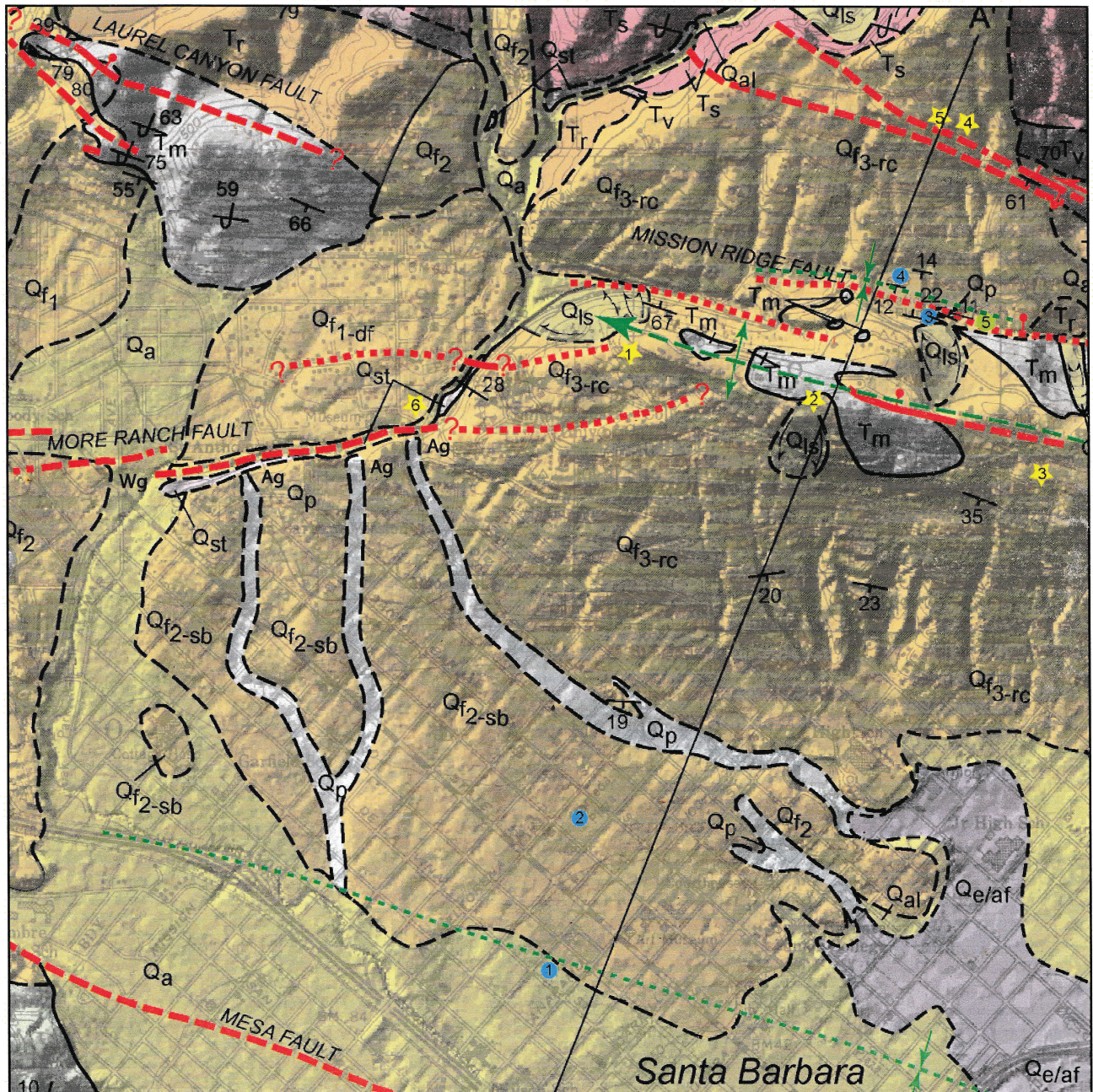


2004 FRIENDS OF THE PLEISTOCENE FIELD TRIP GUIDEBOOK
 SANTA BARBARA FOLD BELT AND BEYOND
 APRIL 15-18, 2004

LEADERS: L. D. Gurrola and E. A. Keller

CONTRIBUTORS: R. West, T. Garcia, A. Duvall, T. Tierney, L. Harrison,
 P. Adams, C. Berlinger, R. Urban, L. Owen, D. Burbank, T. Dunne,
 R. Norris, O. Chadwick, A. Sylvester, T. Dibblee, M. Gabet,
 A. Selting, C. Glavich, D. Revell, D. Valentine, and C. Busby



Cover Page: Geomorphic map showing a part of the downtown Santa Barbara area from Gurrola (2004), Digital Elevation Model and Geology Map of the eastern Santa Barbara Fold Belt, Santa Barbara, California, Ph.D. map, unpub. data., plate 2 of 5.

See website at: <http://www.geol.ucsb.edu/projects/fop2004> for map legend and explanation of units.

Preface

Welcome to the 2004 Friends of the Pleistocene Field Trip, Santa Barbara Fold Belt and Beyond! I am happy that you are here to join us in our celebration of our research and are anticipating an exciting and debate-filled field trip. There are a number of field stops that present different aspects of tectonic and fluvial geomorphology that ensures something of interest for everyone. I hope that you will find value in our research and that you will leave with fresh ideas regarding the geomorphology of the Santa Barbara coastal plain. Enjoy our weather and our geology!

Cheers,

Larry Gurrola

**2004 FRIENDS OF THE PLEISTOCENE FIELD TRIP
SANTA BARBARA FOLD BELT AND BEYOND
ITINERARY AND DRIVING DIRECTIONS**

DAY 1: OPTIONAL DAY

DIRECTIONS: Meet at 12:00pm at the west end of Goleta Beach County Park. Parking is free.

FROM THE NORTH: Exit Southbound CA Hwy 101 at Fairview Road in Goleta. Turn Right and head south toward the sea. After about one mile the road will make a jog to the west near the Santa Barbara Airport before continuing south. After passing the Airport the road will curve left under an overpass. Turn Right into the entrance to Goleta Beach County Park immediately past the overpass. Turn Right at the Stop Sign at the end of the entrance way. Proceed west as far as possible and park. Continue walking to the west end of the lot, nearest to the UCSB campus.

FROM THE SOUTH: Several miles beyond Santa Barbara Exit Northbound CA Hwy 101 onto CA Hwy 217 / Ward Memorial Blvd. toward UCSB/Santa Barbara Airport. Keep to the right and exit at Sandspit Road (toward Santa Barbara Airport). Turn Left at the Stop Sign. Proceed under Hwy 217 and Turn Right into the Goleta Beach County Park entrance. Turn Right at Stop Sign at the end of the entrance. Proceed west as far as possible and park. Continue walking to the west end of the lot, nearest to the UCSB campus.

ITINERARY: The Beach Walk will begin at Goleta Beach and end in Isla Vista at Camino Pescadero, a one-way distance of approximately two miles.

DAY 2: EL CAPITAN CANYON

8:00 a.m. – 10:30 a.m.

DIRECTIONS: Meet at 8:00 a.m. at El Capitan Canyon Resort at 11560 Calle Real, Goleta California. Please park on the side of the road.

FROM THE NORTH: Exit Southbound CA Hwy 101 at exit number 117 – El Capitan State Beach. Turn left on El Capitan State Beach Rd and turn left onto Calle Real. Continue to drive to El Capitan Canyon Resort at 11560 Calle Real and park on the side of the road.

FROM THE SOUTH AND LAKE CACHUMA: Exit the Lake Cachuma campground and turn left (east) onto HWY 154. Drive for approximately 20 miles and turn right onto Calle Real at the first stop light in Santa Barbara, California. Drive for 0.5 miles and merge onto US-101 N via the ramp at the stop sign. Drive for 14.5 miles to exit number 117 – El Capitan State Beach. Take the exit toward El Capitan State Beach and continue driving straight to El Capitan Canyon Resort at 11560 Calle Real and park on the side of the road.

ITINERARY: The Beach Walk will begin at the road in front of El Capitan Canyon Resort.

LUNCH STOP LOCATION WILL BE ANNOUNCED

DAY 2: EAST BEACH TO LOON POINT ONE-WAY BEACH HIKE

12:00 p.m. – 5:00 p.m.

Meet at 12:00 p.m. near the volleyball courts at East Beach. We will be parking our vehicles near East Beach and walking to Loon Point, a 5-mile one-way hike. We have three vans to transport the carpool drivers back to their cars so they can drive back to Loon Point to pick-up their passengers.

Parking may be a little difficult to find but there should be ample room with public parking lots that charge a few dollars for the afternoon. There is also street parking but is more difficult to find depending on the time and weather. The main entrance to East Beach is located at 1400 East Cabrillo Blvd between Chase Palm Park and Andree Clark Beach Refuge. We will meet east of the main entrance near the volleyball courts. Look for a large group of 120 people.

We are allowing extra time for this stop so everyone can find parking. There is parking available along East Cabrillo Blvd, at Andree Clark Bird Refuge on Los Patos Way, and near the intersection of Milpas St. and East Cabrillo Blvd by the softball fields. The bird refuge parking lot is located at the east end of East Cabrillo Blvd. If you want to park at the Bird Refuge, continue to drive on East Cabrillo Blvd and turn left onto Los Patos Way before you drive under the railroad bridge.

DIRECTIONS: Drive east on Calle Real toward El Capitan State Beach Rd. Turn right onto El Capitan State Beach Rd. Merge onto US-101 S and drive for approximately 21 miles to the Milpas exit. Exit the highway on Milpas St. and turn right onto Milpas St. at the stoplight. Drive for 0.3 miles and begin to look for parking as you approach the softball fields. Turn left onto East Cabrillo and drive about 0.2 miles. East beach is located on the right-hand side and the Andree Clark Bird Refuge Lagoon is located on the left-hand side. For those interested in fresh fruits and vegetables, there is a produce store located on the corner of Milpas St. and Calle Puerto Vallarta.

DAY 3: Santa Barbara Point (Formerly Known as Dibblee Point)

8:00 a.m. – 12:00 p.m.

DIRECTIONS: Exit the Lake Cachuma campground and turn left (east) onto HWY 154. Drive for approximately 20 miles and turn left onto US-101 S via the ramp. Drive for approximately 4.0 miles and exit on Castillo St. Turn right onto Castillo St. and drive for 0.3 miles. Turn right onto Shoreline Dr. and drive for 0.9 miles. We will be meeting at the east end of Shoreline Park near the intersection of Shoreline Dr. and La Marina. There are two small parking lots located off Shoreline Drive, west of La Marina. Also, there is public parking available for a small charge at the intersection of Loma Alta and Shoreline Drive across the street from the Santa Barbara City College stadium. Also, there is parking in the residential area across the street from Shoreline Park.

DAY 3: Santa Barbara Old Mission and Rose Garden; Hike to Rocky Nook Park

1:00 p.m. – 3:00 p.m.

We will take a very short hike from the Rose Garden to Rocky Nook Park so you may choose to park in either the residential area of the Rose Garden or at Rocky Nook Park. The Old Mission has parking available but that lot can be quite busy with tour buses and tourists. We will begin our presentations in the Rose Garden Park.

DIRECTIONS: Drive east on Shoreline Dr. back to Castillo St. Turn-left onto Castillo St. for 0.4 miles and drive under the freeway. Merge into the left-hand lane and turn left onto the 101-N ramp. Drive for 1.3 miles and take the Mission St. exit. Turn right onto West Mission St. and drive for 0.8 miles. Turn left onto Laguna St. and begin looking for parking. You may park near the Rose Garden or the Santa Barbara Mission which is located at 2201 Laguna St. We will meet at the water fountain in the Rose Garden which is across the street from the Old Mission. You may also park at Rocky Nook Park which is located north of the Santa Barbara Mission at 610 Mission Canyon Rd. Turn right onto East Los Olivos St. from Laguna St., stay on East Los Olivos St heading north and bear left at the fork in the road. The entrance to Rocky Nook Park is located on the right-hand side of the road immediately after crossing the Mission Creek bridge and where East Olivos St. becomes Mission Canyon Rd.

DAY 3: Skofield Park

3:15 p.m. – 5:00 p.m.

DIRECTIONS: From Laguna St, turn right onto Los Olivos Drive and drive over the Mission Creek Bridge. Continue driving on Los Olivos Drive which becomes Mission Canyon Rd. The road intersects Foothill Rd. at a 3-way stop sign. Turn right onto Footill Rd. and drive for 0.2 miles. Turn left at the stop sign (back) onto Mission Canyon Rd. Continue to drive on Mission Canyon and bear to the right at the fork in the road. Look for Las Canoas St after the crossing bridge and turn right on Las Canoas Rd. Drive for 1.2 miles to Skofield Park which is located at 1819 Las Canoas Rd.

DAY 4: Sedgewick Ranch

8:30 a.m. – 3:00 p.m.

DIRECTIONS: Turn right onto (west) onto HWY 154 from the Lake Cachuma campground. Drive for approximately 6.2 miles and turn right onto Edison St. Continue to drive for 1.1 miles and turn left onto Brinkerhoff Ave. Park at 3566 Brinkerhoff Ave.

**2004 FRIENDS OF THE PLEISTOCENE FIELD TRIP
SANTA BARBARA FOLD BELT AND BEYOND
SPEAKER ITINERARY
APRIL 15-18, 2004**

DAY 1: GOLETA BEACH TO GOLETA POINT AND BEYOND BEACH HIKE

12:00 p.m. – 5 p.m.

SPEAKERS: Robert West, David Valentine, Ed Keller, Bob Norris, Dave Revell, Pete Adams, Christina Belanger, Carrie Glavich, and Arthur Sylvester

TOPIC: Coseismic uplift and formation of marine platforms vs. wave-excavation processes, littoral transport, and beach stabilization.

DAY 2: EL CAPITAN CANYON

8:00 a.m. – 10:30 a.m.

SPEAKERS: Alison Duvall and Doug Burbank

Topic: A. Duvall and D. Burbank will present their research on bedrock stream-incision processes and rates of the Santa Ynez Range.

DAY 2: EAST BEACH TO LOON POINT ONE-WAY BEACH HIKE

12:00 p.m. – 5:00 p.m.

SPEAKERS: Larry Gurrola, Ed Keller, Lewis Owen, and Cathy Busby

TOPIC: Presentations by L. Gurrola, E. Keller, and L. Owen on the active folding and terrace chronology of the Santa Barbara Cemetery-Zoo and Loon Point anticlines. C. Busby will discuss the debris flow characteristics of the Casitas Formation.

DAY 3: Santa Barbara Point (Formerly Known as Dibblee Point)

8:00 a.m. – 12:00 p.m.

SPEAKERS: Ed Keller, Tom Dibblee, Larry Gurrola, Lewis Owen, and Tim Tierney

TOPIC: E. Keller and T. Dibblee will discuss pre-Quaternary and Quaternary tectonic history. Also, T. Tierney will discuss the segmentation of the Santa Ynez Range. L. Gurrola will present research on geology, terrace chronology of the Mesa anticline, and active folding of the Mission Ridge fault system. L. Owen will discuss optical stimulated luminescence analysis of marine terrace deposits.

DAY 3: Santa Barbara Old Mission and Rose Garden

1:00 p.m. – 2:00 p.m.

SPEAKERS: Larry Gurrola and Ed Keller

TOPIC: Active folding and tectonic geomorphology of the Mission Ridge anticline, lateral migration of Mission Creek, and lateral propagation of the Mission Ridge fold

DAY 3: Rocky Nook Park

2:00 p.m. – 3:00 p.m.

SPEAKERS: Robert Urban, Ed Keller, and Larry Gurrola

TOPIC: R. Urban will present research on the Rocky Nook debris flow (Mission diamicton) geomorphology and debris flow hazards. L. Gurrola will discuss Ne21 cosmogenic age-dating of the Rattlesnake alluvial fan; present an exposure of the south-limb of the Mission Ridge anticline and an exposure of a previously unmapped fault.

DAY 3: Skofield Park

3:15 p.m. – 5:00 p.m.

SPEAKERS: Robert Urban, Lee Harrison, and Ed Keller

TOPIC: R. Urban and E. Keller will discuss research of the headscarp region which is the source area of the Rocky Nook debris flow. L. Harrison will present his research on pool formation in Rattlesnake Creek.

DAY 4: Sedgewick Ranch

8:30 a.m. – 3:00 p.m.

SPEAKERS: Tony Garcia, Tom Dunne, and Oliver Chadwick

TOPIC: Presentations on slope erosion and other processes.

DAY 1: GOLETA BEACH TO GOLETA POINT AND BEYOND BEACH HIKE

12:00 p.m. – 5 p.m.

What's the Point?

Robert Brown West, Earth Sciences Department, East Los Angeles College
David Wade Valentine, Map and Imagery Laboratory, UC Santa Barbara

Abstract

Shore platforms are erosion surfaces in bedrock found at the base of sea cliffs. There are two types recognized on rocky coasts throughout the world. The Type-A platform is a sloping abrasion surface found within and below the intertidal zone, whereas the Type-B platform is nearly horizontal and commonly found near the top of the intertidal zone. Type-A surfaces are by far the more common species, while Type-B surfaces, though not as extensive in area, are more commonly found at headlands. Both of these surface forms can be found on UCSB campus beaches. Goleta Point has the most prominent Type-B platform along the local coast (Figure 1).

Two hypotheses for the origin of the Type-B platform at Goleta Point stand in direct conflict each other. One hypothesis calls for rapid emergence of an abrasion surface by coseismic uplift. The alternate hypothesis calls for sea-cliff retreat above the intertidal zone, and invokes storm waves as the primary agent of erosion. In either case, the origin of a shore platform is critically linked to sea cliff retreat, the mode of which is reflected in the form of the sea cliff. Where abrasion dominates we expect to see an abrasion notch at the base of a steep sea cliff. The typical campus sea-cliff profile in bedrock, however, is characterized by a seaward sloping ramp at the base of a steep sea cliff. This form indicates that abrasion is not the primary mode of sea-cliff retreat.

A hypothesis of wave quarrying (excavation) as the dominant mode of sea-cliff retreat is compatible with the typical form of local sea cliffs, which includes such oddities as Type-B platforms. The observational basis in support of the hypothesis is the correlation between the top of the ramp, the top of Type-B platforms, the wetting line, and the line of weathering contrast. Wave quarrying occurs when waves break against the sea cliff; typically during high-tide, storm surges when wave energy is highest and sand is stripped from the beach. The most easily quarried material is in the subaerial weathering level above the ramp. Local Type-B platforms, in general, are the product of wave-quarry, not rapid uplift.

Introduction

What is Goleta (Campus) Point? Is it an uplifted wave-abrasion platform? At what level was it originally cut? How was it cut? These are hotly debated questions amongst a growing number of geoscientists in the Santa Barbara area who are interested in coastal erosion and uplift. Although debate on the origin of shore platforms may have begun over 150 years ago with the published speculations of J.D. Dana, a world-wide consensus has yet to emerge and the debate rages on (Stephenson, 2000). With regards to local seismic hazard, however, significant implications hang in the balance of this debate. Two camps have formed here with opposing views and little agreement.

We, the authors, characterize our camp as the “*eroders*” and the opposition as the “*lifters*”. The argument between our camps centers squarely on the nature of a line. Near the base of the sea cliff this line is ubiquitous. Above this line is found the rough, light rock of the subaerial weathering environment; below is found the smooth, dark rock of the submarine domain (Figure 2). Both camps recognize the correlation in elevation of this line with the upper surface of the Goleta Point platform. While we contend the platform originated *in situ* by exigent processes without significant uplift, the *lifters* contend that it has been displaced by rapid coseismic uplift. If uplift is responsible for platform origin, then its timing, extent, and magnitude could be used to estimate an associated seismic hazard.

GOLETA POINT



Figure 1. Looking south across the Goleta Point shore platform at low tide. The Goleta Point Fault can be traced from the runner in the foreground toward the right side of the distal rocks of the point.

SEA CLIFF SALIENT NEAR CAMPUS STAIRS



Figure 2. Contrast in color and texture of the sea cliff is pronounced at the wetting line. Mojo Hound (25 inches at withers) stands atop a shoreline bench that is coincident with the the wetting line.

In opposition to an uplift interpretation of the Goleta Point platform, we *eroders* have built a body of distinctions that facilitate recognition of the correlation between process and form for various modes of sea-cliff retreat. In the process of describing these forms and their controls we will address the following two questions, which will address concerns of the opposition. 1) Did uplift just happen to align the upper surface of the Goleta Point platform with the boundary dividing light and dark domains? 2) Is the domain boundary a horizon present within the rocks of the sea cliff and gradually exposed with sea cliff retreat?

Shore Platform Origins

In the face of a plethora of terms describing various types of shore platforms, many of which connote genesis in addition to form, Sunamura (1992) recognized two distinct classes he referred to as Type-A and Type-B. Type-A shore platforms are characterized by relative smoothness, broad extent, and concave-upward, seaward slope. They are ordinarily found within and below the intertidal zone and include what is normally referred to as a wave-cut, or abrasion platform. Type-B shore platforms are characterized by relative roughness, limited extent, and horizontal attitude. They are ordinarily found within and above the intertidal zone and include what is often referred to as a shoreline bench. What is missing from Sunamura's definitions is what is ordinarily referred to as the shoreline angle.

In his classic article, *Role of analysis in scientific investigation*, Douglas Johnson (1933) framed the debate between two simple and contrasting hypotheses for the origin of Type-B platforms (referred to as *marine benches*). The first hypothesis calls for rapid emergence of an abrasion surface, by tectonic uplift and, or eustatic sea-level fall. The second hypothesis calls for sea-cliff retreat above the intertidal zone, and invokes storm waves as the primary agent of erosion. Following in Johnson's footsteps we subject these hypotheses to the rigorous scrutiny of scientific analysis with the greatest impartiality prior to acceptance or rejection.

In the case of an emerging platform, if tectonic uplift elevates an abrasion surface into the variable weathering regime near the top of the intertidal zone, then its fine details and smooth surface are likely to be obliterated. In such a case, direct evidence of the abrasion origin of the platform may not be preserved. An alternate approach to assessing this hypothesis is to scrutinize the accepted paradigm for Type-A (abrasion) platform origin.

The seaward sloping surface of a Type-A platform is characterized by relative smoothness as the result of the process of wave abrasion. Abrasion is defined as: rubbing, scouring, or scraping whereby particles of rock are eroded away by friction. Furthermore, the moving agency (in this case water) must be "armed" with rock particles or fragments. On UCSB campus beaches the abrasion surface is formed on the highly fractured, soft shale of the Sisquoc Formation. The slope of the surface is controlled by two factors: 1) the rate of downwearing ($\partial z/\partial t$); and 2) the rate of backwearing ($\partial x/\partial t$). In its simplest form the slope angle (α) of the surface is defined by the relationship: $\tan \alpha = (\partial z/\partial t)/(\partial x/\partial t)$ (West, 1995).

The rate of downwearing is simply the rate of abrasion, which may vary in position and time as a function of: water depth, beach cover, wave climate, and substrate resistance. Water depth appears to be the principal limit to downwearing such that significant submarine abrasion is largely confined to the surf zone (Bradley, 1958). This limit should be reflected in a concave upward profile of the nearshore abrasion surface, in response to a decreasing rate of downwearing with distance from the shoreline. A rapidly emerging nearshore abrasion platform should initially be recognized by its smooth surface and concave upward, seaward slope. The Goleta Point platform, however, has a distinctly horizontal attitude which is more compatible with the form of Type-B platforms than the expected form of an uplifted Type-A platform.

By distinguishing Type-B platforms on a descriptive basis Sunamura (1992) did not end the debate over their origin, but allowed for agreement on gross form. The debate on their origin is then focused on relative position, material, structure, and process. These aspects of the debate have been argued since the early half of the last century (see for instance: Johnson, 1919; Bartrum, 1926; Wentworth, 1938; Edwards, 1941) with progress made in description but little agreement on mechanisms. It is our contention that variability among the many factors influencing coastal erosion provides no anchor for universal comparison, and therefore a review of past and current literature on the subject is not particularly illuminating with reference to our local coast. Instead, we recognize that shore platforms of any type are intimately associated with sea cliff retreat and we focus our attention on modes of sea cliff retreat.

Neither Type-A nor Type-B platforms may come into existence without backwearing, or sea-cliff retreat. The rate of backwearing, however, is a complex issue that includes consideration of both submarine and subaerial processes. To better understand backwearing, or sea-cliff retreat, our analysis of this problem turns to the form of the sea cliff. Where abrasion controls retreat we may expect to see an abrasion notch at the base of a steep sea cliff. The typical campus sea-cliff profile in bedrock, however, is characterized by a seaward sloping ramp at the base of a steep sea cliff. This form indicates that abrasion is not the principal mode of sea-cliff retreat.

Sea Cliff Profiles

Where the bedrock base of campus sea cliffs is exposed its profile occurs in three basic forms of transition from the steep cliff to the seaward sloping abrasion surface, which is only exposed at low tide. The three forms are not mutually exclusive, but are characterized by the strength of development of a single feature in each type. The three features are the notch, the ramp, and the bench, any of which may be present in a given profile. Their distinct forms and relative positions, however, prevent confusion between these elements. By far the most common of these forms is the ramp, which may occur alone, is often crowned with a bench, but is infrequently undercut by a notch (Figure 3).

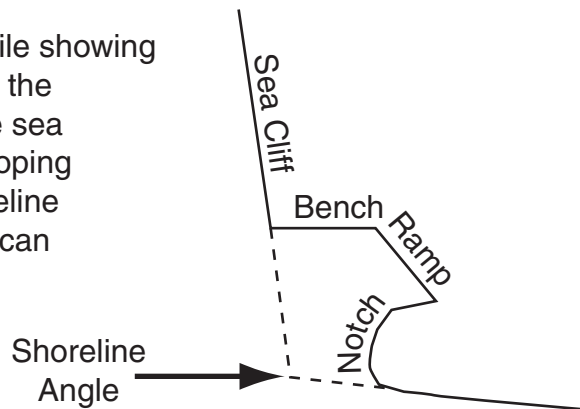
The use of time distinctions, such as “often” in this discussion is purposeful, because these forms appear to be ephemerally contingent upon differential rates of erosion. Wherever the ramp is present it marks a transition between the subaerial and submarine weathering domains. Ramps are particularly well-developed on strata that are abrasion resistant as indicated by a rarity of coincidence with an abrasion notch. If the two occur together, then as the abrasion notch enlarges it does so at the expense of the ramp. The lower part of the ramp is typically dark and smooth like the abrasion surface at its base. The ramp surface increases in lightness and roughness with elevation above its base. A salt encrusted line commonly marks its join with the steep wall of the sea cliff.

Benches are commonly associated with both ramps and abrasion resistant rock. Benches form as the sea cliff above the ramp retreats faster than the ramp. The elevation of a newly carved bench is initially correlative with the wetting line found on the face of the sea cliff. Rapid retreat of the sea cliff during a single storm event reveals the superficial nature of the wetting line. A “stranded” wetting line can be seen immediately west of the sea arch at Fish Rock (Figure 4) where the bench was widened nearly a meter overnight by storm-wave attack in the winter of 1995. The wetting line is distinctly absent from the newly exposed sea cliff despite the bench having extended slightly below the wetted remnant of the former cliff face. The wetting line is apparently imposed superficially and does not represent the intersection of a saturated horizon with the sea cliff.

Clearly the ephemeral nature of the wetting line precludes interpretation as a relict uplift feature. With local sea cliff erosion rates as high as 15cm/yr, narrow benches can also be considered ephemeral features. What then is the significance of the correlation with the elevation of the wetting line and the level of bench formation? The answer lies in the nature of the line.

SEA CLIFF PROFILE FORMS

Figure 3. An idealized sea cliff profile showing all of the forms commonly found at the base of local sea cliffs. Where the sea cliff does not meet the sea ward sloping abrasion platform at a simple shoreline angle, one or more of these forms can be found.



SHORELINE BENCH WEST OF FISH ROCK



Figure 4. Looking west from Fish Rock at a shoreline bench widened during a winter storm in 1995. The prominent siliceous bed in the center of the photograph defined the former sea cliff face prior to the storm. This same bed can be seen in the lower left corner of the photo where it marks the transition from the older, wetted, and abraded bench to the left and the newly exposed bench to the right.

The Light and the Dark

The two domains divided by a line in the sea cliff are largely defined by contrasts in both tone and texture, but have a surprisingly large number of additional contrasts. Where the sea cliff is armored with sandstone rip-rap, however, the wetting line is not as distinct, but the domain of subaerial weathering is recognized by the presence of tafoni in the sandstone blocks.

Subaerial weathering dominates the light and rough domain above the line, where angular blocks of the highly fractured shale are loosened by various wedging processes. When slabs of fractured shale are calved from the cliff face, their collapse forms an ephemeral colluvial slope of angular rubble atop the beach at the cliff's foot. Typically, the newly exposed face reveals a network of roots and thick encrustations of salt. Individually the angular blocks vary in size depending on the shale's original fracture density, but all show evidence of weathering by accumulation of iron oxides, clays, and salts on their fracture faces. The weather weakened rock in the subaerial domain is ripe for mass wasting and wave quarrying.

In contrast, the dark and smooth domain, which is occasionally hidden by a beach, is dominated by abrasion. The fractured shale is almost uniformly beveled and localized relief is largely determined by contrasts in abrasion resistance. When a beach is present, its berm is frequently built up to the elevation of the domain boundary. Where a sea-cliff salient juts boldly seaward into this domain it is typically anchored by a well-defined ramp formed on a layer that is distinct in both domains and whose abrasion resistance exceeds that of adjacent layers. The wetting line rises higher on a salient, which allows algae to maintain a presence on the upper part of the ramp despite the continued threat of abrasion.

Fractures and faults are exploited in contrasting modes in each domain. Blocks pull away from fractures and faults, which exposes more of their surfaces in the light domain; while in the dark domain certain fractures and most faults are preferentially abraded and channeled, which eliminates their surface. Where faults juxtapose rock of greatly contrasting character (such as fracture density, or cement content), differential erosion is markedly enhanced in the domain of abrasion, whereas weathering in the subaerial domain seems to weaken rocks to such an extent that differential erosion is subdued.

Differential erosion is not only distinct between the two domains, but is also distinct across them. This distinction is greatly enhanced by structural control. For instance, where the strike of dipping shale runs parallel to the shoreline, a single abrasion resistant layer may delay retreat of the ramp along a certain length of shoreline such as at Fish Rock (Figure 4). Meanwhile, the same layer, weakened in the subaerial domain, gives way to mass wasting, and wave-quarrying, which allows for differential sea-cliff retreat and the formation of a shoreline bench, or Type-B platform. This mode of differential erosion is distinguished by different processes acting on the same material in two domains of weathering, as opposed to one process acting on two domains of material. Wherever a fault juxtaposes large domains of material with contrasting resistance to abrasion, there is to be found the greatest potential for the style of differential erosion that produces Type-B platforms. Such a place is at Goleta Point.

Goleta Point

Within the emerging Santa Barbara fold and thrust belt can be found a number of northeast trending cross-faults that accommodate steps between various thrust fronts. The Goleta Point fault is such an accommodation structure (Gurrola, 2004, pers. comm.) The fault forms the western boundary of the point's Type-B platform. Differential abrasion has gullied the fault zone below the wetting line, whereas the fault zone above the line for many years defined the west face of a remnant sea stack. Today the sea stack is virtually absent, while only 50 years earlier the sea stack was a robust tower (Figure 5). As the stack has crumbled into the sea its base has been trimmed



Figure 5. Bob Norris below Goleta Point sea stack circa 1950. Note the relatively flat surface of the Type-B platform is the level at which the base of the stack is being trimmed. (Photo by R. M. Norris)



Figure 6. An abrasion notch on the east flank of the Goleta Point rocks is exposed at low tide. Abrasion is concentrated at the base where tools are readily mobilized. The flank above the notch is armored with buckshot barnacles. In deeper water mussels displace the barnacles.

(All photos by R. Brown West except where otherwise noted)

horizontally at the approximate level of the wetting line and benches in the nearby sea cliff. The platform created by erosion of the sea stack is but the newest in a complex of similar features at Goleta Point. The horizontal attitude of the Goleta Point platforms is obvious in relation to the distant horizon of sea-level. All of these relationships suggest the possibility of formation of this entire platform as an extensive bench complex.

Since bench formation is tied to sea cliff retreat, albeit above the wetting line, we may estimate the time needed to produce the Goleta Point platform using an estimated rate of sea cliff retreat for nearby Isla Vista (Norris, 1977). Assuming the platform was progressively exposed from south to north over the 90 meters of its longest axis, it would take only 600 years to retreat the sea cliff at a rate of 15cm/yr. Of course, this scenario could only hold as long as the platform rocks are relatively abrasion resistant while the overlying rocks gradually succumb to a combination of subaerial weathering and infrequent storm-wave attack.

As the adjacent abrasion surface is lowered the platform rocks find themselves in ever deepening water, a condition which may lend itself to preservation of the platform rocks. For instance, waves often reflect off of the distal rocks of the point, or merely wash over their surface, instead of crashing into them. The sides of most of the rocks are covered by a dense armor of mussels as are the tops of the distal rocks. At low tides an abrasion notch is exposed at the base of the nearest rocks (Figure 6) indicating that abrasion is only significant at the level of the adjacent abrasion platform where the abrasive materials are concentrated.

Conclusions

The hypothesis of tectonic uplift of an abrasion surface to explain the origin of the Goleta Point shore platform is inconsistent with evidence provided from the form of the platform itself. Instead of having a seaward slope, similar to the adjacent modern abrasion surfaces, the platform is horizontal in attitude, similar to nearby shoreline benches. A hypothesis of wave quarrying (excavation) as the dominant mode of sea-cliff retreat is compatible with the typical form of local sea cliffs, which includes such oddities as shoreline benches. The observational basis in support of the hypothesis is the correlation in the sea cliff between the top of the ramp, the top of shoreline benches, the wetting line, and the line of weathering contrast. Wave quarrying occurs when waves break against the sea cliff; typically during high-tide, storm surges when wave energy is highest and sand is stripped from the beach. The most easily quarried material is in the subaerial weathering level above the ramp. Shoreline benches and Type-B platforms, in general, are the product of wave-quarry, not rapid uplift.

Two modes of differential erosion are at work at Goleta Point as the consequence of the Goleta Point Fault juxtaposing materials with contrasting resistance to wave abrasion. Lowering by abrasion of the less resistant materials surrounding the Goleta Point rocks has allowed them to become emergent, while retreat by weathering and excavation above the wetting line has allowed for the carving of the bench surface. The abrasion resistant nature of the rocks at Goleta Point has slowed their retreat below the wetting line without reducing abrasion beside or excavation above them. Abrasion resistance appears to be the key to understanding the distribution of ramps and benches at the base of sea cliffs along campus beaches. The Type-B platform at Goleta Point is the product of sea cliff retreat above the wetting line and gradual extension of a broad shoreline bench above relatively abrasion resistant materials.

References

- Bartrum, J. A. 1926. Abnormal shore platforms. *Journal of Geology* 34, 793-806.
- Bradley, W.C., 1958. Submarine abrasion and wave-cut platforms. *Geological Society of America Bulletin* 69, 967-974.
- Edwards, A. B. 1941. Storm-wave platforms. *Journal of Geomorphology* 4, 223-236.
- Gurrola, L. D. 2004, Personal Communication.
- Johnson, D. W. 1919, *Shore processes and shoreline development*. New York, Wiley. 584 pp.
- Johnson, D. 1933. Role of analysis in scientific investigation. *Geological Society of America Bulletin* 44, 461-494.
- Norris, R. M. 1977. Erosion of sea cliffs. In *Geologic hazards in San Diego*, ed. P.L. Abbott and J. K. Victorix. San Diego, CA: San Diego Society of Natural History.
- Stephenson, W. J. 2000. Shore platforms: a neglected coastal feature? *Progress in Physical Geography* 24, 311-327.
- Sunamura, T. 1992. *Geomorphology of rocky coasts*. New York, Wiley. 302 pp.
- Wentworth, C. K. 1939. Marine bench-forming processes II, solution benching. *Journal of Geomorphology* 2, 3-25
- West, R. B., 1995, In situ erosion of Type-B shore platforms of Santa Barbara, California: *Geological Society of America Abstracts with Programs* 27 (6), 343.

Wave Energy Delivery and the Shape of Rocky Coasts: Part 1 – Introduction and Background on Wave Theory

Peter N. Adams
Univ. of California – Santa Cruz

Though responsible for many breathtaking landscapes, the coastal geomorphology of active margins has received much less scientific attention than the depositional landforms and sedimentary processes responsible for decorating passive margins. Some studies have focused on dating marine terraces (Merritts and Bull, 1989; Perg et al., 2001), which form as a result of wave action, tectonic uplift and sea level fluctuation (Anderson et al., 1999), but little work has been done toward understanding the processes responsible for shaping the planform appearance of active margin coasts like that of central California. Some of the factors responsible for sculpting the features we recognize on active margin coasts are depicted on Figure 1 of this section.

When considering geomorphic “damage” inflicted upon a rocky coast, the variable of interest is the delivery power, P_D , of waves. This power is strongly controlled by oceanographic conditions and bathymetry. To better understand the delivery power, one must examine the deep-water wave power, P_0 , and how it is modified through wave transformation.

Deep-Water Wave Height

Deep-water wave height, H_0 , should exert the greatest control on delivery power. The energy density, E_0 , of a deep-water wave is given by

$$E_0 = \frac{1}{8} \rho g H_0^2 \quad (1)$$

where ρ is the density of seawater and g is gravitational acceleration. Deep-water wave power, P_0 , is defined as the energy flux per unit length of wave crest averaged over one wave period (Sunamura, 1992; Komar, 1998),

$$P_0 = E_0 C_0 n = \frac{1}{8} \rho g C_0 n H_0^2 \quad (2)$$

where C_0 is deep-water wave celerity and n describes the shape evolution of a wave as it shoals, a hyperbolic function whose value is 1/2 in deep water and 1 in shallow water. The transformation of waves as they interact with the shelf results in evolution of both their height and celerity. These transformations involve changes in wave geometry both in plan view and in cross section (Fig. 2).

Wave Shoaling

Airy wave theory assumes that in the absence of refraction and bottom friction, wave power is conserved from deep to shallow water. Changes in wave height must therefore result in changes of the opposite sign in celerity (equation 2). This wave-shape evolution can be

expressed as a shoaling coefficient, where H and C are the local wave height and celerity, computed at the breaking wave depth:

$$K_S = \frac{H}{H_0} = \sqrt{\frac{1}{2n} \frac{C_0}{C}} \quad (3)$$

Wave Refraction

As waves approach a coast obliquely, refraction bends the wave crests toward a more coast-parallel orientation. Wave crests can be significantly stretched (Fig. 2), allowing straight-crested offshore waves to distribute their power to a coastline whose shape is irregular and of greater length. Wave-crest stretching decreases wave height, thereby decreasing wave power. This effect is captured in a refraction coefficient, K_R , that further transforms offshore wave height:

$$K_R = \frac{H}{H_0} = \sqrt{\frac{S_0}{S}} = \sqrt{\frac{\cos \alpha_0}{\cos \alpha}} \quad (4)$$

where S_0 and S are the wave-crest lengths between two wave rays in deep and shallow water, respectively, and α_0 and α are angles between wave crests and depth contours in deep water and breaking-wave depth shallow water, respectively (Fig. 2). Incorporating both shoaling and refraction, wave height at the coast can be expressed as.

$$H = H_0 K_S K_R \quad (5)$$

The ratio of the delivery power of waves to their deep-water power simplifies to

$$\frac{P_D}{P_0} = K_R^2 \quad (6)$$

Energy Dissipation

Energy dissipation by bottom interaction is dictated by both the depth at which waves begin to feel bottom and the path length over which dissipation occurs (Anderson et al, 1999). Two oceanographic variables dictate the location at which waves first begin interacting with the sea floor: The wavelength, L (set by wave period, T) and the tide. The water depth, h_f , to which there is significant wave orbital motion is approximately $L/2$. Wave period influences P_D by affecting the wavelength and therefore the water depth at which energy dissipation begins. From Airy wave theory, the wavelength is related to wave period through the dispersion equation (Komar, 1998):

$$L = \frac{g}{2\pi} T^2 \tanh\left(\frac{2\pi h}{L}\right) \quad (7)$$

where h is the water depth. In deep water the hyperbolic tangent function approaches unity, and the water depth at which dissipation begins increases as the square of the wave period: $h_f = (g/4\pi)T^2$. Longer-period waves feel bottom earlier and should lose a larger fraction of their energy to bottom friction.

Waves approaching perpendicular to the bathymetric contours should lose the smallest fraction of their deep-water wave power. In addition, a lower shelf slope increases the ray-path length over which dissipation occurs. Ignoring refraction of the wave, the dissipative path length, R , varies inversely with both the slope of the shelf, θ , and the angle between wave crests and bottom contours, α_0 (Fig. 1), and goes as the square of the wave period:

$$R = \frac{h_f}{\sin(\theta) \cos(\alpha_0)} = \frac{gT^2}{4\pi \sin(\theta) \cos(\alpha_0)} \quad (8)$$

Increases in wave period and deep-water approach angle, and decreases in shelf slope, should lower the fraction of deep-water wave power reaching the coast.

Finally, tide affects water depth and therefore the offshore distance at which waves begin to dissipate energy (Trenhaile, 2000). At high tide, a deep-water wave travels farther unhindered by dissipative interaction with the bottom than at low tide and should result in greater energy imparted to the sea cliff (Fig. 1B). Finally, at low tide, waves break farther offshore, expending most of their energy in the surf zone, severely reducing the energy imparted to the cliffs. We seek quantification of these effects.

Wave Energy Delivery and the Shape of Rocky Coasts: Part 2 – Microseismic Shaking of Sea Cliffs

Peter N. Adams
Univ. of California – Santa Cruz

The morphology of a rocky coast along a tectonically active margin results from the interaction of uplifted resistant coastal bedrock and the destructive energy delivered to the coast by waves. Rocky coasts inspire interesting geomorphic questions about embayment shape, marine-terraces, and the relative roles of climate and lithology in coastline evolution? Lithology of coastal sea cliffs provides one control on rocky-coast evolution and offshore ocean climate provides another. Storm systems generate waves whose power is reduced by energy dissipation during shoaling, the remaining power being expended in the surf zone and at the sea cliffs (Komar, 1998). As a first step toward addressing rocky-coast evolution, we explore the utility of seismically sensed shaking of the sea cliffs as a measure of how offshore wave conditions, shelf bathymetry, and tides dictate the delivery of geomorphically useful energy to a rocky coast.

Deep-water waves begin losing energy through friction when their orbital motions extend to the sea floor (Fig. 1). Long-period waves and those occurring at low tide sense the sea floor further offshore and dissipate a greater fraction of deep-water energy than do short-period waves or those occurring at high tide. The deep-water swell direction and refraction of a wave's ray path dictate the length of wave travel during which energy is dissipated. Wave power is also diminished by stretching of wave crests during refraction. In essence, deep-water wave power, P_0 , is transformed into delivery power, P_D , through a filter that depends on bathymetry and several oceanographic variables. Here we attempt to characterize this filter by using a novel method.

Seismologists have long recognized that microseisms complicate measurements of earthquakes (Longuet-Higgins, 1950; O'Hanlon, 2001). Standing waves on the shelf generate a seismic signal from the constructive interaction of waves reflected from the coast with incoming waves of the same period. Ground motions from the breaking of nearshore surf have also been noted. Distracting as microseisms may be to the seismologists, they are useful to oceanographers as a proxy for wave height, and they provide a record of ground motion in response to wave breaking. Zopf et al. (1976) demonstrated that microseisms could be used to measure wave heights when conventional pressure sensors are unavailable. Tillotson and Komar (1997) compared microseismically measured wave heights to those measured by buoys. Recently, researchers have employed historical seismographic records to hindcast (i.e., statistically predict past) changes in wave climate in the northeast Pacific (Bromirski et al., 1999) and in the North Atlantic (Grevemeyer et al., 2000). To date, however, few studies of coastal geomorphology have employed this valuable data source.

We assembled time series of wave heights and periods to characterize deep-water wave power, and swell directions and tidal elevations to calculate expected energy dissipation. These data were obtained from an NDBC buoy that records deep-water wave statistics and from a NOAA tidal gage. We compared time series of oceanographic variables with cliff shaking observations made with a portable broadband seismometer deployed at the edge of the sea cliff and coupled to the bedrock. We then attempted to define that combination of offshore wave climate and near-coast characteristics that best explains the shaking of the sea cliff.

Microseismic monitoring of wave-energy delivery to sea cliffs provides a rich data set against which to test theories of wave-energy dissipation. Given that seismologists working in coastal regions must commonly filter out the effects of waves, this is truly a case of one scientist's noise being another's signal. With a single stationary instrument, we were party to a natural experiment in which the effects of a wide set of oceanographic variables could be properly explored. Quantitative prediction of cliff shaking requires knowledge of these oceanographic variables and a model that accounts for (1) wave transformation due to shoaling and refraction and (2) dissipation through drag on the seafloor and through nearshore wave-breaking processes. We note that the tide strongly modulates the delivery of energy by controlling the location of wave break relative to the cliff. This experiment places on firmer footing any future modeling of long-term coastal evolution, including the generation of marine terraces and the embayment of coastlines.

Wave Energy Delivery and the Shape of Rocky Coasts: Part 3 – Strain of Sea Cliffs

Peter N. Adams
Univ. of California – Santa Cruz

Steep sea cliffs of tectonically-active coastal landscapes are the product of wave-induced erosion. Rock uplift delivers fresh rock to the nearshore zone to be attacked by waves delivering their geomorphically effective energy. While one can sense qualitatively the energy of impact by waves crashing against a rocky coast, we have yet to fully understand the processes by which waves impart their energy to the shore and how this energy is transformed into erosion.

Traditionally, researchers have concluded that waves perform geomorphic work on rocky coasts by mechanical abrasion and by plucking or quarrying of blocks (Bagnold, 1939; Stephenson and Kirk, 2000; Sunamura, 1992; Trenhaile, 1987). Mechanical abrasion employs sediment grains, entrained by wave orbital motion, as tools to grind away the face of the sea cliff as the water of breaking waves impacts the vertical surface. Quarrying of blocks is thought to occur by hydraulic action when waves striking the sea cliff compress air in cliff face cracks. This exerts an outward stress on the surrounding rock mass which when repeated cause cracks to grow, ultimately detaching blocks (Sanders, 1968). Importantly, in this view the rate-limiting process is the growth of cracks by wave-induced hydraulic blasts. A major focus of rocky coastline geomorphic research is the documentation of the relative efficacy of each of these processes, and the detailed exploration of the physics of each process.

Ocean microseisms, first proposed by Weichert (1904), are ground motions generated by shallow water waves in coastal regions, and are subdivided into primary and secondary types (Bormann, 2002). Primary ocean microseisms involve the conversion of water wave-induced pressure variations to seismic energy, and hence have roughly the same period as the incoming water waves (Haubruch, 1963). Secondary ocean microseisms record pressure variations beneath a standing wave of half the period of the incoming ocean waves. This standing wave exists because the incoming waves are reflected back off the coast, causing superposition of waves traveling in opposite directions (Longuet-Higgins, 1950). This phenomenon was employed by Zopf et al. (1976) to measure ocean waves with a seismometer. The relationship linking microseismic energy and wave climate has been explored in detail by Bromirski and Duennebieer (2002). Recently, several research groups have successfully hindcast ocean wave climates by examining records of long-term microseismic energy collected at coastal seismic stations (Tillotson and Komar, 1997; Bromirski et al., 1999; Bromirski, 2001; Grevemeyer et al., 2000).

To understand how changes in offshore wave climate modulate geomorphic energy delivery to a rocky coast, Adams et al. (2002) used a broadband seismometer to measure ground motions associated with waves impacting a sea cliff. The purpose of this previous study was to document how offshore wave conditions, shelf bathymetry and tides dictate the temporal pattern of energy delivery to the sea cliffs. Their study focused on velocity of ground motion, high pass filtering the data to explore the signal in the frequency band between 1Hz and the Nyquist frequency (50Hz) (Adams et al., 2002). Over the course of that several month-long study, a strong signal in the 0.05–0.1 Hz frequency band (10–20 second period) persisted throughout the time series, but was cautiously ignored, as it was not relevant to the outlined research objectives. In the present study reported here, we revisit this signal explicitly, in a process geomorphology context, asking the questions: (1) How is the long-period (10–20 sec, 0.05–0.1 Hz) ground motion signal related to the incident nearshore wave field? (2) What are the details of the motion exhibited by the seacliff at this frequency? (3) What, if any, strain is the seacliff experiencing at this frequency?

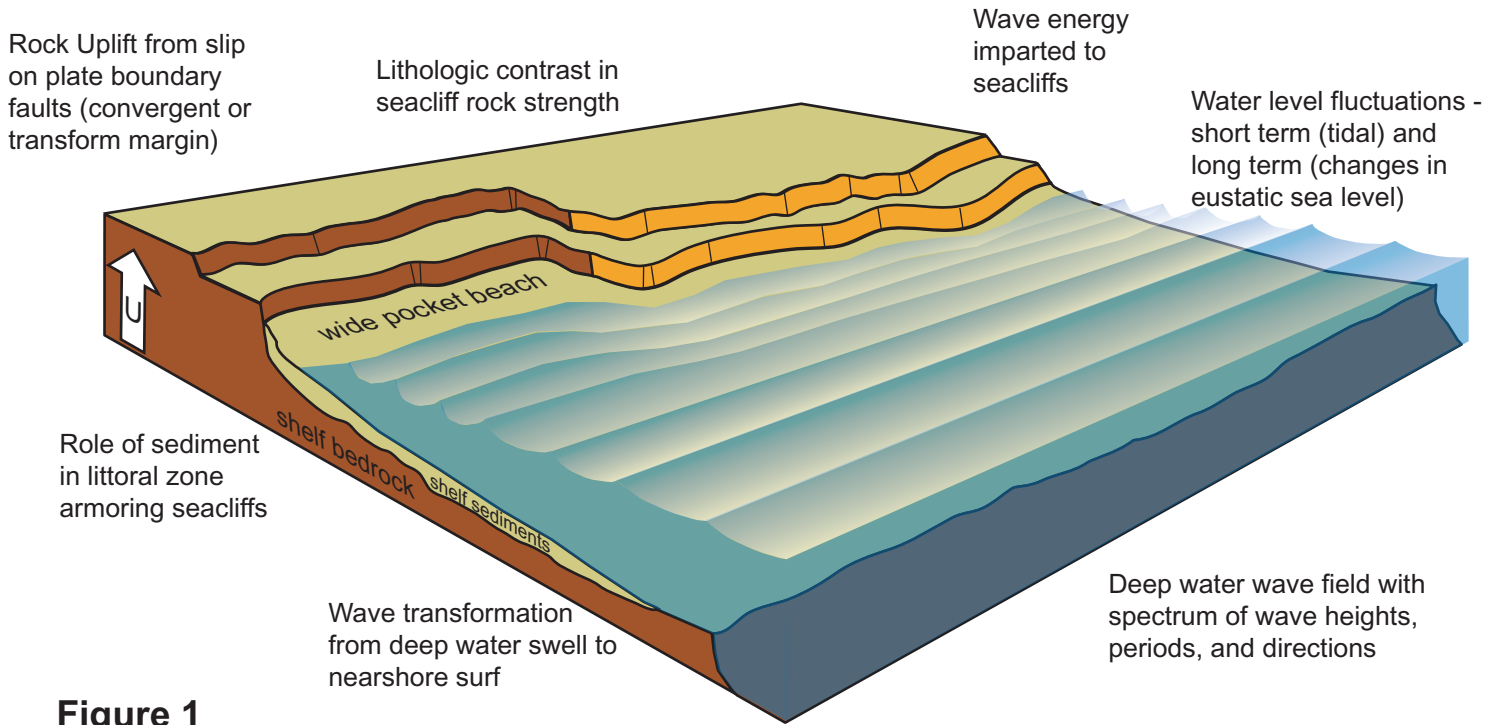


Figure 1

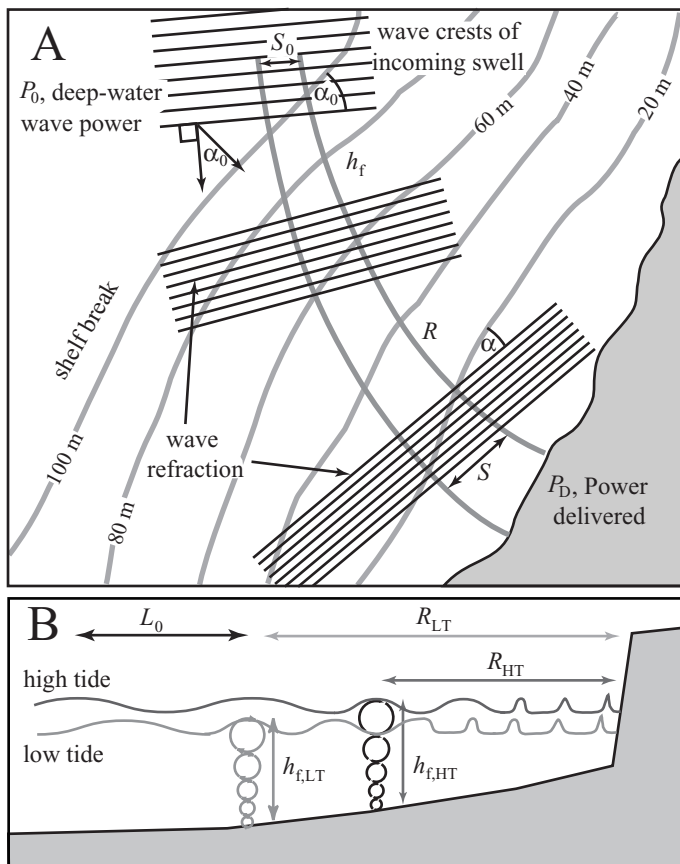


Figure 2

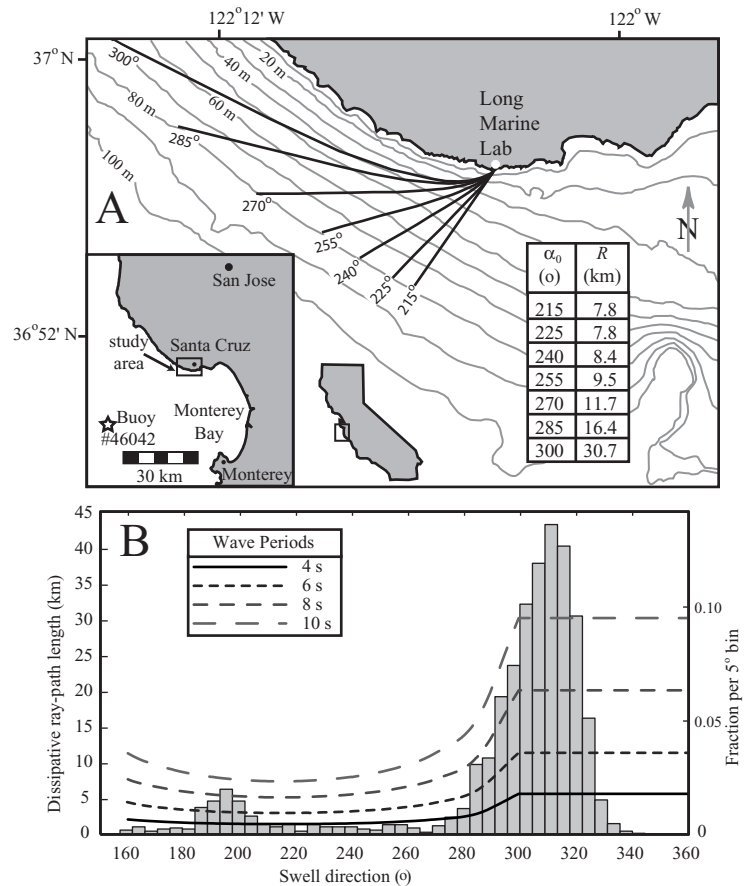


Figure 3

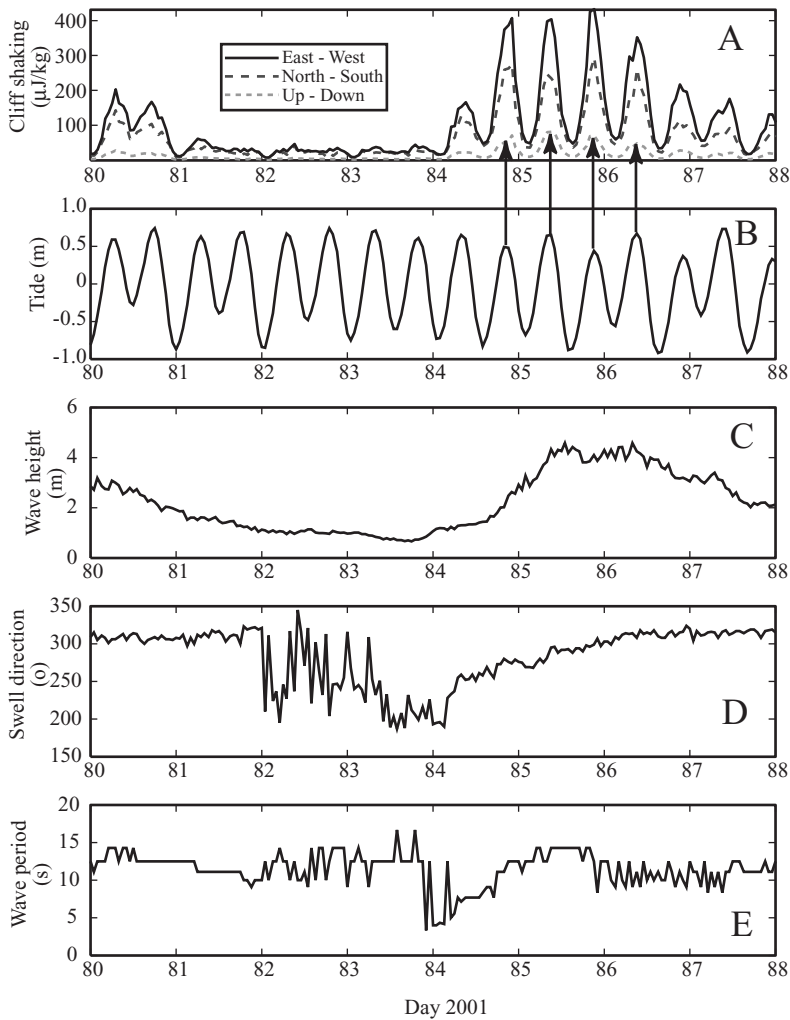
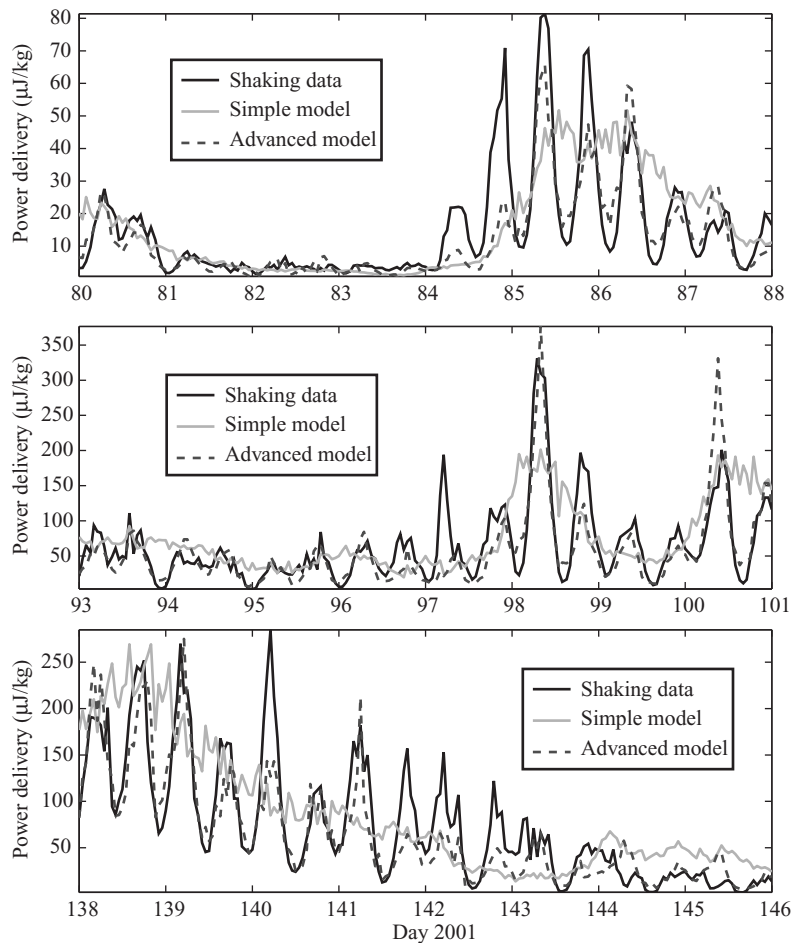


Figure 4. An eight-day record from March 2001. A: Microseismic shaking at cliff edge (three components of ground motion). B: Tidal elevation. C: Offshore significant wave height. D: Swell direction. E: Wave period. Horizontal shaking is considerably stronger than vertical. Note strong correspondence between times of high shaking and times of high tide (shown with arrows) over an interval of large wave heights.

Figure 5. Modeled time series of power delivery for three periods of eight days each, along with microseismic shaking (dark solid line). Note different scales of shaking magnitude for the three plots. Simple model (light gray solid line) employs linear scaling of deep-water wave power, whereas advanced model (dark gray dashed line) incorporates wave shoaling and refraction, tide, dissipation from shelf drag, and temporally-dependent seismic attenuation.



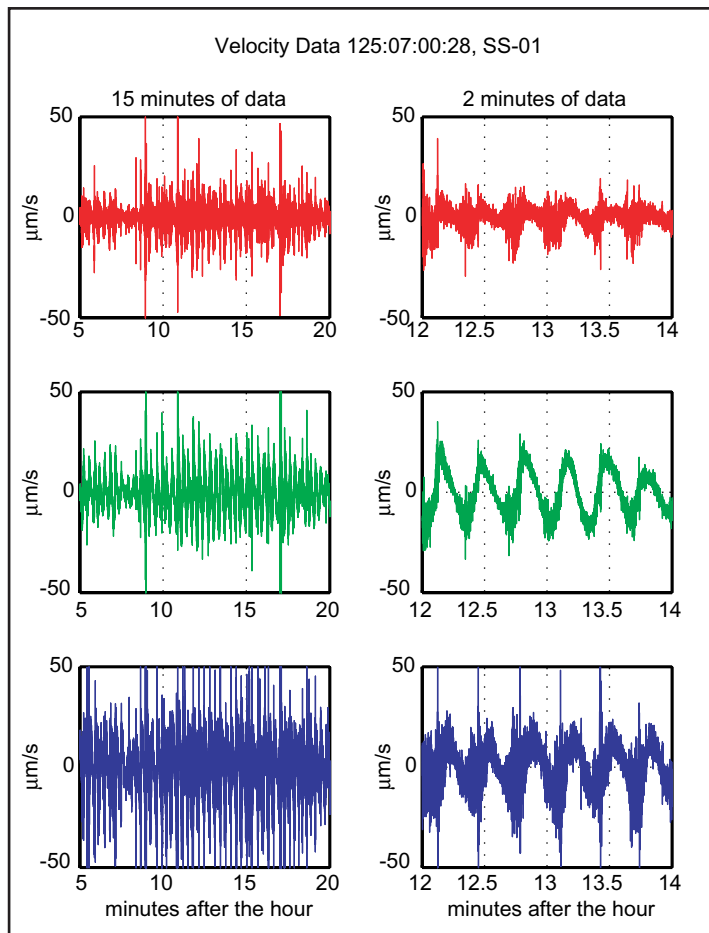


Figure 6.

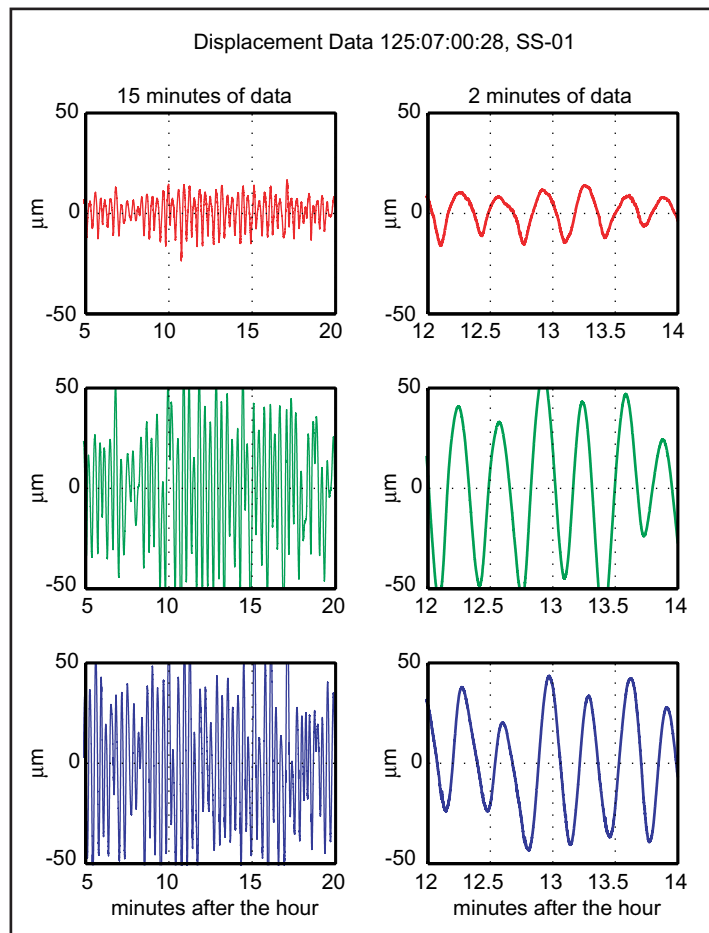


Figure 7.

Figure 8.

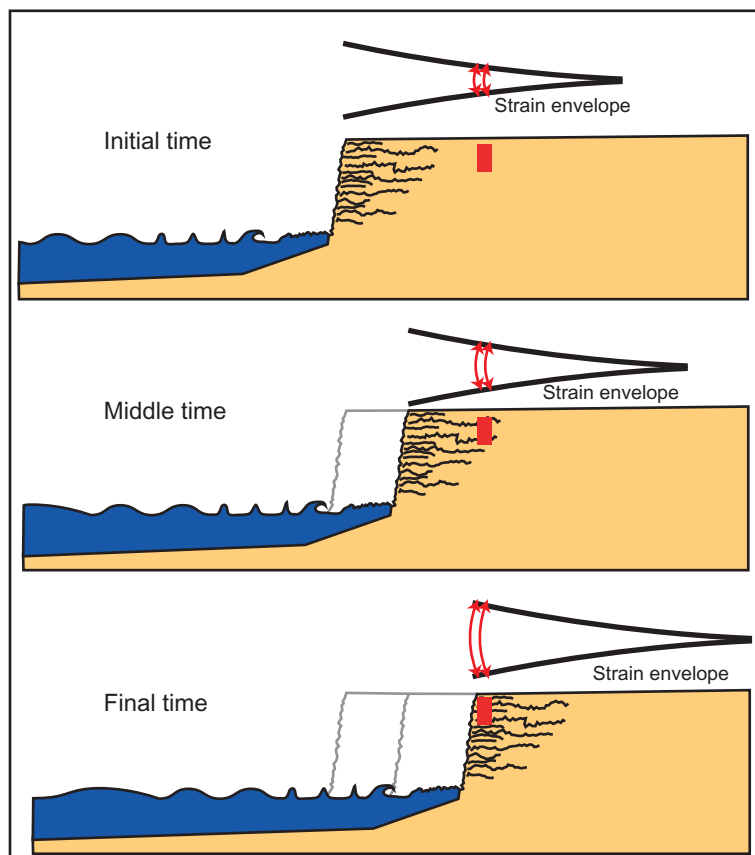
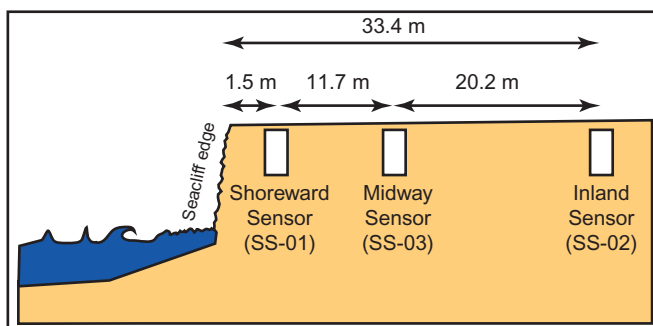


Figure 9.

THE FOLLOWING ARTICLE WAS USED WITH PERMISSION, CALIFORNIA
DEPARTMENT OF CONSERVATION, CALIFORNIA GEOLOGICAL SURVEY

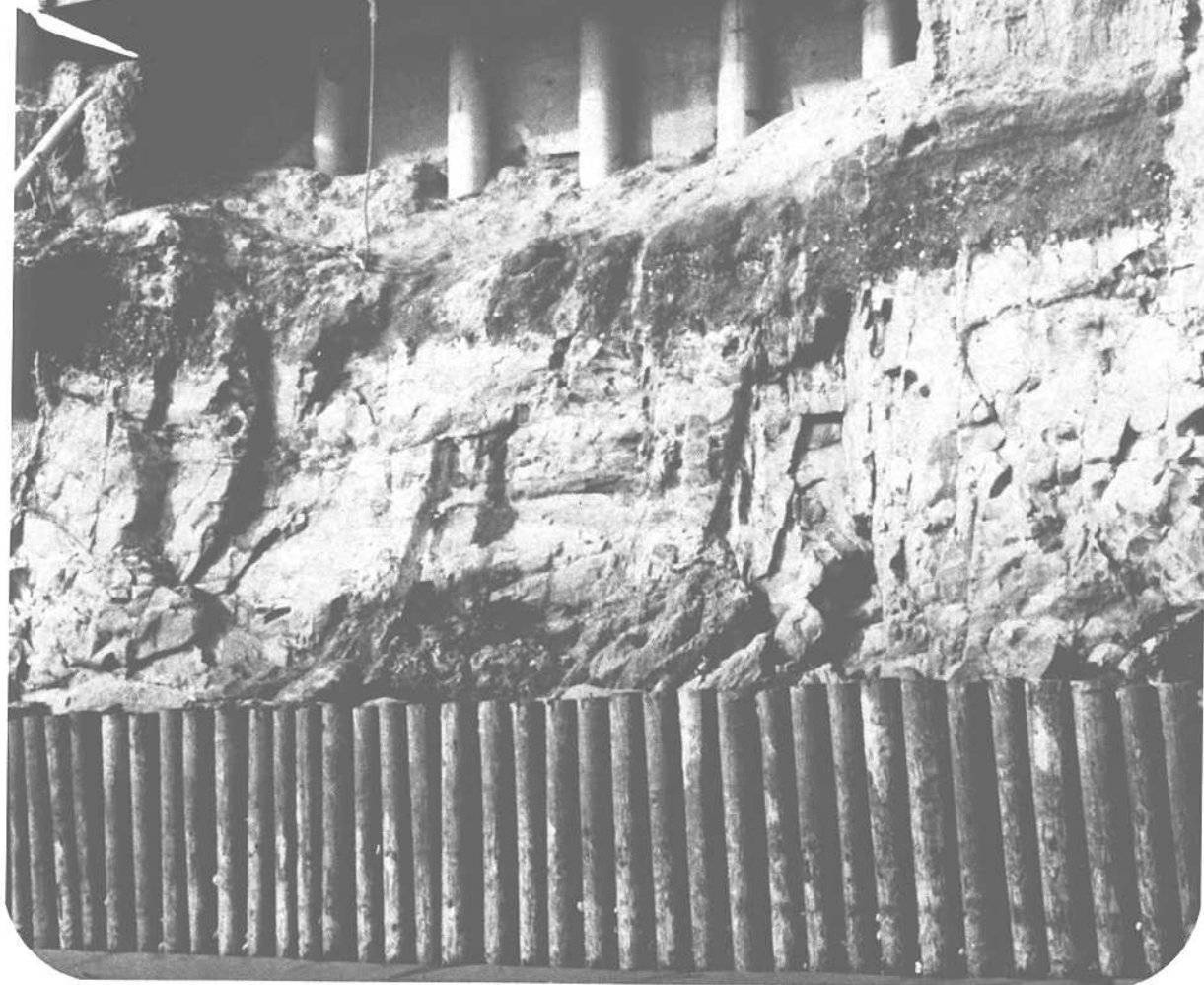
☞ READER SURVEY ENCLOSED

Sea Cliff Erosion

CALIFORNIA GEOLOGY

\$1.00

AUGUST 1990



CALIFORNIA
DEPARTMENT
OF CONSERVATION

Division of Mines and Geology

Understanding California's Geology

Our Resources - Our Hazards

GEORGE DEUKMEJIAN, Governor
STATE OF CALIFORNIA

GORDON K. VAN VLECK, Secretary
THE RESOURCES AGENCY

RANDALL M. WARD, Director
DEPARTMENT OF CONSERVATION

Sea Cliff Erosion: A Major Dilemma

By

ROBERT M. NORRIS,
Professor of Geology, Emeritus
University of California, Santa Barbara

INTRODUCTION

After many years of observation, the author concludes that various engineering structures used as protective measures to reduce or eliminate sea cliff erosion in California are not effective over time. A great deal of time, money, and distress can be avoided if, prior to building structures at or near the top of sea cliffs, an ample zone is allotted for naturally occurring cliff erosion to take place. Because protective devices constructed at the base of sea cliffs provide only temporary protection, and in the long term these partial protective measures always fail, alternatives should be considered.

Geologists have long recognized that all cliffs are inherently unstable, and are only temporary features over geologic time. Cliffs cut in hard crystalline rocks, like El Capitan in Yosemite Valley, are more durable than cliffs cut in soft sedimentary rocks, but both will yield eventually to erosion. On the California coast there are very few durable rock outcrops; most coastal cliffs are cut in relatively weak sedimentary rocks and steep cliffs are eroded by wave action which regularly undercuts the cliffs and removes fallen debris from the cliff base.

In places where the sea has retreated from the cliff base for some years, talus and loose soil and rock (colluvium)* from the cliff face gradually pile up at the base of the cliff and build upward toward the top of the cliff. This process is evident, for example, at San Clemente State Beach, Orange County (Photo 1). Here, the Santa Fe Railroad

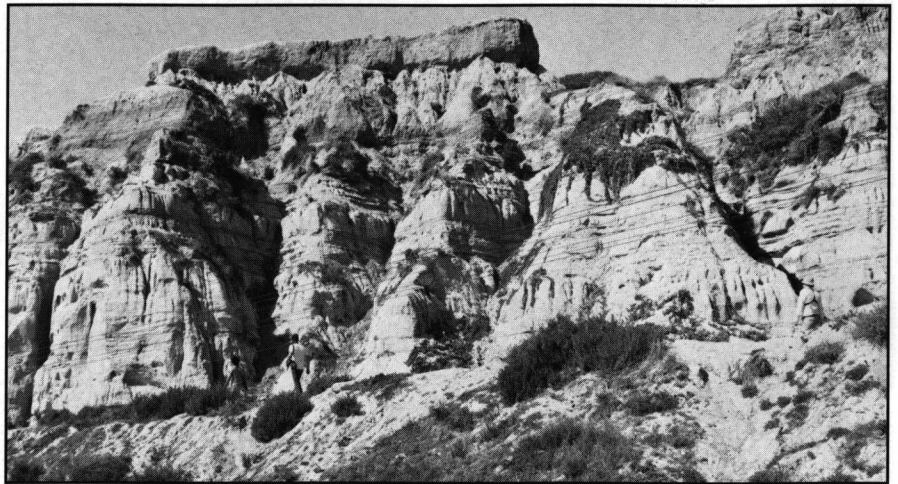


Photo 1. Sea cliff composed of the Capistrano Formation at San Clemente State Beach, Orange County. The Santa Fe Railway at the cliff base protects this cliff from direct marine attack. Nonmarine processes, chiefly rain wash, caused the fluting and badlands topography in this soft rock unit. Note the accumulation of talus at the cliff base. Photos by Robert M. Norris, except as noted.

track constructed along the base of the cliff has protected the cliff for many years from direct wave attack. In the intervening years, the pile of eroded rock and soil accumulating at the cliff base has reached nearly half way up the original cliff at many places. As this erosional process continues, the near-vertical original cliff will be replaced with a gentler slope near the angle of repose* for dry material. Over a period of time, even the top edge of the cliff will wear back or retreat a considerable distance.

SEA CLIFF RETREAT

Marine Erosion

Sea cliff retreat is caused by marine and nonmarine agents, including wave attack, solution, and wind driven salt spray. The main type of marine erosion is direct wave attack at the cliff base. This process frequently quarries

out weak beds at the base of the cliff and eventually undercuts the cliff to the point where the overlying unsupported material collapses onto the beach. Waves also work along joint or fault planes to loosen blocks of rock or soil (Photo 2).

The second type of marine erosion that causes sea cliff retreat is known as solution erosion, a chemical process in which the soluble minerals are dissolved out of rocks. The solution process is effective on limestone cliffs where sea water dissolves the lime in the rocks, resulting in the formation of deep notches. This process is very important on some raised coral islands in the south Pacific Ocean and on the limestone coasts of the Mediterranean and the Adriatic seas. However, only minor amounts of limestone occur along the California coast and solution is not a major cause of sea cliff retreat.

*See Glossary, page 177.

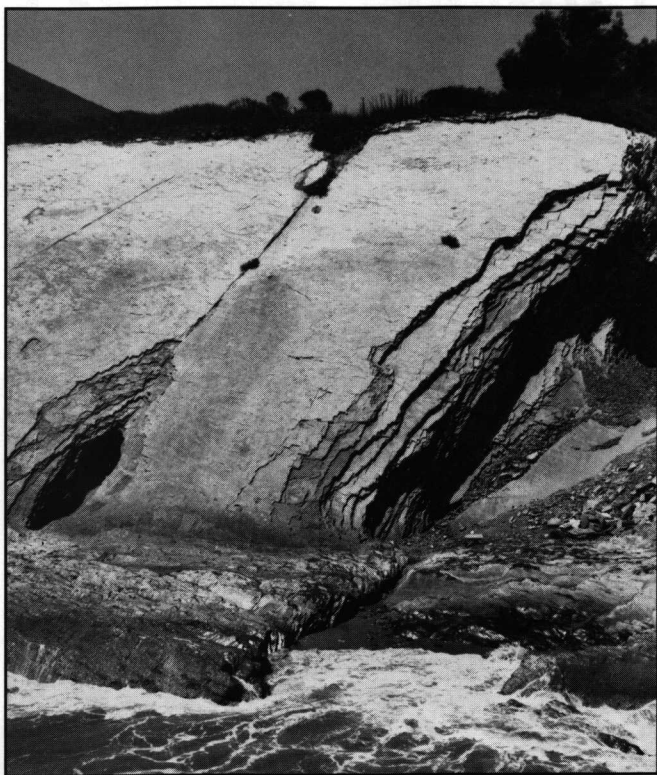


Photo 2. Marine erosion of Monterey Formation at Gaviota State Beach, Santa Barbara County. Wave erosion has cut a rock platform at the base of the cliff and created a small sea cave in a joint crack.

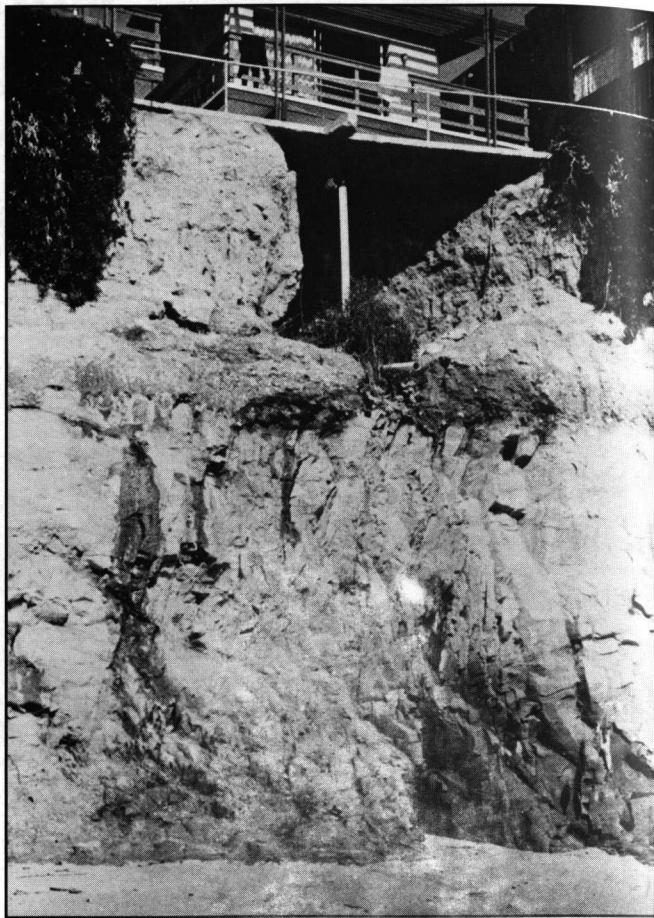
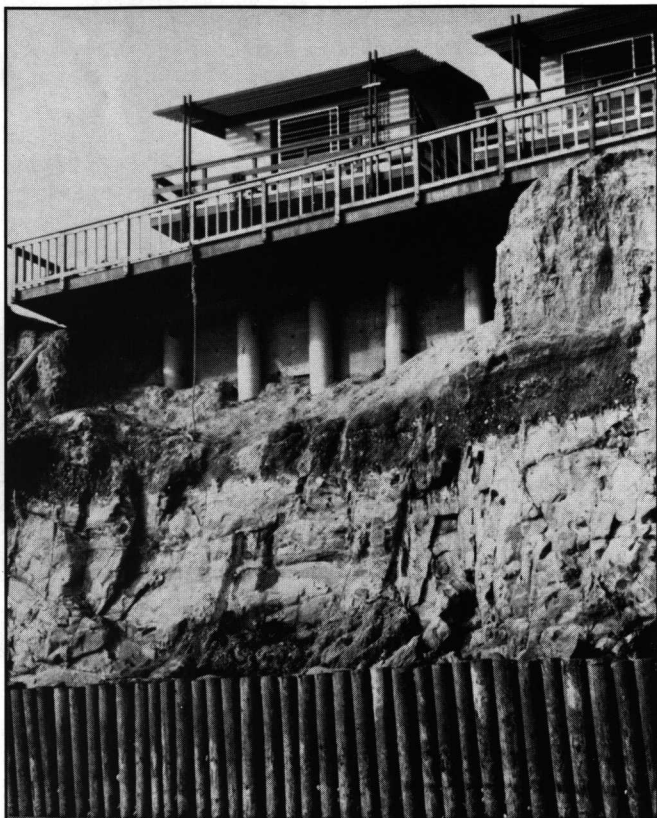


Photo 3. Erosion of sea cliff caused by water from a leaking drain below a concrete porch at a cliff-top house; photo taken in 1974.



◀ Photo 4. Same house (left) shown in Photo 3; photo taken in 1980. Repair work to prevent erosion of the cliff included installation of a drain pipe (extreme left) to prevent water from flowing over the cliff edge and a sea wall of wooden piles constructed at the cliff base.

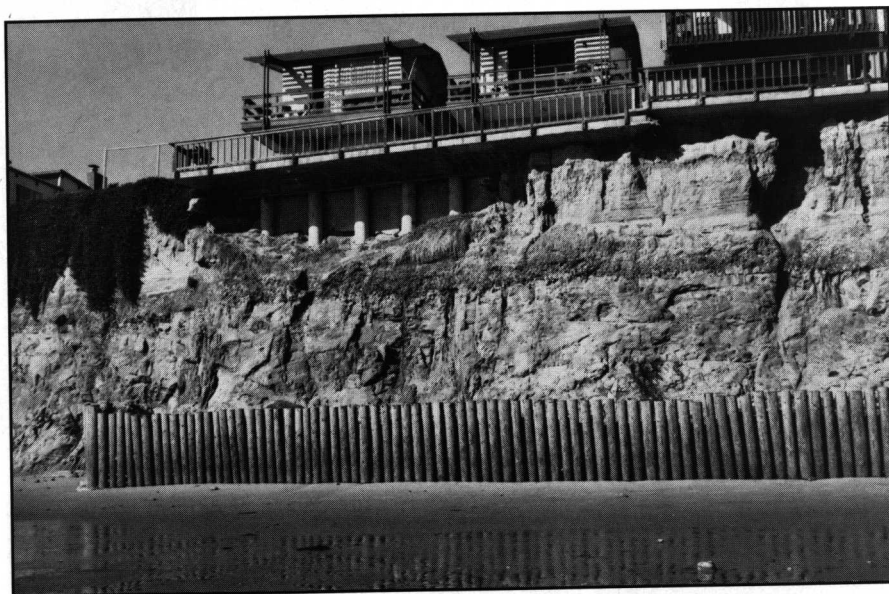
A third type of marine erosion occurs when winds pick up salt spray from waves and drive the spray against sea cliffs. This salty water may be absorbed by porous sedimentary rocks, and as the water evaporates, salt crystals form on the soil and in the porous rocks. The surface of the cliff material slowly flakes off and falls to the beach below. This process affects the entire cliff face, unlike wave erosion and solution erosion which occur only where sea water comes into direct contact with the rocks of the cliff.

Barriers placed at the bottom of the cliff may deter wave erosion, but may have no effect on salt spray or on solution processes.



◀ Photo 5. Same cliff seen in Photos 3 and 4; photo taken in 1987. The sea cliff has retreated back from the edge of the porch of the house (right side of photo). The drain has fallen off; an alcove is developing underneath one building (second from right).

Photo 6. Same cliff shown in Photos 3-5; photo taken in 1989. The alcove under the house on the right has been enlarged.



Nonmarine Erosion

Nonmarine agents responsible for cliff erosion include chemical and mechanical erosion processes, surface drainage water, and rainwater. None of these processes are affected by construction of cliff-base protective structures. Moreover, it is a serious mistake to ignore these processes when designing protective devices because they may account for as much as half of the cliff retreat along portions of the California coast (Photos 3-6).

Erosion is generally a gradual process. Chemical erosion causes oxidation and hydration. These processes may remove cementing materials in rocks, allowing grains to separate from one another. Volume changes by hydration or oxidation can weaken or wedge rocks apart. Mechanical erosion processes, such as the freezing and thawing action of water in crevices, are generally not an important factor in California due to the mild climate along the coast.

Surface water runoff and wind-driven rainwater are important sea cliff erosive agents. Water running over the cliff edge and wind-driven rain causes the fluting* often seen on cliff faces. These

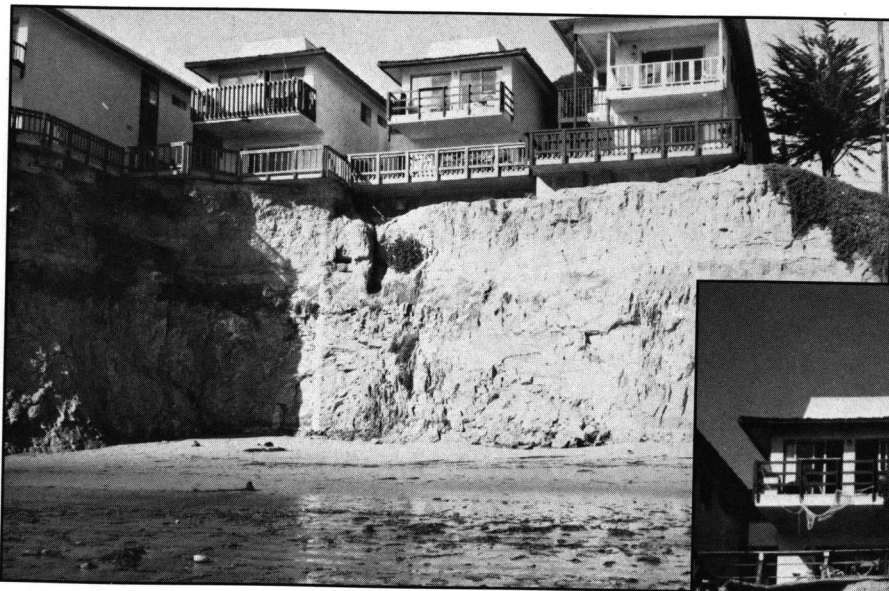
same processes have sculptured badlands topography, such as Red Rock Canyon in Kern County, California and Bryce Canyon in Utah. This type of topography is developed on soft, relatively unconsolidated rocks like mudstones or clayey shales (Photo 1).

Groundwater seeping from a cliff face may cause another kind of nonmarine erosion called spring sapping*, a process which creates alcove-like reentrants on the cliff face, and undermines and weakens the strata above (Photo 7). This process has excavated large valleys on windward parts of the Hawaiian Islands where very large

springs emerge from the porous lava flows. Similar effects occur on the bluffs of the Snake River near Twin Falls, Idaho. However, persistent flows of groundwater and active spring sapping are minor on the generally arid California coast.

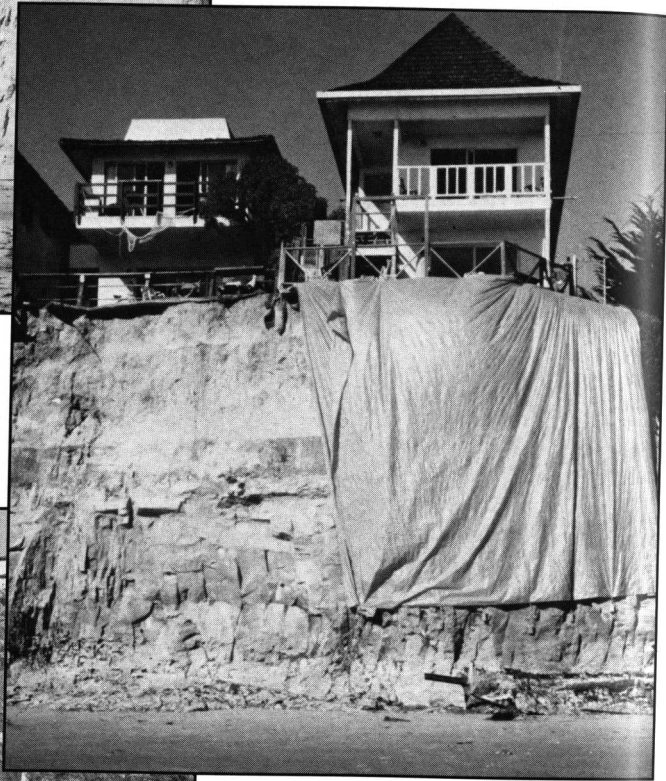
Where coastal developments are not serviced by municipal sewage systems, effluent from septic tanks may cause spring sapping of a sea cliff. Even where well-defined spring sapping does not occur, the septic system effluent will raise the pore pressure in sediments or rocks into which it is introduced, and thus reduce shear strength.

*See Glossary, page 177.

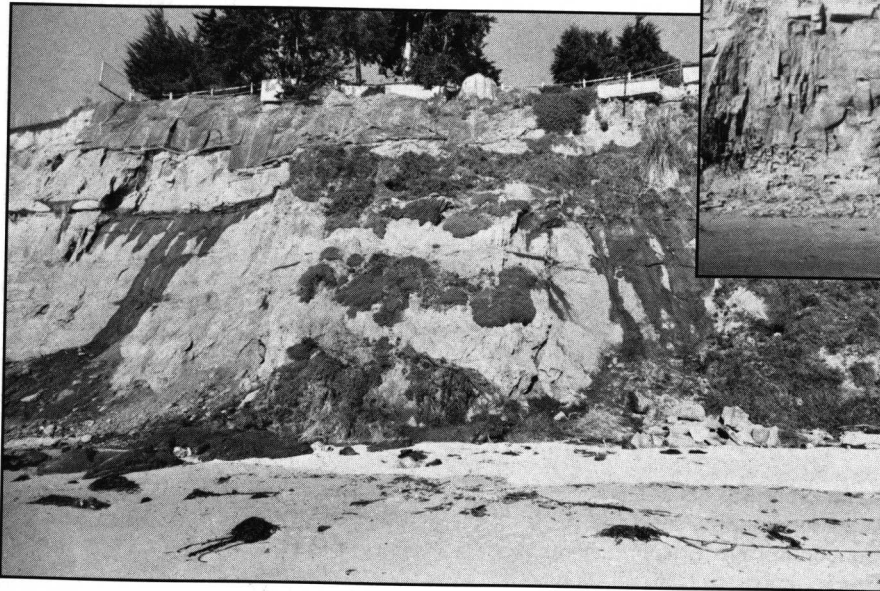


◀ Photo 7. Same cliff top shown in Photo 8. Cliff top beneath porches has retreated and porch railings have been made more secure. Concrete column and foundation are exposed under the porches of the houses.

Photo 8. Plastic sheeting has been hung over the sea cliff to protect it from water draining over the cliff top, Isla Vista, Santa Barbara County. Photo taken in 1986. ▶



◀ Photo 9. Sea cliff at More Ranch Beach, Santa Barbara County; photo taken in 1971. Water is seeping from a permeable zone (dark area) about two-thirds of the way up the cliff. This water causes spring sapping and sloughing of the cliff face. The water is probably draining from septic tanks and garden irrigation on the cliff top.



If bedding, fracture, or joint planes dip seaward, water may move along these planes and rock slides may occur. Installation of sewer systems in developed areas of the coastline can greatly reduce cliff erosion caused by spring sapping.

Property owners can protect cliff-top land from erosion by using drainage systems to carry water away from un-

stable areas and to prevent surface runoff down the cliff face. The cliff top can be stabilized by planting drought-tolerant vegetation. Vegetation that requires regular watering will exacerbate the problem it is meant to correct. Even drought-resistant vegetation may have undesirable effects because roots wedge rocks apart during growth. It is impractical to place plants on the edge of vertical cliffs or on cliffs where the

retreat rate is so rapid vegetation cannot be established.

Plastic sheeting has also been used to protect cliffs from rain wash (Photos 8 and 9). However, constant repair and maintenance are required to keep the plastic in place. Strong winds, especially those occurring during storms, can tear the sheeting and leave the cliff face unprotected when most needed.



◀ Photo 10. Small translational rock slide in the Monterey Formation, Hope Ranch Beach, Santa Barbara County; photo taken in 1984. This was a sudden bedding-plane rock slide, a common occurrence where the thin-bedded Monterey Formation dips steeply seaward.

Photo 11. Rotational slump, Santa Barbara; photo taken in February 1978. Several houses were destroyed by this slide which occurred after a few weeks of heavy rainfall. The head scarp is about 20 feet high. Marine erosion undercut the cliff. The slide was probably triggered by penetration of rainwater into cracks and joints near the cliff edge.

Other Factors

Landslides can occur in dry or wet materials. Movement may be slow, or it may be rapid if it occurs along a concealed bedding plane structure. Therefore, landslides may involve larger blocks of the sea cliff than are affected by weathering processes and may cause dramatic property damage (Photos 10 and 11).

People and animals also affect sea cliff erosion. For example, foot trails up steep cliffs result in increased erosion; burrowing gophers and other animals can weaken soft rocks when the burrows intersect cracks in dry soil. Piping, the development of subterranean channels which are rapidly enlarged by water, may result.

MITIGATION

Prior to slope failure, property owners often realize there is a problem and seek an engineering solution. Because an effective long-term solution is likely to be very expensive, less expensive protective measures, that only defer the problem by slowing — not stopping — the cliff retreat and erosion, are taken. These half-way measures include revetments constructed with large boulders placed at the base of the cliff, gabions (rock-filled baskets) stacked at the cliff



base, piling and other types of sea walls (Photos 4-6). However, any barrier that is not keyed into the bedrock at the cliff base and is not continuous to the cliff top, will eventually fail to provide any protection to buildings and structures at the cliff top. Even where the entire cliff face is protected with a continuous sheet of concrete, if it is not massive and keyed into the bedrock at the base of the cliff, failure will occur within a few years (Photos 12-15).

State and local government agencies involved in zoning and building safety usually do not approve construction of sea walls and other protective structures because these structures occupy beach space, are usually unsightly, require continuing maintenance, and hinder beach access. However, some type of protection is usually authorized once the property owner is able to show building damage is imminent.

SUMMARY

There is no simple engineering solution to save a cliff-top building threatened by erosion. Most remedial measures that are affordable for an individual property owner will only reduce the rate of erosion, not stop it. In the long term, the same problems will occur again and ultimately it will be necessary to condemn and demolish the structure because cliff erosion is part of the on-going geological process. Geologic conditions and common sense suggest that it would be less costly for both property owners and taxpayers if a strip several hundred feet wide landward of all cliff tops was carefully managed.

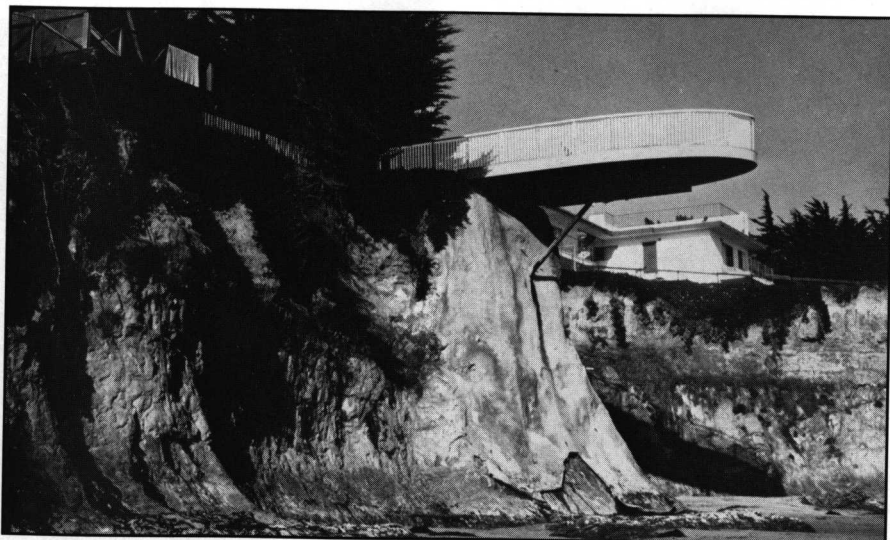


Photo 12. View of a cliff showing a porch projected out from a cliff-top house, Isla Vista, Santa Barbara County. Photo was taken in 1971. Grout was sprayed onto the cliff face to protect the cliff from wave erosion. *Photo courtesy of Duke University Press.*



Photo 13. Same sea cliff and projecting porch shown in Photo 12; photo taken in 1978. Wave erosion has attacked the base of the grout covering, and drainage over the cliff edge has eroded the upper edges of the coating. A covering of jute sacking has been added at the cliff top (left of grout cover). *Photo courtesy of Duke University Press.*

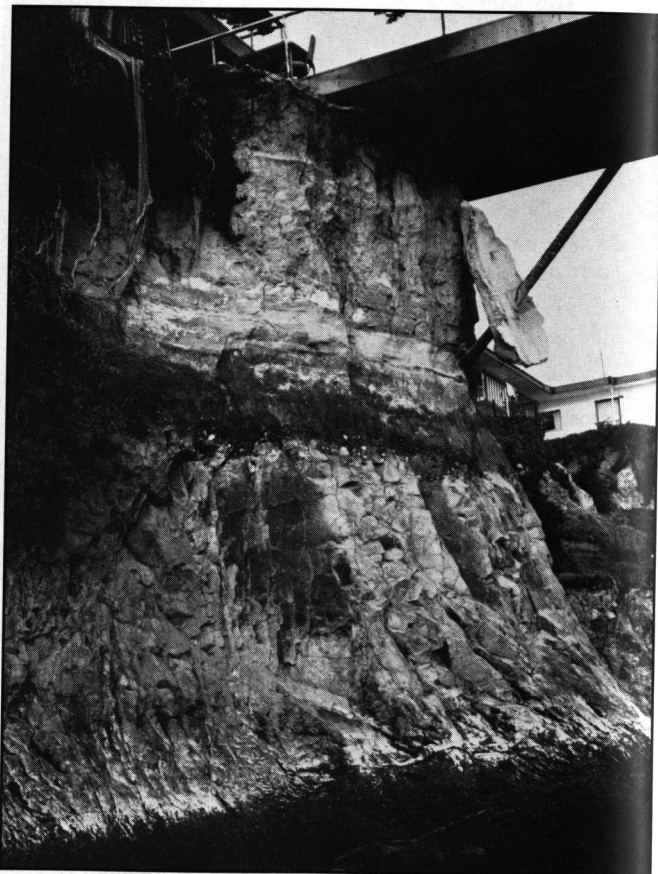


Photo 14. Sea cliff and projecting porch; photo taken in 1980. Only a remnant of the concrete grout cover remains, held in place by the porch support. The concrete covering reduced the rate of cliff retreat as shown by the slight seaward bulge in the lower part of the cliff, but it failed to stop the erosion. *Photo courtesy of Duke University Press.*

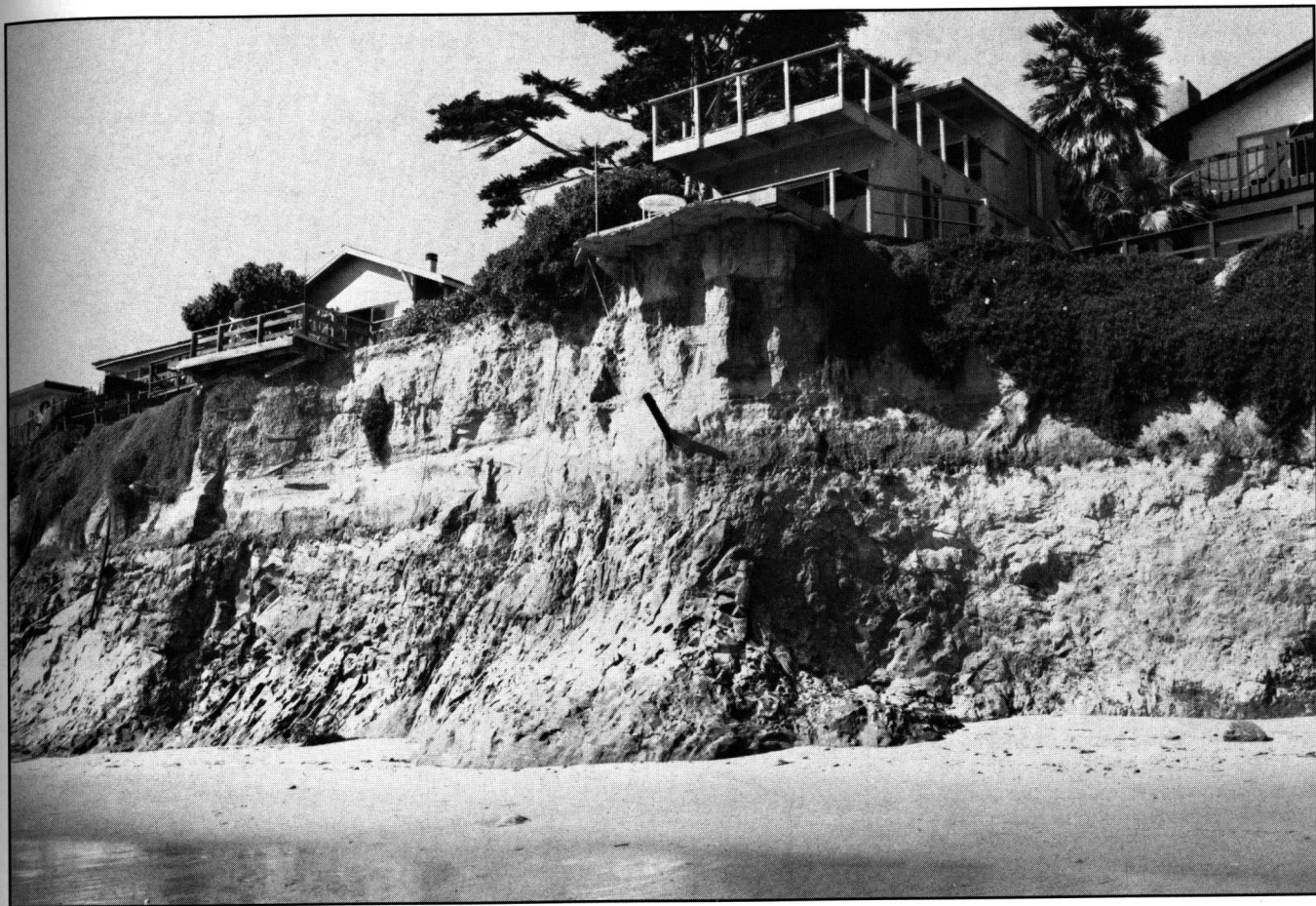


Photo 15. Same sea cliff location shown in Photos 12-14; photo taken in 1987. In 1982, the portion of the porch extending out over the cliff was removed. Continued erosion has caused the cliff to retreat under the edge of the porch area, but some seaward bulge in the cliff is still evident.

REFERENCES

- Griggs, Gary B., and Savoy, Lauret E., editors, 1985, *Living with the California coast*: Duke University Press, Durham, North Carolina, 393 p.
- Norris, Robert M., 1968, Sea cliff retreat near Santa Barbara, California: *Mineral Information Service*, v. 21, no. 6, p. 87-91.
- Norris, Robert M., 1985, Southern Santa Barbara County, Gaviota Beach to Rincon Point, Chapter 15 in Griggs, G., and Savoy L., editors, *Living with the California coast*: Duke University Press, Durham, North Carolina, p. 250-278.
- Pilkey, Orrin H., 1989, The engineering of sand: *Journal of Geological Education*, v. 37, p. 308-311.

GLOSSARY

- angle of repose:** Maximum angle of slope at which loose material comes to rest without sliding.
- colluvium:** A loose mass of fallen soil and rock collected at the base of a slope or cliff.
- fluting:** A vertical channel formed by differential weathering and erosion on the face of a cliff or rock surface.
- spring sapping:** Erosion around a seepage in a cliff face, resulting in retreat of the cliff.



Preliminary environmental assessment of a Pleistocene marine deposit near Isla Vista, California

Christina L. Belanger
Biological Sciences, College of Creative Studies
University of California, Santa Barbara

Summary

Previous studies of the fossiliferous Pleistocene marine deposit near Isla Vista, California have yielded a faunal description of at least 138 mollusc species. These collections only sample the western 0.8 km of the deposit where it nears beach level, probably because of the deposit's less accessible 3-4 m height in its eastern extent. My study samples the eastern 2 km of the exposure, and uses 47 molluscan elements to determine if there is any change in faunal composition or depositional source from the western UCSB campus to Devereux Slough. Preliminary results suggest the entire deposit represents a single fine sandy to muddy sublittoral environment. The abundance of disarticulated pelecypods, shell fragments, and the absence of shells in life position, suggest the fauna was transported and rapidly deposited.

Introduction

A fossiliferous Pleistocene marine deposit is exposed in the marine terrace near Isla Vista, California (Figure 1) and rests with angular unconformity on the Pliocene Sisquoc Formation (Fig 2). The unit consists of two visually distinct, unconsolidated, silty-sand deposits referred to here as yellow brown and gray sediment. Both sediment types contain abundant fossil molluscs, foraminifera, and fragmentary remains of arthropods and echinoderms within the first meter above the contact with the Sisquoc Formation. The deposit is exposed from the western edge of the University of California, Santa Barbara campus to Devereux Slough, an approximate distance of 2.5 km.

Previous research has dated the Pleistocene unit to approximately 45,000 years using uranium series and radiocarbon analysis of a fossil solitary coral found in the terrace (Keller, 2000). Similar dates were also derived from potassium luminescence of feldspar in terrace sands (Spencer and Owen, 1999) and from oxygen isotope signatures from *Olivella biplicata* (Trecker et al., 1998).

Terrace fossil collections were made by Wright (1972) and by the Southern California Paleontological Society from a 0.8 km zone west of Isla Vista to Devereux Slough (Peska, 1987). Foraminiferal studies were also done west of Isla Vista (Barrick, et al., 1989). None of these studies included the eastern extent of the deposit nor did they explicitly record faunal data from the two sediment colors. My ongoing study extends collections approximately 2 km east of the previous study area to determine if the fauna is laterally consistent and to determine if there is any variation in the fauna between the different sediments that may indicate different depositional sources or events. To address these questions, I made collections from two localities within the original collection area (sites 6 and 7), plus five more (sites 1-5) along the 2 km eastern stretch of the terrace (Figure 1). Site 2 was investigated in detail and divided into top, middle, and bottom sections. Site 7 was divided into top and bottom sections based on a natural plane of weakness. At sites 1

and 7, only yellow-brown sediment was present within the fossiliferous zone. At all other sites, fossils were in gray sediment, although yellow-brown unfossiliferous sediment was present above gray unfossiliferous sediment (Figure 2). The fauna and sediment type at each of the seven sites were compared and used to interpret the ecology and the environmental source of the deposit. The results and interpretations presented here are preliminary and are subject to change.

Faunal Characteristics

Previous studies collectively suggest a molluscan fauna of at least 138 taxa (Wright, 1972; Peska, 1987). In the present study, a total of 47 taxa were found in the seven collection sites including 26 species of gastropods and 21 species of pelecypods (Tables 1 and 2). Of these 47 taxa, only 4 are common to abundant in all sections of all seven sites: *Macoma nasuta*, *Nutricula tantilla*, *Olivella biplicata*, and *Alia carinata*. *Bittium spp.*, *Cryptomya californica*, and *Margarites pupillaria* are common to abundant at all sites, but are absent from the lower 20 cm of site 7. *Tellina modesta* is abundant at site 2 and common in sites 6 and 7, but rare or absent in sites 1, 3, 4, and 5. *Protothaca stamina* is abundant in sites 1, 3, 4, 5 and 7, but absent or rare in sites 2 and 6. *Saxidomus nuttalli* is common in site 1 but rare or absent in all other sites.

The most abundant molluscs in the Isla Vista terrace deposit are common in soft-bottom marine environments with sandy to muddy substrate. *Cryptomya californica* is often commensal with mud shrimp and *Urechis sp.*, extending its siphons into their burrows instead of to the surface. *Macoma nasuta* is noted for its tolerance of high salinity and stale-water environments and is very common in mudflats and lagoons. *Nutricula tantilla* is common in the top two centimeters of sandy mud. *Protothaca stamina* is a quiet water species that never lives in shifting sand. *Olivella biplicata* is also a common sandflat gastropod (Ricketts, et al., 1985).

Other common species, including *Alia carinata* and *Margarites sp.*, are found on low intertidal rocks (Smith and Carlton, 1975). Rare species, including *Mytilus sp.*, *Littorina sp.*, *Crepidula spp.*, and others also live on solid substrate, suggesting a rocky shore element is also present (Ricketts, et al., 1985) but these taxa are neither dominant nor are they characteristic of the terrace deposit.

Most of the pelecypods are disarticulated. However *Cryptomya californica* is commonly found articulated at sites 6 and 7. Occasionally, *Macoma nasuta*, *Protothaca stamina* and *Nutricula tantilla* are also found articulated. None of the species found in the Pleistocene unit are in life position. However, the upper 10 cm of the Sisquoc Formation contains numerous rock-boring *Penitella sp.* and *Platyodon sp.* in life position.

Sediment Characteristics

Two visually distinct sediments, yellow-brown and gray, are present in the Isla Vista terrace (Figure 2). The yellow-brown sediment is 0.5- 1.5 m thick and the gray sediment is 0.3 – 1.5 m thick (combined thickness of the deposit is approximately 0.5 – 2.5 m). Both sediments are fossiliferous where within 1 m of the contact with the Sisquoc Formation. At sites 1 and 7, the yellow-brown sediment is in contact with the Sisquoc Formation (Figure 2) and contains fossil material. At all other sites, the gray sediment is in contact with the Sisquoc and contains fossils up to 1m above the contact. At sites 2 and 3, the fossiliferous gray sediment is overlain by unfossiliferous gray sediment.

Yellow-brown unfossiliferous sediment overlies the unfossiliferous gray sediment at sites 2 and 3 and the fossiliferous sediment at sites 4, 5 and 6 (Figure 2).

While the sediments are visually distinct, the grain size distribution is similar at most sites (Tables 3 and 4). In sites 1, 2, 4, 6, and 7, the median grain size is medium sand. At site 3 the median grain size is fine sand and at site 5 the median grain size is coarse sand. However, much of the coarser material in the sediment consists of broken shells and tar aggregates, and the sediment itself is finer than the median grain size suggests (Table 3).

Local accumulations of tar are more frequent in the gray sediments than in the yellow-brown sediments and are often associated with hyper-concentrated, clast-supported shell deposits. Where tar is absent or unconcentrated, shells are matrix supported. In all locations, shells are randomly oriented and are present in higher concentrations than expected in life.

Discussion

Based on current habitat associations, the most abundant taxa in the Isla Vista terrace deposit inhabited a soft-bottom marine environment with sandy to muddy substrate. Rare rocky substrate taxa suggest hard substrate was available but not abundant in the source habitat. While a majority of the fauna certainly lived in fine-grained sediments, it is unclear from my collections whether the fauna occurred in an intertidal or a subtidal setting. However, foraminifera collected 31-256 m west of Camino Majorca suggest a shallow (0-5 m) subtidal environment (Barrick et al., 1989). This is consistent with Wright's interpretation of the terrace deposit as inner sublittoral (Wright, 1972) and the deposit's source was most likely offshore based on the combined faunal evidence.

The recorded sedimentology of the Isla Vista terrace deposit also suggests a fine sand to mud substrate. Fine sandy and muddy substrates occur in protected embayments or offshore below wave turbulence (Valentine, 1961) further indicating the fossil assemblage originated in a quiet water environment. This is consistent with modern habitat associations.

There is lateral variation in the distribution of several species, which may range from very abundant to entirely absent across sample sites. This lateral variation could result from slight differences in sediment characteristics, from depth of oxygen penetration, or from the distribution of non-fossilized members of the community (Little, 2000). The variation seen in the terrace deposit could reflect this patchiness. Further analysis of lateral variation is necessary.

Neither the faunal composition nor the median sediment size vary greatly between the two sediment colors. Thus, the observed color difference may not represent different source environments or different depositional events, but rather different concentrations of tar accretions or differential weathering. Portions of the cliff containing gray sediments are more affected by wave-cut erosion and exposures are renewed continuously. In contrast, where yellow-brown sediment is present, erosion is less frequent and the cliff face has well-developed superficial weathering. The continuity of the fossiliferous sediment regardless of sediment color further supports the interpretation that the different colors do not represent different sources or different events. Any faunal differences between the two sediment colors may be due to local variation in the deposit.

The Pleistocene unit was rapidly deposited over an existing hard substrate as evidenced by numerous rock-boring *Penitella sp.* and *Platyodon sp.* found as whole shells in life position in the upper 10 cm of the Sisquoc. Rapid deposition is further supported by the random orientation, disarticulation of pelecypods, amount of shell fragments, and the abrupt decrease in shell numbers away from the contact with the Sisquoc Formation.

Conclusion

The present preliminary results cannot differentiate between subtidal and intertidal fine sandy to muddy environmental sources because of the faunal similarities between the mollusks in both environments. However, evidence from previous foraminiferal studies suggest the source environment was subtidal. The consistency between the fauna and sediment type indicate that mixing of sediments from other environments has not occurred.

The absence of significant differences in fauna and sediment size between the two sediment colors suggest that the different colors are not the result of different depositional events or different environmental sources. While lateral variation is present, the deposit appears to sample a single environment from the western end of the UCSB campus to Devereux Slough.

Acknowledgments

Thanks go to my advisor, Bruce Tiffney, for introducing me to this project, aiding in collection efforts of the least accessible portions of the deposit, and for extensive discussion and review of the manuscript.

References

- Barrick, R. E., A. E. Beveridge, R. T. Patterson, and J. K. Schubert. 1989. *Journal of Paleontology*, 63(3):261-267.
- Keller, E. A. 2000. Earthquake Hazard of the Santa Barbara Fold Belt, California. unpub. report. 77p.
- Little, C. 2000. *The Biology of Soft Shores and Estuaries*. Oxford: Oxford University Press. 252p.
- Peska, F. 1987. A Late Pleistocene Site at Goleta, California. *Bulletin of the Southern California Paleontological Society*. Vol. 19. no 3-4. p26-30.
- Ricketts, E. F., J. Calvin, J. W. Hedgpeth and D. W. Phillips. 1985. *Between Pacific Tides*. Fifth Edition. Stanford University Press, California. 652p.
- Smith, R. I. and J. T. Carlton. 1975. *Light's Manual: Intertidal Invertebrates of the Central California Coast*. Third Edition. University of California Press, Berkeley.
- Spencer J. and L. Owen. 1999. Luminescence Dating of Santa Barbara Terraces/Raised Beaches: Preliminary Results, unpub. report. 22p.

Trecker, M. A., L. D. Gurrola, and E. A. Keller. 1998. Oxygen Isotope Correlation of Marine Terraces and Uplift of the Mesa Hills, Santa Barbara, California, IN: Steward, I. S. and C. Vita-Finzi, Coastal Tectonics, Geological Society of London, 146: 57-69.

Valentine, J. W. 1961. Paleoecologic molluscan geography of the California Pleistocene. University of California Publications in Geological Sciences. 34(7): 309-442.

Wright, R. H. 1972. Late Pleistocene marine fauna, Goleta, California. Journal of Paleontology, 46(5):688-695.

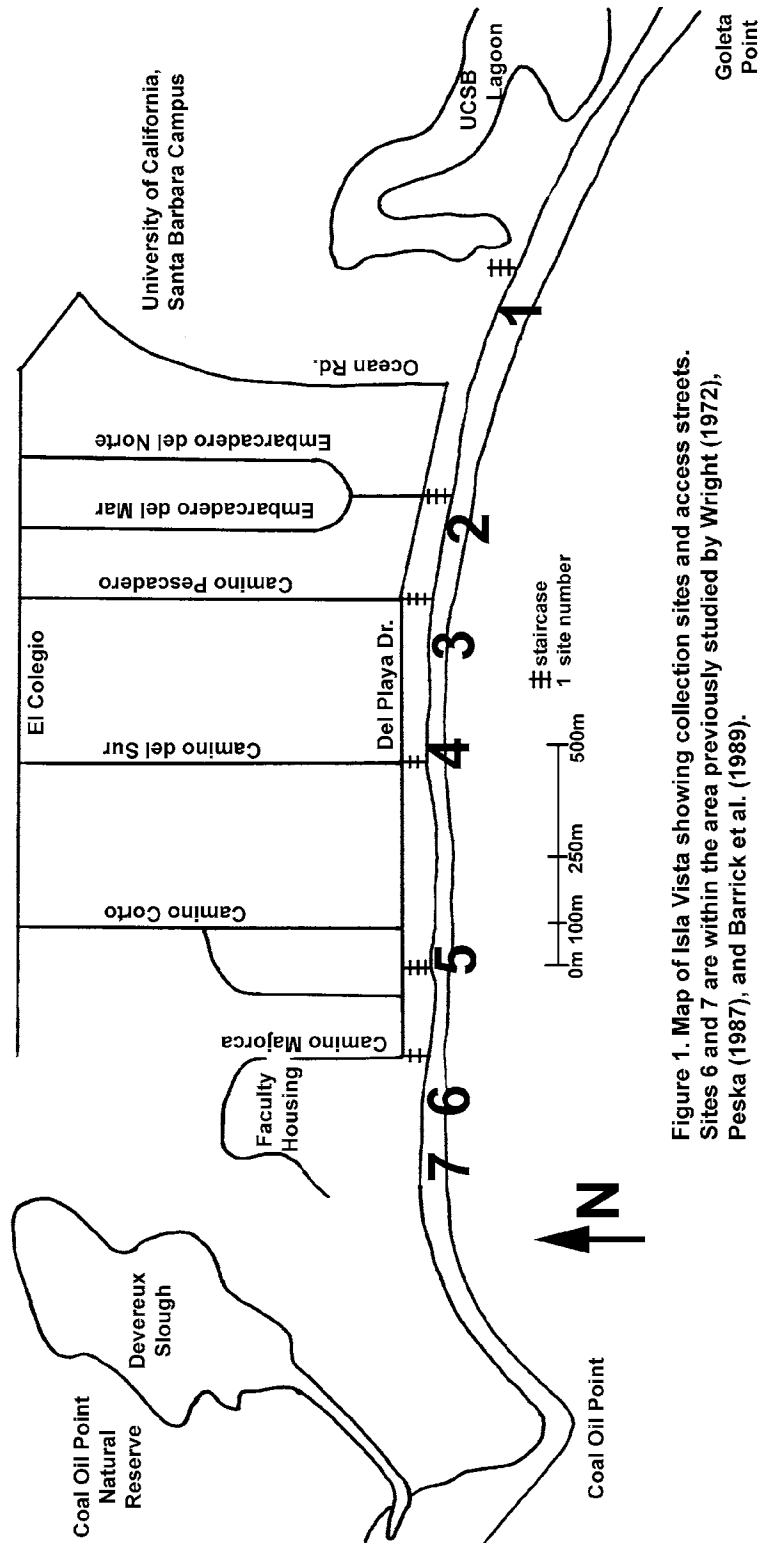


Figure 1. Map of Isla Vista showing collection sites and access streets. Sites 6 and 7 are within the area previously studied by Wright (1972), Peska (1987), and Barrick et al. (1989).

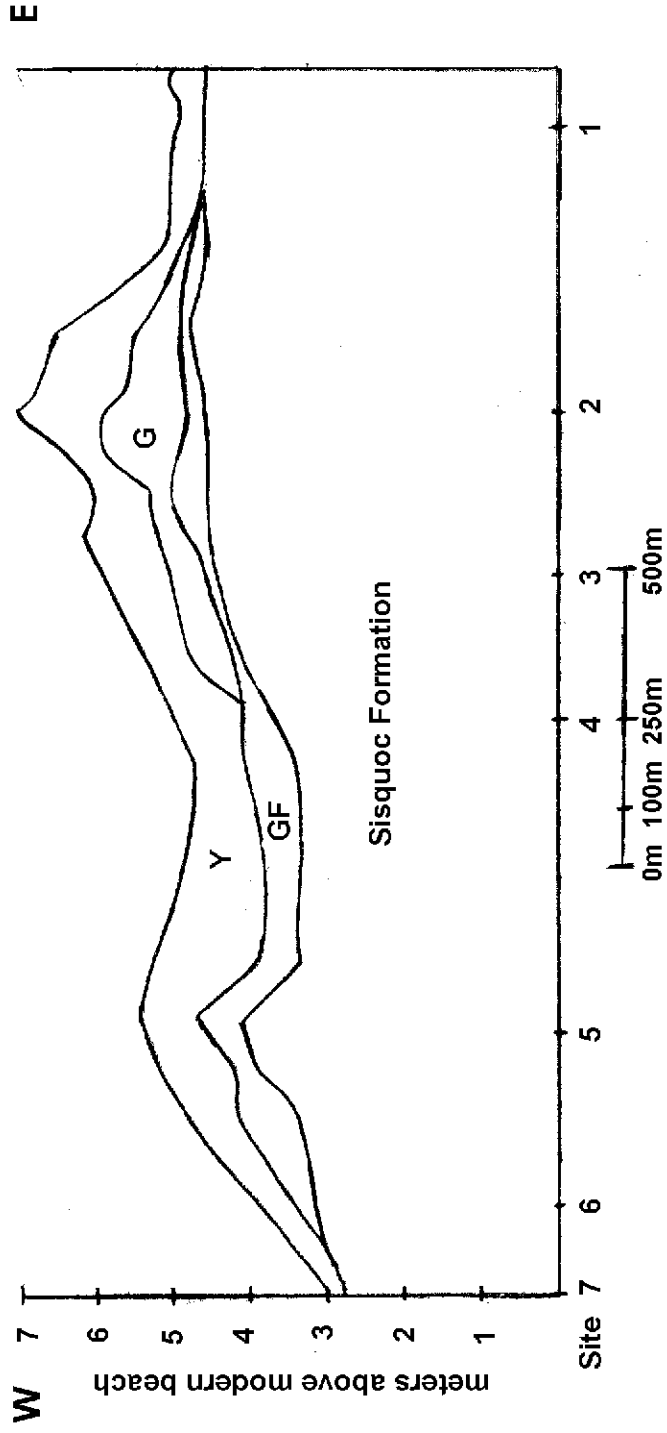


Figure 2. Diagrammatic cross section of the Isla Vista terraces with 1,200x vertical exaggeration. Y= yellow-brown, G= gray, GF= gray fossiliferous. A distinction between yellow-brown fossiliferous and yellow-brown unfossiliferous has not yet been mapped.

Table 2. Preliminary list of pelecypods from Isla Vista terrace near Goleta, California. A= abundant, C= common, R= rare. Sites 6 and 7 are within the area collected by Wright (1972).

	Site 1	Site 2			Site 3	Site 4	Site 5	Site 6	Site 7		Wright, 1972
		Top	Middle	Bottom					Top	Bottom	
Pelecypoda											
Clinocardium sp.								R			R
Cryptomya californica	A	A	A	A	A	A	C	A	C		C
Glans sp.										R	
Lucinisca nuttalli	R	R	R	R			R				R
Macoma expansa			R								R
Macoma indentata										R	R
Macoma inquinata	C						C				C
Macoma nasuta	A	A	A	A	A	A	A	A	A	A	A
Mytilus sp.			R					R		C	R
Nuculana taphria	R		R								R
Nutricola tantilla	A	A	A	A	A	C	C	C	A	R	
Penitella turnerae								R			
Platyodon cancellatus			R		R					C	C
Protothaca staminea	A	C	C		A	A	A	R	C	A	C
Saxidomus giganteus										R	A
Saxidomus nuttalli	C		R		R	R	R				
Solen sp.	R	R	R	R							R
Spisula sp.									R		
Tellina bodegenis			R					R			
Tellina modesta	R	A	A	C	R		R	C	C	R	R
Tresus nuttalli	C		R		R	C		R	R		A

Table 3. Preliminary sediment data reported as percent volume of various sediment grain sizes present at each collection site. Large shells were removed from the sample before sieving. Particle sizes phi -2.00 to 2.00 are primarily shell fragments and clumps of tar.

Site 1			Site 5		
Phi Value	% volume	Cumulative % volume	Phi Value	% volume	Cumulative % volume
-2	7.8	7.8	-2	23.5	23.5
-1	9.7	17.5	-1	17.6	41.1
1	19.4	36.9	1	23.5	64.6
2	9.7	46.6	2	4.7	69.3
3	19.4	66	3	7.1	76.4
4	14.6	80.6	4	11.8	88.2
>4	19.4	100	>4	11.8	100
Site 2			Site 6		
Phi Value	% volume	Cumulative % volume	Phi Value	% volume	Cumulative % volume
-2	5.1	5.1	-2	18.1	18.1
-1	8.9	14	-1	7.2	25.3
1	13	27	1	12	37.3
2	2.6	29.6	2	6	43.3
3	32	61.6	3	14.5	57.8
4	32	93.6	4	24.1	81.9
>4	6.4	100	>4	18.1	100
Site 3			Site 7		
Phi Value	% volume	Cumulative % volume	Phi Value	% volume	Cumulative % volume
-2	8.5	8.5	-2	10.4	10.4
-1	2.8	11.3	-1	10.4	20.8
1	8.5	19.8	1	14.6	35.4
2	2.8	22.6	2	4.3	39.7
3	21	43.6	3	17.3	57
4	28.2	71.8	4	20.6	77.6
>4	28.2	100	>4	22.4	100
Site 4					
Phi Value	% volume	Cumulative % volume			
-2	7.7	7.7			
-1	7.7	15.4			
1	15.4	30.8			
2	12.3	43.1			
3	15.4	58.5			
4	23	81.5			
>4	18.5	100			

Table 4. Preliminary sediment data showing the percentage of phi values 3.00, 4.00 and > 4.00 (medium sand, fine sand and silt). At these sizes, shell fragments and tar aggregations are absent and a better comparison of sediment size between sites can be made.

Phi Value	3.00	4.00	> 4.00
Site 1	36.20%	27.30%	36.20%
Site 2	45.45%	45.45%	1.00%
Site 3	27.20%	36.40%	36.40%
Site 4	27.10%	40.40%	32.50%
Site 5	23.20%	38.40%	38.40%
Site 6	25.50%	42.50%	32.00%
Site 7	28.70%	34.20%	37.10%

BIVALVES

Cryptomya californica (California Soft Shell)

Color: Gray

Length: 3 cm

Mostly smooth oval valves with fine concentric sculpture.

Habitat: Sand of coast and bays.

Range: Gulf of Alaska to Peru.



Lucinisca nuttalli (Nuttall Lucine)

Color: White to gray

Length: 1-2 cm

Nearly circular shaped valves with central beaks and cancellate sculpture.

Habitat: Sandy beaches

Range: Monterey, California to the Gulf of California.



Macoma nasuta (Bent-nosed Macoma)

Color: Off-white, brown, purple

Length: 4-6 cm.

Rounded anterior, angular posterior. Smooth outer surface with commarginal bands of color.

Habitat: Muddy bay bottoms and intertidal zones.

Range: Alaska- Baja California.



Nutricola confusa

Color: Pink to white

Length: 0.5 – 1 cm

Inflated triangle shaped shell has a shiny surface. Very fine commarginal sculpture.

Habitat: Bays and offshore.

Range: Alaska to Baja.



Platydon cancellatus (Boring Softshell)
Color: gray shell.
Length: 6 cm long.
Thin but defined concentric sculpture mark each oval valve.
The beaks are located towards the posterior end of the center of each valve.
Habitat: Protected shorelines, especially in soft sandstones and muds.
Range: Queen Charlotte Island to San Diego.



Protothaca staminea
(Pacific Littleneck)
Color: White
Length: 4-6 cm
Defined by strong radial sculpture with weak commarginal sculpture.
Beak anterior to center.
Habitat: Intertidal zones
Range: Alaska to Baja California.



Saxidomus nuttali (Washington Butter Clam)
Color: Grayish white
Length: 12-15 cm
Fine commarginal sculpture. The valves are oval shaped, and beaks are central on each valve.
Sometimes found in the life position.
Habitat: Bay bottoms
Range : Humboldt, CA to Baja California
Historical Note: Local Chumash tribes used the shells of this species as currency.



GASTROPODS

Alia carinata (Dove Shell)

Color: White

Length: 1-1.5 cm

Smooth shell, defined suture.

Elongate aperture.

Habitat: Low tide mark and deeper.

Range: Alaska to Baja California



Lirobittium attenuatum

Color: Tan to Pink

Length: 1 cm

Cancellate sculpture on rounded whorls. Tear shaped aperture.

Habitat: Low water near rocks.

Range: Alaska to Baja California



Epitonium tinctum (Tinted Wentletrap)

Color: White

Length: 1-1.5 cm

Easily identified by large protruding ridges perpendicular to the whorls.

Circular aperture.

Habitat: Intertidal zone

Range: Vancouver, British Columbia to Baja California



***Homalopoma* sp**

Color: Varies

Length: 0.5-1 cm

Turban shaped shells with strong spiral sculpture. Circular aperture.

Habitat: Mostly intertidal

Range: Alaska to northern Baja California



Littorina planaxis (Eroded
Periwinkle)

Color: White

Length: 1-2 cm

This snail shaped species has whorls that are slightly rounded, with no sculpture. Oval aperture.

Habitat: Rocky reefs

Range: Puget Sound, Washington to Baja California



Nassarius perpunguis (Fat Nassa)

Color: Tan to White

Length: 1.5-2 cm

Cancellate sculpture marks this species. Tear drop shaped aperture.

Habitat: Bay bottoms and lagoons

Range: Point Reyes, California to Baja California.



Olivella sp

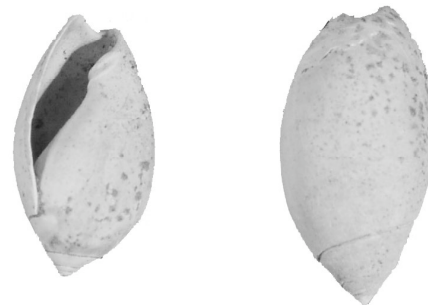
Color: White to Purple

Length: 1-3 cm

Cylindrical shells with smooth highly polished outer surface. Elongate aperture.

Habitat: Lagoons and bay openings.

Range: Alaska to Baja California



Ocinebrina sp

Color: Brown to Tan

Length: 1-3 cm

Genus marked by axial ribs and spiral sculpture. Oval to tear shaped aperture with thickened lip.

Habitat: Low tide mark

Range: Local species found from Monterey Bay, California to Baja California



UCSB Beach: 30 years of Waxing and Waning

By

Arthur Gibbs Sylvester

Geological Sciences, University of California, Santa Barbara

A temporally random set of images of UCSB beach taken from the Anacapa Steps over 30 years illustrates the waxing and waning of a beach, probably due to a combination of a major forest fire that barred the mountain slopes to rapid erosion and several El Niño storms.

Winter storm waves routinely pounded the UCSB cliffs in the 1950s and most of the 1960s. Waves did not attack the cliffs from 1969 to 1983, because they were protected by a 200 m-wide beach upon which grew luxuriant vegetation. The beach also supported volleyball courts and concrete fire rings. Large trees grew along the base of the cliffs, and old-timers say that they used to drive vehicles and camp on the beach. The colossal 1983 El Niño storm changed all that in just two days, tearing out the beach and the trees at the base of the cliff. Storm waves again attacked the cliffs and have so every winter since. The sand barely covers the bedrock platform, and the fire rings and volleyball courts are long gone. Where did all that sand come from and why did it disappear?

A major forest fire burned the south front of the Santa Ynez Mountains from Pt. Conception eastward to San Marcos Pass in 1955, thereby barring the mountain slopes to increased erosion. From 1955 to 1969 several large storms moved sediment from the slopes to the washes. The 1969 El Niño was a giant storm that flushed the accumulated sediment down the washes to the sea, thus moving more sediment into the Santa Barbara Channel in two days than all storms in the previous 25 years combined ((Inman and Jackson, 2001). That voluminous slug of sediment nourished the UCSB beach so that the beach waxed perceptibly and stabilized until the 1983 El Niño tore it away. Subsequent El Niños have been less intense than the 1983 storm and have lacked a fresh supply of sediment to transport, so the beach has been in a more or less metastable state, neither waxing nor waning noticeably, although the cliffs are regularly attacked and eroded by winter storm waves.

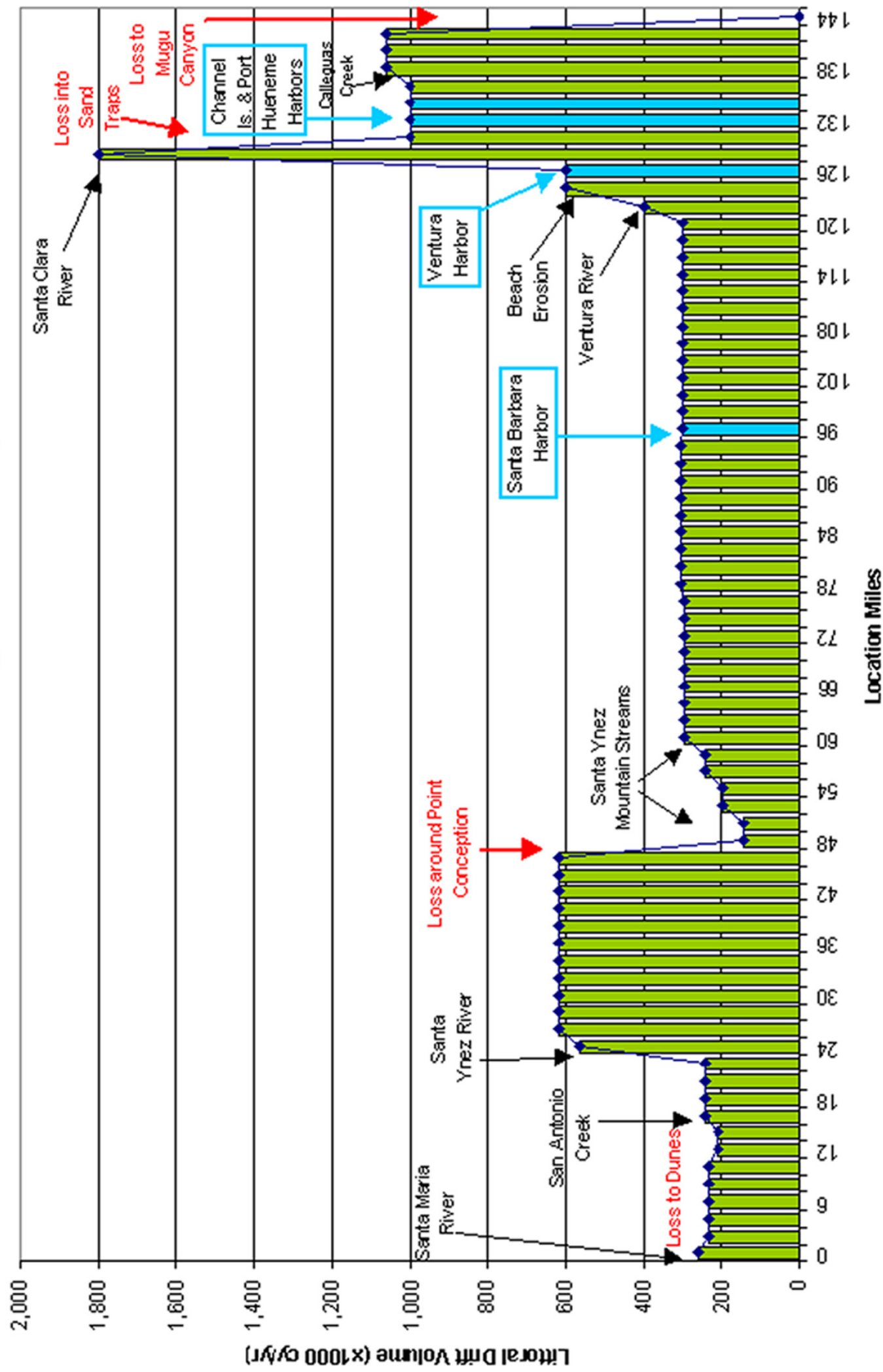


UCSB beach, 28 March 1975. Note width of beach and growth of vegetation both on the beach sand as well as on and below the cliff. Growth includes a volleyball court and a concrete BBQ fire ring in foreground. Vegetation has obliterated sand bar lines that were evident in 1972. ©AGS1975



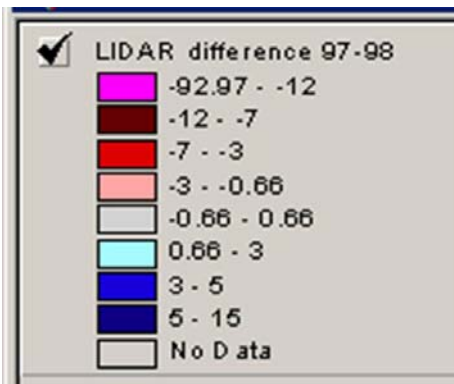
UCSB beach, 26 January 1983, Morning and astronomic high tide, toward tail end of El Niño storm. Storm waves directly batter the cliffs. ©AGS1983.

**Figure 15: Santa Barbara Littoral Cell Longshore Transport Volumes
 Santa Maria River to Mugu Submarine Canyon**



Sediment Budget Caption – Sediment Budget running total (courtesy of Kiki Runyan PhD Dissertation draft with advisor Gary Griggs). Inputs from Rivers were calculated by Cope Willis. [Willis and Griggs 2003 (Geology 2003, vol. 111. p 167-182)]. This running total follows the sediment at the source of the littoral cell (Santa Maria River) with minor losses to sand dunes via eolian transport, and a substantial loss around Pt. Conception. Individual harbor dredge records serve as checkpoints to balance the sediment budget. The loss around Pt. Conception was estimated from sediment yield calculations for the Coast Range watersheds needing to balance the 75 year average dredge records at the Santa Barbara Harbor.

LIDAR figures – LIDAR is a remote sensing laser altimetry which accurately measures elevation to within 15 cm. These figures illustrate the relative shoreline change during the 1997-98 El Nino. The figures result from the subtraction of an April 1998 topographic grid from an October 1997 grid, effectively bracketing the 1997 –1998 El Nino winter and illustrating the relative change. These three figures are a panoramic of the shoreline from Ellwood Mesa to Goleta Beach. Warmer colors represent erosion and cool colors represent accretion.



Elevation change in feet
Oct. 1997 - April 1998

DAY 2: EL CAPITAN CANYON

8:00 a. m. – 10:00 a. m.

Discussion of bedrock channels within the Santa Ynez Mountains: El Capitan Canyon

Alison Duvall, Eric Kirby, and Douglas Burbank

Objective

We will spend this stop in El Capitan Canyon where we will discuss bedrock channel behavior in the Santa Ynez Mountains and observe a section of El Capitan stream, one of the many small bedrock channels that drain the range.

Overview

After a short walk from the road, we will discuss bedrock channel response to variable rates of rock uplift across the southern flank of the range. The range crest, resistant bedrock fins, and several other drainages are also visible from this vantage point. By examining a section of the stream channel in detail, we also consider effects of transitions in underlying bedrock strength on channel process and form. In this short reach of El Capitan stream, a discontinuous carpet of medium to coarse (>20 cm) boulders, derived from resistant sandstone exposed on the upper mountain flanks, rest upon underlying weak substrate in which the stream channel is incised. Coarse bedload coupled with a steeper-than-expected channel gradient, suggest the potential role of resistant sediment in dictating channel gradient along the lower reach of this stream and others like it within the range.

Santa Ynez Bedrock Channels

The southern flank of the Santa Ynez Mountains includes 70+ dominantly bedrock channels (Fig. 1, Table 1). The sub-parallel channels are generally steep, narrow and short with an average channel length of 6.4 km. Drainage areas vary from 0.2 to 12.5 km² with an average of 6.5 km². The study area has a Mediterranean climate characterized by episodic, cool winter storms and a warm, dry spring, summer, and fall. These channels can be divided into two general regions: the low-uplift region comprises streams in the western part of the range where rock-uplift rate is ~0.75 mm/yr and the high-uplift region comprises streams in the eastern part of the range where rock-uplift rate is ~5 mm/yr (Fig. 1). All rock-uplift rate values were derived from flights of marine terraces present along the length of the study-area coastline (please see other stops in this field guide for details).

Bedrock Geology

Bedrock exposed in study-area channels consists of an assemblage of Eocene through Pliocene sedimentary rocks (Dibblee, 1982). Rock units exposed along the flank of the range strike nearly east-west, parallel to the range crest. As a consequence, the pattern of lithologic variations is nearly constant along strike of the range. In the western part of the range (low rock-uplift rate), exposures of resistant (Eocene) sandstone crop out along the range crest and upper mountain flanks. These resistant beds stand in contrast to the soil-mantled hillslopes developed in the less-resistant (Oligocene-Pliocene) sandstone, conglomerate, and

shale along the lower flanks of the range. In this part of the range, a small subset of channels is developed entirely within these less-resistant rocks. In contrast, none of the channels in the eastern (high rock-uplift rate) part of the range (near Ventura, CA) cross major transitions in rock strength and instead, channels erode only the relatively weak Oligocene-Pliocene units.

Results from 1000 Schmidt Hammer measurements of intact rock strength show that the older, predominantly sandstone rocks exposed at higher elevations in the western part of the range are roughly twice as strong (mean Schmidt value and standard error of the mean of 43.8 ± 6.1) as the younger sandstone, shale, and conglomerate units exposed in the lower half of the western range and in the entire eastern part of the range (mean rock strength of 23.4 ± 4.1) (Table 2) (Fig. 2).

Stream-Power Incision Model

Bedrock channel incision is commonly considered to be a detachment-limited process, whereby incision into bedrock occurs because a stream's capacity to entrain and transport particles of sediment exceeds the locally available sediment supply (e.g. Howard, 1994). Using a form of basal shear stress, Howard and Kerby (1983) originally modeled detachment-limited bedrock channel erosion as a power-law function of drainage area (A) (a proxy for discharge) and stream gradient (S):

$$(1) E = KA^m S^n$$

where m and n are positive constants and K is known as the coefficient of erosion. Variables in equation 1 represent the specific relations (Whipple and Tucker, 1999):

$$(2a) m = (2ac/3)(1-b);$$

$$(2b) n = 2a/3;$$

$$(2c) m/n = c(1-b).$$

$$(3) K = k_e k_w^{-n} k_q^{n(1-b)} \rho^{3n/2} g^n$$

where a and k_e are related to the dominant erosion process, rock mass quality, and to some degree sediment load, b and k_w reflect the hydraulic geometry (width) and c and k_q depend on basin hydrology (discharge), ρ is the density of water and g is gravity.

The evolution of bedrock channel profiles is commonly written as a competition between rock uplift and erosion (Howard, 1994; Whipple and Tucker, 1999):

$$(6) \partial z / \partial t = U(x, t) - KA^m S^n$$

where $[\partial z / \partial t]$ is the time rate of change of bed elevation, U is the rock-uplift rate relative to a fixed base level and erosion rate is modeled as described above (Equation 1). For fluvial landscapes where erosion balances rock uplift everywhere along the channel (i.e. channel equilibrium) and under conditions of spatially uniform uplift, rock strength, and erosion process, the equilibrium channel gradient (S_e) decreases as a power function of drainage area according to the relation:

$$(7) S_e = (U/K)^{1/n} A^{-m/n}$$

In equilibrium channels if and only if conditions of uniform U and K exist, then the ratio of m/n sets the rate of change of channel gradient with drainage area and the coefficient $(U/K)^{1/n}$ dictates equilibrium profile gradient. Equation 7 can then be rewritten as:

$$(8a) S = k_s A^{-\theta}$$

$$(8b) k_s = (U/K)^{1/n}$$

$$(8c) \theta = m/n.$$

Equations 8b and 8c highlight two important channel indices: the steepness index (k_s) and the concavity index (θ). The channel “steepness” index (Figure 3) is a relative measure of channel gradient and is useful for comparison of profile gradient among multiple channels. Stream channel concavity (θ) is the downstream rate of change in slope with respect to drainage area (Figure 3). Theoretical predictions indicate that channel concavities should fall within a range of 0.30 – 0.60 given a uniform rock-uplift rate (independent of magnitude), rock erodibility, and climate (Roe et al., 2002; Whipple and Tucker, 1999). Regressions of channel gradient and drainage area data readily provide a direct estimate of both indices from stream profiles (Kirby and Whipple, 2001; Snyder et al., 2000).

Channel Longitudinal Profiles: Concavity and Gradient

The 44 western, low-uplift channels have concavity indices which range between 0.34 and 2.1 (Table 1) with an average and standard error of the mean of 0.83 ± 0.06 (Table 3), a value well above both the theoretically predicted range (0.30 – 0.60) and results published from other field sites (Kirby and Whipple, 2001; Snyder et al., 2000). Nine streams flowing entirely within the weaker Oligocene – Pliocene units along the lower flanks of the range, however, exhibit concavity values within the predicted range (mean concavity index of 0.48 ± 0.04). As an example, Venadito Canyon (#34: Figure 4) has a concavity of 0.4 ± 0.06 , whereas the main trunk (east fork) of El Capitan canyon (#38: Figure 4), which flows down from near the main drainage divide, has a concavity of 0.81 ± 0.03 (Figure 4; Table 1). Steepness indices for streams in the low-uplift region exhibit similar differences in response to transitions in rock strength (Table 3). Mean k_s values for channels developed within the weak rock units is 13.8 ± 4.0 , whereas the mean value is higher (23.9 ± 1.9) for those streams crossing a transition in rock strength.

Within the high-uplift region, all channels are developed within weak Oligocene – Pliocene units (Table 2). The 6 channels in the eastern region of the study area exhibit a mean concavity of 0.6 ± 0.09 (Table 3), similar to channels restricted to uniform lithology in the west. The mean steepness index for the high-uplift stream is 26.1 ± 4.9 , indicating that channels are ~2-3 times as steep as low-uplift streams in analogous weak rock units (Figure 5).

Channel Width

As rivers adjust to spatial or temporal variations in vertical tectonic rates, channel width is likely to be an adjustable channel parameter (Lave and Avouac, 2000; Schumm et al., 2000). A narrower channel should, in theory, focus more erosive energy on a small part of the bed; thereby facilitating more rapid incision. Detailed field surveys of high-flow channel width were carried out in this field site in order to document width variations.

Classically, hydraulic geometry relations describe a downstream trend in channel width (w) with discharge (Q):

$$(9a) \quad w = k_w Q^b$$

where k_w is a dimensional coefficient and b is the width-scaling exponent. Although originally defined by an empirical relationship observed in alluvial rivers, e.g. Leopold and Maddock (1953), similar width scaling has been observed more recently in bedrock rivers as well (Montgomery and Gran, 2001).

Drainage area is often used as a proxy when discharge data is not available. Equation 9a is then rewritten as:

$$(9b) \quad w = k_w k_q^b A^{cb} = k'_w A^{b'}$$

In this field site, channel width data was collected along dominantly bedrock reaches within a tributary to El Capitan stream (low uplift) and Madranio creek (high uplift). Regression analysis of data collected yields k'_w of 0.08 and b' of 0.33 whereas data from Madranio creek (high-uplift region) yields k'_w of 0.007 and b' of 0.42 (Figure 6, Equation 9b); both are similar to observed scaling in bedrock channels (Montgomery and Gran, 2001; Snyder et al., 2003). In order to effectively compare channel widths at specific drainage areas between these two profiles, we fit a regression through each data set with $b = 0.4$. The best-fit width coefficient for the fixed regression for the low-uplift tributary is 0.032 and 0.012 for Madranio creek within the high-uplift region. These data show that the high-uplift channel is significantly (~ 3 times) narrower than the El Capitan tributary at the same drainage area (Fig. 6). Differences in width between the two uplift regions are interpreted to be a result of an increase in rock-uplift rate in the eastern part of the study area.

Channel Gradient and the Role of Sediment

A comparison of channel gradients between the control set of streams restricted to weak substrate and the lower reaches of channels that cross the documented rock-strength transition (such as the main trunk of El Capitan stream) yield a very interesting result. Despite the larger upstream drainage areas, gradients on the lower reaches of high-concavity channels are steeper than gradients on channels developed entirely within the weak substrate (Fig. 7). This observation is strikingly inconsistent with the topographic predictions of a

simple bedrock incision model, where larger drainage areas (and thus, discharge) should result in lower gradients within the same substrate (Whipple and Tucker, 1999).

One reasonable hypothesis for this behavior is that channel gradients along the high-concavity channels are set by the need to convey sediment derived from resistant bedrock upstream (e.g. Sklar and Dietrich, 1998). The high-gradient lower reaches of these channels are mantled with a sporadic blanket of coarse (>20 cm) boulders, most of which comprise resistant sandstone exposed on the upper mountain flanks. Alluvial fan deposits developed at the present-day coastline indicate that most of the rock material is transported through the length of the channels. In contrast, coarse bedload is uncommon in channels restricted to weak rocks (and without a source of allochthonous sediment). Essentially, the transition from hard to weak rocks appears to drive streams into a transport-limited state where the size and strength of coarse bed material dictates local channel gradient.

References

- Dibblee, T.W., Jr., Regional geology of the Transverse Ranges province of Southern California, in *Geology and Mineral Wealth of the California Transverse Ranges*, edited by D.L. Fife, and Minch, J. L., pp. 27-39, South Coast Geological Society, Inc., 1982.
- Howard, A.D., A detachment-limited model of drainage basin evolution, *Water Resources Res.*, 30, 2261-2285, 1994.
- Howard, A.D., and G. Kerby, Channel changes in badlands, *Geological Society of America Bulletin*, 94, 739-752, 1983.
- Kirby, E., and K. Whipple, Quantifying differential rock-uplift rates via stream profile analysis, *Geology*, 29 (5), 415-418, 2001.
- Lave, J., and J.P. Avouac, Active folding of fluvial terraces across the Siwaliks Hills, Himalayas of central Nepal, *Journal of Geophysical Research-Solid Earth*, 105 (B3), 5735 - 5770, 2000.
- Leopold, L.B., and T. Maddock, Hydraulic geometry of streams and some physiographic implications, *U. S. Geological Survey Professional Paper*, 252, 57, 1953.
- Montgomery, D.R., and K.B. Gran, Downstream variations in the width of bedrock channels, *Water Resources Research*, 37 (6), 1841-1846, 2001.
- Roe, G.H., D.R. Montgomery, and B. Hallet, Effects of orographic precipitation variations on the concavity of steady-state river profiles, *Geology*, 30 (2), 143-146, 2002.
- Schumm, S.A., J.F. Dumont, and J.M. Holbrook, *Active Tectonics and Alluvial Rivers*, 276 pp., Cambridge University Press, Cambridge, 2000.
- Sklar, L., and W.E. Dietrich, River longitudinal profiles and bedrock incision models: stream power and the influence of sediment supply, in *River over rock: Fluvial processes in bedrock channels*, edited by E.E. Wohl, pp. 237-260, American Geophysical Union, Washington, D.C., 1998.
- Snyder, N.P., K.X. Whipple, G.E. Tucker, and D.J. Merritts, Landscape response to tectonic forcing: digital elevation model analysis of stream profiles in the Mendocino triple junction region, northern California, *Geological Society of America Bulletin*, 112, 1250-1263, 2000.
- Snyder, N.P., K.X. Whipple, G.E. Tucker, and D.J. Merritts, Channel response to tectonic forcing: field analysis of stream morphology and hydrology in the Mendocino triple junction region, northern California, *Geomorphology*, 2003.

Whipple, K.E., E. Kirby, and S.H. Brocklehurst, Geomorphic limits to climate-induced increases in topographic relief, *Nature*, 401, 39-43, 1999.

TABLE 1: STREAM CHANNEL DATA

No.	Channel Name	Channel Length (km)	Drainage Area (km ²)	Channel Type*	m/n ⁺	k _s ⁺⁺
1	Wood Canyon (west)	7.4	5	T	0.97 +/- 0.15	11.3
2	Wood Canyon (east)	6.6	7	T	0.51 +/- 0.12	14.2
3	Damsite Canyon	6	4.5	T	1.6 +/- 0.26	16.5
4	Canada del Cojo	7	9	T	0.65 +/- 0.10	19.3
5	Canada del Cementerio	4.6	2.5	T	0.62 +/- 0.13	11.6
6	Canada del Gato	4	2.5	U	0.58 +/- 0.06	18
7	Barranca Hondo	4.9	3	T	1.1 +/- 0.11	23.5
8	Canada de la Llegua	4.5	2.5	T	0.87 +/- 0.09	17
9	Arroyo San Augustin	5.2	5.5	T	0.85 +/- 0.06	21.7
10	Canada del Pescado	3.9	1.5	T	0.74 +/- 0.10	13.6
11	Canada de las Agujas	5.4	4	T	0.87 +/- 0.09	18.4
12	Arroyo el Bulito (west)	7	7.5	T	1.8 +/- 0.30	21.4
13	Arroyo el Bulito (east)	6	7	T	2.1 +/- 0.30	22.6
14	Canada del Agua	4.6	3.5	T	0.89 +/- 0.11	16.1
15	Canada del Coyote	3.4	0.5	U	0.35 +/- 0.11	8.75
16	Canada del Sacate (west)	4.6	4.5	T	0.72 +/- 0.06	18.5
17	Canada del Sacate (east)	4.6	4.5	T	0.86 +/- 0.08	19.3
18	Canada de Cuarta	5.2	5	T	0.92 +/- 0.10	18.7
19	Canada de Alegria (west)	6.2	10	T	0.54 +/- 0.06	17.9
20	Canada de Alegria (east)	6	10	T	0.6 +/- 0.06	17.1
21	Canada del Agua Caliente	6	8	T	0.55 +/- 0.08	14.8
22	Canada San Onofre	4.6	6.5	T	0.38 +/- 0.01	53.3
23	Canada del Molino	5.4	4.5	T	1.2 +/- 0.14	39.8
24	Canada de la Posta	4	3	T	0.71 +/- 0.13	38.9
25	Canada de Gallina	1.1	0.2	U	0.48 +/- 0.46	14.2
26	Arroyo Hondo	6.2	10.5	T	0.40 +/- 0.06	37.7
27	Canada de la Huerta	1.4	0.4	U	0.41 +/- 0.09	13.1
28	Canada de la Pila	3.2	1.5	U	0.67 +/- 0.07	19
29	Arroyo Quemado	6.3	9	T	1.9 +/- 0.12	40.1
30	Tajiguas Creek	8.9	12	T	1.6 +/- 0.22	21.5
31	Aguajito Canyon	6.4	12	U	0.53 +/- 0.05	15.8
32	Canada del Refugio	8	12	T	1.2 +/- 0.14	32.4
33	Refugio east fork	10	12	T	0.90 +/- 0.14	47.5
34	Venadito Canyon	6.2	6	U	0.40 +/- 0.06	10.6
35	Las Flores Canyon	7	4	T	0.76 +/- 0.06	21.4
36	Canada del Corral	10.5	11	T	0.58 +/- 0.05	43.8
37	El Capitan Canyon (west)	9.5	12.5	T	0.97 +/- 0.11	51.9
38	El Capitan Canyon (east)	10.2	12.5	T	0.81 +/- 0.03	34.5
39	Canada del Destiladera	3.6	2.5	U	0.34 +/- 0.07	13.9
40	Las Llagas Canyon	6.3	8.5	T	0.77 +/- 0.08	22.7
41	Gato Canyon	10.7	10	T	0.88 +/- 0.06	39.3
42	Las Varas	7.5	9	T	0.69 +/- 0.04	20.9
43	Dos Pueblos (lower fork)	12	9	U	0.54 +/- 0.06	10.9
44	Dos Pueblos (east)	12.1	11	T	0.55 +/- 0.07	46.7
48	Los Sauces Creek (west)	8.5	3.5	U	0.37 +/- 0.06	24.1
46	Los Sauces Creek (east)	8.5	9	U	0.56 +/- 0.07	19.7
47	Javon Canyon	6.3	8	U	0.55 +/- 0.12	27
48	Madranio Creek	5.2	7.5	U	0.54 +/- 0.06	29.4
49	Padre Juan (west)	6.9	9	U	0.58 +/- 0.05	25.4
50	Padre Juan (east)	6.9	9	U	1 +/- 0.06	30.9

Streams in gray shading are within the high-uplift region ($\sim 5 \text{ mm yr}^{-1}$), all others are within the low-uplift region ($\sim 0.75 \text{ mm yr}^{-1}$)

* T = channels that cross a transition from hard to weak rocks, U = channels that erode only rocks of uniform strength

+ m/n = the channel concavity or curvature of the longitudinal profile

++ k_s = steepness index, calculated for each stream using a reference concavity of 0.4

TABLE 2: RELATIVE ROCK STRENGTH DATA

Rock Unit	El Capitan – low uplift			Madranio – high uplift		
	mean “R”	mode	n	mean “R”	mode	n
Pico	N/A	N/A	N/A	15.2 +/- 1.4	15	23
Rincon	below 10	N/A	20	below 10	N/A	20
Monterey	34.9 +/- 6.4	35	40	30.8 +/- 11	32	47
Sisquoc	N/A	N/A	N/A	below 10	N/A	20
Vaqueros	22.7 +/- 4.1	20	144	N/A	N/A	N/A
Sespe	20.9 +/- 5.9	16	290	N/A	N/A	N/A
Gaviota	34.2 +/- 8.6	34	341	N/A	N/A	N/A
Sacate	55 +/- 3.5	55.5	27	N/A	N/A	N/A
Matilija	42.1 +/- 9.6	40	57	N/A	N/A	N/A

Note: all measurements were taken with a Schmidt hammer device on exposed Rocks within or near the channel bed. “N/A” indicates that the rock unit either does not exist in the uplift region or that it was impossible to sample.

TABLE 3: SUMMARY OF MEAN CHANNEL INDICES

Channel Description	# of streams	Concavity* (m/n)	Steepness Index* (k _s)
low uplift (all rock strengths)	43	0.83 (+/- 0.42)	23.9 (+/- 12.3)
low uplift (weak rocks only)	8	0.48 (+/- 0.11)	13.8 (+/- 3.42)
low uplift (transition in strength)	35	0.92 (+/- 0.42)	26.5 (+/- 12.4)
high uplift (weak rocks only)	6	0.6 (+/- 0.21)	26.1 (+/- 4)
weak rocks only (both uplift regions)	14	0.53 (+/- 0.16)	

* mean values and standard error (parentheses) are given. Uncertainties reflect 1 σ standard deviation of the mean.

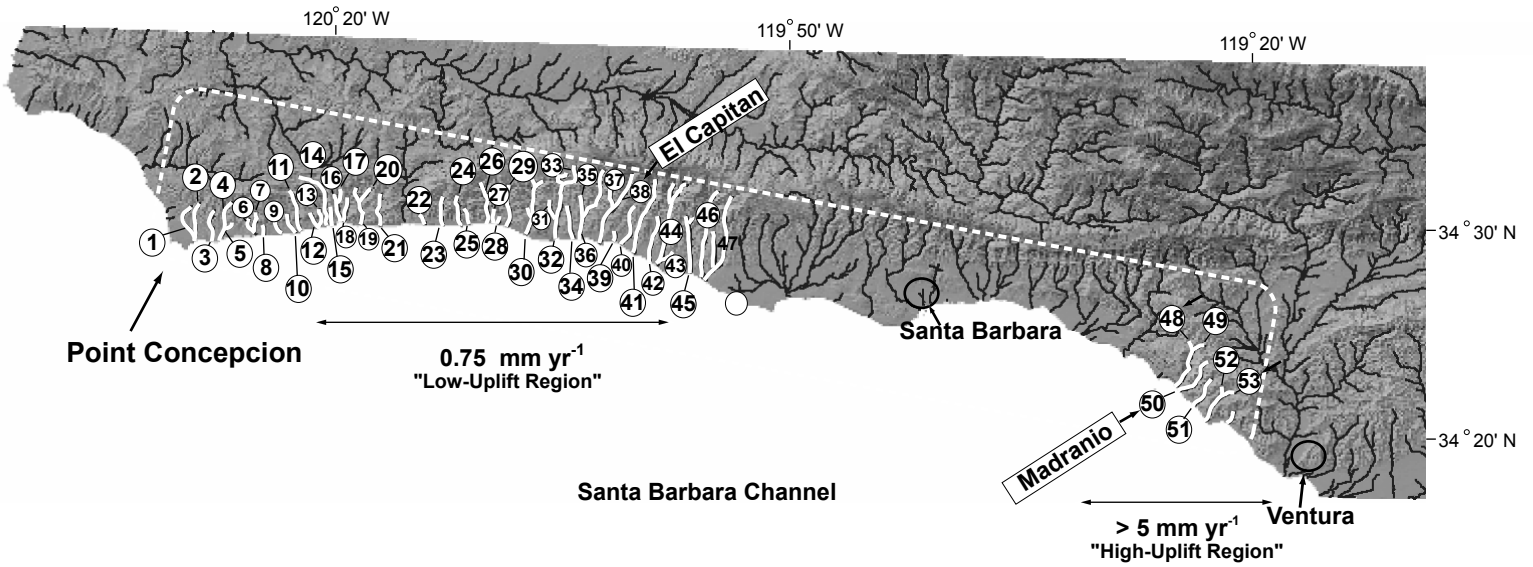


Figure 1. Drainage network of the Santa Ynez Mountains. Streams used in study calculations are numbered. El Capitan Stream (FOP stop) is labeled. Rock-uplift rates derived from marine terrace data are also shown. Note that rock-uplift rates are low ($\sim 0.75 \text{ mm/yr}$) in the west ("low-uplift region") relative to the high rate toward the east near Ventura ($\sim 5 \text{ mm/yr}$) ("high-uplift region").

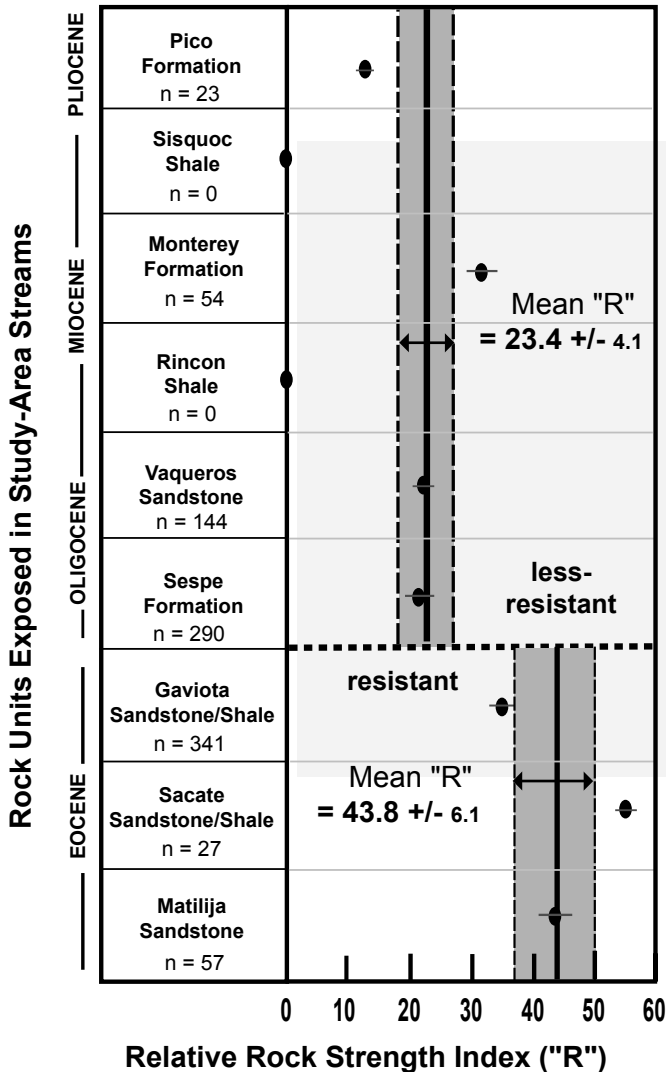


Figure 2. Stratigraphic column of rock units exposed in study-area streams with results of Schmidt hammer test of intact rock strength. The dash line indicates the boundary of the suite of younger, generally less-resistant rocks (the Monterey formation is an exception) and a suite of older, more-resistant rocks that cap the range.

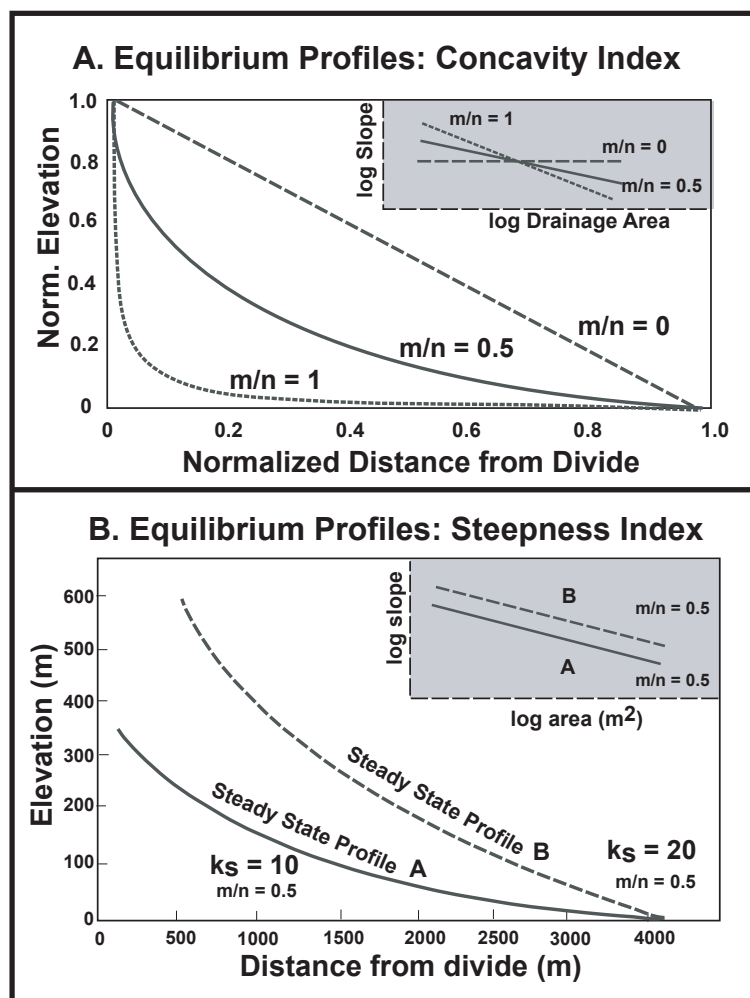


Figure 3. Schematic diagrams of key parameters derived from equilibrium profiles (modified from Whipple and Tucker, 1999). (A) Longitudinal stream-profile concavity is set by the m/n ratio (concavity index). Upper inset shows different m/n values in slope-area space and the main graph shows the same three ratios in elevation-distance space. (B) Two profiles with varying steepness indices. Note that, although stream B is twice as steep as stream A, they have the same concavity.

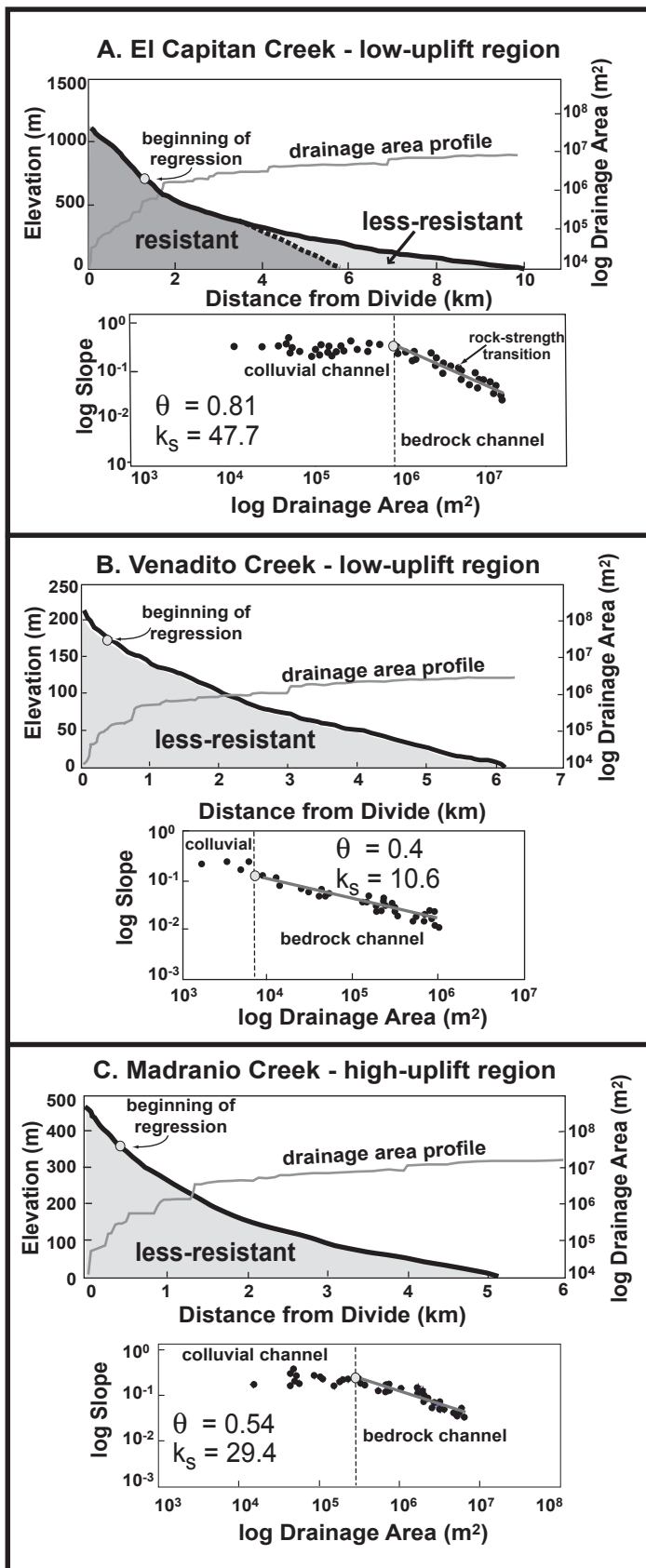


Figure 4. Examples of channel topographic data derived from a digital elevation model (A) El Capitan creek (#38), a low-uplift stream that crosses both resistant and less-resistant rocks, (B) Venadito creek (#34), a low-uplift stream draining only weak rocks, and (C) Madranio creek (#51), a high-uplift stream also eroding only weak rocks. For each stream, the top panel shows the channel profile (black) and drainage area (gray) as a function of downstream distance. The white circle indicates the beginning of the fluvial part of the channel and the linear regression. The lower panel contains the slope and drainage area-data with regression lines. Slopes were calculated at 5-m vertical elevation intervals.

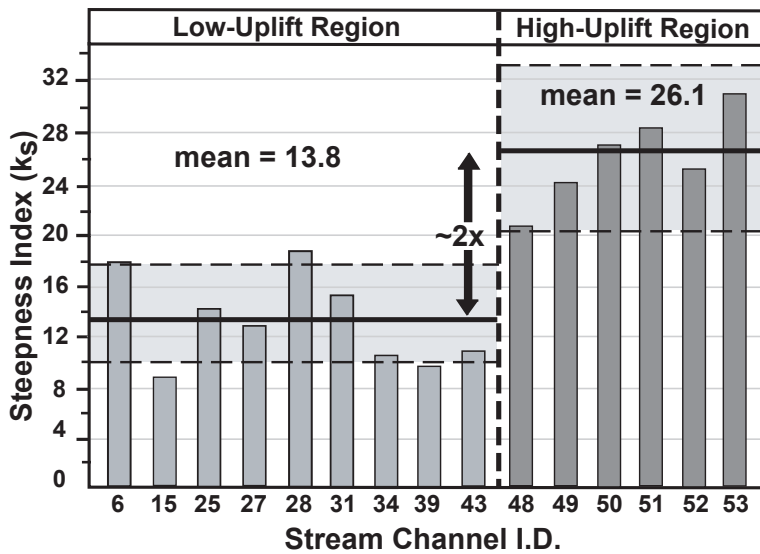


Figure 5. Steepness index (k_s) for all of the weak-rock only channels (identified by stream-channel I.D. #: Figure 1). Mean values and standard error of the mean for each regional dataset indicate an ~ 2 fold increase in k_s in the high-uplift streams.

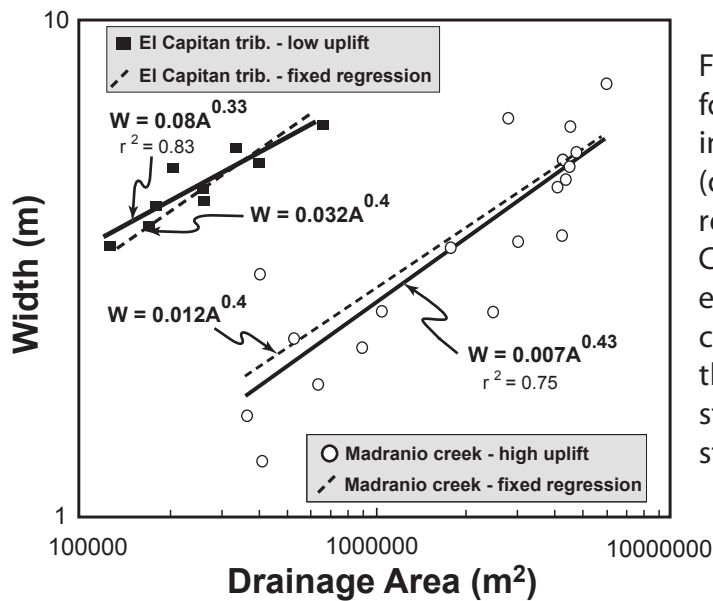


Figure 6. Channel width versus drainage area data for a tributary to El Capitan stream (solid square) in the low-uplift region and Madranio stream (open circle) in the high-uplift region. Power-law regressions through each data set are shown. Channel data for each stream were fixed with an exponent of 0.4 to allow direct comparison of channel width between the two streams. Note that for similar drainage areas, the low-uplift stream is ~ 2.5 times narrower than the high-uplift stream.

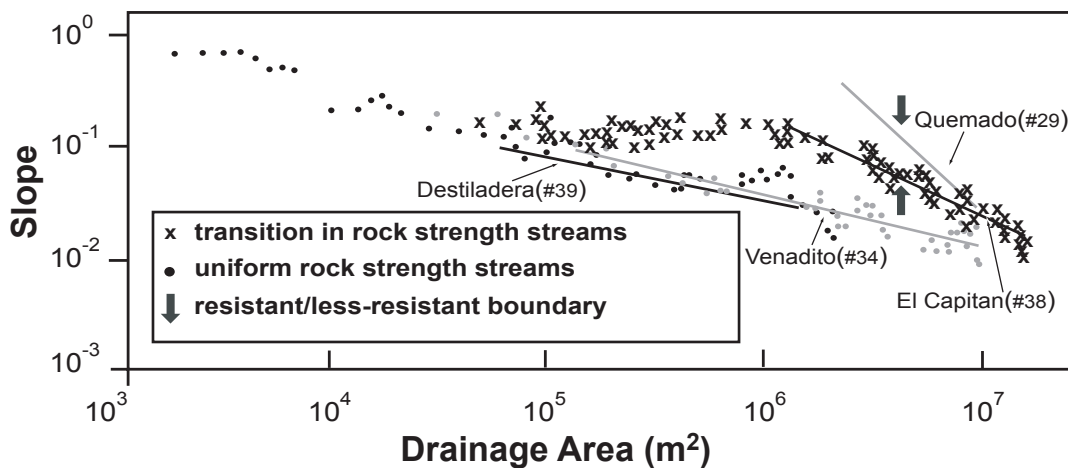


Figure 7. Comparison of channel gradients of low-uplift streams traversing a transition in rock strength (represented by an x) with those confined to weaker rocks (represented by a circle). Arrows indicate where transitions from resistant to less-resistant rocks occur. Note that Quemado (#29) and El Capitan (#38) (rock-strength transitional streams) are steeper than both Venadito (#34) and Destiladera (#39) (streams experiencing uniform rock strength) at the same drainage areas.

DAY 2: EAST BEACH TO LOON POINT BEACH HIKE

12:00 p. m. – 5:00 p. m.

ACTIVE TECTONICS OF THE SANTA BARBARA FOLD BELT, SANTA BARBARA, CALIFORNIA

L. D., Gurrola, E. A. Keller, J. Chen, Lewis Owen, and M. Bell

INTRODUCTION

The Santa Barbara Fold Belt (SBFB) is an active fold belt comprised of generally en echelon folds and reverse (thrust) faults, some of which are blind, on the coastal piedmont of the Santa Ynez Range of the western Transverse Ranges (Fig. 1). These blind reverse and thrust faults are termed seismic sources which warp, tilt, fold and/or fault late Pleistocene-Holocene marine terraces, terrace deposits and alluvial fans. The fold belt is nearly parallel to the coastline, but individual folds are sufficiently oblique to the coast to provide sea cliff exposures in the sea cliff, demonstrating the relationship between faulting and folding.

From east to west (Carpinteria to Goleta), the SBFB is an area of active folding and uplift in a landscape dominated by emergent marine terraces preserved on the flanks of folds (Fig. 2). Anticlinal folds (some with buried faults and some with faults exposed at the surface) are geomorphically expressed as linear topographic highs and ridges, often displaying fold scarps (Gurrola and Keller, 1997a). Linear topographic highs on the Santa Barbara piedmont are mostly the expression of active anticlines. Conversely, synclinal folds are expressed as onshore basins such as coastal sloughs (esteros) or lowlands (Gurrola and Keller, 1997a). At several locations, emergent marine terraces are intensely faulted and folded into hanging wall anticlines and footwall synclines.

Landform assemblages formed on the Santa Barbara Fold Belt (SBFB) permits detailed study to better understand the role of active folding and related (blind) faulting and the resultant earthquake hazards (Fig. 2; Table 1). This guidebook is the result of several theses which investigate the role of active folding in the topographic development of fold belts and the lateral propagation of folds as they develop through time. The SBFB is particularly well-suited for these studies because many of the folds deform marine platforms of known ages, allowing us to calculate rates of tectonic processes during the late Pleistocene and Holocene.

HISTORIC SEISMICITY

Active folding and (blind) reverse faulting in the SBFB present a significant, yet still largely unknown earthquake hazard to the 200,000 people living in Santa Barbara County. Historic seismicity in the SBFB, shown on Table 2, indicates that most of the seismic activity located south of the Santa Ynez Range. A seismic map of the probability of seismic shaking for southern California, based upon historic seismicity suggests the Santa Barbara area can expect 3 to 4 earthquakes per century with shaking that will exceed 0.2 g, the level of activity where damage to older buildings begins (S.C.E.C., 1995).

The historic record of the Santa Barbara area extends back to the establishment of the missions Purisima (Lompoc, California) and Santa Barbara during the late 18th century (Table 2). Since the early 19th century, three large earthquakes have occurred in the SBFB including the 1812, the 1925, and the 1927 events (Sylvester and Mendes, 1981). Seismic data for the 1812 and 1925 events are scarce as seismograph stations were non-existent for the 1812 rupture and only a few were operating in 1925. Those seismograph stations determine the location of the epicenter for the 1925 rupture within a 60 km radius. The 1812 earthquake is the earliest of the three earthquakes, and probably had a magnitude of ~ M_w 7.0. This earthquake produced regional damage throughout northern and southern Santa Barbara County. The seismic source was most likely in the SBFB and perhaps on either the blind decollement, the SYF, the Oak Ridge, the North Channel Slope, or the Pitas Point faults.

A large earthquake occurred near the City of Santa Barbara on 26 June, 1925 and produced extensive damage to the downtown and surrounding areas (Willis, 1925). Estimated modified Mercalli (MM) intensities were approximately MM VII in the downtown area, whereas maximum intensities were approximately MM VIII-IX on the La Mesa hills (Olsen, 1972).

Preceding the 1925 event, voluminous amounts of petroleum were observed along Santa Barbara beaches and a moderate-sized foreshock occurred at 3:27 a.m. The main shock followed at 6:42 a.m. and had

a duration of about forty seconds (Willis, 1925). Olsen and Sylvester (1975) believe that the intensity of shaking indicates a maximum magnitude of $M_{6.3}$ for the main earthquake, however Stein and Hanks (1998) calculate a moment magnitude of M_w 6.8. The fault that ruptured in 1925 has not been identified, but either an offshore or onshore source is possible based on intensity of shaking.

The 1978 M_w 5.9 Santa Barbara earthquake produced localized, moderate damage in Goleta. Following the 1978 event, seismograph stations were installed throughout the Santa Barbara region to gather aftershock data, however the location and geometry of the epicenter remain in dispute due to disagreement among seismologists (e.g., Corbett and Johnson, 1982; Yeats and Olson, 1984). Yeats and Olson (1984) believe that the 1978 M_w 5.9 Santa Barbara earthquake occurred on a south-dipping reverse fault, whereas Corbett and Johnson (1982) argue for a nearshore, low-angle, north-dipping fault. Evidence of localized damage in the areas of the UC Santa Barbara campus and Goleta, California supports the epicenter location of Corbett and Johnson (1982).

TECTONIC FRAMEWORK OF THE SANTA BARBARA FOLD BELT

West of the Ventura Fold Belt (VFB), the SBFB is formed on the south limb of the regional Santa Ynez anticlinorium (SYA). Namson and Davis (1992) argue the anticlinorium is related to a low-angle, north-dipping ramp of a detachment or decollement at 10-12 km depth. If this hypothesis is correct, then slip on the decollement is transferred to the north-verging structures (backthrusts) on the coastal piedmont (including offshore structures) of the SBFB. The west-trending Santa Ynez anticlinorium forms the principal topographic feature of the SBFB. The tectonic framework of the fold belt on the coastal piedmont consists of three sets of faults: 1) west-striking, oblique (reverse-left) slip; 2) northwest-striking oblique (reverse-left) slip faults; and 3) northeast-striking tear faults or lateral ramps (Gurrola et al., 1997a; 1996a).

The 70 km long, south-dipping MRFS is the principal fault on the coastal piedmont that extends from Ellwood beach in Goleta eastward to the Ojai Valley where it is truncated by the north-dipping San Cayetano fault. The MRFS is subdivided into geometric, geomorphic, and structural segments including, from west to east, the More Ranch, the Mission Ridge, and the Arroyo Parida segments (Fig. 2; Table 1) (Gurrola et al., 1997a; Gurrola and Kamerling, 1996b). The 15 km long More Ranch segment strikes through the Goleta basin separating the Goleta and Santa Barbara onshore basins. The More Ranch fault uplifts, from west to east, the Ellwood, the UC Santa Barbara-Isla Vista, and the More Mesa anticlines in the western fold belt.

The 17 km long, blind Mission Ridge segment is the westward, left-step continuation of the More Ranch segment where it truncates the northwest-striking Mesa and San Jose faults. The trace of the Mission Ridge fault is delineated through the urban corridor of Santa Barbara based on fold or fault scarps. The fault forms the Mission Ridge anticline which is the most prominent tectonic feature on the coastal piedmont and the blind fault dips to the south beneath the city of Santa Barbara. The 32 km Arroyo Parida segment strikes north of Carpinteria uplifting the Arroyo Parida ridge in the eastern fold belt and is subdivided into west and east subsegments that are 17 km and 15 km long, respectively. A second set of faults consists of northwest-striking reverse (left-slip?) which form discontinuous folds that are subsidiary to the MRFS. These include the San Jose, the San Pedro, the Lavigia, and the La Mesa faults that are typically several kilometers in length and are abruptly truncated by the MRFS (Table 1).

A third set of faults identified on the coastal piedmont include northeast-striking strike-slip faults that strike at a high-angle to the MRFS and northwest-striking faults (Gurrola and Keller, 1997b; Gurrola and Kamerling, 1996b; Gurrola et al., 1996a). Segments of the MRFS and the northwest-striking faults are defined by similar geometric, geomorphic and structural characteristics. Petroleum data indicates subsurface vertical displacement of Tertiary units for the west- and northwest-striking faults (Olson, 1982; Jackson and Yeats, 1982), however, the mostly blind faults produce folds in the overlying Pleistocene sedimentary units. These sedimentary units deform as fault-propagation folds with hanging wall anticlines (or monoclines) and footwall synclines. In some cases, subsidiary structures such as bending moment faults have propagated up through the fore- and backlimbs of anticlinal folds such as the Ellwood and the Mission Ridge anticlines.

STRUCTURAL STYLE OF QUATERNARY DEFORMATION

Folding and reverse faulting accommodate crustal shortening of the western Transverse Ranges Province. In the SBFB, the amplitude of synclinal basins are an order of magnitude greater than anticlinal folds resulting in relatively deep basins (0.5-1 km) in contrast to anticlines that form moderate (0.05 - 0.25 km) topographic highs.

Topographically, well-expressed folds in the SBFB along with natural and trench exposures allow for limited 3D mapping and analysis of surface and shallow fold deformation. Subsurface data integrated from Jackson and Yeats (1982) and Olson (1982) provide deeper subsurface analysis important to understanding the style of folding. The principal style of fold deformation documented is fault-propagation folding and monoclinical folding associated with basement compressive deformation (Gurrola and Keller, 1997b).

Fault-propagation folds initially develop as an asymmetric anticline-syncline pair formed as the result of displacement on an initially buried reverse fault that propagates to the surface (Fig. 3a) (Suppe, 1985; Suppe and Medwedeff, 1984 and 1990). Subsequent shortening locks up the fold and the propagating reverse fault typically ruptures through the synclinal axis resulting in a faulted hanging wall anticline and foot wall syncline. With subsequent slip, either the syncline or anticline may be faulted away. A growth wedge may form on the forelimb fold scarp that is progressively rotated with faulting.

Basement involved compressive folds form on the hanging wall of thrust ramps as the result of fault propagation and slip producing a monoclinical fold in overlying, stratified cover (Narr and Suppe, 1994). This model involves two stage evolution where an initial phase of layer parallel contraction is followed by later phase of layer parallel extension (Fig. 3b).

The More Ranch fault exposure in the Ellwood seacliff is similar to the basement involved fold deformation model of Narr and Suppe (1994). Late Pleistocene marine terrace sediments form a drape fold and are the result of faulting of Miocene basement rock. The near vertical limb of the monocline is produced by the uplifted block of Monterey and progressively rotates with continued slip.

STRATIGRAPHY

Pre-Quaternary Stratigraphy

Pre-Quaternary strata of the SBFB consist of a section of Eocene through Pliocene rocks that were deposited in a continental margin setting (Dibblee, 1966). These rocks include from oldest to youngest: Coldwater Sandstone; Sespe Formation; Vaqueros Sandstone; Rincon Formation; Monterey Formation; and Sisquoc Formation (Table 3). The Sespe, the Rincon, the Monterey, and the Sisquoc Formations typically form the rocks of the mountain slopes and basement rocks of the coastal piedmont. In some cases, these rocks are locally uplifted in the core of anticlines and along faults, as well as forming the bedrock of which late Pleistocene wave-cut platforms are eroded on.

Quaternary Stratigraphy

Quaternary strata of the SBFB consist of a sequence of Pleistocene and late Pleistocene marine and non-marine strata. The Pleistocene sequences are deposited on, and unconformably overlie pre-Quaternary strata on the coastal piedmont (Table 3). The Quaternary units, from oldest to youngest, include the Santa Barbara Formation, the Casitas Formation, and late Pleistocene-Holocene marine terrace, fanlomerate, alluvial, and fluvial deposits.

Santa Barbara Formation

The Santa Barbara Formation is a shallow marine sequence primarily composed of sandstone and contains minor units of conglomerates, siltstones and claystones. Thickness of the Santa Barbara Formation ranges from 150 m to 625 m thick (Olson, 1982; ;1988a, 1988b). The Santa Barbara Formation is the basal Quaternary unit of the SBFB with poor age control. The Santa Barbara Formation overlies the 1.2 ma Bailey Ash in Ventura (Izett et. al., 1974; Olson, 1982), and the upper Santa Barbara Formation grades into a marine section of lower Casitas Formation.

Based on the maximum age for the Santa Barbara Formation of 1.2 ma, paleomagnetic analysis can indicate if deposition occurred during the Matayama (1.2 ma to 790 ka) or Bruhnes (post 790 ka to late Pleistocene) epoch by determining if magnetic polarization is reverse (Matayama) or normal (Bruhnes). Reconnaissance paleomagnetic analysis suggest normal remnant magnetization for sediments of the Santa Barbara Formation in the La Mesa Hills. Therefore, we believe the Santa Barbara Formation there is younger than 790 ka.

The paleomagnetic data indicate clockwise rotations that mostly range from approximately 0° to 30°, except for two samples (More Mesa) indicative of rotations up to 90°. The paleomagnetic data suggests that localized clockwise rotation occurs adjacent to faults and may be the result of reverse slip with a minor component of left-lateral strike-slip motion.

Casitas Formation

Based on the stratigraphic position with respect to the underlying Santa Barbara, the middle to late Pleistocene Casitas Formation is the result of alluvial deposition on an emergent coastal piedmont. The rocks typically range from pebbly sandstones to gravel and boulder conglomerates with minor units of siltstone and claystone. The basal Casitas Formation grades into the upper Santa Barbara Formation and is exposed in the sea cliffs at Summerland, California (Fig. 2). The basal units consist of regressive sequence of nearshore marine sandstones and siltstones.

Stratigraphic relations suggest the Casitas Formation is younger than the underlying Santa Barbara Formation (Dibblee, 1986a; 1986b; 1966; Olson, 1982). Reconnaissance paleomagnetic analysis of the basal section of the Casitas Formation sampled from the Loon Point and Ortega Hill folds indicate normal remnant magnetization. These paleomagnetic results are in agreement with results from the underlying Santa Barbara Formation and confirm Casitas deposition occurred during the Bruhnes epoch (post-790 ka). The Casitas Formation is older than the age of the overlying, late Pleistocene marine terrace, fanglomerate, and alluvial units and is most likely mid-Pleistocene in age. The Casitas Formation may represent a series of aggradation events related to paleo-sea level highstands (Bull, 1991).

Middle to Late Pleistocene Alluvial and Fluvial Units

Late Pleistocene alluvial fan deposition occurred across the coastal piedmont on south-flowing streams from the Santa Ynez Mountains. Alluvial strata unconformably overlie pre-Quaternary bedrock and Quaternary strata generally thicken southward. Elevated and dissected proximal facies sediments are present on the northern margin of the piedmont and consist of clast-supported fanglomerate deposits. The deposits generally range from coarse boulder to gravel conglomerate deposited as debris flows. Medial to distal facies deposits are present along the coastal margin and consist of matrix-supported alluvial deposits. The alluvial deposits generally range from silt-sandstone to cobble-gravel conglomerates.

Based on mapping and geomorphic expression, there are a minimum of five alluvial fan terrace surfaces and deposits identified on the coastal piedmont. The City of Santa Barbara is located on the oldest fan deposit termed the Rattlesnake Creek fan. Detailed analyses of cosmogenic-produced ^{21}Ne were done on detrital quartz from boulders sampled from five sites on the Rattlesnake Creek alluvial fan. An additional site was analyzed at 1.5 cm depth intervals to 26 cm depth to distinguish the present exposure depth attenuated cosmogenic ^{21}Ne production from prior exhumation, fluvial transport, and depositional environment inherited ^{21}Ne production. Modeled ^{21}Ne inheritance yields corrected ages for fan surface exposure of 59 to 139 ky. The age of the next younger alluvial fan deposit (70-100 ky) infers an age of 100 to 139 ky for the Rattlesnake Creek (Table 4).

Late Pleistocene fluvial strata are present along paleo-stream channels and present day stream channels as terrace deposits. Locally, strath terrace deposits are present on the limbs of anticlinal folds. The age of fluvial units are not well known, but are younger than the underlying Casitas Formation.

Late Pleistocene Marine Terrace Deposits

Marine wave-cut abrasion platforms in the SBFB are eroded on and form unconformities on both Pre-Quaternary and Quaternary strata such as the Sisquoc, the Monterey, the Santa Barbara, and the Casitas Formations. The abrasion platforms are commonly overlain by a thin, basal cobble to pebble conglomerate (boulder line) with overlying marine to non-marine terrace deposits. Typically, the terrace strata are approximately 2 m to 5 m thick and consist of a regressive sequence of nearshore facies marine sands and conglomerate (storm lag) deposits. The deposits grade upward into beach dune (aeolian) deposits and locally, estuarine deposits.

Terrace fossils preserved in pebble to cobble conglomerates or in rocky intertidal, fossiliferous units were sampled in order to obtain solitary corals for uranium series age-dating analysis. Two solitary corals from the UC Santa Barbara terrace and the Santa Barbara City College terrace were analyzed and yield estimated ages of 47 +/- 0.5 Ky and 70 +/- 2.0 Ky, respectively (Table 4). Radiocarbon and OSL data in association with oxygen isotope signatures of fossil mollusks contributed to establishment of the late Pleistocene chronology. Radiocarbon and luminescence samples were obtained from the Loon Point, Santa Barbara Cemetery, Santa Barbara Point, Santa Barbara City College, and UC Santa Barbara terraces (Table 4).

Holocene Alluvial, Fluvial, and Estuary Deposits

Holocene alluvial and fluvial deposits typically consists of clay rich, silt-sandstone and conglomerate units and either cap the late Pleistocene marine terraces or are present along paleo-stream and present day stream channels. An alluvial unit that caps the Loon Point fault terrace (discussed in a later section) is radiocarbon age-dated at 3,980 +/- 40 RCYBP (Table 4).

Holocene colluvial deposits generally consist of brecciated, matrix- to clast-supported conglomerates and are deposited at the base of fold, fault, and sea cliff scarps. Holocene fluvial units typically consist of clay, silt, and sand, and gravel to cobble conglomerate units deposited along active south-flowing stream channels on the coastal piedmont. Holocene estuarine deposits are present in the Goleta Slough, historic El Estero, and historic Las Salinas Estuaries. The estuarine deposits typically consist of organic-rich clays with interbedded silts and fine-grained sands are located in the coastal margins of the piedmont. Commonly, the sediments are poorly consolidated and are characterized by shallow ground water conditions that produce a high potential for liquefaction.

LATE PLEISTOCENE MARINE TERRACE CHRONOLOGY AND CORRELATION

The coastal piedmont of the SBFB is commonly characterized by the presence of marine terraces (Fig. 4). Marine terraces form at sea level highstands as wave-abraded platforms and are subsequently uplifted (Matthews, 1973 and Kern, 1977). In the SBFB, marine platforms are commonly uplifted and preserved on the flanks of active folds. Commonly, as tectonic uplift occurs, a thin veneer of (regressive) marine sands are deposited on the abrasion surface, which are later covered by alluvial and colluvial sediments. The shoreline angle (or strandline) is the intersection of the wave-cut platform with the sea-cliff, and, as it forms within one or two meters of mean (high) sea level (Lajoie et. al, 1979), it is a uniform reference to paleo-sea level (Fig. 4). A rate of uplift is calculated based on the elevation of a shoreline angle of an uplifted terrace and the numerical age of the wave-cut platform at the shoreline angle at the time the shoreline angle formed (usually a highstand) (Muhs, et. al, 1994).

Oxygen Isotope Studies

Studies in southern California have indicated that marine terrace mollusks of different ages preserve distinct isotopic signatures that may be used to correlate undated terraces to those of known age (Muhs, et. al, 1992; Trecker et. al, 1998a and 1998b). The method involves collection of fossil mollusks from dated "calibration sites" in order to establish characteristic isotopic signatures for mollusks from terraces of different ages (i.e. stage 3a, 5a, and 5e). Samples are then collected from undated sites in the same area, and the stable isotopic signatures of these mollusks are statistically compared with those of mollusks from the U-

series dated calibration sites. Changes in oxygen isotopic values during the late Quaternary are largely dependent on changing glacial ice volume and ocean temperatures. Mollusks from terraces formed during periods of relatively higher sea level and lower ice volume (warmer water), preserve lower oxygen isotopic values than those from terraces formed during periods of lower sea level with relatively higher ice volume (cooler water). The gastropod *Olivella biplicata* was chosen for analysis. It was found at most fossil sites, and occurs widely in late Pleistocene marine terrace deposits in California. *Olivella* shells are often the best preserved, and suffer the least damage as they are used by hermit crabs after death (Valentine, 1961). *Olivella* are small, compact, thick shelled monomineralic (aragonite) and grow year round, recording different isotopic values during each season, allowing for averaging of seasonal temperature effects. Finally, *Olivella* lives 8-15 years (Morris et al., 1980), making it possible to average out the effects of an El Niño year, or other climate phenomena that might otherwise skew the isotopic signature.

The oxygen isotope stratigraphy method of correlating terraces that we use requires that multiple samples be analyzed at each site to define an average signature and recognize outliers, as well as to record climate variability at the time of formation of each terrace. Statistical analysis is performed to quantitatively evaluate the data to assist in correlation of terrace deposits. Our results indicate that mollusks from the stage 5a terraces preserve a distinctly different isotopic signature than mollusks from the 3a terraces as well as from the modern wave-cut platform. These isotopic signatures are used to correlate terraces of unknown age to (U-series) dated calibration sites.

Chronology and Rates of Uplift

In the SBFB, we have numerical dates for two marine terraces based on U-series analysis of *Balanophyllia elegans*. The first emergent marine terraces at Isla Vista (UC Santa Barbara) and Bathhouse Beach (Santa Barbara City College) are dated at 47 \pm 0.5 ka and 70 \pm 2 ka, respectively. Due to the fact that terraces are discontinuous in the SBFB, it is necessary to correlate terraces of known age to those of unknown age across changes in topography and structural features (Fig. 5). Often, the shoreline angle is buried by non-marine colluvium and alluvium. However, once elevations of shoreline angles are measured, and uplifted marine platforms are correlated to paleo-sea levels, rates of uplift are calculated.

Establishment of the marine terrace chronology is necessary to estimate the local, vertical rate of surface uplift. Age dating of terrace fossil fauna directly overlying the abrasion platform determines a minimum age of platform formation. Commonly along the California coast, first emergent marine terraces are formed during oxygen isotope stage 5 (80 ka to 125 ka) paleo-sea level highstands (Muhs et al., 1994). However, terraces formed during the stage 3a (45 ka) and 3c paleo-sea level highstands are present along the Santa Barbara and Ventura coasts (Gurrola et al., 1997a; 1997b; Gurrola et al., 1996b; Lajoie et al., 1982). The presence of oxygen isotope substage 3a (45 ka) terraces in the SBFB suggests a high rate of surface uplift exceeding 1 m/ky (Table 4).

Marine terraces are not continuous across the SBFB. As a result, it is necessary to correlate terraces of known age to those of unknown age across changes in topography and change of structure (Fig. 5). Adjacent flights of terraces of known and unknown age are correlated by several methods including numerical age (U-series, ^{14}C , OSL) of terrace fossils and oxygen isotopic signatures of terrace fossils to assign uplifted marine platforms to isotopic stages 3 (45 ka or 60 ka) and 5 (80 ka to 105 ka or 125 ka) (Trecker et al., 1998a and 1998b).

Radiocarbon and/or OSL age-dates compliment the uranium series data for terraces where solitary corals were not found (Table 5). Radiocarbon and OSL samples were obtained from the first emergent terraces at Loon Point, Santa Barbara Cemetery, Santa Barbara Point, Santa Barbara City College, and UC Santa Barbara (Table 5). These age-dated terrace sites allow for the estimation of uplift rates for the first emergent terrace (Fig. 6).

EARTHQUAKE HAZARD

A principal objective of the earthquake hazard assessment is to estimate potential magnitudes of maximum expected earthquakes. In order to estimate potential magnitudes for specific faults in the SBFB, it is necessary to estimate potential rupture lengths or earthquake segments. Earthquake segments are defined by

aseismic or coseismic deformation and are unknown parameters for the most part (McCalpin, 1996) until an earthquake occurs. However, the identification of earthquake or rupture segments may be estimated by geometric, geomorphic, and structural fault segmentation.

Fault Segmentation

Geometric, geomorphic and structural segments of the MRFS including the More Ranch, Mission Ridge, and Arroyo Parida segments, are defined by changes in structural style, geometry, termination of folds, and geomorphology. Mapping of the tectonic geomorphology of reverse faults and related folds identified left-lateral displacement of folds at the More Ranch-Mission Ridge segment boundary, truncation of folds and faults at the Mission Ridge-Arroyo Parida segment boundary, and differential faulting, uplift and related folding at the west-east Arroyo Parida segment boundary. These segment boundaries coincide with faults that strike at a high-angle to the MRFS, termed cross faults (tear faults) (Fig. 2) (Gurrola and Kamerling, 1996b; Gurrola et al., 1996a). The northeast-striking, (cross) faults include, from west to east, the Goleta Point, the Fernald Point, and Rincon Point faults (Gurrola and Kamerling, 1996b; Gurrola et al., 1996a). The northeast-striking faults are subparallel to the present axis of compression and are favorably oriented to behave as tear faults during coseismic deformation.

Potential Rupture Segments

Some recent Santa Barbara area earthquakes show rupture zones limited by boundaries demonstrated to be steeply-dipping cross faults behaving as tears. Tear faults segment larger reverse (and thrust) faults transferring slip to adjacent thrust ramps. Tear fault segment boundaries in the western Transverse Ranges and Los Angeles may limit the size of rupture zones during an earthquake and therefore the potential magnitudes of expected earthquakes. These cross faults or segmentation boundaries are difficult to discover and map, and are often identified after a large earthquake on the basis of aftershock hypocenters and focal mechanism defining near-vertical strike-slip tear faults at the edges of the main shock rupture (Hauksson and Jones, 1989).

Tear faults may control the nucleation or termination of moderate to large earthquakes in the Los Angeles basin and the western Transverse Ranges. The 1994 Northridge earthquake nucleated at the intersection of a thrust ramp and tear fault rupturing up the ramp. Seismicity maps of the 1978 Santa Barbara earthquake (Corbett and Johnson, 1982) reveal an abrupt termination of the earthquake swarm on the eastern boundary. This boundary coincides with the northeast-striking Goleta Point fault and suggests that the fault may behave as a tear fault on the MRFS (Gurrola and Kamerling, 1996a; 1996b; Gurrola et al., 1997b) (Figs. 2).

Assuming that the MRFS is capable of producing earthquakes similar in magnitude to the 1994 Northridge and 1971 San Fernando earthquakes, then we can assume similar rupture lengths, area, and depth. We expect the MRFS would rupture along similar geomorphic/structural segments and the rupture may nucleate or terminate near a tear fault such as the Goleta Point, Fernald Point, or Rincon Point faults.

Earthquake Magnitudes

Wells and Coppersmith (1994) establish a regression relationship between surface rupture length and M_w (moment magnitude) for worldwide earthquakes for all types of displacement and faults. They conclude that the differences in earthquakes for different types of faults with similar rupture lengths were not great. The expected magnitude can be predicted from estimated rupture length. Yeats et. al (1997) argue that the area of rupture on a fault surface is primarily a function of length of rupture and can be used to estimate magnitudes of potential earthquakes.

Estimated moment magnitudes of future earthquakes of seismic sources in the onshore and offshore SBFB are listed on Table 1. Segments of the MRFS vary from 15 to 17 km in length (Fig. 7). Assuming these represent earthquake segments and using the method of Wells and Coppersmith (1994) we estimate a maximum M_w 6.5 earthquake for these segments. If multiple segments were to rupture, then a M_w 6.8 to 7.0

earthquake is possible (Fig. 7). If the entire length of the MRFS were to rupture in one coseismic event, then a **Mw 7** or greater is possible in the onshore SBF. We expect a rupture on the MRFS to; 1) nucleate or terminate near a tear fault, 2) involve at least a 15 to 17 km long fault segment, if not multiple segments and 3) be capable of producing a **Mw 6.5** or larger earthquake. Assuming a vertical, surface displacement of about 1.0 m per event and a faulting rate of 0.4 m/ky on any one segment of the MRFS, then the average return period is approximately 2.5 ky. Given the large number of sources a **Mw 6-7** event is likely to occur much more frequently in the SBF.

Potential maximum magnitudes of northwest-striking faults are shown in Table 1 and are lower in magnitude than along the MRFS due to their short, discontinuous surface lengths. Identified potential rupture lengths also take into account subsurface expression of faults in order to estimate the total potential rupture length. The Mesa and Lavigia faults are the principal northwest-striking faults that are capable of producing a **Mw 6** to 6.4 earthquake. Faults such as the Dos Pueblos (including the Glen Annie fault) and Los Carneros faults are capable of producing maximum magnitude earthquakes of about **Mw 6.0** to 6.1 (Table 1). Other northwest-striking faults are shown in Table 1 and are capable of producing earthquakes of about **Mw 5**.

Estimated earthquakes are consistent with historic seismicity in the SBF. In this century two events of **M 5.9** (1941 and 1978) occurred offshore of Carpinteria and Goleta, respectively. The 1925 **Mw 6.8** Santa Barbara earthquake is the 7th largest out of 40 earthquakes in southern California with **Mw** greater than 6.0 in the 20th century (Stein and Hanks, 1998). If this estimated magnitude is correct, then it released about 1.5 times the energy of the 1994 **Mw 6.7** Northridge earthquake and 2 times as much energy as the 1971 **Mw 6.6** San Fernando earthquake. However, Olsen and Sylvester (1975) report the earthquake to be a **M 6.3** based on their interpretation of seismic records. The 1994 **Mw 6.7** Northridge earthquake is a recent example of the most likely earthquake we expect in the future for the SBF. Unusually large onshore and/or offshore seeps of oil accompanied by small foreshocks may precede some large earthquakes by several hours in the SBF. Seeps were reported about 3 hours prior to the 1925 earthquake (Hamilton, 1969). Smaller **Mw 5-6** earthquakes evidently do not have such precursors or they are too small to be observed.

Potential for Coseismic Uplift and Surface Rupture

The onshore and offshore SBF is characterized by blind reverse and thrust faults that produce active anticlinal and synclinal folds. Although scarce, there is limited evidence for regional prehistoric coseismic uplift. A well-preserved remnant of a prehistoric marine platform is preserved at Goleta Point. The marine platform is about 2 m above mean sea level and is above modern wave-base most of the time. Pholad bore holes preserved in sea cliff exposures approximately 3 m above sea level are preserved along a 35 km length of coast from Goleta Beach to Gaviota, California and suggests regional coseismic uplift of 2 to 3 m. A **Mw 7+** earthquake on an unknown (offshore?) fault is necessary to produce 2 to 3 m of coastal uplift.

Based on the paleoseismic study of the More Ranch segment of the MRFS, a rupture on the More Ranch or Mission Ridge segments is likely to produce surficial uplift associated with bending moment faulting along the anticlinal fold crests. A single segment rupture may produce a surficial (hanging wall block) up to approximately 1 m along with up to 0.5 m of bending moment faulting. If a multiple segment earthquake were to occur on the MRFS, then surficial uplift may be as high as 2 to 3 m on the hanging wall block.

Liquefaction Potential

Areas of potential liquefaction identified in this earthquake hazard assessment include the Goleta Slough, Laguna Blanca, historic El Estero, and Las Salinas (presently known as the Andre Clark Bird Refuge). These areas consist of unconsolidated estuary and alluvial sediments with shallow ground water conditions and are characterized by poor engineering properties. The Goleta Slough and historic El Estero pose a significant liquefaction hazard to the communities of Goleta and downtown Santa Barbara, respectively (Fig. 2).

Goleta Slough is the onshore expression of the footwall syncline formed on the More Ranch segment of the MRFS. The estuary inlet was a natural deepwater harbor in historic times but has been backfilled with unconsolidated fluvial sediments. The historic estuary extended to the north to approximately south of highway 101 and was continuous with Devereaux Slough to the west. The shallow ground water table (1 m to

2 m depth) and fine-grained sediments that are primarily clays, silts and sands are susceptible to potential liquefaction from moderate and larger earthquakes.

Low-lying (20 to 25 m elevation) portions of the city of Santa Barbara are partially located on the historic estuary, El Estero. The estuary was filled in the early twentieth century, in part from debris from the 1925 earthquake. Presently, the site of the estero is characterized by shallow groundwater conditions. Typically estuarine sediments extend to depths of 17 m to 25 m and consist of loose, unconsolidated sands, silts, and clays (Campbell, Clements, and Calvert; pers. oral comm., 2000). As a result, the estuarine and fill sediments have unfavorable engineering properties and are susceptible to liquefaction from a moderate or larger earthquake.

Potential for Amplification of Shaking

The city of Santa Barbara is located in the onshore portion of the Santa Barbara basin and on the hanging wall of the south-dipping, Mission Ridge segment. The synclinal trough extends to depths of 0.3 km, possibly as much as 2 km, and is filled with saturated, unconsolidated sediments (Olson, 1982). Subsurface geometry of the Mission Ridge fault is largely unknown. If the fault is a shallow, low-angle thrust, then the fault may pose a greater shaking hazard to the city of Santa Barbara. Therefore, the city of Santa Barbara is subject to amplified ground shaking during an earthquake due to proximity and location of the Mission Ridge fault, the nature of the underlying structure and basin sediments, and surface effects of the hanging wall block similar to the 1994 Northridge earthquake.

CONCLUSIONS

In summary, the Santa Barbara urban corridor is in an area of known seismicity with an earthquake hazard similar to the cities of Ventura and Los Angeles. The city of Santa Barbara is located on the hanging wall of the blind Mission Ridge segment of the MRFS and is subject to amplified shaking during an earthquake as the result of free surface effects of the hanging wall and possible directivity of seismic waves. Parts of the downtown area are susceptible to liquefaction where the historic El estero (salt marsh) has been filled (in part from debris from the 1925 earthquake (Simmons, pers. comm., 1999) and is susceptible to a tsunami from an earthquake generated in the Santa Barbara Channel.

An earthquake on the MRFS or a fault offshore with a maximum M_w 6.5 to M_w 7.5, respectively will cause extensive damage to the Santa Barbara urban area inflicting several hundred million to a billion or more dollars of property damage, with several to several tens of deaths (depending on the time and day of the earthquake) and thousands of injuries. Associated secondary hazards include potential liquefaction, amplification of shaking, possible inundation by tsunami in the downtown Santa Barbara and Goleta Slough areas.

Based upon development of Quaternary stratigraphy and rates of uplift of wave-cut platforms in the Santa Barbara Fold Belt (SBFB) and investigation of active folding and faulting we conclude:

- First emergent marine terraces in the Santa Barbara Fold Belt range in age from 45 ka to 125 ka which correlates to oxygen isotope stages 3 or 5.
- Rates of surface uplift for marine terraces in the SBFB is approximately 1 to 2 m/ky. This is approximately an order of magnitude higher than was believed prior to our study.
- Tectonic geomorphology of the SBFB suggests that those areas that are topographically high are for the most part elongated hills which are active anticlines which conceal buried reverse faults. Topographically lower areas within the fold belt such as the alluvial fan and El estero areas of the city of Santa Barbara as well as the Goleta Valley and Carpinteria slough are areas of active subsidence associated with synclines.
- The most serious earthquake hazard to the Santa Barbara urban area is active faults and folds within the offshore portion of the Santa Barbara Fold Belt in the Santa Barbara Channel. Several sources including the North Channel Slope, Oak Ridge, and Santa Cruz Island faults are capable of producing an M_w 7.1 to 7.5 event, as is the Santa Ynez fault located about 10 km north of Santa Barbara.

- Faults in the onshore SBF are capable of producing earthquakes of about M_w 5 to 6.5. If several segments of the Mission Ridge Fault System were to rupture simultaneously an earthquake with magnitude of approximately M_w 7 is possible.
- The most likely scenario for a damaging earthquake to the Santa Barbara urban corridor would be a "Northridge-like event" with M_w approximately 6.5. The M_w 6.8 Santa Barbara earthquake in 1925 is the seventh largest out of 40 earthquakes in southern California with M_w greater than 6.0 in the 20th century and a repeat of that event would inflict several hundred million to a billion or more dollars of property damage with several to several tens of deaths (depending upon time of day the earthquake occurs).

ACKNOWLEDGMENTS

Research on the Santa Barbara Fold Belt is funded by the Southern California Earthquake Center award no. USC 572726 and the U.S.G.S National Earthquake Hazards Reduction Program award no. USGS 143HQ97GA-02978. Jim Chen (California Institute of Technology) conducted U-series analyses of sampled terrace corals. Mike Fuller (UC Santa Barbara), Bob Dunn (UCSB), and Chuck Anderson (UCSB) provided assistance and technical support in sedimentary sampling, preparation and paleomagnetic analyses. Cosmogenic ^{21}Ne analyses of alluvial fan terrace boulders were done by Gary Landis (USGS). Oxygen isotope analyses were conducted in James Kennett's lab with Karen Thompson's lab assistance. X-ray diffraction analyses of the U-series dated fossil corals were conducted by Sam Iyengar, and XRD of the *Olivella* shells was conducted by Dave Pierce (UCSB). The Santa Barbara Parks Department permitted fossil sampling by seaciff repelling at Santa Barbara Point.

DESCRIPTION OF FIELD TRIP STOPS

Santa Barbara Point and La Mesa marine terraces

The west-trending Santa Ynez Mountains (anticlinorium) can be observed to the north and is the result of north-south contraction and forms the principal topographic feature of the SBFB. On the southern flank of the Santa Ynez mountains, from west to east these include; the Santa Barbara estero (syncline) and Cemetery uplift (anticline), the Ortega Hill-Loon Point uplift (anticline) and Carpinteria slough (syncline), and Red Mountain uplift (anticline). In Santa Barbara, the Mission Ridge (Riviera) anticline forms the prominent topographic high on the Santa Barbara coastal plain and is the result of uplift on the blind Mission Ridge segment (Fig. 2) (Keller et. al, 1997).

Santa Barbara Point is located at the east end of the La Mesa Hills (Shoreline Park) about 1 km west of the Santa Barbara Harbor and downtown Santa Barbara (Fig. 2). The northwest-trending La Mesa hills inferred to be the expression of a hanging wall anticline on the south-dipping, reverse Mesa fault. The folds plunge offshore to the east at Santa Barbara Point and are truncated to the northwest by the Mission Ridge segment of the MRFS. Along the north facing fold scarp, the forelimb of the anticline is mostly absent due to erosion by Mission Creek where numerous meander scars are present. A remnant of the north-dipping limb is preserved in the northwest La Mesa and the south-dipping limb is poorly exposed in a road cut on Meigs Road.

The La Mesa terraces are uplifted along the Mesa and Lavigia anticlinal folds, which are formed on the hanging walls of the blind, La Mesa and Lavigia reverse faults, respectively. The nearly continuous terrace surfaces and associated strandlines are truncated west of Mesa Lane by the Las Positas water gap and east of Santa Barbara City College (SBCC) by the Mesa fault and subsequent erosion from Mission Creek.

Along the south limb of the fold at SBCC, a marine terrace fossil assemblage is exposed in the sea cliff on the first emergent marine terrace at SBCC, formerly known as Bathhouse Beach (Fig. 8). A fossil coral was obtained from the paleontology collection at the Department of Geological Sciences at UCSB. The coral was a well-preserved, solitary coral (*Balanophyllia elegans*) sampled from the sea cliff exposure at the Bathhouse Beach fossil site.

X-ray diffraction analysis determined the fossil coral to be composed of original aragonite shell material. Uranium series analysis of the fossil coral yielded a measured an initial $^{234}\text{U}/^{238}\text{U}$ activity of 1.164 ± 0.015 which is within the same range as that for modern seawater (Gurrola et al., 1997a). The estimated uranium series age is approximately of 70 ± 2 ka (Table 4). The oxygen isotope analyses of fossil mollusks indicate warmer paleo-ocean water signatures than the UCSB site (Trecker et. al., 1998a and 1998b). Chappell et al. (1996) recognize a paleo-sea level highstand associated with oxygen isotope substage 5a at 70 ± 2 ka with an elevation of -58.5 ± 13.5 m (Fig. 6). Therefore, the first emergent marine terrace at SBCC is best correlated to the 73 ± 2 ka paleo-sea level highstand at isotope substage 5a (Fig. 9).

At SBCC there are five uplifted terraces with associated paleo-shorelines, and one abrasion platform with the strandline removed by erosion, preserved in the same terrace flight as the SBCC site. The approximate paleo-shoreline elevations of the terraces and abrasion platform beginning with the first emergent are 30 ± 1.5 m, 44 ± 1.5 m, 61.5 ± 2.0 m, 75 ± 2.0 m, and 118 ± 3.0 m, respectively (Fig. 9).

Based on the uranium series age of 70 ± 2 ka for the first emergent marine terrace at SBCC, a total surface uplift of approximately 88.5 ± 15 m, a rate of local surface uplift of 1.3 ± 0.20 m/ky. is estimated (Figs. 8 and 9). Assuming a constant rate of uplift and using the method by Bull (1985), the 30 m and the 61.5 m terrace shorelines correlate to paleo-sea level highstands associated with substage 5a. The terraces at approximate elevations of 75 m and the 118 m shorelines correlate to paleo-sea level highstands associated with substage 5c (Fig. 9). The

paleo-shoreline positioned at an elevation of 44 m does not correlate to any paleo-sea level highstands and is most likely formed as the result of coseismic surface uplift of the coastline or a temporary stabilization of sea level fluctuations during sea level transgression or regression.

South of SBCC at Santa Barbara Point, a series of five flights of terraces with associated shorelines are preserved at approximate elevations of 15 +/- 1.0 m, 28 +/- 1.5 m, 47 +/- 2.0 m, 59 +/- 2.0 m, and 76 +/- 2.5 m (Fig. 10). A higher marine abrasion platform with the strandline absent is preserved at an approximate elevation of 127 +/- 3.0 m.

The paleo-shoreline of the first emergent marine terrace at Santa Barbara Point is discontinuous and trends offshore immediately west and east of Santa Barbara Point. The higher terrace strandlines are mappable from the SBCC terrace and the 70 ka terrace shoreline is present as the second emergent terrace at Santa Barbara Point (Fig. 10).

OSL measurements of quartz grains sampled from terrace sands at Santa Barbara Point determine an age of 58 +/- 11 ka for the first emergent terrace (Fig. 8; Table 4). Given the error range assigned to the 58 +/- 11 ka age, the terrace may have formed as a result of paleo-sea level highstands associated with oxygen isotope substage 3a (45 ka) or 3c (58 ka). Oxygen isotope data from fossil mollusks from Santa Barbara Point indicate a cool paleo-ocean temperature associated with stage 3 (Trecker et. al., 1998a and 1998b).

Based on the OSL age of terrace sands, the isotopic signatures of fossil mollusks, and the position of the second emergent terrace at Santa Barbara Point (hypothetically 70 ka), the first emergent terrace is correlated to oxygen isotope substage 3c (58 ka) (Fig. 10). A total surface uplift of approximately 73 +/- 14.5 m and a local vertical rate of surface uplift of 1.3 +/- 0.2 m/ky. are estimated (Fig. 10; Table 4). This is in agreement with the calculated local vertical surface uplift rate of 1.3 +/- 0.20 m/ky. at SBCC.

Assuming a constant rate of terrace uplift and the method by Bull (1985), the flights of terraces at elevations of 59 m, 76 m, and 127 m correlate to oxygen isotope substages 5a (80 ka), 5c (105 ka) and 5e (125 ka), respectively. The paleo-shoreline at an elevation of 47 m does not correlate to a paleo-sea level highstand and is the same strandline as the SBCC terrace at an elevation of 44 m.

West of Santa Barbara Point at Meigs Road, laterally continuous terrace strandlines are geomorphically well-expressed (Fig. 11). The elevations of the terrace strandlines are approximately 34 +/- 1.5 m, 47 +/- 1.5 m, 61 +/- 2.0 m, 75 +/- 2.0 m, and 114 +/- 3.0 m. A mostly stripped marine abrasion platform also occurs at an elevation of approximately 128 +/- 3.0 m.

Based on geomorphic mapping, the 70 ka strandline corresponds to the first emergent shoreline angle (34 +/- 1.5 m) and yields a total surface uplift of 92 +/- 15 m above paleo-sea level at the time of platform erosion (Fig. 11). A local, vertical surface uplift rate of 1.3 +/- 0.2 m/ky is estimated (Fig. 11).

The terrace shorelines are mappable to the west at Mesa Lane, where a small drainage truncates the first and second flights of terrace strandlines (Fig. 12). West of the water gap, terrace shoreline angles are present at approximate elevations of 34.5 +/- 0.5 m, 47 +/- 1.5 m, 61 +/- 2.0 m, 75 +/- 1.0 m, and 114 +/- 1.0 m. A marine abrasion platform is present at an elevation of approximately 128 +/- 3 m, however the surface is entirely stripped of terrace sediments and the shoreline angle removed by erosion.

Based on geomorphic mapping of the 70 ka strandline, a total uplift of 92.5 +/- 14 m and a local vertical uplift rate of 1.3 +/- 0.3 m/ky is estimated (Fig. 12). An assumed constant rate of uplift allows for correlation of the terraces at approximate elevations of 75 m and 114 m to oxygen isotope substages 5a (80 ka) and 5c (105 ka), respectively (Fig. 12). The second and third terrace levels do not correlate to a paleo-sea level highstand and probably are the result of coseismic uplift of the coastline or a temporary stabilization of sea level fluctuations during sea level transgression or regression. West of Mesa Lane, the terrace flights and associated strandlines are truncated by a major, south-flowing water gap (Las Positas water gap) occupied by Arroyo Burro Creek.

Santa Barbara Cemetery Anticline

The Santa Barbara Cemetery anticline is a 2 km long, northwest-trending fold that is well-exposed and trends nearly parallel to the beach seacliff in Montecito (Fig. 13). The anticline folds Quaternary Casitas Fm and the first emergent terrace into a well-expressed, north-facing fold scarp and anticlinal hill. Strata of the Casitas Fm dips approximately 25° to the north at the base of the sea cliff and decreases up section. Looking down the length of the sea cliff the strata of the south-dipping can be observed. Also, some units thin and onlap against the fold crests suggesting that syntectonic Casitas deposition occurred during fold growth and uplift. The wave-cut abrasion platform is warped across the fold crests but keep in mind that the sea cliff is parallel to the fold axis. A synclinal basin is formed to the north and expressed as the present day Santa Barbara coastal lagoon (historic estero). These folds are most likely related to a blind reverse fault. The age of the Santa Barbara marine terrace is estimated at 79 ± 10 ka, based on OSL measurements of K-feldspar from the terrace sand. We calculate a rate of uplift of 0.5 ± 0.06 m/ky for the Santa Barbara Cemetery terrace.

Loon Point

The first emergent terrace at Loon Point terrace, which is the second emergent terrace of the Summerland sequence, is exposed along the modern beach sea cliffs at Loon Point (Fig. 13). The elevation of the shoreline angle is approximately 50 ± 3.0 m and the terrace is synclinally folded below sea level into the Carpinteria syncline to the east. Terrace sands were sampled from the first terrace flight near Loon Point in order to obtain an age-date by optically stimulated luminescence analysis. OSL analysis yielded age estimations of 105 ± 15 ka for and 167 ± 15 ka for quartz and potassium feldspar grains, respectively (Table 4). The oldest first emergent marine terraces preserved in the SBF are no older than 125 ka, therefore the age of the Loon Point terrace is assumed to be 105 ± 15 . The estimated amount of surface uplift is approximately 73.5 ± 3.0 and the estimated surface uplift rate is approximately 0.7 ± 0.1 m/ky (Fig. 14).

The south-dipping, Loon Point fault is exposed in a nearly vertical 25 m high sea cliff exposure and forms a north-verging, asymmetric hanging wall anticline that deforms Casitas Formation and late Pleistocene (105 ka) marine terrace strata near Loon Point (Gurrola et. al, 1998) (Fig. 15). The bluff exposure prevents detailed stratigraphic analysis, however, photo mosaic mapping and subsequent trenching of the fault have provided additional information.

The Loon Point fault strikes approximately N85E at an oblique angle to the sea cliff and the dip of the fault is approximately $32^\circ \pm 5^\circ$ to the south. The fault juxtaposes steeply-inclined strata on the hanging wall against gently-dipping strata on the foot wall. The Loon Point anticline consists of forelimb strata that are overturned against the fault and dip about 88° to the southeast whereas the backlimb strata dips approximately 30° to the south (Fig. 15). The interlimb angle is approximately 57° and is termed a tight fold. The axial surface is moderately inclined and the fold thickens in the hinge area and forelimb.

The strata exposed in the sea cliff consist of a sequence of, from lower to upper, marine facies of Casitas Formation, marine terrace, and alluvial sediments. Shallow marine facies of the Casitas Formation strata are exposed on the footwall and strike at N75W and dip 16SE, whereas non-marine Casitas strata are exposed in the footwall and strike N80E and dip 27SE. A colluvial

growth wedge exhibiting tapering beds overlies the Casitas Formation and is preserved on the forelimb of the fold.

Hangingwall strata of the Casitas Formation beds consists of fluvial and massive debris flow deposits that taper and thicken, indicating syntectonic deposition during fold growth. The wave-cut platform is preserved on the forelimb overlying the growth wedge and identified by a thin cobble conglomerate (boulder line) with clasts that exhibit pholad boreholes. The fault vertically offsets the marine platform approximately 7 m with a dip separation of approximately 10 m. Across the axial surface, the boulder line is eroded out of the sea cliff section and projects into space (Fig. 15). To the east, the boulder line is preserved on the backlimb and can be followed to the east until it disappears below sea level into the Carpinteria syncline to the east.

Paleomagnetic analysis of fine-grained samples of Casitas Fm obtained from the sea cliff strata using continuous thermal demagnetization yield normal remnant magnetization for all sample analyzed. The samples retain normal polarity through high blocking temperatures as field strength is depleted indicating one component of normal magnetization. Therefore, the Casitas Fm is less than 790 ka, and probably is much younger because the underlying Santa Barbara Fm is also less than 790 ka. Several samples from the Loon point sea cliff exhibit magnetic vectors that have been rotated a maximum of 20°-30° clockwise from north suggesting a component of sinistral shear strain

The faulted, asymmetric Loon Point anticline is a fault-propagation fold in which the fold formed as the thrust fault propagated to the surface. Suppe (1985) and Suppe and Medwedeff (1990) describe asymmetric folds with one steep or possibly an overturned limb adjacent to a thrust fault as a fault-propagation fold. They describe these folds as a result of the process of fault propagation and suggest that the fold records deformation that occurs in front of the propagating fault surface which ramps from a detachment at depth. With time, the fault juxtaposes a footwall syncline against a hanging-wall anticline across the fault (Suppe, 1985). As the fault propagates upward, the fault ramp lengthens and commonly, the fault-propagation fold becomes locked and the fault may rupture through the anticlinal or synclinal axial surface, or somewhere in between (Suppe, 1985; Suppe and Medwedeff, 1984 and 1990).

The reverse fault and asymmetric, hanging-wall folds documented in this study are similar to the fault-propagation fold geometry described by Suppe (1985) and Suppe and Medwedeff (1984 and 1990). Absent from the footwall block of the Loon Point fault is an associated syncline (Fig. 3b). Therefore, the fault ruptured through the syncline and is classified as a synclinal fault breakthrough (Suppe and Medwedeff, 1990).

Suppe and Medwedeff (1990) propose two models by which folding occurs in brittle conditions. Both models describe fold-propagation by reverse-faulting. The constant thickness fault-propagation folding model is based on conservation of bedding thickness and bed length. The fixed front anticlinal axial surface model allows for bed thickening or thinning in the steep fore-limbs of the fold. Beds of the Loon Point fold slightly thicken in the steep fore-limb of the anticlinal fold and indicate that this fault-propagation fold can be best described with the fixed front anticlinal axial surface model.

Excavation of a fault trench across the fold scarp of the Loon Point fault-propagation fold revealed a shallow-dipping (40°) reverse fault (Gurrola et. al, 1998) (Fig. 16). The fault juxtaposed marine terrace sands against Quaternary alluvium. The marine sands were absent from the footwall block and were exposed in a secondary trench and surveyed into the fault to measure a vertical displacement of 5 m (Gurrola et al., 1998). Detrital charcoal sampled from a faulted alluvial unit with 2 m of offset yielded a ^{14}C date of 3,980 +/- 40 RCYBP. The age is too young to calculate a reasonable slip rate, however based on approximately 14 m of structural relief across the 105 ka marine terrace, an approximate vertical rate of folding of 0.1 m/ky is calculated for the Loon Point anticline. The Loon Point fault is classified as an active fault and seismic source in the SBFB.

REFERENCES CITED

- Bull, W. B., 1985, Correlation of flights of global marine terraces, IN: Morisawa, M., and Hack, J., eds., Tectonic Geomorphology. Proceedings, Binghamton Geomorphology Symposium, 15th, p. 129-152.
- Chappell, J., Omura, A., Esat, E., McCulloch, M., Pandolfi, J., and Pillans, B., 1996, Reconciliation of late Quaternary sea levels derived from coral terraces at Huon Peninsula with deep sea oxygen isotope records, Earth and Planetary Science Letters 141, p. 227-236.
- Dibblee, T.W., Jr., 1950, Geology of southwestern Santa Barbara County, California: California Department of Natural Resources Division of Mines Bulletin 150, 95 pp., map scale 1:62,500.
- Dibblee, T.W., Jr., 1966, Geology of the central Santa Ynez Mountains, Santa Barbara County, California: California Division of Mines and Geology Bulletin 186, 99 pp., map scale 1:62,500 and 1:31,680.
- Dibblee, T.W., Jr., 1986a, Geologic Map of the Carpinteria quadrangle, Santa Barbara County, California: Dibblee Geological Foundation Map DF-04, scale 1:24000.
- Dibblee, T.W., Jr., 1986b, Geological Map of the Santa Barbara quadrangle, Santa Barbara County, California: Dibblee Geological Foundation Map DF-06, scale 1:24000.
- Dibblee, T.W., Jr., 1988, Geologic Map of the Ventura-Pitas Point quadrangles, Ventura and Santa Barbara Counties, California: Dibblee Geological Foundation Map DF-21, scale 1:24000.
- Dibblee, T. W., Jr., 1988, Geology of the Ventura Basin area, in Ventura Basin: Geologic Introduction and Field Trip Guidebook (M. H. Link, ed.), Pac. Sec. Amer. Assoc. Petroleum Geologists and Los Angeles Basin Geological Society, p. 7-18.
- Gurrola, L. D. and Kamerling, M., 1996a, Role of cross faults as tears in thrust ramps in the Ventura and Santa Barbara Fold Belts, California, 1996: Abstracts for the Southern California Earthquake Center Annual Meeting, p. 49.
- Gurrola, L. D. and Kamerling, M. 1996b, Segmentation of principal east-west trending reverse/thrust fault and earthquake nucleation sites in the western Transverse Ranges, California: EOS, Transactions, AGU, v. 77, no. 46, p. 512..
- Gurrola, L. D., Slayman, R. C., Hartleb, R. D., and Keller, E. A. 1996a, Segmentation of the Mission Ridge Fault System based on geomorphic and structural expression, Santa Barbara Fold Belt, California, 1996: Abstracts for the Southern California Earthquake Center Annual Meeting, p. 49.
- Gurrola, L. D., Chen, J. H., Keller, E. A., and Metcalf, J. G. 1996b, Dating of emergent marine terraces and rate of uplift for the western Santa Barbara Fold Belt, California: GSA Abstracts with Programs, vol. 28, no. 7, p. A-301.
- Gurrola, L. D. and Keller, E. A. 1997a, Tectonic geomorphology of the Santa Barbara fold belt, western Transverse Ranges, California: GSA abstracts with programs, vol. 29, no. 6, p. 344-345.
- Hauksson, E., and Jones, L. M., 1989, The 1987 Whittier Narrows earthquake sequence in Los Angeles, southern California: Seismological and tectonic analysis, Jour. Geophys. Res. 94(7), p. 9569-9589.s
- Izett, G. A., Naeser, C. W., Obradovich, J. D., 1974, Fission track age of zircons from an ash bed in the Pico Fm (Pliocene and Pleistocene) near Ventura, California, in GSA Abstracts with Programs 6(3), p. 197.
- Jackson, P.A., 1981, Structural evolution of Carpinteria basin, western Transverse Ranges, California, unpublished M. S. thesis, Oregon State University, 107 p.

- Jackson, P. A. and Yeats, R. S. 1982, Structural evolution of the Carpinteria basin, western Transverse Ranges, California: The American Association of Petroleum Geologist Bulletin, vol. 66, no. 7, p. 805-829.
- Keller, E. A., Mueller, K., and Gurrola, L D.1997, 'Big Bend' of the San Andreas fault: Hypothesis of tectonic extrusion: GSA abstracts with programs, vol. 29 no. 6, p. A-235.
- Kern, J. P. 1977, Origin and history of upper Pleistocene marine terraces, San Diego, California: Geol. Soc. Amer. Bull., vol. 88, p. 1553-1566.
- Lajoie, K. R., Kern, J. P., Wehmiller, J. F, Kennedy, G. L, Mathieson, S. A., Sarna-Wojcicki, A. M., Yerkes, R. F. and McCrory, P. F. 1979, Quaternary marine shorelines and crustal deformation, San Diego to Santa Barbara, California, In: Abbot, P. L., ed., Geological excursions in the southern California area: Guidebook for field trips, GSA Annual Meeting, Nov. 1979, Department of Geological Sciences, San Diego State University, San Diego, CA., p. 3-16.
- Lajoie, K. R., Sarna-Wojcicki, A. M., and Yerkes, R. F. 1982, Quaternary chronology and rates of crustal deformation in the Ventura area, California, In: Cooper, J. D., ed., Neotectonics in southern California, Guidebook for fieldtrips, Anaheim, CA, p. 43-51.
- Landis, G., Gurrola, L., Selting, A., and Mills-Herring, L., 2002, Evaluation of ^{21}Ne cosmogenic nuclide surface exposure ages from a mid-late Pleistocene alluvial fan and Holocene debris flow, Santa Barbara, CA, Geol. Soc. Amer. Abstracts with Programs Vol. 34, No. 6.
- Matthews, R. K. 1973, Relative elevation of Late Pleistocene high sea level stands: Barbados uplift rates and their implications, IN: CLIMAP program, Quat. Res., vol. 3, no. 1, p. 147-153.
- McCalpin, James P. Paleoseismology. Academic Press, 1996 588 p. Series title: International Geophysics Series Vol. 62
- Morris, R. H., Abbott, D. P, and Haderlie, E. C., 1980, Intertidal Invertebrates of California, : Stanford University Press, p. 290-292.
- Muhs, D. R., Rockwell, T. K., and Kennedy, G. L. 1992, Late Quaternary uplift rates of marine terraces on the Pacific Coasts of North America, southern Oregon to Baja California Sur, IN: Impacts of tectonics on Quaternary coastal evolution, Quat. Inter., vol. 15-16, p. 121-133.
- Muhs, D. R., Miller, G. H., Whelan, J. F., and Kennedy, G. L. 1994; Aminostratigraphy and oxygen isotope stratigraphy of marine terrace deposits, Palos Verdes Hills and San Pedro areas, Los Angeles County, California, In: Quaternary Coasts of the United States: Marine and Lacustrine Systems, SEPM Special Publication no. 48, p. 363-376.
- Narr, W. and Suppe, J. 1994, Kinematics of basement-involved compressive structures: Amer. Jour. Sci. vol. 294, no. 7, p. 802-860.
- Olsen, P. G., and Sylvester, A. G., 1975, The Santa Barbara earthquake, 29 June 1925: California Geology, vol. 28, no. 6, p. 123-131.
- Olson, D. J., 1982, Surface and subsurface geology of the Santa Barbara-Goleta metropolitan area, Santa Barbara County, California: Unpub. M .S. thesis, Oregon State University, 71 p.
- Southern California Earthquake Center, 1995, Seismic Hazards in Southern California: Probable Earthquakes, Working Group on California Earthquake Probabilities, Bull. Seis. Soc. Amer., vol. 85, no. 2, p. 379-439.
- Stein, R., Hanks, T., 1998, Magnitude 6 or greater earthquakes in Southern California during the twentieth century; no evidence for a seismicity or moment deficit, Bull. Seis. Soc. Amer. v.88, No. 3, p. 635-652

- Suppe, J., 1985, *Principles of Structural Geology*: Prentice-Hall, Englewood Cliffs, New Jersey, 537 p.
- Suppe, J., and Medwedeff, D. A., 1984, Fault-propagation folding: *Geol. Soc. Amer. Abst. Prog.* vol. 16, p. 670.
- Suppe, J., and Medwedeff, D. A., 1990, Geometry and kinematics of fault-propagation folding: *Eclogae geol. Helv.* vol. 83, no. 3, p. 409-454.
- Sylvester, A. G. and Mendes, S. H. 1981, Case Studies of Earthquake Damage and Repair: Earthquake History of Santa Barbara, contributions by Hart, G. C. and Huang, S., Guidebook for the Field Seminar; Annual Meeting of the Earthquake Engineering Research Institute, 56 pp.
- Trecker, M. A., Gurrola, L. D., and Keller, E. A. 1998a, Oxygen Isotope Correlation of Marine Terraces and Uplift of the Mesa Hills, Santa Barbara, California: U.S.A, IN: Stewart, I.S and Vita-Finzi, C. (eds), *Coastal Tectonics*, *Geol. Soc. London*, vol. 146, p. 57-69.
- Trecker, M. A., Gurrola, L. D, and Keller, E. A., 1998b, Oxygen-Isotope correlation of marine terraces and uplift of the Mesa Hills, Santa Barbara, California, USA: In: Stewart, I. S. and Vita Finzi, C. (eds.) *Coastal Tectonics: Geological Society of London, Special Publication 146*, p. 57-69.
- United States Geological Survey 1996, USGS response to an urban earthquake Northridge '94: U.S.G.S. *Geol. Surv. Open File Report 96-263*, 78 p.
- Valentine, J. W. 1961, Paleoeologic molluscan geography of the Californian Pleistocene: *University of California Publications in Geolgoical Sciences*, vol. 34, no. 7 p. 309-442.
- Wells, D. L., and Coppersmith, K. J., 1994, New empirical relationships among magnitude, rupture length, rupture width, rupture area, and surface displacement, *Bull. Seis. Soc. Amer.* 84(4), p. 974-1002.
- Willis, B., 1925, A study of the Santa-Barbara earthquake of June 29, 1925: *Seis. Soc. Amer. Bull.*, vol. 15, no. 4, p. 255-278.
- Yeats, R. S, Sieh, K., Allen, C. R., 1997. *The geology of earthquakes*. Oxford, University Press, 568 p.
- Yeats, R. S. and Olson, D. J., 1984, Alternate fault model for the Santa Barbara, California earthquake of 13 August 1978: *Seis. Soc. Amer. Bull*, vol. 74, no. 5, p. 1545-1553.

Table 1. Seismic sources of the onshore and offshore Santa Barbara Fold Belt with associated fault/fold dimensions, activity, and maximum expected earthquakes (M_w). Predicted magnitudes for earthquakes are determined using the methodology of Wells and Coppersmith (1994). Names of seismic source abbreviations for figure 2 are in parenthesis.

- a. We assume fault length is the surface rupture length and may be slightly different than map lengths of seismic sources shown on Figure 2.
- b. Active = demonstrated Holocene (last 10,000 yr.) activity;
 Apparently Active = probably Holocene (geomorphic expression of activity);
 Potentially Active = active in Pleistocene (last 1.65 million years)

Fault	Folds(s)	Length (km)^a	Slip	Vertical rate of faulting (mm/yr)	Activity^b	Max. M_w
<i>Mission Ridge System</i>						
More Ranch segment (MrR)	Ellwood, UCSB, More Mesa anticlines	15	Oblique: reverse-left	0.3 – 0.4	Apparently active	6.4
Mission Ridge segment (MsR)	Mission Ridge, Montecito, Eucalyptus Hill, and Barker Pass anticlines	17	Reverse-(left?)	0.6 – 0.9	Active	6.5
west and east Arroyo Parida segments (AP)		17 15	Oblique: left-lateral reverse	0.4 (Ojai, CA)	Potentially active	6.5 6.4
Northwest Striking Faults						
Mesa (MF)	Mesa anticline	12	Reverse	Unknown	Potentially active	6.3
Lavigia (LF)	Hope Ranch anticline Honda Valley folds	15	Oblique: reverse left-lateral	0.1	Potentially active	6.4
San Jose (SJ)	Goleta Valley anticline	7	Reverse (oblique?)	Unknown	Potentially active	6.1
San Pedro (SP)	unnamed anticlines	8	Oblique: reverse left-lateral	Unknown	Potentially active	6.1
Loon Point (LP)	Loon Point anticline	1	Reverse	Unknown	Active	5.1
Ortega Hill (OH)	Ortega Hill anticline	1	Reverse-(oblique?)	Unknown	Potentially active	5.1
Santa Barbara Cemetery (SBC)	Santa Barbara Cemetery anticline	1	Reverse	0.1	Apparently active	5.1
Los Carneros (LC)		7	left-lateral	Unknown	Potentially active	6.1
Dos Pueblos (DP)		6	left-lateral	Unknown	Potentially active	6.0

Research on the Santa Barbara Fold Belt is supported in part by the UC Santa Barbara, Institute for Crustal Studies, Southern California Earthquake Center and the National Earthquake Hazards Reduction Program. The views and conclusions presented in this guidebook are solely those of the authors.

Table 2. Table of regional historic seismicity of the Santa Barbara Fold Belt (Sylvester and Nicholson, 1975; Sylvester and Mendes, 1981).

Date	Magnitude	Location	Modified Mercalli Scale (MM)	Damage	Measured or Inferred Peak Accel. (g)	Estimated Peak Accel. at Santa Barbara	Distance to Santa Barbara (km)
24 Mar., 1806	?	?	?	Damage to Mission Santa Barbara and Royal Presidio	?	0.05-0.10	?
21 Dec., 1812	7.1+	Santa Barbara Channel	X-XI	Destroyed La Purisma Mission (near Lompoc) and Santa Barbara Mission.; tsunami?	0.60+	0.20-0.40	< 50
9 Jan., 1857	8.2 +	San Andreas fault	X+	Ruptured 300 km of the San Andreas fault; intensity VI-VII at Santa Barbara; > 90 sec. of shaking	0.80+	0.10+	60-190
27 July to 12 Dec., 1902	6.0?	near Los Alamos	VIII-IX	Several EQ's totally destroy Los Alamos	0.40-0.50	0.05	60
29 June, 1925	6.3 or 6.8	Santa Barbara	VIII-IX	Extensive damage to downtown Santa Barbara and city	0.50-0.60	0.40-0.60	< 5
29 June, 1926	5.5?	Santa Barbara	VIII	Moderate damage to Santa Barbara; aftershock of 1925 EQ	0.30	0.20	< 5
4 Nov., 1927	7.3	off Pt. Arguello	VIII+	Tsunami (2m) generated along coast; slight damage to Santa Barbara	0.60++	0.10	100
30 June, 1941	5.9	offshore Carpinteria	VII	Slight damage to Santa Barbara	0.40-0.50	0.10	10
21 July, 1952	7.7	Kern County	XI	Moderate damage to Santa Barbara; liquefaction along Laguna Street paleochannel	0.80+	0.15	85
5 July, 1968	5.2	Santa Barbara Channel	VI	EQ swarm with largest event causing slight damage to Santa Barbara	0.20	0.07-0.10	15
13 Aug., 1978	5.9	off Goleta Pt.	VII-VIII	Moderate damage mainly to UCSB campus	0.44	0.28	< 5

Table 3. Generalized stratigraphic section of the Santa Barbara Fold Belt, California (modified after Dibblee, 1966; Olson, 1982).

SERIES	FORMATION	DESCRIPTION	ESTIMATED THICKNESS
Plio-Pleistocene	Holocene alluvium older alluvium and gravels, fanglomerate Qa, Qoa, Qog, Qf	Gravel, sand, silt; non-marine Older alluvium: gravel, sand, silt; marine terrace deposits capping coastal mesas Fanglomerate: boulders, gravel, sand; non-marine	0 - 75 m (0 - 250')
	Casitas Qca	Buff to brownish-gray pebbly sandstone and cobble gravel; mostly non-marine	?
	Santa Barbara Qsb not in contact	Yellow, fossiliferous, fine sand, local consolidated sandstone, and minor siltstone and claystone; marine (<790 ka in Santa Barbara Fold Belt)	0 - 900 m (0 - 3000')
	"Pico"	Blue-gray siltstone, fine-grained sandstone with a fossiliferous basal conglomerate; marine	
	Sisquoc Tsq	Diatomaceous clay-shale and siltstone; marine	0 - 245 m (0 - 800')
Miocene	Monterey Tm, Tml	Dark brown, laminated siliceous shale, mudstone, and siltstone; bentonite at base; marine	425 - 670 m (1400 - 2200')
	Rincon Tr	Gray to dark brown mudstone and siltstone with occasional bentonite beds and carbonate lenticules; marine	425 - 520 m (1400 - 1700')
Oligocene	Vaqueros Tvq	Gray, thick-bedded sandstone; marine	100 m (325')
	Sespe Tsp, Tspss	Predominantly red sandstone, shale, and conglomerate interbedded with gray to green siltstone; non-marine	760 - 900 m (2500 - 3000')
Eocene	Coldwater Tcw, Tcwsh	Gray, arkosic sandstone, minor siltstone; marine	1000 m (3300')

Table 4. Uranium-series, radiocarbon, and optically stimulated luminescence age results from stream, alluvial, and marine terraces in the SBFB.

Sample Location – Terrace Site	Sample Number	Cosmogenic ²¹ Ne Age (ka)	Uranium Series Age (ka) ^a	Measured C14 Age (RCYBP) ^b	Measured Luminescence Age ^c (ka)	
					Quartz	K-feldspar
UC Santa Barbara- Isla Vista terrace	IV-1-96 IV-2-98		47 +/- 0.5	43,790 +/- 770		40 +/- 3
Ellwood terrace	C-5			35,860 +/- 570		
Ellwood terrace	C-12			37,000 +/- 570		
Ellwood terrace	C-14			47,020 +/- 1,500		
More Mesa terrace	MM-1-96 MM-2-98			36,830 +/- 330		53 +/- 7
Santa Barbara City College terrace	SBCC-1-98 SBCC-2-98		70 +/- 2.0			
Santa Barbara Point	SBP-1-98				336 +/- 64 ^d	58 +/- 11
Santa Barbara Cemetery	SBC-1-98					79 +/- 10
Summerland terrace Loon Point	LP-1-96 LP-2-98			3,990 +/- 40	105 +/- 15	167 +/- 15 ^d
Elings Park South					68 +/- 6	
Cavelleto Terrace	MFH-C-1			2,450 +/- 40		
Rattlesnake Fan		59 – 130				
Rocky Nook Fan		3 – 30				

- Uranium-series and luminescence ages are reported as 1 ka = 1,000 years before present.
- Radiocarbon samples were submitted to Beta Analytic Laboratory for AMS analysis and ages are designated as radiocarbon years before present (RCYBP).
- Optically stimulated luminescence age estimates are based on analysis of quartz and K-feldspar grains (Spencer and Owen, 1999).
- Results are considered maximum ages and the date (336 +/- 64 ka) at Santa Barbara Point and the date (167 +/- 15) at Loon Point are considered unlikely because: 1) the first emergent terrace at Santa Barbara City College has a U-series age of 70 +/- 2 ka, and 2) first emergent terraces throughout the Santa Barbara-Ventura region (when dated) are no older than 125 ka.

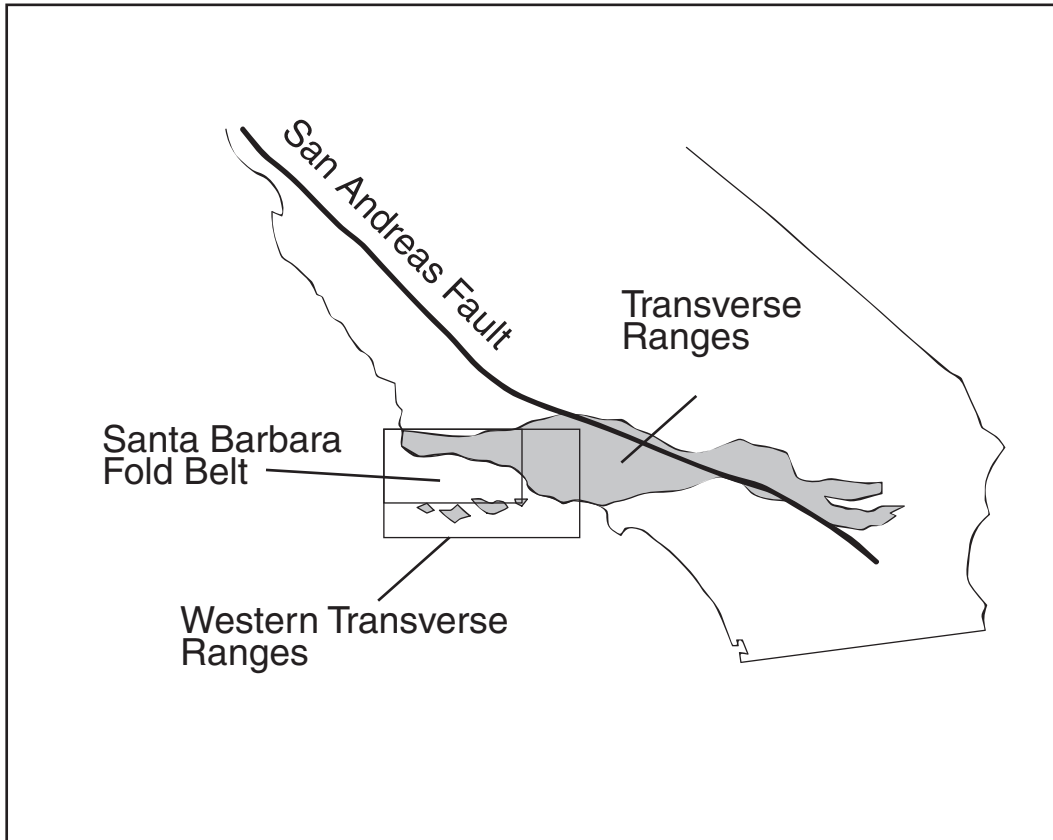


Figure 1. Location of the western transverse Ranges and the Santa Barbara Fold Belt.

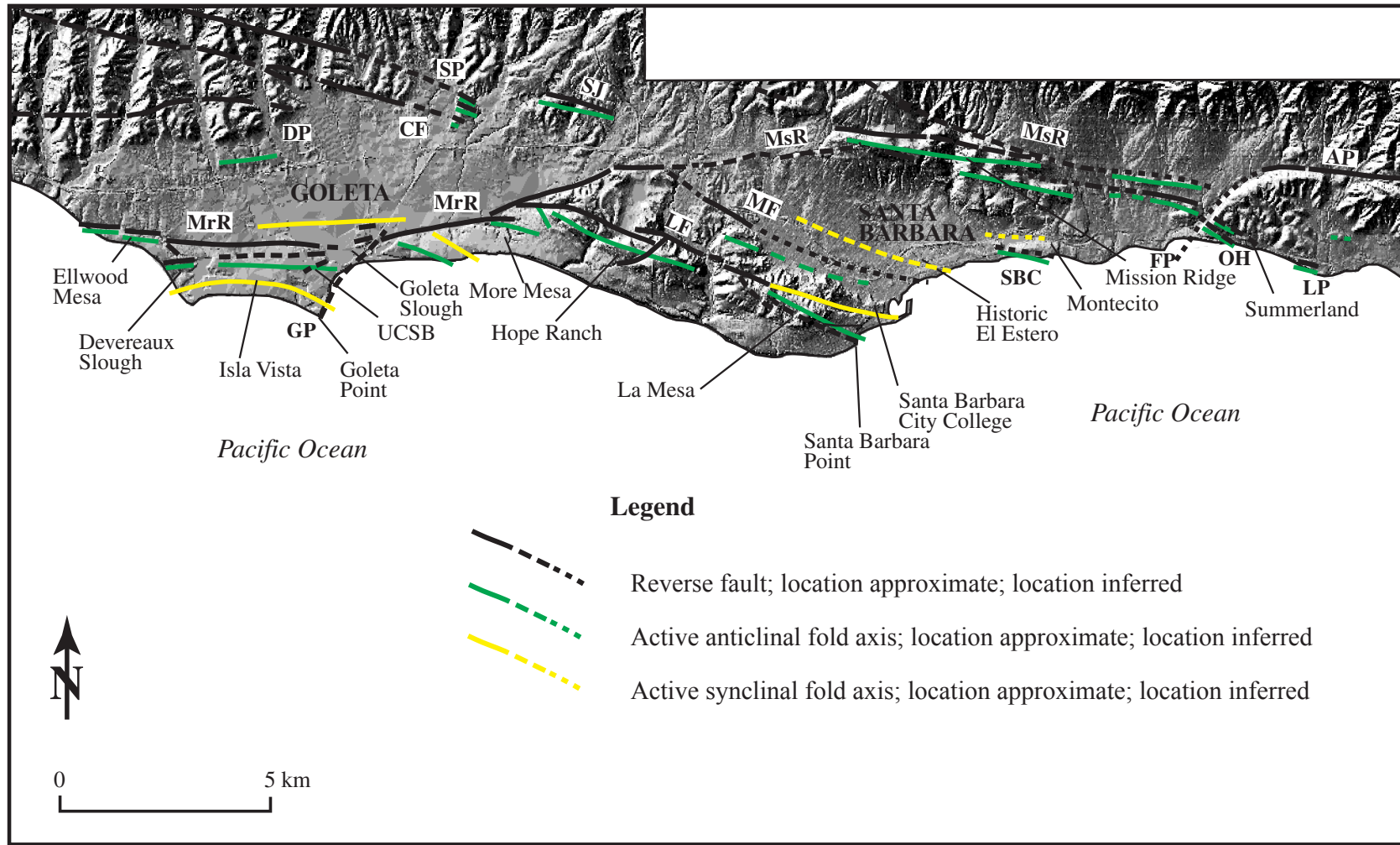
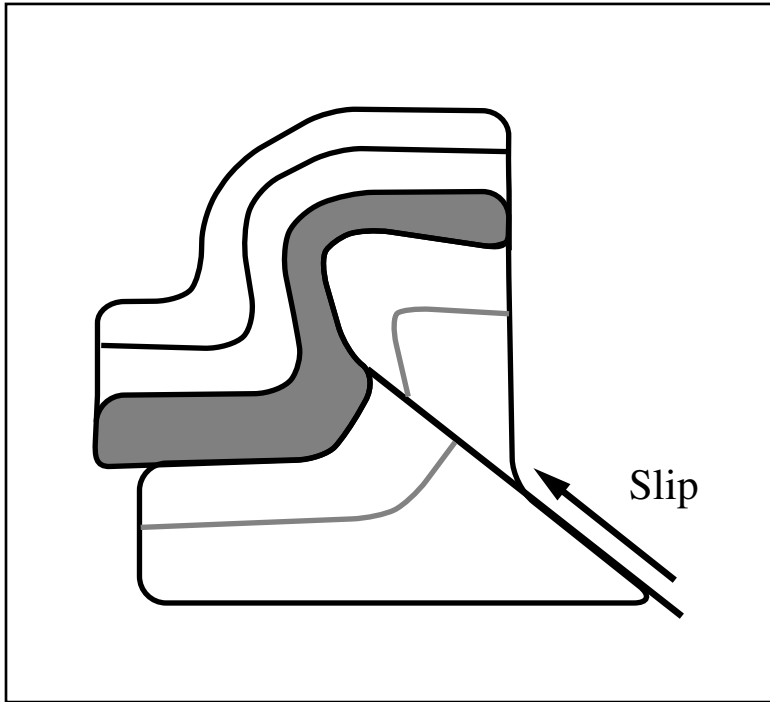


Figure 2. Seismic sources of the onshore Santa Barbara Fold Belt showing south-dipping, reverse faults, some of which are blind, with associated north-verging, hanging wall anticlines and footwall synclines. The Mission Ridge Fault System is subdivided into the More Ranch (MrR), the Mission Ridge (MsR), and the Arroyo Parida (AP) segments. Additional onshore reverse faults include the Dos Pueblos (DP), the Carneros (CF), the Goleta Point (GP), the San Jose (SJ), the San Pedro (SP), the Lavigia (LF), the Mesa (MF), the Santa Barbara Cemetery (SBC), the Ortega Hill (OH), the Fernald Point (FP), and the Loon Point (LP) faults.



Figures 3a. The schematic diagram (lower diagram) illustrates the model of a as the result of basement involved deformation. Note that the Monterey Fm deforms by brittle deformation (i.e., faulting), whereas the unconsolidated, overlying terrace and alluvial sediments deform by ductile folding (Modified after Narr and Suppe, 1994).

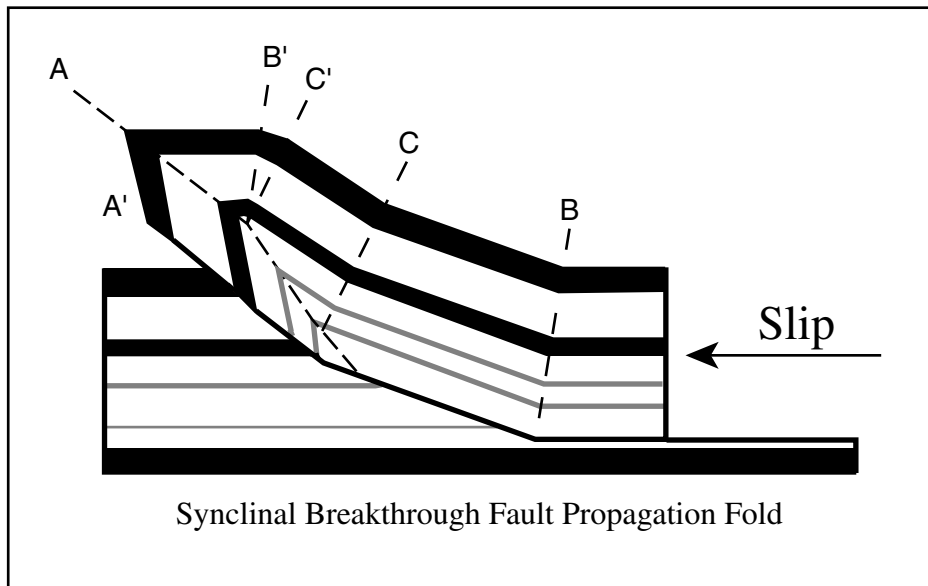


Figure 3b. Upper diagram illustrates the fault-propagation fold model showing the hanging-wall anticline which formed in front of an upward propagating fault tip. The fault ruptures through the synclinal axis (in this case) producing a synclinal breakthrough fold. Active axial surfaces are indicated as dashed lines (Modified after Suppe and Medwedeff, 1990).

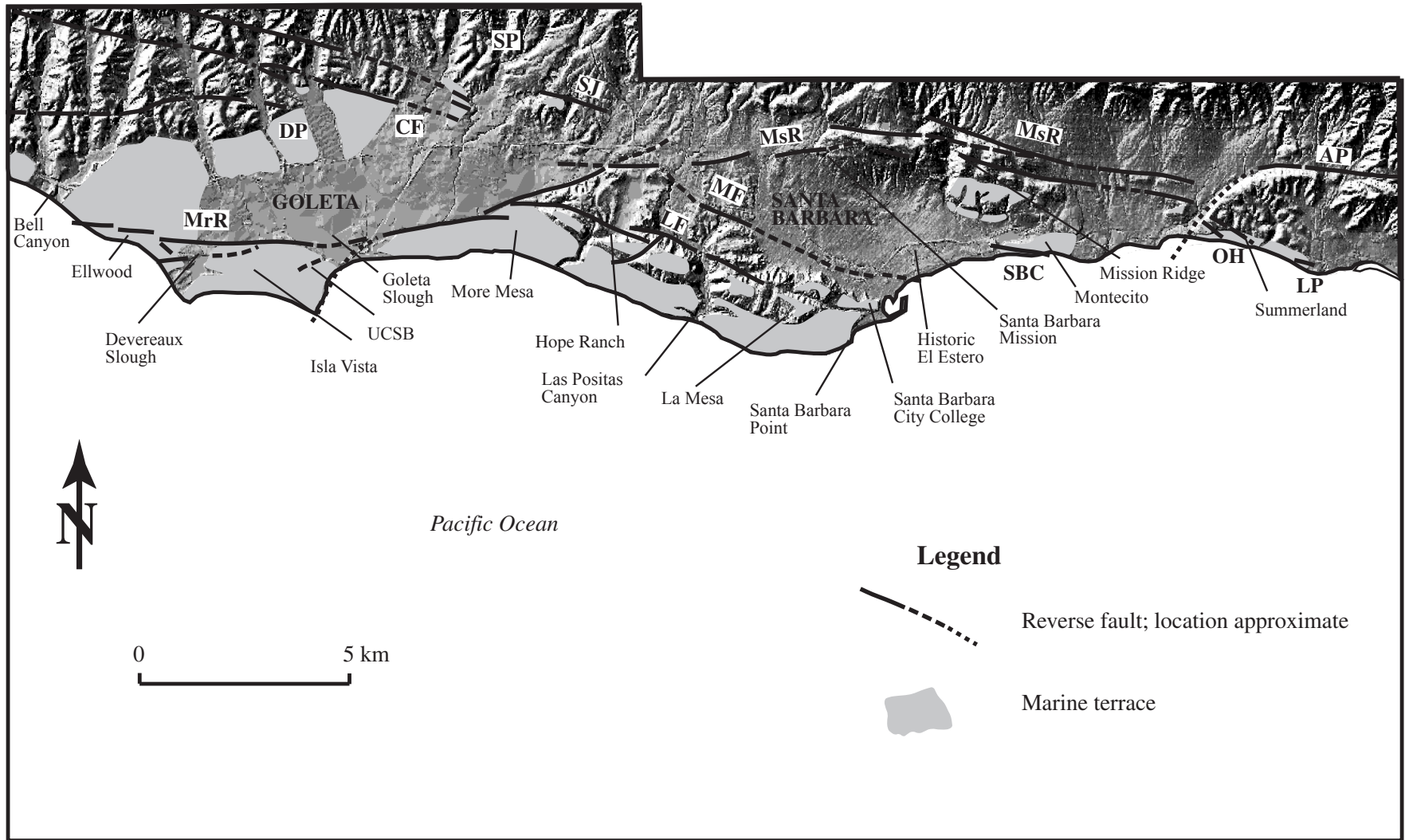


Figure 4. Geomorphic map of uplifted marine terraces preserved on the coastal piedmont of the SBBF. The marine terrace landforms are preserved on anticlinal folds formed as the result of blind reverse and thrust faulting. Fault abbreviations include the More Ranch (MrR), the Mission Ridge (MsR), and the Arroyo Parida (AP) segments. Additional reverse faults include the Dos Pueblos (DP), the Carneros (CF), the San Jose (SJ), the San Pedro (SP), the Lavigia (LF), the Mesa (MF), the Santa Barbara Cemetery (SBC), the Ortega Hill (OH), and the Loon Point (LP) faults.

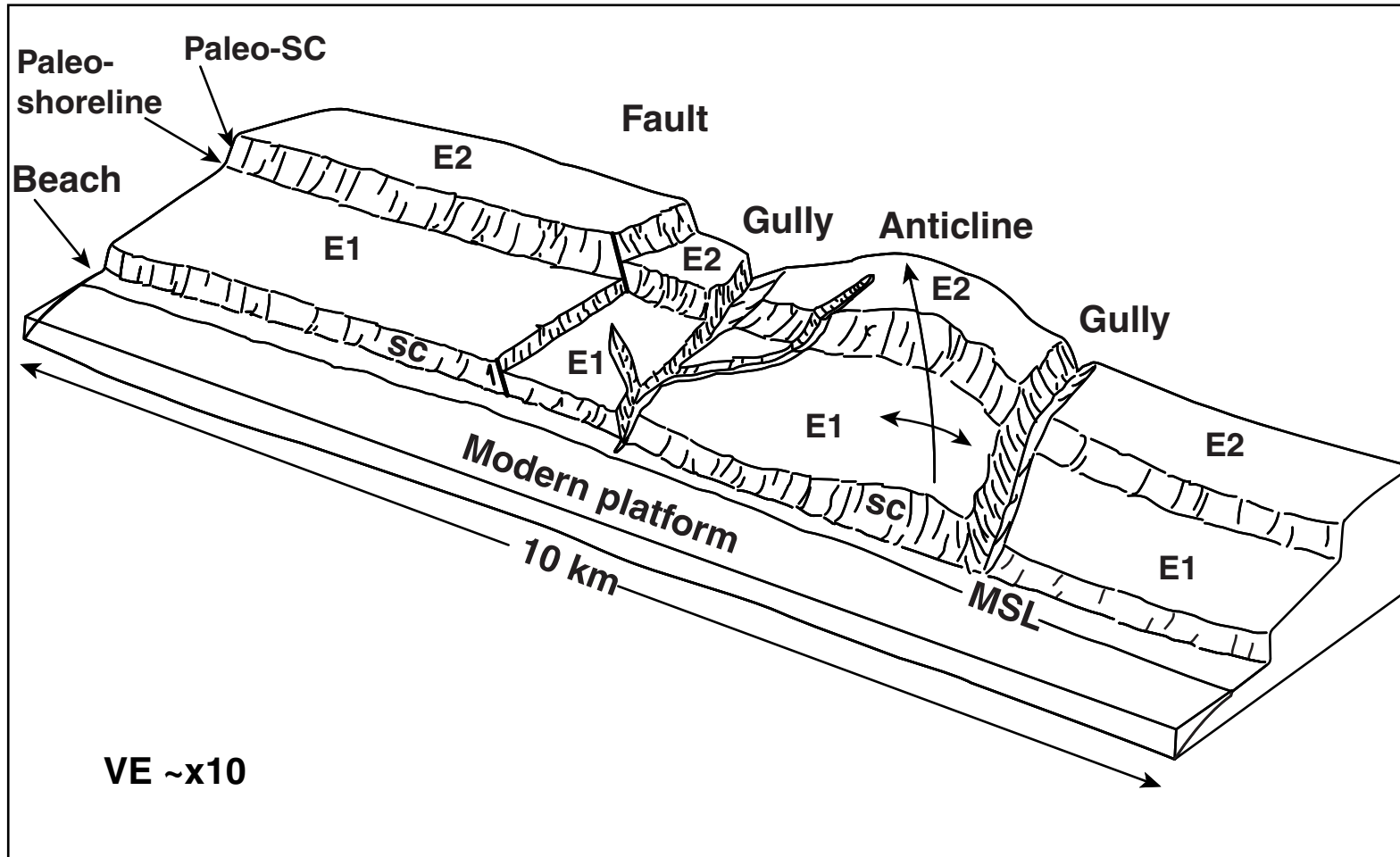


Figure 5. Idealized diagram of a modern wave-cut platform and associated sea cliff (SC) and relation to uplifted marine terraces and associated morphology. The first emergent marine terrace is (E1) and the second emergent terrace (E2) is the next higher terrace. The elevation of the buried marine platform and the associated paleo-sea cliff (Paleo-SC) defines the terrace shoreline angle. The elevation of the terrace shoreline angle is measured in order to calculate total amount of vertical surface uplift. Note that uplifted marine terraces are discontinuous and folded, complicating their correlation (modified after Trecker et al., 1998).

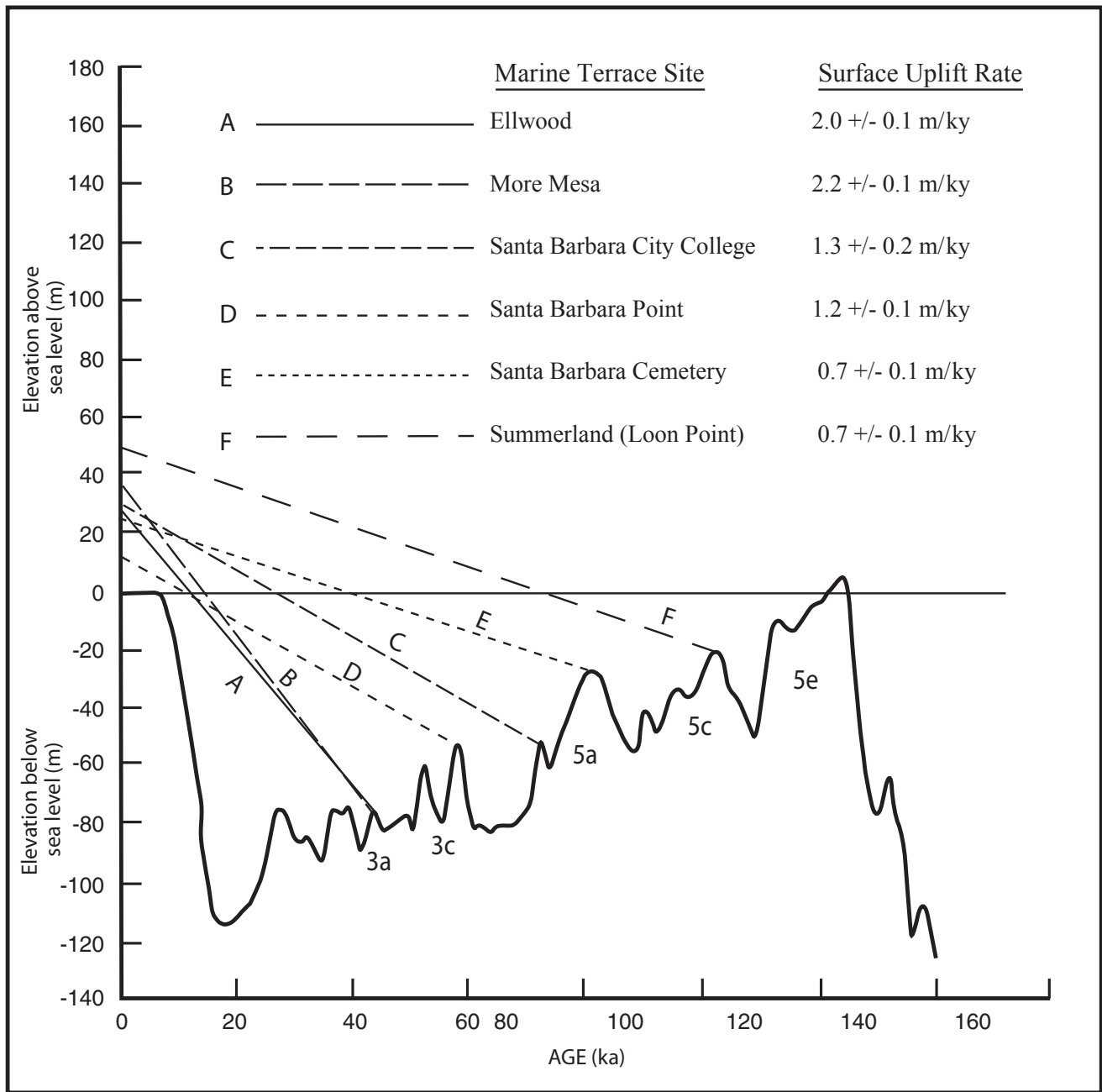


Figure 6. Graph of the late Pleistocene sea level curve (Chappell et al., 1996) with the elevations of the shoreline angles of the first emergent terraces in the SBF. The elevations and ages of the first emergent terraces are correlated to the associated paleo-sea level highstand. The slope of the resultant line is the rate of surface uplift (m/ka) for that terrace.

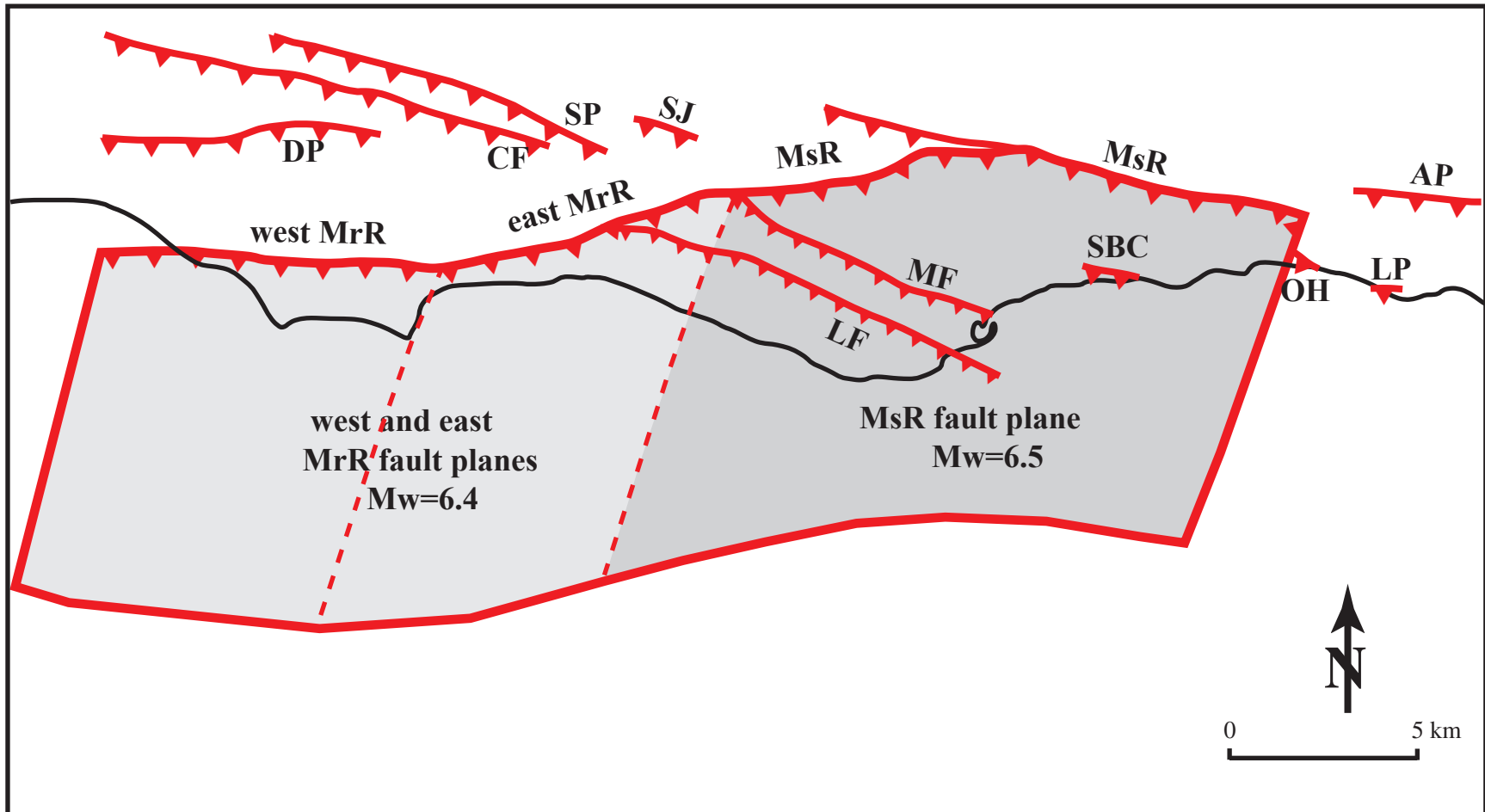


Figure 7. Seismic source map of the Santa Barbara Fold Belt showing extent of the More Ranch (MrR) and Mission Ridge (MsR) fault planes in the subsurface and potential earthquake magnitudes (M_w). Additional onshore reverse faults include the Dos Pueblos (DP), the Carneros (CF), the San Jose (SJ), the San Pedro (SP), the Lavigia (LF), the Mesa (MF), the Santa Barbara Cemetery (SBC), the Ortega Hill (OH), and the Loon Point (LP) faults. Additional structural data are from Dibblee (1986), Olson (1982), Hoover and Associates (1978), and Jackson (1981).

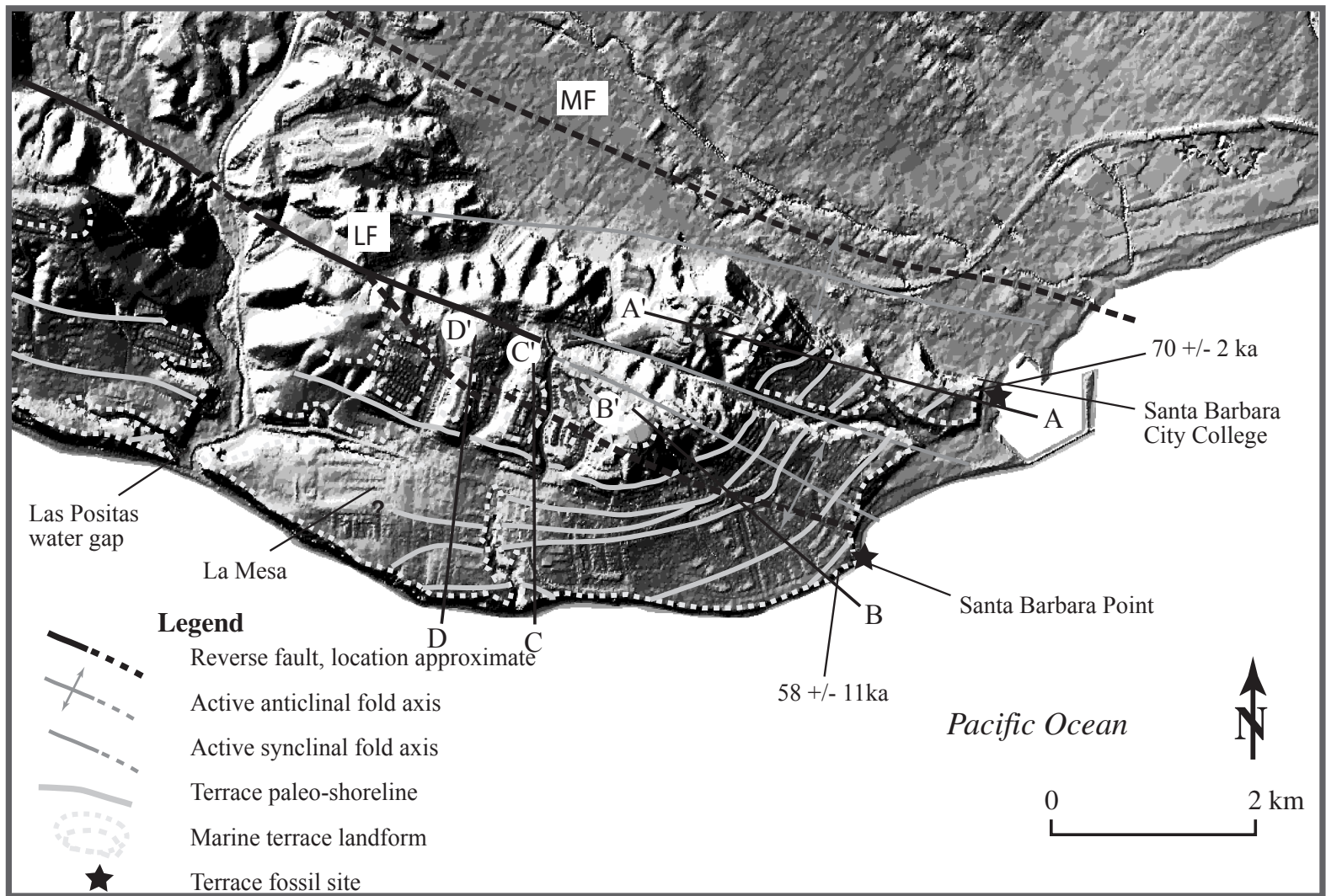


Figure 8. Geomorphic map of the La Mesa anticline and uplifted, marine terraces: (La Mesa fault (MF) and Lavigia fault (LF). Flights of marine terraces are preserved on the south flank and the nose of the east-plunging La Mesa anticline. Sites where u-series and OSL age-dates are labelled and are correlated across the Las Positas water gap. They are truncated by the blind, south-dipping MF. The LF forms a well-expressed fold scarp east of the Las Positas water gap and is expressed as an anticlinal-synclinal fold sequence to the west.

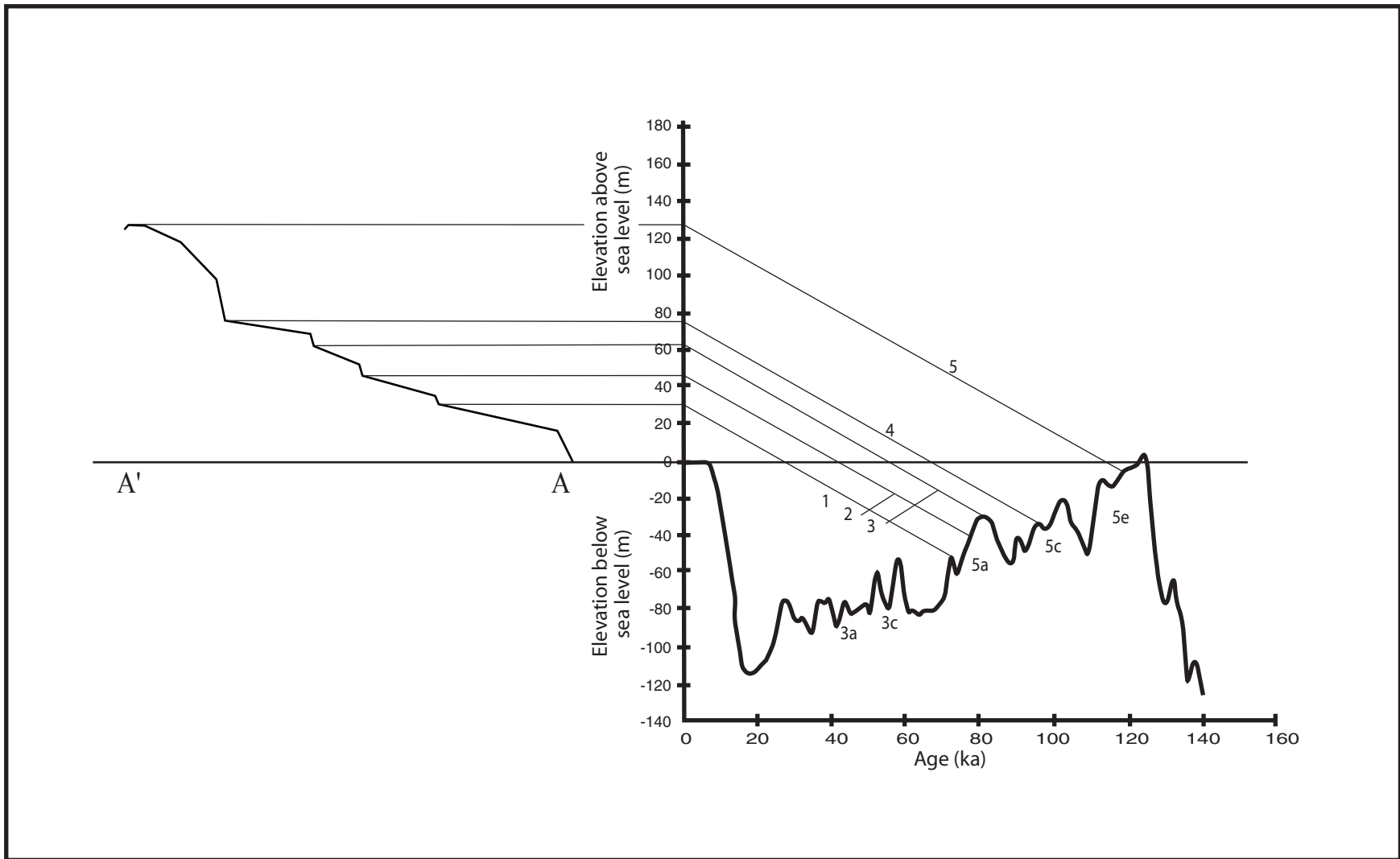


Figure 9. Graph of the late Pleistocene oxygen isotope sea level curve by (Chappell et al., 1996) with profile A-A' and elevations of the five Santa Barbara terrace flights (labelled 1, 2, etc. on the diagram). The first terrace flight is u-series age-dated and correlates to the isotope substage 5a paleo-sea level highstand. The calculated rate of uplift is 1.3 ± 0.2 m/ka. Higher terrace flights are plotted assuming a constant rate of uplift and are correlated to associated paleo-sea level highstands.

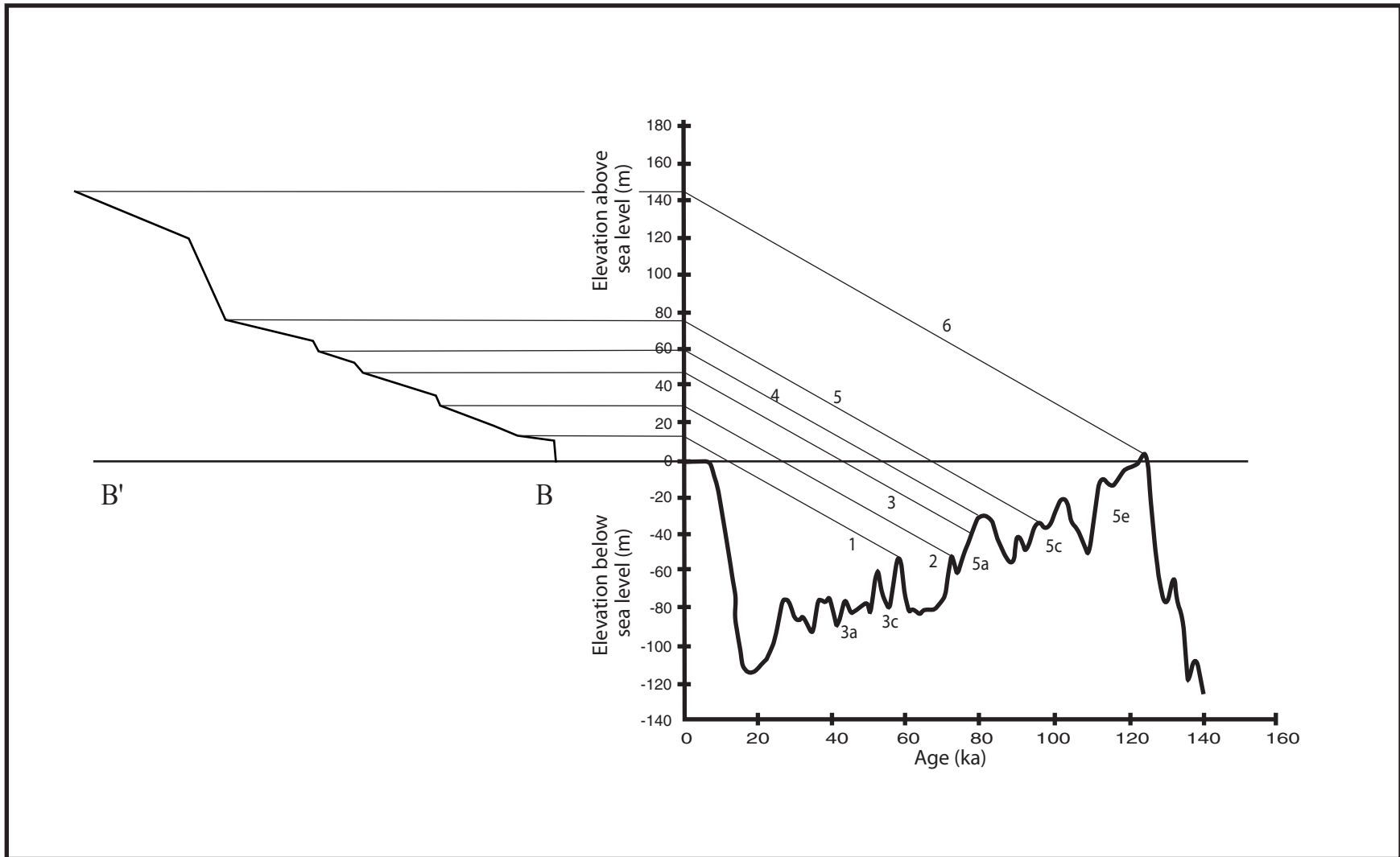


Figure 10. Graph of the late Pleistocene oxygen isotope sea level curve by (Chappell et al., 1996) with profile B-B' and elevations of the six terrace flights terrace flights at Santa Barbara Point (labelled 1, 2, etc. on the diagram). The first and second terrace flight are u-series and OSL age-dated, respectively and correlates to the isotope substage 3a paleo-sea level highstand. The calculated rate of uplift is 1.3 ± 0.2 m/ka. Higher terrace flights are plotted assuming a constant rate of uplift and are correlated to associated paleo-sea level highstands.

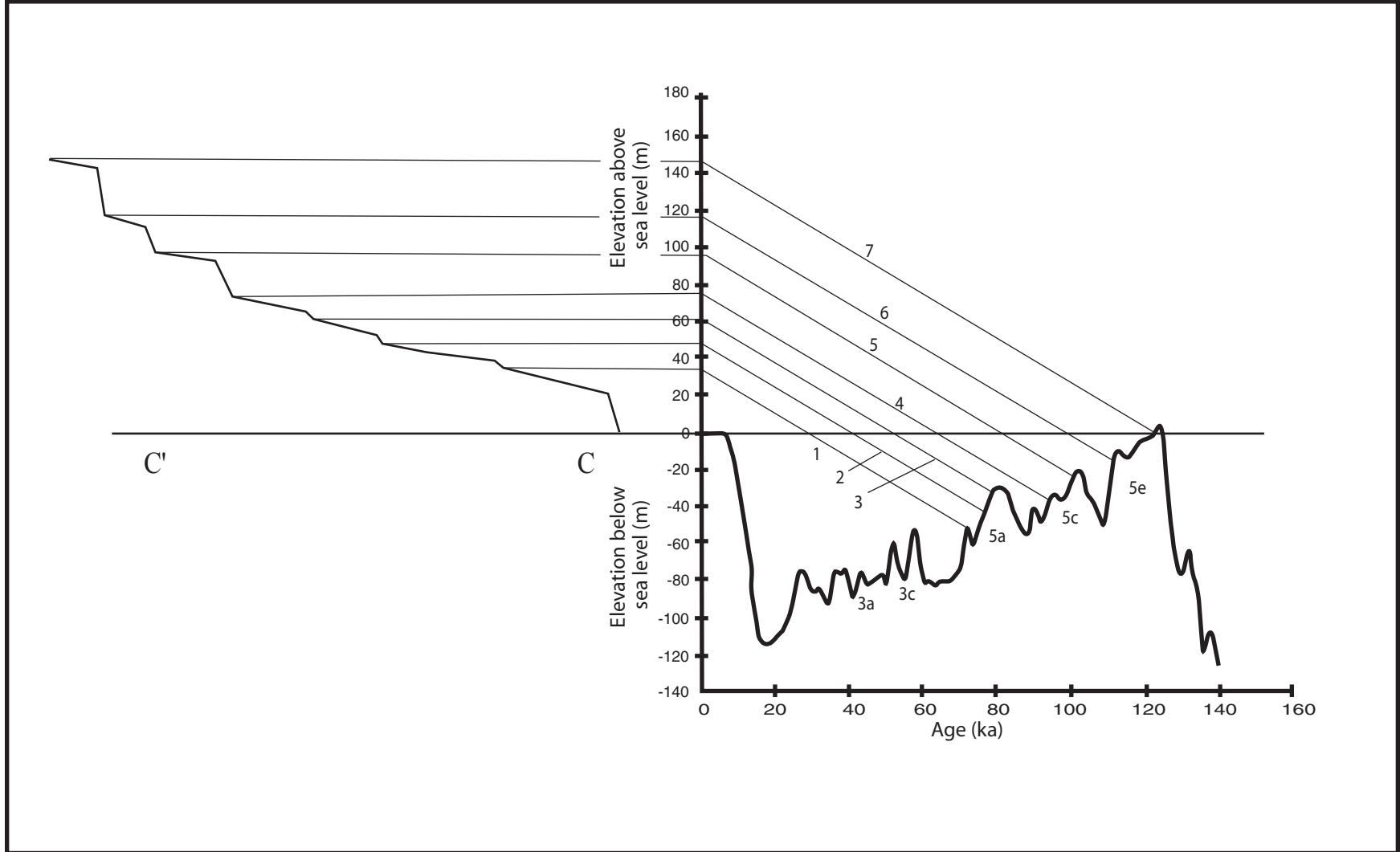


Figure 11. Graph of the late Pleistocene oxygen isotope sea level curve by (Chappell et al., 1996) with profile C-C' and elevations of the Meigs Lane terrace flights (labelled 1, 2, etc. on the diagram). The first terrace flight is u-series and correlates to the isotope stage 3a paleo-sea level highstand. The calculated rate of uplift is 1.3 ± 0.3 m/ka. Higher terrace flights are plotted assuming a constant rate of uplift and are correlated to associated paleo-sea level highstands.

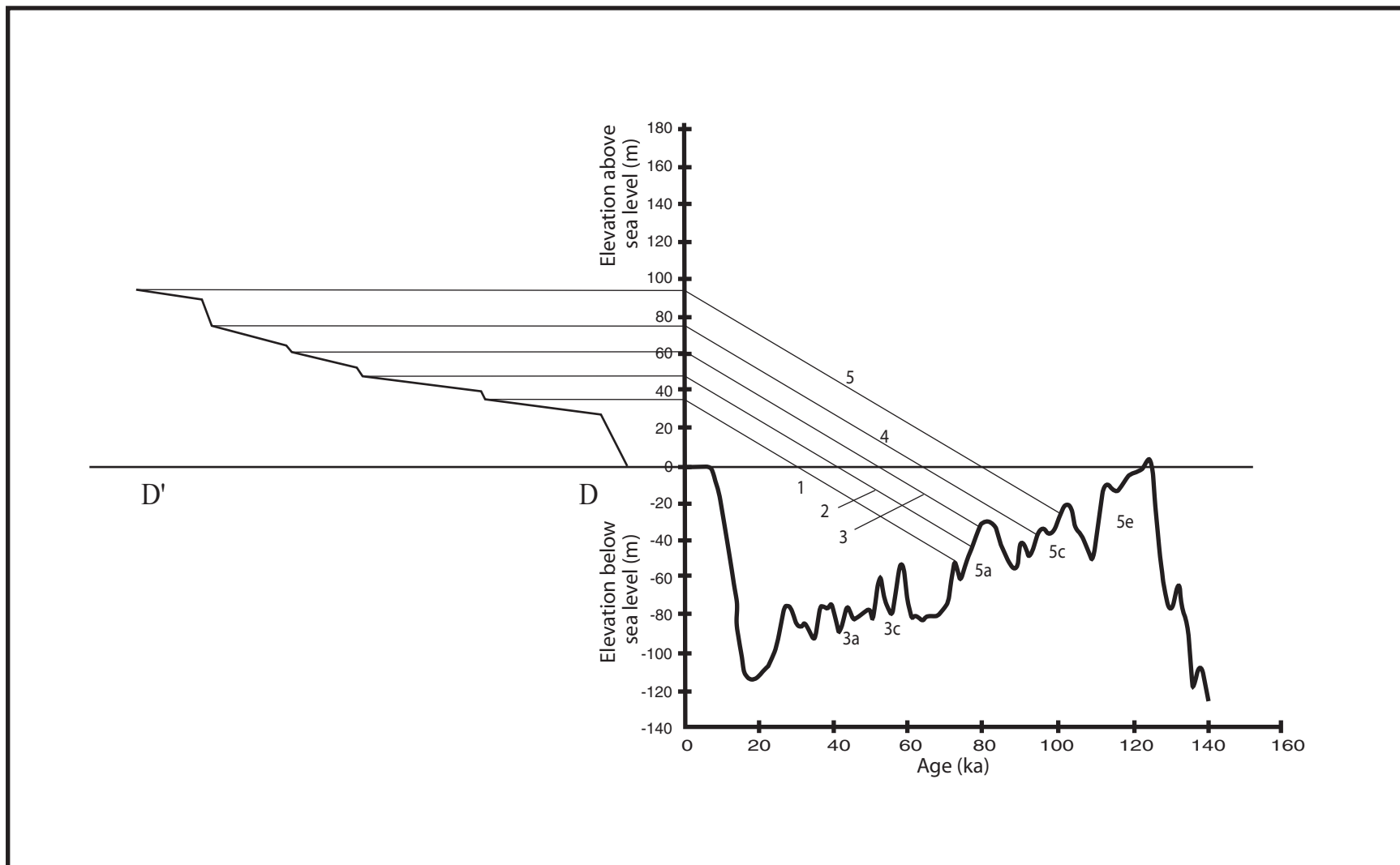


Figure 12. Graph of the late Pleistocene oxygen isotope sea level curve by (Chappell et al., 1996) with profile D-D' and elevations of the Mesa Lane terrace flights (labelled 1, 2, etc. on the diagram). The first terrace flight is u-series age-dated and correlates to the isotope stage 3a paleo-sea level highstand. The calculated rate of uplift is 1.3 ± 0.3 mm/yr. Higher terrace flights are plotted assuming a constant rate of uplift and are correlated to associated paleo-sea level highstands.

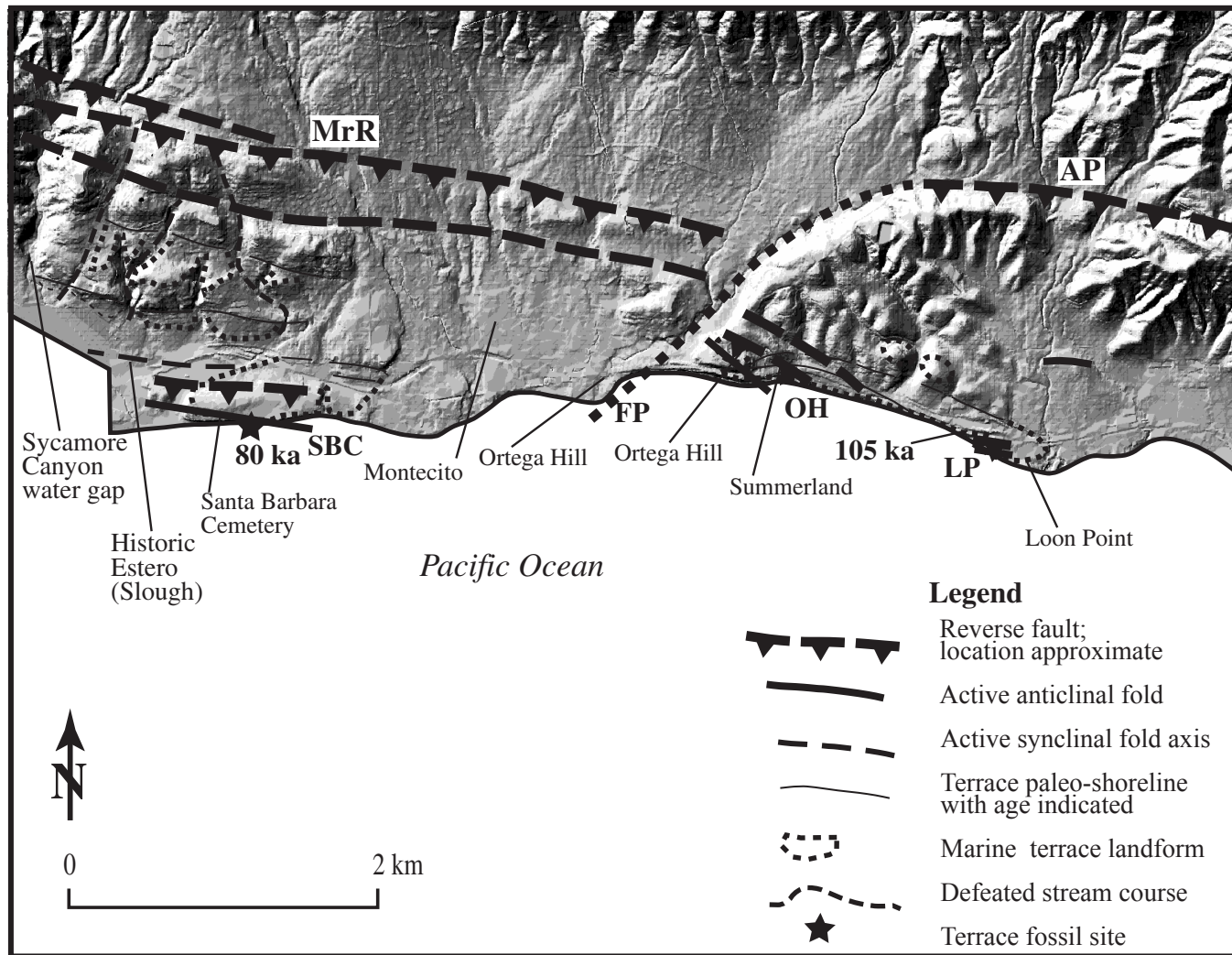


Figure 13. Geomorphic map of the eastern SBFB from Santa Barbara eastward to Summerland. Uplifted marine terraces and the associated paleo-shorelines are shown. The Mission Ridge (MrR), the Fernald Point (FP), the Arroyo Parida (AP), the Santa Barbara Cemetery (SBC), the Ortega Hill (OH), and the Loon Point (LP) faults are shown.

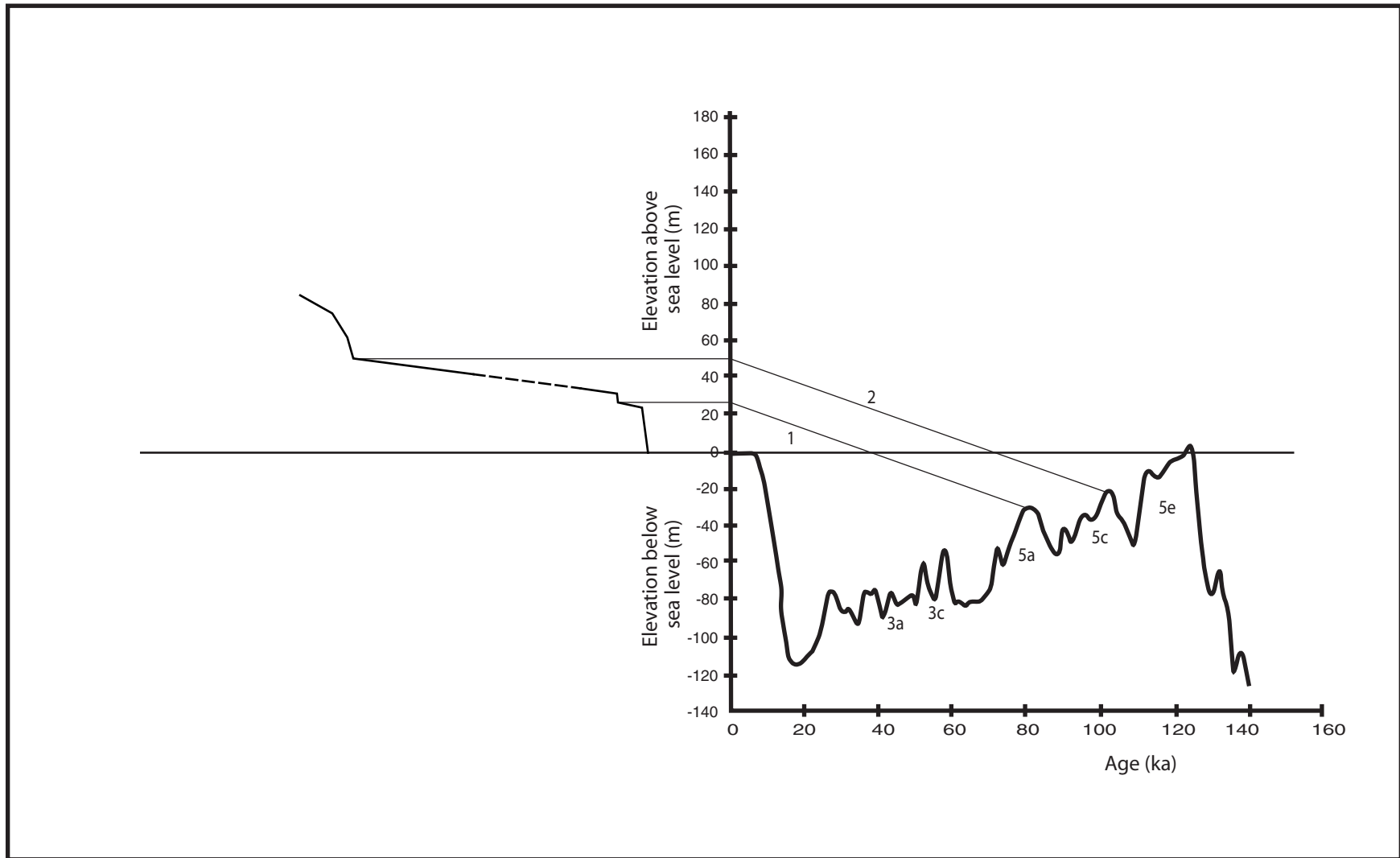


Figure 14. Graph of the late Pleistocene oxygen isotope sea level curve by (Chappell and others, 1996) with the profile and elevations of the two Summerland terrace flights (labelled 1 and 2, on the diagram). The first terrace flight is OSL age-dated and correlates to the isotope stage 5a paleo-sea level highstand. The calculated rate of uplift is 0.7 ± 0.1 m/ka. The next higher terrace flight is plotted assuming a constant rate of uplift and are correlated to the associated paleo-sea level highstand.

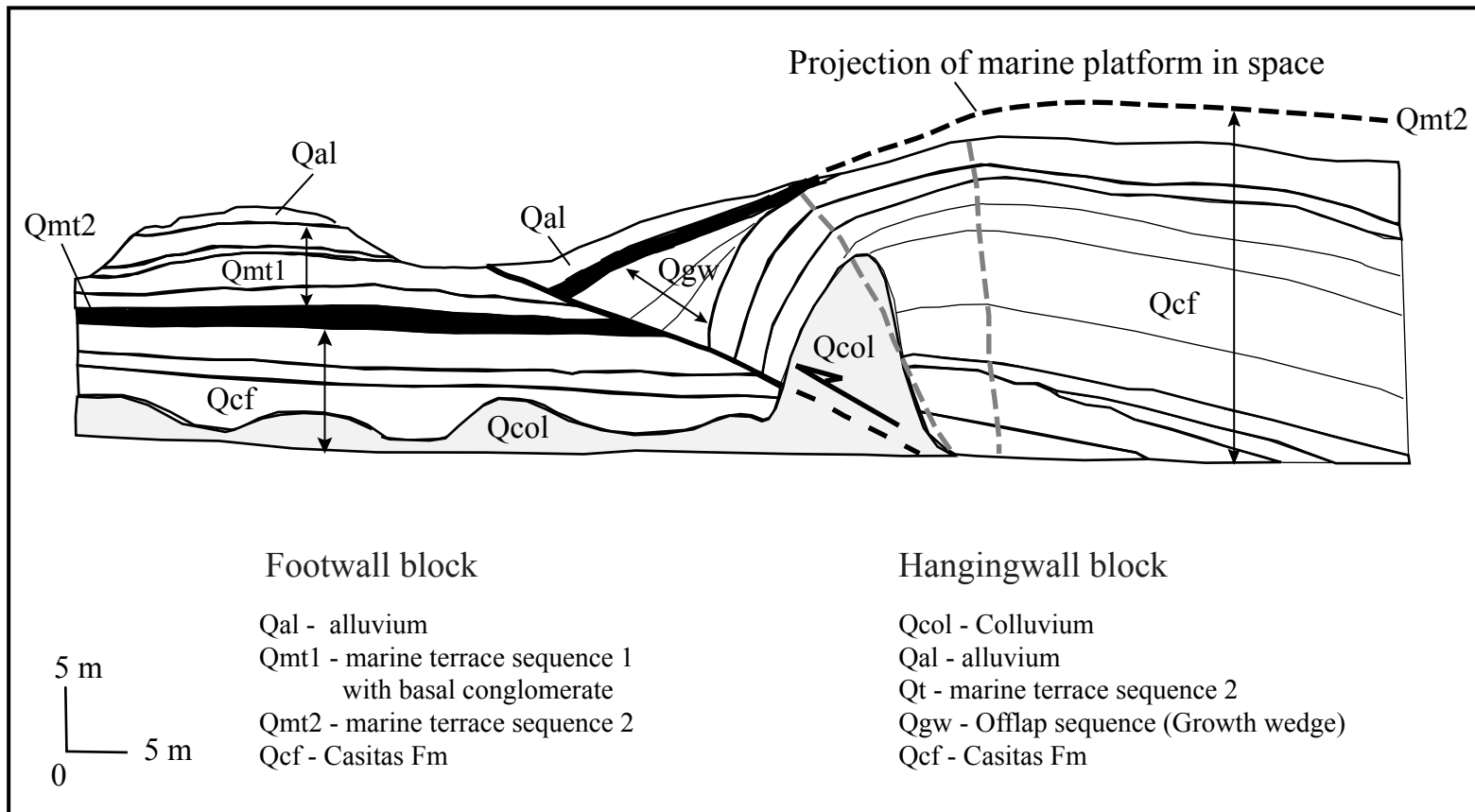


Figure 15. Quaternary stratigraphy of the seacliff exposure of the Loon Point fault-propagation fold. Note the geometry of the growth wedge on the hanging wall fold and the overlying units are rotated into the fault to a lesser degree. Marine terrace sequence 2 projects into space (dashed line) as the result of folding and subsequent erosion. Active axial surfaces (gray dashed lines) are shown.

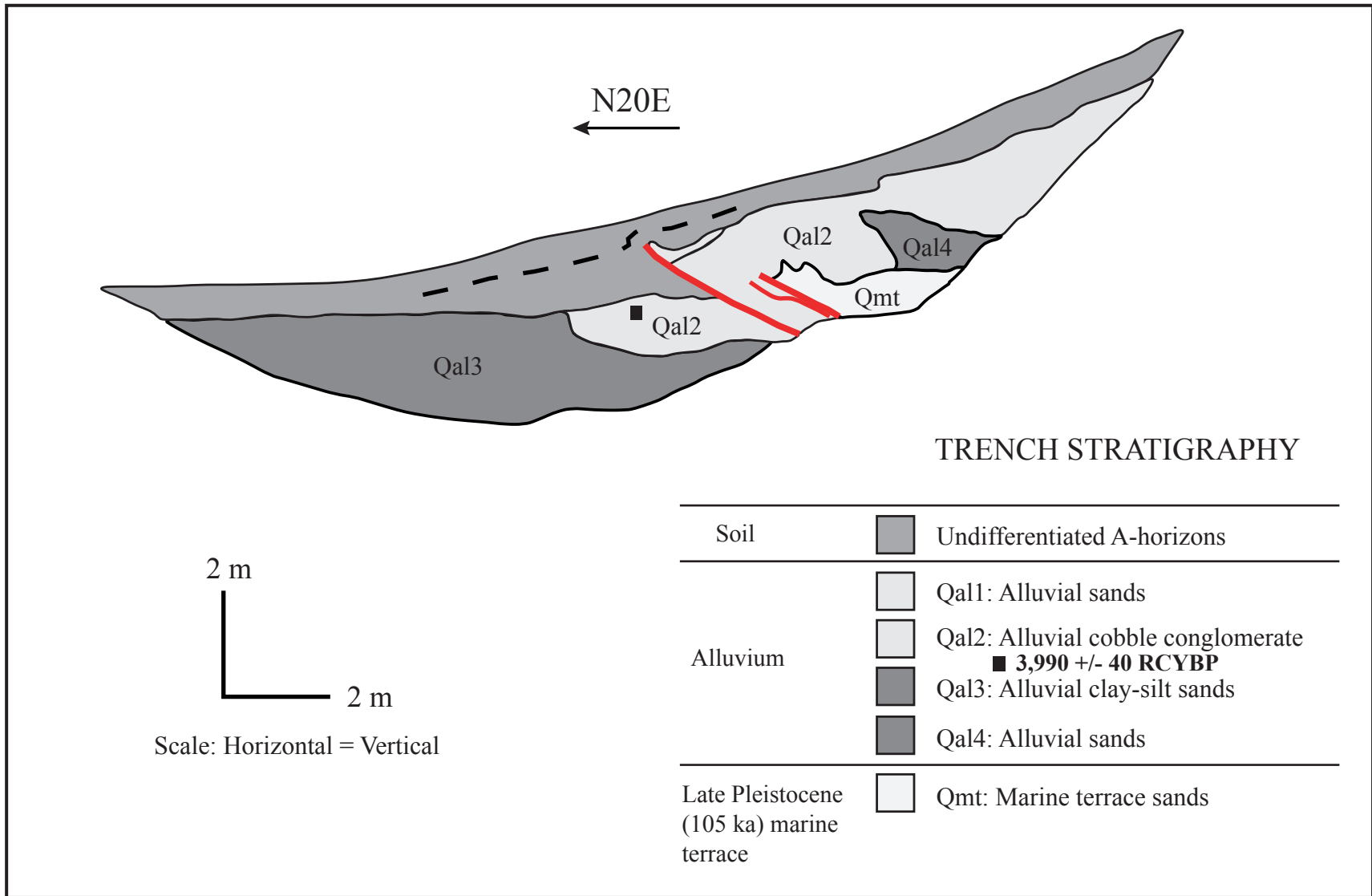


Figure 16. Log of the east trench face of the Loon Point fault, Summerland, California. The top of unit Qa12 is vertically displaced nearly 1 m and radiocarbon analysis of detrital charcoal yields a maximum ¹⁴C age of about 4 ka, therefore the fault is determined to be active.

DAY 3: SANTA BARBARA POINT

8:00 a.m. – 12:00 p.m.

**EARTHQUAKE HAZARD
OF THE
SANTA BARBARA FOLD BELT, CALIFORNIA**
AWARD #1434HQ97GR-02978
L. D. Gurrola and E. A. Keller (PI)
Institute for Crustal Studies
UC Santa Barbara, Santa Barbara, California 93106
(805) 893-4207 office; (805) 893-2314 fax
gurrola@crustal.ucsb.edu keller@magic.ucsb.edu
www.ics.ucsb.edu

INTRODUCTION

The east-west trending Santa Barbara Fold Belt (SBFB) is located on the coastal piedmont of the Santa Ynez Range and offshore in the Santa Barbara Channel. The SBFB is the westward continuation of the Ventura Fold Belt, both located in the southern part of the western Transverse Ranges. The onshore SBFB is expressed topographically by a series anticlinal hills and synclinal basins (Figure 1). This image (Figure 1) is a high resolution digital elevation model with elevation control (0.6 - 1.5 m), from data provided by the Santa Barbara County Flood Control District. The northern boundary of the belt is the Santa Ynez fault and the southern boundary is the Santa Cruz Island fault (Gurrola and Keller, 1997). Santa Barbara is located in a zone of relatively high seismic risk (Figure 2, Southern California Earthquake Center, 1995).

The principal fault of the onshore SBFB is the reverse-slip, Mission Ridge Fault System (MRFS) is approximately 65 km long, subdivided into geomorphic and structural segments, named the More Ranch, the Mission Ridge, and the Arroyo Parida faults (Figure 1) (Gurrola and others, 1996a). The tectonic framework of the SBFB consists of three sets of structures: 1) the east-west striking MRFS; 2) northwest striking reverse faults and associated folds; and 3) northeast striking oblique-slip faults that often form segment boundaries of the MRFS.

INVESTIGATIONS UNDERTAKEN

Seismic hazard assessment of the onshore Santa Barbara Fold Belt includes:

- 1) Identification of potential seismic sources and fault segment boundaries in the SBFB.
- 2) Mapping and establishing chronology of late Pleistocene marine terraces.
- 3) Estimation of rates of uplift.
- 4) Investigation of paleoseismicity of the Loon Point fault-propagation fold and the More Ranch segment of the MRFS.
- 5) Estimation of maximum moment magnitudes of potential earthquakes.

RESULTS

Our research of the onshore SBFB concludes:

- 1) **Seismic sources** of the SBFB are shown in Figure 1 and listed in Table 1. The sources consist mostly of south-dipping reverse faults, many of which are blind, and form topographically well expressed elongated, anticlinal hills. We discovered several potential seismic sources previously unrecognized including faults and folds.
- 2) **Uplifted marine terraces** and associated wave-cut platforms in the SBFB are shown in Figure 3. We establish terrace chronology (Tables 2 and 3) and identify oxygen

isotope stage 3 (40 or 58 ka) (1 ka = 1,000 yr. before present) and stage 5 (82, 105, or 125 ka) terraces. Locally, we identify and map oxygen isotope substages 3c, 5a, and 5c terraces (Gurrola and others; 1996b and 1997b).

3) **Rates of local uplift** based upon marine terrace chronology of the SBFB vary from 1.0 to 2.0 m/ky (mm/yr) (1 ky = 1,000 yrs) (Gurrola and others; 1996b and 1997b). The vertical component of slip on the MRFS has been determined on two sites of the More Ranch segment to be approximately 0.3 m/ky (mm/yr) (Figure 3 and Table 2).

4) **Paleoseismic investigation** of the Loon Point fault, near Summerland, California suggests this fault-propagation fold (Figure 4) most recently ruptured during the pasts 4 ky. A fault trench excavation on the More Ranch segment of the MRFS revealed two paleoearthquakes, the oldest of which occurred approximately 36 ka (Figure 5).

5) **Estimated moment magnitudes** of future earthquakes of seismic sources in the SBFB are listed on Table 1. Segments of the MRFS vary from 15 to 17 km in length. Assuming these represent earthquake segments then, using the method of Wells and Coppersmith (1994) we estimate a maximum M_W 6.5 earthquake on these segments. If multiple segments were to rupture, then a M_W 6.8 to 7.0 (moment magnitude) earthquake is possible. Several sources such as the North Channel Slope, Oak Ridge and Santa Cruz Island faults are capable of producing a M_W 7.1-7.5 event as is the Santa Yñez fault, located about 10 km north of Santa Barbara (Southern California Earthquake Center, 1999). The North Channel Slope fault is considered by the California Division of Mines and Geology (1999) to present the greatest potential seismic hazard to the Santa Barbara area. However, we believe that the Oak Ridge – Mid Channel fault system and associated fold presents a potential equally serious hazard. Assuming a vertical displacement of about 1.0 m per event on a segment of the MRFS, the average return period is approximately 3 ky.

Estimated earthquakes are consistent with historic seismicity in the SBFB. In this century two events of M 5.9 (1941 and 1978) occurred offshore of Carpinteria and Goleta, respectively. The 1925 M_W 6.8 Santa Barbara earthquake is the 7th largest out of 40 earthquakes in southern California with M_W greater than 6.0 in the 20th century (Stein and Hanks, 1998). If this estimated magnitude is correct, then it released about 1.5 times the energy of the 1994 M_W 6.7 Northridge earthquake and 2 times as much energy as the 1971 M_W 6.6 San Fernando earthquake. However, Olsen and Sylvester (1975) report the earthquake to be a M 6.3 based on similar seismic records. The 1994 M_W 6.7 Northridge earthquake is a recent example of the most likely earthquake we expect in the future for the SBFB. Unusually large onshore and/or offshore seeps of oil accompanied by small foreshocks may precede some large earthquakes by several hours in the SBFB. Seeps were reported about 3 hours prior to the 1925 earthquake (Hamilton and others, 1969). Smaller M_W 5-6 earthquakes evidently do not have such precursors or they are too small to be observed

In summary, the Santa Barbara urban corridor is in an area of known seismicity with an earthquake hazard similar to the cities of Ventura and Los Angeles. The city of Santa Barbara is located on the hanging wall of the blind Mission Ridge segment of the MRFS and is subject to amplified shaking during an earthquake as the result of free surface effects of the hanging wall and possible directivity of seismic waves. Parts of the downtown area are susceptible to liquefaction where the historic estero (salt marsh) has been filled (in part from debris from the 1925 earthquake (Simmons, pers. comm., 1999))

and susceptible to a tsunami from an earthquake generated in the Santa Barbara Channel. An earthquake on the MRFS or a fault offshore with a maximum M_W 6.5 to M_W 7.5 could cause extensive damage to the Santa Barbara urban area inflicting several hundred million to a billion or more dollars of property damage, with several to several tens of deaths (depending on the time and day of the earthquake) and thousands of injuries.

NON-TECHNICAL SUMMARY

The Santa Barbara urban corridor is located in a relatively high earthquake risk zone, and is vulnerable to a magnitude 6.5 to 7.5 earthquake, similar to the 1994 Northridge event. The good news is that such an earthquake is very survivable. Most of our one or two story wood-frame buildings will not collapse, although many will be damaged and lose their chimneys. There is concern for older buildings, and those with heavy tile roofing. There is debate concerning the magnitude of the 1925 earthquake as the U.S. Geological Survey lists it as a M_W 6.8 (Stein and Hanks, 1998) whereas, previous study determine it to be a M 6.3 (Olsen and Sylvester, 1975). For hazard preparedness, at a minimum we need to be prepared for the larger (M_W 6.8) earthquake. A M_W 7.1-7.5 event for the North Channel Slope, Santa Ynez, Oak Ridge, or the Santa Cruz Island faults is possible, but less likely than a "Northridge type" event. Several onshore and offshore seismic sources are capable of producing such an earthquake. Unusually large onshore and/or offshore oil seeps accompanied by small foreshocks may precede some large earthquakes by several hours in the Santa Barbara area. A M_W 6.5 to 7.5 earthquake near Santa Barbara would produce damages on the order of several hundred million to a billion or more dollars (damage to infrastructure not included) while inflicting several to several tens of deaths (depending on the time and day of the earthquake) and thousands of injuries to people. Parts of the urban corridor in downtown Santa Barbara and Goleta Slough are vulnerable to liquefaction, amplified ground shaking, and tsunami.

PUBLICATIONS

- Gurrola, L. D., Keller, E. A., Trecker, M. A., and Hartleb, R. 1998, Active folding and buried reverse faulting of the Santa Barbara Fold Belt, California: Geol. Soc. Amer. Field Trip Guide Book Number 11, 43 p.
- Keller, E. A., Gurrola, L. D., and Tierney, T., Geology, 1999, Geomorphic criteria to determine direction of lateral propagation of reverse faulting and folding: Geology, v. 27, no. 6, p. 515-518.
- Trecker, M. A., Gurrola, L. D., and Keller, E. A., 1998, Oxygen-Isotope Correlation of Marine Terraces and Uplift of the Mesa Hills, Santa Barbara, California, USA: In: Stewart, I. S. and Vita Finzi, C. (eds.) Coastal Tectonics: Geological Society of London, Special Publication 146, p. 57-69.
- Gurrola, L. D. and Keller, E. A. 1998, Active folding of emergent marine terraces: Summerland to Carpinteria, Santa Barbara fold belt: California, Geol. Soc. Amer. Abs. with Prog., v. 30, no. 5, p. 17.
- Gurrola, L. D. and Kamerling, M. 1996a, Role of cross faults as tears in thrust ramps in the Ventura and Santa Barbara Fold Belts, California, 1996: Abstracts for the Southern California Earthquake Center Annual Meeting, p. 49.

- Gurrola, L. D. and Kamerling, M. 1996b, Segmentation of principal east-west trending reverse/thrust fault and earthquake nucleation sites in the western Transverse Ranges, California: EOS, Transactions, AGU, v. 77, no. 46, p. 512.
- Hartleb, R., Keller, E. A., and Gurrola, L.D., 1998, Santa Barbara, CA Flood Hazard: A Story of Paleochannels and Earthquakes: Geol. Soc. Amer. Abs. with Prog., v. 30, no. 5, p. 18.
- Keller, E. A., Gurrola, L. D., and Trecker, M. A. 1998, Geomorphic Criteria to Determine Direction and Rate of Lateral Propagation of Reverse Faulting and Folding, Geol. Soc. Amer. Abs. with Prog., v. 30, no. 5, p. 22.
- Keller, E. A. and Gurrola, L. D. 1997a, Can we predict lateral propagation of rupture during earthquakes? Geomorphic indicators of propagation of reverse faults, Santa Barbara Fold Belt, California: Southern California Earthquake Center Annual Meeting, October 1997 p. 69.
- Keller, E. A., Mueller, K., and Gurrola, L D. 1997b, 'Big Bend' of the San Andreas fault: Hypothesis of tectonic extrusion: Geol. Soc. Amer. Abs. with Prog., v. 29, no. 6, p. A-235.
- Ronald, E. C., Keller, E. A., Gurrola, L. D., and Trecker, M. A. 1998, Shoreline Features of the Santa Barbara Fold Belt: A Case of Forensic Seismology: Geol. Soc. Amer. Abs. with Prog., v. 30, no. 5, p. 62.

SCIENTIFIC OUTREACH ACTIVITIES

Leaders: E. A. Keller and L. D. Gurrola

Active Folding and Reverse Faulting: Santa Barbara Fold Belt, California; 2 field trip for Geological Society of America Cordilleran Section Meeting, Long Beach, California, April 5 and 6, 1998.

Session Chairs: E. A. Keller and L. D. Gurrola

Active Folding and Reverse Faulting Session; Geological Society of America Cordilleran Section Meeting, Long Beach, California, April 7-10, 1998.

REFERENCES CITED

- California Division of Mines and Geology, 1999, Santa Barbara Channel faults. Accessed at <http://www.consrv.ca.gov/dmg/shezp/shaking/sntabarb.htm>
- Gurrola, L. D. and Keller, E. A. 1997a, Tectonic geomorphology of the Santa Barbara fold belt, western Transverse Ranges, California: Geol. Soc. Amer. Abs. with Prog., v. 29, no. 6, p. A-344.
- Gurrola, L. D., Chen, J. H., and Keller, E. A., 1997b, Uranium-series age and rate of uplift of the Mesa marine terraces, Santa Barbara Fold Belt, California: Southern California Earthquake Center Annual Meeting, October 1997 p. 64.
- Gurrola, L. D., Slayman, R. C., Hartleb, R. D., and Keller, E. A., 1996a, Segmentation of the Mission Ridge Fault System based on geomorphic and structural expression, Santa Barbara Fold Belt, California, 1996: Abstracts for the Southern California Earthquake Center Annual Meeting, p. 49.
- Gurrola, L. D., Chen, J. H., Keller, E. A., and Metcalf, J. G. 1996b, Dating of emergent marine terraces and rate of uplift for the western Santa Barbara Fold Belt, California: Geol. Soc. Amer. Abstracts with Programs, v. 28, no. 7, p. A-301.
- Hamilton, R. M., Yerkes, R. F., Brown, R. D. Jr., Burford, R. D., and DeNoyer, J. M., 1969, Seismicity and associated affects, Santa Barbara region. In *Geology, Petroleum development and seismicity of the Santa Barbara Channel Region, California*. U.S. Geological Survey Professional Paper 679, p. 47-77.
- Kamerling, M., 1999, personal oral communication.
- Monterey Bay Aquarium Research Institute, 1999, Santa Barbara Basin Expedition 1998: accessed 5/26/99 at <http://www.mbari.org/rd/sbasin/sbbasin.html>
- Southern California Earthquake Center, 1999, Faults of southern California, accessed at <http://www.scecdc.scec.org/faultmap.html>
- Southern California Earthquake Center, 1995, Putting down roots in earthquake country: SCEC, Los Angeles, CA, 28p.
- Spencer, J., and Owen, L., 1999, Luminescence dating of Santa Barbara terraces/raised beaches: preliminary results, unpub. Report, 22 p.
- Stein, R. S., and Hanks, T. C., 1998, M>6 earthquakes in southern California during the twentieth century: No evidence for seismicity or moment deficit: *Bull. Seis. Soc. Amer.*, v. 88, no. 3, p. 635-652.
- Wells, D. L. and Coppersmith, K. J., 1994, New empirical relationships among magnitude, rupture length, rupture width, rupture area, and surface displacement: *Bull. Seis. Soc. Amer.*, v. 84, no. 4, p. 974-1002.

Table 1. Seismic sources of the onshore and offshore Santa Barbara Fold Belt with fault/fold dimensions, activity, and maximum expected earthquake (M_w) are determined using the methodology of Wells and Coppersmith (1994). Names of seismic source abbreviations for Figure 1 are in parenthesis.

Fault	Folds(s)	Length (km)^a	Slip	Vertical rate of faulting (mm/yr)	Activity^b	Max. M_w
<i>Mission Ridge System</i>						
More Ranch segment (MrR)	Ellwood, UCSB, More Mesa anticlines	15	Oblique: reverse-left	0.3	Apparently active	6.4
Mission Ridge segment (MsR)	Mission Ridge, Montecito, Eucalyptus Hill, and Barker Pass anticlines	17	Reverse-(left?)	0.3 – 0.4	Apparently active	6.5
west and east Arroyo Parida segments (AP)		17 15	Oblique: reverse-left	0.4 (Ojai, CA)	Potentially active	6.5 6.4
<i>Northwest striking sources</i>						
Mesa (MF)	Mesa anticline Honda Valley syncline	12	Reverse	Unknown	Potentially active	6.3
Lavigia (LF)	Hope Ranch anticline	15	Reverse	0.1	Potentially active	6.4
San Jose (SJ)	Goleta Valley anticline	7	Reverse-(oblique?)	Unknown	Potentially active	6.1
San Pedro (SP)	unnamed anticlines	8	Oblique: Reverse-left	Unknown	Potentially active	6.1
Loon Point(LP)	Loon Point anticline	1	Reverse	Unknown	Active	5.1
Ortega Hill (OH)	Ortega Hill anticline	1	Reverse-(oblique?)	Unknown	Potentially active	5.1
Santa Barbara Cemetery(SBC)	Santa Barbara Cemetery anticline	1	Reverse	0.1	Apparently active	5.1
Los Carneros (LC)		7	Left	Unknown	Potentially active	6.1
Dos Pueblos (DP)		6	Left	Unknown	Potentially active	6.0
<i>Offshore sources</i>						
Oak Ridge(OR)	Oak Ridge trend	90	Reverse	3.5 to 6.0	Active	7.5 ^c
Pitas Point (PP)	Pitas Point trend	22	Left-reverse	Unknown	Potentially active	6.6 ^c
Red Mountain (RM)		39	Reverse	0.4 to 1.5	Apparently active	6.8 ^d
Rincon Creek (RC)	Rincon Creek anticline	20	Reverse	0.3	Apparently active	6.6
North Channel Slope(NCS)		60	Reverse	2.0	Apparently active	7.1 ^d
Mid Channel (MC)		20	Reverse	Unknown	Active	6.6
Coal Oil Point (COP)	Coal Oil Point anticline	4	Reverse	Unknown	Apparently active	5.8
<i>Other sources</i>						
Santa Yñez		130	Left-reverse	0.1 to 0.7	Active	7.5 ^c

- We assume fault length is the surface rupture length and may be slightly different than map lengths of seismic sources shown on Figure 1.
- Active = demonstrated Holocene (last 10,000 yr.) activity;

Apparently Active = very young (probably Holocene) topographic expression of activity;

Potentially Active = active in Pleistocene (last 1.65 million years)

- c. Data from Southern California Earthquake Center (SCEC, 1999)
- d. Data from California Division of Mines and Geology (1999)

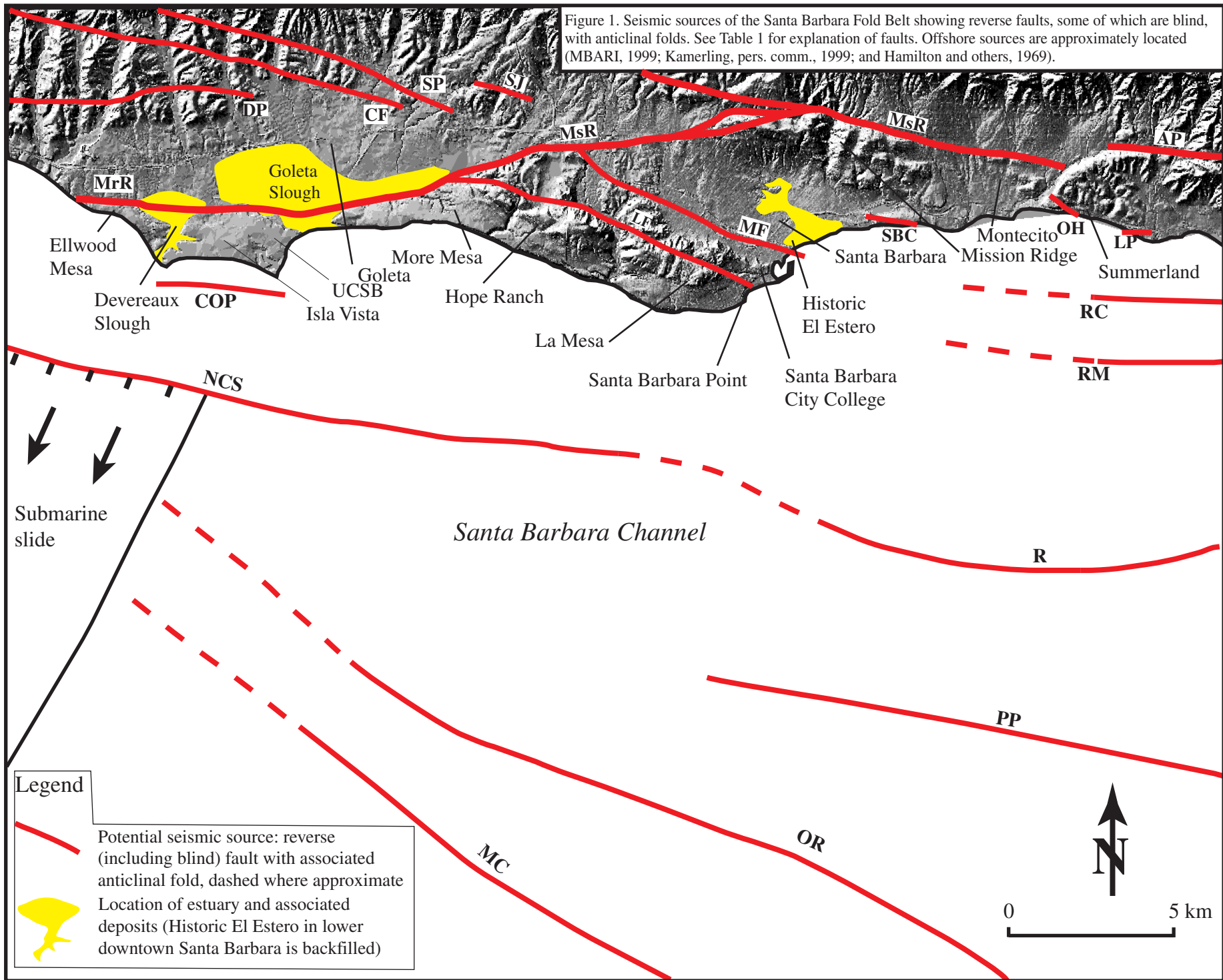
Table 2. Late Pleistocene chronology of marine terraces in the Santa Barbara fold belt. Age-dating methods include uranium series analyses of fossil terrace corals, radiocarbon dating of detrital charcoal, a fossil pholad, and a fossil coral.

Terrace site	Elevation of shoreline angle (m)	Age (ka)	Age-dating method	Vertical uplift rate (m/ka)
Ellwood mesa	27	47 +/- 1.5	Radiocarbon (charcoal)	1.5
Isla Vista - UC Santa Barbara	27	47 +/- 0.5 ka 43.4 +/- 0.8	U-series (coral) Radiocarbon (coral)	1.5
More Mesa	30	36.4 +/- 0.3	Radiocarbon (pholad shell)	1.8
Santa Barbara City College	41	77 +/- 2	U-series (fossil coral)	0.8

Table 3. Optical Stimulated Luminescence measurements and age estimations based on analysis of quartz and K-feldspar grains (Spencer and Owen, 1999). Results are considered maximum ages and the date (336 +/- 64 ka) at Santa Barbara Point is considered unlikely because: 1) the first emergent terrace at Santa Barbara City College has a U-series age of 77 +/- 2 ka, and 2) first emergent terraces throughout the Santa Barbara-Ventura region (when dated) are no older than 125 ka. 1 ka = 1,000 yrs before present.

Terrace Site	Quartz			K-feldspar		
	Paleodose (Gy)	Dose Rate (mGya ⁻¹)	Age (ka)	Paleodose (Gy)	Dose Rate (mGya ⁻¹)	Age (ka)
Santa Barbara Cemetery				262 +/- 25	3.31 +/- 0.3	79 +/- 10
Loon Point	353 +/- 45	3.36 +/- 0.23	105 +/- 15	628 +/- 34	3.76 +/- 0.28	167 +/- 15
Isla Vista				141 +/- 5	3.52 +/- 0.23	40 +/- 3
Santa Barbara Point	1074 +/- 191	3.2 +/- 0.22	336 +/- 64	210 +/- 36	3.61 +/- 0.26	58 +/- 11
Santa Barbara City College	378 +/- 76	3.46 +/- 0.22	109 +/- 23			
More Mesa				231 +/- 24	4.35 +/- 0.32	53 +/- 7

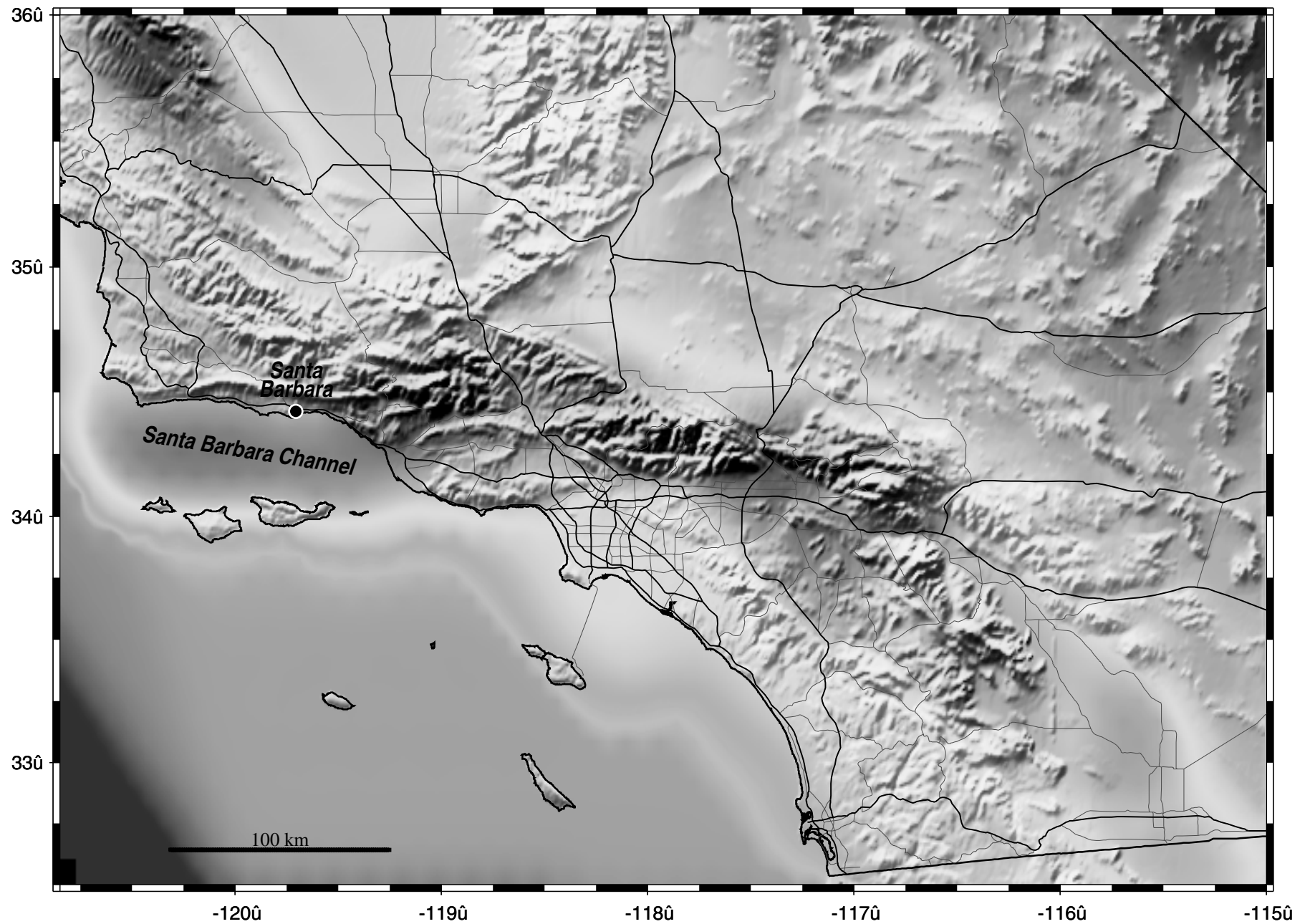
Figure 1. Seismic sources of the Santa Barbara Fold Belt showing reverse faults, some of which are blind, with anticlinal folds. See Table 1 for explanation of faults. Offshore sources are approximately located (MBARI, 1999; Kamerling, pers. comm., 1999; and Hamilton and others, 1969).



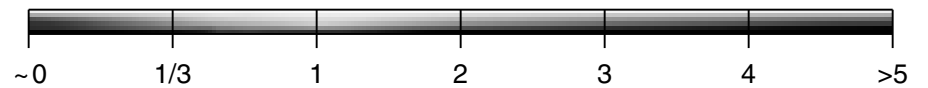
Legend

-  Potential seismic source: reverse (including blind) fault with associated anticlinal fold, dashed where approximate
-  Location of estuary and associated deposits (Historic El Estero in lower downtown Santa Barbara is backfilled)





So. Calif. Earthquake Center (SCEC)



Key - Number of times per century the shaking from earthquakes will exceed 20% the force of gravity. Significant damage to older buildings begins at this level.

GMT Feb 2 13:06 Computer graphics by Ken Hudnut (USGS - Pasadena)

Figure 2. Relative seismic hazard for southern California (SCEC, 1995).

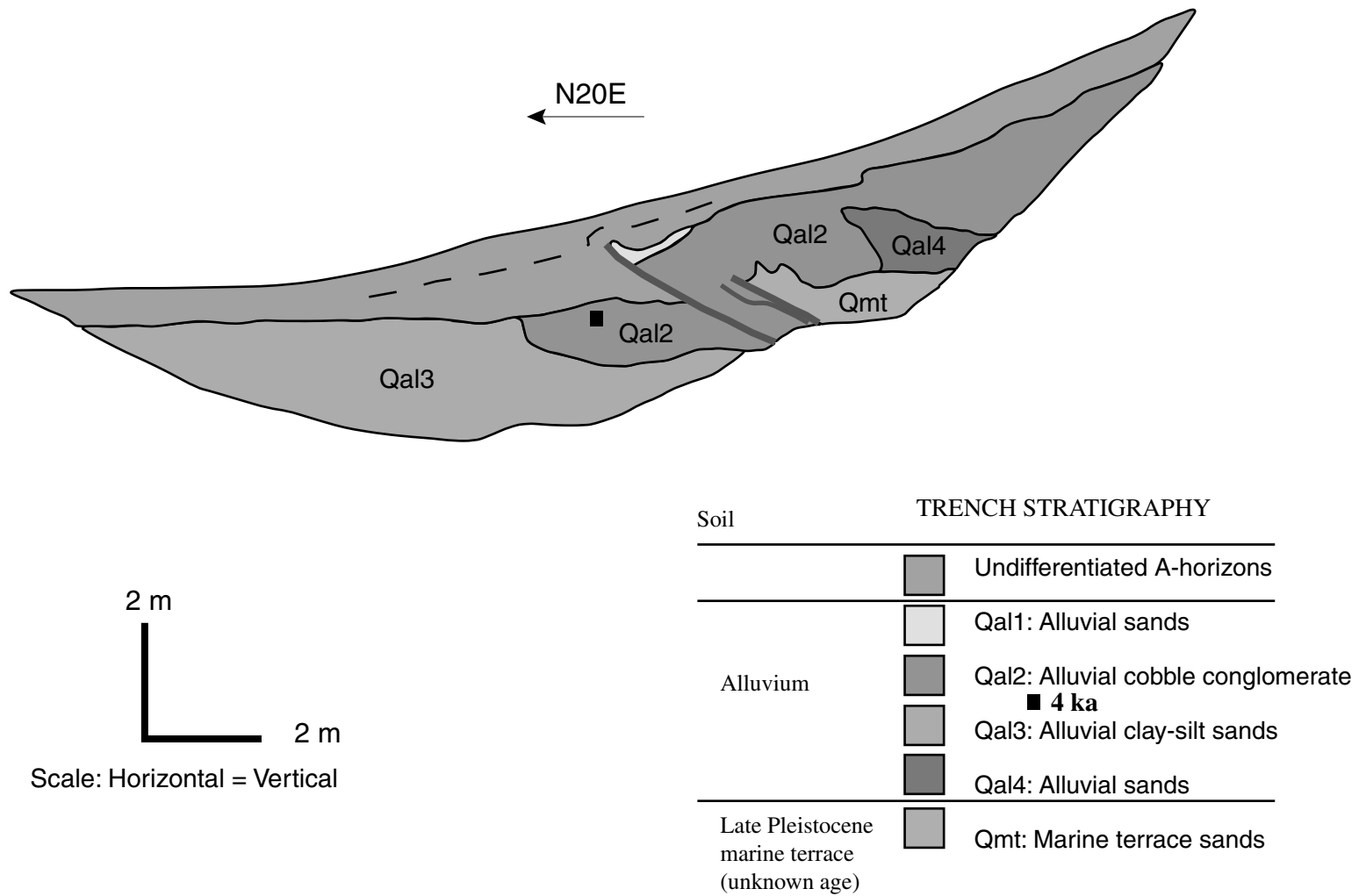


Figure 4. Log of the east trench face of the Loon Point fault, Summerland, California. The top of the marine terrace sands (unit Qmt) is vertically displaced 5 m. The top of unit Qal2 is vertically displaced nearly 1 m and radiocarbon analysis of detrital charcoal yields a maximum ^{14}C age of about 4 ka, therefore the fault is determined to be active.

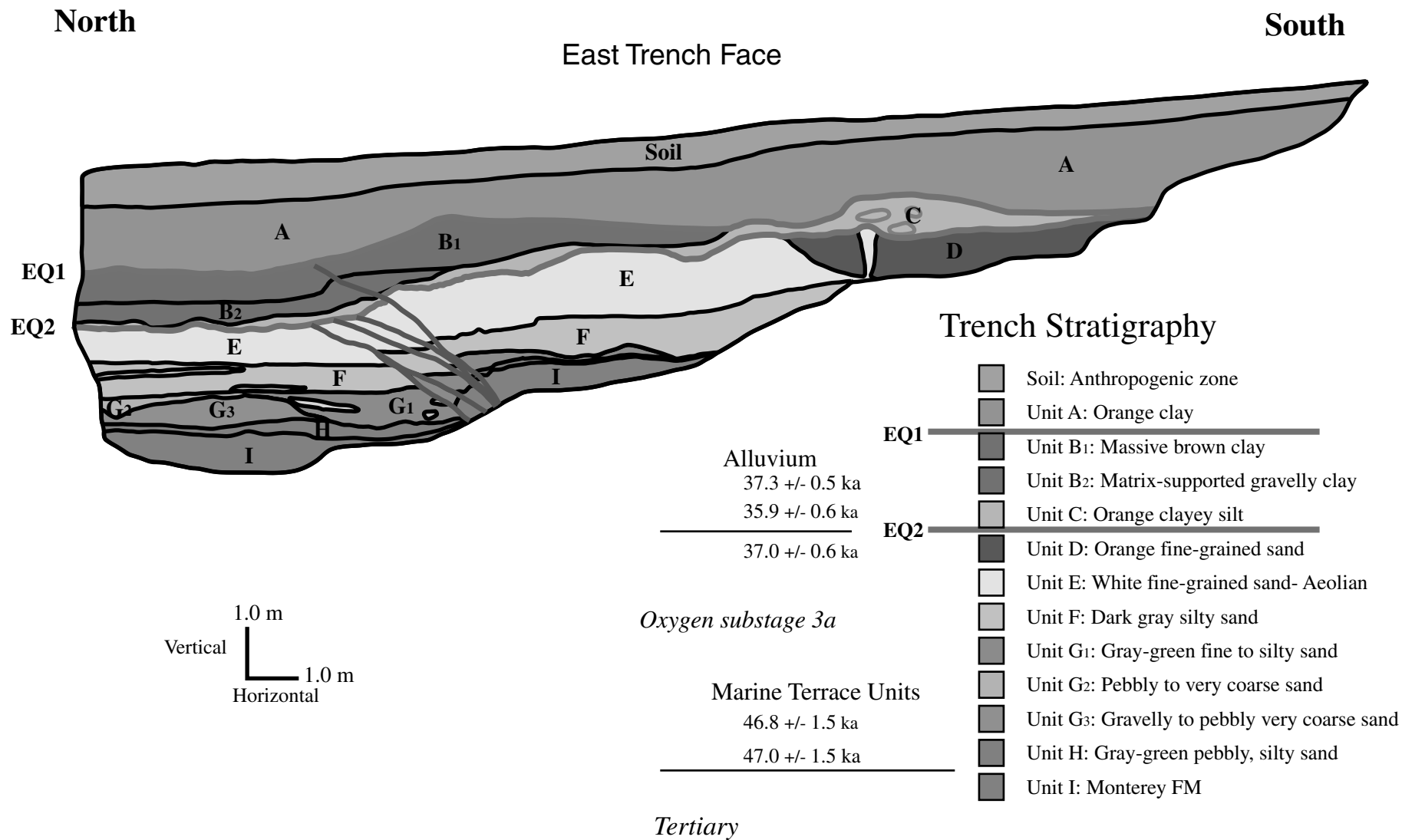


Figure 5. Log of the east trench face of the More Ranch fault folding and faulting of the oxygen isotope substage 3a marine terrace. The wave-cut abrasion platform (contact between units I and H) is vertically offset a total of approximately 1.2 meters. The trench stratigraphy reveals two paleoearthquakes denoted EQ1 and EQ2. that occurred between about 37 ka and 36 ka. The most recent earthquake (EQ1) occurred since 36 ka, however a minimum age of faulting has not been established.

Final Report, July, 2000
Earthquake Hazard of the Santa Barbara Fold Belt, California

NEHRP Award # 99HQGR0081

SCEC Award # 572726

E. A. Keller and L. D. Gurrola

Institute for Crustal Studies

UC Santa Barbara

Santa Barbara, California 93106

(805) 893-4207

Research supported by the U.S. Geological Survey (USGS), Department of Interior, under USGS award 1434-HQ-GR-02978. The views and conclusions contained in this document are those of the authors and should not be interpreted as necessarily representing the official policies, either expressed or implied, of the U.S. government. Parts of this report are from papers and abstracts published as part of the work for the project, and parts are from the Ph.D. dissertation of Larry Gurrola, in preparation. This report is available online at
<http://www.geol.ucsb.edu/~keller/sbeqh.pdf>

TABLE OF CONTENTS

	<u>Page</u>
Technical Abstract	4
Non-Technical Abstract	6
1.0 Introduction	7
1.1 Objectives	8
1.2 Methods Of Study	8
2.0 Tectonic Setting of the Western Transverse Ranges	11
3.0 Tectonic Framework	12
4.0 Historic Seismicity	13
5.0 Stratigraphy	15
5.1 Pre-Quaternary Stratigraphy	15
5.2 Quaternary Stratigraphy	16
5.21 Santa Barbara Formation	17
5.22 Casitas Formation	17
5.23 Late Pleistocene Marine Terrace Deposit	18
5.24 Late Pleistocene Alluvial and Fanglomerate Units	19
5.25 Holocene Alluvial, Fluvial and Colluvial Units	19
6.0 Tectonic Geomorphology of Marine Terraces	19
6.1 Marine Terraces	19
6.2 Marine Terrace Morphology	21
6.3 Marine Terrace Chronology and Rates of Uplift	21
6.4 Emergent Marine Terraces	23
6.41 UCSB Terrace	23
6.42 Ellwood Terraces	25
6.43 More Mesa Terraces	27
6.44 La Mesa Terraces	29
6.45 Montecito Terraces	32
6.46 Summerland Marine Terraces	33
7.0 Tectonic Geomorphology and Paleoseismicity of Folds and Faults	35
7.1 Fault Segmentation	35
7.2 Mission Ridge Fault System (MRFS)	37
7.21 More Ranch Segment	38
7.211 Ellwood Fold	39
7.212 UC Santa Barbara-Isla Vista	46
7.213 More Mesa-Hope Ranch Anticlines	48
7.22 Mission Ridge Segment	48
7.221 Mission Ridge	48
7.222 Montecito Anticline	49
7.3 Northwest-Striking Faults	49
7.31 Goleta Valley Anticline	50
7.32 La Mesa Anticlines	51
7.33 Santa Barbara Cemetery (Zoo) Anticline	51
7.34 Ortega Hill Anticline	52
7.35 Loon Point Fault and Propagation Fold	53
7.351 Paleoseismic Evaluation	55

8.0 Style of Quaternary Folding	56
9.0 Lateral Propagation of Folds: Geomorphic Analysis	57
10.0 Hypothesis of Tectonic Extrusion	59
11.0 Earthquake Magnitudes	62
12.0 Conclusions	64
13.0 Acknowledgments	66
14.0 Bibliography	67
15.0 References Cited	69
Tables 1-5	following text
Figure 1-25	following tables

TECHNICAL ABSTRACT

The Santa Barbara Fold Belt (SBFB) is a linear zone of active folds and (mostly) blind faults on the coastal piedmont and in the Santa Barbara Channel. The fold belt is characterized by several flights of emergent late Pleistocene marine terraces uplifted and preserved on the flanks of active, anticlinal folds. At several locations along the fold belt, the first emergent marine terrace is age-dated through methods that include uranium-series analysis of sampled terrace corals, ^{14}C ages of terrace shells and detrital charcoal, optically stimulated luminescence of terrace sands, and oxygen isotopic signatures of terrace mollusks. These age results are integrated to establish terrace chronology and estimate rates of surface uplift.

The first emergent marine terraces in the western SBFB are approximately 45 ka and correlated to the oxygen isotope stage 3 sea level highstand. Rates of local surface uplift are estimated to be approximately 2 m/ky. Marine terraces preserved in the eastern fold belt range in age from 70 ka to 105 ka and correlate to the oxygen isotope stage 5 sea level highstands. Rates of local surface uplift are estimated to be approximately 1 m/ky.

The onshore portion of the SBFB contains a number of active folds with buried reverse faults. The largest structure is the Mission Ridge Fault System (MRFS) with a vertical slip rate of approximately 0.3 m/ky. Paleoseismic studies of the MRFS at Ellwood Mesa suggest there have been several earthquakes during the late Pleistocene. We expect that the MRFS has an average return period of approximately 3 ky. Reverse faults in the onshore portion of the SBFB are capable of producing earthquakes of M_w 6 to 6.5. If several segments of the MRFS were to rupture simultaneously, an earthquake of approximately 7.0 is possible. A repeat of the 1925 M_w 6.8 Santa Barbara earthquake would likely inflict several hundred million to a billion or more dollars of property damage while inflicting several to several tens of deaths.

NON-TECHNICAL ABSTRACT

The Santa Barbara area exhibits characteristic hills that are formed as the result of faulting. These hills along the coastal area have numerous ancient, raised beaches preserved on them. These beaches contain shells that are used to determine the age of the beach deposit. The estimated ages are used to determine the rate of uplift of the Santa Barbara coastal area.

The Santa Barbara area has ancient beaches that occur above the modern beach that range in age from 45,000 to 105,000 years. The uplift rate of the Santa Barbara area is approximately 1 to 2 mm/yr. This rate is ten times greater than previously estimated.

The Santa Barbara urban corridor is in an area of known seismicity with an earthquake hazard similar to that of the cities of Ventura and Los Angeles. Faults on the onshore portion of the Santa Barbara Fold Belt are capable of producing earthquakes with magnitudes 6 to 6.5 and some faults offshore may produce earthquakes with magnitudes in excess of 7. Damages from an earthquake similar to the 1925 event which devastated downtown Santa Barbara would today cause several hundred million to a billion or more dollars of property damage with several to several tens of deaths.

1.0 INTRODUCTION

The east-west trending Santa Barbara Fold Belt (SBFB) is a linear belt of active folds located on the south flank of the western Transverse Ranges on the coastal piedmont and offshore in the Santa Barbara Channel (Figure 1). Topographically well-expressed folds are the result of mostly blind, active reverse and thrust faulting. Faulted anticlines form linear hills. Intervening low areas such as the sites of the City of Santa Barbara and Goleta Valley are faulted synclines. Coastal erosion has exposed the stratigraphy at several of the anticlines. From Carpinteria west to Ellwood a prominent sea cliff characterizes locations of anticlines and synclines are areas where prominent sea cliffs are not present. Thus the gross geomorphology of the Santa Barbara area is clear; where linear hills are encountered, these landforms are actively growing anticlines being uplifted in response to reverse faulting, often buried. On the other hand, low lying areas that comprise salt marshes and sloughs are faulted synclines, characterized by subsidence. This morphology is clearly shown on the digital elevation models used as the base map for Figures 1 and 2.

The onshore fold belt contains about 12 active and potentially active blind faults with associated surficial folds termed seismic sources (Figure 2 and Table 1). About 10 potential seismic sources were discovered as part of this seismic hazard assessment. Active folding due to blind reverse or thrust faulting in the SBFB presents a significant earthquake hazard to the 200,000 people living in Santa Barbara area (Figure 3).

1.1 OBJECTIVES

Objectives of the tectonic geomorphic study of marine terraces are to: 1) map the distribution of emergent marine terraces and associated paleo-shoreline landforms; 2) estimate the elevation of the shoreline angle; 3) develop an understanding of terrace stratigraphy in order to identify fossil sites and collect samples including fossil solitary

corals and mollusks for chronological analysis; 4) establish late Pleistocene chronology by independent analyses of numerical data through: uranium series analysis of solitary corals; radiocarbon analysis of terrace fossils and organic detritus; optically stimulated luminescence (OSL) of terrace sands, and oxygen isotope signatures of terrace mollusks; and 5) calculate rates of local surface uplift based on terrace chronology.

The objectives of the earthquake hazard assessment of the SBFB are to: 1) identify potential seismic sources; 2) estimate rates of late Pleistocene faulting, folding and uplift; 3) evaluate the style of late Pleistocene deformation; and 4) estimate the earthquake hazard of the SBFB.

1.2 METHODS OF STUDY

The geomorphic study of late Pleistocene, emergent marine terraces of the SBFB includes photogeologic and geomorphic mapping of marine terrace landforms. The terrace landforms were mapped on 1928 (1:18,000 scale) stereo aerial photographs. Commonly, the associated shoreline angle of a particular wave-cut platform is buried and only overlying deposits are exposed in sea cliff and trench exposures, allowing for 3-D mapping, estimation of terrace strata thickness, and collection fossil deposits.

Terrace fossils are rare but most often preserved in the basal conglomerate or in overlying fossiliferous units. Terrace fossil deposits are identified in sea cliff exposures at Ellwood, UC Santa Barbara, More Mesa, Santa Barbara Point, and Santa Barbara City College. Fossil deposits were sampled from sea cliff exposures in order to collect solitary corals for uranium series age-dating and mollusks for oxygen isotopic analysis.

Solitary corals (*Balanopyllia elegans*) are believed to be nearly closed systems with respect to input of uranium from ocean waters following the death of the organism, and therefore provide opportunity for age estimation using uranium-series dating. Fossil mollusks, specifically *Olivella biplicata*, record the oxygen isotope signatures of paleo-ocean temperatures for the sea level highstand at which the terrace formed.

Solitary corals were collected from fossil deposits from the first emergent terraces at UC Santa Barbara and Santa Barbara City College. Initial $^{234}\text{U}/^{238}\text{U}$ ratios of the coral samples from the SBFb were compared to modern day seawater to confirm that there was not an influx of secondary uranium. X-ray diffraction analyses of the samples was used to determine if there was alteration of the original aragonite composition. Terrace corals at both sites were determined to be more than 99% aragonite with no secondary calcite detected. The corals were prepared and analyzed at the Isotope Laboratory, Department of Geological Sciences, California Institute of Technology. The corals provide numerical ages for the first emergent terraces at UC Santa Barbara (UCSB) and Santa Barbara City College (SBCC) allow the correlation of the terraces to late Pleistocene sea level highstand the terraces are assumed to have formed at.

Terrace fossil deposits rarely contain solitary corals; therefore alternative age-dating methods were employed. These include radiocarbon analyses of terrace fossil mollusks and detrital charcoal.

Additionally, terrace sand samples were collected for optically stimulated luminescence (OSL) measurements of terrace potassium feldspar and quartz grains. The OSL data yield maximum ages of deposition of the sands for the UCSB, More Mesa, Santa Barbara Point, Santa Barbara Cemetery, and Loon Point terraces.

Fossil mollusk shells were collected at the Ellwood, UC Santa Barbara, More Mesa, Santa Barbara Point, and SBCC terraces for oxygen isotope analysis (Trecker, 1999). The isotopic signatures are associated the late Pleistocene oxygen isotopic sea level curve and assist in the correlation of terraces from location to location.

Earthquake hazard assessment of the SBFb includes photogeologic, geologic, and geomorphic mapping of Quaternary strata including emergent, late Pleistocene marine terraces preserved on limbs of uplifting, anticlinal folds. The geology of topographically well-exposed folds are exposed in natural and trench exposures, allowing for 3-D mapping, to determine fold geometry, morphology and style of folding.

Review of geologic and geotechnical data and consulting reports were conducted to incorporate unpublished data. Numerous reports involved trench pit excavations for geotechnical, environmental remediation, or fault investigations that revealed both deformed and undeformed Quaternary strata including marine terrace units. During the period of this study (mid- to late 1990s), direct observations and data acquisition at trench pit or borehole drilling investigations were completed to evaluate sites for paleoseismic study. Site-specific investigations include fault-trench excavations along the forelimbs of the Ellwood and Loon Point anticlines to evaluate paleoseismicity of the Mission Ridge fault system and Loon Point fault. Characterization of seismic potential is determined for on land faults in the SBFB based on the rates of deformation from paleoseismic study and fault geometry using method of Wells and Coppersmith (1994).

2.0 TECTONIC SETTING OF THE WESTERN TRANSVERSE RANGES

Shortening across the western Transverse Ranges is the result of strain partitioning associated with right-slip convergence at the "Big Bend" of the San Andreas fault (SCEC, 1995). North-south convergence of about 6 m/ky produces surficial folding formed by blind, reverse (and thrust) faulting (Suppe, 1997).

The SBFB is a continuation of the Ventura Fold Belt. The belt is formed on the south limb of the Santa Ynez anticlinorium, and is bounded north and south by the strike-slip Santa Ynez and Santa Cruz Island faults, respectively. Namson and Davis (1992) argue that the anticlinorium is related to a low-angle, north-dipping ramp of a detachment or decollement at 10-12 km depth. If this hypothesis is correct, then slip on the decollement is transferred to the north-verging structures (backthrusts) on the coastal piedmont (including offshore structures) of the SBFB. Late Pleistocene to Holocene deformation and seismic activity is concentrated on structures south of the Santa Ynez fault on the coastal piedmont and offshore in the Santa Barbara Channel.

3.0 TECTONIC FRAMEWORK

The west-trending Santa Ynez anticlinorium forms the principal topographic feature of the SBFB. The tectonic framework of the fold belt on the coastal piedmont consists of three sets of faults: 1) west-striking, oblique reverse MRFS; 2) northwest-striking oblique reverse faults; and 3) northeast-striking lateral tear faults (Figures 1 and 2).

Segments of the west- and northwest striking faults are defined by geometric, geomorphic and structural characteristics. Segment boundaries of the west and northwest-striking faults are defined by abrupt changes in geometry, geomorphic expression, structural style of deformation, and termination of folds. These segment boundaries coincide with north-east striking faults termed cross faults (Gurrola and Kamerling, 1996). These subtly expressed cross faults may behave as tear faults during coseismic rupture.

Subsurface petroleum data indicates vertical displacement of Tertiary units for the MRFS (Olson, 1982; Jackson and Yeats, 1982). However, the mostly blind MRFS produces folds in the overlying Pleistocene sedimentary units. These sedimentary units deform as fault-propagation folds with hanging wall anticlines (or monoclines) and footwall synclines. In some cases, subsidiary structures such as bending moment faults have propagated up through the fore- and backlimbs of the anticline or syncline such as the Ellwood and the Mission Ridge anticlines.

4.0 HISTORIC SEISMICITY

Historic seismicity in the SBFB shown on Table 2 most seismic activity is located south of the Santa Ynez Range. A seismic map of the probability of seismic shaking for southern California, based upon historic seismicity, and produced by the Southern California Earthquake Center suggests the Santa Barbara area can expect 3 to 4

earthquakes per century with shaking that will exceed 0.2 g, the level of activity where damage to older buildings begins.

The historic record of the Santa Barbara area dates back to the establishment of the missions Purisma and Santa Barbara during the late 18th century (Table 2). Since the early 19th century, three large earthquakes have occurred in the SBFB including the 1812, the 1925, and the 1978 events (Sylvester and Mendes, 1981). Seismologic data for the 1812 and 1925 events are scarce as seismograph stations were non-existent for the 1812 rupture and only a few were operating in 1925. Those seismograph stations determine the location of the epicenter for the 1925 rupture within a 60 km radius.

The 1812 earthquake is the earliest of the three earthquakes, and probably had a magnitude of about M_w 7. The 1812 earthquake produced regional damage throughout northern and southern Santa Barbara County. The seismic source was most likely offshore, perhaps on the offshore Oak Ridge, the North Channel Slope, or the Pitas Point faults.

A large earthquake near the City of Santa Barbara on 26 June, 1925 produced extensive damage to the downtown and surrounding areas (Willis, 1925). Estimated modified Mercalli (MM) intensities were approximately MM VII in the lower, southeast downtown area, whereas maximum intensities were approximately MM VIII-IX at the La Mesa hills (Olsen, 1972).

Preceding the 1925 event, voluminous amounts of petroleum were observed along Santa Barbara beaches and moderate-sized foreshocks began at 3:27 a.m. The main shock followed at 6:42 a.m. and lasted for a duration of about forty seconds (Willis, 1925). Olsen and Sylvester (1975) believe that the intensity of shaking indicates a maximum magnitude of $M_6.3$ for the main earthquake, however, Hanks and Stein (1998) calculate a moment magnitude of M_w 6.8 for the earthquake. The fault that ruptured in 1925 has not been identified, but either offshore or onshore source is possible based on intensity of shaking.

Additional evidence for the estimated **M_w** 6.8 (Hanks and Stein, 1998) is the presence of liquefaction at Goleta Beach. Large waves from storms in the winter of 1997-98 excavated a 3 m high beach scarp at Goleta Beach. The beach scarp exposed 2 to 3 m of convoluted, artificial fill with pervasive soft sediment deformation. The wavelengths of strata convolutions and spacing of vertical dish (dewatering) structures range from one to three meters. These liquefaction features form the lower 1 to 2 m of the scarp and are truncated by overlying, undeformed 1 m thick artificial fill.

Fragments of a Coca-Cola bottle collected from the deformed artificial fill were established to have been manufactured either between 1916 to 1925 or 1945 to 1960. The undeformed, overlying fill is most likely emplaced after 1945, therefore the bottle was most likely manufactured between 1916 and 1925 indicating a pre-1925 age for the deformed artificial fill. The most likely earthquake that produced shaking intensities to produce liquefaction features is the 1925 Santa Barbara earthquake.

The 1978 **M_w** 5.9 Santa Barbara earthquake produced local, moderate damage in the area of Goleta. Following the 1978 event, numerous seismograph stations were installed throughout the Santa Barbara region to gather aftershock data. However, the location and geometry of the epicenter remain in dispute due to disagreement among seismologists (e.g., Corbett and Johnson, 1982; Yeats and Olson, 1984). Yeats and Olson (1984) believe that the 1978 **M_w** 5.9 Santa Barbara earthquake occurred on a south-dipping reverse fault, whereas Corbett and Johnson (1982) argue for a nearshore, low-angle, north-dipping fault. Localized damage in the UC Santa Barbara campus area supports the epicenter location of Corbett and Johnson (1982).

5.0 STRATIGRAPHY

5.1 PRE-QUATERNARY STRATIGRAPHY

Pre-Quaternary strata of the SBFB consist of a section of Eocene through Pliocene rocks that were deposited in a continental margin setting. These rocks include from oldest to youngest: Coldwater Sandstone; Sespe Formation; Vaqueros Sandstone; Rincon Formation; Monterey Formation; and Sisquoc Formation (Table 3). The Sespe, the Rincon, the Monterey, and the Sisquoc Formations typically form the rocks of the mountain slopes and basement rocks of the coastal piedmont. In some cases, these rocks are locally uplifted in the core of anticlines and along faults.

5.2 QUATERNARY STRATIGRAPHY

Quaternary strata of the SBFB consist of a sequence of Pleistocene and late Pleistocene marine and non-marine strata. The Pleistocene sequences are deposited on pre-Quaternary strata on the coastal piedmont (Table 3). The Quaternary units from oldest to youngest include: Santa Barbara Formation; Casitas Formation; and late Pleistocene-Holocene marine terrace deposits; fanlomerate deposits; and other alluvium.

5.21 Santa Barbara Formation

The Santa Barbara Formation is a transgressive marine sandstone with minor units of conglomerates, siltstones and claystones. The Santa Barbara Formation is a basal Quaternary unit with poor age control. However, it overlies the 1.2 ma Bailey Ash in Ventura (Izett et al., 1974; Olson, 1982). Thickness of the Santa Barbara Formation ranges from 150 m to 625 m thick (Olson, 1982; Dibblee, 1988).

Paleomagnetic analyses of the Quaternary Santa Barbara and overlying Casitas Formations were conducted to determine magnetic polarity for relative age-dating and degree of deformation (rotation). Exposed units in Goleta Valley and La Mesa anticlines were sampled for reconnaissance paleomagnetic analyses to determine remnant magnetization polarization (Gurrola, in preparation).

Based on the maximum age for the Santa Barbara Formation of 1.2 ma, paleomagnetic results indicate if deposition occurred during the Matayama (1.2 ma to 790 ka) or Bruhnes (post 790 ka to late Pleistocene) epoch by determining if polarization is reverse (Matayama) or normal (Bruhnes). Paleomagnetic results yield normally magnetized sediments of the Santa Barbara Formation in both the Goleta Valley and La Mesa folds, and are therefore, younger than 790 ka. Clockwise, rotations range from 0° to approximately 30° and are the result of localized rotational deformation near reverse faults with a minor component of sinistral slip (Gurrola, in preparation).

5.22 Casitas Formation

The mostly non-marine Casitas Formation is the result of alluvial deposition on the coastal piedmont in the middle to late Pleistocene. The rocks typically range from pebbly sandstones to gravel and boulder conglomerates. The basal Casitas Formation grades into regressive units of nearshore marine sandstones and siltstones and is exposed in the sea cliff Loon Point at Summerland.

Stratigraphic relations suggest the Casitas Formation is younger than the underlying Santa Barbara Formation (Olson, 1982). Paleomagnetic analysis of the basal section of the Casitas Formation sampled from the Loon Point and Ortega Hill folds indicate normal remnant magnetization. These paleomagnetic results are in agreement with results from the underlying Santa Barbara Formation and confirm Casitas deposition occurred during the Bruhnes epoch (post 790 ka). The Casitas Formation is older than the age of the overlying, late Pleistocene marine terrace and alluvial units and most likely is about 500 to 125 ka, and represents a series of Pleistocene aggradation events.

5.23 Late Pleistocene Marine Terrace Deposits

Wave-cut platforms in the SBF are eroded on Pre-Quaternary strata such as the Sisquoc and the Monterey Formations and Pleistocene Santa Barbara and Casitas

Formations. Wave-cut platforms are commonly overlain by a thin, basal cobble to pebble conglomerate (boulder line) with overlying terrace deposits ranging from a 2 m to 5 m thick section of marine sands with an aeolian cap.

Terrace fossils preserved in the conglomerate or in locally, fossiliferous units were sampled in order to obtain solitary corals for uranium series age-dating analysis. Two solitary corals from the UC Santa Barbara terrace and the Santa Barbara City College terrace were analyzed and yield estimated ages of 47 +/- 0.5 and 70 +/- 2.0, respectively (Table 4).

5.24 Late Pleistocene Alluvial and Fanglomerate Units

Late Pleistocene fanglomerate deposits are generally coarse boulder to gravel conglomerates deposited as alluvial fans. Alluvial fan deposition on the coastal piedmont occurred on south-flowing streams from the Santa Ynez Mountains. Alluvial deposits generally range from silt-sandstone to cobble-gravel conglomerate, which may overlie marine terrace deposits. The ages of late Pleistocene alluvial and fanglomerate units are not known, but are younger than underlying Casitas Formation, and therefore are most likely mid to late Pleistocene in age.

5.25 Holocene Alluvial, Fluvial and Colluvial Units

Holocene alluvium typically consists of clay rich, silt-sandstone and conglomerate units that cap late Pleistocene marine terrace units. An alluvial unit that caps the Loon Point fault terrace (discussed in a later section) is radiocarbon age-dated at 3,980 +/- 40 RCYBP (Table 4). Holocene colluvial units generally consist of brecciated, matrix- to clast-supported conglomerates and are deposited at the base fold, fault, and sea cliff scarps. Holocene fluvial units typically consist of clay, silt, and sand, and gravel to cobble conglomerate units deposited along active south-flowing stream channels on the coastal piedmont.

6.0 TECTONIC GEOMORPHOLOGY OF MARINE TERRACES

6.1 MARINE TERRACES

Several flights of terraces are preserved in the SBF. They are assumed to reflect the formation at interglacial paleo-sea level highstands in conjunction with tectonic uplift (Matthews, 1973; Kern, 1977; Lajoie et al., 1982). Emergent marine terraces originate as eroded, wave-cut platforms forming unconformities on the underlying bedrock. Commonly, as tectonic uplift occurs, a thin veneer of (regressive) marine sands are preserved on the marine platform producing an unconformity which is subsequently covered by alluvial and colluvial sediments.

Late Pleistocene sea level highstands are times when wave-cut platforms and sea cliffs at landward edges of marine platforms are assumed to form. The intersection of the paleo-sea cliff with the wave-cut abrasion platform defines the terrace shoreline angle (Lajoie et al., 1979). The shoreline angle approximates the position of paleo-sea level within one or two meters of mean (high) sea level for that platform level and is the preferred reference to paleo-sea level. However, the shoreline angle is typically buried beneath beach deposits, sea cliff colluvium, and/or alluvium, and as a result the elevation of the shoreline angle is often an estimate.

Fluctuations in late Pleistocene sea levels are well studied for the last 125 ka, and sea level highstands are correlated to coral reef terraces and deep-sea oxygen isotope records (Bloom et al., 1974; Chappell, 1983; Chappell and Shackleton, 1986; Chappell et al., 1996). First emergent terraces of known age are related to the revised paleo-sea level curve by Chappell et al. (1996). A rate of uplift for a particular site is calculated based on the elevation of the shoreline angle of the platform, and the numerical age of the marine terrace, and the elevation of the paleo-sea level highstand of the assumed age of the platform. Muhs et al. (1994a) believe that paleo-sea levels for substages 5a (80 ka) and

5c (105 ka) were closer to present day sea level. If this is the case, then the surface uplift rates calculated in this study are maximum with respect to known sea level curves.

6.2 MARINE TERRACE MORPHOLOGY

Marine terraces are some of the most obvious landforms on the Santa Barbara coastal piedmont. Elevations of wave-cut platform shoreline angles range from approximately 25 m to greater than 200 m. Expression of paleo-shoreline angles are relatively poor, but associated paleo-sea cliffs often form moderate to well-expressed scarps. Paleo-shorelines are often laterally discontinuous across streams that dissect terraces, deformed by folds, and/or buried beneath alluvial fan and colluvial deposits (Figure 4).

A sequence of terraces at a specific site is discussed with respect to the first emergent terrace, which is at the seaward edge. The first emergent terraces at Ellwood, UC Santa Barbara, Santa Barbara Point, Santa Barbara City College, More Mesa, Santa Barbara Cemetery, and Summerland have estimated ages based upon considering several potential chronological methods.

6.3 MARINE TERRACE CHRONOLOGY AND RATES OF UPLIFT

Establishment of the marine terrace chronology is fundamental in order to estimate the vertical rate of surface uplift. Age dating of terrace fossil fauna directly overlying the abrasion platform determines a minimum age of platform formation. Commonly along the California coast, first emergent marine terraces are formed during stage 5 (80 ka to 125 ka) paleo-sea level highstands. However, terraces formed during the substage 3a (45 ka) paleo-sea level highstand are present along the Santa Barbara and Ventura coasts (Lajoie et al., 1982; Gurrola et al., 1997a,b; 1996). Presence of isotope stage 3 terraces suggests a relatively high rate of surface uplift exceeding 1 m/ky.

In order to numerically age-date marine terraces, it is preferable to locate terrace fossil sites, collect solitary corals, and date the corals by uranium-series analysis (Muhs et al., 1992 and 1994b). Marine terrace chronology is then established using the TIMS method (Chen et al., 1986) of uranium series analysis.

The estimated minimum age of the marine terrace allows for assignment to an oxygen isotopic stage and determination of the associated paleo-sea level relative to modern day sea level. Mapping and estimation of the elevation of the shoreline angles of terraces of known ages provide the data necessary to calculate amounts of vertical surface uplift and styles of vertical deformation.

Non-marine, colluvium and alluvium often obscure the shoreline angle and the elevation is determined from shallow subsurface data or from sea cliff exposures. Once the elevations of shoreline angles are estimated, correlation of undated, higher (or lower) flights of terraces to oxygen isotopic stage and sea level highstands can be accomplished using the method outlined by Bull (1985). Because terraces are discontinuous in the SBFB, it is necessary to correlate terraces of known age to those of unknown age across changes in topography and change of structure (Figure 4). Adjacent flights of terraces of known and unknown age are correlated by several methods including numerical age (u-series, carbon 14, OSL) and isotopic signatures of fossils (Trecker et al., 1998).

Solitary coral *Balanophyllia elegans* was analyzed from two marine terraces in the SBFB. A terrace coral was sampled from the Isla Vista terrace and one was obtained from a fossil collection at UC Santa Barbara. The coral from the UC Santa Barbara fossil collection was sampled by Lorenzo Yates from the Santa Barbara City College terrace at a location, immediately east of Point Castillo, formerly named Bathhouse Beach. U-series analyses age-date the Isla Vista (UC Santa Barbara) at 47 ± 0.5 ka and Santa Barbara City College (Bathhouse Beach) at 70 ± 2 ka (Table 4) (Gurrola et al., 1997a; 1998).

Radiocarbon and OSL age-dates compliment the uranium series data for terraces where solitary corals were not found. Radiocarbon and OSL samples were obtained from the Loon Point, Santa Barbara Cemetery, Santa Barbara Point, Santa Barbara City College, and UC Santa Barbara terraces (Table 4).

6.4 EMERGENT MARINE TERRACES

6.41 UCSB Terrace

The first emergent marine terrace at UCSB extends from Devereaux Slough to Goleta Slough and is bounded by the More Ranch fault to the north and the Coil Oil Point fault to the south (Figure 5). A terrace fossil assemblage is exposed on the sea cliff at Isla Vista beach on the first emergent UCSB marine terrace (Figure 5). The fossil site was sampled and a solitary coral obtained for uranium series and radiocarbon analyses.

The well-preserved, fossil solitary coral *Balanophyllia elegans* was collected and analyzed by X-ray diffraction. The X-ray diffraction analysis of the coral determined that the shell material was entirely aragonite and was not re-crystallized. The fossil coral was then uranium-series analyzed and determined to have an initial $^{234}\text{U}/^{238}\text{U}$ ratio similar to that of modern day seawater (Chen et al., 1986). The UCSB terrace coral yielded a uranium-series age of 47 +/- 0.5 ka and a radiocarbon age of 43,400 +/- 800 RCYBP (Table 4).

Terrace sands were sampled at the Isla Vista fossil site to measure potassium feldspar grains for optically simulated luminescence (Spencer and Owen, 1999) (Figure 5). OSL measurements of the terrace sands yield age an estimate of approximately 40 +/- 0.3 ka (Table 4).

Oxygen isotopic signatures of terrace mollusks (*Olivella biplicata*) sampled from the fossil site indicate a cool paleo-ocean temperature (Trecker et al., 1998; Trecker, 1999) which is consistent with the numerical ages from uranium-series, radiocarbon, and

OSL analysis. Therefore the UCSB terrace is assigned to the isotope substage 3a paleo-sea level highstand at approximately 45 ka.

The paleo-shoreline associated with the UCSB terrace is buried on the footwall of the More Ranch segment. The maximum observed elevation of the marine platform is approximately 14.0 +/- 0.5 m yields a calculated, minimum total vertical surface uplift of 79 m and a local vertical surface uplift rate of 1.7 +/- 0.1 mm/yr. (Figure 6). This local uplift rate is the result of folding and faulting on several, adjacent structures including the More Ranch segment to the north and the Coal Oil Point fault to the south (Figure 1).

6.42 Ellwood Terraces

The Ellwood Mesa marine terrace is the first emergent terrace west of Devereaux Slough. The terrace forms a continuous surface to the west margin of study (Figure 2). At Devereaux Creek, the marine terrace is anticlinally folded on the hanging-wall of the More Ranch segment, whereas to the west, the terrace is faulted and vertically offset in a sea cliff exposure. Although the Ellwood terrace is deformed across the More Ranch segment of the MRFS, the marine abrasion platform is mappable across the fault.

Presently the Ellwood terrace strandline is poorly preserved north of the More Ranch segment (Figure 5). Early (1928) aerial photographs reveal that the strandline is moderately expressed and is mappable across the Ellwood terrace westward to where it trends offshore, west of the fault exposure.

The strandline elevation of the Ellwood terrace is approximately 23.5 +/- 1.5 m. Detrital charcoal sampled from the basal terrace unit yielded a radiocarbon age of 47 +/- 1.5 ka and allowed for correlation to the oxygen isotope substage 3a and the UCSB terrace (Figure 6; Table 4). Oxygen isotope signatures of fossil mollusks indicate a cool paleo-ocean water temperature (Trecker et al., 1998) which is consistent with substage 3a. Based on the strandline elevation, the amount of total, vertical uplift for substage 3a is

approximately 65 m (Chappell et al., 1996) yielding a calculated local rate of vertical surface uplift of approximately 1.9 ± 0.1 mm/yr. (Figure 6).

Higher flights of terraces are preserved at 31 ± 1.5 m, 39 ± 1.5 m, 44 ± 1.5 m, 63 ± 1.5 m, and 131 ± 1.5 m and in the Dos Pueblos area of Goleta (Figure 5). The shoreline angles associated with these terraces are moderately to poorly preserved and in places, buried by alluvium. To the west, the highest terrace (131 ± 2.5 m) caps north-south trending ridges and to the east caps the crests of active folds. As a result this terrace is laterally discontinuous due to numerous deeply incised drainages, but by position appears to be the same marine terrace surface from Goleta Valley to the western study area. The terrace surfaces are mostly stripped with little or no marine terrace sediments preserved.

A prominent shoreline angle and associated paleo-sea cliff delineates the next lower (63 ± 1.5 m) terrace (Figure 5). The well-preserved, east-west trending, paleo-sea cliff abruptly truncates north-south trending ridges, forming faceted spurs. This paleo-shoreline is mappable in Goleta where it decreases in elevation eastward to approximately 38 m and is buried beneath alluvium .

Based on a calculated uplift rate of 1.9 ± 0.1 mm/yr (Figure 6), and assuming a constant rate of uplift (Bull, 1985), the 44 ± 1.5 m, 63 ± 1.5 m, and 131 ± 1.5 m terraces correlate to oxygen isotope substages 3c (58 ka) and 5a (71 ka or 81 ka). The shoreline angles at elevations of 31 m and 39 m probably result from strong local earthquakes and associated coseismic surface uplifts (2 to 4 m+) of the coastline. Alternatively, these strandlines may be the result of temporary stabilization or hiatus of sea level fluctuations during sea level transgression or regression.

6.43 More Mesa Terraces

More Mesa is the most laterally continuous and well-expressed marine terrace in the SBFB (Figure 7). The More Mesa terraces are continuous from Las Positas west to

Goleta Slough. More Mesa is located on the hanging wall of the More Ranch fault and the north margin is bounded by the More Ranch segment, which truncates several terrace shorelines.

The first emergent marine terrace is preserved on the axis of a Quaternary syncline and the terrace surface is tilted and down-warped to the north (Figure 7). The terrace forms a 4 km long and nearly 1 km wide surface. The shoreline angle of the first emergent terrace is buried due to the synclinal warping of the terrace and is the least discernible of all terraces.

A fossil locality previously unidentified was discovered on the first emergent terrace in a gully at a sea cliff re-entrant (Figure 7). The age of the terrace is estimated by radiocarbon dating of a pholad shell, optically stimulated luminescence of terrace sand grains, and correlation by isotopic signatures of mollusks.

A fossil pholad shell was sampled and obtained from a rock borehole in growth position. Initial SEM analysis determined that the shell material was unaltered aragonite. The shell yielded a ^{14}C of 36,830 +/- 330 RCYBP (Table 4), however Voelker and others (1998) report a large fluctuation in the calibration of ^{14}C ages between 32-34 ka. They determine a ^{14}C age-offset (correction factor) of approximately 5 +/- 1 ka for the pholad age which results in a calibrated ^{14}C age of approximately 41,830 +/- 1,330 RCYBP.

Oxygen isotope signatures of fossil mollusks sampled from the More Mesa terrace indicate a cool paleo-ocean temperature signature correlating to the UCSB site (Trecker et al., 1998). Additionally, terrace sands were sampled at the fossil site for optically stimulated luminescence dating to estimate an age for potassium feldspar grains. The luminescence analysis estimated an age of 53 +/- 7 ka for terrace sands (Table 4). The error range does not differentiate between oxygen isotope substage 3a and oxygen isotope substage 3c. However, calibrated radiocarbon age of the fossil pholad and the isotopic signatures of the fossil mollusks, combined with the OSL age suggest the More Mesa terrace correlates to oxygen isotope substage 3a at 45 ka (Figure 6; Table 4). The

estimated age of the More Mesa terrace is consistent with other terraces (i.e., Ellwood and Isla Vista-UCSB) uplifted on the hanging wall of the More Ranch fault.

Elevations of the first emergent and higher terrace strandlines are positioned at approximately 35 +/- 0.5 m, 44 +/- 1.5 m, 50 +/- 1.5 m, 59 +/- 1.5 m, and 75 +/- 1.5 m (Figure 7). Wavecut platforms, often partially stripped of sediment are present at elevations of 104 m and 182 m, capping the Lavigia anticline, and their strandlines are absent. Based on the method by Bull (1985), the 38 m, 44 m, 50 m, and 59 m terrace strandlines correlate to the oxygen isotope substages 3a (36 ka to 52 ka). The fourth terrace strandline (59 m) does not correlate to any paleo-sea level highstands and most likely is the result of coseismic rupture and uplift of the coastline.

Total vertical surface uplift for the first emergent terrace is 100 m +/- 7 m. A vertical surface uplift rate of 2.2 +/- 0.3 mm/yr. is estimated based on the age of 45 ka, the elevation of the shoreline angle, and the 45 ka paleo-sea level elevation (Figure 6; Table 4).

6.44 La Mesa Terraces

East of the More Mesa terraces, the La Mesa terraces and associated strandlines are continuous from Los Positas along the southern flank eastward across the Mesa anticline (Figure 8). The terraces are uplifted along the south limb of the La Mesa and Lavigia anticlinal folds, on the hanging walls of the blind, La Mesa and Lavigia reverse faults, respectively. The terraces and associated strandlines are truncated east of SBCC by the Mesa fault and subsequent erosion from Mission Creek.

Along the south limb of the fold at SBCC, a marine terrace fossil assemblage is exposed in the sea cliff on the first emergent marine terrace at SBCC, formerly known as Bathhouse Beach (Figure 8). A fossil coral was obtained from the paleontology collection at the Department of Geological Sciences at UCSB. The coral was a well-

preserved, solitary coral (*Balanophyllia elegans*) sampled from the sea cliff exposure at the Bathhouse Beach fossil site.

X-ray diffraction analysis determined the fossil coral to be composed of original aragonite shell material. Uranium series analysis of the fossil coral yielded a measured an initial $^{234}\text{U}/^{238}\text{U}$ activity of 1.164 ± 0.015 which is within the same range as that for modern seawater (Gurrola et al., 1997b). The estimated uranium series age is approximately of 70 ± 2 ka (Table 4). The oxygen isotope analyses of fossil mollusks indicate warmer paleo-ocean water signatures than the UCSB site (Trecker et al., 1998; 1999). Chappell et al. (1996) recognize a paleo-sea level highstand associated with oxygen isotope substage 5a at 73 ± 2 ka with an elevation of -58.5 ± 13.5 m. Therefore, the first emergent marine terrace at SBCC is best correlated to the 73 ± 2 ka paleo-sea level highstand at isotope substage 5a (Figures 6 and 8).

At SBCC there are four uplifted terraces with associated paleo-shorelines, and one abrasion platform with the strandline removed by erosion, preserved in the same terrace flight as the SBCC site. The approximate paleo-shoreline elevations of the terraces and abrasion platform beginning with the first emergent are 30 ± 1.5 m, 44 ± 1.5 m, 54 ± 2.0 m, 75 ± 2.0 m, and 109 ± 3.0 m, respectively (Figure 8).

Based on the uranium series age of 70 ± 2 ka for the first emergent marine terrace at SBCC, a total surface uplift of approximately 88.5 ± 13.5 m and a rate of local surface uplift of approximately 1.3 ± 0.20 mm/yr. is estimated (Figure 6). Assuming a constant rate of uplift and using the method by Bull (1985), the 30 ± 1.5 m and the 75 ± 2.0 m terrace shorelines correlate to substage 5a and to substage 5c sea level highstands. The paleo-shorelines positioned at elevations of 44 ± 1.5 m and 54 ± 2.0 m do not correlate to any paleo-sea level highstands hypothetically formed as the result of coseismic surface uplift.

South of SBCC at Santa Barbara Point, a series of five flights of terraces with associated shorelines are preserved at approximate elevations of 15 ± 1.0 m, 28 ± 1.5

m, 47 +/- 2.0 m, 57 +/- 2.0 m, and 76 +/- 2.5 m (Figure 8). A higher marine abrasion platform with the strandline absent is preserved at an elevation of approximately 127 +/- 3.0 m.

The paleo-shoreline of the first emergent marine terrace at Santa Barbara Point is discontinuous. To the west the paleo-shoreline trends offshore and to the east is buried by alluvial fan-delta deposits, several terrace shoreline angles are mappable at SBCC. The 70 ka terrace shoreline is apparently present as the second emergent terrace at Santa Barbara Point (Figure 8).

OSL measurements of quartz grains sampled from terrace sands at Santa Barbara Point determine an age of 58 +/- 11 ka for the first emergent terrace (Figure 6; Table 4). Given the error range assigned to the 58 +/- 11 age, the terrace may have formed as a result of paleo-sea level highstands associated with oxygen isotope substage 3a (45 ka) or 3c (58 ka). Oxygen isotope data from fossil mollusks from Santa Barbara Point indicate a cool paleo-ocean temperature (Trecker et al., 1998).

Based on the OSL age of terrace sands, the isotopic signatures of fossil mollusks, and the position of the second emergent terrace at Santa Barbara Point (hypothetically 70 ka), the first emergent terrace is correlated to oxygen isotope substage 3c and a local vertical rate of surface uplift of 1.2 +/- 0.1 mm/yr. is estimated (Figure 6; Table 4). This is in agreement with the calculated local vertical surface uplift rate of 1.25 +/- 0.20 mm/yr. at SBCC. Assuming a constant rate of terrace uplift and the method by Bull (1985), the flight of terraces correlate to oxygen isotope substages 3c (58 ka), 5a (72 and 80 ka), 5c (105 ka) and 5e (125 ka), respectively (Figures 6 and 8).

West of Santa Barbara Point at Meigs Road, laterally continuous terrace strandlines are geomorphically well-expressed (Figure 8). The elevations of the terrace strandlines are approximately 34 +/- 1.5 m, 48 +/- 1.5 m, 61 +/- 2.0 m, 75 +/- 2.0 m, and 114 +/- 3.0 m. A mostly stripped marine abrasion platform also occurs at an elevation of approximately 128 +/- 3.0 m.

Based on geomorphic mapping, the 70 ka strandline corresponds to the first emergent shoreline angle (33 m) which yields total surface uplift of 91.5 +/- 13.5 m above paleo-sealevel at time of platform erosion (Figure 8). A local vertical surface uplift rate of 1.3 +/- 0.2 m/ky. is estimated (Figure 6). Based on an assumed rate of constant uplift, the terraces correlate to the substages 5a (72 and 80 ka) and 5c (105 ka) (Figure 8). The second and third terrace levels do not correlate to a paleo-sea level highstand and may be the result of coseismic surface uplift.

The terrace shorelines are mappable to the west at Mesa Lane, where drainage truncates the first and second flights of terrace strandlines (Figure 8). West of the water gap, we identify terrace shoreline angles at approximate elevations of 35 m, 48 m, 61m, 75 m, and 114 m. A marine abrasion platform positioned at approximately 128 m elevation is present but the shoreline angle is removed by erosion.

6.45 Montecito Terraces

Two, possibly three flights of marine terraces are uplifted and preserved east of Santa Barbara. The first emergent terrace is a 1 to 2 km long surface in the Montecito area, is truncated by surficial drainage and is deformed across the Santa Barbara Cemetery anticlinal fold (Figure 9).

A steep, south-facing paleo-sea cliff is preserved north of the fold at an elevation of approximately 31 +/- 2.0 m. The second emergent terrace is apparently preserved on the south limb of the Mission Ridge anticline where the back edge of the platform coincides with the Montecito fault. The shoreline angle of this marine platform is buried or eroded due to faulting, so the maximum platform elevation of approximately 94 m is measured.

Marine sands were sampled from the first emergent terrace along the modern sea cliff near Butterfly Beach in order to measure OSL of terrace sands (K-feldspar grains). The OSL analysis indicates an age of 79 +/- 10 ka for the terrace sand (Table 4). The

maximum elevation of the first emergent terrace is approximately 25 m and a total surface uplift of 56 m is calculated. A local rate of surface uplift of 0.7 ± 0.1 mm/yr. for the Santa Barbara Cemetery terrace is calculated (Figure 6). The first emergent Montecito terrace is synclinally folded below sea level eastward toward the Romero Creek water gap.

6.46 Summerland Marine Terraces

East of the Romero Creek water gap, three emergent terraces are uplifted and preserved on the hanging wall of the Arroyo Parida segment of the MRFS (Figure 9). The shoreline angle of the first emergent terrace extends 2 km from the Ortega Hill anticline eastward to where it trends offshore. The shoreline angle trends offshore west of the (second emergent) Loon Point terrace (Figure 9).

The shoreline angle of the first terrace increases in elevation westward from approximately 19 ± 1.5 m to 23 ± 1.0 m. The marine platform and associated shoreline angle is exposed in a railroad-cut exposure on the south flank of the Ortega Hill anticline (Figure 9). The wave-cut abrasion platform is inclined about 2° to the southeast and is denoted by a boulder line 0.2 to 1 m thick. The boulder line contains cobble clasts with occasional pholad borings indicating a near-shore beach, depositional environment. The cobble conglomerate is overlain by a thin, discontinuous 0.5 m thick bed composed of well-sorted, medium to fine (beach) sand. The boulder line is terminated against steeply south-dipping, non-marine Casitas strata (paleo-sea cliff) forming a wave-cut notch at an elevation of approximately 23 ± 1.0 m. The age of this marine platform and terrace is unknown.

The first emergent terrace at Loon Point terrace, which is the second emergent terrace of the Summerland sequence, is exposed along the modern beach sea cliffs at Loon Point. The elevation of the shoreline angle is approximately 50 ± 3.0 m, however the terrace is synclinally folded below sea level into the Carpinteria syncline to the east.

Terrace sands were sampled from the first terrace flight near Loon Point in order to obtain an age-date by optically stimulated luminescence analysis. OSL analysis yielded age estimations of 105 +/- 15 ka for and 167 +/- 15 ka for quartz and potassium feldspar grains, respectively (Table 4). The oldest first emergent marine terraces preserved in the SBFB are no older than 125 ka, therefore the age of the Loon Point terrace is assumed to be 105 +/- 15. The estimated amount of surface uplift is approximately 73.5 +/- 3.0 and the estimated surface uplift rate is approximately 0.7 +/- 0.1 mm/yr. (Figure 6; Table 4).

7.0 TECTONIC GEOMORPHOLOGY AND PALEOSEISMICITY OF FOLDS AND FAULTS

The SBFB exhibits numerous geomorphic features related to active, shallow subsurface folding (Gurrola and Keller, 1997a). The belt contains numerous active folds developing on the hanging-walls of blind reverse and thrust faults. These active folds form well-expressed, *en echelon* anticlinal ridges and synclinal basins on the coastal piedmont (Figure 2).

Geomorphic expression of active folds in the SBFB includes forelimb fold scarps, transverse wind (air) and water gaps, deflected and defeated stream courses, and uplifted marine terraces. Anticlinal and monoclinal folds form topographically well-expressed anticlinal ridges or fold scarps, whereas synclinal folds form subsiding basins. We will discuss in greater detail several faults and associated folds including the Mission Ridge Fault System (MRFS) and Loon Point fault. Paleoseismic data, collected for two sites: Ellwood Mesa (More Ranch segment of the MRFS) and Loon Point will be presented.

7.1 FAULT SEGMENTATION

Geometric, geomorphic and structural segments of the MRFS including the More Ranch, Mission Ridge, and Arroyo Parida segments, are defined by changes in structural style, geometry, termination of folds, and geomorphology. Segment boundaries also

coincide with faults that strike at a high-angle to the MRFS, termed cross faults (tear faults) (Figure 1; Gurrola and Kamerling, 1996). Mapping of the tectonic geomorphology of reverse faults and related folds identified left-lateral displacement of folds at the More Ranch-Mission Ridge segment boundary, truncation of folds and subsidiary faults at the Mission Ridge-Arroyo Parida segment boundary, and differential faulting, uplift and related folding at the west-east Arroyo Parida segment boundary. These segment boundaries correlate with northeast-striking cross faults including, from west to east: the Goleta Point, the Fernald Point, and Rincon Point faults (Gurrola and Kamerling, 1996). These NE-striking faults are subparallel to the present axis of compression and are favorably oriented to behave as tear faults during coseismic deformation.

Some recent Santa Barbara area earthquakes show rupture zones limited by boundaries demonstrated to be steeply-dipping cross faults behaving as tears. Tear faults segment larger reverse (and thrust) faults transferring slip to adjacent thrust ramps. Tear fault segment boundaries in the western Transverse Ranges and Los Angeles may limit the size of rupture zones during an earthquake and therefore the potential magnitudes of expected earthquakes. These cross faults or segmentation boundaries are difficult to observe and map, and are often discovered only after a large earthquake on the basis of aftershock hypocenters and focal mechanism defining near-vertical strike-slip tear faults at the edges of the main shock rupture (Hauksson and Jones, 1989).

Tear faults may control the nucleation or termination of moderate to large earthquakes in the Los Angeles basin and the western Transverse Ranges. The 1994 Northridge earthquake nucleated at the intersection of a thrust ramp and tear fault rupturing up the ramp. Corbett and Johnson (1984) map the seismicity associated with the 1978 Santa Barbara earthquake which reveals an abrupt termination of earthquakes on the eastern boundary that coincides with the NE-striking Goleta Point fault (Gurrola and Kamerling, 1996).

If we assume that the MRFS is capable of producing earthquakes similar in magnitude to the 1994 Northridge and 1971 San Fernando earthquakes, then we can assume similar rupture lengths, area, and depth. Therefore, we might expect the MRFS to rupture along two or possibly more geomorphic/structural segments and the rupture may nucleate or terminate near a tear fault such as the Goleta Point, Fernald Point, or Rincon Point faults.

7.2 MISSION RIDGE FAULT SYSTEM (MRFS)

The 70 km long, south-dipping, reverse MRFS is the principal seismic source on the coastal piedmont of Santa Barbara. To the west at Ellwood, the MRFS continues offshore and is expressed as a bathymetric high on the sea floor. To the east at Ojai Valley, the MRFS is truncated by the north-dipping San Cayetano fault.

The MRFS forms prominent, topographically expressed folds whereas other secondary blind reverse faults on the coastal piedmont form shorter, discontinuous landforms (Figure 2). Along strike, the MRFS is characterized by fault-propagation folds associated with active folding. These folds and associated landforms include hanging wall anticlines producing anticlinal ridges and footwall synclines producing synclinal basins.

The MRFS is subdivided into geometric, geomorphic, and structural segments including, from west to east, the More Ranch, the Mission Ridge, and the Arroyo Parida segments (Figures 1 and 2). These left-stepping, en echelon segments exhibit fault geometric, geomorphic, and structural homogeneity along strike. However, abrupt changes in these characteristics occur across what we interpret to be segment boundaries.

The 15 km long More Ranch segment strikes through the Goleta basin and uplifts the More Mesa, the UCSB-Isla Vista, and the Ellwood marine terraces. The 17 km long Mission Ridge segment strikes through the community of Santa Barbara and dips south beneath the urban corridor on the coastal piedmont. The Arroyo Parida segment strikes

north of Carpinteria and can be subdivided into west (17 km long) and east (15 m long) subsegments as well as the 5 km long Santa Ana fault that strikes through northern Ojai Valley terminating at the San Cayetano fault.

MRFS folds, from west to east, include: the Ellwood Mesa anticline; the UCSB and More Mesa-Hope Ranch anticlines on the More Ranch segment; the Mission Ridge anticline on Mission Ridge segment; and the Arroyo Parida uplift on the Arroyo Parida segment. Near the city of Santa Barbara, Mission Ridge (the Riviera) anticline forms the most prominent topographic high on the Santa Barbara coastal plain. The ridge extends for most of the length of the Mission Ridge fault segment.

Emergent flights of late Pleistocene marine terraces are preserved on the flanks of hanging wall anticlines of the MRFS and late Pleistocene terrace chronology of the terraces allows for rates of surface uplift and faulting to be estimated.

7.21 More Ranch Segment

The roughly east to west striking, 17 km long, More Ranch segment is mostly blind along strike and can be subdivided into western and eastern subsegments (Figures 2 and 5). The western subsegment uplifts the Ellwood and UCSB terraces and bounds the south margin of Goleta basin. The Goleta Slough syncline (water gap) is located at the boundary between the segments.. The eastern subsegment uplifts the More Mesa and Hope Ranch anticlines and separates the onshore Goleta and the Santa Barbara basins (Figure 5). The More Ranch segment terminates eastward at a complex segment boundary where it truncates the Mission Ridge segment and the northwest-striking San Jose and Mesa faults (Figure 2).

Tectonic landforms along the western and eastern More Ranch subsegments include flights of late Pleistocene wave-cut platforms on the crests and flanks of anticlinal folds. West to northwest-trending, anticlines are north-verging hanging wall folds with *en echelon*, fore- and/or back limb fold scarps.

Pre-Quaternary strata is exposed in the core of folds and form the bedrock on which the late Pleistocene wave-cut platforms are eroded. The blind More Ranch segment also folds and warps several flights of marine terraces including isotope substage 3a (45 ka) (Figures 5 and 6).

7.211 Ellwood Fold: The westernmost extent of the More Ranch fault is exposed in a sea cliff exposure forming a north-verging, monoclinial fold at Ellwood Beach. However, for most of the length of the fold along strike, the main fault is blind forming a north-verging, hanging wall anticline with associated bending moment faults. The en echelon, west-trending anticlinal folds form a geomorphically well-expressed convex fold scarp on the first emergent 45 ka marine terrace. From Devereaux Creek eastward to the sea cliff exposure of the fault the zone of deformation decreases from approximately 150 m to several meters wide.

The westernmost More Ranch fault is exposed in the modern sea cliff; the fault deforms the first emergent marine terrace and is expressed on the surface as a north-facing fold scarp approximately 5 m high. Aerial photographs from 1929 reveal a several hundred meter long, linear fold scarp with greater relief than what is presently preserved suggesting that the scarp has been denuded due to grading.

The sea cliff exposure reveals a south-dipping, reverse fault that offsets the Miocene Monterey Formation and wave-cut platform (Figure 10). The overlying late Pleistocene marine terrace and fluvial units are folded into a monoclinial drape anticline. The vertical throw on the 45 ka, wave-cut platform is approximately 7 m. A paleosol has formed and is preserved in the lower section of folded, fluvial strata. However the steep terrain of the sea cliff prevents detailed study of the fault exposure.

A channel fill exposed in the sea cliff face is abutted up against the fold scarp on the footwall. The channel is an upstream reach of Devereaux Creek truncated by coastal erosion.

At Devereaux Creek, the More Ranch fault forms a broad, asymmetric, north-facing fold scarp on the Ellwood Mesa. Along the fold scarp, Devereaux Creek flows against the scarp eastward to Devereaux Slough. A left-stepping fold scarp bounds the landward edge of Ellwood terrace and the gently south-sloping terrace surface north of Devereaux Creek. The zone of deformation across the north (fore-) limb of the fold is approximately 150 m wide. The fold exhibits a broad, planar crest with vertical relief of approximately 14 m on the 45 ka Ellwood terrace .

Several trench pits were excavated at various locations on the Ellwood fold at Devereaux Creek as part of a geotechnical investigation by Hoover and Associates (1985) and Santa Barbara County soil remediation projects. Hoover and Associates (1985) identified several parallel, west-striking faults, one of which is equivalent to Dibblee's (1986) mapped trace of the More Ranch fault along the channel of Devereaux Creek.

A trench was excavated for soil remediation to depths up to 10 m and 600 m long in the Devereaux Creek channel. The trench did not reveal offset terrace strata but did expose the geometry of the marine platform and overlying terrace sediments. The main strand of the More Ranch is blind at this site and is expressed as an anticlinal fold.

Paleoseismic investigations involved determining the nature of the deformation of the subsurface wave-cut platform across the fold scarp. This included seismic refraction to determine depth and geometry of the contact between the marine terrace strata and the underlying wave-cut platform eroded on the Sisquoc Formation. Two north-south seismic refraction lines revealed that wave-cut platform terrace sediments are uniform and mantle the deformation on the wave-cut platform. The surface expression of the fold mirrors the geometry of the subsurface wave-cut platform unconformity except where two near vertical offsets were identified on the north-facing fold scarp. These offsets of the marine unconformity were in the approximate location of the faults identified by Hoover and Associates (1985).

Direct sampling of the terrace sediments to shallow depths through continuous drill core-sampling was conducted to verify vertical offsets as faults and determine potential fault-trench locations. A total of eight small diameter (4.5 cm) cores were drilled in a north-south profile from north of Devereaux Creek to the crest of the anticline and were continuously sampled from depths of -1 m to maximum depths of -10 m (Figure 11). The shallow drill core-sampling data corroborated the seismic refraction results of the terrace strata thickness and two faults that vertically offset the wave-cut platform by approximately 1.5 m each.

A fault-trench was excavated on the fold scarp across the southern fault splay to evaluate and characterize earthquake history of the More Ranch fault. The continuous drill-core data revealed greater stratigraphic resolution across the southern fault splay than the northern fault splay on the fold scarp. The location of the 25 m long, 6.5 m deep trench is shown on Figure 12. The southern part of the trench was excavated as a narrow 0.60 m wide slot trench, whereas the northern part of the trench was benched at - 2.0 m to allow easier access to details of faulting at shallow depths. The east trench wall was scraped clean and a 0.5 to 2.0 m grid was constructed for detailed, mapping of terrace and fault contacts.

The fault trench revealed a 3 to 4 m thick, marine terrace sequence and several west-striking, south-dipping, thrust faults that vertically offset and warp the basal marine abrasion unconformity approximately 1.5 m (Figure 13). Generally, the zone of faulting was approximately 0.6 m wide, defined by five fault strands that terminated at different stratigraphic horizons. Dip on the fault strands increased with depth from approximately 25° to 45° .

On both sides of the fault, the trench wall exposed a stratigraphic sequence of, denoted unit I to unit A from bottom to top, Miocene Monterey Formation (unit I), a late Pleistocene wave-cut unconformity, marine terrace sediments (units H-D), and alluvial

cover (units C-B) (Figure 13). Unit A is the anthropogenic zone in which a modern A soil horizon is presently forming.

The terrace sequence includes basal silts (units H and F) that include poorly re-worked angular clasts of the Monterey Formation indicating an offshore marine environment. Units E and D were bimodal, well-sorted, medium to fine-grained sands with locally preserved cross-bedding structure. These units (E and D) are aeolian beach dune deposits indicating subaerial emergence of the marine platform. Alluvial units B and C are massive clays with no structure and are probably the result of alluvial floodplain deposition following regression of the beach environment.

The reverse fault strands juxtaposed dissimilar geologic units including the basal Miocene Monterey Formation (unit I) and lowermost terrace units (H and G). The overlying terrace and alluvial units (F-B) were deformed but were similar on both sides of the fault strands. Unit A was not deformed but is deposited across and mantles the underlying scarp. The footwall terrace section was not only thicker but preserved additional units not exposed in the hangingwall section.

The semi-parallel fault strands offset different sequences of terrace strata up to three different stratigraphic levels or horizons. The stratigraphic horizons were overlain by undeformed strata which are termed seismic or paleo-earthquake horizons. These paleo-earthquake horizons indicate within the trench stratigraphy when slip associated with a paleo-earthquake occurred on the specific fault strand. These seismic horizons or paleo-earthquakes are denoted, from lowest to highest in section, EQ3, EQ2, and EQ1, respectively (Figure 13).

The three seismic horizons, EQ3, EQ2, and EQ1, are positioned between terrace units G and F, units E and C, and units B and A, respectively (Figure 13). The northernmost fault strand corresponded to the lowest seismic horizon (EQ3). The central three fault strands terminate at the middle seismic horizon (EQ2) and the southernmost fault strand terminate at the highest seismic horizon (EQ1).

In stratigraphic order, the orientation of the northernmost fault strand is strike 098° with 39° dip to south and offsets units I, the marine abrasion unconformity, unit H, and unit G with reverse-slip. However, the fault was abruptly terminated by unit F. This fault strand juxtaposes different facies of the Miocene Monterey Formation and unit G. Unit G contains two additional units (G_2 and G_3) in the footwall section not preserved in the hangingwall section. The youngest of unit G (denoted G_1) was mappable across the fault but was texturally very different. The abrasion unconformity and the base of unit G_1 were vertically offset approximately 40 cm.

Detrital charcoal were sampled from units H and G_3 on the footwall section and submitted for accelerated mass spectrometry (AMS) analyses. The measured radiocarbon age of units H and G_3 , are about 47 ka. These age-dates of the basal terrace units are stratigraphically consistent and in agreement with the UCSB terrace age to the east. Unfortunately, organic material was not found in units G_1 and F. The closest overlying unit radiocarbon age-dated was unit D at 37 ka (Table 4). Therefore, vertical slip on the northernmost fault strand is approximately 0.40 m and dip slip along the fault plane is approximately 0.52 m for the earliest paleo-earthquake (EQ3). This paleo-earthquake occurred sometime between about 47 and 37 ka.

The central three fault strands were generally oriented at strike of 099° with dip 30° south and vertically offset units I-E with reverse slip. The thrust fault strands are abruptly terminated at the base of alluvial unit C (Figure 13). The wave-cut platform has a cumulative vertical offset across all three strands of approximately 0.50 m. The uppermost faulted terrace unit (E) was a beach indicating subaerial emergence of the marine platform prior to EQ2. Also, a sand blow injection pipe is preserved within unit D and is truncated by the base of the overlying unit C. Unit E was the source ejecta for the sand blow structure that intrudes unit D and suggests intense shaking was associated with EQ2 and shallow groundwater conditions at the trench site.

The uppermost terrace unit deposited at the trench site prior to EQ2 was unit E and through association unit D (Figure 13). Radiocarbon analyses based on sampled organic detritus from units D and C yield approximate ages of about 37 ka and 36 ka (Table 4). Therefore, EQ2 occurred about 37 ka following emergence of the marine platform.

The southernmost fault strand has a strike of 085° and dip of 44° south and vertically offsets units I-B with reverse displacement. The wave-cut platform has a vertical offset of approximately 0.17 m, however the terrace is warped on the hangingwall section which yields a vertical separation of 0.3 m. This reverse fault reaches the highest stratigraphic level in the trench where it is truncated by alluvial unit A.

The fault strand offsets unit C but deforms unit B through monoclinial folding. There are several pervasive synthetic and antithetic shears within unit B with slickensides that indicate backthrusts. However, the fault is well-expressed with discrete, reverse separation of strata on the west trench wall. The uppermost area on the east trench wall was correlated to the exact same area on the west trench wall for evaluation of EQ1.

On both east and west trench walls, the uppermost faulted alluvial clay unit B can be subdivided into lower (B₂) and upper (B₁) units based on the presence and absence of brecciated Monterey clast respectively (Figure 13). However, on the west trench wall, the fault strand vertically offsets the base of unit B₂ approximately 0.1 m with a dip separation of approximately 0.3 m.

The most recent earthquake faulted and/or folded strata approximately 0.4 m (vertical slip) and occurred post 36 ka. The penultimate earthquake occurred between about 37 ka and the oldest earthquake occurred between 47 ka and 37 ka. Based on radiocarbon age-dating of the basal marine terrace unit we calculate a vertical rate of uplift of about 2 m/ky for the Ellwood Mesa (Figure 6). A vertical rate of folding of 0.22 +/- 0.03 m/ky and a dip slip rate of 0.3 m/ky are calculated at this location.

7.212 UC Santa Barbara-Isla Vista: Detailed studies of the More Ranch segment include: trenching; subsurface mapping; and u-series, OSL and isotope analysis. U-series analysis of a marine terrace fossil coral yielded an age of 47 +/- 0.5 ka for the UCSB-Isla Vista terrace (Table 4) and is a minimum age for the platform. Based on isotopic studies of Greenland GSIP ice cores, Dansgaard-Oeschger event 14 is the most likely candidate for the formation of the UCSB-Isla Vista platform. Chappell et al. (1996) estimate that the paleosea level elevation for oxygen isotope substage 3a at 51 ky is approximately -85 m. The shoreline angle elevation is approximately 25 m for the first emergent (Ellwood) terrace, which correlates to the UCSB-IV terrace and is also collaborated with radiocarbon data. The amount of total vertical uplift in the last 47 to 51 ky is about 110 m yielding an estimated local vertical surface uplift rate of about 2 m/ky. The local vertical uplift rate of the More Mesa terrace is approximately 1.8 m/ky.

Along the western subsegment, geomorphic and subsurface mapping of the first emergent marine terraces at UC Santa Barbara and Isla Vista (UCSB-IV) establish the continuity of the associated wave-cut platforms (Figure 5). The UCSB-Isla Vista platform is broadly folded into an open, north-verging, anticline. A 2 m high, north-facing scarp is present in the subsurface on the marine platform at UC Santa Barbara. However, review of geotechnical trenching data indicate this feature formed as the result of faulting on the north-dipping Campus fault (Figure 14).

The UCSB-IV marine platform is downwarped to the west into a syncline at Devereaux Slough and re-emerges as the first emergent terrace at Ellwood. The Ellwood terrace is folded along strike of the More Ranch fault into a hanging wall anticline or monocline. On the hanging wall, the elevation of the marine platform is approximately 26m, whereas on the footwall, the elevation of the marine platform is approximately 13 m. Therefore, the More Ranch segment offsets the radiocarbon age-dated 47 ka and correlated 125 ka terraces 13 m and 43 m respectively, yielding a vertical rate of faulting

(rock uplift) of about 0.3 m/ky, a rate similar to that at Ellwood and 70 km east near Ventura (Figure 15).

7.213 More Mesa-Hope Ranch anticlines: The first emergent terraces at More Mesa, UCSB, and Ellwood are discontinuous as the result of erosion to the inlet of the Goleta and Devereaux Sloughs. The Goleta Slough is the product of local down warping as a result of left-stepping geometry, complex cross-faulting, and oblique slip (Figures 16 and 17). Along the eastern subsegment, the More Ranch fault forms hanging wall anticlines at More Mesa and Hope Ranch. Flights of marine terraces are preserved on the crests and limbs of these folds and can be correlated to the La Mesa marine terraces (Figures 7 and 8). The first emergent marine terrace at More Mesa extends across a series of northwest-trending folds for a distance of about 1.5 km. The elevation of the associated paleoshoreline is poorly preserved at about 36m.

7.22 Mission Ridge Segment

7.221 Mission Ridge: The south-dipping, blind Mission Ridge segment (MsR) of the MRFS, located just north of the city of Santa Barbara, forms the most prominent tectonic landform on the coastal piedmont (Figure 2). The MsR is not exposed in natural outcrop, but forms a topographically, well-expressed hanging-wall anticlinal fold (Mission Ridge). The fold extends 15 km westward from Montecito to Santa Barbara and varies in height from 25 m to 175 m.

The anticline uplifts and folds late Pleistocene fanglomerates and pre-Quaternary strata. Mission Ridge is the result of hanging-wall folding and the core of the anticline consists of Tertiary Rincon and Monterey Formations unconformably overlain by Quaternary fanglomerate. Near Las Alturas Road a fault investigation exposed the Monterey-fanglomerate unconformity which is dipping nearly 50° to the south. A river bank exposure in Rocky Nook Park near the Mission exposes south-dipping backlimb

fanglomerate deposits at approximately 20°. A road cut outcrop on Mountain Drive exposes alluvial forelimb strata dipping approximately 65° to the north. These deposits are part of a steep north limb (forelimb), suggesting that Mission Ridge is a hanging-wall anticlinal fold.

7.222 Montecito anticline: The Montecito anticline is a 2 km long hanging-wall fold formed on the Mission Ridge fault segment. The fold deforms Quaternary fanglomerate and produces a surficial fold scarp. Geotechnical studies document that the fold is cored by Tertiary Rincon Fm in the shallow subsurface (Slayman, pers. comm., 1997). Though there are no exposed limbs of the fold, the alluvial terrace is warped and exhibits a fold morphology. Buckled street curbs, road and sidewalk cracking, and a sloping tennis court suggest this fold may be active and deforming aseismically.

7.3 NORTHWEST-STRIKING FAULTS

A number of faults and associated folds in the SBFBS strike roughly northwest. These folds include: Goleta Valley anticline; La Mesa anticline; and the cemetery anticline; Ortega Hill anticline; and Loon Point anticline (Figure 2). These more northwest-striking features are often truncated by the MRFS (see Figures 2 and 5). We hypothesize that those faults and folds truncated by the MRFS are older and have been rotated clockwise with the Transverse Ranges (Luyendyk, 1991), and may be evidence for continued Quaternary rotation.

7.31 Goleta Valley Anticline

In the Goleta basin, the Goleta Valley anticline forms a well-expressed linear anticlinal hill that is located immediately north of HWY 101. The anticline is a 2 km long, northwest-trending, north-verging fold formed on the hanging wall of the south-dipping, reverse San Jose fault (Figure 5). The fold plunges westward and deforms

Tertiary Rincon Fm, Quaternary Santa Barbara Fm and fanlomerate as well as overlying marine terrace deposits. On the south limb, dips in the Santa Barbara Fm range from 20° to 35° whereas on the north limb the fanlomerate dips about 40°. On the forelimb of the anticline, the San Jose fault scarp is well-expressed immediately south of Cathedral Oaks Road.

Well-developed drainages with moderately-incised valleys and associated wind (air) gaps are preserved on the anticline. At the western end of the anticline, San Antonio Creek is diverted to the west by the anticline and together with the presence of wind (air) gaps and apparent older more eroded topography may indicate westward propagation of the Goleta Valley anticline (Figure 18).

7.32 La Mesa Anticlines

The northwest-trending La Mesa hills are the expression of a hanging-wall anticline on the south-dipping, reverse Mesa fault. The folds plunge offshore to the east at Santa Barbara Point are truncated to the northwest by the Mission Ridge segment of the MRFS. Along the north facing fold scarp, the forelimb of the anticline is mostly absent due to erosion by Mission Creek where two prominent meander scars north of Santa Barbara City College are present. A remnant of the north-dipping limb is reported by Dibblee (1986) and the south-dipping limb is poorly exposed in a road cut on Meigs Road.

The Mesa anticline folds wave-cut platforms of stage 3 and stage 5 near Santa Barbara Point. The rate of surface uplift of about 1 m/ky for the Mesa (Figures 6 and 19) probably represents combined deformation on several (blind) structures, one of which is the Mesa fault.

7.33 Santa Barbara Cemetery (Zoo) Anticline

The Santa Barbara Cemetery (Zoo) anticline is a 2 km long, northwest-trending fold that is exposed in the seacliff just east of East Beach (Figures 2 and 9). The anticline folds Quaternary Casitas Formation and the first emergent terrace into a steepened north-facing fold scarp and anticlinal hill. Strata of the Casitas Formation dip approximately 25° to the north at the base of the sea cliff and decreases up section. East along the exposure of the sea cliff the strata of the south-dipping limb are exposed. Some units thin and onlap against the fold crests suggesting that syntectonic Casitas deposition occurred during fold growth and uplift. The wave-cut platform is warped across the fold crests, and the sea cliff is nearly parallel to the fold axis providing apparent dips. A synclinal basin is formed to the north and expressed as part of the now mostly filled Santa Barbara coastal lagoon (historic El Estero). These folds are most likely related to a blind reverse fault.

7.34 Ortega Hill Anticline

At the left-stepping segment boundary of the MRFS, the strike-slip (?) Fernald Point fault strikes at a high angle to the MRFS and truncates northwest-striking, hanging-wall folds such as the Ortega Hill anticline. The fold is the prominent topographic landform immediately to the west (Figure 9). Ortega Hill is the expression of an anticlinal fold deforming Quaternary Casitas Formation and overlying late Pleistocene terraces sediments. Strata of the Casitas Formation dip approximately 50° to the south whereas strata on the north limb dip 30° to the north. The trend of the anticline is northwest and plunges to the southeast. The fold is open with interlimb angle of approximately $100^{\circ} \pm 5^{\circ}$. Structural studies suggest that the Ortega Hill anticline is contemporaneous with and forms part of the north limb of the Carpinteria basin (Jackson, 1981; Jackson and Yeats, 1982).

7.35 Loon Point Fault and Propagation Fold

At Loon Point (Figure 9), Casitas Formation and a late Pleistocene (oxygen isotope SC at 105 ka, Table 4) marine terrace are folded and faulted by a low-angle reverse fault (Figure 20). The nearly vertical 30 m high sea cliff prevents detailed stratigraphic analysis, however, photographic mosaic mapping and subsequent trenching of the fault have provided additional information.

The Loon Point fault strikes approximately $085^{\circ} \pm 5^{\circ}$ with a dip of $30^{\circ} \pm 4^{\circ}$ to the south. The fault juxtaposes steeply-inclined strata on the hanging wall against gently-dipping strata on the foot wall. The forelimb strata, although clearly defined, are inaccessible due to steep slopes. The forelimb of the fold is overturned dipping about 80° to the southeast and terminates against the fault. A colluvial growth wedge exhibiting tapering beds is preserved on the forelimb.

The position of the wave-cut platform is preserved on the forelimb overlying the growth wedge and identified by a thin cobble conglomerate (boulder line) with pholad boreholes. The age of the marine terrace is most likely either 45 ka or 81 ka, the age of the first emergent marine terraces in the SBF. Across the axial surface, the boulder line is eroded out of the sea cliff section and projects into space (Figure 20). To the east, the boulder line is preserved on the back limb and can be followed to the east until it disappears below sealevel.

The backlimb strata on average strike 080° and dip 27° to the southeast and consist of Casitas Formation, marine terrace, and alluvial sediments. Strata of the Casitas Formation beds at Loon Point consists of fluvial and massive debris flow deposits that taper and thicken, indicating syntectonic deposition during fold growth. The interlimb angle is approximately 57° and is a tight fold. The axial surface is moderately inclined and the fold thickens in the hinge area and forelimb. Displacement is south-side up with

associated north-directed fold vergence. Strata on the foot wall strike 075° and dip 16° to the southeast.

The faulted, asymmetric Loon Point anticline is a fault-propagation fold in which the fold formed as the thrust fault propagated to the surface. Suppe (1985) and Suppe and Medwedeff (1990) describe asymmetric folds with one steep or possibly an overturned limb adjacent to a thrust fault as a fault-propagation fold. They describe these folds as a result of the process of fault propagation and suggest that the fold records deformation that occurs in front of the propagating fault surface which ramps from a detachment at depth. With time, the fault juxtaposes a foot wall syncline against a hanging-wall anticline across the fault (Suppe, 1985). As the fault propagates upward, the fault ramp lengthens and commonly, the fault-propagation fold becomes locked and the fault may rupture through the anticlinal or synclinal axial surface, or somewhere in between (Suppe, 1985; Suppe and Medwedeff, 1984 and 1990).

The reverse fault and asymmetric, hanging-wall folds documented in this study are similar to the fault-propagation fold geometry described by Suppe (1985) and Suppe and Medwedeff (1984 and 1990). Absent from the foot wall block of the Loon Point fault is an associated syncline (Figure 20). Therefore, the fault ruptured through the syncline and is classified as a synclinal fault breakthrough (Suppe and Medwedeff, 1990).

Suppe and Medwedeff (1990) propose two models by which folding occurs in brittle conditions. Both models describe fold-propagation by reverse-faulting. The constant thickness fault-propagation folding model is based on conservation of bedding thickness and bed length. The fixed front anticlinal axial surface model allows for bed thickening or thinning in the steep fore-limbs of the fold. Beds of the Loon Point fold thicken in the steep fore-limb of the anticlinal fold and indicates that this fault-propagation fold can be best described with the fixed front anticlinal axial surface model.

7.351 Paleoseismic Evaluation: Excavation of a fault trench across the fold scarp of the Loon Point fault-propagation fold revealed a shallow-dipping reverse fault (Figure 21). The fault juxtaposed marine terrace sands against Quaternary alluvium. The marine sands were absent from the foot wall block and were exposed in a secondary trench and surveyed into the fault to measure a vertical displacement of 5 m (Gurrola et al., 1998). In the seacliff exposure, the marine abrasion platform is folded and vertically offset several m. Several buried (A-horizon) soils are preserved and the lowermost A-horizons appear to be folded. Detrital charcoal sampled from a faulted alluvial unit with 2 m of offset yielded a ^{14}C date of about 4 ka (Table 4). The age is too young to calculate a reasonable slip rate. The Loon Point fault is classified as an active fault and seismic source in the SBFB.

8.0 STYLE OF QUATERNARY FOLDING

Folding and reverse faulting accommodate crustal shortening of the western Transverse Ranges Province. In the SBFB, the amplitude of synclinal basins are an order of magnitude greater than anticlinal folds resulting in relatively deep basins (0.5-1 km) in contrast to anticlines with moderate (0.05 - 0.25 km) topographic relief.

Topographically, well-expressed folds in the SBFB along with natural and trench exposures allow for 3D mapping and analysis of surface and shallow fold deformation. Subsurface data integrated from Jackson and Yeats (1982) and Olson (1982) provide deeper subsurface data important to understanding the style of folding. The principal style of fold deformation documented is fault-propagation folding and monoclinical folding associated with basement compressive deformation.

Fault-propagation folds initially develop as a geomorphically expressed, asymmetric anticline-syncline pair formed as the result of displacement on an initially buried reverse fault that propagates to the surface (Suppe, 1985; Suppe and Medwedeff, 1984 and 1990). Subsequent shortening locks up the fold and the propagating reverse

fault typically ruptures through the synclinal axis resulting in a faulted hanging-wall anticline and foot wall syncline. With subsequent slip, either the syncline or anticline may provide critical data concerning direction and rate of lateral propagation (Keller et al., 1999).

9.0 LATERAL PROPAGATION OF FOLDS: GEOMORPHIC ANALYSIS

The SBFB contains numerous folds developing on the hanging-walls of buried reverse faults. The lateral propagation or growth of folds is an important active tectonic process with important ramifications concerning modeling deformation and mechanics of folding and reverse fault (Keller et al., 1999). Fold deformation is intimately related to reverse faulting (Davis, 1983; Jackson et al., 1996) and surface folding produced by a buried propagating fault provides critical data concerning direction and rate of lateral propagation.

Lateral propagation of folds at rates of several cm/yr (approximately ten times the vertical rate of displacement on the fault producing the fold) is perhaps the most rapid tectonic process not yet well understood (Keller et al., 1999).

Geomorphic relationships are a primary way to demonstrate lateral propagation of folds (Jackson et al., 1996; Keller et al., 1999). Geomorphic indicators of lateral fold propagation resulting from buried reverse faulting include (in direction of propagation): (1) decrease in drainage density and degree of dissection; (2) decrease in elevation of wind gaps; (3) decrease in relief of the topographic profile along the crest of the fold (i.e., a fold plunges in the direction of propagation); (4) development of characteristic drainage patterns; (5) deformation of progressively younger materials, and (6) decrease in rotation and inclination of the forelimb. As a result of style of folding and variable geomorphic response, all of the criteria may not be evident at a particular fold.

The six geomorphic criteria are consistent with but not proof of lateral propagation, because the criteria are consistent (given specific scenarios) with both fold propagation and

fold rotation models of fold growth. Criteria 4 and 5 are strong evidence of lateral propagation, and if there are at least two wind or wind and water gaps (from the same stream), then this is very strong evidence of lateral propagation. Assuming that the stream can only be in one place at a time, the model of rotation is unlikely to produce two wind gaps or a wind and water gap at lower elevations in the direction of fold growth. There could be only one wind gap and one diversion. Once a stream is defeated by uplift in the rotation model it would be deflected to the nose of the fold (which is fixed, in that model) and would not form another gap.

Topographic profiles along the crest, profiles normal to the fold, and digital elevation models can help identify geomorphic parameters of folds. The elevations of wind gaps along an anticline are measured directly, and we postulate, as did Jackson et al. (1996), that these elevations are usually lower in the direction of propagation. The topographic profile along the crest of the fold, may reveal the direction of fold plunge. These relationships are shown for the apparent westward propagation of Mission Ridge at Santa Barbara, California (Figures 22 and 23). Jackson et al. (1996) argue that drainage parallel to a fold will likely be diverted in the direction of propagation. As the diversion develops, streams are captured and the drainage basin area increases until there is sufficient stream power to temporarily maintain a channel at the nose of a fold where propagation has not yet occurred. As fold propagation continues this area becomes a water gap, and eventually may become a new wind (air) gap if the channel is defeated by uplift or stream capture. If this occurs, then the channel is diverted again in the direction of propagation and may make several passes around the fold as the drainage develops. In some folds there may be several wind (air) gaps produced in this manner and the major drainage will be repeatedly diverted around the nose of the fold. In this sense, the streams are antecedent where they cross an active fold as their position is established at the nose of the fold before folding and uplift propagates through the area. These relationships are clearly shown for Mission Ridge (Figure 23). Streams are diverted in the direction of propagation, and for Mission Ridge where there are two wind

(air) gaps and the elevation of the gaps decreases in the direction of propagation. This is strong evidence that the ridge is propagating westward. Finally, dissection of the fold decreases to the west as does limb rotation (Figure 23).

10.0 HYPOTHESIS OF TECTONIC EXTRUSION

Shortening across the western Transverse Ranges is the result of right-slip and contraction in the vicinity of the “Big Bend” of the San Andreas Fault System (SAF). Right-slip along the “Big Bend” produces (north and south of the SAF) parallel to sub-parallel faults with predominantly left-slip strike slip faults and reverse faults with a left-slip component (if they have a component of strike-slip). Major folds and (buried) faults tend to propagate laterally to the west, south of the San Andreas fault, and to the east, north of the SAF. We hypothesize that the lateral propagation of fault rupture during earthquakes will tend to be to the west, south of the SAF; and to the east, north of the SAF (Figure 24) (Keller et al., 1997). North and south of the extrusion zone, plate bounding deformation terminates and this may coincide with the left-lateral, Santa Cruz Island and White Wolf faults, respectively.

The concept of tectonic extrusion has been used in a variety of tectonic settings including the Mediterranean region (McKenzie, 1972); Asia (Tapponnier et al., 1982); and the Los Angeles Region (Walls et al., 1998). The driving mechanisms for each of these locations is somewhat different, depending upon specifics of the regional tectonic framework. In the case of the "Big Bend" of the San Andreas Fault, the extrusion is evidently driven by the contraction produced by the bend in conjunction with the orientation of left-lateral strike-slip faults such as the White Wolf, Santa Ynez and Santa Cruz Island faults. An analogy that has sometimes been drawn is the squeezing of a watermelon seed between the thumb and index finger until it pops laterally. In the case of the "Big Bend" we might envision two watermelons seeds being squeezed with one extruding to the east north of the fault and the second to the west south of the fault.

In order for a fault to propagate laterally it must rupture and displace new ground in the direction of propagation. Thus, earthquake ruptures would hypothetically tend to propagate in the same direction as the growth of the fault and associated folds. It has been argued that as total fault displacement for repeated earthquakes increases so does total fault length (Cowie and Scholz, 1992; and Jackson et al., 1996). The hypothesis that direction of rupture during earthquakes would tend to be the same as the direction of propagation of the fault that produced the earthquake is highly speculative. This leads to the question: Can we predict lateral direction of rupture during earthquakes? The answer to this question is possibly "yes" in specific instances for buried reverse faults that have produced an anticline with surficial expression for which a single direction of lateral propagation may be determined. In other cases, a fold may propagate laterally in two directions, and some earthquakes may rupture laterally in a direction opposite to the direction of the propagation of the fold. Nevertheless, we hypothesize that the dominant direction of lateral propagation of rupture during moderate to large earthquakes will be in the direction of the fold propagation.

Although there is a very limited data set for which to test the hypotheses of lateral propagation of faulting and folding as well as rupture during earthquake, Table 5 provides some examples from southern California earthquakes. The table lists earthquakes and location relative to the San Andreas Fault, direction of lateral propagation of rupture and lateral component of displacement. Also indicated are whether or not a particular event supports the hypothesis of westward propagation of structure and rupture during earthquake, and predicted left-oblique component of displacement.

The majority of earthquakes for which data is available concerning direction of propagation of rupture and sense of lateral displacement tend to support the hypothesis that fault rupture during moderate to large earthquakes tends to have a westward component of propagation south of the SAF and an eastward component, north of the SAF. The evidence is particularly good for the 1952 M_w 7.5 Kern County earthquake which is north of the San

Andreas fault, has left-oblique displacement during the event, and the rupture propagated to the northeast as indicated by the pattern of aftershocks. The 1975 San Fernando M_W 6.6 earthquake had a left-lateral component of slip which apparently increased from east to west (Palmer and Henyey, 1971), but the direction of propagation of the rupture was up and to the southeast. However, the fault is reasonably far removed from the influence of the "Big Bend" and more likely to be within the tectonic framework of the Los Angeles Basin. The 1978 Santa Barbara earthquake was characterized by left-oblique displacement and there is evidence from the aftershock locations that the direction of propagation of the rupture was to the northwest (Corbett and Johnson, 1982; Yeats and Olson, 1984). Finally the 1994 Northridge M_W 6.7 demonstrated a component of northwest direction of lateral propagation of rupture, based upon aftershock locations (USGS, 1996). Thus the earthquakes of 1952, 1978, and 1994 for which data exists concerning the direction of propagation of rupture, support the hypothesis that there is a tendency for rupture propagation to have an eastward component north of the San Andreas fault and a westward component south of the fault.

This hypothesis has important ramifications for earthquake hazards because earthquake damage is often most severe in the direction of a propagating rupture (Benioff, 1955; USGS, 1996) (Figure 25). Anticipating potential direction of rupture during earthquakes will allow for better modeling of potential damages to human structures as a result of seismic shaking.

11.0 EARTHQUAKE MAGNITUDES

Estimated moment magnitudes of future earthquakes of seismic sources in the onshore and offshore SBF are listed on Table 1. Segments of the MRFS vary from 15 to 17 km in length. Assuming these represent earthquake segments then, using the method of Wells and Coppersmith (1994) we estimate a maximum M_W 6.5 earthquake on these segments. If multiple segments were to rupture, then a M_W 6.8 to 7.0 (moment

magnitude) earthquake is possible. Assuming a vertical displacement of about 1.0 m per event on a segment of the MRFS, the average return period is approximately 3 ky.

Several seismic sources such as the North Channel Slope, Oak Ridge and Santa Cruz Island faults are capable of producing a M_{W} 7.1-7.5 event as is the Santa Yñez fault, located about 10 km north of Santa Barbara. We believe that the Oak Ridge fault system and associated fold presents a potentially serious hazard.

Estimated earthquakes are consistent with historic seismicity in the SBFB. In this century two events of M 5.9 (1941 and 1978) occurred offshore of Carpinteria and Goleta, respectively. The 1925 M_{W} 6.8 Santa Barbara earthquake is the 7th largest out of 40 earthquakes in southern California with M_{W} greater than 6.0 in the 20th century (Stein and Hanks, 1998). If this estimated magnitude is correct, then it released about 1.5 times the energy of the 1994 M_{W} 6.7 Northridge earthquake and 2 times as much energy as the 1971 M_{W} 6.6 San Fernando earthquake. However, Olsen and Sylvester (1975) report the earthquake to be a M 6.3 based on similar seismic records. The 1994 M_{W} 6.7 Northridge earthquake is a recent example of the most likely earthquake we expect in the future for the SBFB. Unusually large onshore and/or offshore seeps of oil accompanied by small foreshocks may precede some large earthquakes by several hours in the SBFB. Seeps were reported about 3 hours prior to the 1925 earthquake (Hamilton, 1969). Smaller M_{W} 5-6 earthquakes evidently do not have such precursors or they are too small to be observed

In summary, the Santa Barbara urban corridor is in an area of known seismicity with an earthquake hazard similar to the cities of Ventura and Los Angeles. The city of Santa Barbara is located on the hanging wall of the blind Mission Ridge segment of the MRFS and is subject to amplified shaking during an earthquake as the result of free surface effects of the hanging wall and possible directivity of seismic waves. Parts of the downtown area are susceptible to liquefaction where the historic el estero (salt marsh) has been filled (in part from debris from the 1925 earthquake (Simmons, pers. comm.,

1999)) and is susceptible to a tsunami from an earthquake generated in the Santa Barbara Channel. An earthquake on the MRFS or a fault offshore with a maximum M_w 6.5 to M_w 7.5 respectively will cause extensive damage to the Santa Barbara urban area inflicting several hundred million to a billion or more dollars of property damage, with several to several tens of deaths (depending on the time and day of the earthquake) and thousands of injuries.

12.0 CONCLUSIONS

Based upon development of Quaternary stratigraphy and rates of uplift for wave-cut platforms in the Santa Barbara Fold Belt (SBFB) and investigation of active folding and faulting we conclude:

- First emergent marine terraces in the Santa Barbara Fold Belt range in age from 45 ky to 125 ky. That is, oxygen isotope stage 3 or 5.
- Rates of surface uplift for marine terraces in the SBFB is approximately 1 to 2 mm/ky. This is approximately an order of magnitude higher than was believed prior to our study.
- Tectonic geomorphology of the SBFB suggests that those areas that are topographically high are for the most part elongated hills which are active anticlines which conceal buried reverse faults. Topographically lower areas within the fold belt such as the alluvial fan and el estero areas of the city of Santa Barbara as well as the Goleta Valley and Carpinteria slough are areas of active subsidence associated with faulted synclines.
- Active folds and reverse faults in the SBFB predominately are propagating to the west, consistent with the hypothesis of tectonic extrusion.
- The most serious earthquake hazard to the Santa Barbara urban area is active faults and folds within the offshore portion of the Santa Barbara Fold Belt in the Santa Barbara Channel. Several sources including the North Channel Slope, Oak Ridge, and

Santa Cruz Island faults are capable of producing an M_W 7.1 to 7.5 event, as is the Santa Ynez fault located about 10 km north of Santa Barbara.

- Faults in the onshore SBF are capable of producing earthquakes of M_W 6.0 to 6.5. If several segments of the Mission Ridge Fault System were to rupture simultaneously an earthquake with magnitude of approximately M_W 7 is possible.
- The most likely scenario for a damaging earthquake to the Santa Barbara urban corridor would be a "Northridge-like event" with M_W approximately 6.5. The M_W 6.8 Santa Barbara earthquake in 1925 is the seventh largest out of 40 earthquakes in southern California with M_W greater than 6.0 in the 20th century and a repeat of that event would inflict several hundred million to a billion or more dollars of property damage with several to several tens of deaths (depending upon time of day the earthquake occurs).

13.0 ACKNOWLEDGMENTS

Research on the Santa Barbara Fold Belt is funded by the Southern California Earthquake Center award no. USC 572726 and the U.S.G.S National Earthquake Hazards Reduction Program awards nos. 143HQ97GA-02978 and 99HQGR0081. We thank Brian Baca and Bill Tracy (Santa Barbara County), Roger Slayman (CFS Inc.), Mike Hoover, Dean May (La Cumbre Mutual Water Co.), and Bill Hanna (UCSB) for providing and sharing geotechnical data. Jim Chen conducted u-series analyses of sampled terrace corals. Mike Fuller, Bob Dunn, and Chuck Anderson provided assistance and technical support in sedimentary sampling, preparation and paleomagnetic analyses. Oxygen isotope analyses were conducted in James Kennett's lab with Karen Thompson's lab assistance. X-ray diffraction analyses of the u-series dated fossil corals was conducted by Sam Iyengar, and XRD of the *Olivella* shells was conducted by Dave Pierce (UCSB). OSL analysis was conducted by J. Spencer and L. Owen from UC Riverside. David Valentine produced DEM graphics, David Crouch and Steve Brown drafted several

illustrations, and Yann Ricard provided computer support. We benefited from fruitful discussions in the field with Barry Keller, Butch Brown, and Ray Coudray. The Santa Barbara Parks Department permitted fossil sampling by seacliff repelling at Santa Barbara Point. Reading of the manuscript by A. Selting and T. Tierney is appreciated.

14.0 BIBLIOGRAPHY

Publications resulting from this project:

Gurrola, L. D. and Kamerling, M. 1996a, Role of cross faults as tears in thrust ramps in the Ventura and Santa Barbara Fold Belts, California, 1996: Abstracts for the Southern California Earthquake Center Annual Meeting, p. 49.

Gurrola, L. D. and Kamerling, M. 1996b, Segmentation of principal east-west trending reverse/thrust fault and earthquake nucleation sites in the western Transverse Ranges, California: EOS, Transactions, AGU, v. 77, no. 46, p. 512.

Gurrola, L. D. and Keller, E. A. 1998, Active folding of emergent marine terraces: Summerland to Carpinteria, Santa Barbara fold belt: California, Geol. Soc. Amer. Abs. with Prog., v. 30, no. 5, p. 17.

Gurrola, L. D. and Keller, E. A., 1997, Seismic hazards of the Santa Barbara fold belt, California, Geol. Soc. Amer. Abs. with Prog., v. 31, no. 7, p. 474.

Gurrola, L. D., Keller, E. A., Trecker, M. A., Hartleb, R., and Dibblee Jr., T. W., 1998, Active folding and buried reverse faulting of the Santa Barbara Fold Belt, California: Geol. Soc. Amer. Field Trip Guide Book Number 11, 43 p.

Gurrola, L. D., Keller, E. A., Dibblee Jr., T. W., Trecker, M., and Hartleb, R. 1999, Active folding and blind reverse faulting of the Santa Barbara Fold Belt, California: Coasts Geological Society Field Trip Guide Book, 86 p.

- Hartleb, R., Keller, E. A., and Gurrola, L.D., 1998, Santa Barbara, CA Flood Hazard: A Story of Paleochannels and Earthquakes: *Geol. Soc. Amer. Abs. with Prog.*, v. 30, no. 5, p. 18.
- Keller, E. A. and Gurrola, L. D. 1997a, Can we predict lateral propagation of rupture during earthquakes? Geomorphic indicators of propagation of reverse faults, Santa Barbara Fold Belt, California: Southern California Earthquake Center Annual Meeting, October 1997 p. 69.
- Keller, E. A., Gurrola, L. D., and Tierney, T., 1999, Geomorphic criteria to determine direction of lateral propagation of reverse faulting and folding: *Geology*, v. 27, no. 6, p. 515-518.
- Keller, E. A., Gurrola, L. D., and Trecker, M. A. 1998, Geomorphic Criteria to Determine Direction and Rate of Lateral Propagation of Reverse Faulting and Folding, *Geol. Soc. Amer. Abs. with Prog.*, v. 30, no. 5, p. 22.
- Keller, E. A., Mueller, K., and Gurrola, L D. 1997b, 'Big Bend' of the San Andreas fault: Hypothesis of tectonic extrusion: *Geol. Soc. Amer. Abs. with Prog.*, v. 29, no. 6, p. A-235.
- Ronald, E. C., Keller, E. A., Gurrola, L. D., and Trecker, M. A. 1998, Shoreline Features of the Santa Barbara Fold Belt: A Case of Forensic Seismology: *Geol. Soc. Amer. Abs. with Prog.*, v. 30, no. 5, p. 62.
- Trecker, M. A., Gurrola, L. D, and Keller, E. A., 1998, Oxygen-Isotope correlation of marine terraces and uplift of the Mesa Hills, Santa Barbara, California, USA: In: Stewart, I. S. and Vita Finzi, C. (eds.) *Coastal Tectonics: Geological Society of London, Special Publication 146*, p. 57-69.

15.0 REFERENCES CITED

- Benioff, H., 1955, Mechanism and strain characteristics of the White Wolf fault as indicated by the aftershock sequence. In G. B. Okeshott (ed.) Earthquakes in Kern County, California during 1952. California Division of Mines Bulletin 171, p. 199-202.
- Bloom, A. L., Broecker, W. S., Chappell, J., Matthews, R. K., and Mesolella, K. J. 1974, Quaternary sea level fluctuations on a tectonic coasts; new $^{230}\text{Th}/^{234}\text{U}$ dates from the Huon Peninsula, New Guinea, *Quat. Res.* 4, p. 185-205.
- Bull, W. B., 1985, Correlation of flights of global marine terraces, IN: Morisawa, M., and Hack, J., eds., *Tectonic Geomorphology. Proceedings, Binghamton Geomorphology Symposium, 15th*, p. 129-152.
- Chappell, J. 1983, A revised sea-level record for the last 300,000 years from Papua, New Guinea: *Search*, vol. 14, no. 3-4, p. 99-101.
- Chappell, J. and Shackleton, N. J. 1986, Oxygen isotopes and sea level: *Nature*, vol. 324, p. 137-140.
- Chappell, J., Omura, A., Esat, E., McCulloch, M., Pandolfi, J., and Pillans, B., 1996, Reconciliation of late Quaternary sea levels derived from coral terraces at Huon Peninsula with deep sea oxygen isotope records, *Earth and Planetary Science Letters* 141, p. 227-236.
- Chen, J. H., Edwards, R. L., and Wasserburg, G. J., 1986, ^{238}U , ^{234}U , and ^{233}Th in sea water, *Earth and Planetary Science Letters*, vol. 80, p. 241-251.
- Corbett, E. J., and Johnson, 1982, The Santa Barbara, California earthquake of 13 August 1978, *Bull. Seism. Soc. Amer.* 72, p. 2201-2226.
- Cowie, P. A., and Scholz, C. H., 1992, Growth of faults by accumulation of seismic slip, *Journal of Geophysical Research* 97(B7), p. 11,085-11,095.
- Davis, T. L., 1983, Late Cenozoic structure and tectonic history of the western "Big Bend" of the San Andreas fault and adjacent San Emigdio Mountains [Ph.D. thesis], Santa Barbara, University of California, 508 p.

- Dibblee, T.W., Jr. 1986, Geologic map of the Santa Barbara quadrangle, (Ehrenspeck, ed.), Dibblee Geological Foundation.
- Dibblee, T. W., Jr., 1988, Geology of the Ventura Basin area, *in* Ventura Basin: Geologic Introduction and Field Trip Guidebook (M. H. Link, ed.), Pac. Sec. Amer. Assoc. Petroleum Geologists and Los Angeles Basin Geological Society, p. 7-18.
- Gurrola, L. D. 1993, Structural analysis of a fault-propagation fold and tectonic geomorphology of the Summerland coastal region, Summerland, California, unpub. research report, University of California, Santa Barbara, 21 p.
- Gurrola, L. D. and Kamerling, M. 1996, Role of cross faults as tears in thrust ramps in the Ventura and Santa Barbara Fold Belts, California, 1996: Abstracts for the Southern California Earthquake Center Annual Meeting, p. 49.
- Gurrola, L. D. and Keller, E. A. 1997b, Tectonic geomorphology of the Santa Barbara fold belt, western Transverse Ranges, California: GSA abstracts with programs, vol. 29, no. 6, p. 344-345.
- Gurrola, L. D. and Keller, E. A. 1997c, Style of Quaternary Deformation of an Active Fold Belt: The Santa Barbara Fold Belt, Western Transverse Ranges, California: EOS, Transactions, AGU, vol. 78, no. 46, p. F632.
- Gurrola, L. D., Chen, J. H., and Keller, E. A., 1997a, Uranium-series age and rate of uplift of the Mesa marine terraces, Santa Barbara Fold Belt, California: Southern California Earthquake Center Annual Meeting, October 1997 p. 64.
- Gurrola, L. D., Chen, J. H., Keller, E. A., and Metcalf, J. G. 1996, Dating of emergent marine terraces and rate of uplift for the western Santa Barbara Fold Belt, California: GSA Abstracts with Programs, vol. 28, no. 7, p. A-301.
- Gurrola L. D., Keller, E. A., Dibblee Jr., T. W., Dolan, J., Campbell, S., and Hoover, M. 1998 Active Folding of Emergent Marine Terraces; Summerland to Carpinteria, Santa Barbara Fold Belt, California. The Geological Society of America, Abstracts with Programs, Cordilleran Section, 30(5):8107.

- Hamilton, R. M., 1969, Geology, petroleum development, and seismicity of the Santa Barbara channel region, California, U.S. Geological Survey Professional Paper 1044-9612, p. 47-68.
- Hauksson, E., and Jones, L. M., 1989, The 1987 Whittier Narrows earthquake sequence in Los Angeles, southern California: Seismological and tectonic analysis, *Jour. Geophys. Res.* 94(7), p. 9569-9589.
- Hoover and Associates, 1985, Unpublished report.
- Izett, G. A., Naeser, C. W., Obradovich, J. D., 1974, Fission track age of zircons from an ash bed in the Pico Fm (Pliocene and Pleistocene) near Ventura, California, *in* GSA Abstracts with Programs 6(3), p. 197.
- Jackson, P.A., 1981, Structural evolution of Carpinteria basin, western Transverse Ranges, California, unpub. M.S. thesis, Oregon State University, 107 p.
- Jackson, P. A. and Yeats, R. S. 1982, Structural evolution of the Carpinteria basin, western Transverse Ranges, California: *The American Association of Petroleum Geologist Bulletin*, vol. 66, no. 7, p. 805-829.
- Jackson, J., Norris, R., and Youngson, J 1996, The structural evolution of active fault and fold systems in central Otago, New Zealand; evidence revealed by drainage patterns: *Jour. Struct. Geol.*, vol. 18, no. 2-3, p. 217-234.
- Keller, E. A., Gurrola, L. D., and Tierney, T., 1999, Geomorphic criteria to determine direction of lateral propagation of reverse faulting and folding: *Geology*, v. 27, no. 6, p. 515-518.
- Keller, E. A., Mueller, K., and Gurrola, L D. 1997, 'Big Bend' of the San Andreas fault: Hypothesis of tectonic extrusion: *GSA abstracts with programs*, vol. 29 no. 6, p. A-235.
- Kern, J. P. 1977, Origin and history of upper Pleistocene marine terraces, San Diego, California: *Geol. Soc. Amer. Bull.*, vol. 88, p. 1553-1566.

- Lajoie, K. R., Sarna-Wojcicki, A. M., and Yerkes, R. F. 1982, Quaternary chronology and rates of crustal deformation in the Ventura area, California, In: Cooper, J. D., ed., Neotectonics in southern California, Guidebook for fieldtrips, Anaheim, CA, p. 43-51.
- Lajoie, K. R., Kern, J. P., Wehmler, J. F, Kennedy, G. L, Mathieson, S. A., Sarna-Wojcicki, A. M., Yerkes, R. F. and McCrory, P. F. 1979, Quaternary marine shorelines and crustal deformation, San Diego to Santa Barbara, California, In: Abbot, P. L., ed., Geological excursions in the southern California area: Guidebook for field trips, GSA Annual Meeting, Nov. 1979, Department of Geological Sciences, San Diego State University, San Diego, CA., p. 3-16.
- Luyendyk, B. P., 1991, A model for Neogene crustal rotations, transtension, and transpression in southern California, Geological Society of America Bulletin 103(11), p. 1528-1536.
- MacKenzie, D. 1972, Active tectonics of the Mediterranean region: R. Astron. Soc. Geophys., vol. 30, no. 2, p. 109-185.
- Matthews, R. K. 1973, Relative elevation of Late Pleistocene high sea level stands: Barbados uplift rates and their implications, IN: CLIMAP program, Quat. Res., vol. 3, no. 1, p. 147-153.
- Muhs, D. R., Rockwell, T. K., and Kennedy, G. L. 1992, Late Quaternary uplift rates of marine terraces on the Pacific Coasts of North America, southern Oregon to Baja California Sur, IN: Impacts of tectonics on Quaternary coastal evolution, Quat. Inter., vol. 15-16, p. 121-133.
- Muhs, D. R., Rockwell, T. K., and Kennedy, G. L. 1994a, Uranium-series ages of marine terrace corals from the Pacific Coast of North America and implications for last-interglacial sea level history, Quaternary Research, vol. 42, p. 72-87.
- Muhs, D. R., Miller, G. H., Whelan, J. F., and Kennedy, G. L. 1994b; Aminostratigraphy and oxygen isotope stratigraphy of marineterrace deposits, Palos Verdes Hills and

- San Pedro areas, Los Angeles County, California, In: Quaternary Coasts of the United States: Marine and Lacustrine Systems, SEPM Special Publication no. 48, p. 363-376.
- Namson, J. and Davis, T. 1992, Late Cenozoic thrust ramps of Southern California: Final report of 1991 to the Southern California Earthquake Center.
- Okeshott, G. B. (ed.), 1955, Earthquakes in Kern County, California during 1952. California Division of Mines Bulletin 171, 277 p.
- Olson, D. J., 1982, Surface and subsurface geology of the Santa Barbara-Goleta metropolitan area, Santa Barbara County, California: Unpub. M .S. thesis, Oregon State University, 71 p.
- Olsen, P. G., and Sylvester, A. G., 1975, The Santa Barbara earthquake, 29 June 1925: California Geology, vol. 28, no. 6, p. 123-131.
- Palmer, D. F., and Henyey, T. L., 1971, San Fernando earthquake of 9 February 1971, Pattern of faulting, Science, v. 172, p. 712-715.
- Southern California Earthquake Center, 1995, Seismic Hazards in Southern California: Probable Earthquakes, Working Group on California Earthquake Probabilities, Bull. Seis. Soc. Amer., vol. 85, no. 2, p. 379-439.
- Spencer J. and Owen, L., 1999, Luminescence Dating of Santa Barbara Terraces/Raised Beaches: Preliminary Results, unpub. report, 22 p.
- Stein, R. S., and Hanks, T. C., 1998, M>6 earthquakes in southern California during the twentieth century: No evidence for seismicity or moment deficit, Bull. Seis. Soc. Amer. 88(3), p. 635-652.
- Suppe, J., 1985, Principles of Structural Geology: Prentice-Hall, Englewood Cliffs, New Jersey, 537 p.
- Suppe, J., 1997, Mapping and kinematic analysis of compressive growth structure to define slip rates, Princeton University, 154 p.

- Suppe, J., and Medwedeff, D. A., 1984, Fault-propagation folding: *Geol. Soc. Amer. Abst. Prog.* vol. 16, p. 670.
- Suppe, J., and Medwedeff, D. A., 1990, Geometry and kinematics of fault-propagation folding: *Eclogae geol. Helv.* vol. 83, no. 3, p. 409-454.
- Sylvester, A. G. and Mendes, S. H. 1981, Case Studies of Earthquake Damage and Repair: Earthquake History of Santa Barbara, contributions by Hart, G. C. and Huang, S., Guidebook for the Field Seminar; Annual Meeting of the Earthquake Engineering Research Institute, 56 pp.
- Tapponnier, P., Peltzer G., Ledan, A.Y. 1982, Propagating extrusion tectonics in eastern Asia: *EOS*, vol. 63, no. 45. p. 1097.
- Trecker, M.A., 1999, Oxygen isotope stratigraphy as a means of correlating deformed marine terraces, unpub. M. S. thesis, Univ. Calif., Santa Barbara, 74 pp.
- Trecker, M. A., Gurrola, L. D., and Keller, E. A. 1998, Oxygen Isotope Correlation of Marine Terraces and Uplift of the Mesa Hills, Santa Barbara, California: U.S.A, IN: Stewart, I.S and Vita-Finzi, C. (eds), Coastal Tectonics, *Geol. Soc. London*, vol. 146, p. 57-69.
- United States Geological Survey, 1996, USGS response to an urban earthquake Northridge '94, U.S.G.S. Geol. Surv. Open File Report 96-263, 78 pp.
- Voelker, A., Sarnthein, M., Grootes, P., Erlenkeuser, H., Laj, C., Mazaud, A., Nadeau, M., and Schleicher, M., 1998, Correlation of Marine ^{14}C Ages from the Nordic Seas with the GISP2 Isotope Record: Implications for ^{14}C Calibration Beyond 25 ka BP, *Radiocarbon*, vol. 40, no. 1, p. 517-534.
- Wallace, R (ed.) 1990, The San Andreas Fault System, California: U. S. Geol. Surv. Prof. Paper 1515, 283 p.
- Walls, C., Rockwell, T., Mueller, K., Bock, Y., Williams, S., Pfanner, J., Dolan, J., and Fang, P., 1998, Escape tectonics in the Los Angeles metropolitan region and implications for seismic risk, *Nature*, vol. 394, p. 356-360.

Wells, D. L., and Coppersmith, K. J., 1994, New empirical relationships among magnitude, rupture length, rupture width, rupture area, and surface displacement, *Bull. Seis. Soc. Amer.* 84(4), p. 974-1002.

Willis, B., 1925, A study of the Santa-Barbara earthquake of June 29, 1925: *Seis. Soc. Amer. Bull.*, vol. 15, no. 4, p. 255-278.

Yeats, R. S. and Olson, D. J., 1984, Alternate fault model for the Santa Barbara, California earthquake of 13 August 1978: *Seis. Soc. Amer. Bull.*, vol. 74, no. 5, p. 1545-1553.

Table 1. Seismic sources of the onshore and offshore Santa Barbara Fold Belt with fault/fold dimensions, activity, and maximum expected earthquake (M_w) are determined using the methodology of Wells and Coppersmith (1994). Names of seismic source abbreviations for Figure 1 are in parenthesis.

Fault	Folds(s)	Length (km) ^a	Slip	Vertical rate of faulting (mm/yr)	Activity ^b	Max. M_w
<i>Mission Ridge System</i>						
More Ranch segment (MrR)	Ellwood, UCSB, More Mesa anticlines	15	Oblique: reverse-left	0.3	Apparently active	6.4
Mission Ridge segment (MsR)	Mission Ridge, Montecito, Eucalyptus Hill, and Barker Pass anticlines	17	Reverse-(left?)	0.3 – 0.4	Apparently active	6.5
west and east Arroyo Parida segments (AP)		17 15	Oblique: reverse-left	0.4 (Ojai, CA)	Potentially active	6.5 6.4
<i>Northwest striking sources</i>						
Mesa (MF)	Mesa anticline Honda Valley syncline	12	Reverse	Unknown	Potentially active	6.3
Lavigia (LF)	Hope Ranch anticline	15	Reverse	0.1	Potentially active	6.4
San Jose (SJ)	Goleta Valley anticline	7	Reverse-(oblique?)	Unknown	Potentially active	6.1
San Pedro (SP)	unnamed anticlines	8	Oblique: Reverse-left	Unknown	Potentially active	6.1
Loon Point(LP)	Loon Point anticline	1	Reverse	Unknown	Active	5.1
Ortega Hill (OH)	Ortega Hill anticline	1	Reverse-(oblique?)	Unknown	Potentially active	5.1
Santa Barbara Cemetery(SBC)	Santa Barbara Cemetery anticline	1	Reverse	0.1	Apparently active	5.1
Los Carneros (C)		7	Left	Unknown	Potentially active	6.1
Dos Pueblos (DP)		6	Left	Unknown	Potentially active	6.0
<i>Offshore sources</i>						
Oak Ridge(OR)	Oak Ridge trend	90	Reverse	3.5 to 6.0	Active	7.5 ^c
Pitas Point (PP)	Pitas Point trend	22	Left-reverse	Unknown	Potentially active	6.6 ^c
Red Mountain (RM)		39	Reverse	0.4 to 1.5	Apparently active	6.8 ^d
Rincon Creek (RC)	Rincon Creek anticline	20	Reverse	0.3	Apparently active	6.6
North Channel Slope(NCS)		60	Reverse	2.0	Apparently active	7.1 ^d
Mid Channel (MC)		20	Reverse	Unknown	Active	6.6
Coal Oil Point (COP)	Coal Oil Point anticline	4	Reverse	Unknown	Apparently active	5.8
<i>Other sources</i>						
Santa Yñez		130	Left-reverse	0.1 to 0.7	Active	7.5 ^c

- We assume fault length is the surface rupture length and may be slightly different than map lengths of seismic sources shown on Figure 1.
- Active = demonstrated Holocene (last 10,000 yr.) activity;
Apparently Active = very young (probably Holocene) topographic expression of activity;
Potentially Active = active in Pleistocene (last 1.65 million years)
- Data from Southern California Earthquake Center (SCEC, 1999)
- Data from California Division of Mines and Geology (1999)

Table 2. Table of regional historic seismicity of the Santa Barbara Fold Belt (Nicholson, pers. comm., 1999).

Date	Magnitude	Location	Modified Mercalli Scale (MM)	Damage	Measured or Inferred Peak Accel. (g)	Estimated Peak Accel. at Santa Barbara	Distance to Santa Barbara (km)
24 Mar., 1806	?	?	?	Damage to Mission Santa Barbara and Royal Presidio	?	0.05-0.10	?
21 Dec., 1812	7.1+	Santa Barbara Channel	X-XI	Destroyed La Purisma Mission (near Lompoc) and Santa Barbara Mission,; tsunami?	0.60+	0.20-0.40	< 50
9 Jan., 1857	8.2 +	San Andreas fault	X+	Ruptured 300 km of the San Andreas fault; intensity VI-VII at Santa Barbara; > 90 sec. of shaking	0.80+	0.10+	60-190
27 July to 12 Dec., 1902	6.0?	near Los Alamos	VIII-IX	Several EQ's totally destroy Los Alamos	0.40-0.50	0.05	60
29 June, 1925	6.3 or 6.8	Santa Barbara	VIII-IX	Extensive damage to downtown Santa Barbara and city	0.50-0.60	0.40-0.60	< 5
29 June, 1926	5.5?	Santa Barbara	VIII	Moderate damage to Santa Barbara; aftershock of 1925 EQ	0.30	0.20	< 5
4 Nov., 1927	7.3	off Pt. Arguello	VIII+	Tsunami (2m) generated along coast; slight damage to Santa Barbara	0.60++	0.10	100
30 June, 1941	5.9	offshore Carpinteria	VII	Slight damage to Santa Barbara	0.40-0.50	0.10	10
21 July, 1952	7.7	Kern County	XI	Moderate damage to Santa Barbara; liquefaction along Laguna Street paleochannel	0.80+	0.15	85
5 July, 1968	5.2	Santa Barbara Channel	VI	EQ swarm with largest event causing slight damage to Santa Barbara	0.20	0.07-0.10	15
13 Aug., 1978	5.9	off Goleta Pt.	VII-VIII	Moderate damage mainly to UCSB campus	0.44	0.28	< 5

Table 3. Generalized stratigraphic section of the Santa Barbara Fold Belt, California (modified after Dibblee, 1966; Olson, 1982).

SERIES	FORMATION	DESCRIPTION	ESTIMATED THICKNESS
Plio-Pleistocene	Holocene alluvium older alluvium and gravels, fanglomerate Qa, Qoa, Qog, Qf	Gravel, sand, silt; non-marine Older alluvium: gravel, sand, silt; marine terrace deposits capping coastal mesas Fanglomerate: boulders, gravel, sand; non-marine	0 - 75 m (0 - 250')
	Casitas Qca	Buff to brownish-gray pebbly sandstone and cobble gravel; non-marine	?
	Santa Barbara Qsb not in contact	Yellow, fossiliferous, fine sand, local consolidated sandstone, and minor siltstone and claystone; marine (<790 ka in Santa Barbara Fold Belt)	0 - 900 m (0 - 3000')
	"Pico"	Blue-gray siltstone, fine-grained sandstone with a fossiliferous basal conglomerate; marine	
	Sisquoc Tsq	Diatomaceous clay-shale and siltstone; marine	0 - 245 m (0 - 800')
Miocene	Monterey Tm, Tml	Dark brown, laminated siliceous shale, mudstone, and siltstone; bentonite at base; marine	425 - 670 m (1400 - 2200')
	Rincon Tr	Gray to dark brown mudstone and siltstone with occasional bentonite beds and carbonate lenticules; marine	425 - 520 m (1400 - 1700')
Oligocene	Vaqueros Tvq	Gray, thick-bedded sandstone; marine	100 m (325')
	Sespe Tsp, Tspss	Predominantly red sandstone, shale, and conglomerate interbedded with gray to green siltstone; non-marine	760 - 900 m (2500 - 3000')
Eocene	Coldwater Tcw, Tcwsh	Gray, arkosic sandstone, minor siltstone; marine	1000 m (3300')

Table 4. Uranium-series, radiocarbon, and optically stimulated luminescence age results from terraces in the SBFB.

Sample Location – Terrace Site	Sample Number	Uranium Series Age (ka) ^a	Measured C14 Age (RCYBP) ^b	Measured Luminescence Age ^c (ka)	
				Quartz	K-feldspar
UC Santa Barbara- Isla Vista terrace	IV-1-96 IV-2-98	47 +/- 0.5	43,790 +/- 770		40 +/- 3
Ellwood terrace	C-5		35,860 +/- 570		
Ellwood terrace	C-12		37,000 +/- 570		
Ellwood terrace	C-14		47,020 +/- 1,500		
More Mesa terrace	MM-1-96 MM-2-98		36,830 +/- 330		53 +/- 7
Santa Barbara City College terrace	SBCC-1-98 SBCC-2-98	70 +/- 2.0		109 +/- 23	
Santa Barbara Point	SBP-1-98			336 +/- 64 ^d	58 +/- 11
Santa Barbara Cemetery	SBC-1-98				79 +/- 10
Summerland terrace Loon Point	LP-1-96 LP-2-98		3,990 +/- 40 yr	105 +/- 15	167 +/- 15 ^d

- a. Uranium-series and luminescence ages are reported as 1 ka = 1,000 years before present.
- b. Radiocarbon samples were submitted to Beta Analytic Laboratory for AMS analysis and ages are designated as radiocarbon years before present (RCYBP).
- c. Optically stimulated luminescence age estimates are based on analysis of quartz and K-feldspar grains (Spencer and Owen, 1999).
- d. Results are considered maximum ages and the date (336 +/- 64 ka) at Santa Barbara Point and the date (167 +/- 15) at Loon Point are considered unlikely because: 1) the first emergent terrace at Santa Barbara City College has a U-series age of 70 +/- 2 ka, and 2) first emergent terraces throughout the Santa Barbara-Ventura region (when dated) are no older than 125 ka.

Table 5. Selected examples of southern California earthquakes.

Earthquake	Approximate Magnitude	Location Relative To San Andreas Fault	Direction of Lateral Propagation of Rupture	Aftershock Locations	Lateral Component of Displacement	Supports Hypothesis? YES (Y) NO (N)	Comments References
1925 Santa Barbara	6.3	south	west (?)	not known	probably left-oblique		many uncertainties
1952 Kern Co.	7.5	north	northeast	all northeast	left-oblique	Y (displacement)	Oakeshott, 1955
1971 San Fernando	6.6	south	probably to southeast	mostly southeast	left-oblique	Y (displacement) N (propagation)	left-lateral component of slip apparently increases east to west (Palmer and Henyey, 1971)
1978 Santa Barbara	5.9	south	northwest	northwest	left-oblique	Y	Corbett & Johnson, 1982; Yeats & Olson, 1984
1994 Northridge	6.7	south	northwest	mostly northwest	not known	Y	USGS, 1996

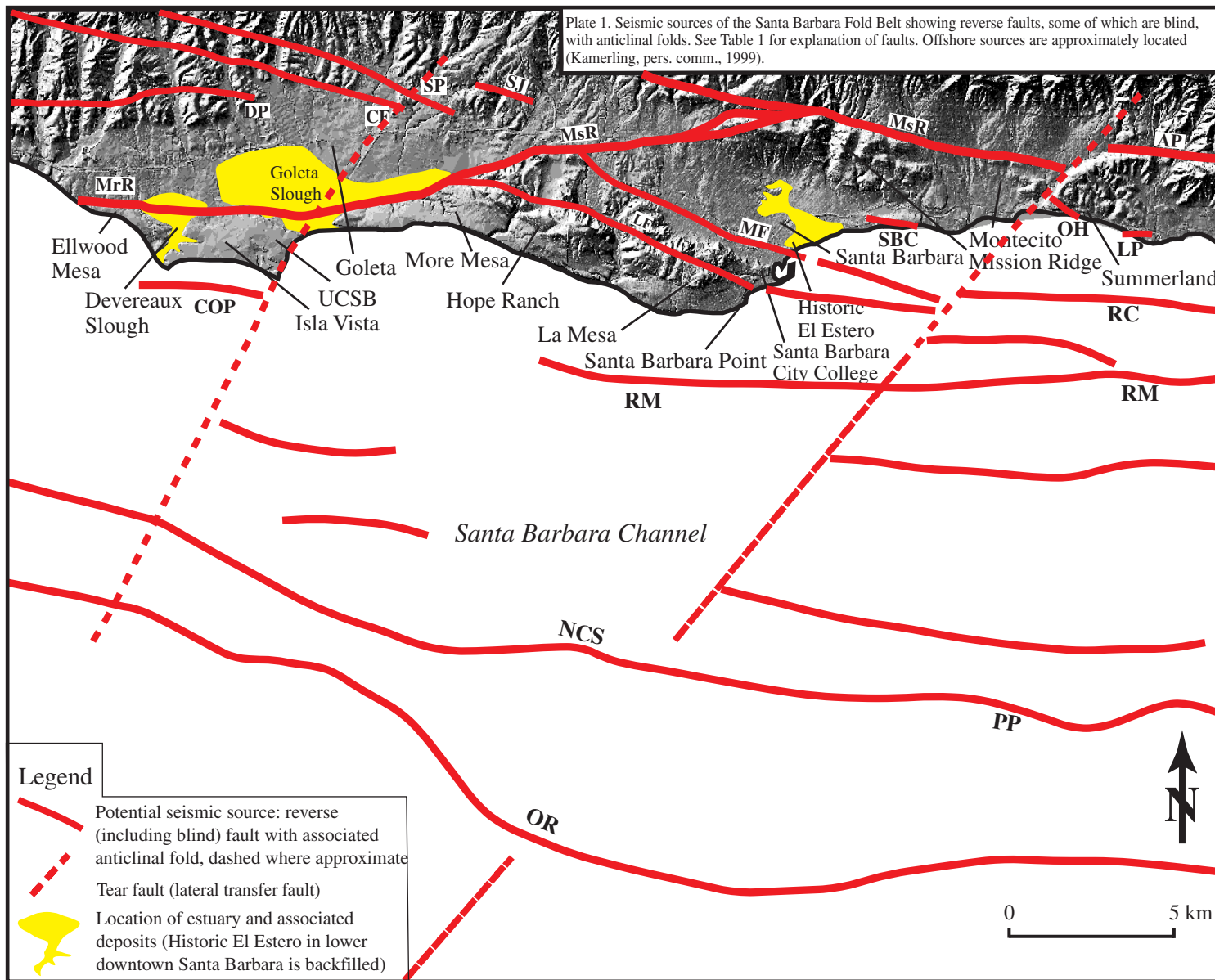


Figure 1. Seismic sources of the Santa Barbara Fold Belt showing reverse faults, some of which are blind, with anticlinal folds. Offshore sources are approximately located (Kamerling, pers. comm., 1999). The Mission Ridge Fault System is subdivided into the More Ranch (MrR), the Mission Ridge (MsR), and the Arroyo Parida (AP) segments. Additional onshore seismic sources include the Dos Pueblos (DP), the Carneros (CF), the San Jose (SJ), the San Pedro (SP), the Lavigia (LF), the Mesa (MF), the Santa Barbara Cemetery, the Ortega Hill (OH), and the Loon Point (LP) faults.

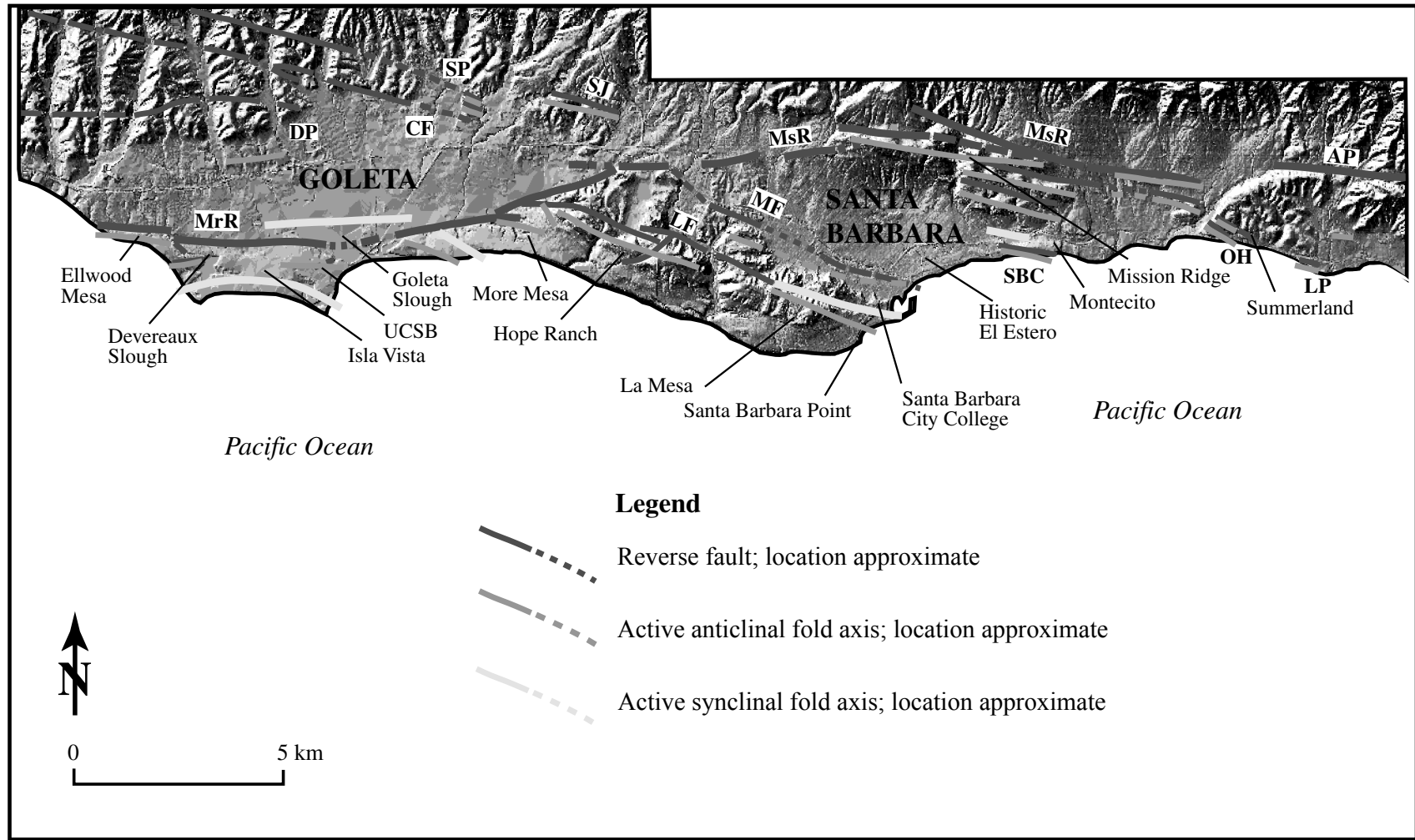
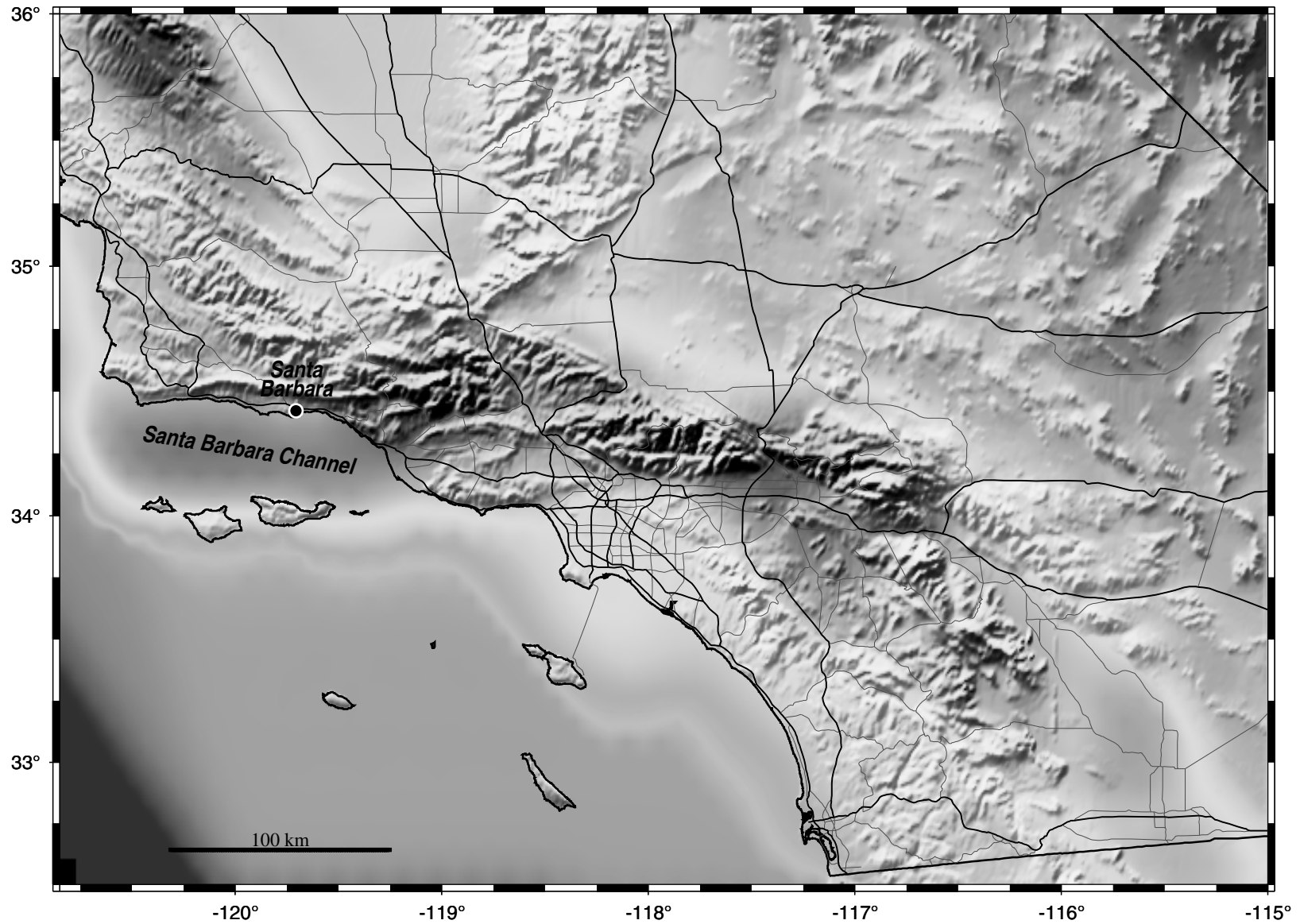
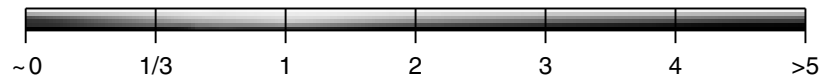


Figure 2. Seismic sources of the onshore Santa Barbara Fold Belt showing south-dipping, reverse faults, some of which are blind, with associated north-verging, hanging wall anticlines and footwall synclines. The Mission Ridge Fault System is subdivided into the More Ranch (MrR), the Mission Ridge (MsR), and the Arroyo Parida (AP) segments. Additional onshore reverse faults include the Dos Pueblos (DP), the Carneros (CF), the San Jose (SJ), the San Pedro (SP), the Lavigia (LF), the Mesa (MF), the Santa Barbara Cemetery (SBC), the Ortega Hill (OH), and the Loon Point (LP) faults.



So. Calif. Earthquake Center (SCEC)

GMT Feb 2 13:06 Computer graphics by Ken Hudnut (USGS - Pasadena)



Key - Number of times per century the shaking from earthquakes will exceed 20% the force of gravity. Significant damage to older buildings begins at this level.

Figure 3. Relative seismic hazard for southern California (SCEC, 1995).

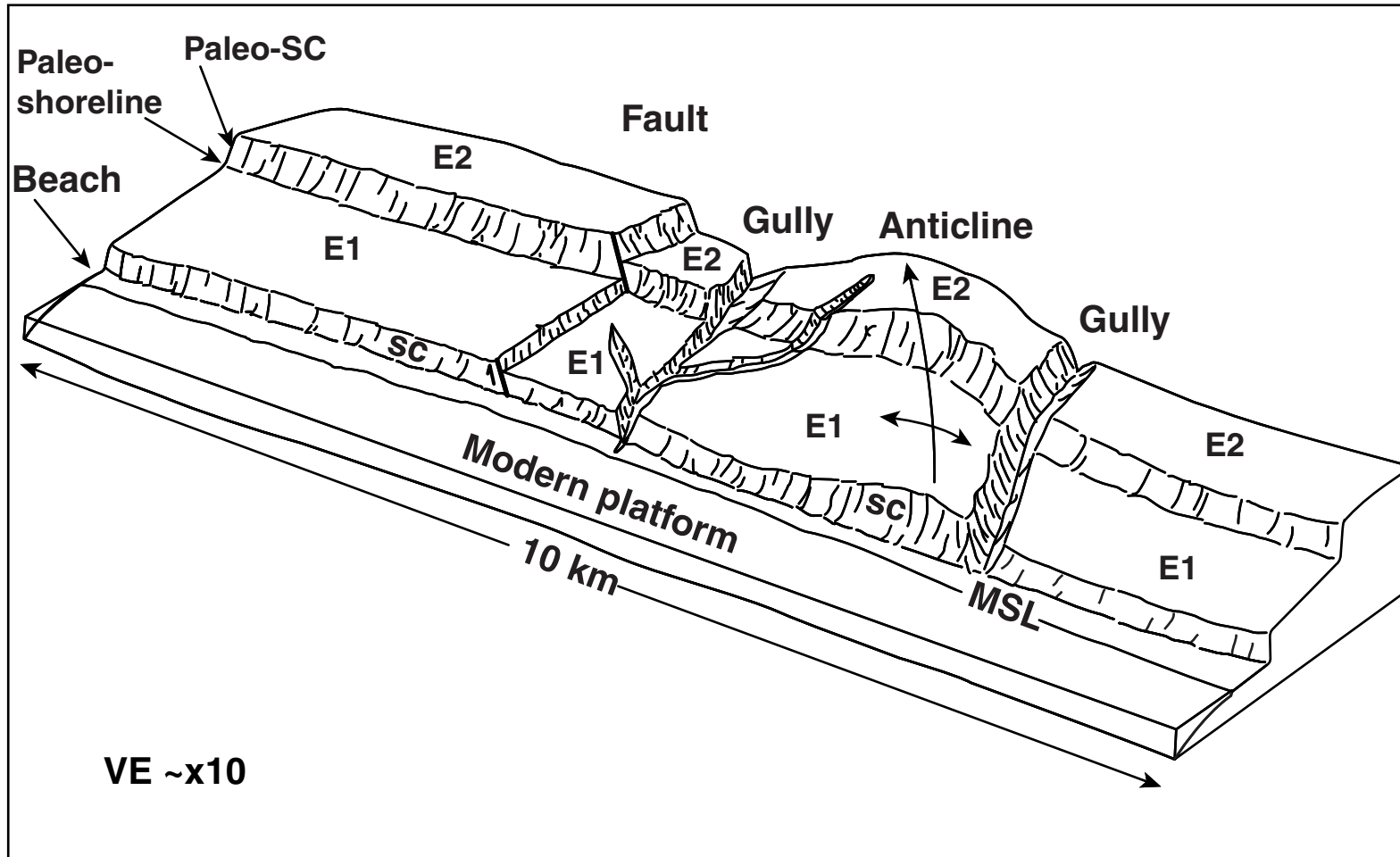


Figure 4. Idealized diagram of a modern wave-cut platform and associated sea cliff (SC) and relation to uplifted marine terraces and associated morphology. The first emergent marine terrace is (E1) and the second emergent terrace (E2) is the next higher terrace. The elevation of the buried marine platform and the associated paleo-sea cliff (Paleo-SC) defines the terrace shoreline angle. The elevation of the terrace shoreline angle is measured in order to calculate total amount of vertical surface uplift. Note that uplifted marine terraces are discontinuous and folded, complicating their correlation (modified after Trecker et al., 1998).

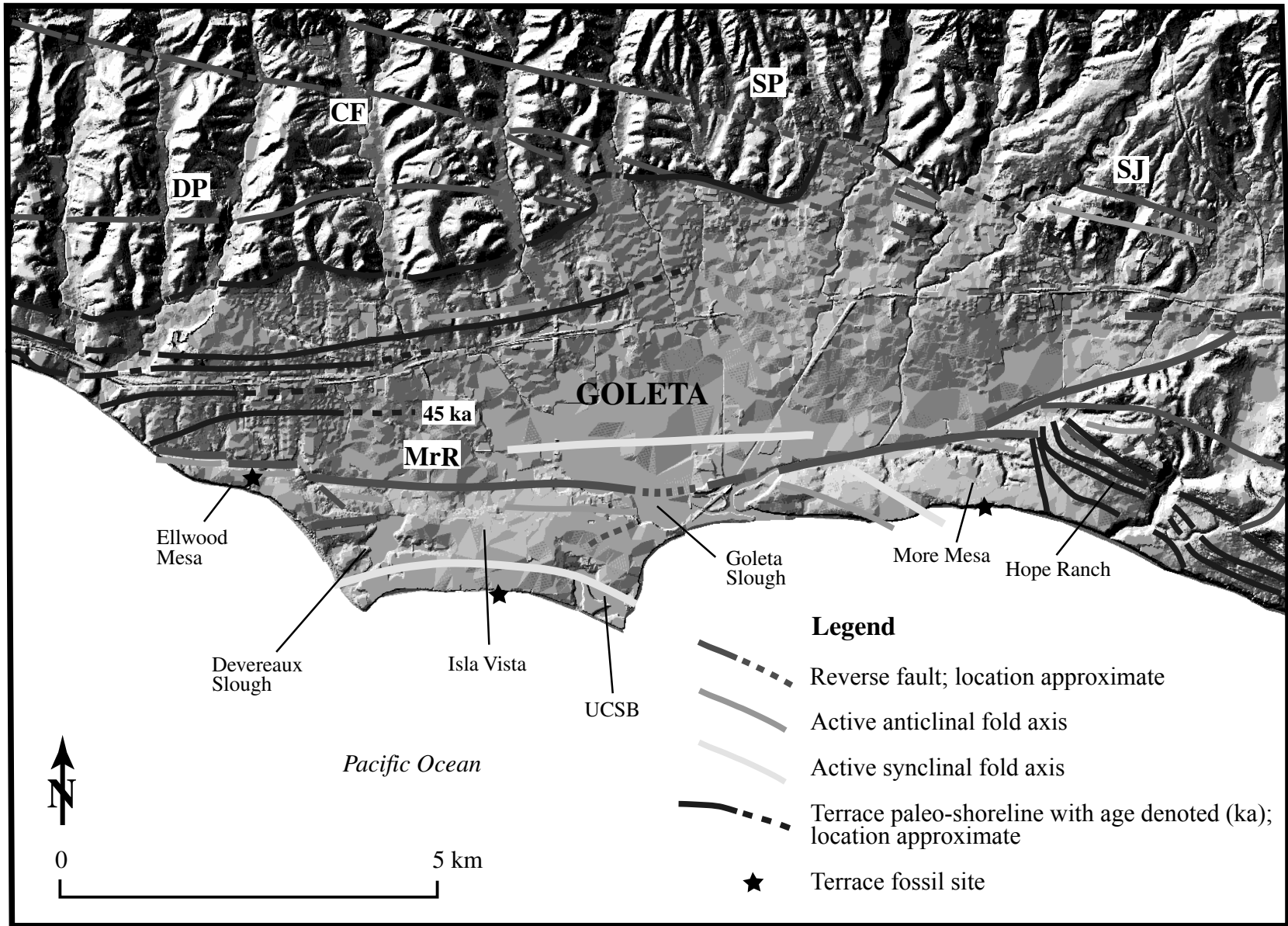


Figure 5. Geomorphologic map of the Ellwood and UC Santa Barbara campus area showing shoreline angle and the positions of the associated paleo-shorelines. Note that the paleo-shorelines are discontinuous at drainages and eroded across the More Ranch fault (MrR). Other faults include the Carneros (CF), the Dos Pueblos (DP), the San Jose (SJ), and the San Pedro (SP) faults.

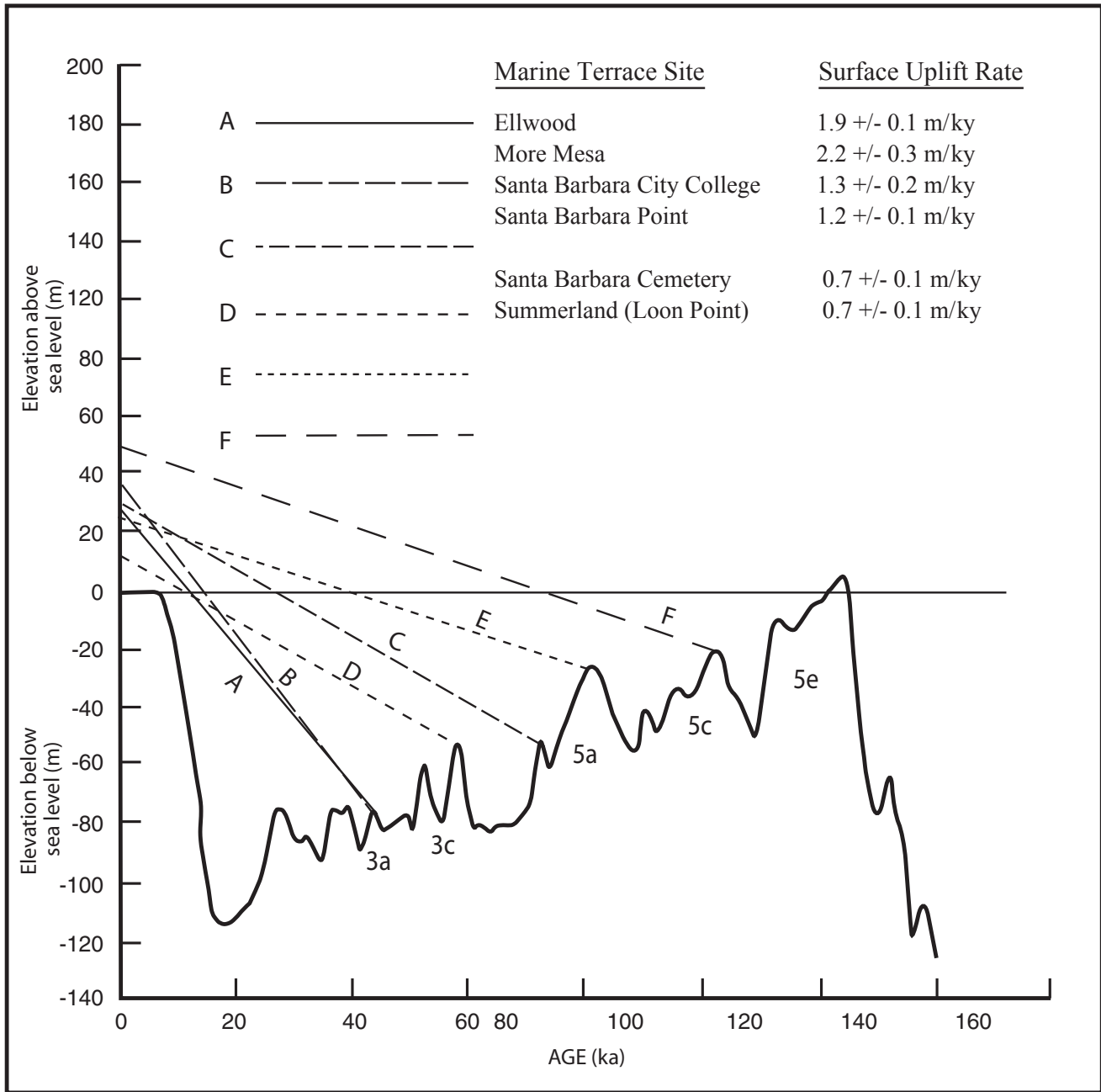


Figure 6. Graph of the late Pleistocene sea level curve (Chappell and others, 1996) with the elevations of the shoreline angles of the first emergent terraces in the SBF. The elevations and ages of the first emergent terraces are plotted, and the slope of the resultant line is the rate of surface uplift (m/ky) for that terrace.

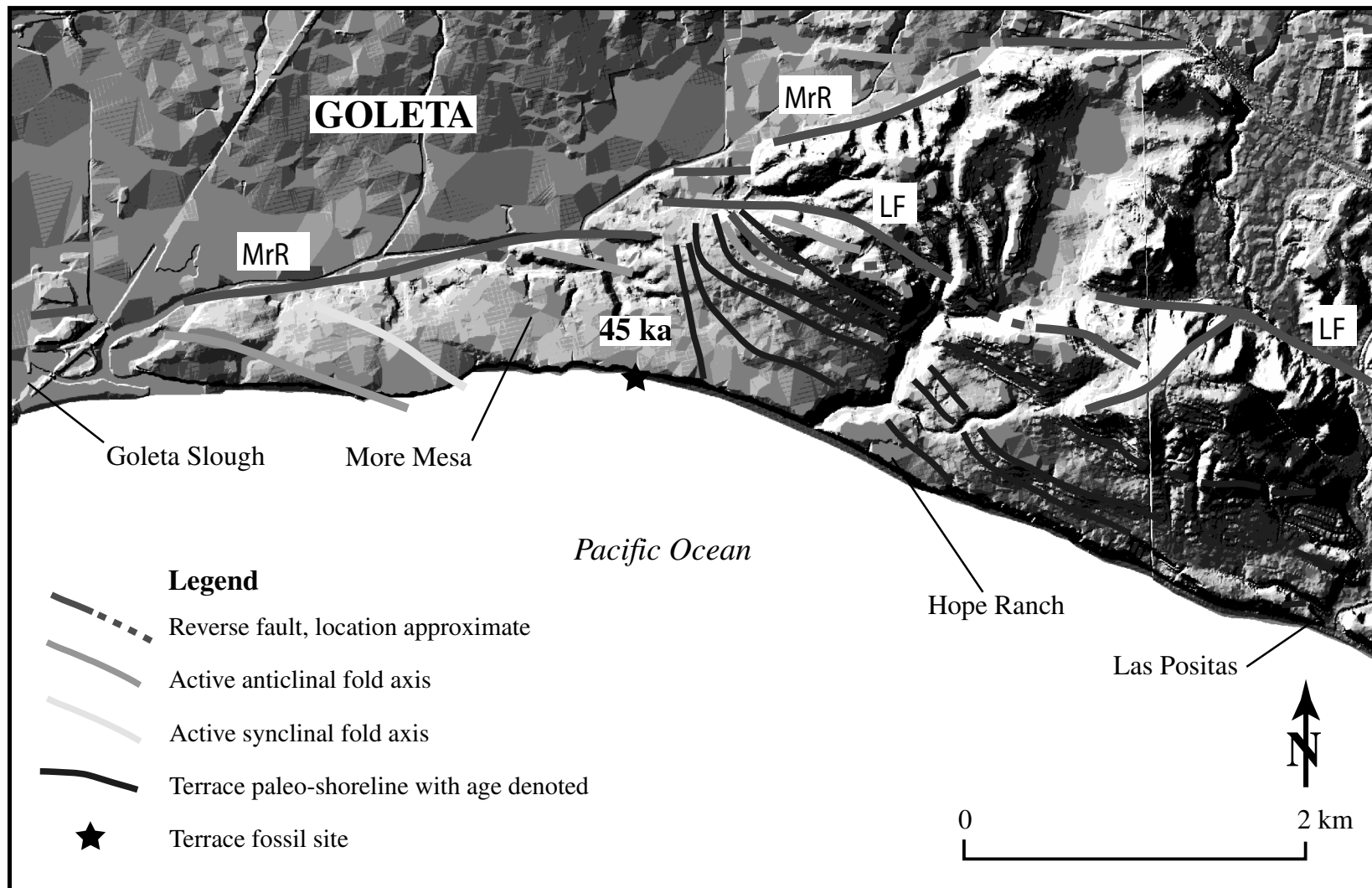


Figure 7. Geomorphic map of More Mesa marine terraces on the hanging wall of the More Ranch (MrR) and Lavigia (LF) faults. The position of the five emergent terraces and associated paleo-shorelines are shown. The first emergent terrace is age-dated at approximately 42 ka and correlated to isotope substage 3a and yields a surface uplift rate of 2.2 ± 0.2 mm/yr.

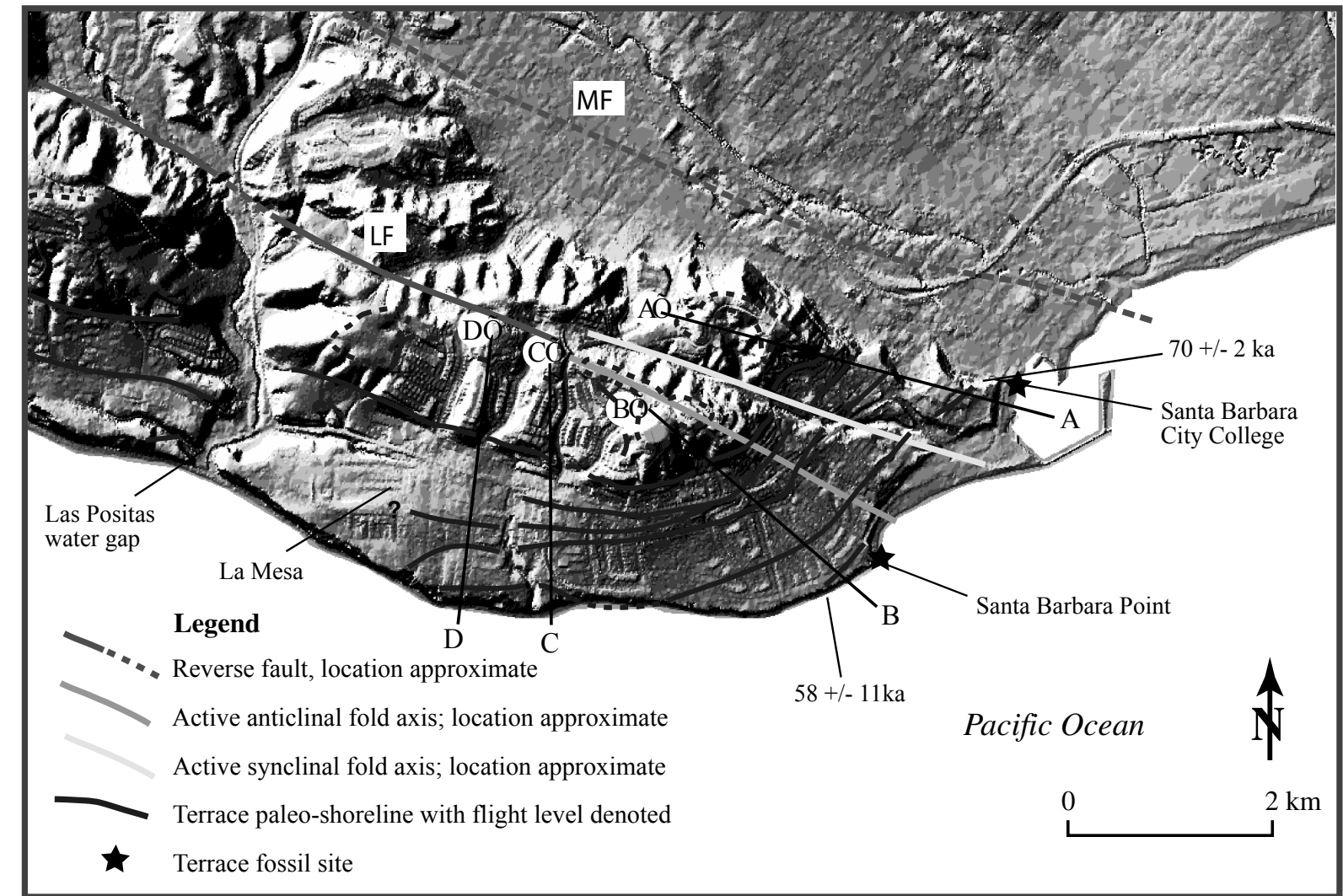


Figure 8. Geomorphic map of the La Mesa anticline and uplifted, marine terraces: (La Mesa fault (MF) and Lavigia fault (LF). Flights of marine terraces (denoted 1, 2, 3, etc.) are preserved on the south flank and the nose of the east-plunging La Mesa anticline. Sites where u-series and OSL age-dates are labelled and are correlated across the Las Positas water gap. They are truncated by the blind, south-dipping MF. The LF forms a well-expressed fold scarp east of the Las Positas water gap and is expressed as an anticlinal-synclinal fold sequence to the west.

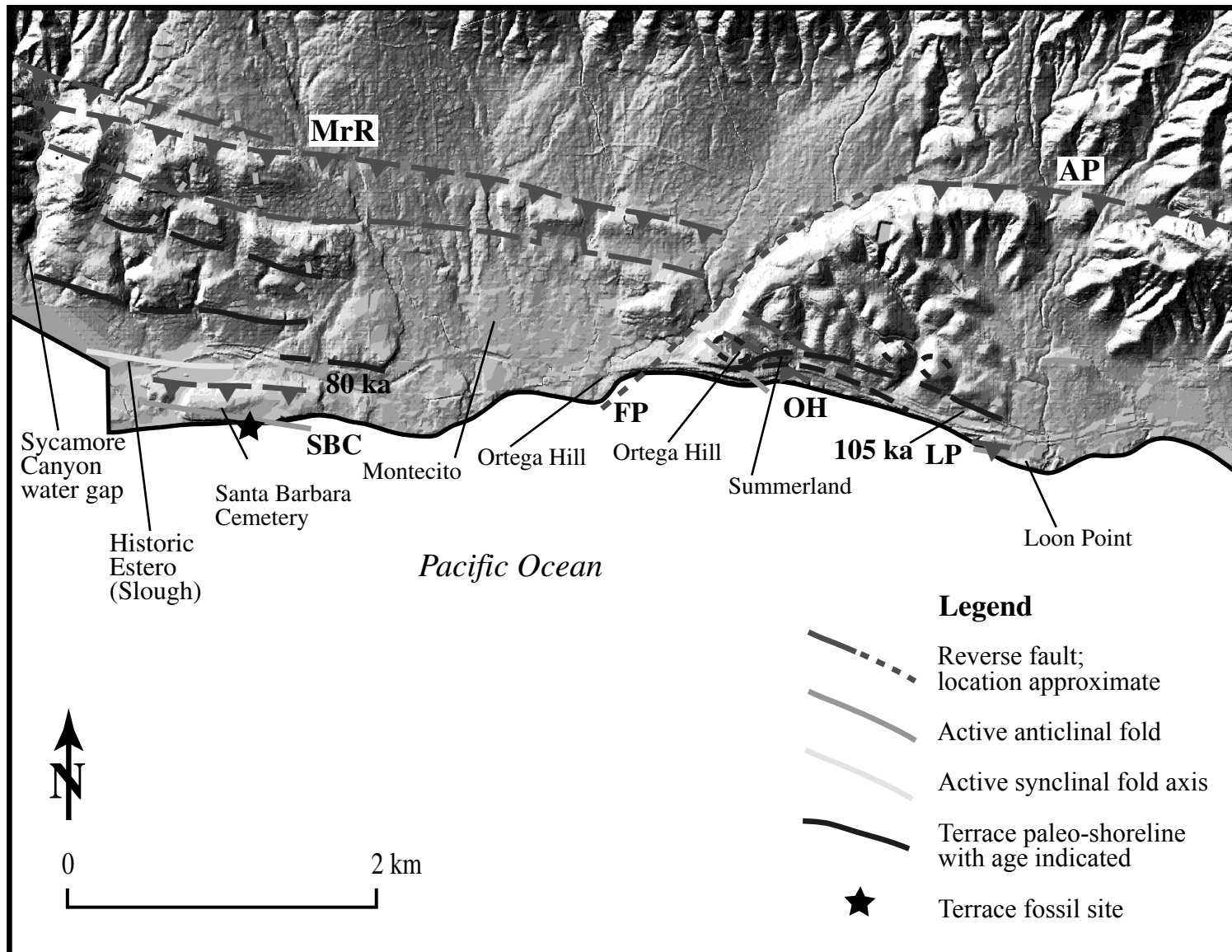


Figure 9. Geomorphic map of the eastern SBFB from Santa Barbara eastward to Summerland. Uplifted marine terraces and the associated paleo-shorelines are shown. The Mission Ridge (MrR), the Fernald Point (FP), the Arroyo Parida (AP), the Santa Barbara Cemetery (SBC), the Ortega Hill (OH), and the Loon Point (LP) faults are shown.

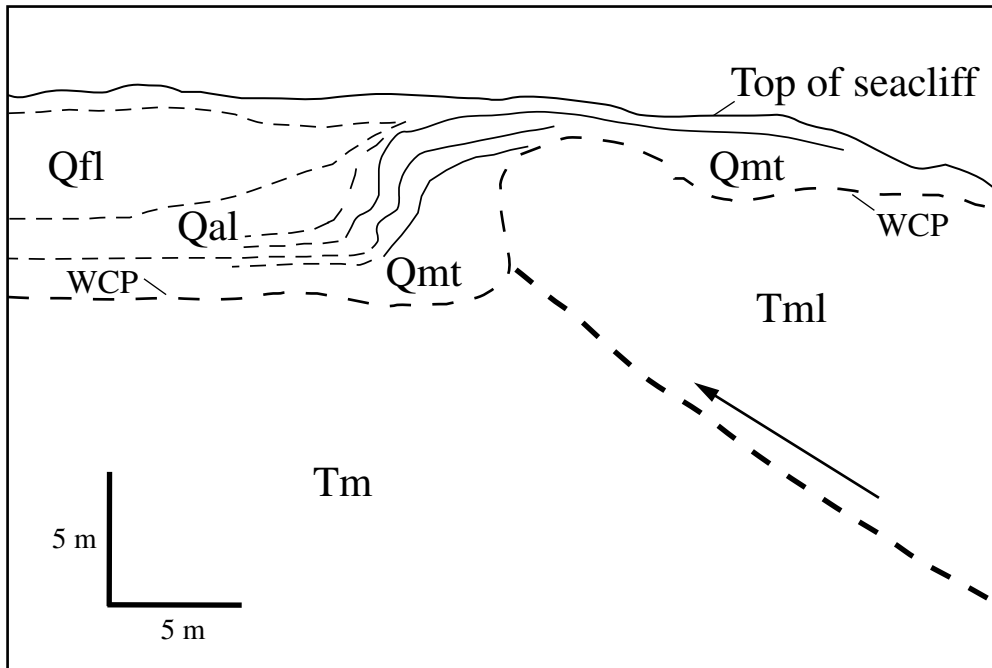
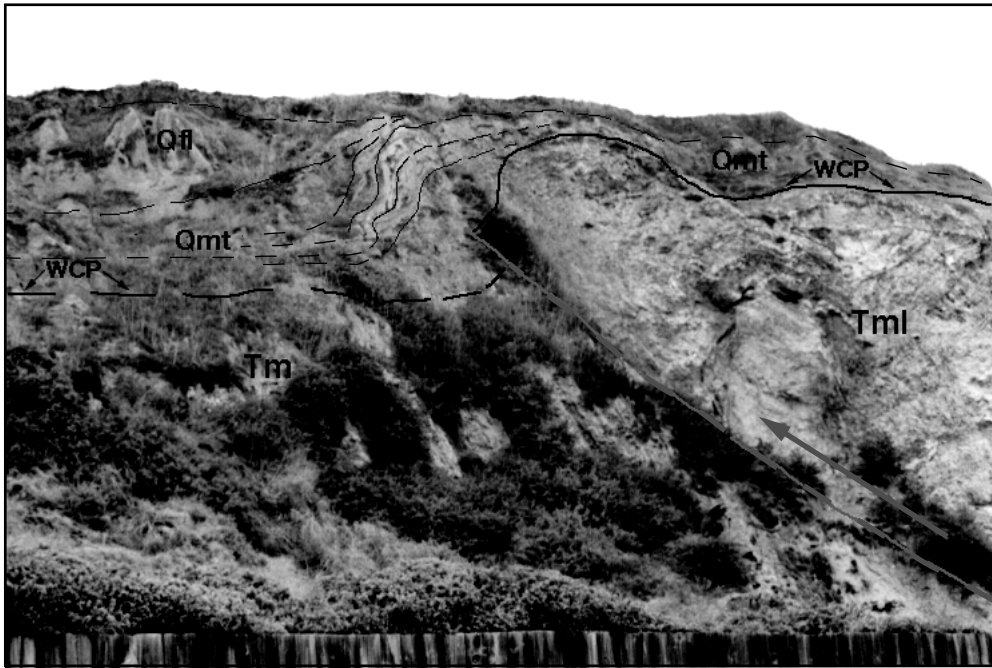


Figure 10. Photograph and sketch of the More Ranch fault seacliff exposure at Ellwood. The drape anticline folds Quaternary marine terrace (Qmt), alluvial (Qal) and fluvial (Qfl) sediments. The wave-cut platform (WCP) on top of Tertiary Monterey Formation (Tm and Tml-lower member) is vertically offset about 6 m.

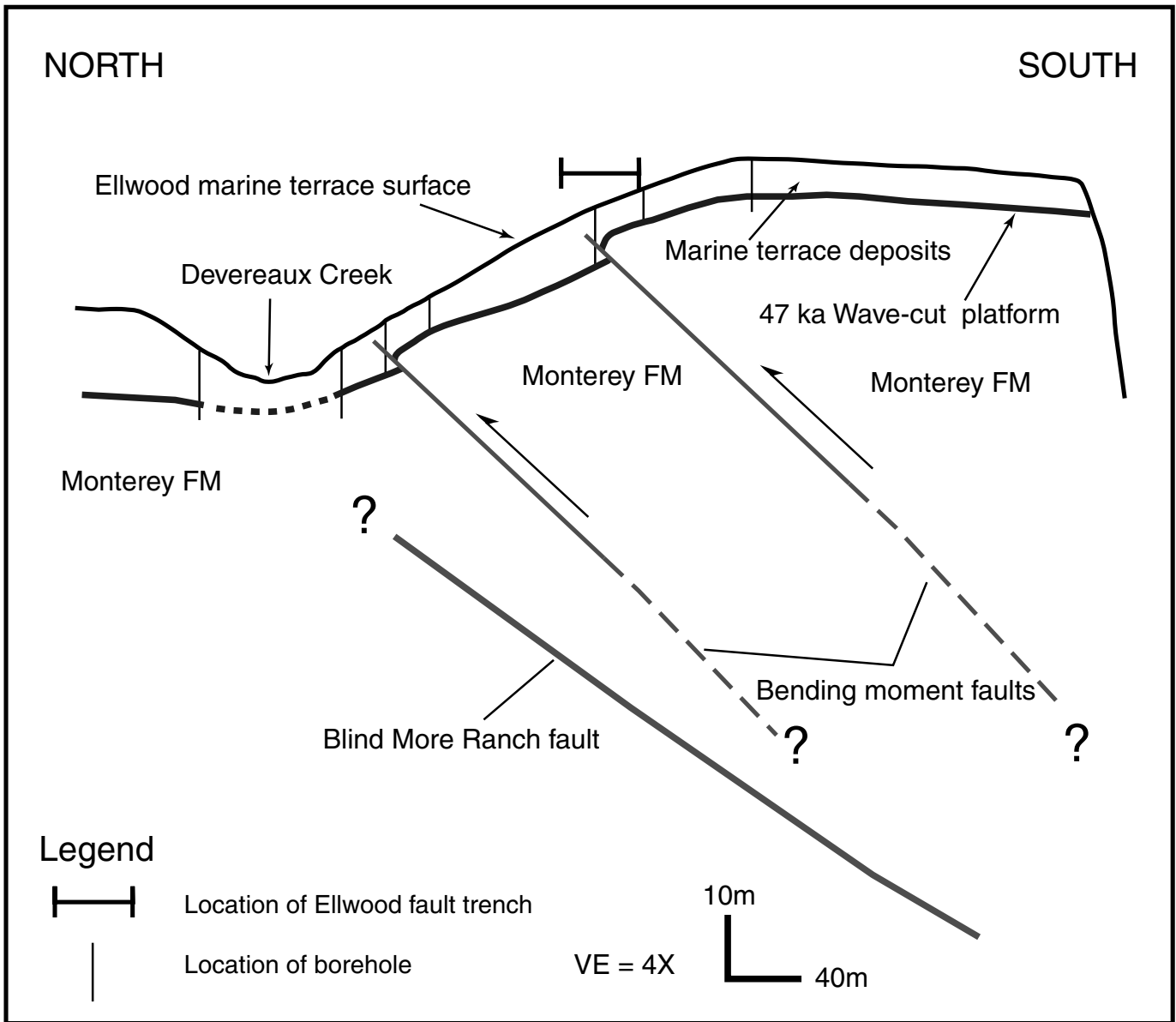


Figure 11. Subsurface profile of the Ellwood wave-cut platform and terrace based on shallow, continuous-core sampling of small-diameter boreholes and surface elevation surveys. The borehole data is supplemented with data from previous geotechnical and environmental excavations. The subsurface profile shows the relationship of bending moment faults to the blind trace of the More Ranch segment.

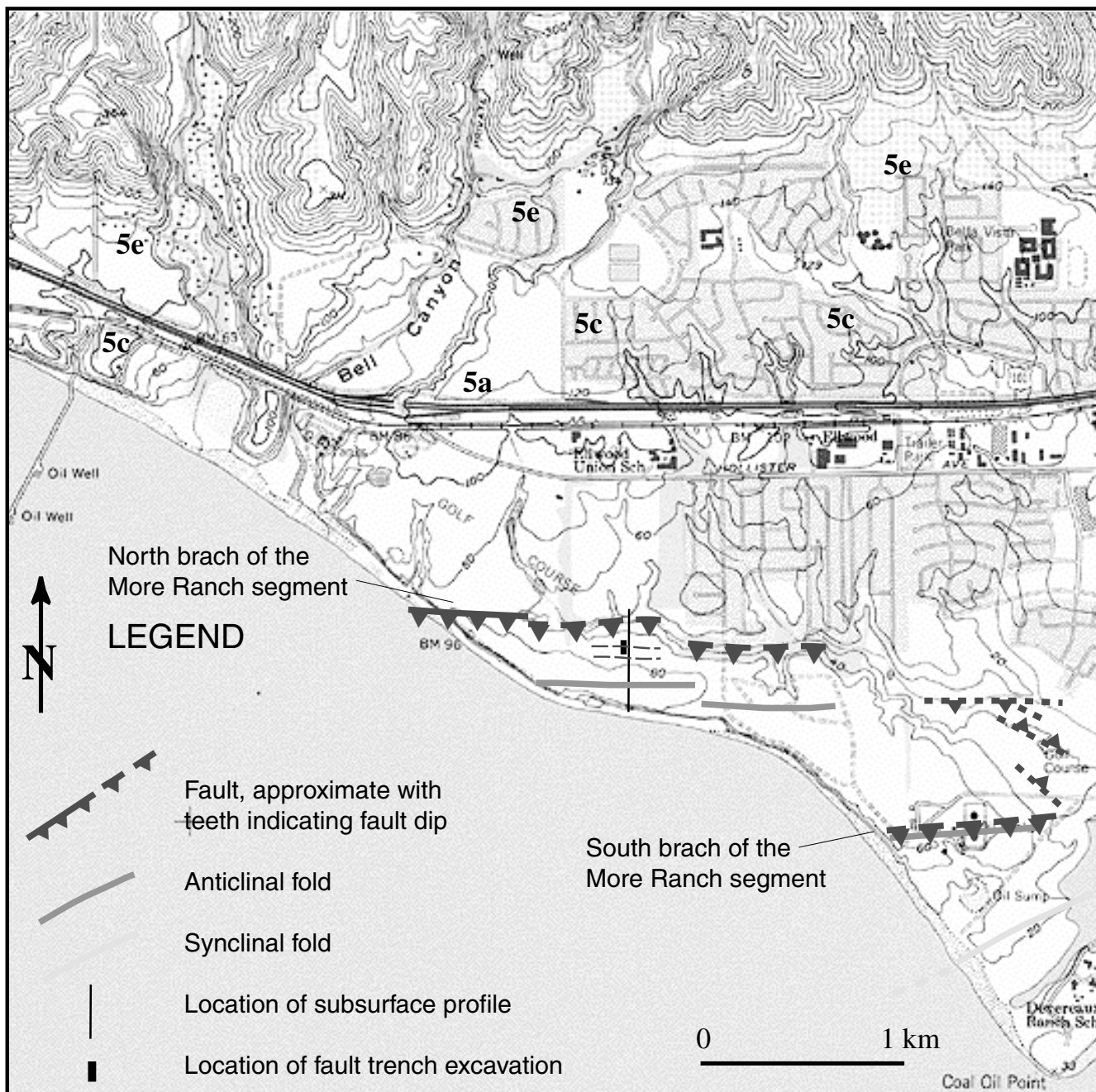


Figure 12. Map of the Ellwood Beach area showing the locations of the north and south branches of the More Ranch fault and location of fault trench. The north branch of the More Ranch fault is exposed at its western extent, however the fault is blind east of the sea cliff exposure and mapped based on the projection of the fault plane to the surface. A north-south profile (Figure 11) of the wave-cut platform and terrace is constructed across bending moments formed on the forelimb of the Ellwood anticline.

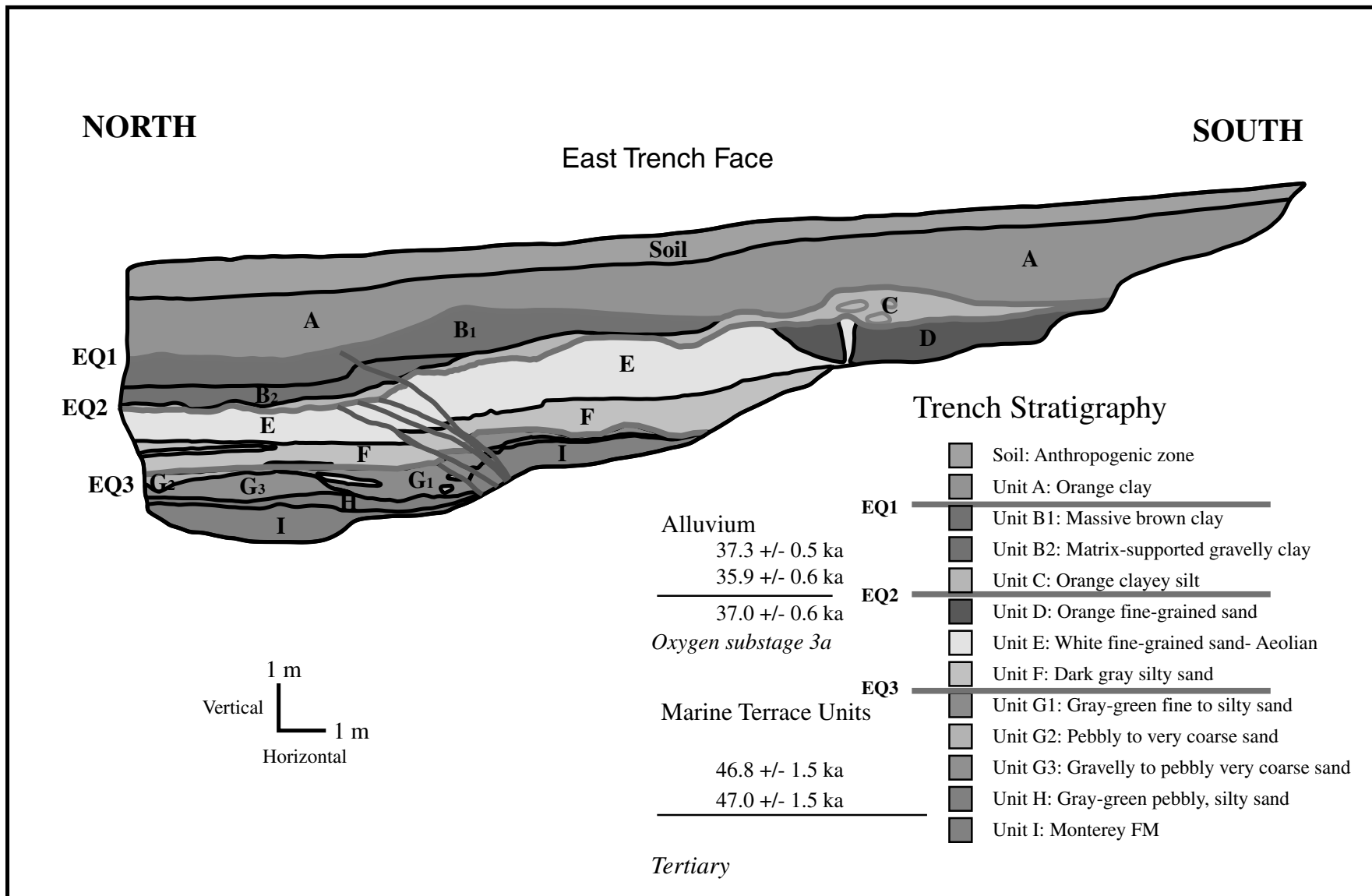
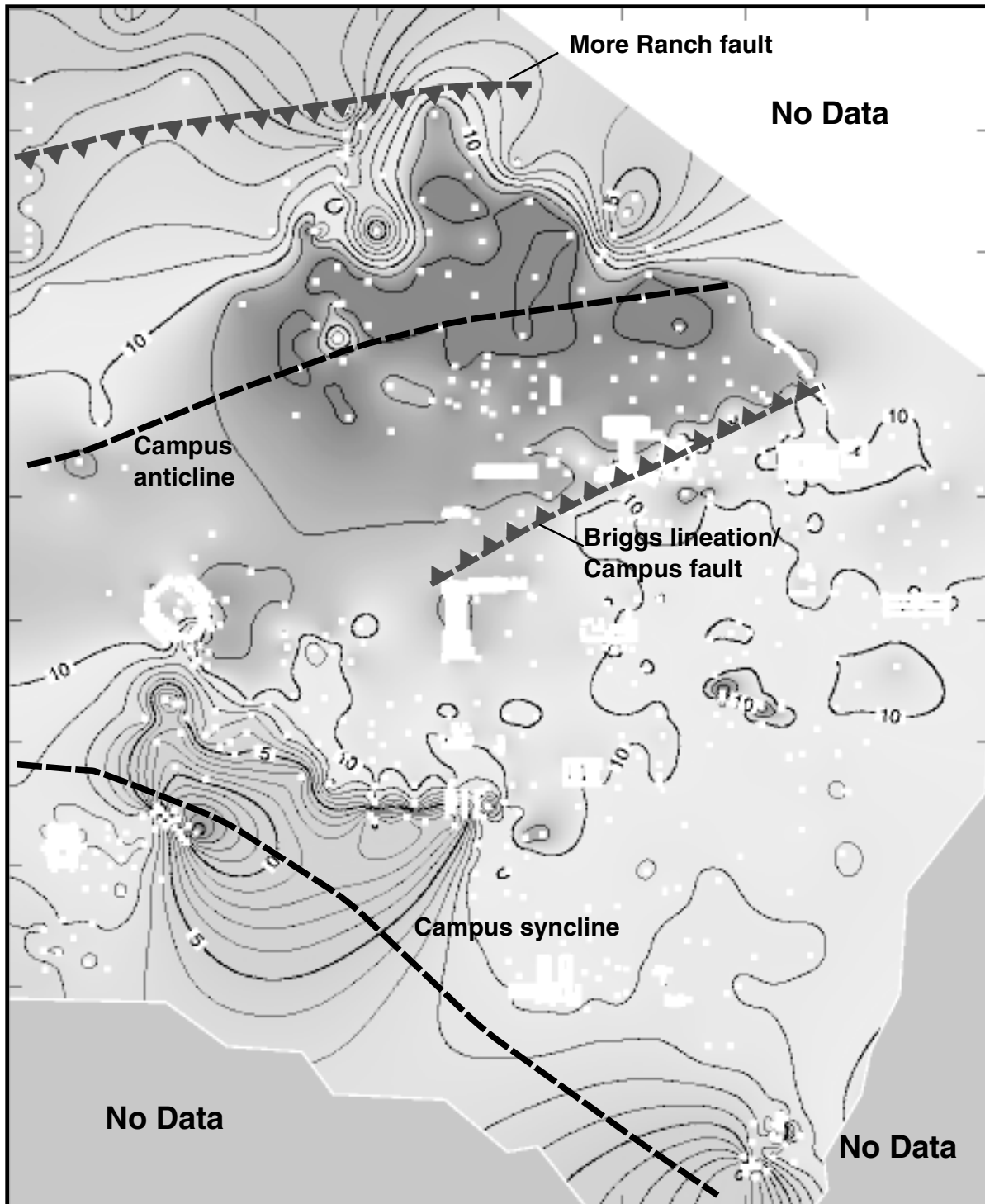
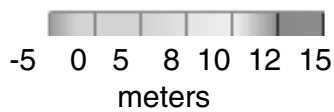


Figure 13. Trench log of the east trench face of the More Ranch fault folding and faulting oxygen isotope substage 3a marine terrace. The wave-cut platform (contact between units I and H) is vertically offset a total of approximately 1.2 m. The trench stratigraphy reveals three paleoearthquakes denoted EQ1, EQ2, and EQ3. EQ2 and EQ3 occurred approximately about 37 ka and between 47 ka and 37 ka respectively. The most recent earthquake (EQ1) occurred since 36 ka, however a minimum age of faulting has not been established.



Contour Interval = 1.0 meter



Horizontal Scale



Figure 14. Subsurface topographic map of the 45 ka UCSB marine platform showing fault and fold features related to the More Ranch segment. A south-facing scarp (Briggs lineation) is believed to have formed as the result of uplift due to a north-dipping fault termed the Campus fault.

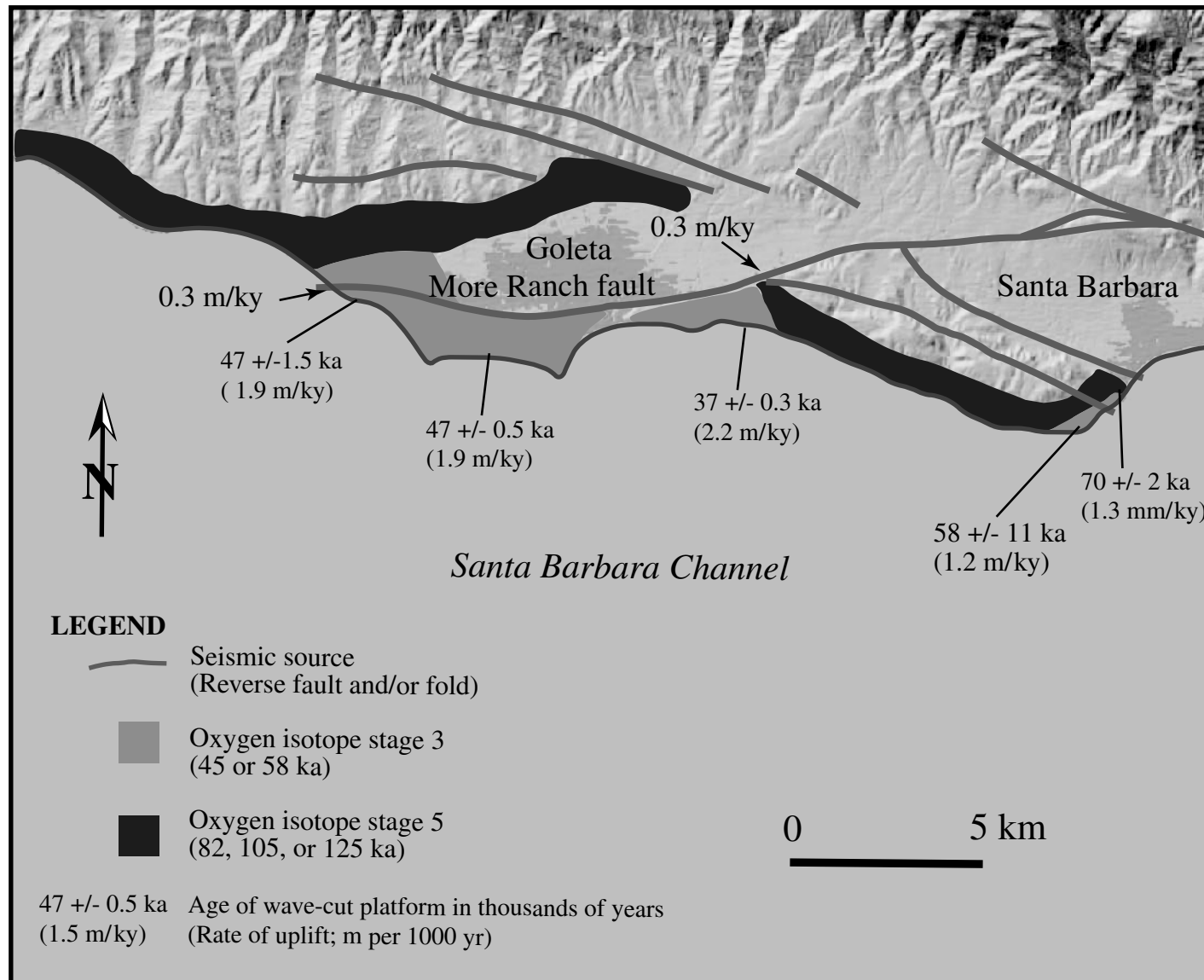
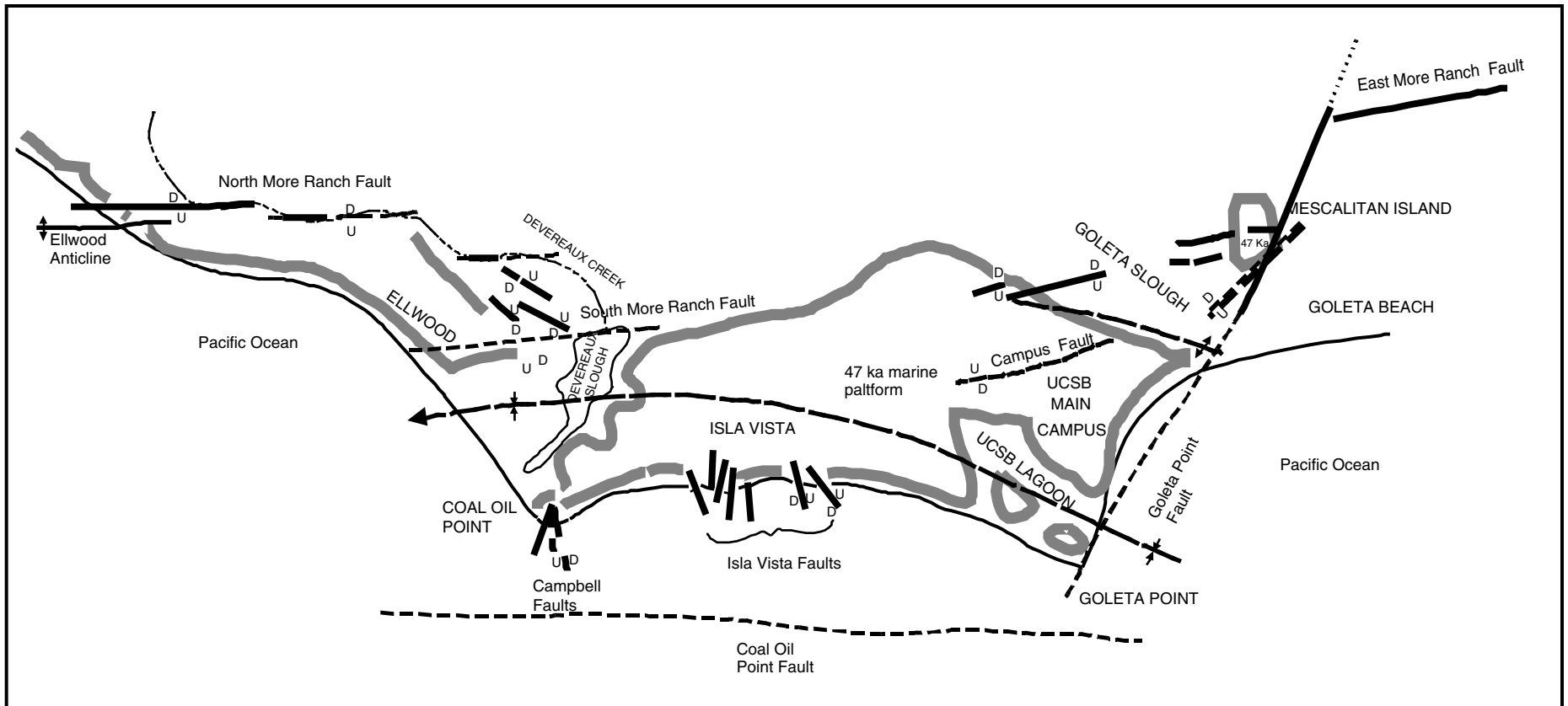


Figure 15. Late Pleistocene marine terraces of the western Santa Barbara Fold Belt. Uranium series ages of fossil terrace corals and radiocarbon (^{14}C) ages of terrace charcoal and a fossil pholad sampled are shown. Vertical surface uplift rates are shown as are faulting rates for the More Ranch fault where oxygen isotope stages 3 and 5 are vertically displaced.



- Symbols**
- Fault; dashed where approximately located; showing relative sense of displacement and dip direction.
 - Anticline, approximately located; showing direction of plunge.
 - Syncline, approximately located; showing direction of plunge.
 - Edge of elevated coastal mesa.

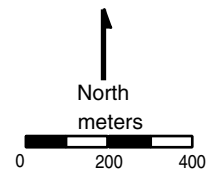


Figure 16. Local fault map and associated geomorphology of the UCSB campus area.

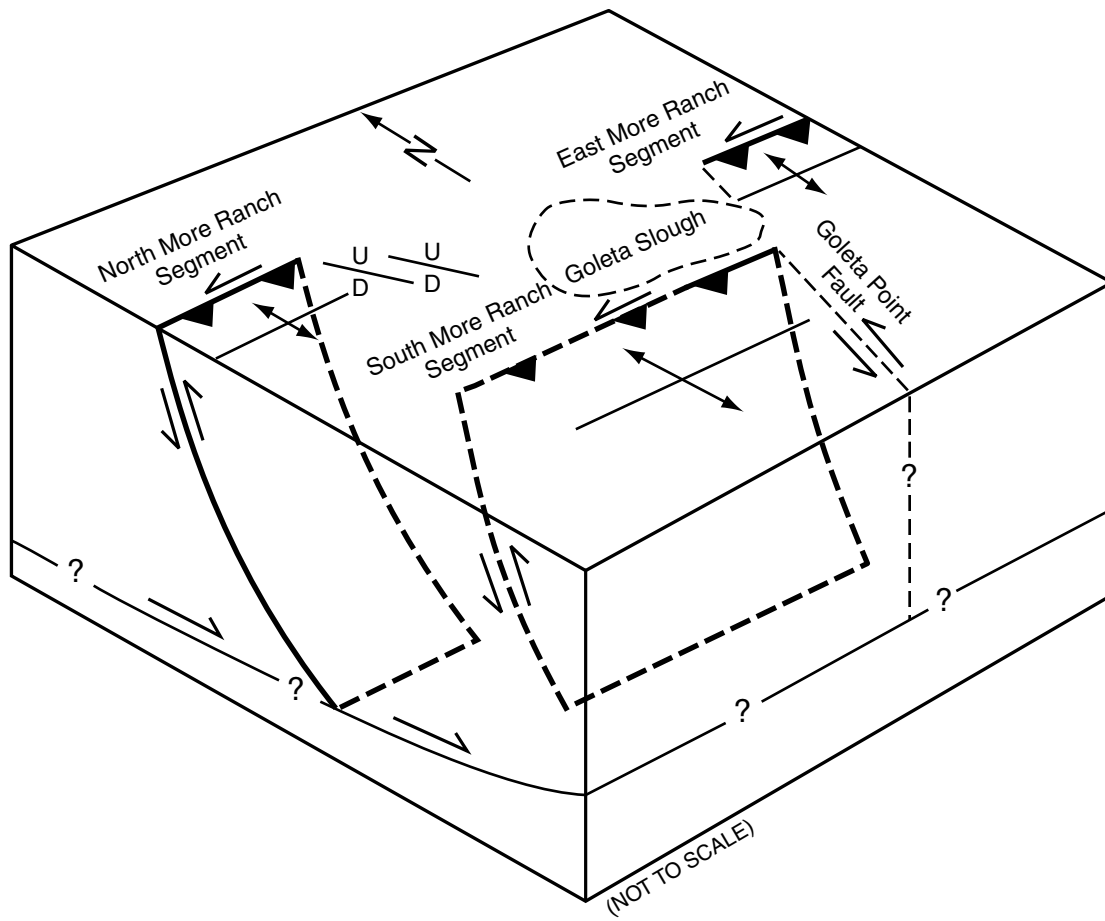


Figure 17. Tectonic geomorphology associated with oblique slip along the More Ranch segment and the relationship to northeast and northwest-striking cross faults (Gurrola, 1997).

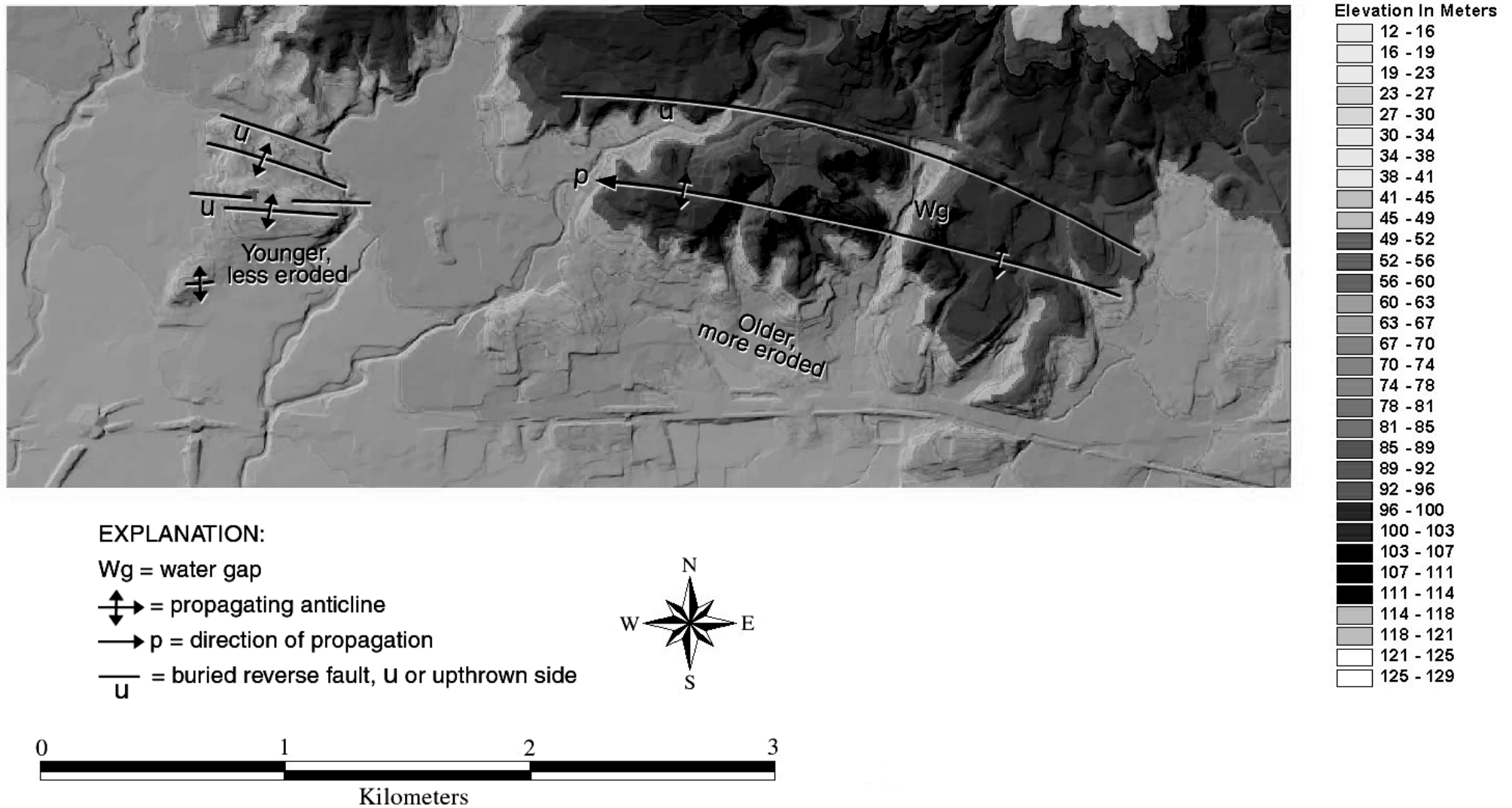


Figure 18. Image of the Goleta Valley anticline which apparently is propagating westward. Evidence for this includes the fact that the eastern portion of the fold is more eroded and probably represents older topography than the less eroded and presumably younger topography to the west.

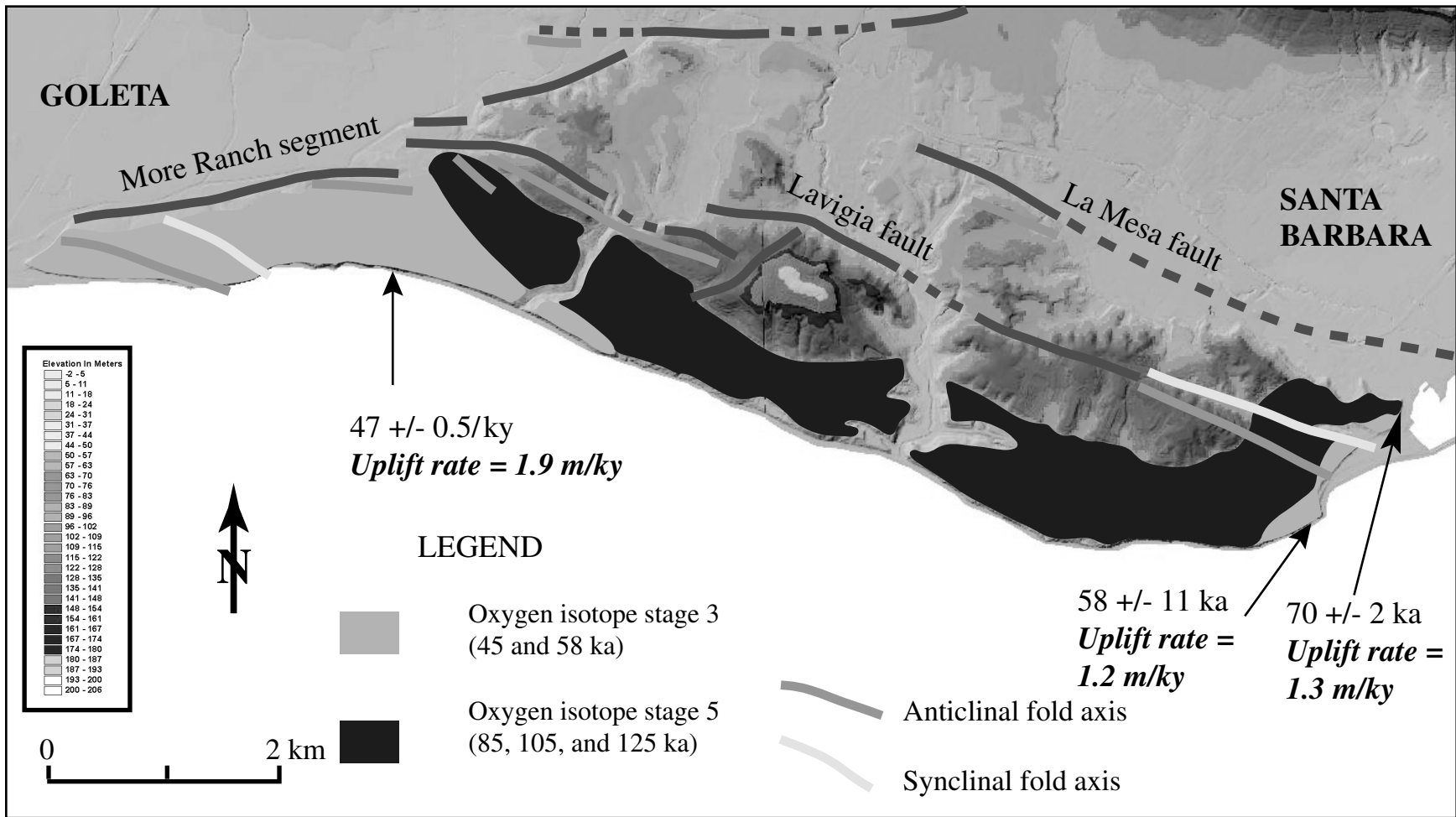


Figure 19. La Mesa to Hope Ranch area showing rates of surface uplift based upon first emergent marine platforms of oxygen-isotope stages 3 and 5.

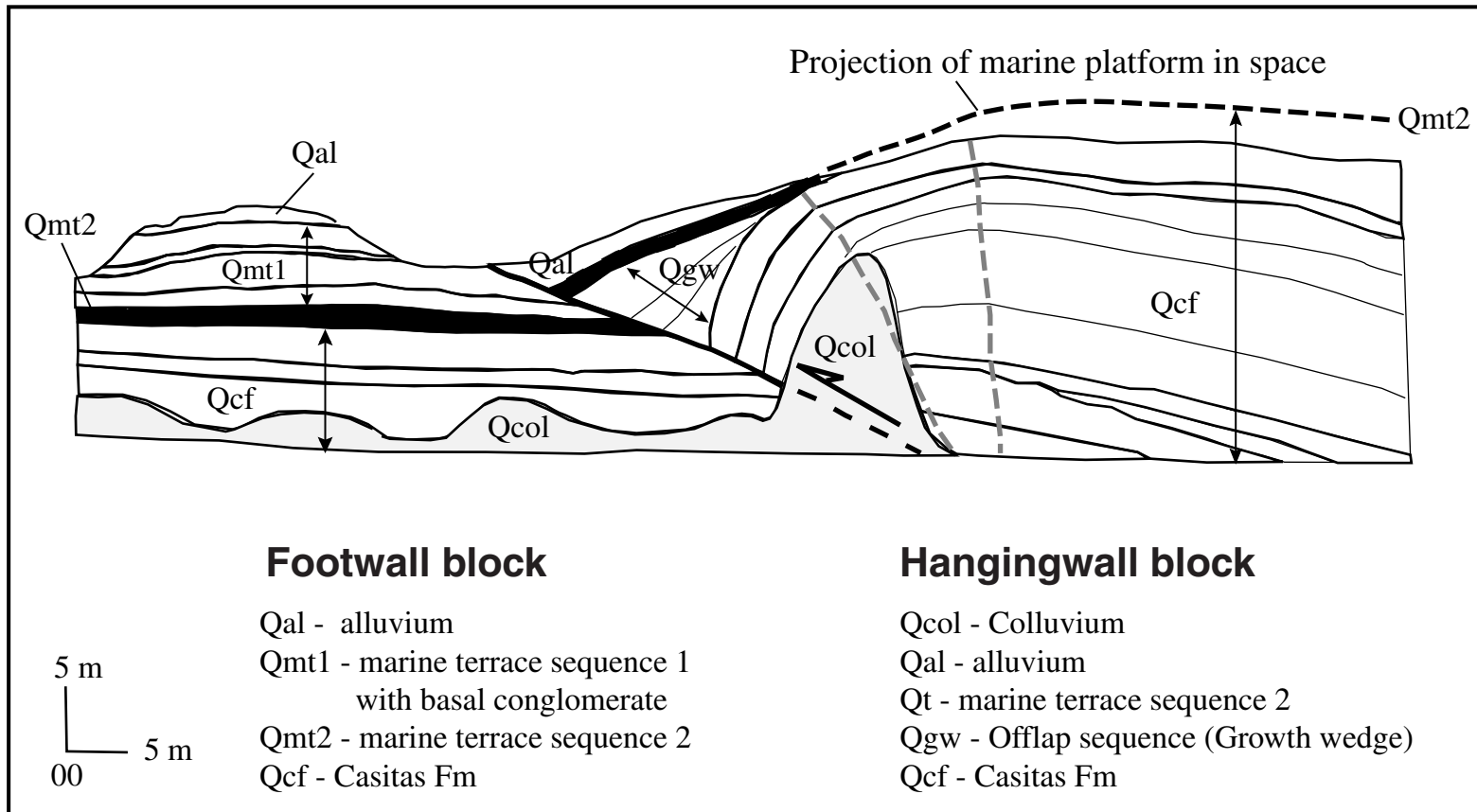


Figure 20. Quaternary stratigraphy of the seacliff exposure (oblique to the fault) of the Loon Point fault-propagation fold. Note the geometry of the growth wedge on the hanging wall fold and that overlying units are rotated into the fault to a lesser degree. Marine terrace sequence 2 projects into space (dashed line) as the result of folding and subsequent erosion. Active axial surfaces (gray dashed lines) are shown.

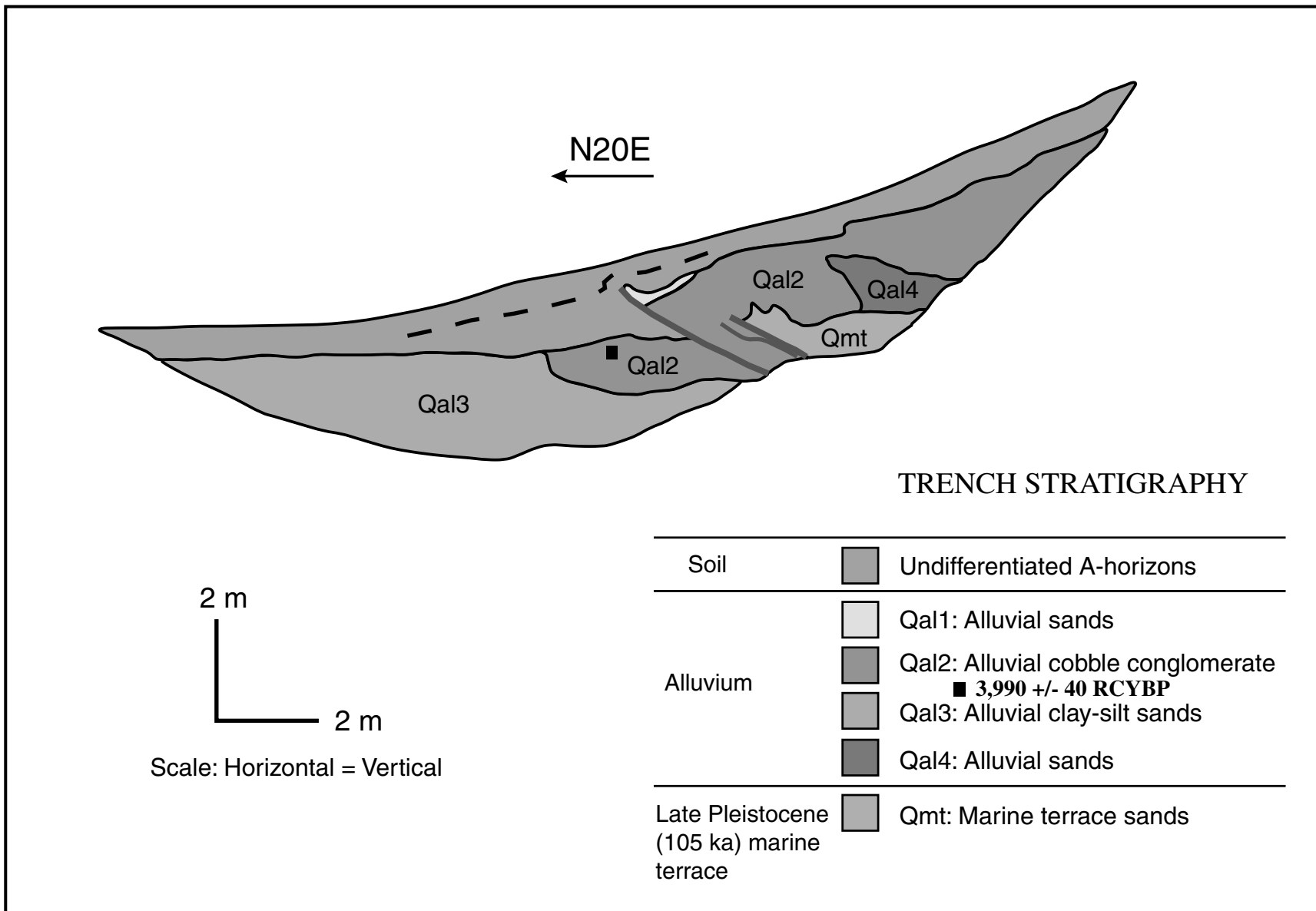


Figure 21. Log of the east trench face of the Loon Point fault, Summerland, California. The top of unit Qa12 is vertically displaced nearly 1 m and radiocarbon analysis of detrital charcoal yields a maximum ¹⁴C age of about 4 ka, therefore the fault is determined to be active.

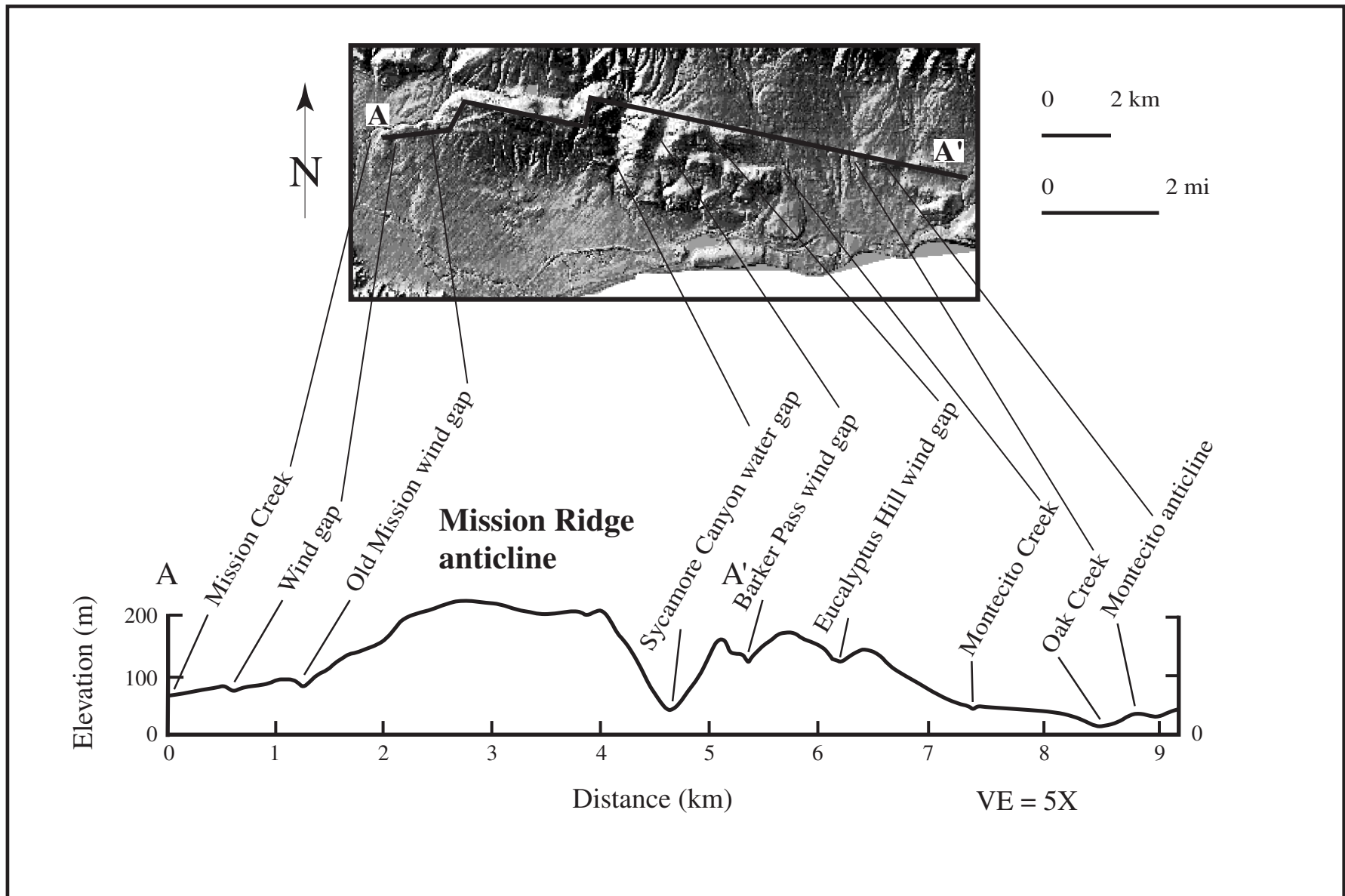


Figure 22. Longitudinal profile of the Mission Ridge anticline showing tectonic geomorphology from Santa Barbara to Montecito. Note the topographic expressions of water and wind (air) gaps as well as the decrease in elevation westward and eastward (Gurrola, 1998)

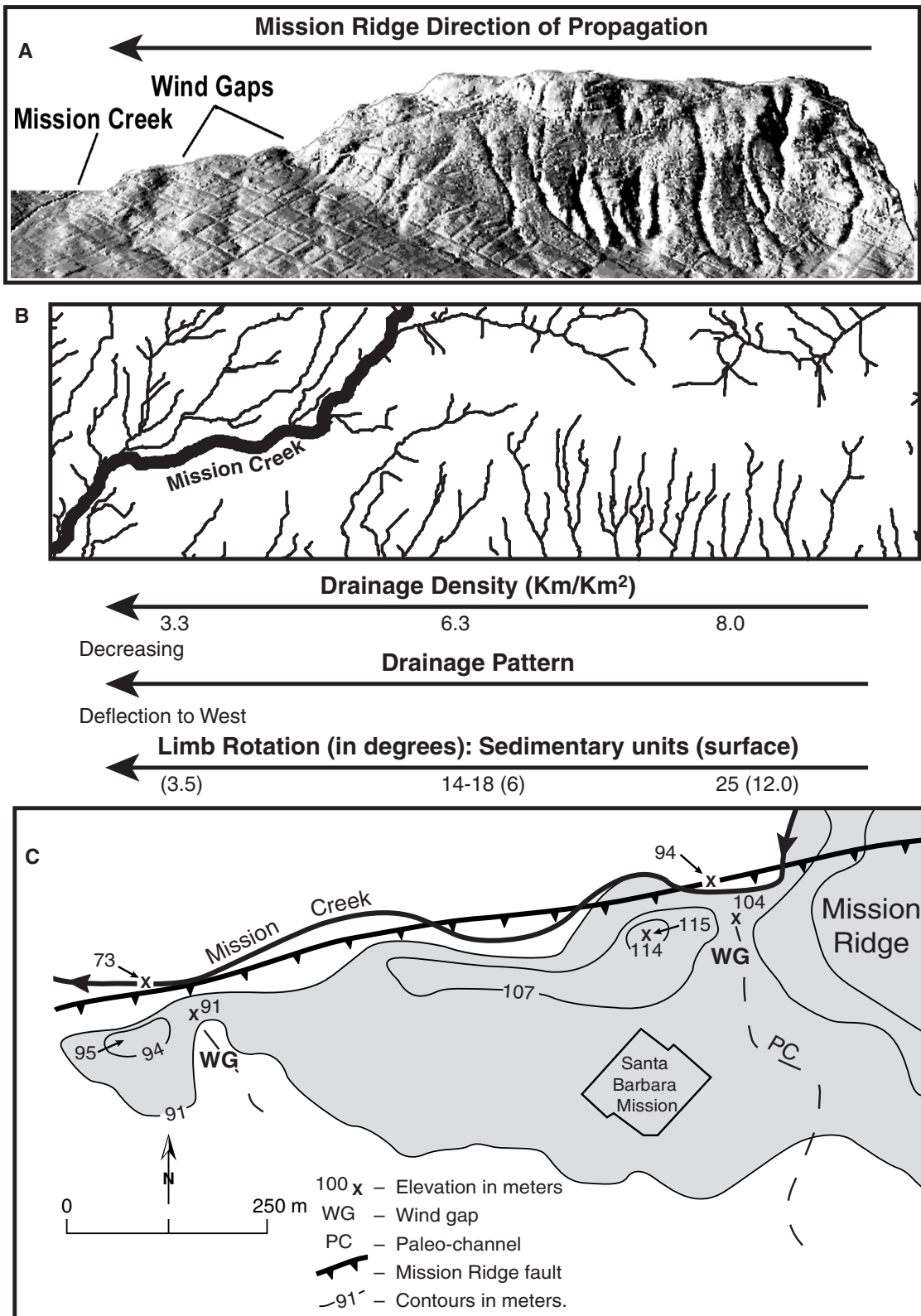


Figure 23. Diagrams of western Mission Ridge showing westward propagation of the Mission Ridge fold (Keller and others, 1999). The location of wind (air) gaps on the 3 m² DEM is shown in A; decrease in drainage density, drainage pattern deflection to the west, and decrease of limb rotation to the west are shown on B; and decrease in wind gap elevations and the locations of associated paleochannels are shown on C.

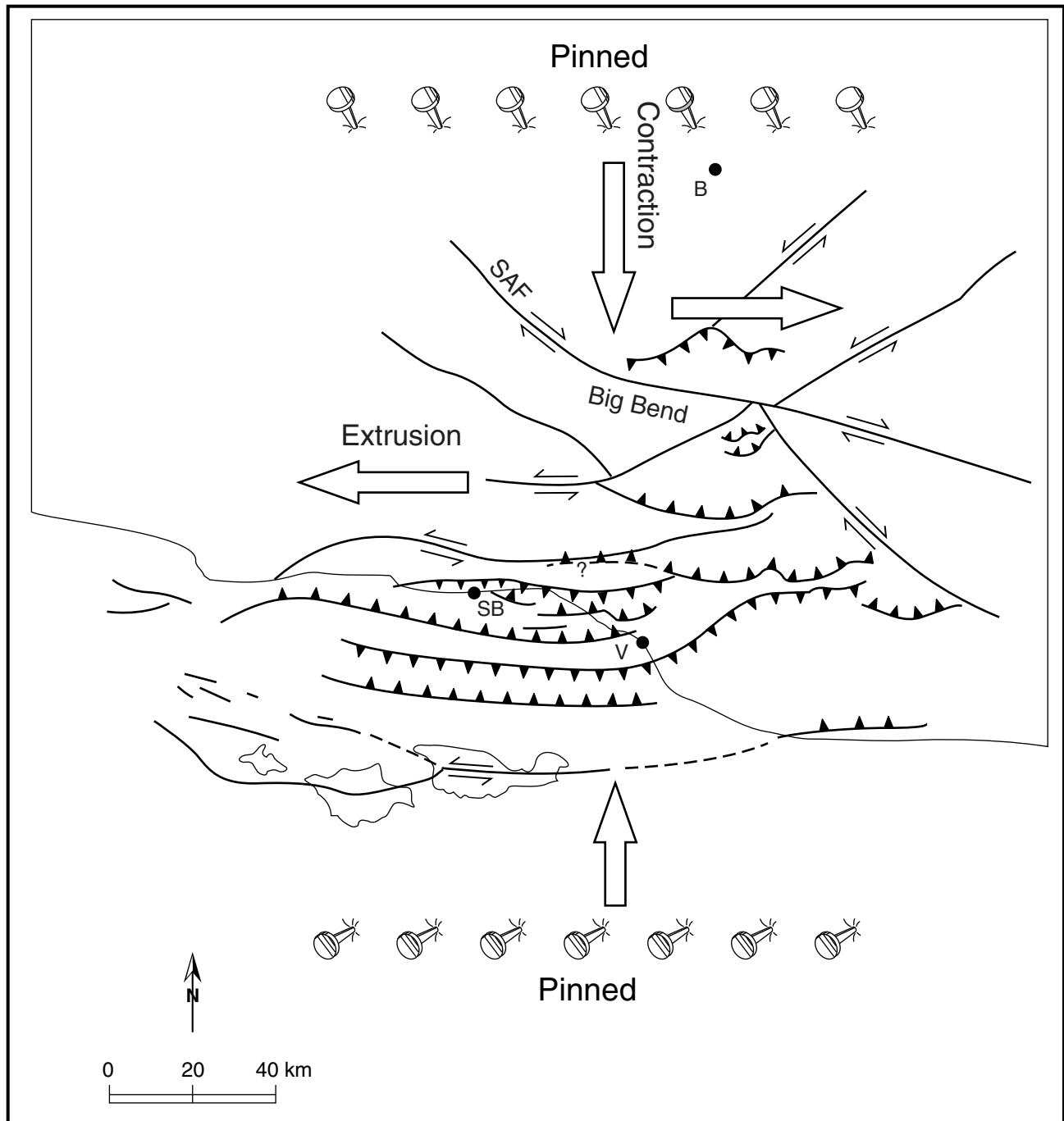
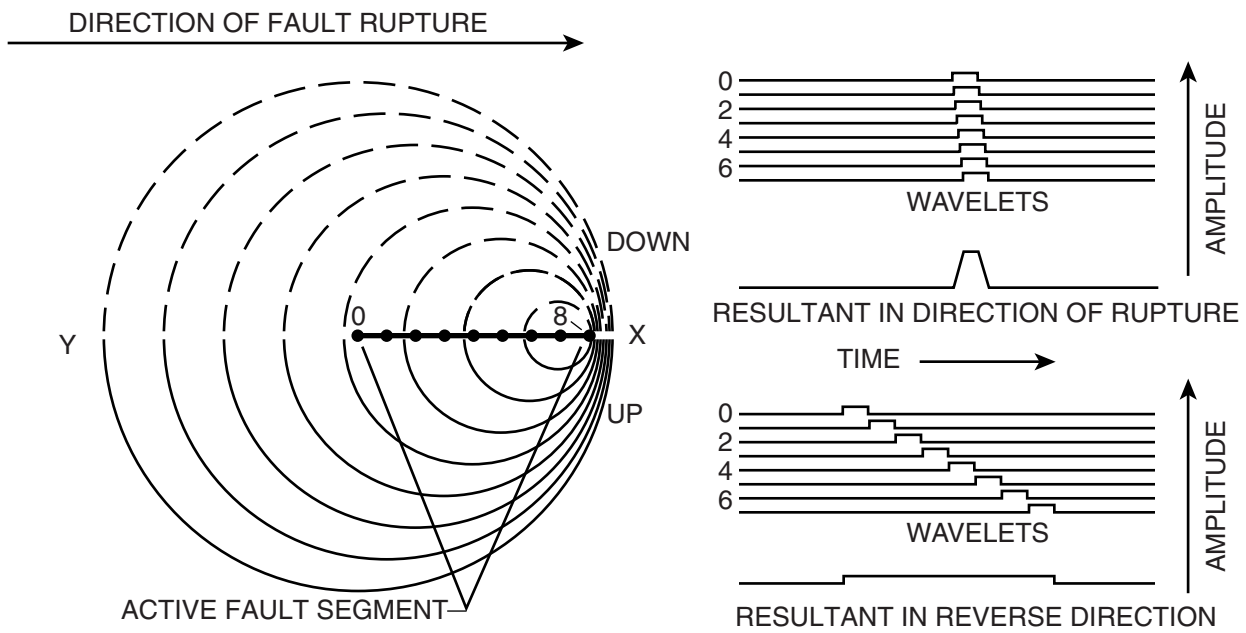


Figure 24. Tectonic model of westward extrusion south of the San Andreas Fault and eastward extrusion north of the San Andreas fault (Modified after Wallace, 1990). SB = Santa Barbara and V = Ventura.



After H. Benioff, 1955

Figure 25. Concept of directivity increasing the amplitude of seismic waves in the direction that a rupture propagates. After Benioff, 1955.

TECTONIC GEOMORPHOLOGY OF THE GREATER SANTA YNEZ MOUNTAINS

Timothy Tierney

Department of Geological Sciences
University of California at Santa Barbara
Santa Barbara, California, 93106

ABSTRACT

The Santa Ynez Mountains of southern California represent an opportunity to study pristine mountain tectonic geomorphology in a setting relatively uncomplicated by geomorphic or tectonic overprinting. This mountain range has a distinct crest along 110km (Matilija Creek west to Jalama Beach) of its 130km length (Matilija Creek west to Point Arguello). Hereafter known as the “greater Santa Ynez Mountains,” this portion of the range was chosen for study because it additionally has well-defined flanks, is either still or recently active, and is composed of strata that were likely previously undeformed.

Within the greater Santa Ynez Mountains, five range segments are defined as the lengths between boundary points where crest strike, crest elevation, and range width each shift abruptly between relatively stable average values. There is exact correspondence between these boundaries and structures striking transverse to the range, strongly implying a tectonic origin for the segments.

Water gaps at two range segment boundaries imply that range segments either grew together or paused during lateral propagation at these points, and possibly at other boundaries as well. Westward decrease in mountain front sinuosity in the westernmost segment implies that this segment has propagated westward over time. These results indicate that range segments have lengthened over time and interacted at their margins in a manner similar to folds within fold belts (Jackson and others, 1996).

Mean elevations within the study area increase from west to east, corresponding with a) eastward-increasing marine terrace uplift rates, b) increasing proximity to the San Andreas fault, c) increasing proximity to the tectonic “hinge” of the rotated western Transverse Ranges terrane, and d) a shift north of the range from a tectonic basin (Santa Maria Basin) to a tectonic uplift (San Rafael Mountains).

Range segment lengths are 25km, 15km, 25km, 25km, and 20km respectively. Because these segments may provide stopping points for rupture on the structure(s) responsible for the range (the Santa Ynez fault, and other inferred or suspected structures) the maximum segment length is used to predict a maximum likely earthquake magnitude of M6.7 for this structure(s) (Wells and Coppersmith, 1994).

The primacy of tectonics over erosion in the range is represented by four factors. The ratio of segment relief to width (r/w) increases from west to east in correspondence with increasing elevation and indicates a landform growing increasingly out of erosional equilibrium. The stream profiles within the two range water gaps are convex, indicating their ongoing or recent deformation. A 10km section of range crest in the easternmost segment is developed in a shale-dominated rock unit rather than in a primarily sandstone unit as is elsewhere. The tectonic signal contained within the mountain front sinuosity of the westernmost segment has not yet been counter balanced by erosion.

Analysis of covariance upon the basin hypsometric integrals for all crest-draining south flank basins reveals no linear trends in value either within or among range segments at the 95% confidence level. This erosional equivalence indicates either that all

range segments arose at the same time and without lateral propagation, or else that the hypsometric method of analysis failed due to rapid achievement of dynamic equilibrium within the basins. Given the theoretical sensitivity of the hypsometric method to perturbation and the other evidence in favor of segment lateral propagation, the latter interpretation is favored here.

1. THE SANTA YNEZ MOUNTAINS UPLIFT

The Santa Ynez Mountains uplift is that part of the western Transverse Ranges located along the north border of the rotated western Transverse Ranges (WTR) terrane (Dibblee, 1982b). The primary feature of this uplift is the Santa Ynez-Topatopa range, extending some 160km from Point Arguello in the west to Castaic Creek in the east (Figures 1 and 2). This range is divided by Matilija Creek (the main tributary of the Ventura River) into the Santa Ynez and Topatopa mountains in the west and east, respectively. Matilija Creek is interpreted to be an antecedent drainage which has produced a water gap in what would have otherwise been a continuous range (Dibblee, 1982b). Lesser ridges produced by reverse faulting and folding (Gurrola, pers. commun., 2000) along the south flank of the Santa Ynez-Topatopa range include Mission Ridge, Arroyo Parida Ridge (Figure 2), Laguna Ridge, Rincon Mountain, Red Mountain and Sulphur Mountain (Figure 1), and are also considered part of the Santa Ynez Mountain uplift (Dibblee, 1982b).

The Santa Ynez Mountain uplift is the result of the convergence of the WTR terrane with other terranes along its north edge. On its northwest margin, the WTR terrane is converging with the Santa Maria Basin, a tectonic basin now composed of unroofed Franciscan Formation overlain by Monterey Formation. On its northeast margin, the WTR terrane has been converging (Luyendyk et al, 1980) with the San Rafael Mountains (aka Nelson's (1925) Little Pine Mountain block), an uplifted area composed of forearc basin rocks.

The Santa Ynez Mountain uplift is believed to be no older than the Pliocene, because upper Cenozoic sequence rock units of Plio-Pleistocene age (Dibblee 1995) found within the upper parts of the adjacent Ventura (Pico Fm., Mudpit Shale, Saugus Fm., Santa Barbara Fm., Casitas Fm) and Santa Maria Basins (Careaga Sand, and Paso Robles Fm.) are interpreted to be derived from erosion of the Santa Ynez Mountains (Dibblee, 1982b; Dibblee, 1995). The Santa Ynez-Topatopa Range is believed to have first emerged during Pliocene time, followed by the adjacent, lower crests during Pleistocene time (Dibblee, 1982a).

2. GEOMORPHOLOGY, STRATA, AND STRUCTURE

From west to east (Figure 3D), the greater Santa Ynez Mountains step up from low western elevations (388m) to a local elevation maximum at Santa Ynez Peak (1310m). Further east, they descend into a distinctive saddle at San Marcos Pass (700m), beyond which they achieve their greatest heights (1200 – 1400m). These highlands contain another, more subtly expressed saddle at Romero Saddle (1000m). Throughout its length, the crest is nearer to the north flank of the range than the south flank, so that the former is the narrower of the two by about 10% on average (Figure 3A). In most areas where the mountain flanks are well defined, they trend parallel to the range crest. Crest and flanks both parallel the strike of strata within the range.

This report relies upon the geologic maps of the Dibblee Geological Foundation (15 maps:1985, 1986, 1987, 1988) and the stratigraphy of Dibblee (1950 and 1966). For the purposes of this study, these strata are generalized into “nonresistant” and “resistant” units. Soft units are shales and resistant units are sandstones and coarser units. The siliceous upper Monterey shale is exceptional, being also characterized as resistant (Table 1).

Name	Symbol	Resistance
Quaternary Units	Qa, Qoa, Qg, Qls	soft
Sisquoc shale	Tsq	soft
Monterey shale: Upper/ Lower	Tm-u / Tm-l	HARD / soft
Rincon shale	Tr	soft
Vaqueros sandstone	Tvq	HARD
Sespe Formation	Tsp	HARD
Alegria Formation	Ta	HARD
Gaviota Formation	Tg	HARD
Sacate Formation	Tsa	HARD
Cozy Dell shale	Tcd	soft
Matilija sandstone	Tma	HARD
Anita shale	Tan	soft
Jalama sandstone / shale	Kj-ss / Kj-sh	HARD / soft

Table 1. Stratigraphy and hardness classification.

The Santa Ynez Mountains consist of sedimentary strata consisting mainly of upper Cretaceous, Eocene, Oligocene and Miocene rocks that strike parallel to the range crest and flanks (Figure 3C). These strata dip primarily south at moderate angles, but are locally steepened and overturned. Due to their strike parallel to the range crest, the same rock units are generally present throughout the range.

A principal structure of the Santa Ynez Mountains is the Santa Ynez fault (Figure 3C), which abuts the north flank of the mountains, paralleling the range crest and defining the range’s north flank between Gaviota Canyon and Matilija Creek. Dibblee (1966) described this fault as left-oblique with south-side up, with displacement of “several miles” (p. 66) in both dimensions. Dibblee (1966) described the fault as dipping 46° south beneath Santa Ynez Peak, steepening to vertical in the vicinity of Romero Saddle, and overturning to dip steeply north along with the strata at Matilija Creek. Kerr and Schenck (1927) named this area of overturned strata centered about Matilija Creek as the Matilija Overturn.

West of Gaviota Canyon the Santa Ynez fault splays into a north and south branch. The north branch strikes west and splays into additional parallel strands, including the Gaviotito, Pacifico and Bulito faults, which cross and disrupt the range crest into several parallel ridges. The south branch of the Santa Ynez fault strikes southwest, crossing the range transverse to Gaviota Canyon before going offshore. Displacement on all subsidiary faults is interpreted as left-oblique, with south side up (Dibblee, 1950).

Uplift of the Santa Ynez Mountains is possibly the effect of north-south shortening accommodated by a deep thrust ramp connected to reverse faults which dip

beneath the range from the north and south (Namson and Davis, 1998). The Santa Ynez fault would be the northerly of these reverse faults, and its range-parallel strike clearly establishes its relevance to the range's uplift. The opposite fault to the south has not been positively identified from among several possibilities, and the deep thrust ramp beneath the range is only hypothesized.

2.1 CREST GEOMETRY

The crest of the Santa Ynez Mountains appears to be a single linear feature, but closer examination reveals several curious anomalies. In map view (Figure 3B) the crest makes several clear deviations from a linear trend. These take the form of breaks in continuity (Gaviota Canyon and San Marcos Pass), a zone of crest trifurcation (Upper Bulito and Upper Santa Anita Canyons), as well as changes in strike (35° at Refugio Pass, 30° at Romero Saddle). A profile view of the crest reveals similar deviations, here taking the form of abrupt shifts in average crest elevation (388m to 759m across Gaviota Canyon; 759m to 1005m across Refugio Pass), and elevation saddles at San Marcos Pass (650m) and Romero Saddle (1000m) (Figure 3C). Plotting map and profile view together (Figure 3) reveals that there is a good correspondence between anomalies in each dimension.

2.2 GEOMORPHIC RANGE SEGMENTS AND SEGMENT BOUNDARIES

Mountain range segments are defined in this report as areas of distinct geomorphology, characterized by differences in average range width and elevation values as well as crest geometry in terms of continuity and trend. Range segment boundaries are defined geomorphically as elevation lows marking points of value shift among range segments parameters. Five geomorphic range segments are defined and named, from west to east, the San Julian, Gaviota, Naples, Montecito, and Carpinteria range segments (Table 2).

Range Segment	Length	Avg Width	Avg Elev	S, N Flank Elev.	Relief/Width
San Julian	25km	5255m	388m	20m, 175m	0.06
Gaviota	15km	6788m	759m	35m, 220m	0.09
Naples	25km	8436m	1005m	100m, 430m	0.09
Montecito	25km	6791m	1085m	230m, 500m	0.11
Carpinteria	20km	5006m	1248m	350m, 630m	0.15

Table 2. Summary of statistics describing range segments of the Santa Ynez Mountains.

Average range crest elevations were determined by extracting elevation values from crest DEM cells, truncating each segment by 15% on either side in order to eliminate "edge effects" where elevations dropped off. Statistical analysis of elevation variation indicates that these differences are significant at the 95% confidence level.

Relief/width ratio for each segment is calculated using Formula 1, which takes the average value of the north/south flank elevations as a base.

$$R/W = [CE - (SFE + NFE) / 2] \div \text{width}$$

R/W = relief/width
 CE = crest elevation
 SFE = south flank elevation
 NFE = north flank elevation

Formula 1

The boundaries between the range segments are as important as the range segments themselves (Figure 3D; Table 3). The San Julian and Gaviota range segments are separated by the Gaviota Canyon boundary. The Gaviota and Naples range segments are separated by the Refugio Pass boundary. The Naples and Montecito range segments are separated by the San Marcos Pass boundary. The Romero Saddle boundary separates the Montecito and Carpinteria range segments. The Carpinteria range segment is separated from the Topatopa Range by the Matilija Creek boundary.

Range Segment Boundary	Δ elevation	Δ strike	Offset crest?
Gaviota Cyn	371m = 96%	-	yes
Refugio Pass	246m = 32%	35°	-
San Marcos Pass	80m = 08%	-	yes
Romero Saddle	163m = 15%	30°	-
Matilija Creek	252m > 20%	-	yes

Table 3. Summary of statistics describing range segment boundaries of the Santa Ynez Mountains.

2.2.1 Mountain front sinuosity within the San Julian range segment

Mountain-front sinuosity is a measure of the relative importance of erosion over uplift in the determination of topography (Keller and Pinter, 1996). It is measured by computing the ratio between the mountain-front length measured along the break in slope at the foot of the mountain and that length measured in straight-line segments parallel to the trend of the range. High sinuosity values are indicative of erosional dominance, because mountain-fronts presumably begin as linear features along faults or fold limbs and become embayed by erosion as uplift wanes.

Caution was used in selecting areas for Mfs analysis, because as a morphometric method it is highly sensitive to conditions other than tectonic signal. Only mountain fronts which 1) are adjacent to a tectonically inactive area; 2) are not adjacent to range-parallel drainage that could “bevel” back the mountain front; and 3) exhibit uniform bedrock geology were analyzed.

The only area within the greater Santa Ynez Mountains meeting these criteria was the westernmost part of the south flank of the San Julian range segment, extending 20km east from Jalama Beach to Canada de la Cuarta, about 5km short of Gaviota Canyon (Figure 4). Conditions along this front are highly regular: a narrow coastal plain generally exists between the front and the sea and strata of continuous thickness parallel the front, which is continuous in the upper member of the Monterey shale.

Mountain fronts (Figure 4) are identified using DEM-derived elevation and ground slope maps. Study of the slope map reveals that coastal plain surfaces have slope values of 11° or less, and mountain surfaces have slope values greater than 16°. The transitional slope values between the plains and mountains commonly exist within a narrow band, and this area is mapped as the break in slope. Nevertheless, the mapping process remains interpretive, with difficult areas including narrow canyons and regions lacking well-defined transitional slope zones from piedmont to mountain slope. Sinuosities were calculated at 5km intervals along the trend of the range.

The method revealed a decrease in sinuosity towards the west, indicative of western propagation of the segment during uplift.

2.2.2 Gaviota canyon range segment boundary

The boundary between the San Julian and the Gaviota range segments is expressed geomorphically as Gaviota Canyon, one of two water gaps within the Santa Ynez-Topotopa range. The range crest steps right and changes sharply in elevation at this point, from 388m on the west side to over 800m on the east side.

The geologic boundary between the two range segments is the south branch of the Santa Ynez fault, which does not strictly coincide with Gaviota Canyon, but rather cuts across it diagonally. Gaviota Canyon and neighboring canyons (Alegria & Agua Caliente, both to the west) show minor left-deflection where they cross the fault. Gaviota Creek drains lands north of the range to the ocean through Gaviota Canyon, one of two water gaps in the Santa Ynez-Topatopa range. Its profile shows clear convexity where it crosses the range (Figure 5).

The lower elevation of the San Julian range segment relative to the Gaviota range segment is probably related to the bifurcation of the Santa Ynez fault at Gaviota Canyon, allowing the left-reverse (south side up) south branch of the Santa Ynez fault to act as a tear fault accommodating differing amounts of shortening along either side of its trace.

Left-deflection of Alegria, Agua Caliente and Gaviota drainages by the South Branch of the Santa Ynez fault indicates that these streams must have predated the fault, establishing courses that have since become deflected. Among these the water-gap at Gaviota Creek indicates that among them, it at least is antecedent to the range. Considering the elevation difference across Gaviota Canyon, the antecedence of Gaviota Creek implies that its present location was once an area of low relief, where the adjacent range segments either propagated together from opposite directions or else the entire range paused in its lateral propagation long enough for this water gap to become established. Among these alternatives, evidence for westward lateral propagation of the San Julian range segment supports the option of antecedent drainage being a result of a pause in western range propagation at this location.

Convexity in the longitudinal profile of Gaviota Creek where it crosses the range at Gaviota Canyon indicates that the stream bed is subject to deformation of ongoing or recent origin. This is consistent with the hypothesis of the ongoing or recent uplift of the study area.

2.2.3 Displacement on the south branch of the Santa Ynez fault

In map view, the pattern of offset rock units appears to indicate dextral slip on this fault, in contrast to the interpretation (Dibblee, 1950) of this fault as left-reverse. The dextral offset pattern is an illusion produced by the combination of south-dipping strata and south side up dip-slip, which have overwhelmed the true left slip map pattern. Sinistral motion on the fault is further implied by left-deflection of Alegria, Agua Caliente, and Gaviota drainages where they cross the south branch of the Santa Ynez fault.

Rockwell et al (1992) estimated a vertical rate for the south branch of the Santa Ynez fault of 0.05mm/yr and a “low” horizontal rate. These rates were based upon their observation of clear and measurable vertical separation but no clear horizontal separation.

Bedding geometry allows prediction of the horizontal rate. Dips on either side of the south branch of the Santa Ynez fault are about 30° south, and identical rock units are in approximate alignment across the fault due to the fact that the bedding dip balances against sinistral motion of the fault to produce the illusion of no horizontal movement. The ratio of horizontal:vertical slip necessary for this balance is 1.732:1 ($\sin 30^\circ / \cos 30^\circ$). Multiplying this ratio against the estimate for vertical rate yields a horizontal rate of 0.086mm/yr. These rates only apply to recent fault history, back to the age of the offset terraces (stage 7) that yielded them. A vertical rate of 0.05mm/yr produces the 371m elevation difference across Gaviota Canyon in 7.4 million years if there is no erosion, meaning that these rates were probably greater in the past because the Santa Ynez Mountains are believed to be no older than the Pliocene.

Total slip on the fault is unknown, but may also be estimated. Multiplying the 371m elevation difference across Gaviota Canyon by 1.732 yields a horizontal displacement of 643m. Since this discounts differential vertical erosion, these figures must be regarded as a minimum.

2.2.4 Refugio Pass range segment boundary

Refugio Pass is the geomorphic boundary (Figure 3D) between the Gaviota and Naples range segments, forming a distinctive (600m) low in the crest elevation profile. Across this lowpoint the crest trend changes by 35° from east-northeast to east-southeast. Directly north of this point, the Brush Peak anticline as well the two Refugio Pass faults (informal name) diverge from the Santa Ynez fault and trend east-southeast along the north flank of the range, marking the geologic boundary between the neighboring range segments. Displacement on both of these faults is interpreted as south side up (Dibblee Geological Foundation map DF 15(1988)).

The Brush Peak anticline and the informally-named Refugio Pass faults which emerge and trend east from this area are interpreted to have helped accommodate the additional shortening that has caused the Naples range segment to the east to achieve higher elevations than the Gaviota range segment.

2.2.5 San Marcos Pass range segment boundary

San Marcos Pass is a topographic saddle with a southeast trending axis. It corresponds with two syncline-anticline pairs (the Brush Peak anticline, the Painted Cave and Laural Canyon synclines, and another unnamed anticline) that have similar trends. These synclines and anticlines correspond with local canyons and ridges, respectively.

The coincidence of a structural and topographic saddle at this point in which even individual folds correspond with ridges and canyons is interpreted to indicate that topography here is a direct result of tectonics. The entire zone is interpreted to be produced by “pinching” between the rise of range segments on either side. Dibblee (1966) made a similar interpretation for this area.

2.2.6 Romero Saddle range segment boundary

Romero Saddle is the geomorphic and geologic boundary between the Montecito and Carpinteria range segments (Figure 3D). Geomorphically, it is the low point in a broad saddle between both range segments (1000m) and marks a 30° change in crest strike. Geologically, the saddle coincides with the oldest rocks in the range, the center of

the Montecito Overturn (Figure 3E) and the informally-named Romero Saddle fault. To the north of this range segment, the right-oblique (north-side up) Little Pine fault and the San Rafael Mountains intersect the Santa Ynez Range (Figure 3E).

At Romero Saddle, the contact between the Franciscan formation and younger rocks is mapped as a fault, and another unnamed fault splays from this fault striking southeast. This report informally refers to this splay as the Romero Saddle fault (Figure 3C), which is interpreted to be right-oblique, with north side up (Dibblee Geological Foundation map DF 11(1987)).

Strata veer left (north) as they strike toward the Romero Saddle fault from the west. These are right-lateral drag features that show the opposite sense of motion due to being overturned. Dibblee (1966) incorrectly interpreted these as left-drag features, but properly labels the fault as dextral in later mapping (Dibblee Geological Foundation map DF 04(1986)).

North of the Santa Ynez at this location, the Little Pine fault diverges from its southeast strike to turn parallel to the Santa Ynez range before being truncated by the Juncal Camp fault. Dibblee (1966) described the Little Pine fault as steepening from north dipping to vertical as it approaches the Santa Ynez Mountains. Nelson (1925) mapped the fault as offsetting the Pleistocene Paso Robles Formation, which is derived from the erosion of the Santa Ynez Mountains (Dibblee 1982a), indicating the Little Pine fault has remained active since the uplift of the Santa Ynez Mountains began.

The Juncal Camp fault is described by Page et al (1951) as dipping steeply and truncating the Little Pine fault and itself being truncated by the Santa Ynez fault, indicating that it is intermediate among these three structures in age. Schroeter (1972) interpreted 960m of south-side up displacement in the central part of this fault, which appears to decrease away into the east and west.

Lower crest elevations within the Montecito range segment coincide with crest development within the Jalama formation, predominately a shale unit. Even though the crest is typically found in the thin sandstone beds within this unit, the shale dominance contrasts sharply with the sandstone-dominated units (Matilija and Sacate) that host the crest elsewhere in the range.

2.2.7 The Romero Saddle fault

East-side up motion on the informally-named Romero Saddle fault is interpreted to be responsible for higher elevations in the Carpinteria range segment to the east of this structure. This fault is interpreted to be related to the Little Pine fault, with which it shares a similar sense of motion, similar strike, and into which it projects. The Little Pine fault assumes a parallel course to the Santa Ynez range at close proximity, and the Romero Saddle fault may be a rebreaking of the Little Pine fault along its original path. The fact that the Little Pine fault has been active subsequent to the uplift of the Santa Ynez range is consistent with this hypothesis.

2.2.8 The Montecito Overturn

Bedding dips within the Montecito range segment steepen east of San Marcos Pass to become overturned, forming what Dibblee (1982a) named the Montecito overturn. The overturn begins along the south flank and eventually widens across the entire range to the Santa Ynez fault at Romero Saddle.

Dibblee (1966 and 1982b) accounts for eastern steepening and overturn of the otherwise south-dipping Santa Ynez fault and south-bowing of the range crest at this location by impingement of the Santa Ynez uplift upon the San Rafael range, which has been uplifted and thrust southwestward by the Little Pine fault.

The coincidence of the Franciscan-cored Montecito Overturn, the intersection with the San Rafael range, and the steepening of both the Santa Ynez and Little Pine faults at this point suggest that these features share a common explanation.

Overtured strata are interpreted here to be the result of intense constriction which caused these strata to assume southward dips while still at depth. This pre-uplift south-dip, combined with south-tilting resulting from uplift, resulted in overturn. The hypothesized constriction could be the result of impingement of the Santa Ynez uplift upon the San Rafael uplift, itself executed in part by the Little Pine fault. Steepening of the Santa Ynez and Little Pine faults as they approach one another in this area is consistent with this hypothesis.

Page et al. (1951) and Dibblee (1966) suggested that some form of “cold intrusion” of Franciscan rock is responsible for the Montecito Overturn. Examination of the extent of the overturn (Figures 3C and 3E) reveals that while it is indeed centered about a lens of Franciscan rock, its east-west extent is too wide to be readily attributable to overturn via cold intrusion of this rock. Franciscan rock is here interpreted to be in situ, and the result of intensified uplift that has exposed older rocks in this part of the range than elsewhere. This is in general agreement with later interpretations offered by Dibblee (1982b).

Shale rock occupies the crest for 15km coincident with the Montecito overturn because the overturned geometry naturally places this unit (Juncal) into the highest elevations during uplift. The fact that this rock has not yet eroded away to place the crest into sandstone as it is elsewhere in the range indicates that erosional equilibrium has not yet been established. This condition is interpreted to be a result of the recency of uplift, which is consistent with the hypothesis of the landscape being tectonically controlled.

2.2.9 Matilija Creek range segment boundary

Matilija Creek, a major tributary to the Ventura River, forms the boundary between the Carpinteria range segment and the remainder of the Santa Ynez-Topatopa range to the east. This boundary is marked by a dramatic topographic low (a water gap) and a left-step in the crest. It separates the higher Topotopa crests from the lower Santa Ynez crests. Curiously, this boundary does not coincide with any mapped structure, setting it apart from others, but there is reason to believe that some unmapped structure may be present (Figure 6). North of the range, the reverse (south-side up) Old Man fault intersects the range at this geomorphic boundary and may continue south of it unmapped. South of the range a “displacement transfer zone” exists (Huftile and Yeats, 1995), where north-south shortening shifts across major east-west trending structures. A structure accommodating this transfer may be hidden beneath Matilija Creek.

Considering the geomorphic differences across this boundary, the antecedent stream here is probably the result of either a pause in lateral range propagation or else two separate range segments propagating together at this point rather than of downcutting through a single rising mass of rock.

Matilija Creek displays a subtle convexity where it crosses the range, which is obscured by the Matilija Reservoir. To compensate for this circumstance, the profile for a tributary to Matilija Creek (the North Fork of Matilija Creek) that joins it just downstream of the reservoir was also generated. The profile for the North Fork of Matilija Creek shows clear convexity prior to merging with Matilija Creek downstream of the reservoir. These convexities (Figure 5) indicate that the stream beds are subject to deformation of ongoing or recent origin. This is consistent with the hypothesis of the ongoing or recent uplift of the study area.

2.3 GEOMORPHIC SEGMENTATION OF TECTONIC ORIGIN AND IMPLICATIONS FOR SEISMIC HAZARD

Range segments are interpreted to be the result of structural segmentation of the Santa Ynez fault, based upon the coincidence of every major structure splaying from the Santa Ynez fault with a range segment boundary (Figure 3; Table 4). Differences in range segment elevations are interpreted to be the result of varying shortening rates or amounts across each range segment, accommodated by boundary structures, indicating that range segmentation is of tectonic origin.

Range Segment Boundary	Corresponding Structure
Gaviota Canyon	south branch of the Santa Ynez fault
Refugio Pass	Refugio Pass faults
San Marcos Pass	San Marcos Pass folds
Romero Saddle	Romero Saddle fault
Matilija Creek	hidden?

Table 4. Range segment boundaries and their corresponding structures.

Based upon the above, each range segment boundary may therefore represent a stopping point for rupture, allowing use of the maximum segment length of 25km (Table 2) in computing potential earthquake magnitudes of the Santa Ynez fault or other structures responsible for uplift of the range. The magnitude charts of Wells and Coppersmith (1994) indicate the magnitude for a 25km rupture is roughly magnitude 6.7 (Figure 7).

Given that elevation differences among the segments are interpreted to represent differences in local shortening, increasing relief/width ratio represents a landscape that is growing increasingly out of erosional equilibrium as it grows higher, indicating that elevation differences are of recent origin. This trend matches that found in coastal terrace uplift rates (Figure 3F), which, from west to east, increase from 0.15m/ky to 8m/ky (Rockwell et al, 1992; Metcalf, 1994; Gurrola et al, 2001; Muhs et al, 1992). The trend additionally coincides with a) increasing proximity to the San Andreas fault, b) increasing proximity to the tectonic “hinge” of the rotated western Transverse Ranges terrane, and c) a shift north of the range from a tectonic basin (Santa Maria Basin) to a tectonic uplift (San Rafael Mountains).

3 HYPSONOMETRIC ANALYSIS

3.1 THE HYPSONOMETRIC METHOD

The distribution of elevation across an area of land may be described by the hypsonometric curve, created by plotting normalized height versus normalized area for the landscape under consideration (Strahler 1952). The area beneath the curve is known as the hypsonometric integral, and is taken to represent the percent of uneroded rock in the landscape. Because it is scale-independent, hypsonometric analysis allows comparison between areas of different size.

High values of the hypsonometric integral correspond with convex shapes for the hypsonometric curve and are commonly interpreted to represent relatively uneroded landscapes incised by narrow canyons. Intermediate values correspond with a sublinear or convex-concave curve forms. Lower values for the hypsonometric integral correspond with concave shapes for the hypsonometric curve, and are generally taken to represent old landscapes with few remaining highlands. Strahler (1952) termed these three states youthful (convex), mature (linear), or old (concave) basins (Figure 8A), consistent with the cycle of erosion of Davis (1899).

Hypsonometry is employed in this study to discover relative degrees of erosion of the topography for the different range segments. Relative degree of erosion serves as a proxy for range segment age.

Without DEM analysis, such a study entails human extraction of data from topographic maps. Elevation minimum and maximum values are manually picked, and elevation populations are extracted by point counting. Point counts typically consists of 50 points, with the human operator interpolating values between topographic contour lines.

The value of the hypsonometric integral is determined by the following equation (Pike and Wilson, 1971):

$$\text{Hypsonometric Integral} = \frac{(\text{mean elevation}) - (\text{minimum elevation})}{(\text{maximum elevation}) - (\text{minimum elevation})}$$

Formula 2

A DEM allows the analysis of all elevation points within the study area up to the resolution of the digital data. DEM analysis results in faster analysis, more reliable results, and easier production of hypsonometric curves and hypsonometric integral values. Drainage basins analyzed within this report typically were represented by over 1000 DEM cells.

3.2 WEAKNESSES OF THE HYPSONOMETRIC METHOD

Like all morphometric methods, hypsonometry requires thoughtful application in order to produce valid results.

One must be cognizant of the workings and limitations of this method in order to avoid errors in its application and interpretation.

The hypsometric method assumes a flat parent landscape that was uplifted vertically. Only such a landscape can produce a hypsometric integral approaching 1.0 prior to erosion (Figure 8B-1). Uplift may also take place by means of tilting or doming that produce initial landscapes with uneroded values significantly less than 1.0. Landscapes produced under one tectonic style (i.e., faulting) may therefore not be directly comparable to those created under a different tectonic style (i.e., folding).

The hypsometric method is also extremely sensitive to the values assigned for minimum and maximum elevations, making it vulnerable to error when these initial values have been removed from the landscape by erosion of peaks or filling of valleys. Loss of original elevation maxima artificially inflates hypsometric integral values (Figure 8B-2). Loss of elevation minima artificially decreases hypsometric integral values (Figure 8B-3).

3.3 HYSOMETRIC RESULTS

The individual watershed was chosen as the unit of analysis in this study (Figure 14), due to its natural boundaries. All south-facing watersheds that extend to the range crest were analyzed. Watersheds failing to meet this criterion were omitted from study because they do not represent adjustment of the land to the full tectonic signal in the landscape. The results from the analysis of watersheds within the study area are shown in Figure 6C.

3.3.1 Statistical analysis of hypsometric results

An analysis of covariance (ANCOVA) (Montgomery, 2001) was performed on the hypsometric data, treating range segment and axial distance along the mountain front as independent variables and hypsometric integral as the dependant variable. The purpose of this procedure was to determine if mean hypsometric values vary between range segments and if there are any trends in values within single range segments. P-values for range segment, axial location, and the interaction term were all found to be insignificant at the 95% confidence level, so a "simplified" ANCOVA was run, omitting the interaction term. Again, p-values for group and distance were found to be insignificant at the 95% confidence level. These results indicate that range segment and axial distance have no effect on hypsometric integral.

3.3.2 Interpretation of statistical results

ANCOVA results may be explained in two ways:

Explanation 1: The equivalence of hypsometric values both among and within range segments indicates erosional equivalence, in turn indicating age equivalence. All range segments are equally old, and each range segment emerged without lateral propagation.

Explanation 2: Basin geometries reach equilibrium more rapidly than tectonics perturb them. This second explanation implies that Strahler's "old age" form for basins is rarely achieved, because the basins instead settle into a "mature" form as their final state according to Hack's (1960) concept of dynamic equilibrium.

Given the variability of conditions within the study area (resistant & nonresistant rock crests, channel backfilling, discharge areas, ambiguous basin boundaries) and the

sensitivity of the hypsometric method to errors in minimum and maximum elevation values, the uniformity of results favors the second explanation.

7. CONCLUSIONS

The greater Santa Ynez Mountains show clear geomorphic segmentation which is closely tied to structure within the range, indicating a tectonic origin. Distinct geomorphic changes across discrete boundaries coincident with range-transverse structure is interpreted to indicate that these structures are accommodating differences in tectonic rates and styles within different range segments. Some range segments have propagated laterally during uplift, only later impinging upon neighboring segments. Segment boundary structures may provide stopping points for fault rupture, allowing for seismic hazard estimation. Eastward-increasing elevation among range segments is interpreted to be the result of increasing accumulated strain, corresponding with several regional trends.

References

Crouch, J.K., and Suppe, J., 1993, Late Cenozoic tectonic evolution of the Los Angeles basin and inner California borderland: A model for core-complex like crustal extension: Geological Society of America Bulletin, v. 105, p. 1415-1434.

Delcaillau, B., and 7 other authors, 1998, Morphotectonic evidence from lateral propagation of an active frontal fold; Pakushan anticline, foothills of Taiwan. *Geomorphology* v. 24, 263-290.

Dibblee Geological Foundation, various geologic quadrangle maps, scale 1:24,000.

DF-01, 1985, Wheeler Springs, by T.W. Dibblee Jr.

DF-02, 1985, Old Man Mountain, by T.W. Dibblee Jr.; Ehrenspeck, H.E., ed.

DF-03, 1986, Hildreth Peak, by T.W. Dibblee Jr.; Ehrenspeck, H.E., ed.

DF-04, 1986, Carpinteria, by T.W. Dibblee Jr.; Ehrenspeck, H.E., ed.

DF-06, 1986, Santa Barbara, by T.W. Dibblee Jr.; Ehrenspeck, H.E., ed.

DF-07, 1986, Goleta, by T.W. Dibblee Jr.; Ehrenspeck, H.E., ed.

DF-08, 1987, San Marcos Pass, by T.W. Dibblee Jr.; Ehrenspeck, H.E., ed.

DF-09, 1987, Dos Pueblos, by T.W. Dibblee Jr.; Ehrenspeck, H.E., ed.

DF-10, 1987, Lake Cachuma, by T.W. Dibblee Jr.; Ehrenspeck, H.E., ed.

DF-11, 1987, White Ledge Peak, by T.W. Dibblee Jr.; Ehrenspeck, H.E., ed.

DF-12, 1987, Matilija, by T.W. Dibblee Jr.; Ehrenspeck, H.E., ed.

DF-15, 1988, Santa Ynez and Tajiguas, by T.W. Dibblee Jr.; Ehrenspeck, H.E., ed.

DF-16, 1988, Solvang and Gaviota, by T.W. Dibblee Jr.; Ehrenspeck, H.E., ed.

DF-17, 1988, Santa Rosa Hills and Sacate, by T.W. Dibblee Jr.; Ehrenspeck, H.E., ed.

DF-18, 1988, Lompoc Hills and Point Conception, by T.W. Dibblee Jr.; Ehrenspeck, H.E., ed.

Dibblee, T.W., Jr., 1950, Geology of southwestern Santa Barbara County, California: California Department of Natural Resources Division of Mines Bulletin 150, 95 pp., map scale 1:62,500.

Dibblee, T.W., Jr., 1966, Geology of the central Santa Ynez Mountains, Santa Barbara County, California: California Division of Mines and Geology Bulletin 186, 99 pp., map scale 1:62,500 and 1:31,680.

Dibblee, T.W., Jr., 1982a, Regional geology of the Transverse Ranges province of southern California, *in* Fife, D.L., and Minch, J.A., eds., Geology and mineral wealth of the California Transverse Ranges, Mason Hill volume: South Coast Geological Society Guidebook No. 10, p. 7-26.

Dibblee, T.W., Jr., 1982b, Geology of the Santa Ynez–Topatopa Mountains, southern California, *in* Fife, D.L., and Minch, J.A., eds., *Geology and mineral wealth of the California Transverse Ranges*, Mason Hill volume: South Coast Geological Society Guidebook No. 10, p. 41-56.

Dibblee, T.W., Jr., 1995, Tectonic and depositional environment of the middle and upper Cenozoic sequences of the coastal southern California region, *in* Fritche, A.E., ed., 1995, *Cenozoic paleogeography of the western United States—II: Pacific Section*, SEPM, book 75, p. 212-245.

Dickinson, W.R., 1995, Paleogene depositional systems of the western Transverse Ranges and adjacent southernmost Coast Ranges, California *in* Fritche, A.E., ed., 1995, *Cenozoic paleogeography of the western United States—II: Pacific Section*, SEPM, book 75, p. 53-83.

Gurrola, L.D. and others, 2001, Neotectonics of the Santa Barbara Fold Belt, southern California, *in* Dunne, G. and Cooper, J., compilers, *Geologic excursions in southwestern California*, Pacific section SEPM Book No. 89, p. 21 – 100.

Hack, J.T., 1960, Interpretation of erosional topography in humid temperate regions. *American Journal of Science*, 258A: 80-97.

Huftile, G., and Yeats, R.S., 1995, Convergence rates across a displacement zone in the western Transverse Ranges near Ventura, California: *Journal of Geophysical Research* v. 100, No. B2, pp. 2043 – 2067.

Jackson, J., Norris, R., and Youngson, J., 1996, The structural evolution of active fault and fold systems in central Otago, New Zealand: evidence revealed by drainage patterns. *Journal of Structural Geology*, v. 18, No. 2/3, p. 217-234.

Keller, E.A., Gurrola, L.D., and Tierney, T.E., 1999, Geomorphic criteria to determine direction of lateral propagation of reverse faulting and folding. *Geology*, v. 27; no 6; p. 515-518.

Keller, E.A., and Pinter, N., 1996, *Active Tectonics: Earthquakes, Uplift, and Landscape*. Prentice Hall: Upper Saddle River, 338 pages.

Kerr, P.F., Schenck, H.G., 1927, the significance of the Matilija Overturn: *Geological Society of America Bulletin*, v. 39, p. 1087-1102.

Luyendyk, B.P., Kamerling, M.J., and Terres, R.R., 1980, Geometric model for neogene crustal rotations in southern California: *Geological Society of America Bulletin*, v. 91, p. 211–217.

Metcalf, J.G., 1994, Morphology, chronology, and deformation of pleistocene marine terraces, southwestern Santa Barbara County, California: University of California at Santa Barbara, unpublished MA thesis.

Mertes, L.A.K., Hickman, M., Walternberger, B., Bortman, A.L., Inlander, E., McKenzie, C., and Dvorsky, J., 1998, Synoptic views of sediment plumes and coastal geography of the Santa Barbara Basin, California: *Hydrological Processes*, v. 12, p. 967-979

Muhs, D.R., Rockwell, T.K., and Kennedy, G.L., 1992, Late quaternary uplift rates of marine terraces on the Pacific coast of North America, southern Oregon to Baja California Sur: *Quaternary International*, v15/16, pp. 121–133.

Namson J. and Davis, T., 1988, Structural transect of the western Transverse Ranges, California. *Geology*, v. 16, pp. 675-679.

Nelson, R.N., 1925, Geology of the hydrographic basin of the upper Santa Ynez River, California: *Bulletin of the California University Department of Geological Sciences*, v15, p. 162-187.

Nicholson, C., Sorlein, C.C., Atwater, T., Crowell, J.C., and Luyendyk, B.P., 1994, Microplate capture, rotation of the western Transverse Ranges, and initiation of the San Andreas transform as a low-angle fault system: *Geology*, v. 22, p. 491-495.

Page, B.M., Marks, J.G., Walker, G.W., 1951, Stratigraphy and structure of mountains north-east of Santa Barbara, California. *AAPG Bulletin*, v. 35, n. 8, pp. 1727-1780.

Pike, R.J., and Wilson, S.E., 1971, Elevation-relief ratio, hypsometric integral and geomorphic area-altitude analysis. *Geological society of America Bulletin*, 82: 1079-1084.

Rockwell, T.K., Nolan, J., Johnson, D.L., and Patterson, R.H., 1992, Ages and deformation of marine terraces between Point Conception and Gaviota, western Transverse Ranges, California *in* *Quaternary Coasts of the United States: Marine and Lacustrine Systems*, SEPM Special Publication No. 48, p. 333–341.

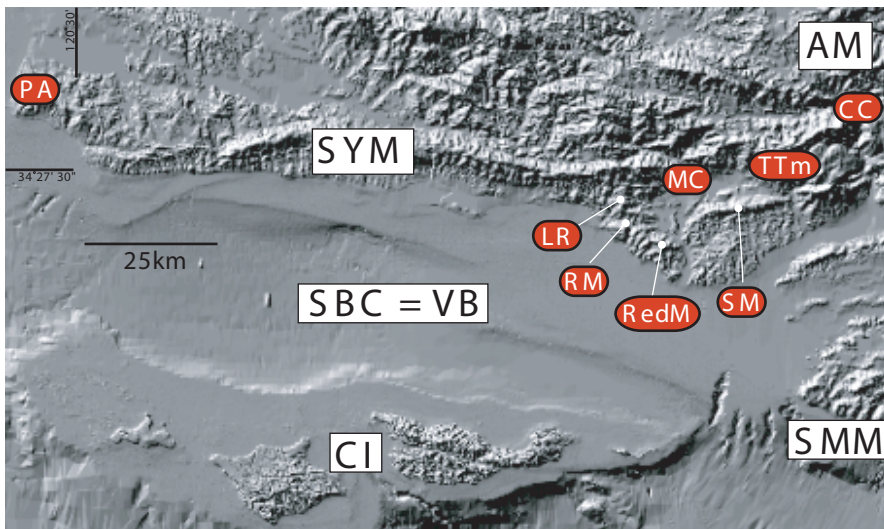
Schroeter, C.E., 1972, Stratigraphy and structure of the Juncal Camp - Santa Ynez fault slice, southeastern Santa Barbara County, California: University of California at Santa Barbara, unpublished Master's thesis.

Strahler, A.N., 1952, Hypsometric (area-altitude) analysis of erosional topography. *Geological Society of America Bulletin*, 63: 1117-1142

USGS, California 7.5 minute DEMs. URL:
http://edc.usgs.gov/doc/edchome/ndcdb/7_min_dem/states/CA.html
Access date: 8/99

Wells, D.L., and K.J. Coppersmith, 1994. New empirical relationships among magnitude, rupture length, rupture width, rupture area and surface displacement. *Bulletin of the Seismological Society of America*, 84 (4): 974-1002.

Yeats, R.S., Huffile, G.J., and Grigsby, F.B., 1988, Oak Ridge fault, Ventura fold belt, and the Sisar decollement, Ventura basin, California: *Geology*, v. 16, p. 1112 – 1116.



PRIMARY FEATURES

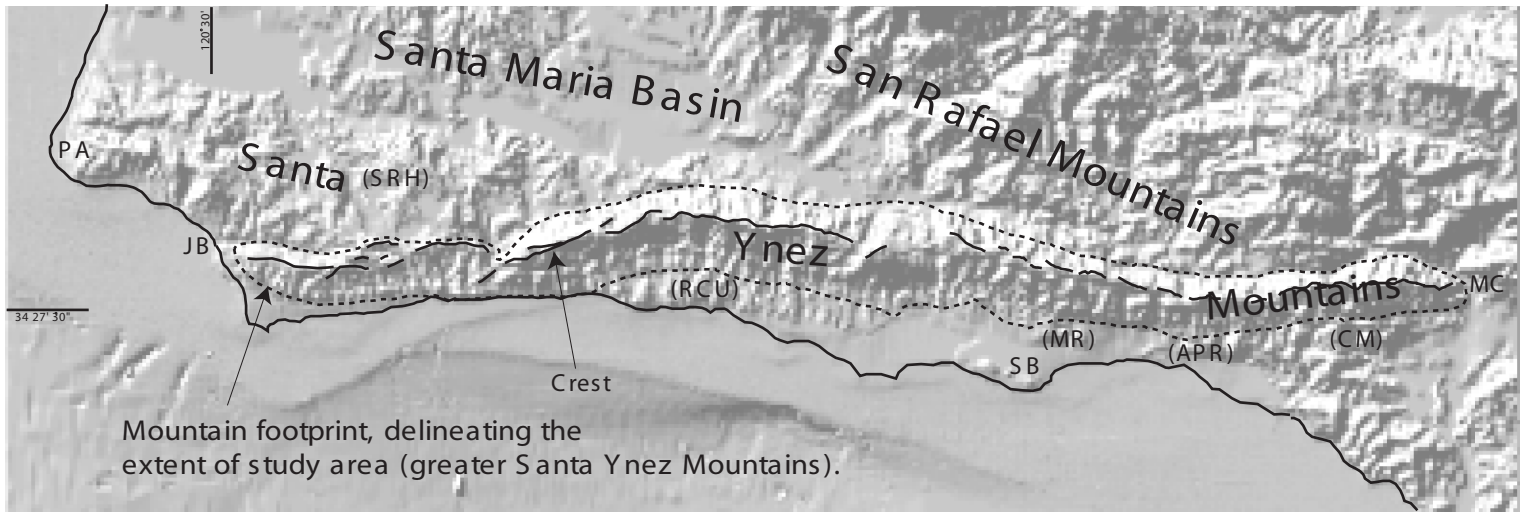
SYM = Santa Ynez Mtns
 AM = Alamo Mtns
 SBC = Santa Barbara Channel
 VB = Ventura Basin
 CI = Channel Islands
 SMM = Santa Monica Mtns

SECONDARY FEATURES

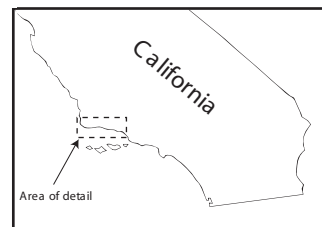
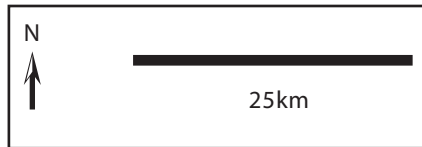
PA = Point Arguello SM = Sulphur Mountain
 MC = Matilija Creek RedM = Red Mountain
 LR = Laguna Ridge TTm = Topatopa Mtns.
 RM = Rincon Mountain CC = Castaic Creek

Figure 1, The Transverse Ranges and the western Transverse Ranges.

A) The Transverse Ranges in relation to the San Andreas fault. B) The western Transverse Ranges, with its geographic boundaries defined by the Santa Ynez Mtns. (SYM), Alamo Mtns. (AM), Santa Monica Mtns. (SMM), and the Channel Islands (CI). Point Arguello (PA) and Matilija Creek (MC) define the axial extent of the Santa Ynez Mountains (SYM). Laguna Ridge (LR), Rincon Mountain (RM), Red Mountain (RedM), Sulphur Mountain (SM) and the Topatopa Mountains are ranges assigned along with the Santa Ynez Mountains (SYM) as belonging to the Santa Ynez Mountain uplift. See Figure 2 for additional uplifts assigned to this event. Shaded relief image from Mertes et al (1998).



Mountain footprint, delineating the extent of study area (greater Santa Ynez Mountains).



ADJACENT UPLIFTS
 (SRH) = Santa Rosa Hills
 (MR) = Mission Ridge
 (APR) = Arroyo Parida Ridge
 (CM) = Chismahoo Mtn
 (RCU) = Refugio-Carneros Uplift

GEOGRAPHIC REFERENCES
 PA = Point Arguello
 JB = Jalama Beach
 SB = Santa Barbara
 MC = Matilija Creek

Figure 2, Study area.

A distinct crest marks the axial extent of the greater Santa Ynez Mountains. The mountain footprint is delineated by the extent of the flanks descending from this crest and is the scope of this study. The footprint abuts adjacent uplifts in several locations, making exact location of boundaries interpretive.

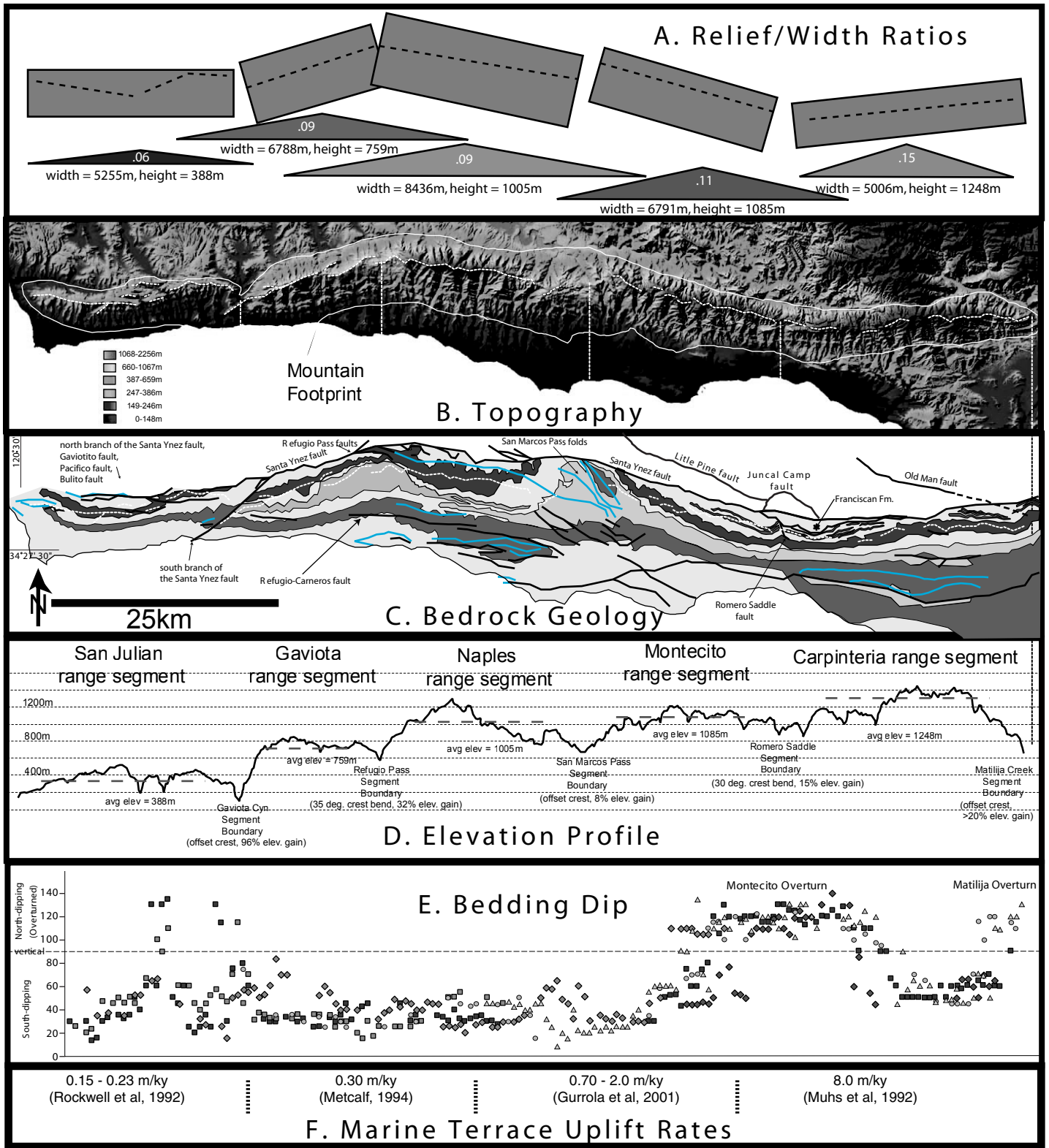
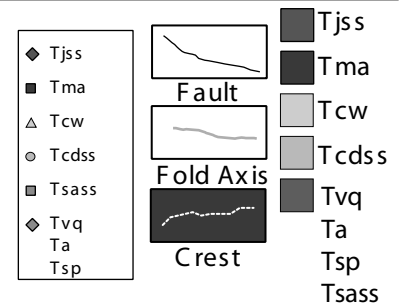


Figure 3, range segments and related data.

A) Segment relief/width ratios, with generalized mountain profiles. B) Shaded relief, with crest and range footprint marked. C) Simplified geologic map with individual sandstone units shown and shales in grey. Stratigraphy is from Dibblee (1950, 1966). D) Crest profile. E) South flank dips for sandstone units. F) Marine terrace uplift rates.



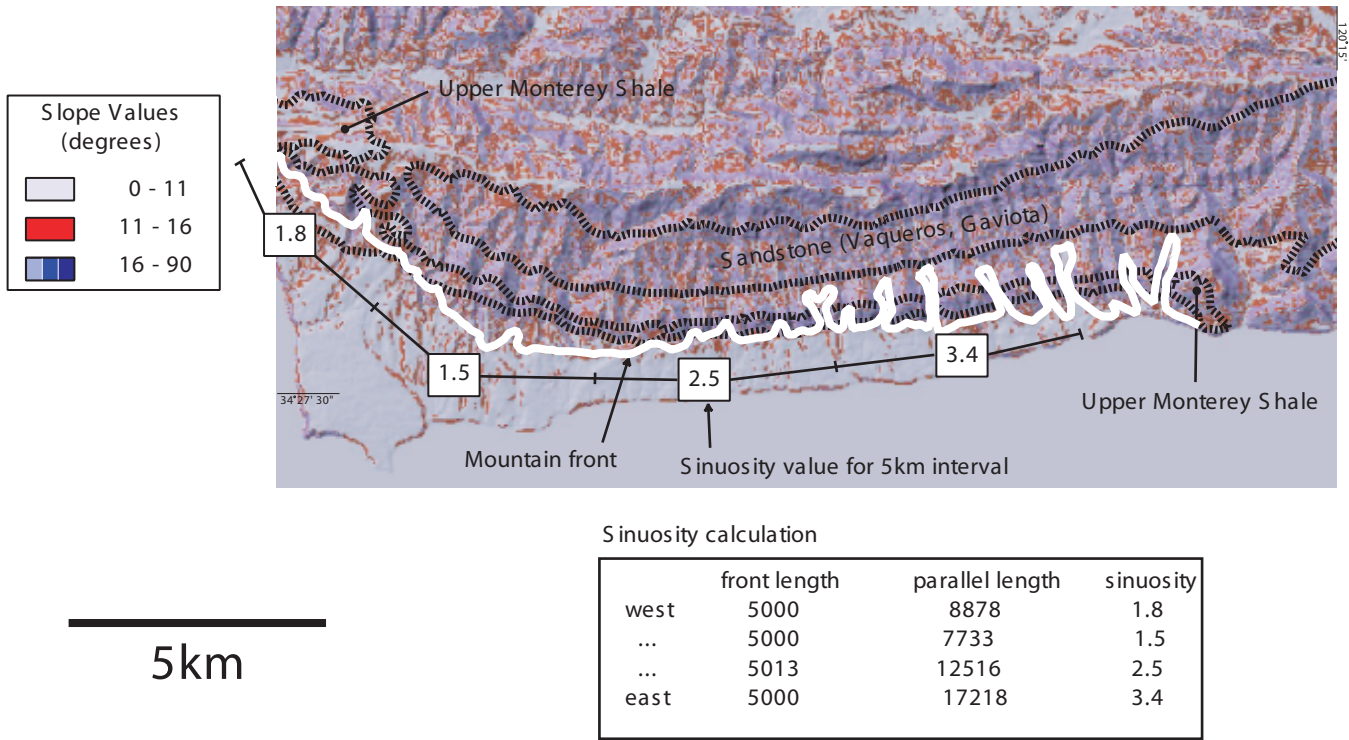


Figure 4. Mountain front S inuosity of the San Julian range segment. The mountain front is traced in white. Values for mountain front sinuosity calculated along arbitrary 5km intervals are shown in adjacent boxes. Black dotted lines outline outcrops of "hard" upper Monterey shale and Vaqueros sandstone (stratigraphy is from Dibblee (1950).

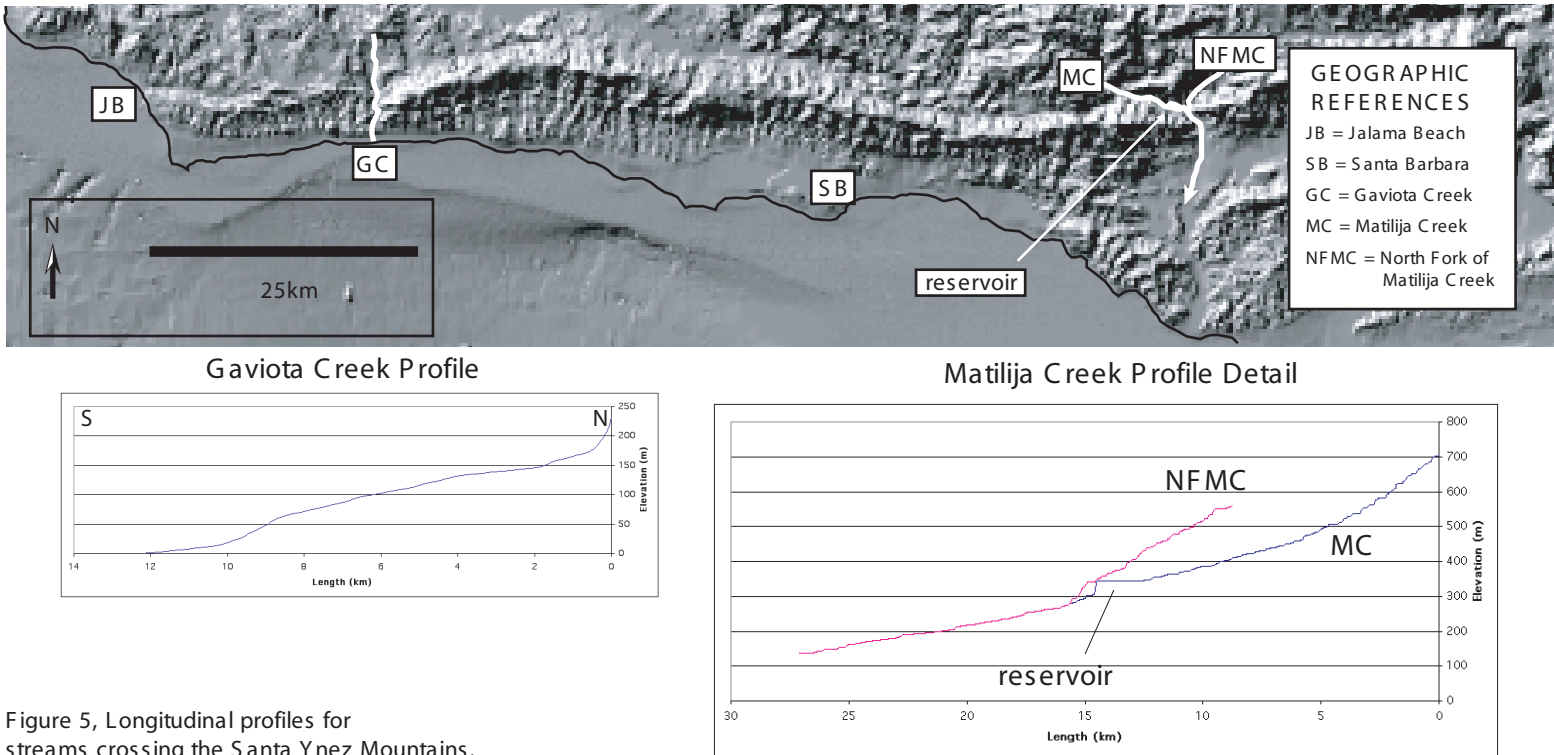


Figure 5, Longitudinal profiles for streams crossing the Santa Ynez Mountains.

The longitudinal profiles of streams crossing the Santa Ynez Mountains all display convexities where they cross the range, consistent with the hypothesis that the Santa Ynez Mountains are of recent or ongoing origin. Gaviota Creek displays the most pronounced convexity. Matilija Creek displays more subtle convexity which is partially obscured by the presence of a reservoir, but the North Fork of Matilija Creek displays clear convexity before merging with Matilija Creek downstream of the reservoir.

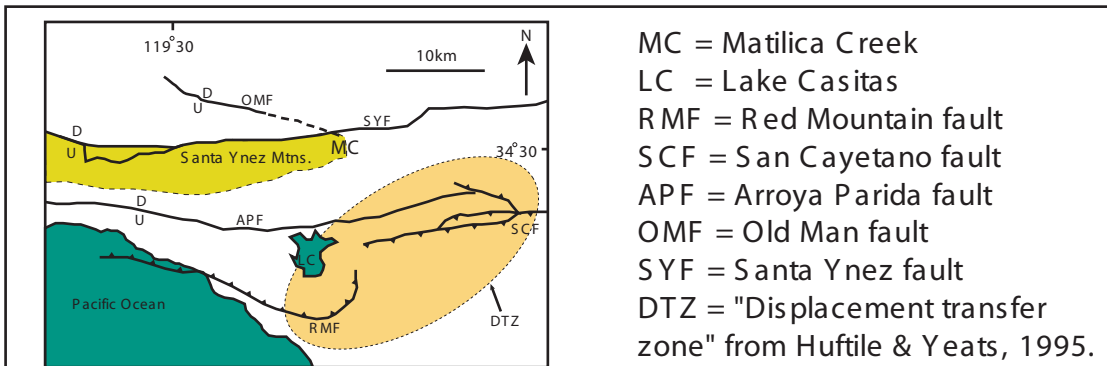


Figure 6. Postulated structures at the Matilija Creek range segment boundary. Matilija Creek differs from other range segment boundaries identified in this thesis in not corresponding with a mapped structure transverse to the Santa Ynez Mountains, but the geometry of local structure suggests that some unmapped structure may exist at this location. To the north, the Old Man fault intersects the Santa Ynez Mountains at the Matilija Creek range segment boundary, and may continue across the range beneath the alluvium of Matilija Creek. To the south, Huftile and Yeats (1995) identify a "displacement transfer zone" where north-south shortening shifts from the Red Mountain fault to the San Cayetano fault. A structure accommodating this transfer may be hidden beneath alluvium of Matilija Creek.

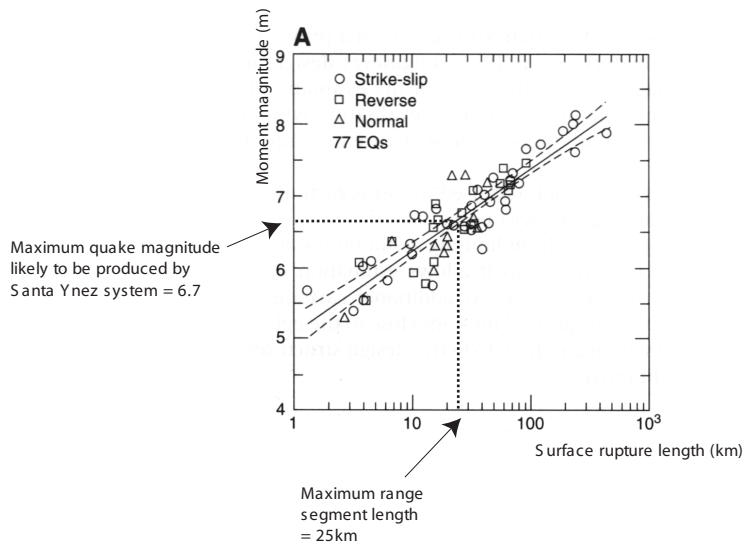
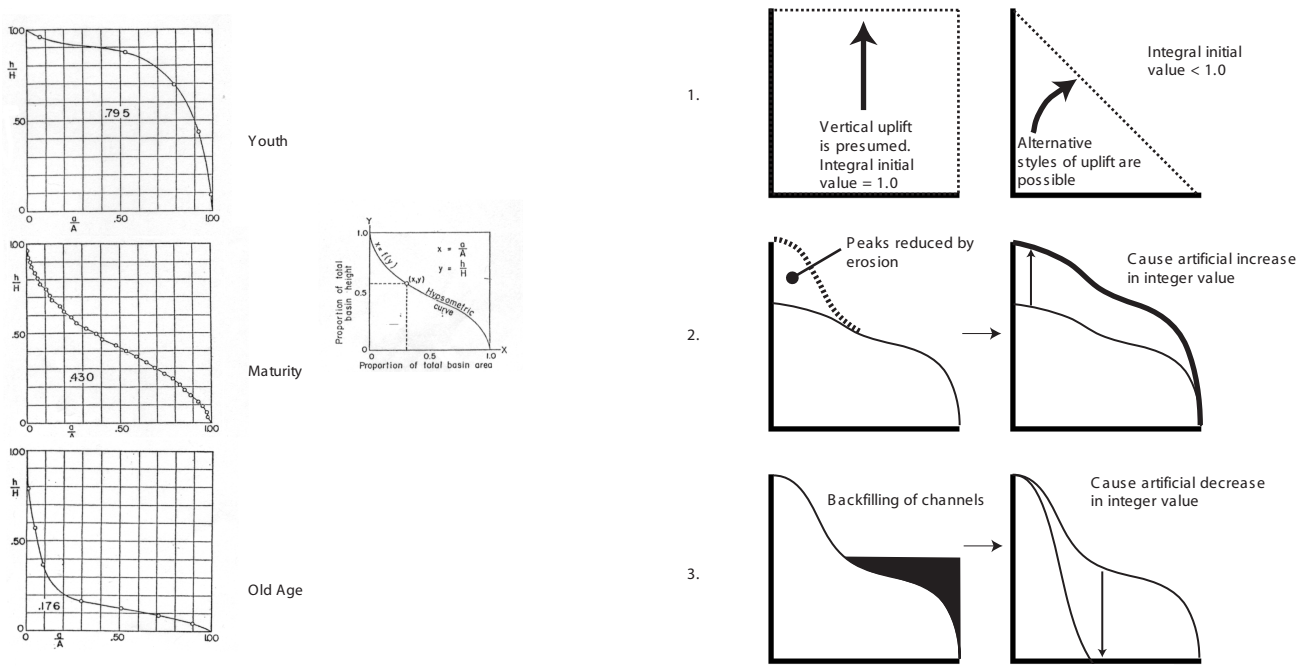
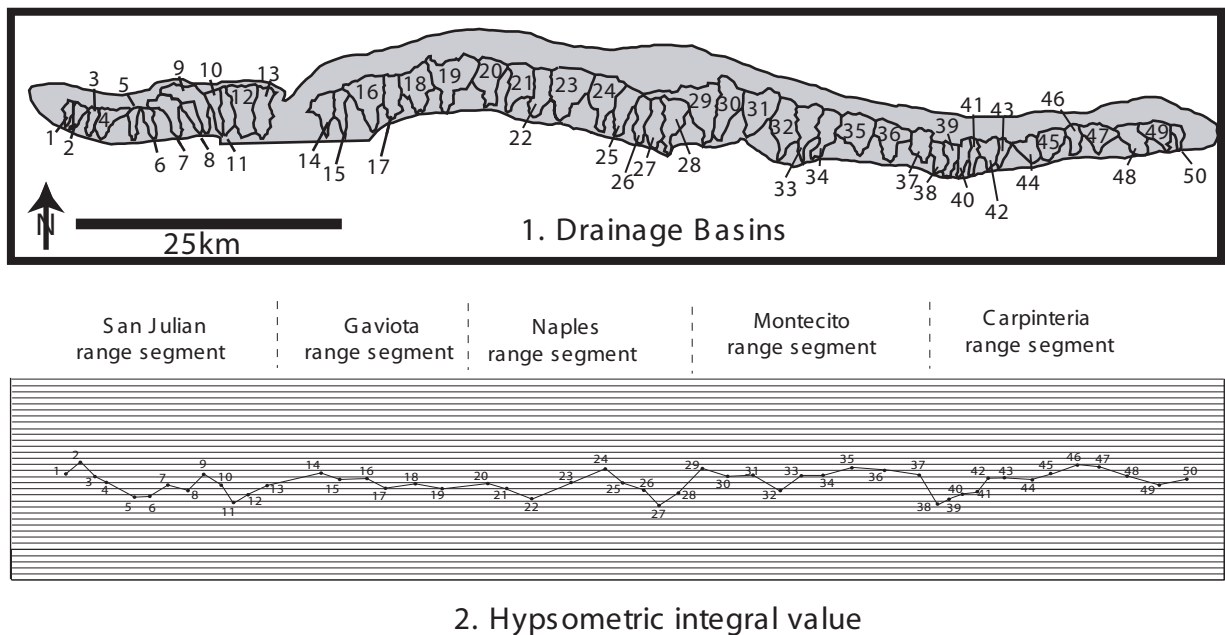


Figure 7. Relationship between fault length and quake magnitude. The chart above (Wells and Coppersmith, 1994) plots the relationship between earthquake magnitude and fault length, as represented in proxy by surface rupture length. Plotting the maximum range segment length for the study area reveals that the greatest magnitude quake likely to be produced by structures responsible for the Santa Ynez Mountains is 6.7.



A) Forms of the hypsometric curve. The hypsometric curve represents the amount of uneroded rock within a basin. S trahler (1952) identified three principal forms for the hypsometric curve, representing the landscape evolution stages of Davis (1899).

B) Weaknesses of the hypsometric method. 1) errors introduced when assumptions underlying the method are incorrect. 2) errors introduced when landscape no longer "remembers" value of original elevation highs due to erosion. 3) errors introduced when landscape no longer "remembers" value of original elevation lows due to backfilling.



C) Hypsometric analysis of the greater Santa Ynez Mountains. 1) Basins subjected to analysis: every south flank basin reaching the range crest. 2) Results of analysis: a statistically-flat trend, both within and among range segments.

Figure 8, Hypsometry
 A) General forms of the hypsometric curve. B) Weaknesses of the hypsometric method explained.
 C) Hypsometric data gathered from the greater Santa Ynez Mountains.

**DAY 3: SANTA BARBAR MISSION AND ROSE GARDEN;
HIKE TO ROCKY NOOK PARK**

1:00 p.m. – 3:00 p.m.

TECTONIC GEOMORPHOLOGY, ACTIVE FOLDING, AND EARTHQUAKE HAZARD OF THE MISSION RIDGE FAULT SYSTEM, SANTA BARBARA, CALIFORNIA

[GURROLA, Larry D.](#) and KELLER, E. A., Geological Sciences, UC Santa Barbara, Santa Barbara, 93106, lgurrola@umail.ucsb.edu

Investigation of the Mission Ridge fault on the Santa Barbara, California coastal piedmont identified potential seismic sources, several of which are expressed as anticlinal folds with tectonic geomorphic expression. The folds deform late Pleistocene alluvial fan and marine terraces age-dated by radiocarbon, uranium-series, optical stimulated luminescence, oxygen-isotope stratigraphy, and/or cosmogenic ^{21}Ne analyses. Trench excavations across the forelimbs of folds of the Mission Ridge fault reveal active deformation including bending moment faulting and hanging-wall warping.

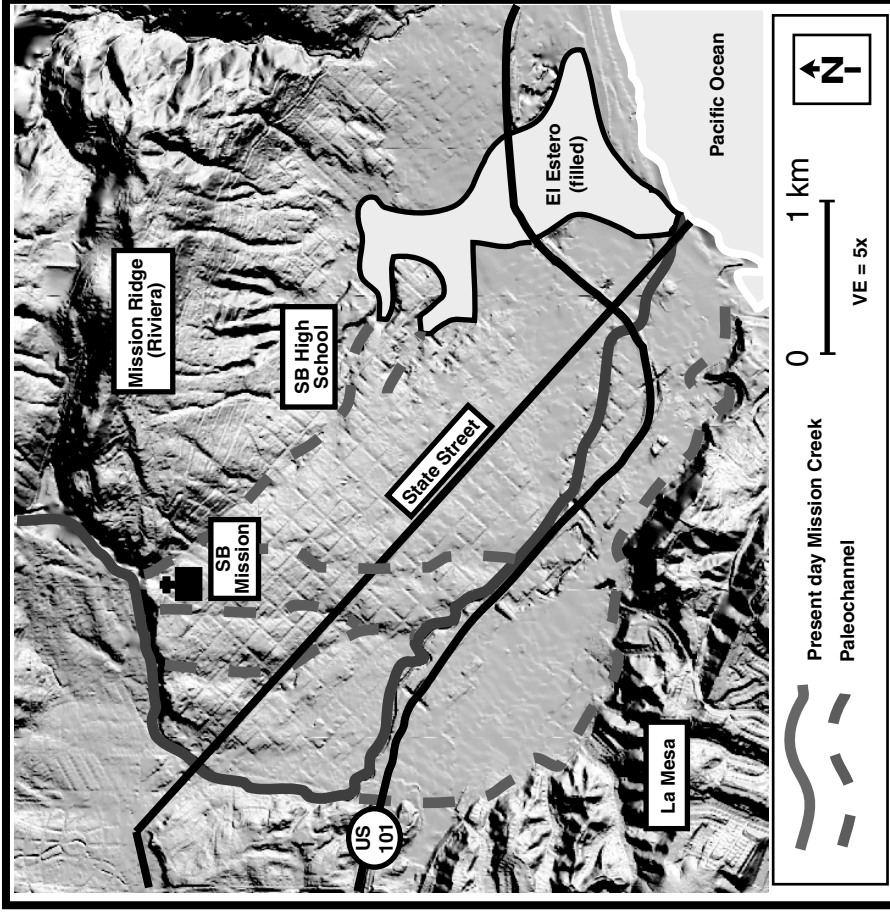
The westernmost segment of the Mission Ridge fault, the More Ranch fault, is exposed in a sea cliff exposure at Ellwood Beach. Vertical separation of the 44 ka marine abrasion platform due to faulting is approximately 7 m, whereas a monoclinical drape fold is formed in the terrace sediments. Analyses of continuous-drill core samples, seismic refraction data, and trench excavations on the More Ranch fault collected approximately 2 km east of the sea cliff exposure suggest: that the 44 ka marine terrace is anticlinally folded; fold relief across the 44 ka marine platform is approximately 14 m; and the estimated vertical rate of deformation is 0.32 m/ky.

Trench excavations across the Mission Ridge segment of the Mission Ridge fault system exposed 100 ka to 139 ka alluvial fan deposits, probably related to the 125 ka sea level highstand, folded with 90 m of vertical relief. From this evidence, the vertical rate of deformation is 0.75 ± 0.15 m/ky. A trench pit excavation across part of the northern limb of the Mission Ridge anticline exposed fluvial and alluvial sediments that are increasingly tilted with depth. The fluvial units dip approximately 10° to the north and form part of the forelimb of the fold. Radiocarbon analyses of an organic peat horizon determine an age-date of 1690 A.D. or 1730 A.D. for the fluvial deposits. Based on the arrival of Spanish settlers in 1782, we interpret that an earthquake occurred on the Mission Ridge segment between 1690 A.D. and 1730 A.D. Considering that the entire Mission Ridge fault consists of three segments, our seismic hazard analysis suggests that if one of the segments ruptured an earthquake of $M_w 6.5$ would likely result. If all three segments ruptured, an earthquake of $M_w 6.8$ to $M_w 7.0$ would likely occur.

Santa Barbara, CA Flood Hazard: A Story of Paleochannels and Earthquakes

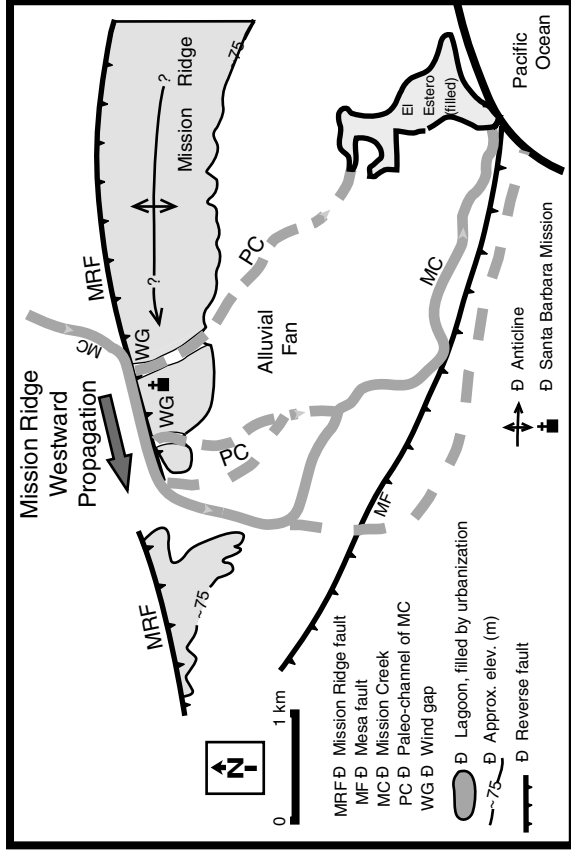
E.A. Keller, R.D. Hartleb, L.D. Gurrrola
University of California at Santa Barbara

Mission Creek in late Pleistocene time flowed south from the Santa Ynez Mountains, through a series of distributary channels of an alluvial fan upon which much of the city of Santa Barbara is now built, discharging into a lagoon (El Estero). These channels are present today as paleochannels in a completely urbanized environment. Uplift and lateral propagation of the western end of Mission Ridge (assumed to be a result of earthquakes of the Mission Ridge fault) near the fan head resulted in westward diversion of Mission Creek. Total deflection of approximately 1 km is delineated by wind gaps which decrease in elevation to the west. Though masked by urbanization, the paleochannels are still expressed in the topography and, along with other drainages on the south flank of Mission Ridge, contribute runoff to the now-filled El Estero lagoon in lower Santa Barbara.



High resolution (3-m grid spacing) DEM of downtown Santa Barbara, California created from 2 and 5-foot CI topographic data. (Elevation data from Santa Barbara County Flood Control).

Schematic diagram showing tectonic geomorphology of downtown Santa Barbara, California.



DAY 3: SKOFIELD PARK

3:00 p.m. – 5:00 p.m.

Pool formation in boulder-bed streams: Implications from 1-D and 2-D hydraulic modeling

Lee R. Harrison^{1*} and Edward A. Keller¹

Abstract. The mechanism by which pools form along a stream is a fundamental aspect of channel form and process. Most of the previous studies of pool formation have focused largely on alluvial rivers and relatively few studies exist on pool evolution in boulder-bed channels. Here, we use high-resolution digital terrain data and a computational flow modeling approach to investigate the interactions between boulder-large roughness elements, channel hydraulics and pool formation along a 48 m reach on Rattlesnake Creek, near Santa Barbara, CA. One and two-dimensional flow modeling were used to predict the velocity and shear stress distribution over the reach for a range of discharges. Flow modeling is based on numerical solution of the one-dimensional energy equation and the depth-integrated equations of conservation of mass and momentum. Results from the 1-D simulations identified that a flow reversal occurred above a discharge of approximately 4.0 cms, likely due to changes in the effective channel width at varying flows. Two-dimensional velocity predictions indicated that strong flow convergence develops below a boulder-constriction at the pool-head and translates a high-velocity jet through the pool center. The jet is enhanced by ponding of water upstream of the constriction and the development of an eddy zone on the lee side of the boulder that concentrates flow through the pool center. The predicted flow patterns suggest that boulder-large roughness elements act to increase local flow acceleration, turbulence and sediment transport capacity. Based on the analysis of channel hydraulics the existing pool morphology on this study reach appears to be formed and maintained by moderate flows with a recurrence interval of 1-2 years.

Introduction

The mechanism by which pools form along a stream is a fundamental aspect of channel form and process. Pools form freely in alluvial channels by the interaction of flow and sediment. In mountain channels with rough, irregular boundaries, pools are often forced by local obstructions, such as boulders, bedrock or debris jams (Keller and Swanson, 1979; Lisle, 1986; Montgomery et al. 1995). In the latter case, the roughness elements cause flow convergence, acceleration and enhanced sediment transport capacity at high discharges and force downstream morphology and the occurrence of pools. While it is widely recognized that flow convergence and bed scour are associated with flow obstructions, there has not been any quantitative analysis on pool formation in boulder-bed streams of the chaparral environment. Here we test the hypothesis that pools in these systems evolve due to velocity or shear stress reversals caused by boulder roughness elements.

Pools can be defined as deep areas with low velocities at low discharge, where riffles are high points in the bed topography, with steeper water surface slopes and faster velocities at low flow relative to pools. Many studies on pool-riffle sequences have tested the velocity reversal hypothesis (Keller, 1971), including Lisle (1979), Costa (1983), O'Connor et al. (1986) Keller

¹ Department of Geological Sciences, University of California at Santa Barbara.

* Correspondence to: lharrison@umail.ucsb.edu.

and Florsheim (1993), Carling and Wood (1994), Sear (1996), Thompson et al., (1998, 1999), and Cao et al. (2003). The velocity reversal hypothesis suggests that there is a hierarchical reversal in the magnitude of velocity over a riffle-pool sequence. At low discharge, well below bankfull, the velocity in the riffle exceeds that in the pool. Bed material moved out of the riffle is deposited in the adjacent pool. At high flow, at or near bankfull, the velocity of the pool exceeds that of the riffle. Thus, pools scour during these high flow events and fill during low flow.

In addition to their geomorphic significance, pools provide important habitat for the maintenance of viable fish populations, which rely upon pools and riffles throughout different stages of their life-cycle. Deep pools that provide important summer low-flow habitat, are found sporadically in boulder-bed channels, and it is more common to find step-pool morphology. Pool habitat has been suggested to be a primary limiting factor of juvenile trout in southern California (Spina, 2002). Therefore, an analysis of the processes that govern pool formation will provide useful data for understanding the habitat availability within boulder-bed streams.

The direct study of pool formation in natural streams is difficult because channel scour occurs during high magnitude, low frequency flows. The recurrence intervals between such discharge events is often very long relative to the time span of most research projects, and conditions within the channel commonly make direct field measurements hazardous or impossible. Consequently, computational hydraulic modeling offers an excellent opportunity to collect data relating channel hydraulics to processes thought to be important in pool genesis. Here we examine the interaction between flow hydraulics, topography and pool formation in a typical boulder-bed stream using one-dimensional (1-D) and two-dimensional (2-D) numerical modeling.

Study Area

Mountain streams in the chaparral environment are distinguished from other steep mountain channels by the unique linkage between the fire-cycle, vegetation and sediment production. Hillside vegetation periodically burns and sediment production increases dramatically following wildfire. During the decades between wildfire, much less sediment is mobilized. Occasional high magnitude debris flows deliver voluminous large boulders to stream channels (Florsheim et al., 1991). The combination of large debris flow-delivered boulders and low volumes of available finer gravel are characteristic of boulder-bed channels in southern California.

Rattlesnake Creek (Figure 1A), located near Santa Barbara, CA, was selected for the present study because it has easily accessible steep boulder-bed and bedrock channels and an abundant steelhead population. Rattlesnake Creek descends from an elevation of 1,164 m near the crest of the Santa Ynez Mountains and enters Mission Creek at an elevation of 149 m. Rattlesnake Creek is typical of many watersheds found in coastal southern California. The channels are deeply incised and are characterized by channel beds of large boulders that are generally not transported by stream flow. Around these boulder mosaics, common channel forms such as pools, riffles, step-pools and cascades evolve.

The geologic units encountered in the study area include Quaternary and Tertiary age deposits of marine and non-marine origin. The Tertiary units encountered in the study area include: the Juncal, Matilija, Cozy Dell, Coldwater, Sespe, and Monterey formations. The Juncal, Matilija, Cozy Dell and Coldwater formations are present in the upper Rattlesnake Creek drainage basin and serve as potential sediment sources for Rattlesnake Canyon. The channel

gravel deposits are modern sediments present in Rattlesnake Creek. The coarse sediments that make up the gravel unit are dominantly supplied by the erosion of debris flow deposits by Mission and Rattlesnake creeks. These boulder and cobble-rich stream sediments obstruct flow in the channel and exert a significant control on the morphology of the creek.

Field Measurements

Topographic data were acquired in March, April and May of 2003 using a Leica TC 805 electronic total station over a 48 m stream reach on Rattlesnake Creek. Channel reach attributes are listed in Table 1. The reach consists of a pool-riffle sequence with a large boulder-constriction directly above the pool (Figures 1B, 2A and 2B).

Real-time flow data is recorded at study site 1 by a pressure transducer installed by the Santa Barbara Coastal LTER Project. This flow data was used for hydraulic calculations at the study site. Flow events at the site are generally of short duration and peak flow often lasts less than one hour. The study site had a peak flow of 3.11 m³/s on March 15, 2003 with lower flows averaging below 0.5 m³/s. Water surface elevations from two near bankfull events and two intermediate storms were collected with the total station. This data has been used to calibrate the modeled flow predictions.

Survey data was used to develop a three-dimensional model of streambed topography using ArcGIS v 8.0 (Figure 3). A Digital terrain model was computed from the topographic data by creating a triangulated irregular network (TIN) using the ArcGIS 3-D Analyst extension. The digital terrain model of the bed surface was used in the hydraulic calculations.

Capturing the three-dimensional topography allows for fine-scale flow calculations, which is crucial in channels with rough irregular boundaries. An investigation was carried out on site 1 of Rattlesnake Creek with the aim of determining topographical survey point densities necessary for an accurate description of meso-scale (e.g. pool, riffle) stream morphology. In areas of high boulder frequency survey point density was 20 points/m² to capture complex topography. Average point density over the reach is 4 points/m². In addition, the terrain models document the baseline morphologic conditions. Additional terrain models have been developed for storm events during the 2003-2004 water year to monitor scour and fill patterns over time.

During the winter of 2003, grain size distributions were measured in the pool and riffle environments using a random pebble count method. The random grain size survey included the measurement of 100 samples from different geomorphic environment. Sediment data from the pool center, pool exit and the riffle were sampled separately to characterize the bed roughness. The grain roughness height k_s was estimated as 3 times the d_{84} for each morphologic environment (e.g. pool-head, center, exit or riffle).

Model Descriptions

One-Dimensional Hydraulic Modeling

Hydraulic computations were performed with HEC-RAS v 3.0 (USACOE, 2001), a one-dimensional model that calculates the water surface depth and slope by solving the basic energy equation between cross-sections:

$$Y_2 + Z_2 + \frac{\alpha_2 V_2^2}{2g} = Y_1 + Z_1 + \frac{\alpha_1 V_1^2}{2g} + h_e \quad (1)$$

Where Y_1, Y_2 = depth of water at cross-sections; Z_1, Z_2 = elevation of the main channel; $a_1 V_1, a_2 V_2$ = Velocity Head and h_e = Energy Head Loss.

The primary data requirement for HEC-RAS is cross-sectional data that can be easily extracted from the digital terrain models using the HEC-GeoRas extension in ArcGIS. Additional data inputs are known water surface elevation or energy slope, Manning's n value, expansion/contraction coefficients and discharge. One-dimensional step-backwater models are capable of handling subcritical and supercritical flow and have been used in bedrock mountain channels more than any other type of model (Miller and Cluer, 1998). This approach is well established and has been used successfully to address geomorphic questions by several authors (O'Connor, 1986, Keller and Florsheim, 1993).

The goal of the 1-D modeling was to reconstruct the cross-sectional distribution of hydraulic variables such as velocity, depth, and shear stress over a range of stream discharge values. These computations are useful in identification of maximum and minimum values of water surface slope and shear stress throughout the stream reach.

Two-Dimensional Flow Modeling

In order to constrain the effects of in-stream obstructions on the flow hydraulics a 2-D computational model was employed. River 2-D (Steffler et al., 2002) is a hydrodynamic model designed to handle complicated flow conditions, such as those present in boulder-bed channels. River 2-D solves the depth-integrated form of the conservation of mass (2) and momentum (3,4) equations.

$$\frac{\partial H}{\partial t} + \frac{\partial(HU)}{\partial x} + \frac{\partial(HV)}{\partial y} = 0 \quad (2)$$

$$\frac{\partial(HU)}{\partial t} + \frac{\partial(HUU)}{\partial x} + \frac{\partial(HUV)}{\partial y} + \frac{g}{2} \frac{\partial}{\partial x} H^2 = gH (S_{ox} - S_{fx}) + \frac{1}{\rho} \left(\frac{\partial}{\partial x} (H \tau_{xx}) + \frac{\partial}{\partial y} (H \tau_{xy}) \right) \quad (3)$$

$$\frac{\partial(HV)}{\partial t} + \frac{\partial(HUV)}{\partial x} + \frac{\partial(HVV)}{\partial y} + \frac{g}{2} \frac{\partial}{\partial y} H^2 = gH (S_{oy} - S_{fy}) + \frac{1}{\rho} \left(\frac{\partial}{\partial x} (H \tau_{yx}) + \frac{\partial}{\partial y} (H \tau_{yy}) \right) \quad (4)$$

Where H = depth of water; U, V = velocities in Cartesian space; x, y, t = Cartesian coordinates and time; ρ = fluid density; g = acceleration due to gravity; S_o = bed slope; S_f = friction slope and τ = turbulent stress tensor.

River 2-D is a finite element model featuring subcritical-supercritical solution capabilities. Input data include channel bed topography, roughness and transverse eddy viscosity distributions and initial flow conditions. This method has been used to document detailed simulation of local interactions between flow patterns and channel features (Crowder and Diplas, 2000). The 2-D modeling provides detailed representation of velocity vectors and changes in water surface elevation around boulders and in areas of supercritical flow.

A finite element mesh boundary has been designed as an overlay on the topography map and was refined to include greater detail in areas with high topographic complexity (Figure 4). Obtaining accurate representation of bed topography has proven to be the most critical aspect of the 2-D modeling phase.

Results

Sediment Data

Based on the sediment data of the channel bed, the coarsest particles are found on the downstream riffle, with a d_{50} value of 150 mm. Several cobble and small boulders (≤ 300 mm) are found in the pool center though it is mostly fine gravels with a d_{50} of 28 mm. Bed material in the pool-exit slope ranged from 10-60 mm with a d_{50} of 25 mm. The pool demonstrated sediment sorting with coarser sediment in the pool center and downstream fining in the pool-exit slope. This data was used to set the roughness values (Manning's n and k_s) in the flow models.

One-Dimensional Flow Simulation

The results from Hec-Ras identified that a reversal in mean velocity occurs between the pool-center and riffle-center above a discharge of roughly 5 cms. There was a shear stress reversal between the pool-center and riffle-center at approximately 8 cms. The velocity and shear stress are consistently higher at the constriction relative to the pool and riffle. Shear stress and velocity reversals occur between the pool-center and riffle-tail at a discharge of roughly 4 cms (Figure 5).

The reversals in velocity and shear stress are likely due to decreased cross-sectional area in the pool at roughly bankfull discharge (Table 2) and the steep energy gradient caused by the constriction (Table 3). Above an estimated discharge of $7.73 \text{ m}^3/\text{s}$ the energy gradient over the pool become steeper than the adjacent riffle. The increased water surface gradient caused by water ponded behind the boulder constriction is translated downstream causing higher mean velocity and shear stress at the pool head relative to the riffle.

The flow event at which the reversal occurs is approximately the bankfull discharge event on this stream (USACOE, 1984), suggesting that the pool-riffle sequence on this reach is maintained by flows with a recurrence interval between 1 to 2 years. These results are consistent with findings by others who have reported velocity or shear stress reversals (Keller, 1971, Lisle, 1979, O'Connor, 1986 and Keller and Florsheim, 1993) at flows of this frequency.

Two-Dimensional Flow Simulation

The upper portion of the reach on Rattlesnake Creek is a hydraulically steep part of the channel where rapidly varied flow exists during high flows. Field observations during flood conditions on March 15, 2003 indicated that water was ponded behind the 2 m boulder above the pool, located at cross-section 6. The locally steepened water surface slope created a hydraulic jump adjacent to the boulder and a high velocity core was transferred through the center of the pool downstream from cross-section 6 (Figure 6).

These field observations lead us to perform model runs comparing a range of discharges from a bankfull discharge event to a flow of roughly 1/10th bankfull. Figures 7A and 7B show the results from the low and high flow model runs. The low flow runs of 7A show that the velocity is higher in the riffle than in the pool as predicted by HEC-RAS. Similarly, the high flow run found higher velocities in the pool compared to the riffle (Figure 7B).

River 2-D predictions indicated that strong transverse velocity gradients were present through the pool at higher modeled discharges. At a flow of 0.5 cms (roughly 1/10th bankfull discharge), velocities are estimated at 0.6 m/s and 1.3 m/s for the pool and riffle, respectively. During discharges of 5.15 cms (approximate bankfull discharge), the maximum velocity in the pool center increased to nearly 3.0 m/s, while the maximum velocity over the riffle is estimated at approximately 2.5 cms. These results are consistent with those predicted by HEC-RAS,

though the reversal appears to be limited to a narrow jet that occurs through the pool head and pool center.

Discussion

Pool Formation and Maintenance

In Rattlesnake Creek, individual debris flow deposits within the channel, constrict roughly 10% – 50% of the active channel width and clearly influence local hydraulics. The boulders converge flow at high discharges, acting to enhance the formation and maintenance of pools. Based on the flow simulations, the presence of the constriction in channel width creates maximum velocities, shear stress and energy gradients at the pool head. The primary peak zone of flow competence remains at the pool head over the entire range of modeled flows. The implication of this is that pools are forced by the debris flow deposits in a similar mechanism documented in streams with large woody debris (Montgomery et al., 1995; Lisle, 1986). Thus pool formation in boulder-bed channels is dependent upon the delivery of large boulders during landslides and debris flow activity.

At this field site, the boulder-obstruction below XS-6 acts to pond water behind it, creating a steep water surface profile and a transverse current towards the channel centerline (Figure 10). The cross-channel pressure gradient caused by the build-up of water behind the boulder and the development of an eddy zone on the lee side of the boulder concentrates flow through the pool center. Thus, the high velocity core is steered by the channel topography. These model runs are consistent with results from Thompson et al (1998, 1999) and with our field observations of the flow dynamics.

The modeling results suggest that the pool morphology on Rattlesnake Creek is maintained by a discharge between 4-5 cms, slightly below bankfull. At flows of this magnitude, flow is strongly converged by the lateral-constriction present between XS-6 and XS-5. Model results of a five-year storm indicate that the boulder-LRE is drowned out and is not able to converge the flow into one high velocity core. During these events, a second high velocity zone is steered toward the point bar (Figure 9) and would likely change the asymmetric nature of the cross-section over time. If the bar-pool morphology is altered by a large storm, it is likely that higher flows would be required to cause pool scour. This offers further support that the pools in these channels are formed and maintained by events with a return period of approximately 1-2 years.

Effective Width

Results from the one-dimensional analysis indicate that the reversal in flow competency is likely due to changes in cross-sectional width at varying flows. In addition, the 2-D velocity vectors in figures 8A and 8B demonstrate that only a portion of the flow is responsible for scouring bed material. Cherkauer (1973) developed the concept of looking at the effective width of a pool-riffle sequence, which corresponds to the active extent of flow. After we eliminate the dead water zone, the lowest five percent (close to 1 standard deviation) of the velocity range (Figures 8A, 8B), patterns of effective width begin to emerge. The ratio of flow width in pools to riffles is one measure of flow convergence. At low flow ($Q = 0.5$ cms), the ratio of effective width between pools and riffles is roughly 1:1 with some divergence in the pool itself, implying that there is uniform flow with little flow convergence. At high flow ($Q = 5.15$ cms) the width ratio between the pool and riffle is about 1:3, demonstrating the strong convergent flow patterns at the pool head. This suggests that when considering restoration designs, boulders should be

placed in areas that replicate natural convergence and divergence patterns in order to maximize pool area and depth.

Future Research

A challenge in hydraulic modeling efforts is effectively capturing complex flow patterns and calibrating the predictions with measured field data. In this study, we have been able to calibrate flow predictions with observed water surface elevations but have not been able to collect velocity data during storm conditions due to hazardous conditions in the channel.

To address these issues, an experimental approach has been designed to further test the importance of channel width and height constrictions on pool formation, using an existing flume facility at the Ocean Engineering Laboratory at University of California at Santa Barbara. Based on the physical data collected in this study, we will develop a scaled replica of the pool in the flume channel. Documentation of the 3-D velocity profile using an Acoustic Doppler Velocimeter (ADV) will be conducted on the model pool. Velocity data will be collected first using a non-erodible bed to act as a control. The methods will be repeated with a mobile bed using sediments that have been scaled to match natural grain size distributions. Comparison of the two data sets will shed light on how pools build by using the before (fixed bed) and after (erodible bed) topography. The flume and hydraulic modeling data will be combined to increase our understanding of how pools form in boulder-bed channels.

Summary and Conclusion

Modeling of a laterally constricted pool-riffle sequence indicates that channel hydraulics are largely controlled by the presence of debris-flow delivered boulders. Results from the 1-D simulations identified that a flow reversal occurred above a discharge of approximately 4.0 cms, likely due to changes in the effective channel width at varying flows. Two-dimensional velocity predictions indicated that strong flow convergence develops below a boulder-constriction at the pool-head and translates a high-velocity jet through the pool center. The jet is enhanced by ponding of water upstream of the constriction and the development of an eddy zone on the lee side of the boulder that concentrates flow through the pool center. The predicted flow patterns suggest that boulder-large roughness elements act to increase local flow acceleration, turbulence and sediment transport capacity. Based on the analysis of channel hydraulics the existing pool morphology on this study reach appears to be formed and maintained by moderate flows with a recurrence interval of 1-2 years. Pool formation in boulder-bed channels thus can be viewed as a stochastic process that is largely dependent on debris flow processes and the distribution of in-channel boulder deposits.

References

- Cao, Z., Carling, P., and Oakey, R. (2003). *Flow reversal over a natural pool-riffle sequence: A computational study*. *Earth Surface Processes and Landforms*, 28, 689-705.
- Carling, P.A. and Wood, N. (1994). *Simulation of flow over pool-riffle topography: a consideration of the velocity reversal hypothesis*. *Earth Surface Processes and Landforms*, 19, 319-332.
- Cherkauer, D.S. (1973). *Minimization of power expenditure in a riffle-pool alluvial channel*. *Water Resources Research*, 9, 1613-1628.
- Costa, J. E. (1983). *Paleohydraulic Reconstruction of Flash-Flood Peaks from Boulder Deposits in the Colorado Front Range*. *Geological Society of America Bulletin*, volume 94. 986-1004.
- Crowder, D.W. and Diplas, P. (2000). *Using two-dimensional hydrodynamic models at scales of ecological importance*. *Journal of Hydrology*, 230 172-191.
- Florsheim, J. A. & Keller, E. A. & Best, D.W. (1991) *Fluvial Sediment Transport in Response to Moderate Storm Flows Following Chaparral Wildfire, Ventura County, Southern California*. *Geological Society of America Bulletin*, volume 103. 504-511.
- Keller, E. A. (1971). *Areal sorting of bed-load material: The hypothesis of velocity reversal*. *Geological Society of America Bulletin*, volume 82. 753-756.
- Keller, E.A. and Swanson, F.J. (1979). *Effects of large organic material on channel form fluvial processes*. *Earth Surface Processes* 4, 361-380.
- Keller, E.A. and J.L. Florsheim. 1993. *Velocity - reversal hypothesis: A model approach*. *Earth Surface Processes and Landforms* 18:733-748.
- Lisle, T.E. (1979). *A sorting mechanism for a pool-riffle sequence: summary*. *Geological Society of America*. 90, 616-617.
- Lisle, T. E. (1986). *Stabilization of a gravel channel by large streamside obstructions and bedrock bends, Jacoby Creek, northwestern California*. *Geological Society of America Bulletin* 97: 999-1011.
- Miller, A.J. and Cluer, B.L. (1998). *Modeling considerations for simulation of flow in bedrock channels*. In: eds. Tinkler, K.J and Wohl, E.E. *Rivers over rock: Fluvial processes in bedrock channels*. *Geophysical Monograph*. 107. p. 61.
- Montgomery, D.R., Buffington, J.M., Smith, R.D., Schmidt, K.M., and Pess, G. (1995). *Pool spacing in forest channels*. *Water Resources Research*. V. 31, No. 4, 1097-1105.
- O'Connor, J.E., Webb R.H., V.R Baker (1986). *Paleohydrology of pool and riffle pattern development; Boulder Creek, Utah*. *Geological Society of America Bulletin*, volume 97. 410-420.
- Sear, D.A. (1996). *Sediment transport processes in pool-riffle sequences*. *Earth Surface Processes and Landforms*. 21, 241-262.

- Spina, A.P. (2002). *Habitat associations of steelhead trout near the southern extent of their range*. California Fish and Game. 88 (3) 1-15.
- Steffler, Peter and Blackburn, Julia. (2002) *Two-Dimensional Depth Averaged Model of River Hydrodynamics and Fish Habitat: User's Manual*. University of Alberta, Canada.
- Thompson, D.M. J.M Nelson and E.E Wohl (1998). *Interactions between pool geometry and hydraulics*. Water Resources. Res. 34, 3673-3681.
- Thompson, D.M., Wohl, Ellen E. and Jarrett, Robert D. (1999). *Velocity reversals and sediment sorting in pools and riffles controlled by channel constrictions*. Geomorphology. 229-241.
- U.S. Army Corps of Engineers. (2001). *HEC-RAS Users Manual*. Hydrologic Engineering Center, Davis, California.
- U.S. Army Corps of Engineers. (1984). *Debris deposition study for without-project and with-project conditions, Santa Barbara County streams Mission Creek and Rattlesnake Creek*. Newport Beach, CA.

Figures

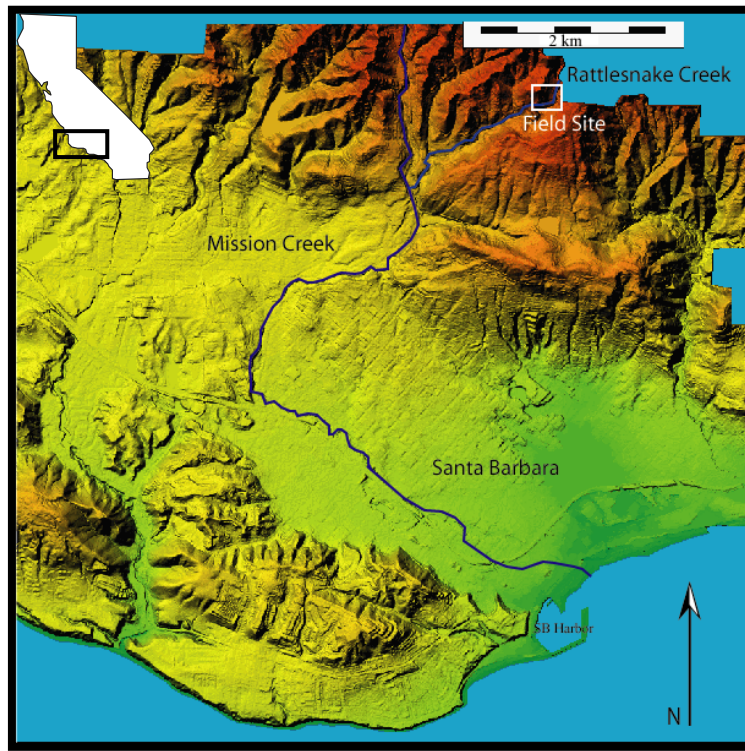


Figure 1.A. Digital Elevation Model (DEM) of Santa Barbara showing Rattlesnake Creek, the major tributary to Mission Creek.

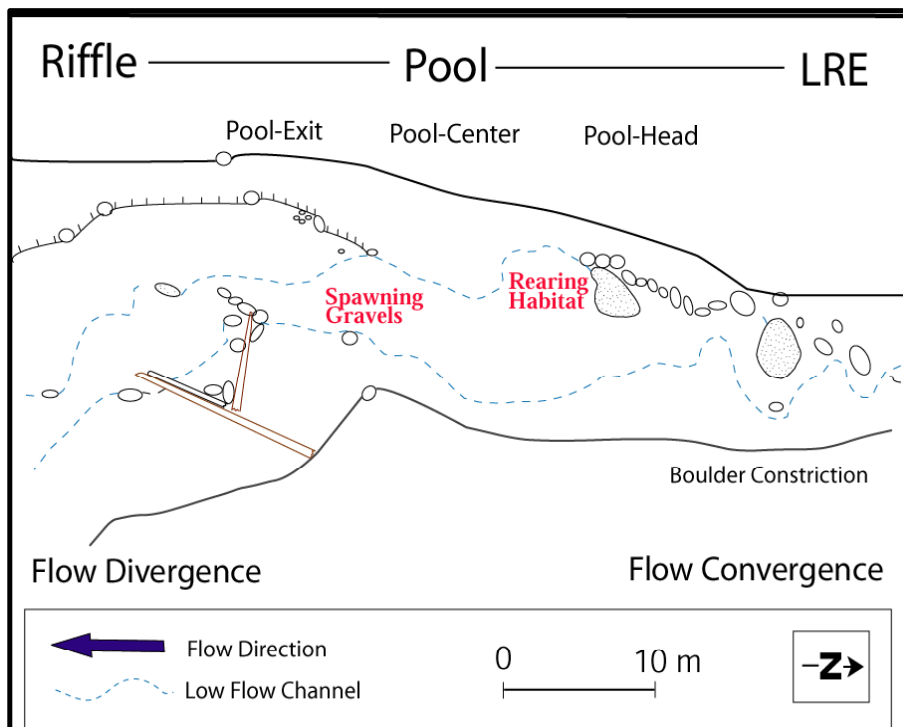


Figure 1.B. Plan view map of 48 m study reach showing boulder-constriction, pool and adjacent riffle.



Figure 2A. Upstream view of boulder riffle on Rattlesnake Creek, showing width expansion from XS-3 to XS-1. Discharge is 0.5 cms.



Figure 2B. Upstream view of the pool on Rattlesnake Creek. Boulder Constriction is shown at XS-6. Discharge is 0.5 cms.

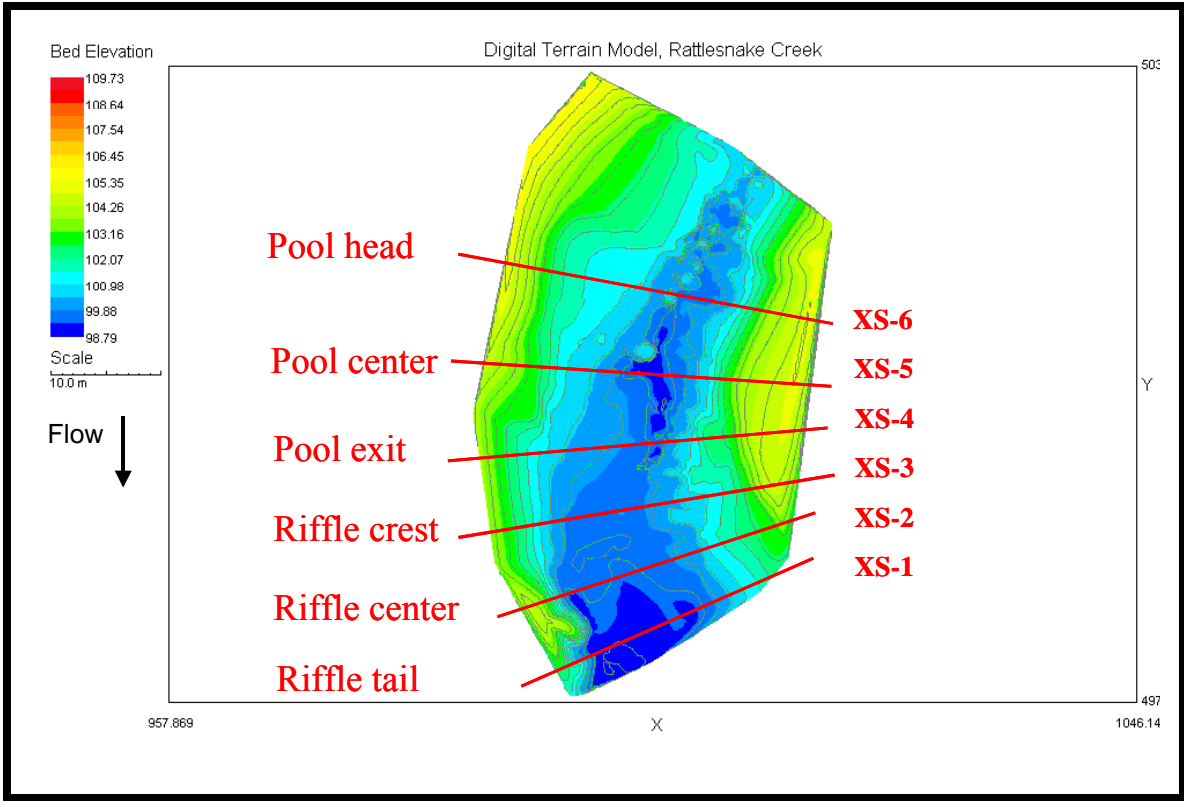


Figure 3. Digital terrain model of the Rattlesnake Creek bed surface. The major morphologic units are shown along sample cross-sections. Contour interval is 0.5 m.

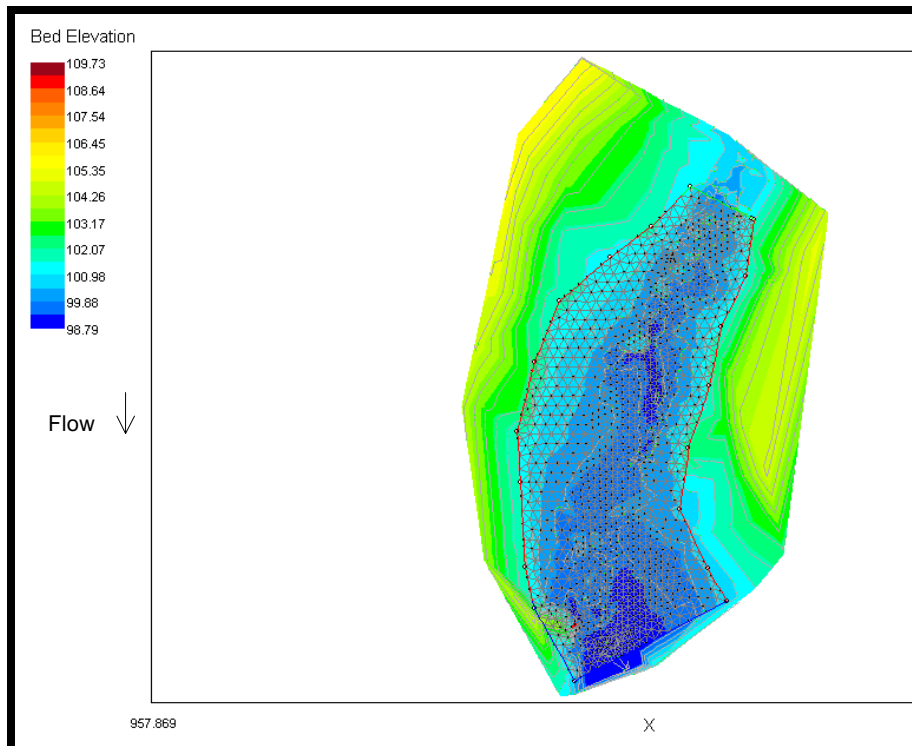


Figure 4. Rattlesnake Creek bed surface and computational mesh used in River 2-D calculations. Contour interval is 0.5 m.

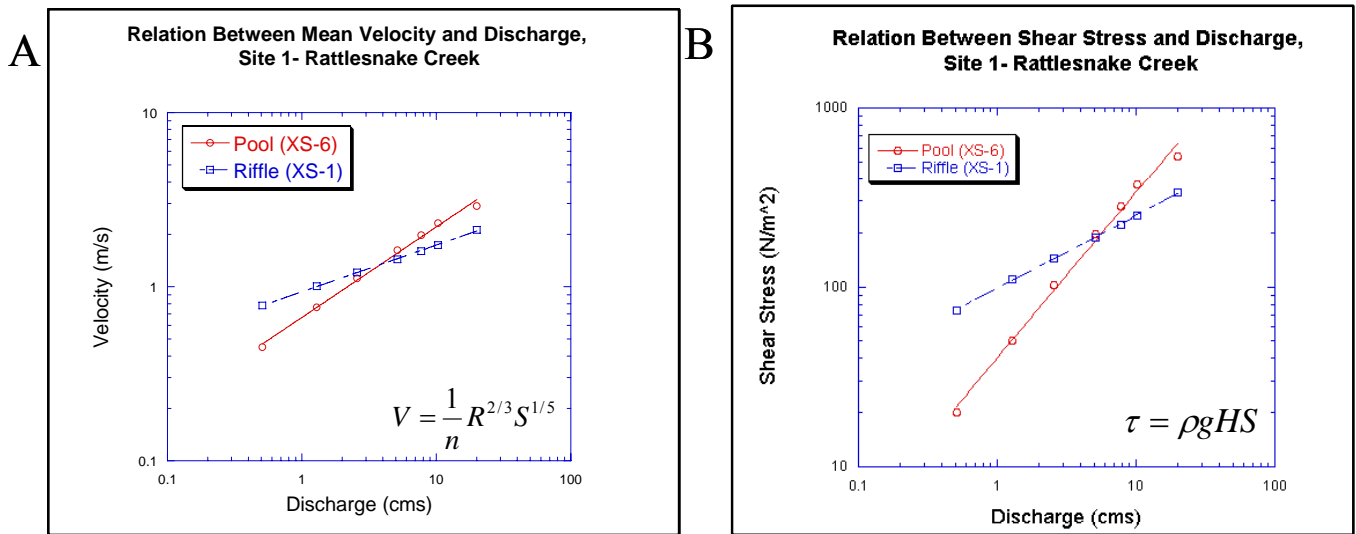


Figure 5. Discharge plotted versus A) modeled velocity and B) shear stress between the pool head and downstream riffle. Results indicate that above a discharge of roughly 5 cms a threshold exists and predicted velocity and shear stress in the pool head exceeds that on the riffle. This suggests that above the threshold discharge of 5 cms (approximately $Q_{1.5}$) the pool will experience scour while the riffle will fill.

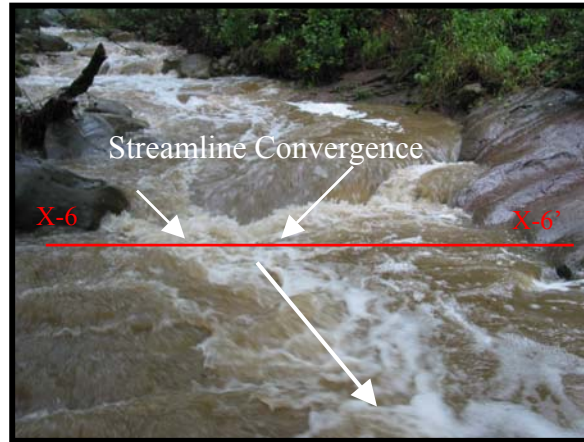


Figure 6. Upstream view of boulder constriction above main pool. Constriction width is approximately 25% of the active channel width. Discharge is 3.11 cms.

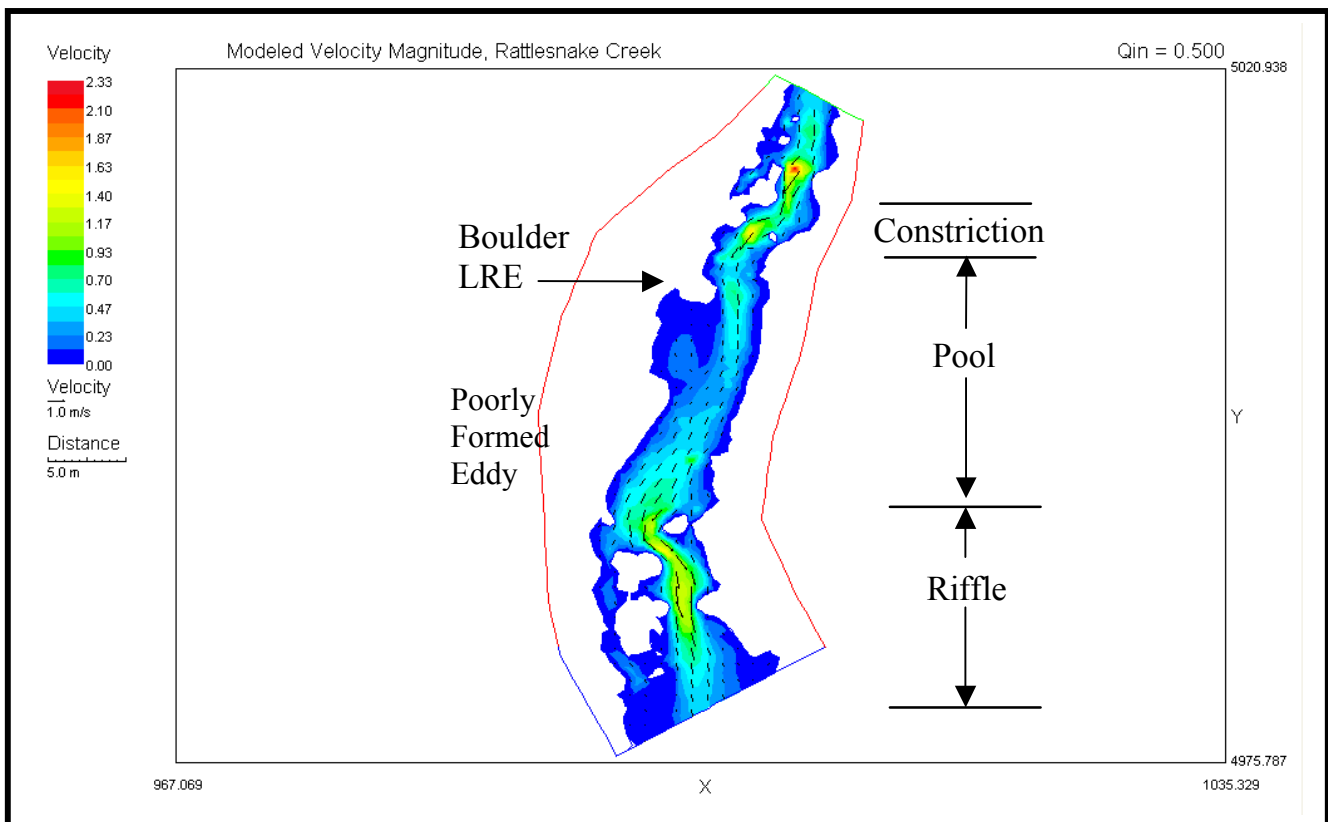


Figure 7A. Modeled Velocity Vectors at 10 Percent of Bankfull Discharge. Note higher flow over the riffle relative to the pool.

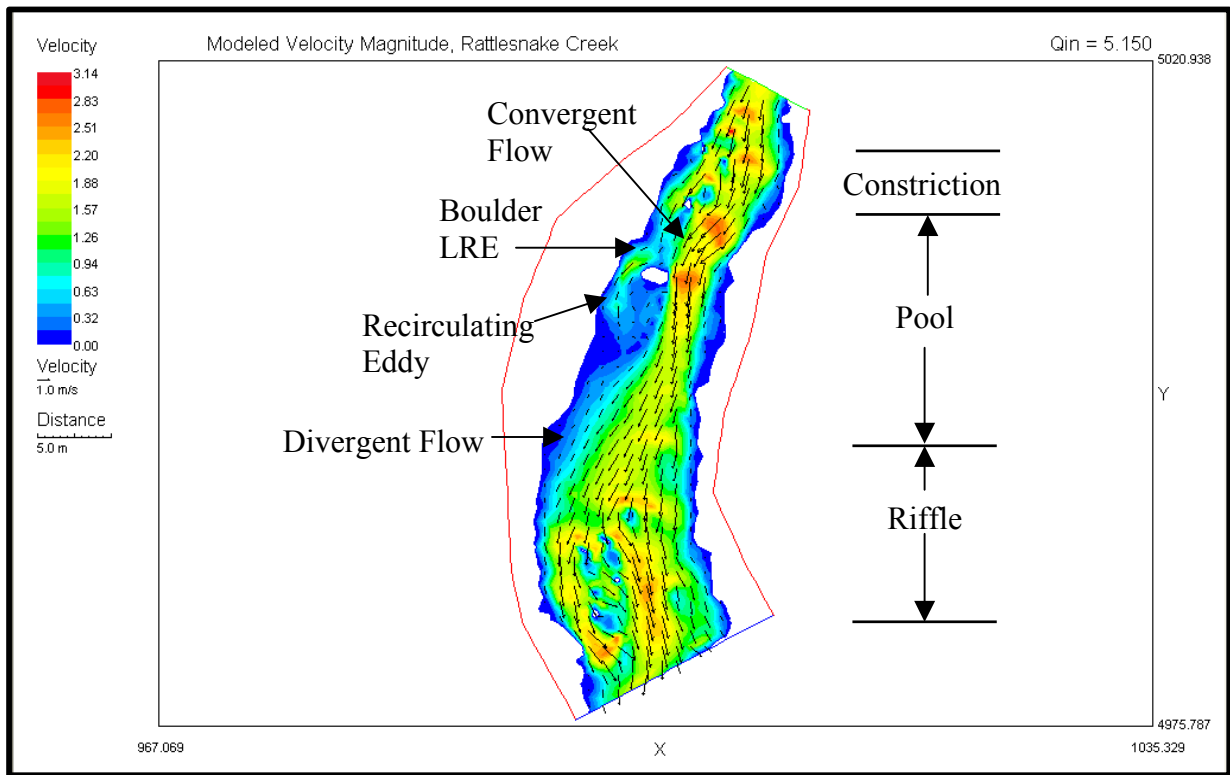


Figure 7B. Modeled velocity vectors at bankfull discharge. Convergent flow below the constriction is concentrated through the pool center creating an area of maximum scour.

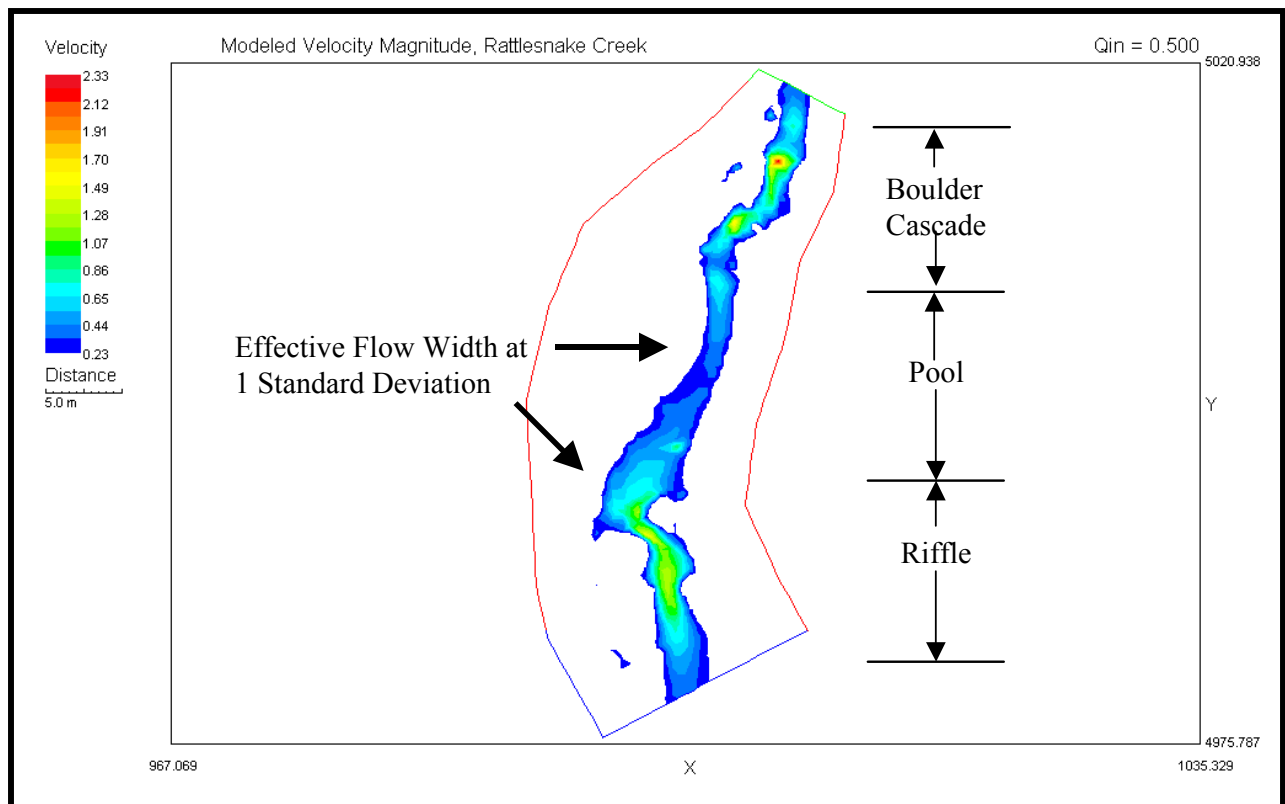


Figure 8A. Modeled Velocity Vectors at 10% of Bankfull Discharge.

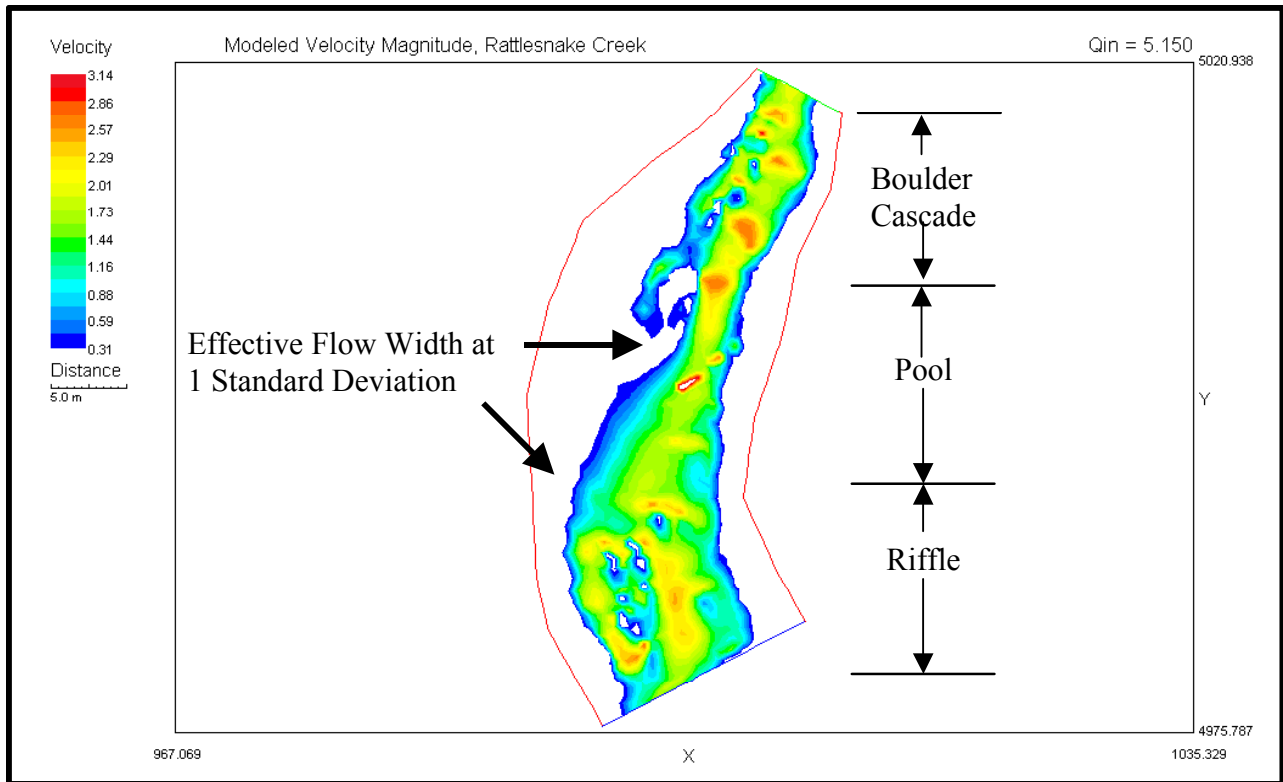


Figure 8B. Modeled Velocity Vectors at Bankfull Discharge. Notice the strong increase in bankfull width as the flow passes through the pool center into the riffle.

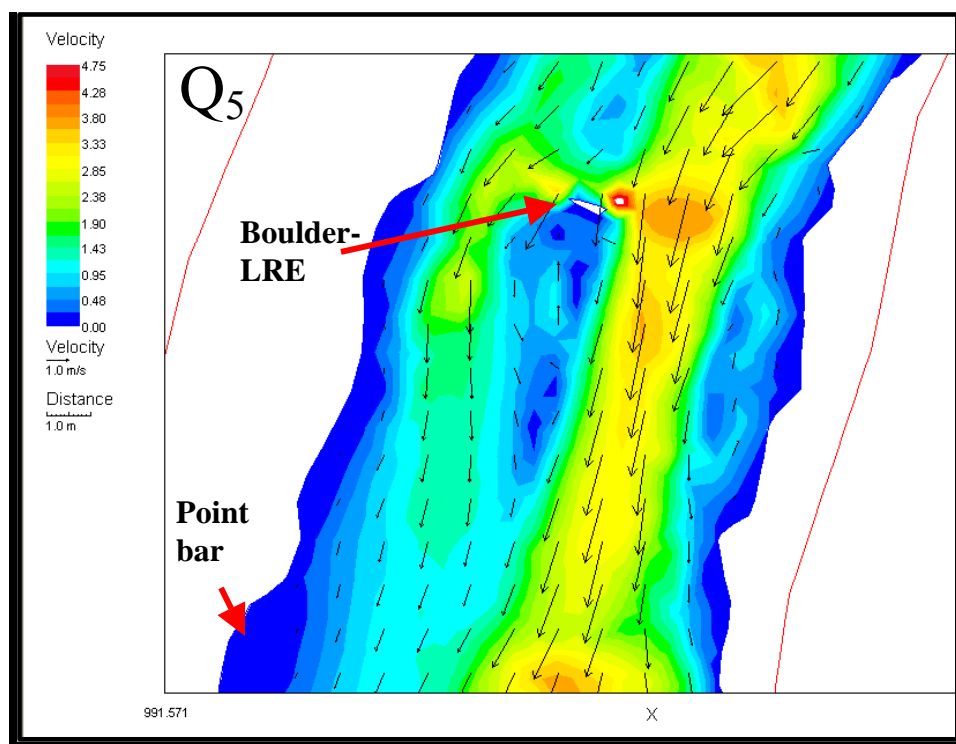


Figure 9. The boulder-LRE is drowned out above bankfull discharge. A second high velocity zone is steered toward the point bar suggesting that the existing morphology is maintained by lower flows.

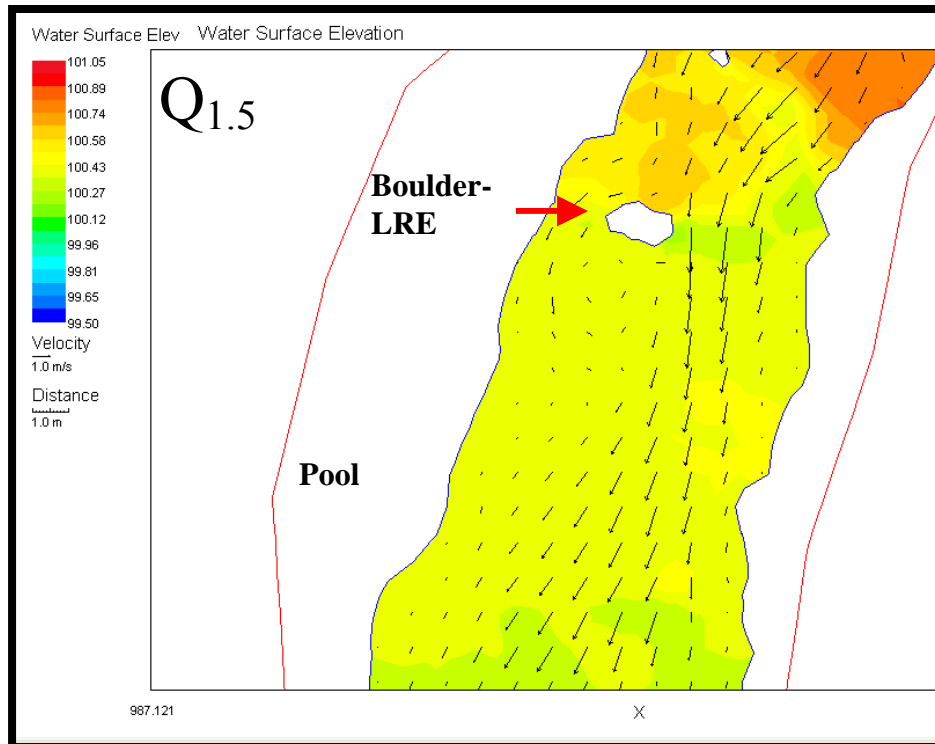


Figure 10. Water is ponded behind the boulder-constriction creating steep water surface slopes and a transverse pressure gradient above the pool head. The backwater effect acts to enhance the high velocity core through the pool center.

Tables

Table 1

Channel Reach attributes

Geometric Feature	Approximate Physical Dimensions
Channel-bed gradient*	0.02
Constriction width	6.4 m
Pool width	12.0 m
Pool length	19.8 m
Maximum pool depth (moderate flow)*	1.10m
Residual pool depth	0.9 m
Riffle width	14.6
Riffle length	17.4 m

*Measured along channel thalweg

Table 2

Predicted cross-sectional areas of flow

Discharge (m ³ /s)	Cross-sectional area of flow		
	Constriction (XS-6) (m ²)	Pool (XS-5) (m ²)	Riffle (XS-1) (m ²)
1.29	0.93	1.77	1.46
2.57	1.53	2.48	2.46
5.15*	2.55	3.58	3.83
7.73	3.66	4.48	4.95
10.3	4.58	5.27	5.93
20	7.61	8.21	9.04

*Estimated bankfull discharge

Table 3

Energy Gradient calculated in Hec-Ras on Rattlesnake Creek

Discharge (m ³ /s)	Energy Gradient		
	Pool maximum near constriction (m/m)	Pool average (m/m)	Middle portion of riffle (m/m)
1.29	0.010	0.010	0.011
2.57	0.015	0.012	0.015
5.15*	0.023	0.017	0.018
7.73	0.028	0.021	0.020
10.3	0.035	0.024	0.021
20	0.040	0.029	0.025

*Estimated bankfull discharge

**Friends of the Pleistocene
Spring 2004**

**THE DEBRIS FLOW ORIGIN OF THE MISSION DIAMICTON AND ASSOCIATED
GEOHAZARDS TO THE CITY OF SANTA BARBARA, CALIFORNIA**

Robert J. Urban¹ and Amy J. Selting²

ABSTRACT

A large debris flow fan, comprised of deposits of the Mission diamicton, associated with the failure of a landslide dam, is recognized in the residential development of the foothills of the City of Santa Barbara, California. The Skofield landslide dam and associated slope failures ($10.3 \times 10^6 \text{ m}^3$) contributed to the genesis of the Mission diamicton ($9.2 \times 10^6 \text{ m}^3$). The Mission diamicton represents multiple episodes of debris flow history. Geophysical investigations identified the 8.7-meter average thickness of Mission diamicton piedmont deposits. The Skofield landslide failure occurred in bedrock of the Sespe Formation and mobilized overlying mid- to late- Pleistocene fan conglomerate. Radiocarbon dating of Mission diamicton deposits indicates the deposits are younger than $1000 \pm 40 \text{ ka}$ in age. Quantitative geohazard evaluation and spatial analysis of Rattlesnake Canyon were used to identify critical slope orientations for present day slope instability, which allows for the recognition that slope failure, landslide dam formation, and associated debris flows from landslide dam failure pose threats to the City of Santa Barbara and perhaps the Santa Barbara coastal region.

INTRODUCTION

The city of Santa Barbara, California is located on a tectonically deformed late Pleistocene alluvial fan, part of the coastal piedmont found at the base of the south flank of the Santa Ynez Range (Fig. 1). An alluvial fan with an unusual morphology is located on the piedmont of the southern flank of the Santa Ynez coastal mountain range, within the City of Santa Barbara, California and the Transverse Range geomorphic provenance (Fig. 1). Though many alluvial fans are present on the coastal piedmont of the Santa Ynez Range in the Santa Barbara region, the lobate and digitate morphology of the fan indicate that debris flow processes were a dominant mechanism for the formation of this fan. The morphologically distinct debris flow fan is evident on the Santa Barbara 3m grid DEM (digital elevation model) (Fig. 1). The high-resolution (0.66m) photo-realistic rendering of the digital terrain model (DTM), generated by Urban (2002), best depicts the detailed morphology of the debris flow fan (Fig. 2).

The pristine morphology of the approximately 1 square kilometer lobate and digitate fan suggests a young age. The sediments, termed the *Mission diamicton*, that comprise the debris flow fan include a debris flow event or events resulting from the failure of a landslide dam, formed by the

¹URS Corporation, 130 Robin Hill Road,
Suite 100
Santa Barbara, CA 93117 805.964.6010

² Headwaters Academy
408 W. Garfield St.
Bozeman, MT 59715 406.585.9997

Skofield landslide (Figs. 1 and 3). Previous work has referred to the debris flow deposits comprising the fan as the *Mission debris flow* (Selting and Urban, 2001; Selting, 2000 and 2002). Recent work has identified that though the bulk of Mission diamicton sediment was provided by the Skofield landslide dam failure, additional large volume landslides up and downstream from the Skofield landslide provided supplementary sediment to the Mission diamicton (Urban, 2003 and 2004).

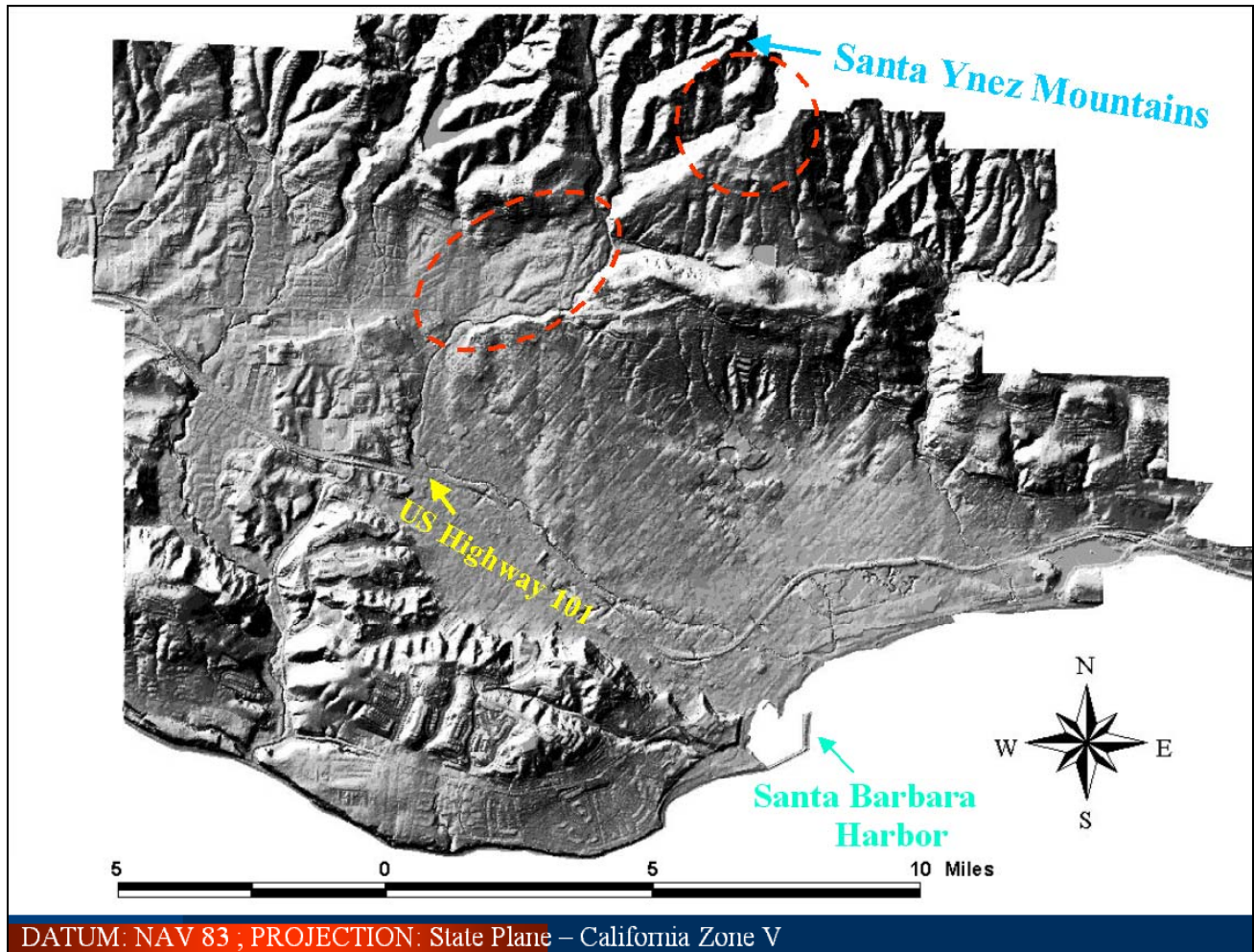


Figure 1. The 3-meter grid digital elevation model (DEM) of the City of Santa Barbara, California depicting the regional topography. The red dashed ellipse indicates the region of the Mission diamicton piedmont deposits. The red dashed circle indicates the location of the Skofield landslide. Figure from Urban (2004).

The debris flows resulting from the failure of the Skofield landslide dam include an event of unknown duration, hereafter called the *Mission debris flow*. Additional large volume slope failures in Rattlesnake Canyon also constitute debris flow materials in the Mission diamicton. Because the debris flow deposits investigated are comprised of sediments derived from multiple sources, the name, *Mission diamicton*, is adapted for the cumulative debris flow deposits (Urban, 2003 and 2004). The name, Mission diamicton, does not imply a singular genetic history. The name, Mission diamicton, is derived from the close proximity of piedmont deposits to the Santa Barbara Mission and the term, *diamicton*, is a non-genetic term that describes unconsolidated poorly-sorted sediments with a bimodal sedimentologic signature. The Mission diamicton is comprised of large diameter boulders in a matrix dominated by sand.

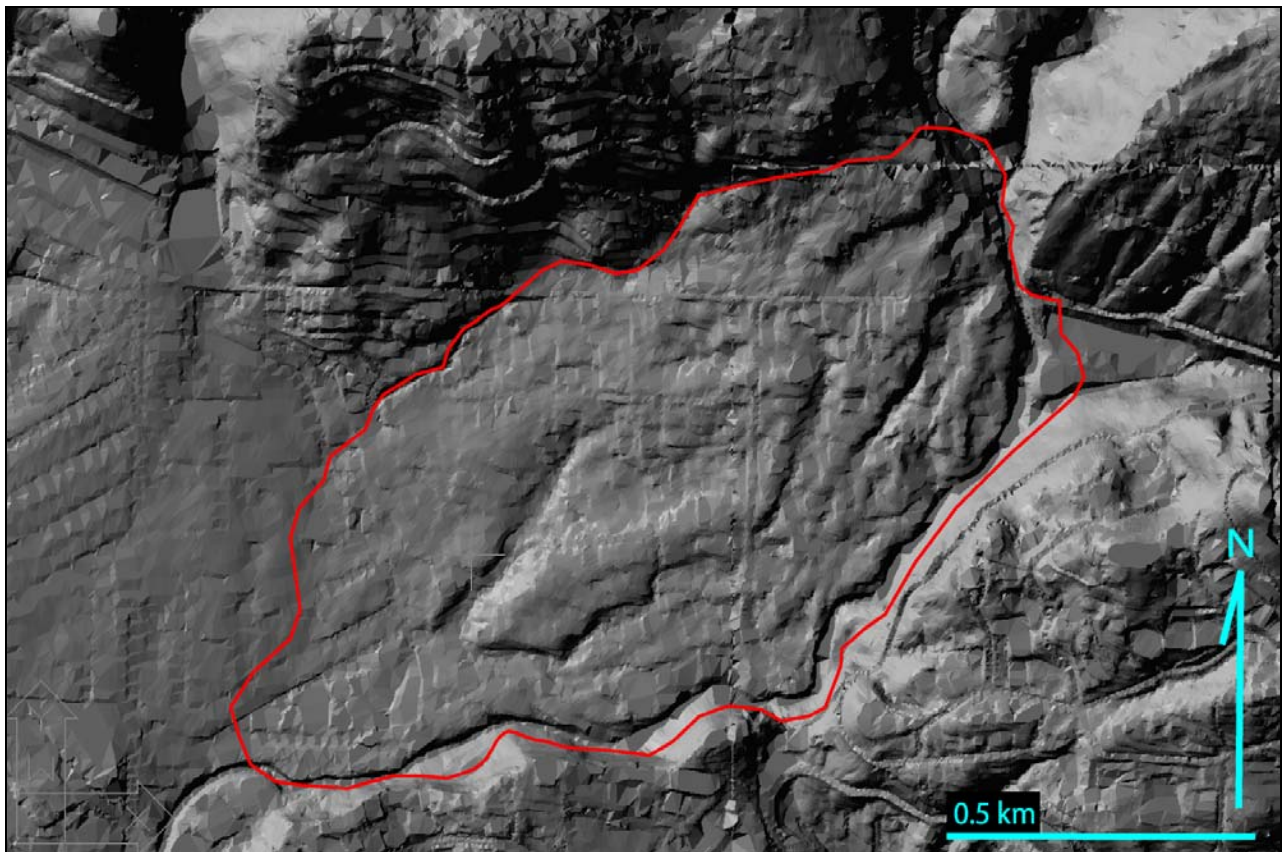


Figure 2. Photo-realistic render of the digital terrain model triangulated-irregular-network (TIN) for the Mission diamicton piedmont deposits. The red line indicates the approximate boundary of the Mission diamicton piedmont deposits. Piedmont deposits have characteristic digitate and lobate morphology indicative of debris flow depositional processes. The complex morphology and lack of paired levees within the fan deposits makes interpretation of debris flow sequence history impractical. Linear features trending north-south and east-west, respectively, are streets. Figure from Urban (2004).

The close proximity of urban development to the steep topography of the rising Santa Ynez Range poses geologic hazards to the habitants of the City of Santa Barbara in the forms of mass movements and associated processes such as the formation of landslide dams and their subsequent failure. Landslides, debris slides, and debris flows have historically affected residents of the Santa Barbara region (Keller, 1999).

Debris Flows

Debris flows are a type of gravity gravity-driven mass movement composed of highly concentrated mixtures of water, sediment, and air. There are three important factors influencing the formation of debris flows: the presence of unconsolidated material, presence of steep slopes, and the availability of suitable quantities of water (Johnson and Rodine, 1984).

Debris flows can be fast moving and have the capacity to carry large boulders for long distances. Debris flows are well known for their ability to transport large volumes of material over long distances as a result of the flow rheology and channel geometry. For these reasons, debris

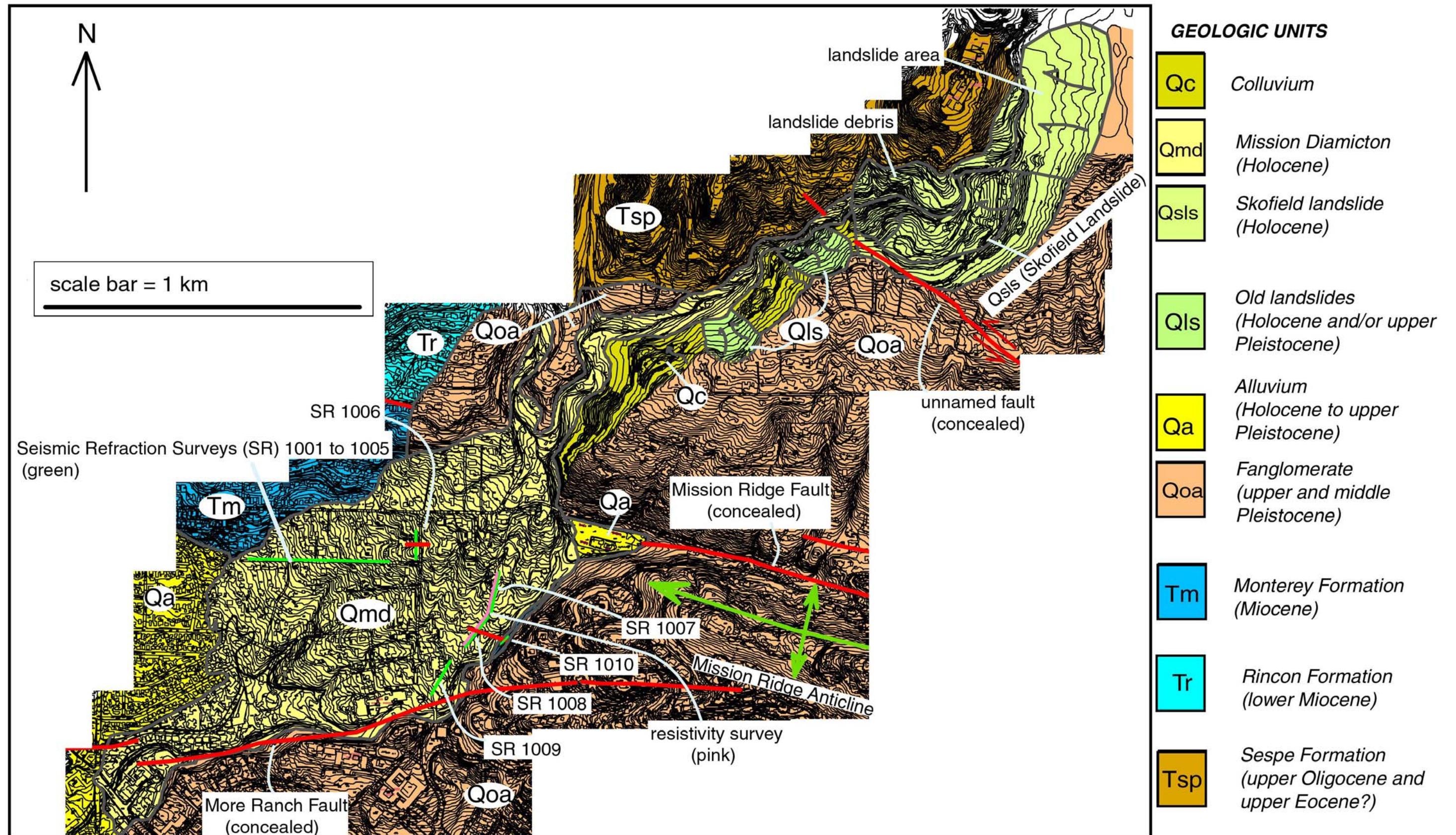


Figure 3. Geologic map of the Mission diamicton and associated features, Santa Barbara, California. Seismic refraction surveys indicated with bright green lines and abbreviated (SR). Resistivity survey indicated with pink line parallel to refraction surveys 1006 and 1007. Red lines indicate locations of concealed faults. Major green arrow indicates anticline axis and direction of plunge. Minor green arrows indicate dip direction of anticline limbs. Anticline and fault locations modified from Gurrola (2002). Fault locations within body of the Mission diamicton based on geophysical evidence. Figure from Urban (2004).

flows have the potential to cause significant damage and pose a significant geohazard in debris flow initiation and run-out areas. There is a frequency magnitude relationship in debris flow occurrence; historical large magnitude catastrophic debris flows are rare events.

The characteristic transport processes of debris flows tend to generate depositional landforms with a distinct morphology. Debris flow deposition commonly constructs flat topped, lobate landforms with steep fronted lateral and terminal margins. Levees of coarse boulders often outline channels on the flow surface. Occasionally debris flow lobes are accompanied with paired levees delineating a debris flow slug of sediment. Channels are commonly blocked by debris plugs, which divert successive pulses of the flow (Whipple and Dunne, 1992). This process can result in a complex flow surface morphology consisting of breached levees, plugged and abandoned channels, compound levees, and multiple digitate lobes (Wells and Harvey, 1987).

There are several sedimentary characteristics typical of debris flow deposits. The deposits are generally massive and poorly sorted, with particle sizes ranging from clay to unusually large boulders. They have matrix-supported fabrics characterized by large clasts enveloped by finer sediment and occasionally display normal or reverse grading.

Landslides are a common initiating mechanism of large debris flows (Johnson and Rodine, 1984). One way by which landslides generate debris flow events is through the formation and failure of a landslide dam. Debris flows initiated in this manner have been responsible for extensive loss of life and property (Costa and Schuster, 1987). Nearly half of all fatalities resulting from major landslide disasters of the twentieth century are attributable to landslide dam failures (Evans and DeGraff, 1997).

THE MISSION DIAMICTON

Areal Extent

The piedmont deposits of the Mission diamicton cover 1.01 km² of the City of Santa Barbara and surrounding area (Figs. 1 and 3) (Urban, 1999). The Mission diamicton extends a distance of approximately 3.8 km from its terminus on the piedmont to its last traceable extent in Rattlesnake Canyon near Skofield Park (Fig. 3) (Urban, 1999). On the piedmont, the deposit is roughly diamond shaped and measures approximately 800m across at its widest point. In Rattlesnake Canyon, the deposit is constrained by canyon topography to an average width of approximately 80m (Urban, 2003 and 2004).

Volume

Although Mission Creek has incised as much as 4m into the deposit, there is not a reliable exposure of the Mission diamicton basal surface within the body of the debris flow fan deposits. Volumetric estimates have utilized field relationships and surrounding topography (Urban 1999 and 2000; Selting and Urban, 2001) predicting an average thickness of 9m for piedmont deposits and an estimated volume of $9.1 \times 10^6 \text{ m}^3$ assuming pancake geometry for piedmont deposits. Selting (2002) used pancake and tapered wedge geometric models to calculate an estimated a volume for the piedmont deposits of $10.9 \times 10^6 \text{ m}^3 \pm 20\%$. However, Urban (2002) demonstrated with 3-dimensional modeling utilizing topography in the study area, that without defining the basal surface of the Mission diamicton, end member models for the Mission diamicton piedmont deposits of a pancake or tapered wedge geometries yield volumes of approximately $10 \times 10^6 \text{ m}^3$ to $30 \times 10^6 \text{ m}^3$.

To determine the source(s) of the Mission diamicton using volumetric methods in combination with geologic evidence, the basal surface of the Mission diamicton needed to be defined.

To identify the basal surface of the Mission diamicton, Urban (2002 and 2003) performed geophysical investigations, utilizing seismic and resistivity methods, of the Mission diamicton piedmont deposits. The combination of processed seismic refraction data, utilizing two-way travel time and tomographic analyses and borehole data, were used to identify the 8.7m average thickness of the Mission diamicton piedmont deposit (Urban, 2003 and 2004). Data from east-west and north-south transects of seismic refraction surveys were processed to construct a 3-dimensional model of piedmont deposits to precisely calculate volume in the AutoDesk Land Development desktop R2 geographic information system environment (Figs. 3 and 4). The generally pancake geometry of the Mission diamicton deposits is calculated to be $8.71 \times 10^6 \text{ m}^3$ (Urban, 2003 and 2004).

In addition to identifying the thickness of the Mission diamicton deposits, two additional findings were revealed by bulk velocity calculations and tomographic analysis of refraction data. First, two of the generally north-south trending refraction survey tomographic models depict lateral velocity contrasts that are correlative to regional faulting (Fig. 4) (Urban, 2003 & 2004). Second, the tomographic analyses, bulk velocity calculations utilizing geotechnical material properties, and borehole data were utilized to identify that the Mission diamicton is generally underlain by mid- to late-Pleistocene fanglomerate (Urban, 2003 & 2004).

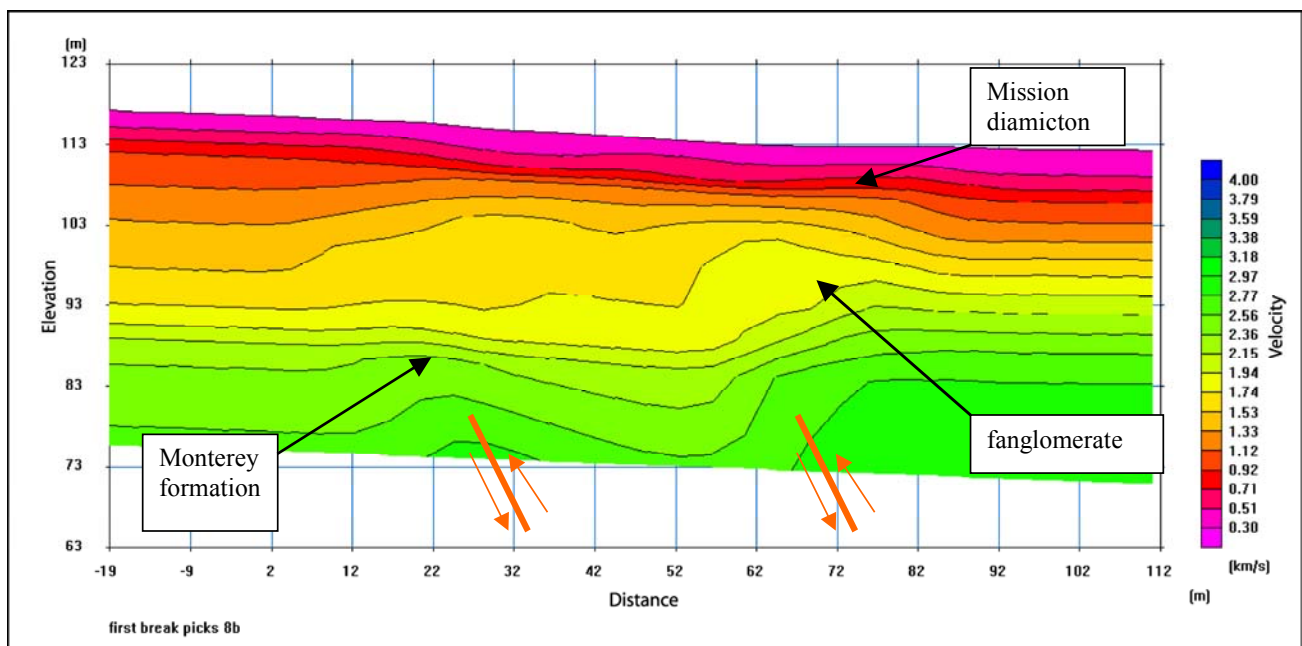


Figure 4. Tomographic analysis velocity model for survey 1008. Survey trends approximately N036E from right to left. Figure from Urban (2004).

The complex geometry of Rattlesnake Canyon and lack of 3-dimensional information regarding geologic contacts makes digital terrain modeling of the Mission diamicton canyon deposits impractical. Therefore, a generic volumetric analysis of the Mission diamicton canyon deposits was accomplished by using a general fill terrace geometry observed throughout Rattlesnake Canyon (Urban, 2003 and 2004). The Mission diamicton canyon deposits have distinct fill terrace morphology and is typically 80m in width (Fig 5). An approximately 4m thickness of debris flow deposits is observed for 1500m in Rattlesnake Canyon. The resultant volume of Mission diamicton deposits in Rattlesnake Canyon is approximately $0.5 \times 10^6 \text{ m}^3$. The total volume of Mission

diamicton deposits is therefore $9.21 \times 10^6 \text{ m}^3$ (Urban, 2003 and 2004). The piedmont portion of the Mission diamicton contains approximately 95% of the total volume of the deposit.

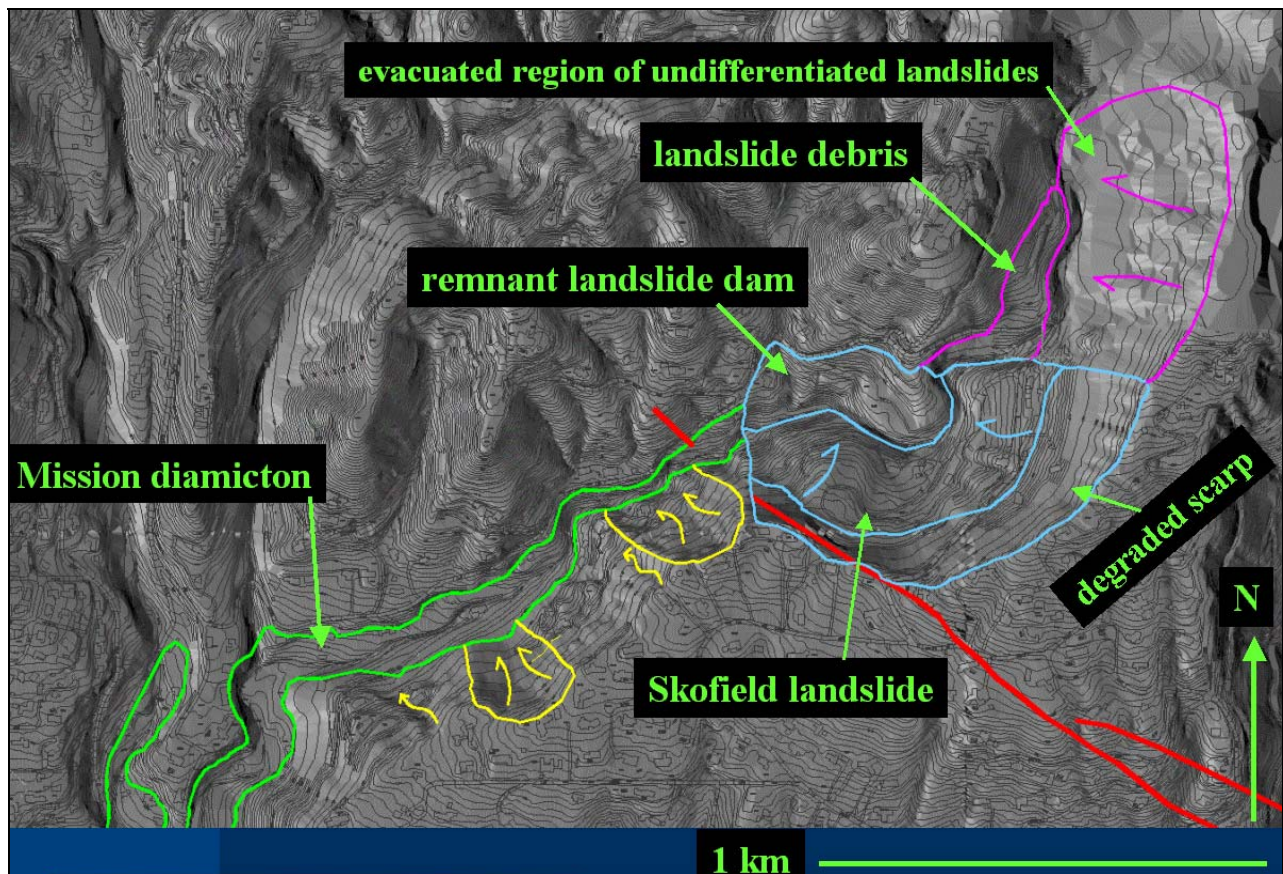


Figure 5. Photo-realistic render of Rattlesnake Canyon. Mission diamicton within green, other large evacuated regions of slope failures indicated by yellow, unnamed fault mapped by Gurrola (2002) indicated by red (no distinction made between concealed/unconcealed fault), Skofield landslide and dam deposits indicated by blue, and region of undifferentiated slope failures and landslide debris presumably related to the failure of the Skofield landslide dam indicated by purple. Topographic contours, streets, and man-made structures indicated by black lines. Figure from Urban (2002).

Sedimentology

The Mission diamicton has many sedimentary characteristics common to modern debris flows. Stream cuts expose generally massive and poorly sorted sediments with a bimodal character consisting of large (0.5m to 7m diameter) sandstone boulders within a matrix of finer sediment that ranges from clay to cobble size material (Urban, 2000; Selting and Urban, 2001). The matrix-supported fabric is dominated by sand size particles. Though the deposit generally lacks internal structure, local preservation of inversely graded debris flow depositional sequences are preserved (Fig. 6) (Urban, 2002). The gross Mission diamicton is inversely graded with the largest diameter boulders concentrated near or at the surface of the deposit.

Large tan to gray arkosic sandstone boulders are the dominant boulder type in the Mission diamicton. The boulders are predominantly sub-rounded but also occur as sub-angular. Arkosic sandstone boulders, characteristic of the Coldwater formation origin, are present in the Mission diamicton. Other boulder clasts originating from the Juncal, Matilija, and Sespe Formations are

present in the Mission diamicton but are not as ubiquitous as Coldwater formation clasts. The Mission diamicton has a remarkable lithologic similarity to sediments present in the nearby mid- to late-Pleistocene fanglomerate deposits (Urban, 1999; Selting 2000). Weathering rinds on the Mission diamicton boulders are typically ablated and replaced with lichen growth. One of the distinguishing characteristics of Mission diamicton boulders from nearby fanglomerate deposit boulders is that the majority of the Mission diamicton boulders lack oxidation-weathering rinds found on fanglomerate boulders (Fig. 7) (Urban, 2002). It appears that mobilization of the fanglomerate boulders could ablate the weathering rinds of fanglomerate boulders and form the deposits of the Mission diamicton.



Figure 6. Multiple debris flow sequences exposed in the Mission Creek stream-cut near the confluence with Rattlesnake Creek. Rock hammer, separating two debris flows in the Mission diamicton, is for scale. Here is a classic debris flow sedimentary sequence of fine grain materials followed by inversely graded clasts in fine-grain matrix. At the top of this sequence and out of the photograph range are the large clasts such as those depicted in Figure 7. Figure from Urban (2004).

The large boulders pepper the surface of the Mission diamicton and depositional features indicating debris flow deposition include boulder berms such as the clast-supported boulder berm that is located at the entrance of Rocky Nook Park (Fig. 8). The large boulders of the Mission diamicton are concentrated near or at the surface of the deposit as identifiable in stream cut exposures and resistivity data (Fig. 9) (Urban, 2003 and 2004).



Figure 7a. Weathering rinds missing from the Mission diamicton boulders in this boulder berm are replaced by lichen growth. Hammer in red circle for scale. Figure from Urban (2004).



Figure 7b. Weathering rinds present on the fanglomerate deposits. Silver camera in red circle for scale. Figure from Urban (2004).



Figure 8. Boulder berm located at the entrance to Rocky Nook Park. For scale, the author is sitting on one of the Coldwater formation clasts that are both of typical size and type for clasts on the surface of the Mission diamicton piedmont deposits. Boulder berms are associated with debris flow deposition. Figure from Urban (2004).

Morphology

The morphologic expression of the Mission diamicton on the piedmont is typical of many modern debris flows. It is characterized by both digitate and lobate morphology, with the relatively flat-topped lobes sloping gently to the south and southwest and having blunt and terminal margins. Selting (2002) offers an interpretation of debris flow deposition based on morphology. However, Urban (2002) identified that the morphologic lobes do not typically occur with paired boulder levees that would delineate the boundary of actual depositional lobes. It is possible that flood and outwash waters could have channelized an individual lobe to give the morphologic expression of two or more debris flow lobes (Urban, 2002). The high-resolution 0.66m DTM generated by Urban (2002) depicts compound lobes that were once believed to be singular debris flow lobes as visible on the 3m grid DEM (Fig. 2).

The subtle morphologic features of the Mission diamicton are obscured by urban development throughout most of the areal deposit extent. But owing to the low level of human disturbance, the best-preserved debris flow morphology is found in Rocky Nook Park where boulder

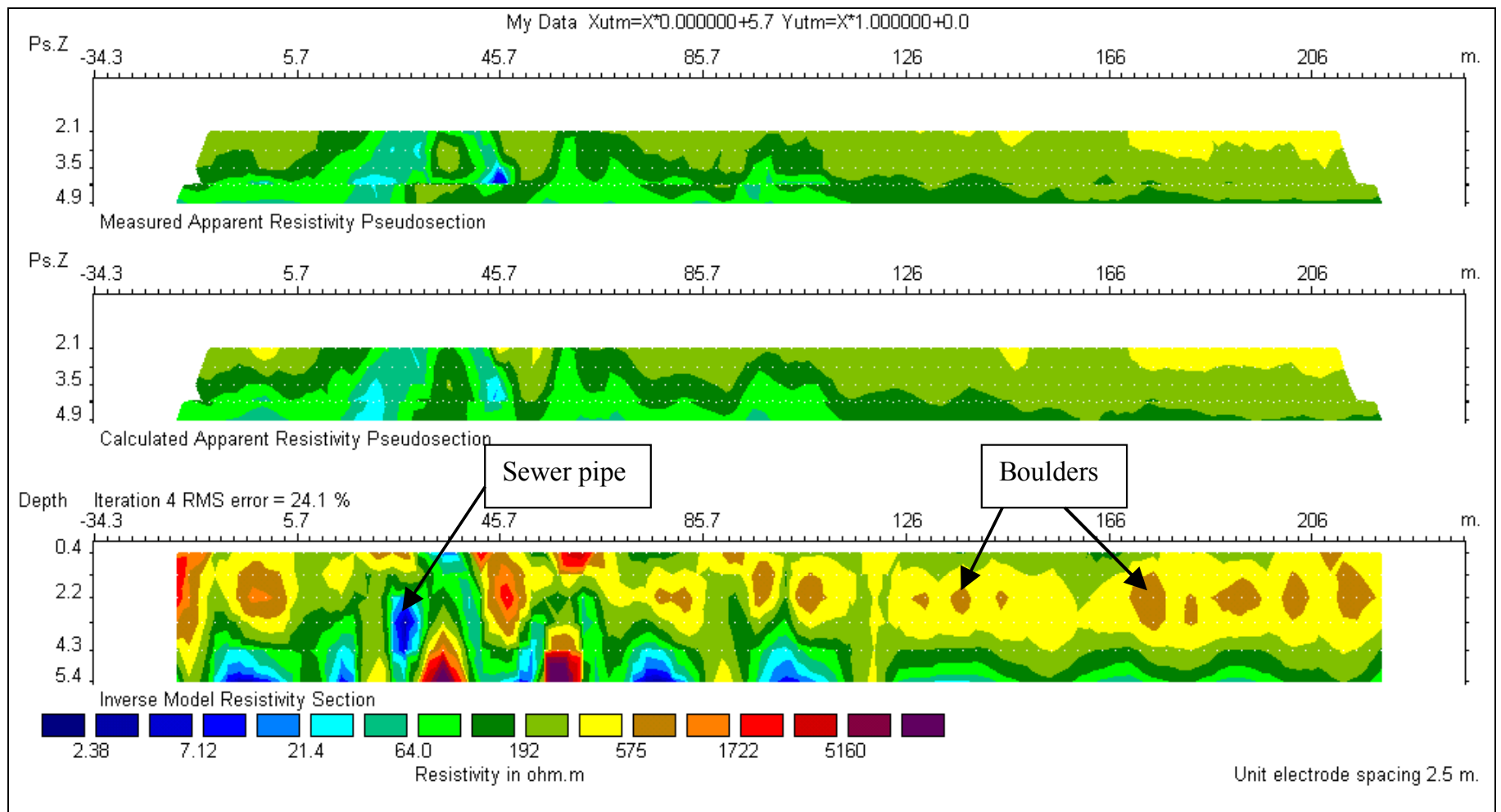


Figure 9. Resistivity Pseudosections and Model resistivity section. Resistivity survey approximately parallels seismic refraction surveys 1008 to 1007 from left to right. Figure from Urban (2004).

levees, abandoned channels, and coarse terminal lobes can be identified at the surface. Lobes with 1m to 5m high boulder fronts and flanks and paired levees that outline former channels are traceable through the park up to 100m.

In Rattlesnake Canyon, the morphology of the Mission diamicton is typically less complicated than its piedmont counterpart. The debris flow deposits generates boulder terraces 3 to 6 m above the active stream channel. The 80m average width fill terraces have identifiable morphology on the 0.6m DTM generated by Urban (2003) (Fig. 5).

BULK SOURCE OF THE MISSION DIAMICTON: SKOFIELD LANDSLIDE

The identification of a source area or areas is an important step towards understanding the origin of the Mission diamicton. Any location proposed as a source must at least satisfy the following criteria. First, the proposed source(s) must be in a location that agrees with the mapped extent of the flow. Second, the source(s) must be capable of producing the sedimentary characteristics of the Mission diamicton. Third, the source(s) must be capable of producing a volume of debris of the same order of magnitude as the Mission diamicton. A large landslide and additional areas of slope failure in the vicinity of Skofield Park satisfies all three criteria and offers engaging insight into the origin of the deposit.

The Mission diamicton can be traced from the piedmont up Rattlesnake Canyon to the vicinity of Skofield Park (Fig. 3). The deposit is absent just beyond Skofield Park. Morphological examination of the upper drainage basin reveals a scarp and remnants of an old and historically inactive landslide, herein named the Skofield landslide. Urban (2002) identified an additional exhumed landslide area is just north of and in addition to the Skofield landslide (Fig. 3). Located on the southeast side of Rattlesnake Canyon, a large arcuate scarp defines the edge of a bowl shaped depression that is the Skofield landslide.

The Skofield landslide and adjacent area of slope failures displaces and exposes a large volume of coarse-grained fanglomerate from the canyon rim onto the canyon bottom. This fanglomerate is the uplifted remnant of an old alluvial fan system. For the purpose of this study, the uplifted fanglomerate extends from the bluff above Skofield Park, south to the Santa Barbara piedmont where the fanglomerate is folded by the Mission Ridge fault into an elongated anticlinal and westerly propagating ridge.

Sedimentary similarities

Table 1 (modified from Selting and Urban, 2001) compares the sedimentary features of the uplifted fanglomerate and the Mission diamicton. This table highlights several similarities between the two deposits. Both of the deposits are coarse grained and poorly sorted. The fanglomerate has the appropriate clast sizes to produce the boulders within the Mission diamicton. However, boulders in the Mission diamicton typically are more subrounded than fanglomerate counterparts. The sedimentary characteristics of the deposits have enough similarity to indicate that the fanglomerate was a viable source of sediment for the Mission diamicton.

There are some differences between the fanglomerate and the diamicton. Weathering rinds that are typical of fanglomerate boulders are often ablated and replaced by lichen growth on the Mission diamicton boulders. It appears that mobilization of the fanglomerate could produce the Mission diamicton. The Mission diamicton typically has a higher percentage of matrix as compared to the fanglomerate. Mission diamicton locally preserves reddish toned matrix not attributable to direct oxidation but rather to the coloration inherent in source material. Interestingly, a significant portion of the exhumed region at the Skofield landslide must have been derived from Sespe

formation bedrock, which has reddish colored sandstone, siltstone, and claystone beds (Figs. 10 and 11).

TABLE 1		
Sedimentary Feature	Mission Diamicton	Fanglomerate
Coarse or fine grained deposit	Coarse	Coarse
Degree of sorting	Poor	Poor
Bimodal character	Yes	Yes
Fabric	Matrix supported	Matrix supported
Range of particle size	Large boulders to clay	Large boulders to clay
Dominant rock type of boulders	Gray to buff arkosic sandstone	Gray to buff arkosic sandstone
Matrix composition	Sand to cobble with minor fines	Sand to cobble with minor fines
Degree of boulder rounding	Dominantly sub-rounded	Sub-angular to sub-rounded
Grading	Mass inverse, locally inverse	Some, inverse and normal

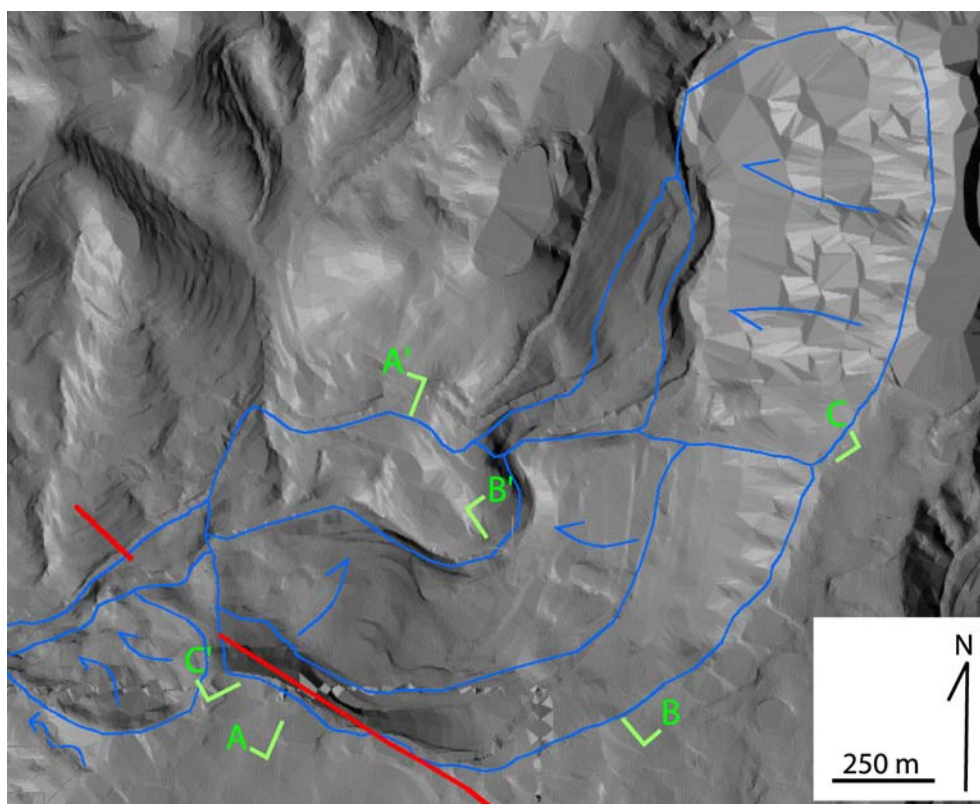


Figure 10. Photo-realistic render of the Skofield landslide region. Landslide and landslide deposits depicted within blue area. Unnamed fault mapped by Gurrola (2002) indicated by red line with no distinction between concealed/unconcealed. Tick points for cross-sections in Figures 11 and 13 indicated with green. Figure from Urban (2004).

Volumetric Similarities

Volumetric calculations for the Mission diamicton and Skofield landslide and adjacent area of slope failures indicate that both volumes are of the same order of magnitude. Topographic profiles of the Skofield landslide were used to approximate pre-slope failure canyon topography (Fig. 11). The exhumed volume in the area of the Skofield landslide and region of slope failures just to the north was accomplished with the use of the AutoDesk Land Development Desktop, a program

used routinely in the consulting industry for cut-and-fill volumetric calculations (Urban, 2003 and 2004). These volumetric calculations incorporated source areas not previously identified by earlier estimates of source volume (Urban, 2000; Selting 2002).

The volumetric calculations presented herein are of the Skofield landslide and area of slope failures adjacent to the north and adjacent to the Skofield landslide (Urban, 2003). The calculations involve generating and comparing a 3-dimensional triangulated irregular network (TIN) of both the modern day topographic surface and an interpreted paleosurface. The pre-slope failure topography was interpreted by joining the termination points of the Skofield landslide head scarp crown. The general trend of Rattlesnake Canyon was used to estimate the projection of the paleoslope trend in the area of slope failures just north of the Skofield landslide. Existing topography was joined to the interpreted trends of the canyon rim paleosurface in the Skofield landslide area. Figure 12 depicts the TIN for the interpreted paleosurface in the Skofield landslide area.

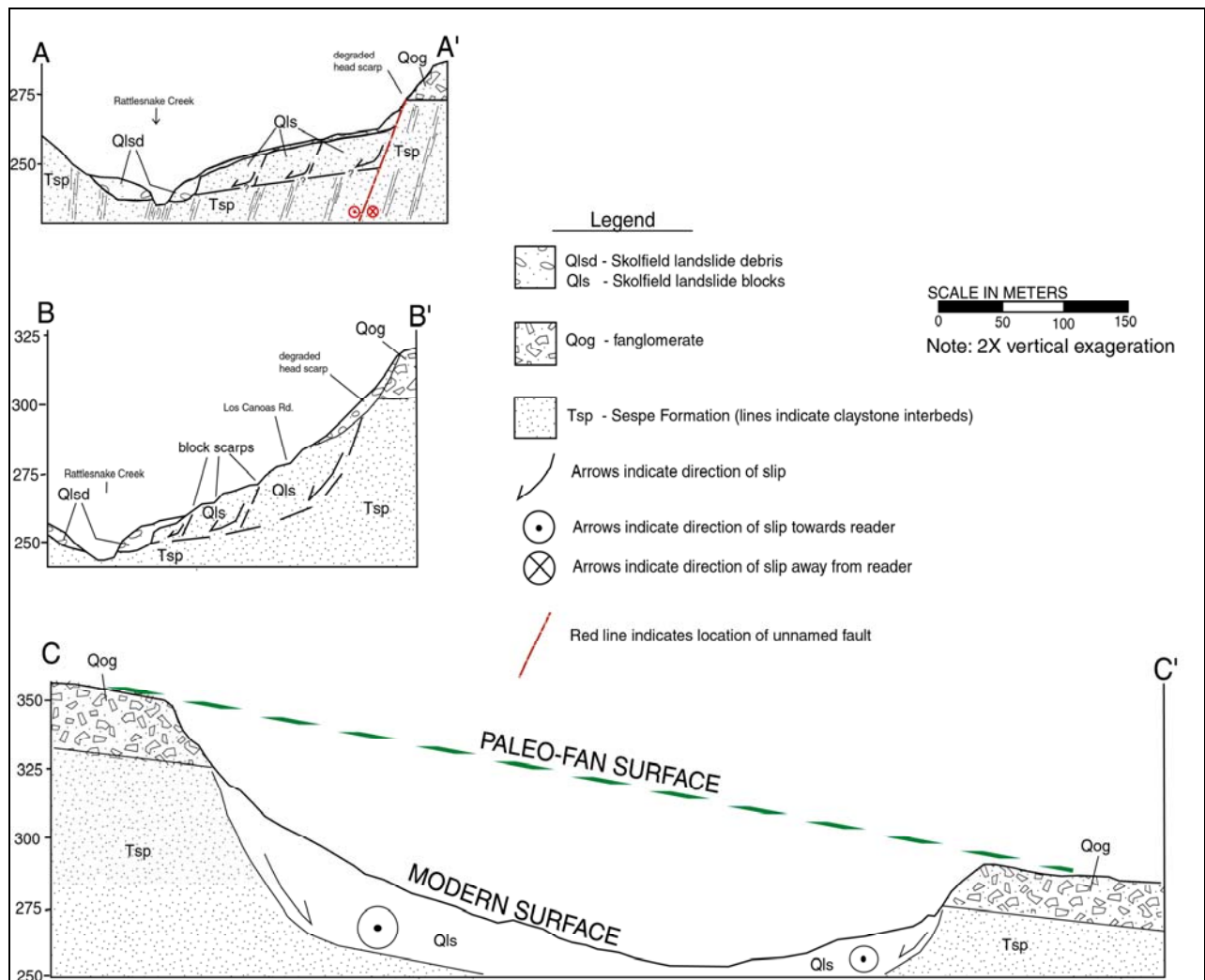


Figure 11. Diagrammatic cross-sections of the Skofield landslide region. Landslide debris has similar sedimentologic characteristics as the spatially higher fanglomerate deposits (see sections A and B). Basal failure plane of the Skofield landslide is unknown. Figure from Urban (2002).

The total exhumed volume of material in the Skofield landslide area is calculated to be approximately $10.3 \times 10^6 \text{ m}^3$ (Urban, 2003). The calculated amount of exhumed material from the Skofield landslide area ($10.3 \times 10^6 \text{ m}^3$) is larger than the calculated volume of material present in the

Mission diamicton ($9.21 \times 10^6 \text{ m}^3$). If any natural topographic modification was applied to the interpreted paleosurface utilized in the Skofield landslide area volumetric calculations, then the volume would decrease and more closely match the Mission diamicton calculated volume. However, the volumetric calculations for both the hypothesized primary source and deposits differ only by approximately 11-12% and indicate good volumetric correlation.

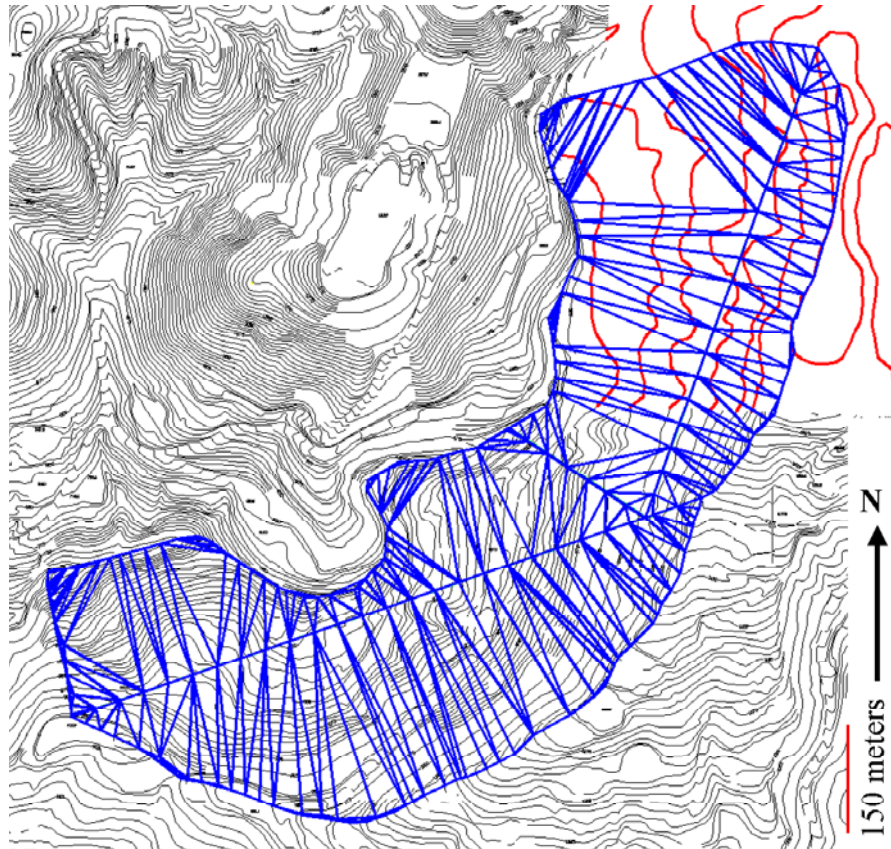


Figure 12. Triangulated-Irregular-Network (TIN) of the Skofield landslide region. Topographic contours indicated by black lines. USGS topographic contour intervals, approximately 12 meters (40 feet), digitized from USGS Santa Barbara Quadrangle are indicated by red lines. The TIN is indicated by blue lines networking into triangles that represent the three-dimensional paleo-topographic surface. The TIN depicts the paleo-topographic surface interpreted for the Skofield landslide region prior to slope failures. Figure from Urban (2004).

Skofield Landslide Failure Kinematics

The arcuate head scarp of the Skofield landslide and head scarp of slope failures to the north are distinct in the typically dendritic drainage pattern in the Santa Ynez Mountains (Fig. 5). The body of the Skofield landslide contains smaller sub-blocks separated by scarps that are visible in the field and in topographic profile (Urban, 2000 and 2004; Selting, 2002). Utilizing ground-penetrating radar (GPR), Urban (2003 & 2004) identified bedrock offsets along the body scarps supporting the hypothesis that the Skofield landslide is comprised of multiple sub-blocks. The Skofield landslide has features of a compound and complex landslide that has characteristics of both rotational and translational kinematics (Urban, 2004).

Based on cross sections through the Skofield landslide, failure had to have occurred within the Sespe formation in order to produce the modern topographic setting (Fig. 11) (Urban, 2000). Rockslide slope failures in Rattlesnake Canyon often removes buttressing support and allows for debris sliding in the overlying fanglomerate. It appears that this mode of failure may represent the kinematics of failure for the Skofield landslide area.

Sespe formation rock discontinuity orientations and friction angles were measured in Rattlesnake Canyon near the Skofield landslide. Urban (2003 & 2004) identified that Sespe formation slopes steeper than 30 degrees from horizontal were in excess of their limiting equilibrium for stability by allowing discontinuities with respective friction angles to daylight. In addition,

Urban (2003 & 2004) also demonstrated with limiting equilibrium stability analyses that overlying fanglomerate was unstable when slopes exceeded 30 degrees from horizontal. The geometry of the slope failures for the fanglomerate was typically thin rotational failure. The stability analyses of Rattlesnake Canyon geologic materials indicates that failure of the Skofield landslide was probably along discontinuities constraining Sespe formation block size and progressional rotational failure in the overlying fanglomerate as buttressing support was removed. Figure 13 depicts an interpreted sequence of failure of the Skofield landslide, landslide dam formation, and subsequent landslide dam failure (Urban, 2004).

DEBRIS FLOW ORIGIN OF THE MISSION DIAMICTON

Debris flows generated by the failure of landslide dams have been responsible for extensive loss of life and property throughout the world (Costa and Schuster, 1987). A remarkable example of this phenomenon is the 1985 failure of the Bairaman landslide dam in Papua, New Guinea. The dam formed when a M 7.1 earthquake triggered extensive landsliding in the bedrock of the Bairaman river valley, filling the drainage with $180 \times 10^6 \text{ m}^3$ of debris (King et al., 1989). When it was feared that the temporary lake would overtop the landslide dam, downstream inhabitants were evacuated and the dam was trenched to force its breach. The breach generated a debris flow with an estimated volume of $120 \times 10^6 \text{ m}^3$ that destroyed downstream communities (King et al., 1989).

The morphology and deposits of the Skofield landslide area indicate that the Skofield landslide acted as a dam in the Rattlesnake Creek drainage basin. This landslide dam would have blocked Rattlesnake Creek, producing a temporary lake. Overtopping and resultant incision or mechanical failure of the dam would have sent debris-laden slurry down canyon to be deposited as the Mission diamicton. This interpretation is supported by the presence of an area of anomalous topography and landslide debris found on both sides of Rattlesnake Canyon in the Skofield Park area. The anomalous topography and landslide debris opposite of the Skofield landslide is interpreted as remnants of the landslide dam. Urban (2003) identified fine-grained sediment with macroscopic charcoal fragments that is stratigraphically placed above stream deposits and below landslide debris. These deposits are located a short distance upstream of the remnants of the Skofield landslide dam and interpreted to be deposits from a temporary lake (Urban, 2004). Selting (2002) also identified fine-grained deposits at an elevation above the landslide debris and interpreted these deposits to be from a temporary lake.

Selting (2002) documents additional evidence for the existence of a landslide dam formed by the Skofield landslide. Selting (2002) provided boulder size distribution data that indicates a mean decrease in boulder size in the Mission diamicton from the Skofield landslide to piedmont deposits. In addition, Selting (2002) identified a large nickpoint in Rattlesnake Creek. The nickpoint is located where the landslide dam is believed to have been present (Selting, 2002). Furthermore, the location of the nickpoint coincides with the location of the highest concentration of very large boulders (diameter $\geq 5\text{m}$) in the field area. The concentration of boulders with diameters greater than 3m within the nickpoint is four to six times higher than the concentration at two other sampling locations within Rattlesnake Canyon (Selting, 2002).

A landslide dam in Rattlesnake Canyon would have impounded a lake of unknown size and residence time. The longevity of landslide dams is highly variable and dependent on the geometry of the channel, the size and orientation of the landslide, the type of material making up the obstruction, and the rate of fluvial input into the impounded lake (Schuster and Costa, 1986). In a survey of 63 landslide dam failures, Schuster and Costa (1986) found that 91% of the observed failures occurred within a year of formation. Landslide dams that persisted for longer duration commonly involved large volumes of obstructing debris in a channel that is narrow relative to the

size of displaced material. In general, material that was well graded (engineering sense of the term, an even distribution of a large range in particle sizes) and had a larger mean particle size was most stable (Schuster and Costa, 1986). Debris dams composed of well-indurated bedrock also tend to be more stable than those dominated by soil and soft rock (Schuster and Costa, 1986).

The Skofield landslide has many of the characteristics necessary to generate a landslide dam. It is likely that the proposed landslide dam lasted long enough to impound a lake that reached into the upper Rattlesnake Creek drainage basin. Such an impounded lake appears to have lasted long enough to develop fine-grained lacustrine deposits still preserved upstream of the Skofield landslide.

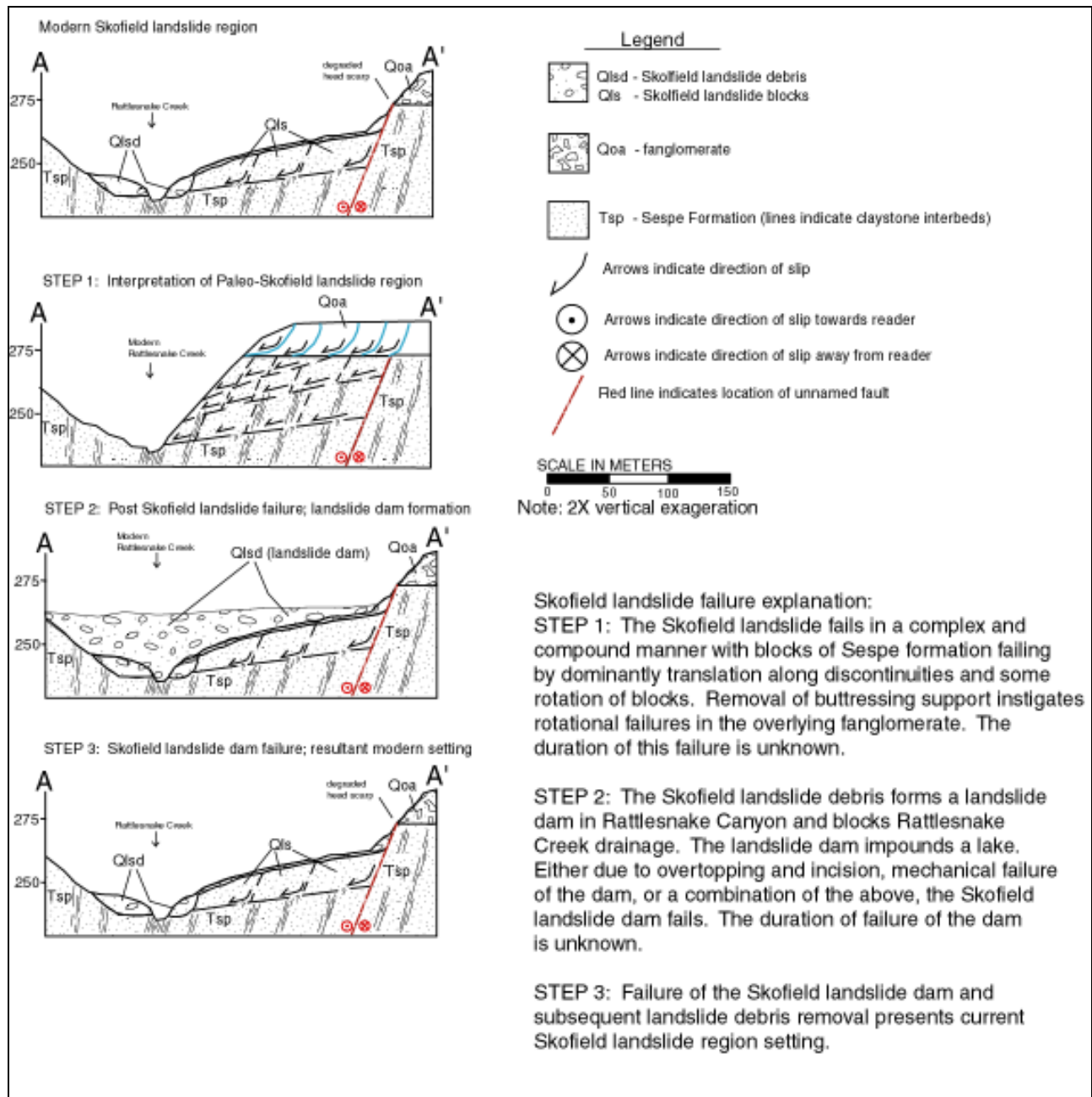


Figure 13. Diagrammatic cross-sections of the Skofield landslide failure. Section A to A' is located on Figure 10. The diagrammatic cross-sections illustrate the compound and complex kinematics of the Skofield landslide failure and the formation of the Skofield landslide dam. Figure from Urban (2004).

AGE OF THE MISSION DIAMICTON AND SKOFIELD LANDSLIDE

The absolute age of the Mission diamicton is important for understanding conditions that were conducive to generation of this deposit and evaluating the geohazard posed by the deposit to the City of Santa Barbara. Selting and Urban (2001) indicate that the Mission debris flow is younger than the presence of Mission Ridge (Figure 3). The Mission Ridge geomorphic feature is being formed by uplift and faulting associated with fault propagation for the More Ranch-Mission Ridge fault system. By calculations of regional folding and uplift rates of marine terraces, Gurrola et al. (1999) estimate that Mission Ridge was in place by 45 ka. Keller (1999) documents an abandoned paleochannel of Mission Creek exists between the Santa Barbara Mission and Rocky Nook Park. The lack of debris flow deposits in this paleochannel is evidence that Mission Ridge had already been in place and Mission Creek was diverted to its current position due to the westerly propagating Mission Ridge.

Based on the geophysical investigation by Urban (2002 & 2003), the paleosurface on which the Mission diamicton rests is approximately half of the elevation of the portions of Mission Ridge just to the east. The orientation of the geologic contact between the Mission diamicton and underlying fanglomerate deposits is not congruent with the slope of the modern day topographic surface of the Mission Ridge or piedmont regions out of the study area. If the Mission diamicton was deposited at the early stages of the Mission Ridge development, then the geologic contact between the Mission diamicton and underlying fanglomerate deposits should be oriented congruent with the modern topographic surfaces expressed in nearby portions of Mission Ridge. But the slope orientation of the geologic contact between the Mission diamicton and underlying geologic materials is not congruent with the modern topography of nearby Mission Ridge regions.

Geometric relationships of the Mission diamicton and topographic slopes of nearby portions of Mission Ridge and alluvial slopes to the west of Mission diamicton piedmont deposits imply that the Mission diamicton was deposited on a topographic surface which was very near the elevation of the geologic contact between the Mission diamicton and underlying materials. The geometric and geologic relationships and uplift rates of Mission Ridge suggest that the Mission diamicton is actually less than 22.5 ka.

Additional evidence that the Mission diamicton is much younger than 45 ka is the pristine morphology of the debris fan comprised of the Mission diamicton and the weakly developed soils from the Mission diamicton. The Mission diamicton piedmont deposits compose a debris flow fan with pristine morphology depicting debris flow lobes. In addition, weak A horizon soils have developed on the Mission diamicton. Keller (2002 personal commun.) believes that the weakly developed soils indicate that the Mission diamicton is less than 10 ka.

Modern historical records do not document the occurrence of the geologic processes such as a large volume debris flows in the region where the Mission diamicton is now deposited. No reports indicating a large landslide or a debris flow exist from written records as early as 1782 when the settlement of non-indigenous people to the Santa Barbara region began (Selting and Urban, 2001). The age of the Mission diamicton is therefore definitely younger than 45 ka but older than 1748 A.D. Weakly developed soils suggest that the Mission diamicton may be Holocene in age.

Radiocarbon Dating

Constraining the age of the Mission diamicton is important for understanding and evaluating the geologic hazards posed by the deposit to the City of Santa Barbara and nearby region. The benefits of absolute dating the Mission diamicton include further constraining the depositional age of

the deposits, which can then be used to assess paleo-environmental conditions that influenced the genesis of the deposits. Paleo-environmental conditions that may have influenced the genesis of the Mission diamicton include the climatic regime(s), seismic inputs, and/or external perturbations such as a fire.

Because of the importance in further constraining the age of the Mission diamicton in terms of evaluating the geologic hazards posed by the deposits, field collection of charcoal samples for radiocarbon dating was accomplished (Urban, 2003 and 2004). A total of 10 bulk samples of sediment to pick microscopic charcoal, two samples with visible charcoal pieces, were collected from the Mission diamicton and one from interpreted lake deposits stratigraphically below Skofield landslide debris. Because of costs associated with radiometric dating, only two of the samples could be absolute dated. The two samples dated were chosen based on geologic relationships that could best constrain the age of the Skofield landslide failure and one debris flow levee in the Mission diamicton.

At the two chosen sample locations, visible pieces of detrital charcoal were collected. At one location, a charcoal sample was collected from a sandy clay horizon identified and interpreted by Urban (2003 and 2004) to be deposits from a temporary lake and are stratigraphically just below Skofield landslide debris. At a second location, a sample was collected from a debris flow levee deposited directly on Sespe formation bedrock and just downstream of the Skofield landslide (Urban, 2004).

Radiocarbon Dating Results

The charcoal samples were dated using radiometric methods and results provided by the Center for Accelerator Mass Spectrometry (CAMS), Lawrence Livermore National Laboratory, Livermore, California. The U. S. Geological Survey provided funding for radiometric dating of the charcoal samples. Sample 02-01-03-A1-K was collected within landslide debris near the toe of the Skofield landslide and is reported as an age of 1000 ± 40 years. Sample 01-20-03-B1-H was collected within a singular debris flow deposit of a channel levee downstream of the Skofield landslide in Rattlesnake Canyon and is reported as an age of 1460 ± 40 years. The radiocarbon dates were calibrated by Gurrola (2004 personal commun.) utilizing the OxCAL radiocarbon calibration program. Sample 02-01-03-A1-K is dated to have originated with a 95.4 percent probability between 970 and 1160 AD. Sample 01-20-03-B1-H is dated to have originated with a 95.4 percent probability between 530 and 670 AD.

The ages of the samples indicate that the formation of a landslide dam in the Skofield landslide region and debris flows of the Mission diamicton was occurring at the time when indigenous people, the Chumash, were in the area (Urban, 2004). No known reports or heritage of a story indicate a singular large catastrophic landslide or debris flow event that would be characterized by the entire Mission diamicton if the deposit represents a single debris flow event. Though, documentation of a Chumash story or report of a singular debris flow event does not exclude the possibility of such an event.

The following scenarios, proposed by Urban (2004), can resolve the radiocarbon age difference between the Skofield landslide and the Mission diamicton.

- 1) The youngest radiocarbon date is approximately when the formation of the Skofield landslide dam and Mission diamicton occurred. The older radiocarbon date represents a piece of charcoal approximately 400 years older than the age of the Mission diamicton.
- 2) The Skofield landslide dam was a long-lived feature that either failed much later than its formation or provided episodic debris flows over a long duration.

- 3) The formation and failure of landslide dams in Rattlesnake Canyon occurs episodically in a variety of magnitudes and the failure of the Skofield landslide dam is one such large event.

DISCUSSION

The bulk of the Mission diamicton is believed to have been deposited as the Mission debris flow, resultant from the failure of a landslide dam formed by the Skofield landslide. The failure of the landslide dam is of an unknown duration but occurred at least in part approximately 1,000 years ago.

Evidence of two other large exhumed landslides, located downstream of the Skofield landslide area, in Rattlesnake Canyon have been mapped by Urban (2003 & 2004) (Fig. 5). The landslide debris that would be represented by the size of these landslides is not present in Rattlesnake Canyon. Presumably, these landslides would have blocked the narrow and confined Rattlesnake Canyon topography and formed landslide dams that would have failed, sending debris flows out onto the Santa Barbara piedmont and deposited as part of the Mission diamicton.

Other diamictons are present on the Santa Ynez piedmont and are interpreted to have originated from debris flows. Borchardt et al. (1982) and Schlemmon (1980) describe an A2 soil horizon in the Point Conception region to the west of Santa Barbara, with physical properties characteristic of a diamicton, which is thought to have originated from a mudflow approximately 1,000 years ago. The presence of the Point Conception diamicton may indicate climatic and/or seismic conditions conducive to mudflow and debris flow initiation at this time.

The combination of the young age of the Mission diamicton and the Point Conception diamicton, described by Borchardt et al. (1982) and Schlemmon (1980) suggest regional conditions conducive to slope failure and debris flow initiation. Both diamictons have similar ages of approximately 1,000 years old. The presence of the two diamictons suggests that either climatic and/or seismic conditions were available in the Transverse geomorphic provenance at this time. Both wet conditions such as a severe rainstorm and a seismic event are capable of initiating slope failures that could result in a debris flow. Evidence of the two young debris flow events in the region indicates a geohazard warranting evaluation.

The Mission diamicton highlights the hazards associated with the urbanization of proximal areas of alluvial fans, as seen in Santa Barbara. Such areas are commonly subjected to the periodic flushing of coarse sediment derived from the hillslopes and floors of the drainage basin. Evidence of other diamictons, representative of debris flow origin, in the region indicate a regional hazard. At least a bulk of the Mission diamicton is represented by sediment derived from a single landslide dam. The occurrence of this type of large event should remind the geologist or urban planner that mass movements on all scales are prevalent in the steep headwaters of the south flank of the Santa Ynez range. Such slope failures are eventually transmitted down basin to the urbanized piedmont with the potential for catastrophic consequences.

GEOHAZARD EVALUATION

The Mission diamicton represents large volume debris flows that principally originated as the result of the failure of a landslide dam formed by the Skofield landslide. The geohazards identified by this study and posed by the Mission diamicton include: slope failures, landslide dam formation and failure, and debris flows resultant of the failure of landslide dams. Residential development and public infrastructure of both the City and County of Santa Barbara are within the immediate

boundaries of the geologically related features, the Mission diamicton and Skofield landslide region. Over 300 residential homes and public infrastructure is now within the approximate 1 square kilometer region of the Mission diamicton piedmont deposits. Numerous residential homes within Rattlesnake Canyon are located on debris flow fill terraces and on or located within potentially affected regions by slope failure.

Landslide dams have historically affected residents of the Santa Barbara region. A modern natural landslide dam in nearby Los Positas Creek has been documented by Keller (1999). Evans and DeGraff (1997) estimate that almost half of all fatalities resulting from major landslide disasters of the twentieth century are related to natural landslide dam failures. Because the Santa Barbara region has now been identified as having a history of landslide dam formation and because landslide dams have a disproportionate weight in affecting the life and property of humans, the need to evaluate the geologic hazards posed by the Mission diamicton is mandatory.

Geohazard evaluation requires identification of geologic phenomenon occurring (or may occur) in a region that can or may affect or cause effect on inhabitants. As part an investigation to evaluate the geohazards posed by the Mission diamicton, Urban (2003 and 2004) performed field identification of geologic hazards and collection of data for a quantitative geohazard analysis. This analysis is summarized herein.

The Sespe formation in Rattlesnake Canyon has ubiquitous joints (fractures) observable in outcrop. Rock slope failures are identifiable in Rattlesnake Canyon and failure in the Sespe Formation has allowed mobilization of overlying fanglomerate deposits. Some of these slope failures have impeded portions of the Rattlesnake Canyon drainage.

Sespe Formation Rockslide Analysis

A field reconnaissance collection of joint and bedding orientations was accomplished according to the methods of Nickelsen and Hough (1967) and performed a kinematic analysis of rock slope stability (Urban, 2003 and 2004). The cone of friction for discontinuities was determined by collecting representative samples of joints where discontinuity orientation were measured. Joint sets were tested for friction angle according to Markland's Test.

Each discontinuity set had at least one sample that has a minimum friction angle value of 30 degrees. Therefore, a cone of friction of 30 degrees was used in the geohazard analysis of rock slope stability for all of the discontinuity sets. An equal area stereonet projection of joint and bedding orientations and the cone of friction was determined for discontinuities. The equal area stereonet projection of discontinuities and cone of friction allows the direct observation that there is the potential for wedge and planar failure of the Sespe formation within Rattlesnake Canyon. The geometric relationships conducive for each type of failure, either wedge or planar, with respect to discontinuity sets was queried in ESRI's ArcView 3.2 GIS environment to identify all slopes within Rattlesnake Canyon with appropriate slope angles and aspects that allow discontinuities to daylight.

Fanglomerate Landslide Analysis

An analysis of landslide potential for fanglomerate materials was also accomplished for evaluating slope failure potential (Urban, 2003 and 2004). Because modern debris slides were evident in 1995 aerial photographs after severe rainstorms, a limit equilibrium slope stability analysis of circular and irregular shaped failure surfaces was accomplished. Geotechnical data from geotechnical consultant reports were collected at the City of Santa Barbara Public Works offices and utilized for the slope stability analysis.

The fanglomerate materials in Rattlesnake Canyon were analyzed according to limit equilibrium slope stability methods utilizing the Bishop method for circular failures and the Janbu

method for random failure surface geometries. The pre- and post-processor STEDwin 2.74, developed by Harold Van Aller, was used for inputting geotechnical data and slope geometries as well as generating the graphical presentation of the results of the stability analyses. STEDwin utilizes the slope stability analysis software PC STABL, developed by Purdue University, which is a geotechnical and academia tested computer program for solving two-dimensional limiting equilibrium slope stability methods. PC STABL and STEDwin are commonly used software programs in the geotechnical and engineering geology professions for the analysis of slope stability.

Fabricated slopes consisting of geotechnical data obtained from geotechnical consultant data for the fanglomerate were input into STEDwin for analysis. For geohazard evaluation purposes, the most conservative estimation of the level of geohazard or identification of slope failure potential was accomplished by using the weakest shear strength of the geologic materials. Slope angles for the fanglomerate materials were increased and analyzed for both Janbu and Bishop methods, respectively, until the factor of safety became less than one (1). At a slope angle when the factor of safety became less than one, the driving forces have become greater than the resisting forces to slope failure and therefore the slope is in a state of disequilibrium. The slope angle for which the fanglomerate materials are in a state where forces driving slope movement exceeds forces resisting slope movement, and therefore critical state of failure, is determined to be 30 degrees. A query in ESRI's GIS program ArcView 3.2, identifies all slopes at or exceeding 30 degrees in the fanglomerate materials and identifies locations of all slopes that are at or exceeding their respective critical orientation for failure.

Both the results of the rockslide analysis of the Sespe formation and limit equilibrium methods analysis of fanglomerate materials were queried in the ArcView GIS environment to identify all slopes within Rattlesnake Canyon on the 3m grid DEM that are either at or exceeding their respective critical orientations for failure. The spatial distribution of slopes that are at or exceeding their critical orientation for failure as determined by this analysis is presented in Figure 14.

Slope Stability Geohazard Evaluation Limitations

Though the geohazard evaluation of slope failure potential in Rattlesnake Canyon identifies various regions with slopes that are either at or exceeding their critical orientation for failure, there are a few limitations to this slope stability geohazard evaluation method. The slope stability analysis of fanglomerate material slopes is limited by the type and availability of geotechnical data on the fanglomerate materials. Geotechnical data available for the fanglomerate materials at the City of Santa Barbara Public Works is limited in areal extent. The limitation that this presents in this slope stability analysis is that the available geotechnical data may not accurately characterize the distribution of shear strength for the fanglomerate materials throughout Rattlesnake Canyon. Also, the samples from which density and shear strength information were used in the analysis were at depths less than the total depth of the fanglomerate slopes analyzed for stability. If samples were collected at varying depths and their appropriate geotechnical information are input into the stability analysis, the global slope stability analysis results could change. In addition, shear strength data collected for the fanglomerate may have only originated from samples collected from the fanglomerate matrix. The additional shear strength that would be gained by adding large diameter clasts is not incorporated into this stability analysis.

Though there is the limitation of the amount and type of sampling used in the analysis of the fanglomerate slope stability analysis, it is the belief that the slope stability analysis presented herein is a good first order approximation to the stability of slopes in Rattlesnake Canyon. The slope stability analysis and identification of slopes at or exceeding their critical orientation for failure

identifies that slopes in Rattlesnake Canyon warrant the need for further investigation of the slope failure geohazard in this region.

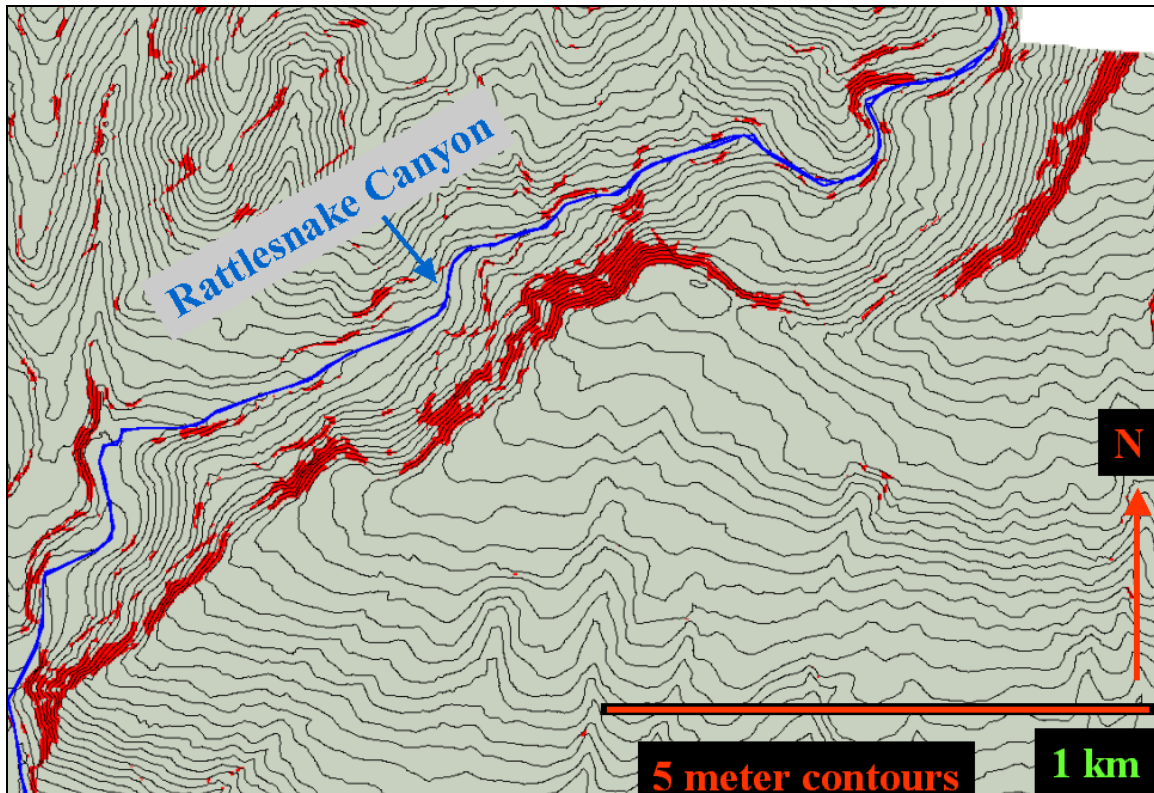


Figure 14a. Geographic information system (GIS) analysis of critically oriented slopes in Rattlesnake Canyon. Red zones are locations where slopes are at or exceeding the critical orientations according to the limit equilibrium slope stability analysis of Sespe formation and fanglomerate slopes. Figure from Urban (2004).

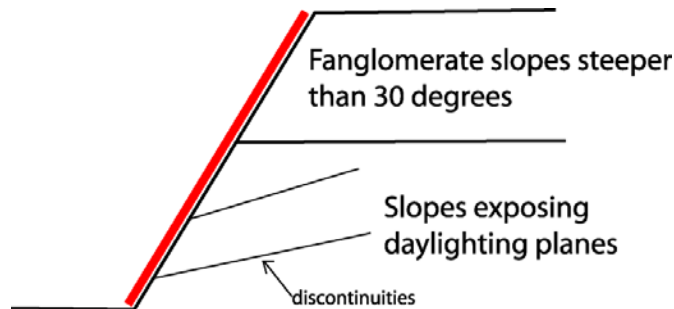


Figure 14b. Diagrammatic cross-sectional sketch of slopes orientations identified as red zones in Figure 14a. Figure from Urban (2004).

Geohazard Evaluation Discussion

The slope stability geohazard evaluation identifies slopes that are either at or exceeding their respective critical orientations for failure. The identification of slope failure potential in Rattlesnake Canyon indicates that the potential for landslide dam formation exists and subsequently geologic events represented by the Mission debris flow and cumulative Mission diamicton have a modern potential to occur. Rattlesnake Canyon, as well as the vast majority of canyons in the Santa Ynez mountain range, is narrow and confined with steep slopes. Narrow and confined canyons with steep

slopes are conditions which Costa and Schuster (1987) identify as conditions that are conducive to the formation of landslide dams.

CONCLUSIONS

The Mission diamicton produces a unique landform in the Santa Barbara Urban Corridor. The debris flow deposits that comprise the Mission diamicton can be traced to the location of the Skofield landslide in Rattlesnake Canyon. The sedimentary characteristics of the Mission diamicton indicate that its clast and matrix components were primarily derived from fanglomerate and Sespe formation in the upper Rattlesnake Creek drainage basin. Sespe formation bedrock failure mobilized overlying fanglomerate onto the canyon floor. The remnants of this landslide, the Skofield landslide, are still visible in the field, on digital models of the area, and in cross section. The volume of landslide debris evacuated from this location is of the same order of magnitude as the Mission diamicton as determined through geophysical investigation and 3-dimensional volumetric modeling.

The role of landslide dams in debris flow generation is well documented. Large damaging debris flows also occur without the necessity of a landslide dam, provided sufficient water and sediment are available, but that explanation does not appear to fit the characteristics of the Mission diamicton and Skofield landslide. The topography of the upper Rattlesnake Canyon, and the properties of the Skofield landslide have characteristics amenable to landslide dam formation. These include location in a narrow confined canyon and the presence of a large volume of coarse-grained debris. Based on evidence collected by the authors, we conclude that the bulk of the Mission diamicton originated from the breach of a landslide dam generated by the Skofield landslide.

The young age of the Mission diamicton and Skofield landslide, as well as regionally proximal diamictons of debris flow origin, suggest a regional hazard under modern climatic conditions. A quantitative geohazard evaluation of Rattlesnake Canyon identifies slopes that are at or exceeding their critical orientation for stability. Unstable slopes in Rattlesnake Canyon could provide landslides able to block the narrow and confined canyon topography, forming landslide dams. These landslide dams could then fail and provide debris flows that could travel onto areas inhabited by residents of the City of Santa Barbara.

ACKNOWLEDGEMENTS

The authors would like to thank Dr. E.A. Keller for introduction to this project, guidance, and insight.

Mr. Urban would additionally like to thank: Dr. John W. Williams and Dr. Donald Reed at San Jose State University for technical and general enlightenment; Dr. Debbie Harden for geomorphic discussion; Rob Huggins, Craig Lippus, and Douglas Groom at Geometrics, Inc. for generously donating geophysical instruments and software for the geophysical investigations; Mr. Harold Van Aller for donating STEDWin for performing the slope stability analysis; Scott Minor at the USGS for arranging for radiocarbon dating; field assistants: Jadin Urban, Zoi Urban, Mark Swank, Chanie Wossen, and Kevin Ingham during the geophysical investigations; Amy Berberi for a power supply during the geophysical investigations; Autodesk, Inc. for providing software for terrain modeling; Dr. Arthur Sylvester for teaching the importance of field competence and being rigorous; Larry Gurrola for radiocarbon date calibration and thoughtful discussion in the field; Alphonse Odisho and Ginny Smith at San Jose State University for technical support; and Mae, Jadin, Zoi, and Noelle Urban for easing the challenges of this work.

Mrs. Selting Williams would like to thank Larry Gurrola for his acumen in the field and his vast knowledge of Santa Barbara geology; as well as Tim Tierney, Tom Dibblee, Art Sylvester, Tanya Atwater, and Jim Boles for their guidance, discussion, feedback, and support of this work. I also thank the USGS for financial support of my research and especially Scott Minor and Karl Kellogg of the USGS Earth Surface Processes team. Most importantly: thank you Ted for your support, intellect, and sense of humor; your contributions are immeasurable.

REFERENCES

- Borchardt, Rice, and Treiman, 1982, Mudflow deposition and horizonation in Holocene soils near Point Conception, California [unpublished paper] available at: <http://www.soiltectonics.com/mudflow.htm>
- Costa, J.E., 1986, Physical Geomorphology of Debris Flows, in Costa, J.E., and Fleisher, P.J., eds., Developments and applications of geomorphology: Berlin; New York, Springer-Verlag, p.372.
- Costa, J.E., and Schuster, R.L., 1987, The formation and failure of natural dams: Dept. of Interior, U.S. Geological Survey; Books and Open File Reports distributor, 87-392
- Evans, S.G., and DeGraff, J.V., 1997, Major landslide disasters of the millennium: GSA 1997 annual meeting, Abstracts with Programs, v. 29, no.6, p. 285.
- Gurrola, L.D., Keller, E.A., Trecker, M.A., Hartleb, R.D., and Dibblee, T.W., 1999, Active folding and buried reverse faulting of the Santa Barbara fold belt, California, Coast Geological Society Field Trip Guide Book.
- Gurrola, L.D., 2002, Digital Elevation, Topographic, and Tectonic Geomorphology Map of the Eastern Santa Barbara Fold Belt, Santa Barbara, California, [unpublished Dissertation map]: University of California at Santa Barbara.
- Hoover and Associates, 1984, Summary of Monitoring Well Construction, Mission Canyon Wastewater Facilities Project, available at the City of Santa Barbara Public Works Department.
- Johnson, A.M., and Rodine, J.R., 1984 Debris Flow, in Brunsden, D., and Prior, D., eds., Slope Instability: New York, John Wiley & Sons, Ch. 8 p. 257-361.
- Keller, E.A., 1999, The natural history of Mission Creek: A story of earthquakes and debris flows, available at the Santa Barbara Natural History Museum, p.8.
- King, J., Lovejoy, I., and Schuster, R.L., 1989, The 1985 Bairaman landslide dam and resulting debris flow, Papua New Guinea: Quarterly Journal of Engineering Geology, London, v. 22, p 257-270.
- Nickelsen, R. and Hough, V., 1967, Jointing in the Appalachian Plateau of Pennsylvania: Geological Society of America Bulletin, v.78, p.609-630.
- Schuster, R., and Costa, J., 1986, A Perspective on Landslide Dams, in Schuster, R., ed., Landslide dams: Process, Risk, and Mitigation: Geotechnical Special Publication No. 3: Seattle, American Society of Civil Engineers.
- Shlemon, R.J., 1980, Soil-stratigraphy of the proposed LNG site, Little Cojo Bay, Santa Barbara County, California. Report submitted to Dames & Moore (Los Angeles) on behalf of Western LNG Terminal Associates (Los Angeles), Dames and Moore Job No. 00011-168-02, 26 p.
- Selting, A.J., 2000, Morphology, Process and Hazard of the Mission debris flow: Paper associated with comprehensive exam project. University of California at Santa Barbara.
- Selting, A.J., 2002, The Mission debris flow: an example of debris flow initiation by the failure of a prehistoric landslide dam in Santa Barbara, California [Masters thesis]: University of California at Santa Barbara.
- Selting, A.J. and Urban, R.J., 2001. Investigation of the Mission Debris Flow Deposit, Santa Barbara, California: 2001 Geological Society of America Cordilleran Section Annual Meeting Field Guide.
- Urban, R.J., 1999, Preliminary report of the Santa Barbara massive debris flow and associated natural landslide dam, Santa Barbara, California [unpublished undergraduate individual project thesis]: University of California at Santa Barbara.

- Urban R.J., 2000, The Santa Barbara catastrophic debris flow and associated natural landslide dam failure [unpublished undergraduate individual project thesis]: University of California at Santa Barbara.
- Urban, R.J., 2002, The Massive Mission Debris Flow and Skofield Landslide, Santa Barbara, California: Association of Engineering Geologists Program with Abstracts 2002 Annual Meeting.
- Urban, R.J., 2003, The Debris Flow Origin of the Mission Diamicton and Associated Geohazards to the City of Santa Barbara, Santa Barbara County, California. Presentation to the San Francisco Section of the Association of Engineering Geologists and Association of Engineering Geologists Program with Abstracts 2003 Annual Meeting.
- Urban, R.J., 2004, The Mission Diamicton and Associated Geohazards, Santa Barbara, California [Masters of Science Thesis]: San Jose State University.
- Wells, S.G., and Harvey, A.M., 1987, Sedimentologic and geomorphic variations in storm-generated alluvial fans, Howgill Fells, northwest England: Geological Society of America Bulletin, v. 98, p. 182-198.
- Whipple, K.X., and Dunne, T., 1992, The influence of debris-flow rheology on fan morphology, Owens Valley, California: Geological Society of America Bulletin, v. 104, p. 887-900.

DAY 4: SEDGEWICK RANCH

8:30 p.m. – 3:00 p.m.

Stream capture in the Figueroa-Mountain piedmont: a working hypothesis to explain the morphology of the Lisque Creek drainage basin, Sedgwick Natural Reserve, Santa Barbara County, California

Antonio F. Garcia¹ and Oliver A. Chadwick²

1, Physics Department, Cal Poly State University; 2, Geography Department, University of California, Santa Barbara

The surficial geology of the Sedgwick Reserve south of the Little Pine Fault provides clues regarding the long term drainage-network history of the Figueroa-Mountain piedmont. Lisque Creek is a tributary of Figueroa Creek, which flows from Figueroa Mountain to the Santa Ynez River. A surficial geologic survey of the Lisque Creek catchment was conducted during Summer 1998, which followed the 1997-98 El Niño winter. The survey shows that channelized flow occurred in only a few low order streams. In contrast, Figueroa Creek has been geomorphically active from at least ca. 1.3 ka (radiocarbon years) through the Winter of 1997-98. The absence of a stream channel during years of relatively high precipitation like the 1997-98 El Niño winter suggests that the Lisque Creek trunk valley is underfit with respect to runoff generated in the catchment. One hypothesis that explains the underfit character of the Lisque Creek drainage is that Alamo Pintado Creek captured the upper part of the Lisque Creek drainage. The objective of this excursion is to evaluate this hypothesis by observing and discussing the drainage-basin geomorphology of the Lisque Creek and Figueroa Creek drainages.

A stochastic sediment delivery model for a steep Mediterranean landscape

Emmanuel J. Gabet

Department of Geology, University of Montana, Missoula, Montana, USA

Thomas Dunne

Donald Bren School of Environmental Science and Management and Department of Geological Sciences, University of California, Santa Barbara, Santa Barbara, California, USA

Received 20 May 2003; accepted 17 June 2003; published 6 September 2003.

[1] It is a truism in geomorphology that climatic events operate on a landscape to drive sediment transport processes, yet few investigations have formally linked climate and terrain characteristics with geomorphological processes. In this study, we incorporate sediment transport equations derived from fieldwork into a computer model that predicts the delivery of sediment from hillslopes in a steep Mediterranean landscape near Santa Barbara, California. The sediment transport equations are driven by rainstorms and fires that are stochastically generated from probability distributions. The model is used to compare the rates and processes of sediment delivery under two vegetation types: coastal sage scrub and grasslands. Conversion of vegetation from sage to exotic grasses is a common land management strategy in the region and may also be engendered by regional climate change due to global warming. Results from the model suggest that (1) approximately 40% more sediment is delivered from grasslands ($98 \text{ t km}^{-2} \text{ yr}^{-1}$) than the sage scrub ($71 \text{ t km}^{-2} \text{ yr}^{-1}$) and (2) chronic soil creep processes dominate under grasslands whereas catastrophic processes dominate under coastal sage scrub. Results from the model also suggest that changes in the spatial distribution of vegetation arising from climate change will have a greater effect on sediment delivery than changes in the magnitude and frequency of meteorological events. *INDEX TERMS*: 1824 Hydrology: Geomorphology (1625); 1815 Hydrology: Erosion and sedimentation; 1803 Hydrology: Anthropogenic effects; 1869 Hydrology: Stochastic processes; *KEYWORDS*: geomorphology, landslides, erosion, fire, hillslopes, semiarid

Citation: Gabet, E. J., and T. Dunne, A stochastic sediment delivery model for a steep Mediterranean landscape, *Water Resour. Res.*, 39(9), 1237, doi:10.1029/2003WR002341, 2003.

1. Introduction

1.1. Background

[2] With frequent fires, infrequent but intense rainfall, and sparse vegetative cover, the delivery of sediment from hillslopes in hilly Mediterranean landscapes is strongly episodic [Rice, 1982]. Whether sediment is delivered as a steady trickle or as large pulses can affect a wide range of geomorphic processes. For example, sediment delivery may come in the form of debris flows, which can cause significant property damage and the loss of life. Sediment production from hillslopes may overwhelm the transport capacity of the fluvial network and lead to flooding as well as the destruction of riverine habitats. Finally, over geological timescales, the frequency and magnitude of sediment delivery may control rates of bedrock incision [Sklar and Dietrich, 1998].

[3] In the absence of anthropogenic disturbances, climate ultimately determines the nature of sediment delivery. Climate regulates sediment production directly through meteorological events and, indirectly, by controlling the

distribution of vegetation communities. For example, sediment transport by tree-throw contributes to soil creep in forested regions [Denny and Goodlett, 1956; Gabet *et al.*, 2003] but is not relevant in areas that are too dry for trees to grow. The influence of climate on the spatial pattern of vegetation communities, however, may be overridden by anthropogenic modifications. Indeed, in the Southwest United States, hillslopes are often cleared of brush and converted to grasslands. This conversion is usually done to increase forage for livestock [Rice and Foggin, 1971] but may also be done to reduce fire hazards and increase water yields [Hibbert, 1971]. A well-documented result of this land management strategy has been an increase in the frequency of landsliding on converted hillslopes [Corbett and Rice, 1966; Bailey and Rice, 1969; Rice and Foggin, 1971; Terwilliger and Waldron, 1991; Gabet and Dunne, 2002]. In light of predictions that under a warmer climate, the distribution of grasslands in California will increase at the expense of shrub communities [Field *et al.*, 1999], the effects of this management strategy may presage an underappreciated consequence of global climate change.

[4] A fundamental tenet in geomorphology holds that climatic events operating on a landscape drive sediment

transport processes and hillslope evolution. *Rice* [1982] proposed a conceptual model that recognizes the stochastic nature of rainstorms and fires and their effects on shallow landslides, but, to date, few studies have formally (i.e., mathematically) linked climate and sediment transport. *Kirkby* [1976] applied a frequency distribution of daily rainfall to drive a process-based, hillslope hydrology model. With this model, he predicted annual runoff and related it to rates of sediment transport to model the evolution of hillslope profiles. *Dunne* [1991] demonstrated how variations in the frequency distributions of rainfall intensity and duration alter both the temporal pattern of sediment flux from hillslopes and the shape of hillslope profiles. *Dunne* [1991] also illustrated how the stochastic nature of climate is related to the spatial and temporal distribution of landsliding in the Pacific Northwest. *Benda and Dunne* [1997a, 1997b] furthered this approach with a process-based model of bedrock hollow-filling and landslide initiation. Their model combines random sequences of rainstorms and fires drawn from probability density functions (pdf's) with a landscape defined by a spatial distribution of characteristics (e.g., hillslope gradient, soil depth) also described by pdf's. *Iida* [1999] demonstrated the utility of rainfall pdf's for predicting the susceptibility of slopes to shallow landsliding. Finally, *Tucker and Bras* [2000] modeled the effects of rainfall variability on the evolution of drainage basins, illustrating that erosional thresholds can have morphological consequences.

[5] In this contribution, we expand upon the approach presented by *Benda and Dunne* [1997a, 1997b] and apply it to a hilly, semiarid watershed with a Mediterranean climate and two vegetation communities. The model proposed here includes all the dominant processes that we observed over a period of 5 years that encompassed a fire and the highest recorded annual rainfall in the region. The governing equations for the sediment transport processes have been developed and calibrated through fieldwork, and we assume that we have not overlooked any important process. With this model, we explore the effects of vegetation conversion and climate change on sediment production.

1.2. Field Area and Sediment Transport Processes

[6] The fieldwork and modeling efforts are centered on a hilly watershed in Sedgwick Reserve in the Santa Ynez Valley, near Santa Barbara, California (Figure 1). Located in the western portion of the Transverse Ranges, the field site is underlain by the Paso Robles Formation, a Pliocene fanglomerate shed from the ancestral San Rafael Range [Dibblee, 1993]. The Paso Robles has been incised to produce gentle to steep rolling hillslopes with slope angles up to 45° and relief ranging from 30 to 50 m. The climate is Mediterranean with an average annual rainfall of 50 cm. The two main vegetation communities are coastal sage scrub (primarily *Artemisia californica* and *Salvia leucophylla*) and exotic grasses (various species of *Bromus* and *Avena*). Presently, grazing occurs on the grasslands at relatively low stocking rates ($40 \text{ cow days ha}^{-1} \text{ yr}^{-1}$).

[7] Few of the lower-order valleys at Sedgwick have channels, and there is approximately 1 m of fill in the first-order valleys. Little is known about the regional history, but presumably, the valleys began to fill with colluvium sometime after the region emerged from the latest glacial maximum, 16,500 years B.P. [Kennett and

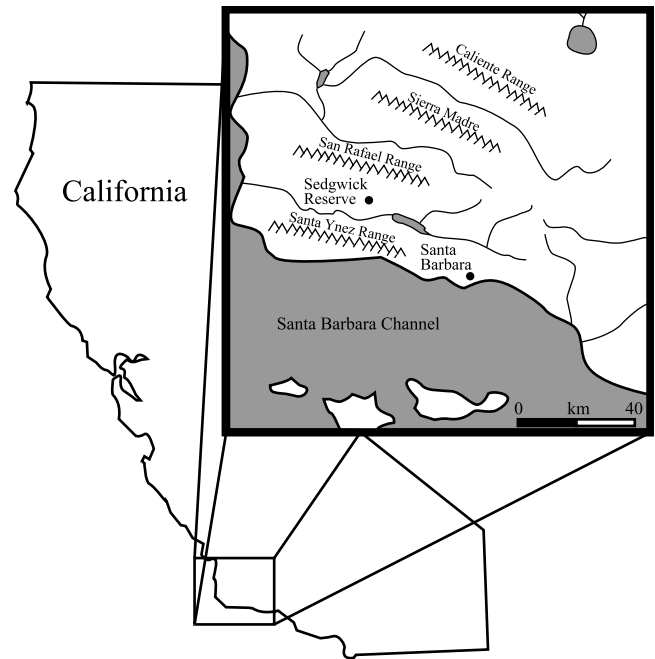


Figure 1. Site map for Sedgwick Reserve.

Ingram, 1995]. Under the drier conditions, the hillslope sediment delivery processes may have gained an advantage over the fluvial sediment transport processes. There is evidence that the channel network is beginning to expand after this phase of contraction. A knickpoint has been advancing up the main channel, Figueroa Creek, and tributary knickpoints are just beginning to form where the main knickpoint has moved past tributary valleys.

[8] Sediment is delivered to the valley bottoms at Sedgwick Reserve by three types of processes. The first, soil creep (*sensu lato*), includes bioturbation [Gabet, 2000] and dry ravel [Gabet, 2003b]. Second, sediment may be delivered by shallow landslides issuing from bedrock hollows [Gabet and Dunne, 2002]. Hollows accumulate sediment from adjacent hillslopes, and as the soil in a hollow thickens over time, it becomes increasingly susceptible to fail as a shallow landslide during heavy rainfall [Campbell, 1975; Dietrich and Dunne, 1978]. Fire may increase the likelihood of failure by destroying vegetation that increases soil strength through root cohesion. When a hollow is evacuated, it fills up again and the cycle repeats itself. The third important sediment delivery mechanism in this landscape is by thin debris flow (TDF) [Wells, 1987; Gabet, 2003a]. This process is limited to sage scrub vegetation and occurs when waxy organic molecules, vaporized during a fire from burning vegetation, recondense within the soil. This hydrophobic layer, deposited 1–2 cm below the soil surface, leads to a shallow perched water table during rainstorms. If pore pressures within this layer become sufficiently high, TDFs are triggered, stripping the top layer of soil [Wells, 1987; Gabet, 2003a]. Field observations indicate that the sediment flux from TDFs and the soil creep processes are not limited by the supply of sediment.

[9] Field observations and an extensive program of rainfall simulation experiments on plots that had undergone a variety of different treatments (i.e., trampled, burnt,

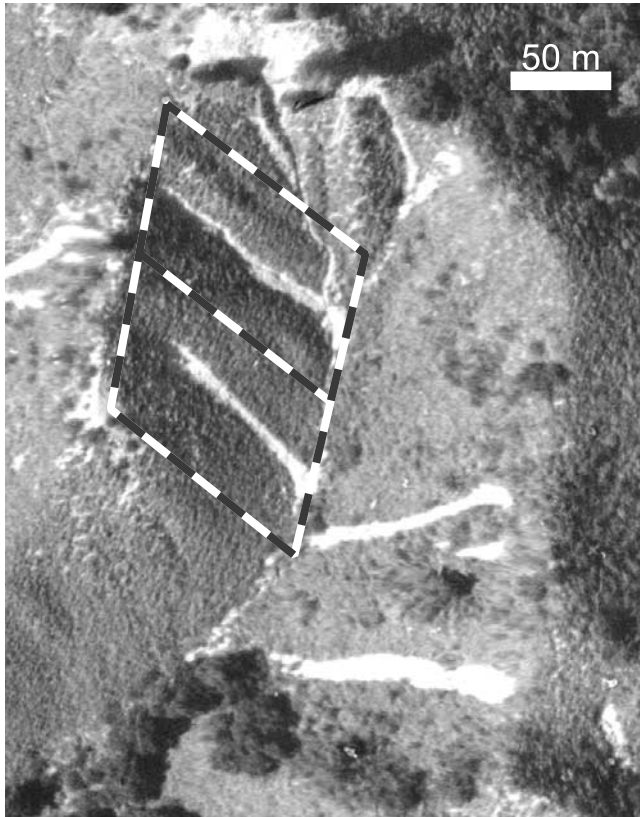


Figure 2. Aerial photo of a typical first-order valley at Sedgwick Reserve. The photograph was taken soon after a powerful El Niño-generated storm triggered more than 150 shallow landslides in the field area. In the coastal sage scrub, all of the landslides issued from bedrock hollows and mobilized as debris flows. The dashed lines demonstrate how the hillslopes may be represented as a series of rectangular strips, extending from one spur ridge to the next and encompassing a bedrock hollow.

mechanically denuded) suggest that overland flow does not appear to be an important transport process in either the sage or the grasslands. Infiltration capacities in the sage are sufficiently high to prevent the generation of Horton overland flow [Fierer and Gabet, 2002]. Even after a series of storms delivered rainfall to burnt hillslopes in the sage and triggered TDFs [Gabet, 2003a], there was no evidence of sediment transport by overland flow (e.g., the presence of rills or delta-like deposits of fine-grained material at the base of the slopes). In the grasslands, sediment transport by surface runoff is limited by the detachment of soil particles by raindrop impact [Gabet and Dunne, 2003]. Because the grazing pressure at Sedgwick Reserve is relatively light, the vegetation cover remains sufficiently high to shield the ground surface so that the annual sediment loss by overland flow is estimated to be 3–4 orders of magnitude less than by biogenic soil creep. This estimate is supported by observations made by the Sedgwick Reserve manager, who reported seeing clear water flowing down the hillslopes during intense rainfall (M. Williams, personal communication, 2001). Additionally, we did not observe any evidence of significant sediment transport from overland flow (e.g.,

rill formation or fine-grained deposits) on burnt grassland slopes.

2. Model Description

2.1. Model Domain

[10] A 2.1-km² watershed located in Sedgwick Reserve provides the topographic attributes for the model (Figure 2). In the model, the watershed is represented as a collection of 533 hillslope strips. Extending from the valley floor to the divide, hillslope strips are defined by three geometrical characteristics: length, width, and slope angle (Figure 3). Field observations and the U.S. Geological Survey (USGS) Los Olivos topographic map were used to measure the lengths and widths of hillslope strips where the width is defined as the distance between spur ridges that delimit the bedrock hollows. These measurements indicate that strip lengths and widths are normally distributed with means of 70 ± 10 m (1 standard deviation) and 35 ± 5 m (1 standard deviation), respectively. The distribution of slope angles was compiled from a digital elevation model (DEM) with 2-m spacing. The distribution of slope angles greater than 25° follows a Poisson distribution with a mean of 32° and a maximum of 45°. A minimum slope angle of 25° was chosen because it is a local threshold for TDFs [Gabet, 2003a] and debris flows mobilized from shallow landslides [Gabet and Dunne, 2002]. Additionally, 70% percent of the surface area of the modeled watershed is steeper than 25° so the flux from these hillslopes will dominate the total sediment delivered. Finally, a bedrock hollow, the source for shallow landslides, is “embedded” near the top of each strip (Figure 3). Figure 2 shows how this simple approximation of a rectangular strip with an embedded hollow may be appropriate for this landscape.

2.2. Climate

2.2.1. Rainstorms

[11] The climate is characterized as a series of rainstorms and fires. An annual sequence of rainstorms is determined

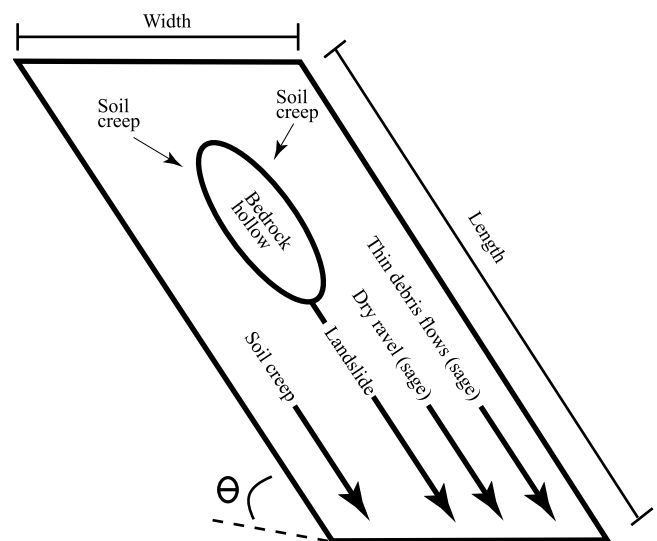


Figure 3. Hillslope strip. The modeled watershed is divided into 533 hillslopes strips, each with different topographic attributes. The potential transport processes operating on each strip are indicated.

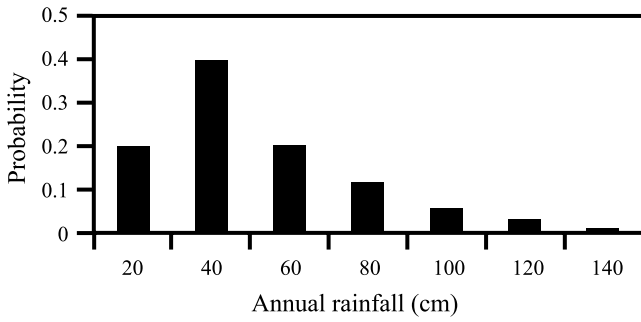


Figure 4. Probabilities of total annual rainfall. The data are from Cachuma Reservoir, 20 km southeast of Sedgwick Ranch.

by randomly selecting values from probability distributions for three variables. The first is total annual rainfall, and its probability distribution is based on 16 years of monthly rainfall records from nearby Cachuma Reservoir (Figure 4). The other two variables are storm duration and 1-hour precipitation intensity. These both follow independent exponential pdf's [Eagleson, 1972; Beven, 1987]:

$$P(i) = \left(\frac{1}{M_i}\right) e^{-i/M_i} \quad (1)$$

$$P(\tau) = \left(\frac{1}{M_\tau}\right) e^{-\tau/M_\tau} \quad (2)$$

where $P()$ is the probability distribution function, i is 1-hour precipitation intensity (cm h^{-1}), and τ is storm duration (hours). Because only monthly rainfall totals were kept at Cachuma Reservoir, values for the mean intensity ($M_i = 0.18 \text{ cm h}^{-1}$) and mean duration ($M_\tau = 14$ hours) were determined from 12 years of hourly rainfall records from different local rain gauges (Buellton Fire Station and Figueroa Mountain Ranger Station; National Oceanic and Atmospheric Administration). The yearly sequence of storms is determined by randomly choosing an annual rainfall total from the pdf. Storm durations and intensities are then randomly chosen from their respective pdf's until the annual total is reached. The rainfall records in the area are relatively short, so we must make the assumption that they have captured a representative sample of the total population of rainstorms. It is encouraging to note that the hourly rainfall records include both the driest year and the wettest year recorded over the 16-year Cachuma Reservoir monthly data.

2.2.2. Fires

[12] Similar to the rainstorms, the generation of fires is also stochastic. Explicit fire models typically require input such as fuel load, wind direction, and topography [e.g., Davis and Burrows, 1993]. Rather than creating a complex fire submodel with data requirements beyond the scope of the sediment transport model, we have developed a stochastic approach that accurately produces the two critical characteristics of the fire regime: fire size distribution and average recurrence interval.

[13] The fire submodel has two components: fire ignition and fire propagation. Each cell in the model

domain has a yearly ignition probability (I_p) determined with

$$I_p = B_p(1 - e^{gt_f}) \quad (3)$$

where B_p is base ignition probability, g is a vegetation growth constant (yr^{-1}), and t_f is time since the last fire (years).

[14] According to this function, the ignition probability increases as vegetation regrows after a fire, asymptotically approaching a maximum as the plant matures (values for g are discussed later with equation (9b)). At the yearly time step, a random number is chosen for each cell and compared to I_p . Any cell that has a random number smaller than I_p becomes the locus for a fire. When a fire is ignited, another random number is selected and compared to a probability distribution of fire sizes. The distribution of fire sizes in the region may be approximated by a negative exponential function (J. Keeley, U.S. Geological Survey, personal communication, 2000)

$$P(F) = \left(\frac{1}{M_F}\right) e^{-F/M_F} \quad (4)$$

where F is fire size (ha) and M_F is mean fire size. The fire propagates radially from the ignited cell into neighboring cells until the chosen size is attained. After a cell is burned, t_f is reset to zero. Over time, the landscape becomes a mosaic of vegetation of different age classes (Figure 5). It

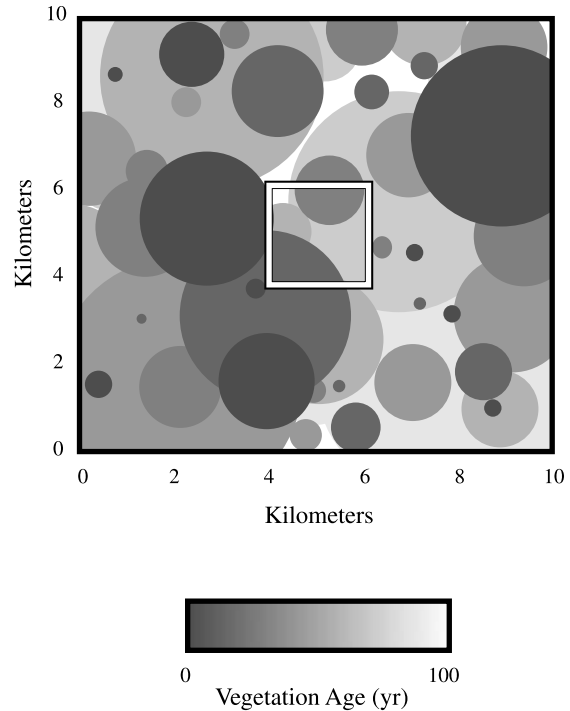


Figure 5. Distribution of vegetation ages in model domain. Vegetation age at any cell is an indicator of the time since the previous fire. To avoid edge effects, the sediment transport model domain (outlined in white box) occupies a small area (2.1 km^2) in the middle of the larger fire submodel (100 km^2).

might be argued that propagation of the fire should be dependent on vegetation age; however, *Keeley et al.* [1999] concluded that brushland fires burn equally well through all age classes. It might also be argued that fires rarely propagate radially from an ignition point. This simplification, however, may be appropriate because we are interested in understanding the temporal pattern of sediment loading rather than the spatial distribution of sediment delivery to a topologically defined channel network. Therefore the average fire recurrence interval on a hillslope is more important than the particular location of a burnt hillslope.

[15] This fire submodel depends on only two variables, the base ignition probability and the mean fire size. *Keeley et al.* [1999] report that the pre-1951 mean brush fire size for Santa Barbara County is 1622 ha and 2341 ha after 1951; however, these averages are higher than the true average because small fires are often not recorded by government agencies [*Keeley et al.*, 1999]. Nonetheless, by assuming a negative exponential distribution of fire sizes, the frequency of fires >100 ha presented by *Keeley et al.* [1999] can be used to reconstruct the entire distribution of fire sizes to yield a post-1950 mean fire size of 650 ha.

[16] The base ignition probability, in contrast, is determined by inverse modeling. *Keeley et al.* [1999] report a post-1950 fire rotation interval of 81 years. Because the fire rotation interval is equal to the average vegetation age [*Wagner*, 1978], the base ignition probability can be determined iteratively. An initial B_p is chosen and the model is run until the average vegetation age for the entire model domain becomes approximately constant. This average age is then compared to the desired fire rotation interval and B_p is adjusted until they match.

[17] We are not aware of any data on fire size and recurrence interval for grassland fires for the region, so we use the same fire parameters for the grasslands as for the coastal sage scrub. The effects of this limitation are minimal because of the relative insensitivity of the grassland transport processes to fire. First, there was no evidence of soil hydrophobicity, increased runoff rates, or rill formation in burnt grasslands after a fire on the property adjacent to Sedgwick Reserve. Second, grass regrows after the first rains of the winter season so that any loss of root strength that would increase the likelihood of shallow landslides would be minor. Finally, the rapid regrowth of grass would quickly shield the bare soil from raindrop impact.

2.3. Infiltration

[18] One of the first-order controls on hillslope sediment transport processes is the partitioning of rainfall between surface and subsurface flow. Average values for the infiltration capacity, 14 cm h⁻¹ for sage and 0.5 cm h⁻¹ for grassland, were measured with a rainfall simulator [*Fierer and Gabet*, 2002; *Gabet and Dunne*, 2003]. The creation of a hydrophobic layer in the sage scrub soil during a fire, however, can reduce infiltration capacities [*DeBano*, 1981]. A study by *Cerda* [1998] in eastern Spain indicates that recovery of the prefire infiltration capacity occurs within 4–5 years in Mediterranean shrubland. Although the vegetation community in *Cerda's* [1998] study differs from the vegetation in this study, we are interested in the rate of decay of hydrophobicity, rather than the absolute values of infiltration capacity. Assuming that temporal

changes in soil hydrophobicity in coastal sage are similar to chaparral, *Cerda's* [1998] data indicate that changes in infiltration capacity (f_i ; cm h⁻¹) at the yearly time step can be calculated as follows:

$$f(t) = f_i + (f_f - f_i)e^{-kt} \quad (5)$$

where f_i is prefire infiltration capacity, f_f is infiltration capacity immediately after the fire, and k is a constant (year⁻¹).

[19] On the basis of *Cerda's* data [1998], k varies between 0.7 and 1.2, and we use an intermediate value of 1. From *Gabet* [2003a], f_f is taken to be 0 cm h⁻¹ at a depth 1.5 cm below the surface of the soil.

2.4. Soil Creep

[20] The flux from slope-dependent soil creep processes is calculated as an average annual rate and is independent of rainstorms and fires. Soil creep in the sage is primarily by dry ravel, the downslope movement of individual particles by rolling, sliding, and bouncing. The annual specific mass flux by this process (i.e., flux per unit contour width of hillslope), q_s (kg m⁻¹ yr⁻¹), is determined with [*Gabet*, 2003b]

$$q_s = \frac{\kappa}{\mu \cos \theta - \sin \theta} \quad (6)$$

where κ is 0.056 kg m⁻¹ yr⁻¹ and μ is 1.01. The value given here for the coefficient of kinetic friction, μ , is greater than the one inferred from sediment trap data by *Gabet* [2003b]. Vegetation density and lithology vary slightly throughout Sedgwick Reserve, and therefore the friction coefficient may differ from one hillslope to the next. For consistency, we set μ just higher than 1.0, the steepest gradient for soil-mantled hillslopes at Sedgwick Reserve. Because of the highly nonlinear nature of equation (6), we would prefer to assign μ values to individual hillslope strips from a pdf; however, we do not have sufficient field data to determine the spatial frequency of μ .

[21] The dominant creep process in the grasslands appears to be bioturbation by pocket gophers, and its specific mass flux is calculated as a function of slope with [*Gabet*, 2000]

$$q_s = \frac{19(\tan \theta)^3 - 20.4(\tan \theta)^2 + 7.3(\tan \theta) + 3.7(\tan \theta)^{0.4}}{\cos \theta} \quad (7)$$

The above equation is divided by $\cos \theta$ to account for the total flux, rather than just the horizontal component of flux as presented by *Gabet* [2000].

2.5. Shallow Landslides

[22] A stability analysis is performed at every yearly time step on each bedrock hollow to determine whether a shallow landslide is triggered. *Reistenberg and Sovonick-Dunford* [1983] and *Gabet and Dunne* [2002] demonstrated that the commonly used infinite-slope stability analysis [e.g., *Selby*, 1993] needs to be expanded when lateral root reinforcement is important. Neither the roots of coastal sage nor grass penetrate the bedrock, and therefore the root reinforcement on the modeled hillslopes is entirely in the lateral direction. To account for lateral root reinforcement,

we use the stability analysis derived by *Gabet and Dunne* [2002] where the factor of safety (S) is calculated with

$$S = \frac{C'_{rl} \left(\frac{2z_{rd} \cos \theta}{\sin \alpha} \right) + C_s \left(w + \frac{2z \cos \theta}{\sin \alpha} \right) + wz(\gamma_s - m\gamma_w) \cos^2 \theta \tan \phi}{wz\gamma_s \cos \theta \sin \theta} \quad (8)$$

where

- C'_{rl} effective lateral root cohesion (kPa);
- C_s soil cohesion (kPa);
- m fraction of the soil column that is saturated;
- w failure width (m);
- z failure depth (m);
- z_{rd} rooting depth (m);
- α side-scarp angle (deg);
- ϕ internal angle of friction (deg);
- γ_s unit weight of wet soil (kN m^{-3});
- γ_w unit weight of water (kN m^{-3});
- θ hillslope angle (deg).

Values for the constants above are summarized in Table 1.

[23] The lateral root reinforcement (the first term on the left-hand side of equation (8)) depends on the rooting depth and the lateral root cohesion. Root cohesion can vary in time because of plant death and regrowth. To simulate root decay and regrowth after a fire, the effective lateral root cohesion (C'_{rl}) is calculated with

$$C'_{rl} = C_{rl}(G + D) \quad (9a)$$

$$G = 1 - e^{-gr} \quad (9b)$$

$$D = e^{-dn} \quad (9c)$$

$$G + D \leq 1 \quad (9d)$$

where

- C_{rl} maximum lateral root cohesion (kPa);
- D root decay factor;
- G root growth factor;
- d, n root decay constants;
- g vegetation growth constant;

the same as in equation (3). Following *Sidle* [1992], the decay of root cohesion is represented by an exponential function (9c). However, whereas *Sidle* [1992] suggests the use of a sigmoid function for the growth curve, we choose a simpler function (9b) that reflects the dearth of appropriate data for coastal sage scrub vegetation. The root growth curve is calibrated to aboveground growth data for sage vegetation [*Horton and Kraebel*, 1955], yielding a value of 0.15 for g . No published data exist for d and n for coastal sage, so they must be estimated indirectly. Some types of vegetation in Mediterranean ecosystems resprout after fires, and therefore root decay would be minimal. However, the dominant species at Sedgwick, California, sagebrush and black sage, typically are not resprouters [*Horton and Kraebel*, 1955; *Keeley*, 1986]. As a starting point for estimating values for d and n , there is a 90% decrease in root strength 8 years after death for Douglas fire [*Burroughs*

Table 1. Values for Constants in Stability Analysis

Constant	Value
C_s	1.2 kPa
z_{rd} (grass)	0.15 m
z_{rd} (sage)	1.00 m
α	45°
ϕ	32°
γ_s	13.9 kN m^{-3}
γ_w	9.8 kN m^{-3}

and *Thomas*, 1977]. If we assume that sage roots experience a 90% decrease in strength after 4 years, values for d and n would be 0.8 and 0.7, respectively. It is simpler to estimate the constants (g, d, n) for the grass because grass will grow back immediately after a fire with the onset of rains and the fine grass roots likely decay quickly as well. Therefore, to simulate these rapid response times, g is 3, d is 2.8, and n is 0.7, such that both root growth and root decay reach 95% of their maximum after 1 year. Finally, the value for C_{rl} is 1 kPa for grass and 3 kPa for sage [*Terwilliger and Waldron*, 1991].

[24] Whereas root strengths determine the vulnerability of soils to failure, it is the rise in pore pressure during storms that triggers the landslides, and therefore the degree of saturation (m) in the bedrock hollows must be determined for the stability analysis. Following *Dunne* [1991] and *Benda and Dunne* [1997b], the convergent bedrock topography into a hollow is idealized as a conical depression. The peak saturated soil thickness (H) at any point x along a horizontal radius can be calculated with

$$H = I_e x(r - 0.5x)/K \sin \theta(r - x) \quad \text{if } x < x_s \quad (10a)$$

$$H = I_e x_s(r - 0.5x_s)/K \sin \theta(r - x) \quad \text{if } x > x_s \quad (10b)$$

$$x_s = K \sin \theta \cos \theta T/p \quad (10c)$$

where x_s is the downslope distance beyond which subsurface flow attains steady state. I_e is the average effective rainfall intensity (mm h^{-1}) for a storm of duration T , and only the largest storm of the model year is considered [*Benda and Dunne*, 1997b]. The effective rainfall intensity reflects the limits imposed by the infiltration capacity to properly account for the effects of soil hydrophobicity after a fire. From field measurements, the average saturated hydraulic conductivity (K) is 0.65 m h^{-1} and the colluvium's drainable porosity (p) is 0.2 (O. Chadwick, University of California, Santa Barbara, personal communication, 2001). The radius of the cone, r , is 50 m, an average from measurements of hollows at Sedgwick Reserve. Again, following *Benda and Dunne* [1997b], pore pressures are not calculated at every horizontal radial distance x [*Dunne*, 1991]. Instead, the pore pressure is calculated at 15 m, a radial distance included in most of the failures observed at Sedgwick Reserve. With the value for H determined with (10), m in equation (8) is calculated with

$$m = \frac{H}{z \cos \theta} \quad (11)$$

[25] Surveys of the failures at Sedgwick Reserve revealed a systematic decline in failure width with increasing slope in the sage [Gabet and Dunne, 2002]. From the data presented by Gabet and Dunne [2002], failure width in equation (8) is calculated as a function of slope with

$$w = 12(\theta - 31)^{-0.5} \quad (12)$$

For slopes less than 32° , failure widths are set at 13 m. Because there was no apparent relationship between failure width and slope in the grasslands, the average width for grassland failures (5 m) is used [Gabet and Dunne, 2002]. Failure volumes are determined as the product of the width, the soil depth at failure, and the failure length calculated from the average length/width ratio (2.7) [Gabet and Dunne, 2002].

2.6. Hollow Filling

[26] After a bedrock hollow is evacuated, the landslide scar is refilled by sediment transported from adjacent slopes by soil creep. The net volume (V) of sediment coming into the hollow per meter length of scar (l) can be calculated as a function of time since the previous landslide (t_i) with

$$\frac{V(t_i)}{l} = \frac{2q_s t_i \sin \lambda}{\rho_s} \quad (13)$$

where ρ_s is the dry bulk density of the soil and λ is the convergence angle into the hollow [Reneau and Dietrich, 1991]. Landslide scars are represented as troughs with side-scarps at an angle α [Gabet and Dunne, 2002] such that the soil depth in each hollow (z) can be expressed as a function of time since the previous landslide with [Benda and Dunne, 1997b]:

$$z(t_i) = \left[(w^2 + 4V(t_i) \cot \alpha)^{0.5} - w \right] \frac{\tan \alpha}{2} \quad (14)$$

Average values from Sedgwick Reserve for ρ_s and λ are 1190 kg m^{-3} and 32° , respectively.

2.7. Postfire Transport Processes

[27] In addition to background dry ravel, there is a form of dry ravel associated with fire. In steep semiarid environments with shrubby vegetation, transport by dry ravel after a fire can be extensive, as sediment that has accumulated behind litter and vegetation is released when the vegetation is burned [Wells, 1987; Florsheim et al., 1991]. From sediment traps installed in coastal sage scrub in anticipation of a prescribed fire near Sedgwick Reserve, the specific flux of sediment from postfire dry ravel can be determined with equation (6) with a value of $0.03 \text{ kg m}^{-1} \text{ fire}^{-1}$ for κ and 1.01 for μ . The amount of postfire dry ravel reported here is less than what has been observed elsewhere. For example, Wells [1987] observed that small channels in the San Dimas Experimental Forest, near Los Angeles, were completely filled with dry ravel deposits immediately after a fire in shrubby vegetation. Davis et al. [1989] found that 0.20 m^3 of dry ravel deposits were delivered per meter length of channel in the month following a chaparral fire near Santa Barbara. Assuming a bulk density of 1300 kg m^{-3} for the deposit and assuming that the deposits accumulated from both sides of the channel, the specific mass flux was

then 130 kg m^{-1} . This is significantly more than what was observed near Sedgwick Reserve; for example, equation (6) parameterized with the values for κ and μ above predicts a specific mass flux of 0.20 kg m^{-1} . A difference in lithology is the most likely explanation for the discordance between the rates of postfire dry ravel at Sedgwick Reserve and those reported by Davis et al. [1989]. The watershed studied by Davis et al. [1989] is underlain by shale and sandstone and the clasts in the postfire dry ravel deposits were well sorted, with an average size of 4 mm [Florsheim et al., 1991]. In contrast, the fanglomerate at Sedgwick Reserve weathers into particle sizes that range from clay to gravel. A greater variance in particle size will decrease the flux by increasing the effective roughness of the surface [Kirkby and Statham, 1974]. Additionally, the soils at Sedgwick Reserve are generally high in smectitic clays [Shipman, 1972], and the cohesion from these clays may inhibit raveling.

[28] Along with dry ravel, thin debris flows (TDFs) are also limited to the coastal sage scrub. Gabet [2003a] has developed a numerical model for TDFs that couples subsurface flow routing through the top 1–2 cm of soil with an infinite-slope stability analysis. The TDF model predicts the location and timing of these shallow failures during rainstorms such that the mass of sediment transported across a unit contour width of slope by TDF may be determined with [Gabet, 2003a]

$$\frac{\text{mass}}{\text{unit width}} = ALz_t \rho_{st} \quad (15)$$

where

A fraction of area covered by TDF scars;

L length of TDF scar (m);

z_t failure depth (m);

ρ_{st} bulk density of the top layer of soil (kg m^{-3}).

L is determined with the model described above; from field observations, d is 1.5 cm and A is 0.60 [Gabet, 2003a]. The bulk density of the upper layer of soil, adjusted for organic content, is 560 kg m^{-3} [Gabet, 2003a].

[29] Many simulation runs of the TDF model described by Gabet [2003a] were done to determine the excess rainfall (i.e., $i - f$) thresholds necessary for triggering TDFs at various slope angles. These runs indicated that only about 0.3 cm of rain will cause TDFs, which agrees well with Wells [1987]. In the larger model presented here, when the rainfall threshold is reached, the sediment delivered to the base of the hillslope is determined with equation (15).

2.8. Model Operation

[30] The algorithm for the model is shown in Figure 6. The climate parameters, mean rainfall intensity, mean storm duration, mean fire size, and fire recurrence interval are specified at the beginning of each run and can be changed at any time during the run. Similarly, vegetation type, which determines the suite of relevant transport processes, is specified for each hillslope strip at the start of the model simulation and can be changed at any time. The initial soil depth in each bedrock hollow is determined by randomly assigning a value for t_i , the time since the last landslide (see equations (13) and (14)). Values for t_i are normally distributed with a mean of 100 years such that initial soil depths are less than 0.20 m. Because slope angles and soil depths

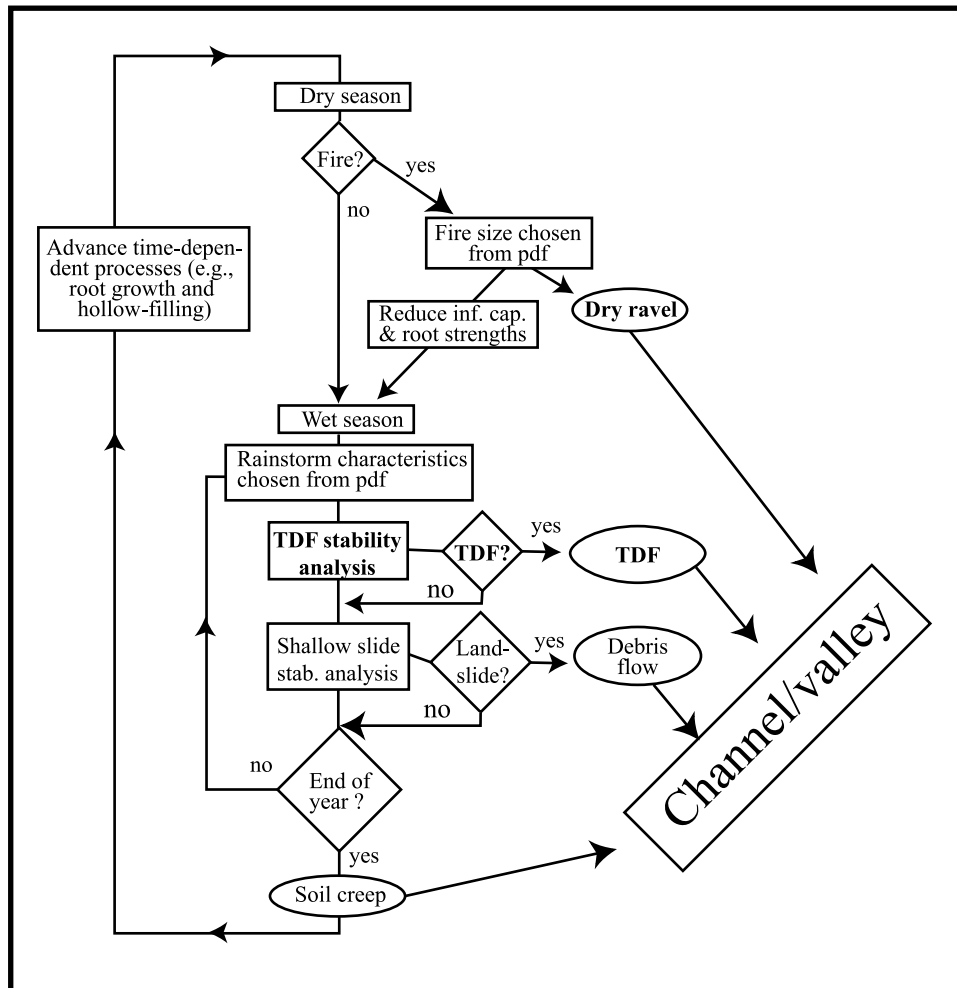


Figure 6. Algorithm for the sediment delivery model. Ovals represent sediment transport processes. Processes in bold type occur only in the coastal sage scrub.

(via t_i) are independently chosen from pdf's, there is a risk that a number of hollows will be initially unstable and fail immediately once the model runs begin. Initial depths therefore are low to avoid artificially synchronizing the cycle of filling and failing among the hollows. To further reduce the effect of the initial conditions, each simulation is run for 5000 years before the results are considered.

[31] To summarize the spatial parameterization of the model, Figure 3 illustrates the geometrical properties of an individual hillslope strip and the transport processes that deliver sediment to the channel network. An example of the sediment output for an individual strip vegetated by coastal sage is shown in Figure 7. For the first 8 years, the only sediment comes from soil creep. In the eighth year, there is a fire on the strip, causing a pulse of sediment from dry ravel and TDFs. Because of the hydrophobic layer and the lag in the root strength loss, there is no landslide in that year. The following year, however, the combination of high rainfall and loss of root strength leads to the evacuation of the bedrock hollow.

[32] At the watershed scale, the processes described above are repeated for all 533 strips. The model records the annual amount of sediment delivered to the base of each hillslope but does not route the sediment down the channel

network. Watersheds in California have valley floors in various stages of aggradation and degradation, and therefore the fate of sediment once it reaches the base of the hillslope is dependent on processes beyond the scope of this model.

3. Results and Discussion

3.1. Model Test

[33] The main high-resolution prediction of the model, a time series of sediment production, cannot be tested because there are no long-term records of sediment discharge from Sedgwick Reserve. However, results from the model can be used to predict an average rate of sediment delivery that can be compared to a rate determined from a sedimentation survey at nearby Gibraltar Reservoir (approximately 40 km southeast of Sedgwick Reserve). In contrast to Sedgwick Reserve, active channels are connected to the base of the hillslopes and there is little storage of colluvium on the footslopes. This tight linkage between the hillslopes and the fluvial network suggests that averaged over several years, the sediment yield from the Gibraltar watershed may be equivalent to the total amount of sediment produced from the hillslopes.

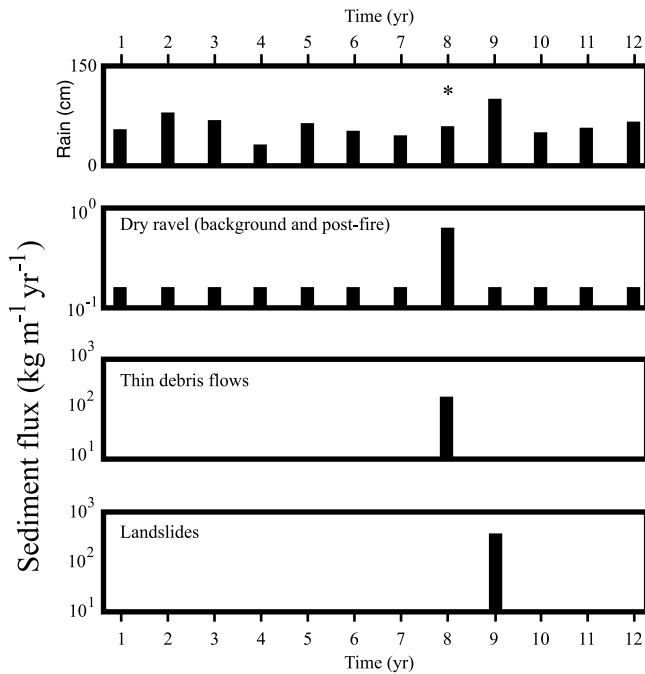


Figure 7. Illustration of the sediment delivery from one hillslope strip with sage vegetation. The top panel is the annual rainfall with a fire in the eighth year indicated by an asterisk. The second panel is the sediment flux from dry ravel and includes both the background rate and the pulse of dry ravel after a fire. The third panel represents the sediment delivered from TDFs during rainstorms after the fire. The bottom panel is the delivery of sediment from a shallow landslide.

[34] The watershed upstream of the Gibraltar Reservoir is steeper than the one modeled at Sedgwick Reserve so the topographic attributes must be redefined. From an analysis of the USGS Little Pine Mountain quadrangle, the average hillslope length is approximately 110 m and the average slope angle is 36° . With these hillslope parameters and a coastal sage scrub vegetation cover, the model predicts an average sediment yield of $128 \text{ t km}^{-2} \text{ yr}^{-1}$. Data from the Santa Barbara County Water Agency (SBCWA) indicate that averaged over 25 years, the volumetric sediment yield from the Gibraltar Reservoir watershed is approximately $640 \text{ m}^3 \text{ km}^{-2} \text{ yr}^{-1}$. Although the bulk density of the sediment has not been measured (K. Goodenough, SBCWA, personal communication, 2001), bulk densities for fine-grained reservoir deposits may vary from 370 to 530 kg m^{-3} [Meade, 1966]. With these values, the mass sediment yield into Gibraltar Reservoir is $250\text{--}360 \text{ t km}^{-2} \text{ yr}^{-1}$.

[35] The predicted rate is 25% less than the lowest rate estimated from the reservoir data. It is possible that we have overlooked an important transport process; however, the difference between the model results and the calculated sediment yield is likely to be due to an underprediction in the rates of dry ravel. As previously noted, the soils at Sedgwick Reserve do not appear to be as susceptible to dry ravel as coarser soils. In contrast, the lithology of the Gibraltar Reservoir watershed is dominated by shales and sandstones, similar to the bedrock that produced the high rates of postfire dry ravel measured by Davis *et al.* [1989].

To approximately match Davis *et al.*'s [1989] data, the value of κ is increased to $33 \text{ kg m}^{-1} \text{ fire}^{-1}$ in equation (5). Additionally, data reported by Anderson *et al.* [1959] and Krammes [1965] from the San Gabriel Mountains in southern California may be used to estimate a value of $2.5 \text{ kg m}^{-1} \text{ yr}^{-1}$ for background dry ravel. The San Gabriel Mountains are granitic, producing sand-sized weathered material [Anderson *et al.*, 1959], similar to the regolith in the Gibraltar watershed. With these new values, the predicted yield becomes $346 \text{ t km}^{-2} \text{ yr}^{-1}$, suggesting that the model is capturing the essence of sediment delivery in this type of landscape. Ideally, we would have used a detailed fire and precipitation record from the Gibraltar watershed to drive the model; unfortunately none exist. However, the watershed may be large enough (520 km^2) that it may integrate the range of climatic events represented in the model run. Additionally, surveys from other reservoirs in the region (Juncal, Twitchell, and Bradbury) record sediment yields similar to the Gibraltar watershed (SBCWA).

3.2. Vegetation Change at Sedgwick Reserve

[36] As previously noted, human-induced vegetation conversion from native scrub to exotic grasses is a common practice in the region. Additionally, coupled climate-vegetation models predict that in the next 100 years, grassy savanna communities may replace shrublands throughout the Coast Ranges of California [Field *et al.*, 1999]. To investigate the effects of vegetation change on sediment delivery, the model was run under sage for 10,000 years and then run under grasslands for another 10,000 years. Ten thousand years was chosen because the model runs must be long enough such that differences resulting from changes in the model parameters can be distinguished from variations caused by the stochastic forcing.

[37] From Figures 8 and 9, there are noticeable differences in sediment delivery between the sage and the grasslands. In the coastal sage scrub, there is greater interannual variability in annual sediment delivery, whereas in the grasslands, sediment delivery events are relatively muted. Figure 9 also shows that the rate of soil creep is approximately 4 times greater in the grasslands than in the coastal sage. Average rates of annual sediment delivery and spatially averaged soil erosion rates for both vegetation types are listed in Table 2. These results suggest that sediment delivery is 38% higher under grassland than coastal sage.

[38] The primary reason for the marked difference in the nature of sediment delivery between the two vegetation covers is attributable to the difference in relevant transport processes. The relative magnitudes of the different processes are compared in Figure 10. In the sage, 70% of the total sediment delivered is by catastrophic processes: TDFs and landslides. This indicates that sediment delivery in the sage is strongly linked to the occurrence of fires. In contrast, soil creep accounts for 72% of the sediment production in the grasslands. Because of the absence of TDFs in the grasslands, sediment production is not as sensitive to fires. Therefore vegetation conversion changes not only the magnitude of sediment supply but also the nature of sediment delivery from catastrophic to chronic. Finally, the relatively weak contribution of grass roots to overall soil strength, as well as its rapid regrowth after a fire, decouples the occurrence of landslides from the fire regime.

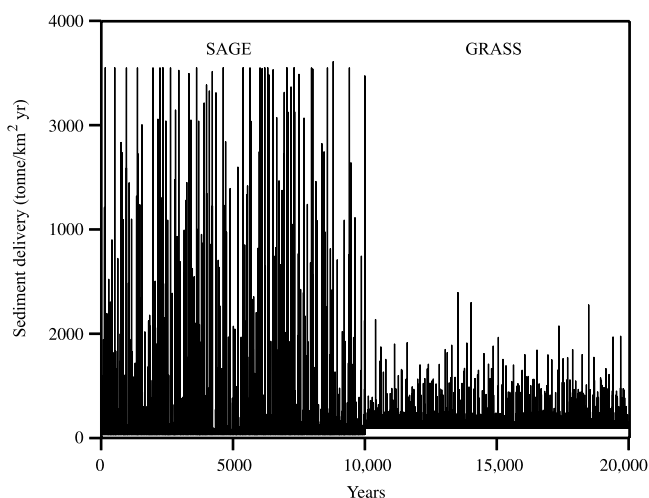


Figure 8. Predicted annual sediment delivery with vegetation conversion. The first 10,000 years are with sage vegetation and the last 10,000 years with grass. The amount of sediment delivered each year in the sage has a higher interannual variability than in the grasslands (note that the maximum sediment delivery occurs in the coastal sage each time the entire model domain burns). In the grasslands, the sediment pulses are significantly attenuated relative to the coastal sage scrub.

[39] Results from the model also suggest that the grassland hollows will fail more often than coastal sage hollows (Table 2). In the grasslands, the bedrock hollows fill up more rapidly because of higher rates of soil creep and they fail with thinner soil depths because of the weaker root reinforcement. Additionally, the predicted spike in landslide frequency soon after vegetation conversion (at 10,000 years in Figure 11) is a phenomenon commonly observed

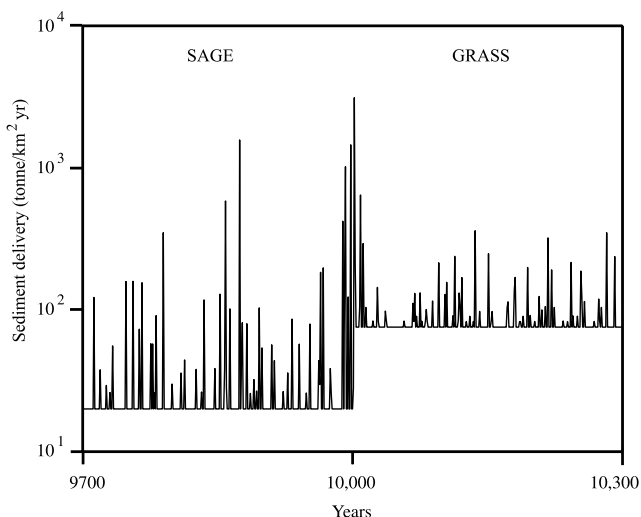


Figure 9. The 600 years bracketing the vegetation conversion. The differences in the magnitude of sediment delivery events between vegetation types are apparent. The flux from soil creep, the baseline sediment delivery, is greater in the grasslands than in the sage, accounting for the higher average rates of sediment loading. Note the semilogarithmic scale.

Table 2. Average Predicted Rates of Sediment Production, Rates of Soil Erosion, and Landslide Frequency^a

	Production, t km ⁻² yr ⁻¹	Erosion, mm kyr ⁻¹	Landslides, slides km ⁻² yr ⁻¹
Present climate			
Sage scrub	71	60	0.58
Grassland	98	82	1.28
2 × CO ₂			
Sage scrub	80	68	0.61
Grassland	100	84	1.55

^aAll differences between vegetation types and climates are statistically significant ($p < 0.005$). The predicted increase in “2 × CO₂” climate scenario is based on results from *Giorgio et al.* [1994] and *Davis and Michaelsen* [1995].

throughout the region [*Corbett and Rice*, 1966; *Bailey and Rice*, 1969; *Rice et al.*, 1969; *Rice and Foggin*, 1971; *Terwilliger and Waldron*, 1991; *Gabet and Dunne*, 2002]. This transient increase in landsliding is likely due to a temporary disequilibrium between the prevailing root reinforcement and soil depths [*Rice and Foggin*, 1971; *Gabet and Dunne*, 2002]. *Gabet and Dunne* [2002] have demonstrated that an abrupt decrease in root reinforcement caused by vegetation conversion increases the likelihood of shallow landsliding on hillslopes that were previously stable.

3.3. Climate Change at Sedgwick Reserve

[40] Given the importance of climate for sediment delivery, it is valuable to consider how global climate change may alter the nature of sediment production. A recently published report has described several potential consequences of global warming in California [*Field et al.*, 1999]. On the basis of general circulation models, the report foresees an increase in winter rains followed by drier summers due to increases in dry, offshore winds (Santa Ana winds). Drier summers would likely increase the frequency and intensity of wildfires throughout the state, particularly in southern California [*Field et al.*, 1999]. *Giorgi et al.* [1994] predicted an approximately 30% increase in winter rainfall and a 4°C rise in summer temperatures in California with a doubling of atmospheric CO₂. Given these estimates, *Davis and Michaelsen* [1995] used an explicit fire ignition

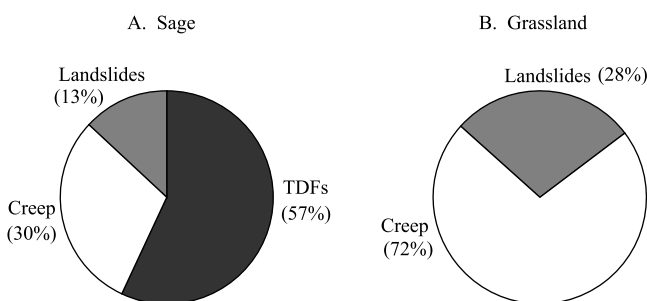


Figure 10. (a) Relative proportions of sediment contributed by each transport process in the sage scrub. The majority of sediment is delivered episodically by TDFs and landslides. (b) Proportions of sediment contributed by each process in the grasslands. The majority of sediment is delivered by soil creep, indicating that sediment delivery in the grasslands tends to occur as a steady trickle rather than as large, infrequent pulses.

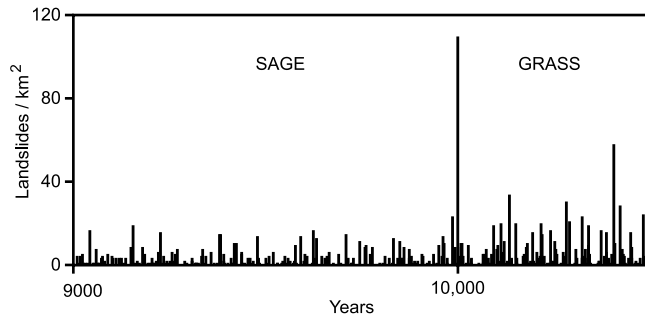


Figure 11. Changes in landslide frequency with vegetation conversion at 10,000 years. Because of the faster rates of hollow-filling and the weaker root reinforcement, landslides occur more frequently in the grasslands. The spike in landslide frequency immediately after the vegetation conversion is a commonly observed phenomenon throughout Mediterranean landscapes and is due to a sudden disequilibrium between soil depths and root reinforcement.

and propagation model to forecast a 17% decrease in the fire recurrence interval in central coastal California.

[41] The model presented here can be used to examine the effects of the predicted changes in the rainfall and fire regimes. First, the annual distribution of rainfall (Figure 4) is shifted to increase the average annual rainfall by 30%, from 50 to 65 cm yr^{-1} . Increased annual rainfall may be accommodated by a rise in the number of storms, storm duration, or rainfall intensity. Climate models suggest that rainfall may become more intense [Houghton *et al.*, 1992] so the average rainfall intensity is increased from 0.18 to 0.23 cm h^{-1} . Second, to account for the change in the fire recurrence interval, the base ignition probability in equation (3) is adjusted to produce a fire recurrence interval of 67 years, instead of 81 years. However, the effect of climate change on the fire recurrence interval is likely more complicated than the simple adjustment made here because the present recurrence interval is largely due to regional fire suppression [Keeley *et al.*, 1999].

[42] The results (Table 2) indicate that climate change will increase the sediment delivery from coastal sage hillslopes by 10% but will only increase the delivery from grassland hillslopes by 2%. This difference would be expected since the sediment delivery processes on sage hillslopes are more sensitive to fires. In both types of vegetation, however, the frequency of landsliding increases due to the more frequent fires that reduce root reinforcement and the larger storms. The increase in storm intensity directly affects the landslide stability analysis through equations (8), (10), and (11) such that the hollows reach a critical saturation more often. The increase in landslide frequency implies that failure volumes will be smaller and that average soil depths in the hollows will decrease [Gabet and Dunne, 2002].

[43] On coastal sage hillslopes, the modeled increase in sediment production due to vegetation conversion is nearly 4 times greater than the increase due to climate change. This result leads to the interesting speculation that climatic changes, expressed as purely meteorological phenomena, may only have a minimal impact on changes in sediment production. In contrast, changes in vegetation community

driven by regional climate change may have much greater consequences.

4. Conclusion

[44] Sediment loading to channels affects a range of concerns, including debris flow hazards, water quality, and reservoir sedimentation. In this contribution, we present a computer model that drives field-based hillslope sediment transport equations with stochastically generated rainstorms and fires. The model is used to examine how land management strategies and climate change may alter both the rates and the processes of sediment delivery. The results suggest that conversion of coastal sage scrub to grassland, a common practice, increases sediment delivery by approximately 38% but that the sediment delivery regime switches from being dominated by catastrophic processes (e.g., thin debris flows) to being dominated by chronic soil creep processes. The results from the model also suggest that changes in vegetation engendered by changes in climate will increase sediment production more than changes in the climatic events themselves.

[66] **Acknowledgments.** We thank M. Williams, R. Skillins, and V. Boucher of Sedgwick Reserve for their enthusiastic help in facilitating the fieldwork. We are grateful for the help that C. Marcinkovich generously provided in the coding of the model, and we thank the reviewers for their insightful comments. Supplies and salary for E. Gabet were supported by U.C. Water Resources grant UCAL-W-917, NSF-SGER DEB9813669, a Sigma Xi grant, and a Mildred Mathias grant.

References

- Anderson, H. W., G. B. Coleman, and P. J. Zinke, Summer slides and winter scour, dry-wet erosion in Southern California mountains, *U.S. For. Serv. Pac. Southwest For. Range Exp. Stn. Tech. Pap.*, PSW-36, PSW-36, 1959.
- Bailey, R. G., and R. M. Rice, Soil slippage: An indicator of slope instability on chaparral watersheds of southern California, *Prof. Geogr.*, 21(3), 172–177, 1969.
- Benda, L., and T. Dunne, Stochastic forcing of sediment routing and storage in channel networks, *Water Resour. Res.*, 33, 2849–2863, 1997a.
- Benda, L., and T. Dunne, Stochastic forcing of sediment supply to channel networks from landsliding and debris flow, *Water Resour. Res.*, 33, 2865–2880, 1997b.
- Beven, K., Towards the use of catchment geomorphology in flood frequency predictions, *Earth Surf. Processes Landforms*, 12, 69–82, 1987.
- Burroughs, E. R., and B. R. Thomas, Declining root strength in Douglas-fir after felling as a factor in slope stability, *USDA For. Serv. Res. Pap.*, INT-190, 1977.
- Campbell, R. H., Soil slips, debris flows, and rainstorms in the Santa Monica Mountains and vicinity, southern California, *U.S. Geol. Surv. Prof.*, 851, 1975.
- Cerda, A., Changes in overland flow and infiltration after a rangeland fire in a Mediterranean scrubland, *Hydrol. Processes*, 12, 1031–1042, 1998.
- Corbett, E. S., and R. M. Rice, Soil slippage increased by brush conversion, *U.S. For. Serv. Pac. Southwest For. Range Exp. Stn. Res. Note*, PSW-128, 1–8, 1966.
- Davis, F. W., and D. A. Burrows, Modeling fire regime in Mediterranean landscapes, in *Patch Dynamics*, edited by S. Levin, T. Powell, and J. Steele, pp. 247–259, Springer-Verlag, New York, 1993.
- Davis, F. W., and J. Michaelsen, Sensitivity of fire regime in chaparral ecosystems to climate change, in *Global Change and Mediterranean-Type Ecosystems*, edited by J. M. Moreno and W. C. Oechel, pp. 435–456, Springer-Verlag, New York, 1995.
- Davis, F. W., E. A. Keller, A. Parikh, and J. Florsheim, Recovery of the chaparral riparian zone after wildfire, *USDA For. Serv. Gen. Tech. Rep. PSW-110*, 194–203, 1989.
- DeBano, L. F., Water repellent soils: A state of the art, *USDA For. Serv. Res. Pap.*, PSW-46, 1–21, 1981.
- Denny, C., and J. Goodlett, Microrelief resulting from fallen trees, *U.S. Geol. Surv. Prof. Publ.*, 288, 59–68, 1956.

- Dibblee, T. W. J., Geologic map of the Los Olivos Quadrangle, *Map DF-44*, Dibblee Geol. Found., Santa Barbara, Calif., 1993.
- Dietrich, W. E., and T. Dunne, Sediment budget for a small catchment in mountainous terrain, *Z. Geomorphol. Suppl.*, 29, 191–206, 1978.
- Dunne, T., Stochastic aspects of the relations between climate, hydrology and landform evolution, *Trans. Jpn. Geomorphol. Union*, 12(1), 1–24, 1991.
- Eagleson, P. S., Dynamics of flood frequency, *Water Resour. Res.*, 8(4), 878–898, 1972.
- Field, C. B., et al., Confronting climate change in California: Ecological impacts on the Golden State, Union of Concerned Sci. and the Ecol. Soc. of Am., Washington, D. C., 1999.
- Fierer, N. G., and E. G. Gabet, Transport of carbon and nitrogen by surface runoff from hillslopes in the Central Coast region of California, *J. Environ. Qual.*, 31, 1207–1213, 2002.
- Florsheim, J. L., E. A. Keller, and D. W. Best, Fluvial sediment transport in response to moderate storm flows following chaparral wildfire, Ventura County, southern California, *Geol. Soc. Am. Bull.*, 103, 504–511, 1991.
- Gabet, E. J., Gopher bioturbation: Field evidence for nonlinear hillslope diffusion, *Earth Surf. Processes Landforms*, 25(13), 1419–1428, 2000.
- Gabet, E. J., Post-fire thin debris flows: Field observations of sediment transport and numerical modeling, *Earth Surf. Processes Landforms*, in press, 2003a.
- Gabet, E. J., Sediment transport by dry ravel, *J. Geophys. Res.*, 108(B1), 2049, doi:10.1029/2001JB001686, 2003b.
- Gabet, E. J., and T. Dunne, Landslides on coastal sage-scrub and grassland hillslopes in a severe El Niño winter: The effects of vegetation conversion on sediment delivery, *Geol. Soc. Am. Bull.*, 114(8), 983–990, 2002.
- Gabet, E. J., and T. Dunne, Sediment detachment by rainpower, *Water Resour. Res.*, 39(1), 1002, doi:10.1029/2001WR000656, 2003.
- Gabet, E. J., O. J. Reichman, and E. Seabloom, The effects of bioturbation on soil processes and sediment transport, *Annu. Rev. Earth Planet. Sci.*, 31, 259–273, 2003.
- Giorgi, F., F. S. Brodeur, and G. T. Bates, Regional climate change scenarios over the United States produced with a nested regional climate model, *J. Clim.*, 7(3), 375–399, 1994.
- Hibbert, A. R., Increases in streamflow after converting chaparral to grass, *Water Resour. Res.*, 7(1), 71–80, 1971.
- Horton, J. S., and C. J. Kraebel, Development of vegetation after fire in the chamise chaparral of southern California, *Ecology*, 36(2), 244–262, 1955.
- Houghton, J., B. Callander, and S. Varney (Eds.), Climate change 1992: The supplementary report to the IPCC scientific assessment, 199 pp., Cambridge Univ. Press, New York, 1992.
- Iida, T., A stochastic hydro-geomorphological model for shallow landsliding due to rainstorm, *Catena*, 34, 293–313, 1999.
- Keeley, J. A., Resilience of Mediterranean shrub communities to fires, *Ecology*, 45, 243–245, 1986.
- Keeley, J. E., C. J. Fotheringham, and M. Morais, Reexamining fire suppression impacts on brushland fire regimes, *Science*, 284, 1829–1832, 1999.
- Kennett, J. P., and B. L. Ingram, A 20,000-year record of ocean circulation and climate change from the Santa Barbara basin, *Nature*, 377, 510–514, 1995.
- Kirkby, M. J., Hydrological slope models: The influence of climate, in *Geomorphology and Climate*, edited by E. Derbyshire, pp. 247–268, John Wiley, Hoboken, N. J., 1976.
- Kirkby, M. J., and I. Statham, Surface stone movement and scree formation, *J. Geol.*, 83, 349–362, 1974.
- Krammes, J. S., Seasonal debris movement from steep mountainside slopes in southern California, in *Proceedings of the Federal Inter-Agency Sedimentation Conference*, U.S. Dep. of Agric. Misc. Publ. 970, 85–88, 1965.
- Meade, R. H., Factors influencing the early stages of the compaction of clays and sands—Review, *J. Sediment. Petrol.*, 36(4), 1085–1101, 1966.
- Reistenberg, M. M., and S. Sovonick-Dunford, The role of woody vegetation in stabilizing slopes in the Cincinnati area, Ohio, *Geol. Soc. Am. Bull.*, 94, 506–518, 1983.
- Reneau, S. L., and W. E. Dietrich, Erosion rates in the southern Oregon Coast Range: Evidence for an equilibrium between hillslope erosion and sediment yield, *Earth Surf. Processes Landforms*, 16, 307–322, 1991.
- Rice, R. M., Sedimentation in the chaparral: How do you handle unusual events?, in *Sediment Budgets and Routing in Forested Drainage Basins*, edited by F. J. Swanson et al., pp. 39–49, U.S. Dep. of Agric. For. Serv., 1982.
- Rice, R. M., and G. T. Foggin, Effect of high intensity storms on soil slippage on mountainous watersheds in southern California, *Water Resour. Res.*, 7(6), 1485–1496, 1971.
- Rice, R. M., E. S. Corbett, and R. G. Bailey, Soil slips related to vegetation, topography, and soil in southern California, *Water Resour. Res.*, 5(3), 647–659, 1969.
- Selby, M. J., *Hillslope Materials and Processes*, Oxford Univ. Press, New York, 1993.
- Shipman, G. E., *Soil Survey of Northern Santa Barbara Area, California*, U.S. Dep. of Agric. Soil Conserv. Serv., Washington, D. C., 1972.
- Sidle, R. C., A theoretical model of the effects of timber harvesting on slope stability, *Water Resour. Res.*, 28(7), 1897–1910, 1992.
- Sklar, L., and W. E. Dietrich, River longitudinal profiles and bedrock incision models: Stream power and the influence of sediment supply, in *Rivers Over Rock: Fluvial Processes in Bedrock Channels*, *Geophys. Monogr. Ser.*, vol. 107, edited by K. J. Tinkler and E. E. Wohl, pp. 237–260, AGU, Washington, D. C., 1998.
- Terwilliger, V. J., and L. J. Waldron, Effects of root reinforcement on soil-slip patterns in the Transverse Ranges of southern California, *Geol. Soc. Am. Bull.*, 103, 775–785, 1991.
- Tucker, G. E., and R. L. Bras, A stochastic approach to modeling the role of rainfall variability in drainage basin evolution, *Water Resour. Res.*, 36(7), 1953–1964, 2000.
- Wagner, C. E. V., Age-class distribution and the forest fire cycle, *Can. J. For. Res.*, 8, 220–227, 1978.
- Wells, W. G., The effects of fire on the generation of debris flows in southern California, *Rev. Eng. Geol.*, 7, 105–114, 1987.

T. Dunne, Donald Bren School of Environmental Science and Management and Department of Geological Sciences, University of California, Santa Barbara, Santa Barbara, CA 93106, USA.

E. J. Gabet, Department of Geology, University of Montana, Missoula, MT 59812, USA. (manny.gabet@mso.umt.edu)

Landslides on coastal sage-scrub and grassland hillslopes in a severe El Niño winter: The effects of vegetation conversion on sediment delivery

Emmanuel J. Gabet*

Department of Geological Sciences, University of California, Santa Barbara, California 93106, USA

Thomas Dunne

Donald Bren School of Environmental Science and Management and Department of Geological Sciences, University of California, Santa Barbara, Santa Barbara, California 93106, USA

ABSTRACT

During the 1997–1998 El Niño, record rainfall triggered >150 shallow landslides within a 9.5 km² area near Santa Barbara, California. They were studied to analyze the sediment delivery to valley floors from landslides in coastal sage scrub and converted grasslands. The conversion of coastal sage to grasslands, primarily to provide pasturage for cattle, is common in the region, and the landscape's response may affect water quality, reservoir infilling, and debris flow hazards. We explore the relationship between lateral-root reinforcement and landslide volume by developing a slope-stability analysis that incorporates root cohesion along the sides of the failure. The stability analysis correctly predicts an inverse relationship between landslide volume and hillslope angle in the sage. The volumes of failures in the grasslands do not vary systematically with slope and are generally smaller than those in the sage. From aerial-photograph analysis and field mapping, we find that there are 22.9 failures per square kilometer in the grasslands compared to 13.2 failures per square kilometer in the sage. Despite the lower failure density in the coastal sage, greater failure volumes and longer transport distances delivered more sediment to valley floors, with a specific volumetric flux of $2.8 \times 10^{-2} \text{ m}^3\text{m}^{-1}$ for this El Niño compared to $1.7 \times 10^{-2} \text{ m}^3\text{m}^{-1}$ in the grasslands. We conclude that the conversion from vegetation with stronger and deeper roots (coastal sage) to vegetation with weaker and shallower roots (grass) has caused a pulse of increased landsliding in the grasslands because the soils are currently too thick for the prevailing root reinforcement. We suggest that, over time, soils in the grassland hollows will become thinner as the evacuation by landslides is repeated until the landsliding rate declines to balance the soil supplied from local colluvium production and diffusive processes upslope.

Keywords: debris flows, geomorphology, landslides, sediment supply, sediment transport, slope stability.

*E-mail: egabet@bren.ucsb.edu.

INTRODUCTION

The El Niño event of 1997–1998 struck the coast of Santa Barbara County, California, with exceptional ferocity, producing the single wettest month and the second wettest year that the region has experienced in more than 100 yr. On the night of February 3–4, 1998, after several days of heavy rainfall (Fig. 1), more than 150 shallow landslides were triggered in a 9.5 km² area at Sedgwick Ranch, 60 km north of Santa Barbara. Although Sedgwick Ranch has a range of vegetation communities, including pine forest, the landslides were limited to hillslopes vegetated by coastal sage scrub (Fig. 2A) or exotic grasses (Fig. 2B). Whereas all the failures in the sage mobilized as debris flows, the failures in the grass took a variety of different forms, including debris flows, disintegrating soil slips (Kesseli, 1943), and slumps (*sensu* Kesseli, 1943).

Shallow landslides, or *soil slips* (Kesseli, 1943; Corbett and Rice, 1966), are characterized by a failure surface at the soil-bedrock contact and typically occur in bedrock hollows, which are unchannelized swales on hillslopes (e.g., Reneau et al., 1990). Hollows accumulate sediment transported from adjacent slopes for hundreds to thousands of years (e.g., Campbell, 1975; Reneau et al., 1990), and as the soil in a hollow thickens over time, it becomes increasingly prone to failure during heavy rainfall (Rice et al., 1969). After failure, the hollow begins filling up again, and the cycle repeats itself (Dietrich and Dunne, 1978). Land-management strategies may amplify the susceptibility of hillslopes to landsliding. In the Pacific Northwest, for example, increased shallow landsliding has been attributed to logging that has decreased the contribution of tree roots to slope stability (Montgomery et al., 2000). In drier regions of the American West, hillslopes are cleared of brush and converted to grasslands primarily to increase forage for livestock (Rice and Foggin, 1971) and, secondarily, to reduce fire hazards and increase water yields (Hibbert, 1971). As in the logged forests, this management strategy has decreased soil reinforcement by roots (Terwilliger and Waldron, 1991) and increased landsliding in converted areas of southern California (Corbett and Rice, 1966; Bailey and Rice, 1969; Rice et al., 1969; Rice and Foggin, 1971).

Understanding the effect of vegetation conversion on landslide frequency in southern California and similar areas is critical because studies by Rice and Foggin (1971) and Scott (1971) suggest that shallow

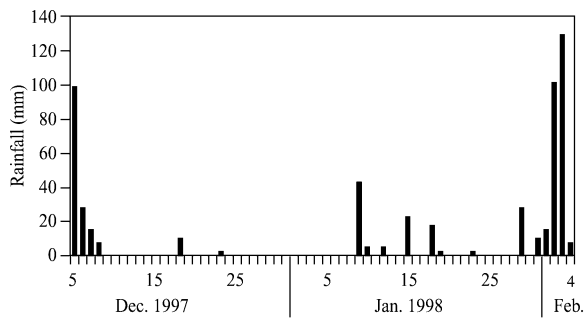


Figure 1. Daily rainfall totals from Figueroa Mountain Ranger Station (elev. 976 m), 3 km northeast of Sedgwick Ranch (elev. 480 m). The difference in elevations suggests that the totals would have been less at Sedgwick Ranch. The landsliding occurred on the night between February 3 and 4, 1998. Data provided by NOAA (National Oceanic and Atmospheric Administration).

landslides may be responsible for the majority of sediment issuing from small watersheds. Increased rates of sediment delivery from hillslopes may affect a number of important concerns such as water quality and the infilling of reservoirs constructed for water storage and flood control (Lustig, 1965; Rice and Foggin, 1971). Additionally, the proliferation of housing developments on alluvial fans exacerbates the danger from debris flows (Campbell, 1975) and flooding (Scott, 1971), which are both linked to landsliding (Rice and Foggin, 1971). Finally, examining the effects of human-induced vegetation change on sediment production may provide insights into the effects of climatically driven vegetation change.

We studied the landslides triggered by the 1997–1998 El Niño to gain a better understanding of shallow landsliding in this environment and the role of vegetation conversion in affecting the rates and mechanics of this process. We are motivated by three questions. First, how does root reinforcement influence the volume of a failure? Second, how do the landscape-scale sediment fluxes to valley floors compare between hillslopes covered by sage and those converted to grass? Third, what are some of the long-term geomorphic consequences of vegetation conversion to hillslope processes?

FIELD SITE

Sedgwick Ranch, a reserve in the University of California Natural Reserve System, is located on the northern margin of the Santa Ynez Valley, in the western Transverse Ranges. The ranch is bisected by the Little Pine fault, which separates Pleistocene fanglomerates of the Paso Robles Formation on one side from serpentinites and graywackes of the Franciscan Formation on the other (Dibblee, 1993). The landslides triggered in 1998 occurred where the Paso Robles Formation has been incised by small streams to produce gentle to moderately steep, rolling hillslopes with an average relief of 60–100 m. Hillslope gradients are controlled by the bedrock; weakly consolidated mudstone underlies most of this area and supports slopes up to 32°. Steeper hillslopes (32°–45°) are supported by interbeds of cemented conglomerate. Soil textures range from sandy loams to silty clays.

The semiarid Mediterranean climate averages 50 cm of annual rainfall. Many hillslopes at Sedgwick Ranch are currently vegetated by exotic, annual grasses (various species of *Bromus* and *Avena*), although grass is not found on slopes steeper than 35° where coastal sage scrub still dominates (mainly *Artemisia californica* and *Salvia leucophylla*). The spatial distribution of the two vegetation types is distinct; only a narrow range of overlap (<10 m) exists where they abut. The history of vegetation conversion at Sedgwick Ranch is not known, but the earliest aerial photographs indicate that the present distribution of vegetation was established before the 1930s. Hamilton (1997) proposed that most nonnative grasslands in the region were formerly dominated by coastal sage scrub, and there is substantial evidence indicating that sage was the original vegetation on the grassland slopes at Sedgwick Ranch. On some hillslopes, the boundary between the grasslands and the sage is sharp, and they grow side by side, separated only by a fence. Additionally, in many cases, grass grows on the lower part of the slopes where gradients are more gentle, whereas the steeper, upper parts are dominated by sage. This distribution suggests that the gentler slopes were manually cleared, whereas the steeper ones were left undisturbed (Campbell, 1975). Finally, remnants of roots with diameters of 5–10 mm have been found in soil pits excavated on the grass slopes, an indication that these slopes were once covered by shrubs rather than native bunch grasses. Clearing slopes of coastal sage mechanically or by prescribed burn continues to be a common practice in the region.

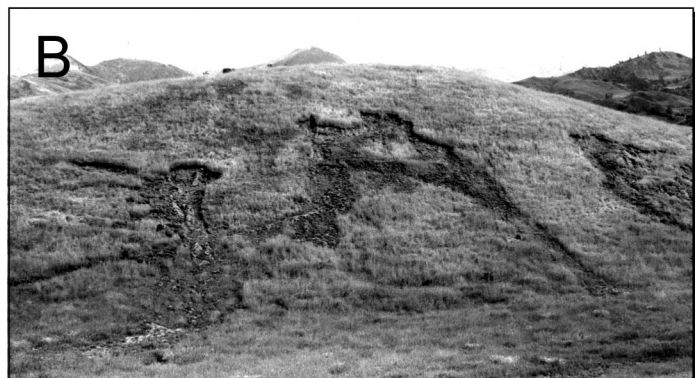
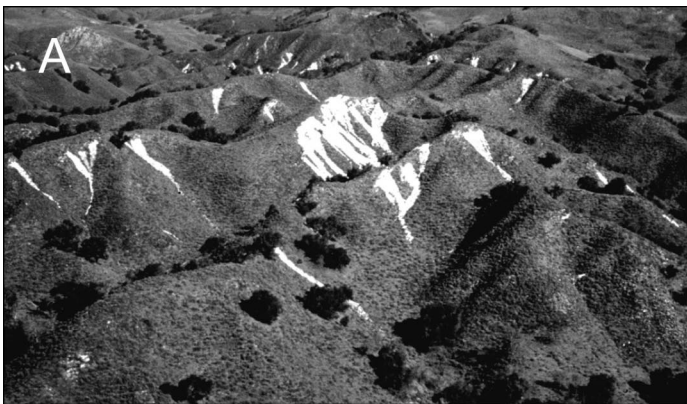


Figure 2. (A) Shallow landslides (white areas) in the sage. Note that the failures originated in hillslope concavities (hollows). (B) Landslides in the converted grasslands triggered on flat and convex parts of the hillslope.

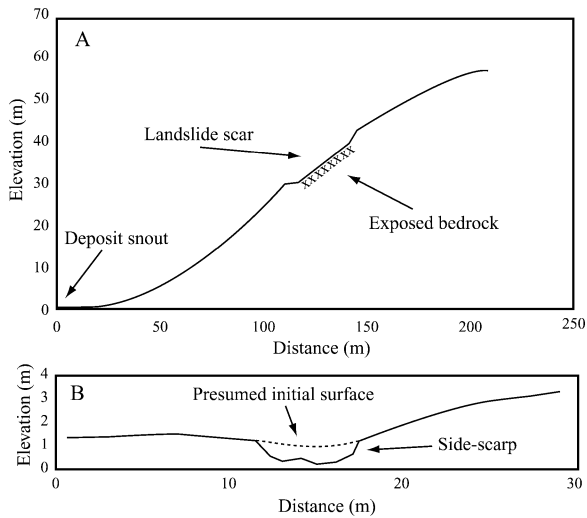


Figure 3. (A) Longitudinal profile of hillslope with landslide scar. (B) Cross section of scar shown in longitudinal profile. The initial surface was reconstructed from the adjacent topography. (Both figures have 2× vertical exaggeration.)

METHODS

Mapping

Two months after the landsliding occurred, stereo color aerial photographs at 1:21 000 scale were taken of the field site. These were used to identify and map the landslides onto the U.S. Geological Survey Los Olivos 7.5' topographic map. Smaller slides that were difficult to see on the photographs were mapped in the field.

A vegetation map was created from the aerial photographs to determine the area covered by each vegetation type. Because we were specifically interested in landsliding, only hillslopes steeper than 15°, the lowest slope observed with a failure, were included in the area calculations.

Surveying

A subset of 31 landslides was randomly chosen to sample the range of failure sizes and hillslope gradients. These were surveyed with a tape, stadia rod, and level. A longitudinal profile of each failure was surveyed from the hillslope divide, down the failure scar, to the snout of the deposit (Fig. 3A). During the longitudinal survey, the location of the center of mass of each deposit was visually estimated to determine transport distance. Three to five cross sections were surveyed across each failure, and the initial surface was reconstructed from the surrounding topography (Fig. 3B) to estimate volumes of sediment evacuated. Data from these surveys are presented in Table 1.

A Tesco variably loaded shear vane was used to measure, in situ, the internal angle of friction and cohesion of soils at the landslide sites. The blades of the vane only penetrate to a depth of 0.5 cm so that the effect of roots on the measurements is minimized.

LANDSLIDE VOLUMES

The volume of individual failures is an important factor in sediment delivery, and the debris flows in the sage were generally larger than

TABLE 1. LANDSLIDES CHARACTERISTICS

Site	Scar angle (°)	Area (m ²)	Volume (m ³)	Depth (m)	Width (m)	Length (m)	Length Width	Run-out distance (m)	Snout angle (°)	C.O.M. distance* (m)
Slumps on grass slopes										
1	31	26			4.8	6.6	0.7			
2	29	26			5.9	5.2	1.1			
3	27	63			7.6	8.0	1.0			
4	23	99			10.0	10.1	1.0			
5	17	142			13.4	11.0	1.2			
6	26	142			11.0	12.9	0.9			
Avg	26	83			9	8.8	1.1			
1σ	5	53			2.9	3.3	0.2			
Disintegrating soil slips on grass slopes										
1	23	204	62	0.30	11.0	41.0	3.7	36	25	30
2	23	154	40	0.26	6.9	26.1	3.8	56	22	63
3	23	389	131	0.34	14.0	39.7	2.8	196	5	190
Avg	23	249	78	0.30	10.6	35.6	3.4	96	17	94
1σ	0	123	48	0.04	3.6	8.3	0.6	87	11	85
Debris flows on grass slopes										
1	29	114	84	0.74	5.4	25.6	4.7	36	20	22
4	29	32	11	0.34	2.8	12.7	4.5	27	6	13
6	30	64	33	0.52	6.9	9.4	1.4	130	3	95
9	30	92	50	0.54	6.1	14.4	2.4	66	8	54
15	25	65	28	0.43	6.1	10.7	1.8	48	20	12
19	27	52	23	0.44	4.6	12.5	2.7	C	C	C
20	32	15	6	0.37	3.4	4.4	1.3	C	C	C
Avg	29	62	33	0.48	5.0	12.8	2.7	61	11	39
1σ	2	34	27	0.13	1.5	6.5	1.4	41	8	35
Debris flows on sage slopes										
3	32	257	160	0.62	12.2	20.7	1.7	132	7	27.4
5	32	173	89	0.51	17.0	11.6	0.7	74	7	26.1
7	43	35	13	0.37	3.2	10.8	3.4	26	18	20.4
8	34	110	70	0.64	7.3	15.1	2.1	C	C	C
10	32	216	114	0.53	8.8	24.7	2.8	63	10	43.5
11	35	103	72	0.70	8.8	12.5	1.4	C	C	C
12	35	145	75	0.52	7.2	22.0	3.1	C	C	C
13	37	117	52	0.44	8.3	14.6	1.8	C	C	C
14	35	108	46	0.43	4.4	24.8	5.6	C	C	C
16	35	206	145	0.70	8.2	25.3	3.1	86	20	42.8
17	45	41	11	0.27	3.0	13.7	4.6	7	30	10.1
23	39	111	45	0.41	6.2	22.3	3.6	73	3	55.5
24	39	96	44	0.46	5.8	15.8	2.7	C	C	C
25	40	248	91	0.37	9.2	27.1	3.0	C	C	C
26	34	106	64	0.60	7.7	13.3	1.7	39	0	27.7
Avg	37	138	73	0.5	7.1	18.3	2.7	54	13	36
1σ	4	68	43	0.13	3.5	5.7	1.2	31	12	18

Note: Avg—average, 1σ—1 standard deviation. The scars of the disintegrating soil slips appeared to have been the result of several failures coalescing. Depth, width, and length data are averages for each failure. Snout angle refers to the slope at which the snout was deposited. C indicates that a portion of the deposit was removed by channelized flow, and, therefore, the distance measurements could not be made. Soil depth, volume, and run-out distance are not given for slumps because they did not evacuate the scar.

*C.O.M. distance is the distance from the middle of the scar to the center of mass of the deposit.

those in the grass (Table 1). Although the size of the disintegrating soil slips in the grass was approximately equal to that of the debris flows in the sage, the disintegrating soil slips appeared to have been composed of several smaller failures. On the sage-covered slopes, a physical relationship between failure volume and hillslope angle is suggested by the inverse relationship between the two (Table 1) and is revealed by an examination of the various forces on a failing soil mass. The commonly used infinite-slope stability analysis for shallow landslides (Selby, 1993) can predict soil depths at failure (Dietrich et al., 1995), but because it assumes that the failing mass is infinitely long and wide, it cannot be used to determine failure length and width. This stability analysis only considers root cohesion in the vertical direction, and it is usually applied in forested regions where cohesive reinforcement occurs along the basal surface (e.g., Sidle, 1987). In environments where roots do not penetrate bedrock and fail to anchor the soil ver-

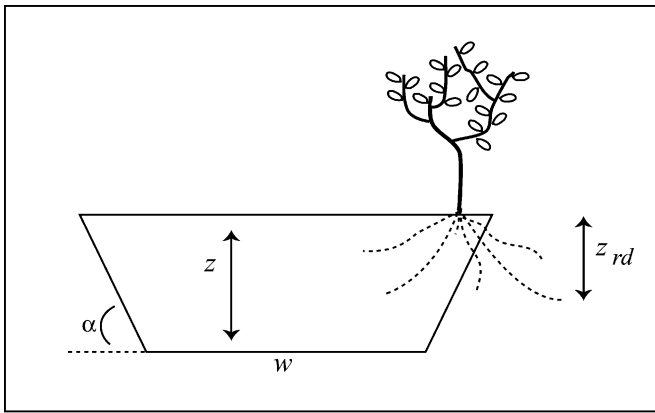


Figure 4. Illustration of the geometrical relationships pertaining to the cohesion terms in the stability analysis (compare with the cross section in Fig. 3B). Soil cohesion is applied to the perimeter of the failure: $W + 2z \cos \theta / \sin \alpha$. Root cohesion only acts over the perimeter to the extent of the rooting depth: $2z_{rd} \cos \theta / \sin \alpha$.

tically, root reinforcement is solely in the lateral direction. This distinction is critical because accounting for the lateral reinforcement of roots in a stability analysis requires modification of the infinite-slope model. The infinite-slope model only considers stresses and strengths on the basal slip surface, so it should not be used when lateral-root reinforcement is important.

Others have adapted the infinite-slope model to account for lateral-root contributions, and this approach has allowed for the examination of the relationship between failure dimensions and root cohesion. Reneau and Dietrich (1987) investigated the link between lateral-root cohesion and failure size by modifying the stability analysis derived by Reistenberg and Sovonick-Dunford (1983). However, their approach does not produce unique solutions for landslide dimensions. Terwilliger and Waldron (1991) presented a three-dimensional analysis to study the effects of root-cohesion distributions on failure size. Their analysis considers many important details of slope stability, such as the mechanical behavior of roots during the initial moments of failure.

In contrast to Terwilliger and Waldron (1991), we derive a simpler analysis with fewer data requirements to examine the relationship between hillslope angle and failure volume at Sedgwick Ranch. Instead of the infinite-slope model, which assumes that the forces on the sides of the failure are negligible, we present a force balance that considers the forces on a slice of hillslope taken parallel to the contour lines and that accounts for reinforcement along the side scarps of the failures (Fig. 4). To include the forces along the edges of the failure mass, the stability analysis presented here is derived so that the terms represent forces per unit length of slope, rather than forces per unit area of slope. We assume, therefore, a landslide that is infinitely long but with a finite width.

Shallow-landslide stability analyses are typically idealized as a block on an inclined plane (e.g., Selby, 1993), and the ratio of the resisting forces to the disturbing forces defines the factor of safety (f) so that the block is stable when $f > 1$. The forces per unit length can be resolved by assuming that the block is sufficiently long relative to the width so that the difference between the forces on the uphill and downhill ends of the block is negligible (e.g., Selby, 1993). The disturbing force is the downslope component of the weight of the block:

$$\frac{F_s}{l} = wz\gamma_s \cos \theta \sin \theta, \tag{1}$$

where

- F_s = shear force (kN)
- l = failure length (m)
- w = failure width (m)
- z = soil depth measured vertically (m)
- γ_s = unit weight of wet soil (kN m^{-3})
- θ = hillslope angle ($^\circ$)

The resisting force includes the effective normal component of the weight of the block mediated by the internal angle of friction (ϕ) (Selby, 1993),

$$\frac{F_f}{l} = wz(\gamma_s - m\gamma_w) \cos^2 \theta \tan \phi, \tag{2}$$

where

- F_f = frictional resistance (kN)
- m = fraction of the soil column that is saturated
- γ_w = unit weight of water (kN m^{-3}).

In addition to friction, soil strength is provided by soil cohesion and lateral-root reinforcement. Soil cohesion acts over the entire perimeter of the failure surface, whereas root reinforcement acts over the perimeter only to the extent of the rooting depth (Fig. 4) so that

$$R_s = C_s \left(w + \frac{2z \cos \theta}{\sin \alpha} \right) \text{ and} \tag{3a}$$

$$R_r = C_{rl} \left(\frac{2z_{rd} \cos \theta}{\sin \alpha} \right), \tag{3b}$$

where

- C_{rl} = lateral root cohesion (kPa)
- C_s = soil cohesion (kPa)
- R_r = total reinforcement by roots (kN m^{-1})
- R_s = total reinforcement from soil cohesion (kN m^{-1})
- z_{rd} = rooting depth measured vertically (m)
- α = angle of side-scarp ($^\circ$).

Lateral earth forces were calculated (Craig, 1978) and found to account for only 10% of the total resistance, so we consider them negligible given the uncertainty in the other terms. The resisting force is the sum of the frictional and cohesive forces (e.g., Craig, 1978), so the factor of safety is then

$$f = \frac{C_s \left(w + \frac{2z \cos \theta}{\sin \alpha} \right) + C_{rl} \left(\frac{2z_{rd} \cos \theta}{\sin \alpha} \right) + wz(\gamma_s - m\gamma_w) \cos^2 \theta \tan \phi}{wz\gamma_s \cos \theta \sin \theta}. \tag{4}$$

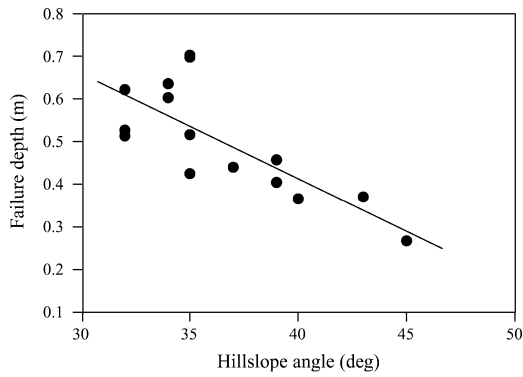


Figure 5. Average failure depth (z) vs. hillslope angle (θ). The line is the least-squares linear regression ($r^2 = 0.58$).

Again, because roots did not penetrate bedrock in any of the surveyed landslides at Sedgwick Ranch, we have not included a vertical root-anchoring term. Equation 4 can be solved for the failure width (i.e., $f = 1$) at different slope angles,

$$w = \frac{C_s \left(\frac{2z \cos \theta}{\sin \alpha} \right) + C_{ri} \left(\frac{2z_{rd} \cos \theta}{\sin \alpha} \right)}{z \cos \theta [\gamma_s \sin \theta - (\gamma_s - m\gamma_w) \cos \theta \tan \phi] - C_s}. \quad (5)$$

To demonstrate the dependence of failure width on hillslope angle and to compare the results to the field data, equation 5 is parameterized to reflect the average conditions on sage-covered slopes at Sedgwick Ranch. An average failure depth for each landslide was determined by dividing the failure volume by the planform area. For failures in the sage, Figure 5 shows a monotonic decline in average failure depth with slope ($r^2 = 0.58$, $n = 15$, $p < 0.005$),

$$z = 1.41 - 0.025\theta, \quad (6)$$

so that z in equation 5 can be calculated as a function of slope angle.

We set the rooting depth (z_{rd}) equal to the soil depth (z) at all gradients because, although we have observed long roots in the sage (>1 m), they were unable to penetrate the bedrock and were limited to growing along the soil-bedrock contact. Terwilliger and Waldron (1990) measured the root-cohesion contributions of chaparral and grass with direct shear tests and determined a root cohesion value of 3 kPa for chaparral. The soils that Terwilliger and Waldron (1990) sampled were primarily vegetated by chamise (*Adenostoma fasciculatum*), which grows taller than the coastal sage vegetation studied here. However, chamise roots are relatively thin (Hellmers et al., 1955), suggesting that using the root-cohesion values measured by Terwilliger and Waldron (1990) in the chamise may be appropriate for the sage.

There are two other important caveats to our root-cohesion representation. First, we assume that root cohesion does not change with depth, whereas Hellmers et al. (1955) noted that the highest concentrations of sage roots are near the soil surface. However, given the uncertainty in the root-cohesion values, we consider a uniform vertical root-cohesion distribution to be adequate, and this assumption is supported by data from Terwilliger and Waldron (1991). Second, the lateral distribution of root cohesion is also assumed to be uniform. Whereas Terwilliger and Waldron (1991) explicitly represented the lateral heterogeneity of chaparral root cohesion in their stability analysis,

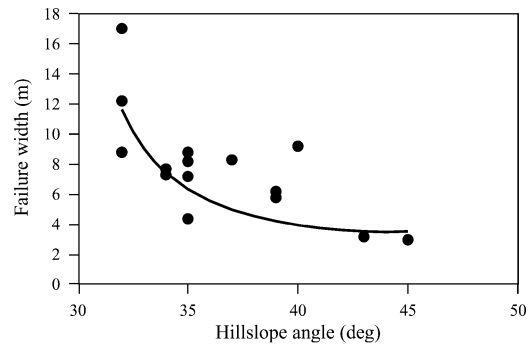


Figure 6. Comparison of predicted failure widths (line) and surveyed widths (points) as a function of hillslope angle for shallow landslides in the sage ($r^2 = 0.37$). Predicted widths were determined with Equation 5 and suggest that root cohesion exerts a dominant control on failure widths when lateral-root reinforcement is significant.

the dense cover of coastal sage scrub at Sedgwick Ranch suggests that the assumption of a laterally homogeneous root-cohesion distribution may be suitable.

Average values from Sedgwick Ranch for the side scarp angle and the unit weight of wet soil are 45° and $17.7 \text{ kN}\cdot\text{m}^{-3}$, respectively, and the unit weight of water is $9.81 \text{ kN}\cdot\text{m}^{-3}$. The angle of internal friction, 32° , is an average determined from 10 sites measured in situ at Sedgwick Ranch with a variably loaded shear vane. Unfortunately, the soil-cohesion values measured with the shear vane are unreliable because of the sensitivity of soil cohesion to water content (Selby, 1993). Ideally, these tests would be done on saturated soils to replicate the conditions at failure; however, they were done when the soils were damp. Consequently, there are no measured constraints on the parameter C_s . We are also unable to set constraints on m , a hydrological variable that depends on rainfall amounts and site-specific topography. These two variables, therefore, are used to fit equation 5 to the data. Thus, rather than trying to accurately reproduce the conditions at failure with incomplete data, we seek to explain the observed trend in failure volumes.

Various combinations of realistic values for C_s and m provide reasonable matches between equation 5 and the surveyed failure widths. In Figure 6, the field data for the failures in the sage are compared to the predicted failure widths with values of 0.7 kPa and 0.5 for C_s and m , respectively. Alternatively, the decrease in failure widths with increasing slope might also be explained otherwise. Bedrock hollows are generally narrower on steep slopes, and the width of the hollow sets an upper limit on the width of the failure contained within it. Of course, the width of the hollows themselves may be a long-term consequence of narrower failures on steeper slopes.

Landslide volumes on the sage-covered hillslopes can be calculated as a function of slope as the product of the widths predicted in Figure 6, the lengths determined from the average length/width ratio (2.7; Table 1), and the slope-dependent soil depths (equation 6). Figure 7 demonstrates that the stability analysis derived here may be used in conjunction with field data to predict landslide volumes. This finding may have important applications and could be integrated into topographically based models for shallow-landslide hazards (e.g., Dietrich et al., 1995), wherever the soil-depth function and the length/width relationships are defined from local data. Finally, the steep increase in failure widths as slopes become more gentle (Fig. 6) suggests that there

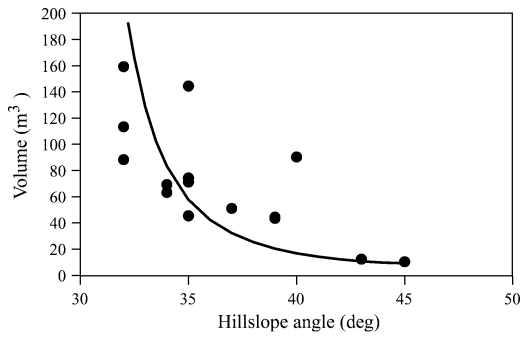


Figure 7. Comparison of predicted volumes (line) and surveyed volumes (points) as a function of hillslope angle for shallow landslides in the sage. Predicted volumes are calculated as the product of the slope-dependent soil depths (equation 6), the widths predicted in Figure 6, and the lengths determined from the average length/width ratio (Table 1). The predicted volumes are similar to the surveyed volumes ($r^2 = 0.46$; $r^2 = 0.53$ without the outlier at 40°).

TABLE 2. PARAMETER VALUES

C_{ri} (grass)*	1 kPa
C_s	0.7 kPa
w^{\dagger}	5 m
z^{\dagger}	0.48 m
z_{rd}^{\dagger}	0.15 m
α^{\dagger}	45°
ϕ^{\dagger}	32°

*Terwilliger and Waldron (1991).

[†]Average value from field data.

is a minimum angle at which slopes will fail in the sage-covered areas; indeed, there were no observed failures in the sage at slopes of $<32^\circ$.

On the grass-covered hillslopes, there is no apparent trend in the volumes of failures with slope (Table 1), possibly owing to the relatively weaker contribution of grass roots to the total soil strength. This relationship can be appreciated analytically if

$$R_s \gg R_r \tag{7a}$$

and

$$w \gg z. \tag{7b}$$

With the data presented in Table 2, values for the reinforcement from soil cohesion (R_s) and apparent root cohesion (R_r) are $4.3 \text{ kN}\cdot\text{m}^{-1}$ and $0.4 \text{ kN}\cdot\text{m}^{-1}$, respectively; furthermore, failure widths (w) are generally an order of magnitude greater than failure depths (z ; Table 1). With the conditions in equations 7a and 7b satisfied for grassland failures, equation 4 then becomes the familiar infinite-slope stability analysis (e.g., Selby, 1993),

$$f = \frac{C_s + z(\gamma_s - m\gamma_w)\cos^2\theta \tan \phi}{z\gamma_s \cos \theta \sin \theta}, \tag{8}$$

The width variable in equation 4 cancels out in equation 8, implying that the forces involved are no longer width dependent. For this reason, the widths of the failures on the grass slopes may be determined by factors not represented in a simple force balance.

Because the grasslands at Sedgwick Ranch are on gentler slopes, it is difficult to separate the effects of slope and vegetation on landslide volume; nonetheless, the data suggest that failures in the grasslands are smaller than those in the sage. Additionally, Rice and Foggin (1971) found that failures in converted grasslands are typically smaller than those in the brush for similar slope angles. However, this observation may not be always true; for example, Rice et al. (1969) reported larger landslides on grasslands than on brush-covered slopes.

SEDIMENT TRANSPORT

Debris-Flow Deposits

With landslide volume, the distance traveled by the failed soil mass is also an important variable in determining the magnitude of the sediment flux. Many of the lower-order valleys at Sedgwick Ranch are unchanneled, so the deposits of 13 of the 22 debris flows are intact, thus allowing measurement of transport distances. Most deposits were clearly defined and had lobate snouts 0.1–0.5 m high. In many cases, there was evidence that some fine-grained material continued farther, probably as the mass drained, but this material represents $<1\%$ of the whole failure. The runout distances of the deposits (Table 1) reflect the strong control that hillslope length has on transport distance. Most failures stopped when the snout reached the valley floor, with the tail of the deposit sometimes resting at steeper slopes. This configuration suggests that once the snout stopped, the rest of the mass was unable to flow around it and subsequently drained, solidifying in place. The center of mass of the deposit was generally located about two-thirds of the way along the total runout distance, indicating that the sediment was distributed along the length of the runout.

The snouts of the majority of the deposits stopped on slopes at or $<10^\circ$ (Table 1), similar to values compiled by Whipple (1994). The sage-scrub vegetation, however, arrested the soil mass of the smaller failures on relatively steep slopes (Table 1). On the grass slopes, the degree of liquefaction rather than the landslide volume seemed to have determined the depositional slope. The more fluidized failures stopped on the gentler slopes, whereas the more block-like failures stopped on steeper slopes.

Sediment Flux

The specific volumetric flux (q_s) is the rate at which a volume of soil is transported across a unit contour width of hillslope. In the following analysis, we only consider the failures with significant amounts of displacement—i.e., the disintegrating soil slips and the debris flows—and will hereafter refer to them as “mobilized failures.” Also, because we are interested in sediment transport by landsliding, we do not consider fluvial transport of landslide sediment that reached the channels. By using the average center of mass transport distances (\bar{d} ; Table 1), the average volumes (\bar{V} ; Table 1), and a failure density (adjusted to include only the mobilized failures for the grass-covered slopes), a landscape-scale sediment flux for this El Niño event can be calculated with

$$q_s = \bar{d} \times \bar{V} \times f_{\text{failure}} \tag{9}$$

There are 2.92 km^2 of grass-covered hillslopes and 6.53 km^2 of sage-covered hillslopes at Sedgwick Ranch. There were a total of 67 failures in the grass and 86 in the sage, producing a failure density of 22.9 failures per square kilometer in the grassland and 13.2 failures per

square kilometer in the sage. Whereas all the sage failures converted to debris flows, debris flows accounted for only 56% of the grass failures; disintegrating soil slips and slumps accounted for 22% each. These data yield a flux of $1.7 \times 10^{-2} \text{ m}^3 \cdot \text{m}^{-1}$ per event for the grass slopes and $2.8 \times 10^{-2} \text{ m}^3 \cdot \text{m}^{-1}$ per event for the sage slopes. Long-term sediment fluxes cannot be estimated because the recurrence interval of events of this magnitude is not known for the region, but there is no indication of a widespread occurrence of shallow failures in aerial photographs of the area dating back to the 1930s. However, because the sage and grass grow back rapidly, evidence for recent widespread landsliding may be undetectable.

In contrast to the results found here, Rice et al. (1969) and Rice and Foggin (1971) concluded that landsliding in converted grasslands produced more sediment than landsliding in the native shrub vegetation. These studies (Rice et al., 1969; Rice and Foggin, 1971), however, compared sediment production from hillslopes of similar gradients with different vegetation covers, whereas our data are somewhat confounded by the unequal distribution of vegetation types across the range of hillslope gradients.

Despite the much higher failure density on the grass slopes at Sedgwick Ranch, the total sediment flux from these slides was less than those on the sage-covered slopes. Although the failures in the grass occurred on gentler slopes, other factors that influence both the size of the failures and the transport distance limited their sediment delivery to the valley floors. Terwilliger and Waldron (1991) suggested that spatially homogeneous root-cohesion distributions may explain smaller failures in grasslands. Additionally, weaker grass roots will allow a soil mass to fail with a lower degree of saturation, thereby reducing the potential for liquefaction and the transport of soil significant distances.

LONG-TERM EFFECTS OF VEGETATION CONVERSION

The replacement of the native sage by exotic grasses appears to have caused a pulse of landsliding on converted hillslopes at Sedgwick Ranch. Similar observations have been made by others in southern California (Corbett and Rice, 1966; Bailey and Rice, 1969; Rice et al., 1969; Rice and Foggin, 1971; Terwilliger and Waldron, 1991). Terwilliger and Waldron (1991) suggested that spatial differences in root-cohesion distributions between chaparral and grass may be responsible for a greater occurrence of landsliding on recently converted grassland slopes. Although this suggestion may be correct, we prefer a more fundamental explanation, initially mentioned by Rice and Foggin (1971). In general, slope stability depends on a balance between root reinforcement and soil depth, so that stronger roots allow soils to become deeper before they fail. Over time, maximum soil depths in bed-rock hollows will come into equilibrium with the prevailing root reinforcement. If the hillslopes have a permanent drop in root reinforcement, then the soils will be too thick for the new root conditions, and landsliding should increase. To demonstrate this effect, stable soil depths under sage or grass cover were calculated as a function of hillslope angle by means of equation 4. We parameterized equation 4 with the same values as for Figure 6 with one exception: The failure width was set at 5 m for all slope angles to facilitate the comparison of stable soil depths for a range of slope angles for both vegetation types. The values for the grass-root parameters, C_{ri} and z_{rd} , are shown in Table 2. Figure 8 demonstrates that there is a range of soil depths that are stable under sage but unstable under grass. The lowering of root reinforcement by vegetation conversion, therefore, may render a larger part of the landscape vulnerable to landsliding. The importance of root reinforcement in slope stability is further emphasized by the

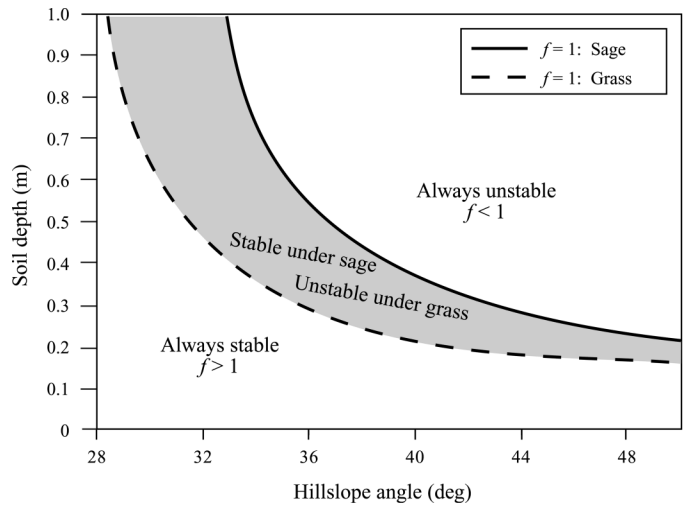


Figure 8. Stability analysis results for varying soil depths under sage or grass at different hillslope angles. The shaded area represents soil depths that are stable under sage but unstable under grass for identical soil-cohesion values and hydrological conditions. The “stability” line for the sage converges on the grass “stability” line because the root reinforcement in the sage is limited by the soil depth (i.e., $z_{rd} = z$). Failure depths do not decrease linearly with slope angle as in Figure 5 because failure width is assumed to be identical for all slopes.

observation that there were no failures in the pine forest at Sedgwick Ranch, despite topographic characteristics similar to the sage and grassland hillslopes that failed.

A disequilibrium between root reinforcement and soil depths at Sedgwick Ranch is supported by field observations. First, there were nearly twice as many failures in the grass as in the sage, despite the generally lower hillslope gradients. This finding suggests that the grass slopes are currently more susceptible to failure. Second, failure depths, and therefore soil depths, were similar between the sage failures and the grass failures (Table 1), suggesting that soil depths in the grasslands may be relict features from a time when root reinforcement was higher. Finally, there were some failures on planar hillslopes in the grass (Fig. 2B), whereas all the failures in the sage were in hollows. Typically, shallow landslides occur in hollows owing to the long-term accumulation of sediment that results in thicker soils and the convergence of subsurface flow that leads to higher pore pressures (e.g., Hack and Goodlett, 1960; Dietrich and Dunne, 1978). Landslides on planar slopes, therefore, may again be an indication of soils that are too deep for the present root cohesion.

After this initial pulse of landsliding wanes, the frequency of landsliding will adjust to the new root conditions. The landsliding frequency should depend on the rate of hollow filling by both in situ soil production and soil transport into the hollow (Dietrich et al., 1995), root reinforcement, and the climate. If climate and the rate of hollow filling remain constant, landslide frequency on the converted hillslopes will remain elevated relative to that on the sage-covered hillslopes (Fig. 9). This difference can be explained simply in terms of mass conservation whereby the input of sediment into the hollows is balanced by the output from landsliding. Because the sediment storage within the hollows is limited by the root reinforcement and the grass roots can support only a thinner mantle of soil, the frequency of landsliding must increase to maintain the same sediment output.

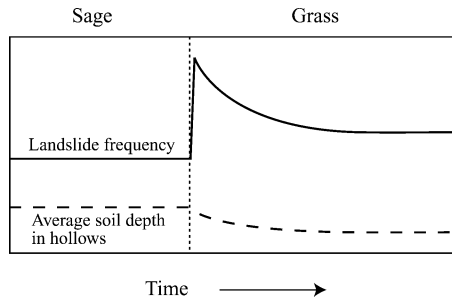


Figure 9. Transient and long-term effects of vegetation conversion from sage scrub to grass on soil depth in the bedrock hollows and the frequency of landsliding. The decline in root reinforcement triggers a pulse of landsliding throughout the landscape as the soils—which are initially thicker than grass can support—become more susceptible to failure. As soil depths in the grass-covered hollows reach a new equilibrium thickness, the frequency of landslides decreases from the peak rate but remains higher than in the sage-covered hollows if the rate of colluvium deepening remains constant under the change of vegetation.

CONCLUSIONS

The El Niño event of 1997–1998 brought record amounts of rainfall to the Santa Barbara region in California and triggered more than 150 shallow landslides at Sedgwick Ranch. The landslides were limited to coastal sage-scrub and converted grassland hillslopes, thus giving us the opportunity to study the mechanics of shallow landslides and to quantify the effects of vegetation conversion on sediment delivery to valley floors by landsliding. We present a slope-stability analysis that accounts for lateral-root reinforcement and accurately predicts an inverse relationship between hillslope angle and landslide volume in the sage. Field surveys indicate that volumes of failures in the grassland are not slope dependent and are generally smaller than those in the sage. To compare the sediment delivery from sage and converted grassland slopes, landscape-scale sediment fluxes were calculated for both. Although the spatial landslide frequency was higher in the grasslands, this factor was compensated by smaller volumes and shorter transport distances so that the failures on the sage hillslopes delivered more sediment to the valley floors. We suggest that the greater frequency of failures in the grasslands is due to a disequilibrium between soil depths and the ability of the grass roots to reinforce the soil. Over time, the soil in the grassland hollows will attain a shallower equilibrium depth.

ACKNOWLEDGMENTS

We thank J. Gabet and B. Newton for help with surveying and field observations and W. Dietrich for discussions. T. Biggs is thanked for reviewing an earlier draft of the manuscript. D. Montgomery and K. Schmidt are gratefully acknowledged for their helpful reviews. Supplies and salary for E. Gabet were supported by University of California Water Resources grant UCAL-W-917, a Sigma Xi grant, and a Mildred Mathias grant. Aerial photographs were paid for with funds from National Science Foundation grant SGER DEB9813669.

REFERENCES CITED

- Bailey, R.G., and Rice, R.M., 1969, Soil slippage: An indicator of slope instability on chaparral watersheds of southern California: *Professional Geographer*, v. 21, no. 3, p. 172–177.
- Campbell, R.H., 1975, Soil slips, debris flows, and rainstorms in the Santa Monica Mountains and vicinity, southern California: U.S. Geological Survey Professional Paper 851, 51 p.
- Corbett, E.S., and Rice, R.M., 1966, Soil slippage increased by brush conversion: Berkeley, California, U.S. Forest Service Pacific Southwest Forest and Range Experiment Station Research Note, PSW-128, p. 1–8.
- Craig, R.F., 1978, *Soil mechanics*: New York, Van Nostrand Reinhold Company Ltd., 318 p.
- Dibblee, T.W.J., 1993, Geologic map of the Figueroa Mountain Quadrangle: Santa Barbara, California, Dibblee Geological Foundation, scale 1:24,000.
- Dietrich, W.E., and Dunne, T., 1978, Sediment budget for a small catchment in mountainous terrain: *Zeitschrift für Geomorphologie*, suppl. band 29, p. 191–206.
- Dietrich, W.E., Reiss, R., Hsu, M.L., and Montgomery, D.R., 1995, A process-based model for colluvial soil depth and shallow landsliding using digital elevation data: *Hydrological Processes*, v. 9, p. 383–400.
- Hack, J.T., and Goodlett, J.C., 1960, Geomorphology and forest ecology of a mountain region in the Central Appalachians: U.S. Geological Survey Professional Paper 347, 66 p.
- Hamilton, J.G., 1997, Changing perceptions of pre-European grasslands in California: *Madrone*, v. 44, no. 4, p. 311–333.
- Hellmers, H., Horton, J.S., Juhren, G., and O'Keefe, J., 1955, Root systems of some chaparral plants in southern California: *Ecology*, v. 36, p. 667–678.
- Hibbert, A.R., 1971, Increases in streamflow after converting chaparral to grass: *Water Resources Research*, v. 7, p. 71–80.
- Kesseli, J.E., 1943, Disintegrating soil slips of the coast ranges of central California: *Journal of Geology*, v. 11, p. 342–352.
- Lustig, L.K., 1965, Sediment yield of the Castaic watershed, western Los Angeles County, California—A quantitative geomorphic approach: U.S. Geological Survey Professional Paper 422-F, 23 p.
- Montgomery, D.R., Schmidt, K.M., Greenberg, H.M., and Dietrich, W.E., 2000, Forest clearing and regional landsliding: *Geology*, v. 28, p. 311–314.
- Reistenberg, M.M., and Sovonick-Dunford, S., 1983, The role of woody vegetation in stabilizing slopes in the Cincinnati area, Ohio: *Geological Society of America Bulletin*, v. 94, p. 506–518.
- Reneau, S.L., and Dietrich, W.E., 1987, Size and location of colluvial landslides in a steep forested landscape, in Beschta, R.L., Blinn, T., Grant, C.E., Ice, G.G., and Swanson, F.J., eds., *Erosion and sedimentation in the Pacific Rim*: Wallingford, UK, International Association of Hydrological Sciences Press, p. 39–48.
- Reneau, S., Dietrich, W.E., Donahue, D.J., Hull, A.J., and Rubin, M., 1990, Late Quaternary history of colluvial deposition and erosion in hollows, central California coast ranges: *Geological Society of America Bulletin*, v. 102, p. 969–982.
- Rice, R.M., and Foggini, G.T.B., 1971, Effect of high intensity storms on soil slippage on mountainous watersheds in southern California: *Water Resources Research*, v. 7, p. 1485–1496.
- Rice, R.M., Corbett, E.S., and Bailey, R.G., 1969, Soil slips related to vegetation, topography, and soil in southern California: *Water Resources Research*, v. 5, p. 647–659.
- Scott, K.M., 1971, Origin and sedimentology of 1969 debris flows near Glendora, California: U.S. Geological Survey Professional Paper 750-C, 6 p.
- Selby, M.J., 1993, *Hillslope materials and processes*: Oxford, Oxford University Press, 451 p.
- Sidle, R.C., 1987, A dynamic model of slope stability in zero-order basins, in Beschta, R.L., Blinn, T., Grant, C.E., Ice, G.G., and Swanson, F.J., eds., *Erosion and sedimentation in the Pacific Rim*: Wallingford, UK, International Association of Hydrological Sciences Press, p. 101–110.
- Terwilliger, V.J., and Waldron, L.J., 1990, Assessing the contribution of roots to the strength of undisturbed, slip prone soils: *Catena*, v. 17, p. 151–162.
- Terwilliger, V.J., and Waldron, L.J., 1991, Effects of root reinforcement on soil-slip patterns in the Transverse Ranges of southern California: *Geological Society of America Bulletin*, v. 103, p. 775–785.
- Whipple, K.X., 1994, *Debris-flow fans: Process and form* [Ph.D. thesis]: Seattle, University of Washington, 205 p.

MANUSCRIPT RECEIVED BY THE SOCIETY SEPTEMBER 17, 2001

REVISED MANUSCRIPT RECEIVED FEBRUARY 4, 2002

MANUSCRIPT ACCEPTED MARCH 4, 2002

Printed in the USA